Photoabsorption and photodissociation in molecular nitrogen

Alan N. Heays

A thesis submitted for the degree of
Doctor of Philosophy of
The Australian National University

November, 2010

Declaration

This thesis is an account of research undertaken between February 2006 and November 2010 at The Research School of Physics and Engineering, The Australian National University, Canberra, Australia.

Except where acknowledged in the customary manner, the material presented in this thesis is, to the best of my knowledge, original and has not been submitted in whole or part for a degree in any university.

Alan N. Heays
November, 2010

Abstract

The photoabsorption and photodissociation of molecular nitrogen at extreme-ultraviolet wavelengths has been precisely modelled by solution of the coupled Schrödinger equation, for the purposes of elucidating the spectroscopy and predissociation dynamics of N_2 and for practical application to its photochemistry. The physically realistic model is capable of reliable extrapolation beyond the database of spectroscopic information necessary for its construction, to energies in the range of 100 000 to 118 000 cm^{-1} and, with some caveats, beyond this; and for any temperature, rotational state, and isotopomer of N_2. The model simulated spectra have an effectively-infinite resolution, and reproduce the rotational level energies of all electric-dipole-allowed $^1\Pi_u$ and $^1\Sigma_u^+$ states, and their absorption f-values, to spectroscopic accuracy over its entire range. The predissociated lineshapes of calculated transitions are accurately reproduced, as is the background continuum, even where a dissociation limit is crossed.

The highly perturbed spectrum is shown to arise from multi-channel effects which can only be reproduced by a coupled treatment which includes the effects of homogeneous and heterogeneous interactions. Unbound dissociative states are permitted in the model formulation and a complex of $^3\Pi_u$ and $^3\Sigma_u^+$ states is shown to be responsible for the predissociation of singlet levels via spin-orbit interaction. The spectroscopic parameters of triplet states, and the variation of $^1\Pi_u$ predissociation rates over multiple orders of magnitude has been accurately modelled for all isotopomers and energies up to 111 000 cm^{-1}. The transformation of the calculated dissociative wavefunctions into a basis of asymptotically well-defined atomic states allows for the calculation of their predissociation branching ratios. New and accurate determinations have been made of potential-energy curves for the coupled states, the off-diagonal matrix elements that mix them, and the electronic transition moments responsible for their optical excitation, including, in some cases, their dependence on internuclear distance.

New supporting laboratory measurements of rotationally-resolved absolute f-values and predissociation linewidths have been made for many transitions, some of which have not been previously observed. These various experiments employ synchrotron and laser radiation as well as electron-impact excitation, and make detections by means of a grating spectrometer, Fourier-transform spectrometer, and the detection of photofragments. Analysis of these studies is facilitated by the coupled-channels modelling, which is then informed by the resulting new data.

The characteristics of the coupled-channels model are an ideal match to the immediate need for N_2 spectra by photochemical modellers of planetary atmospheres, because of its realistic extensibility to variable real-world conditions. An application of the model to the atmosphere of Titan is presented here, which explains the unusual observed ratio of nitrogen isotopes in terms of the details of N_2 photoabsorption. Another use of modelled spectra is presented here, for the analysis of the terrestrial dayglow. The applicability of the coupled-channels model is quite broad and further investigations which utilise it are underway.

Acknowledgements

Many thanks to the excellent supervisory powers of Prof. Brenton Lewis, the consummate spectroscopist, and Dr. Stephen Gibson. Further thanks to my friends and family in and out of Canberra for awesome friendliness and familiarity. Additional thanks to the various collaborators on the N_2 project, particularly Prof. Glenn Stark, for many interesting opportunities and an excess of raw data. Yet more thanks, to the works of Herzberg [54], Lefebvre-Brion and Field [90], and all the rest.

Contents

List of Figures

List of Tables

Chapter 1

Introduction

There are two aims prompting the study presented in this thesis. First, the nitrogen molecule is a fascinating problem in molecular spectroscopy, and many of its physical properties remain unexplained despite being an object of study for many decades. A resurgence of interest has led to many new experimental and theoretical investigations, referenced below, and this thesis seeks to decipher much of this new knowledge into a new picture of the molecule's quantum states, including an understanding of the phenomenon of predissociation. A second motivation for this work was originally proposed by members of the Harvard Center for Astrophysics, who identified the complete lack of a realistic model of N_2 photodissociation, despite the significance of this process to a number of real world photochemical applications. Pursuit of these two goals has been, fortuitously, mutually beneficial. The development of a quantitative model has necessitated a detailed study of the molecules fundamental properties, but also made such a study possible.

The large, and growing, quantity of high resolution data that has been collected in absorption [14, 17, 18, 155, 189], emission [130, 132, 133, 134, 135], ionisation [104, 147, 148, 149, 150, 151, 152, 179], and dissociation [52, 181, 182] experiments has, until now, not been integrated with the maturing theoretical interpretation of the excited states of N_2 [12, 13, 30, 49, 89, 104, 145, 153]. The assignment of logical progressions of electric-dipole-allowed bands excited from the ground state and appearing in the extreme-ultraviolet (XUV) has long been hindered by large perturbations between electronic states. The magnitude of these interactions makes it abundantly clear that any attempt to understand the XUV spectrum of N_2, even qualitatively, in terms of simple Born-Oppenheimer electronic states is completely futile.

More recent experiments have made progress on an additional aspect of the N_2 spectrum. Diffuse absorption lines and missing emission bands have betrayed the existence of a haphazardly variable tendency of N_2 excited by XUV radiation to predissociate [13, 23, 52, 53, 55, 73, 103, 131, 147, 148, 149, 150, 151, 152, 155, 173, 179, 181, 182, 183, 191]. The mechanism responsible has been gradually resolved theoretically [13, 30, 49, 53, 93, 103, 104] and is due to the interplay of several triplet states, invisible to electric-dipole excitation, and some of which are unbound. These are perturbed by one another and, critically, coupled to the co-energetic singlet states by spin-orbit interaction. Thus, the accidental predissociation that complicates the N_2 spectrum requires an accurate understanding of many singlet states, further triplet states, and a multitude of perturbing interactions.

Chapters 2 and 3 describe the theoretical underpinnings of the quantum-mechanical study of diatomic molecules, and the state of experimental and theoretical knowledge concerning N_2 spectroscopy. Neither of these chapters is exhaustive. Instead, they seek to outline the information which was most useful to the original work that follows.

The accumulation of N_2 spectroscopic knowledge is now sufficiently deep and broad that it may be utilised for the construction of an advanced semi-empirical coupled-channels quantum-mechanical model of the states responsible for the dipole-allowed XUV spectrum, and their dissociative perturbers, and which is the objective of the research detailed in this thesis.

The coupled-channels method [40, 90, 117, 118, 167, 174] does not calculate the properties of isolated electronic states, and then include the effect of state interactions as perturbations. Instead, during the mechanics of calculation, these interactions are treated simultaneously to the potential-energy curves representing each state. This approach has the advantage of implicitly including the perturbative interactions of all vibrational levels of all bound states, as well as the unbound continua, in a single calculation. An alternative, and commonly-performed, theoretical treatment of N_2 involves the localised deperturbation of a finite number of interacting levels [26, 30, 94, 109, 177, 179, 186, 188, 189]. Such studies do not require a sophisticated model of the wavefunction and frequently produce precise and useful results, but are largely phenomenological and lacking in predictive power. Alternatively, there also exist treatments of N_2 from fundamental principles [9, 24, 25, 33, 34, 42, 42, 92, 122, 128, 145], but the attainment of spectroscopic accuracy by these *ab initio* methods lies beyond the theoretical and computational powers of the present day. The modelling of this thesis seeks to be, at once, global and quantitative, and herein lies the need for a semi-empirical approach, part way between purely phenomenological and *ab initio* techniques. The coupled-channels method reduces the entire electronic wavefunction to a parameterisation by means of potential-energy curves and interaction matrix-elements. It is the fixing of these aspects of the model that requires an ample experimental database. However, because the Schrödinger equation of nuclear motion is solved explicitly, the coupled-channels technique is, nonetheless, capable of great predictive power. That is, model interpolation, and some extrapolation, of the known spectrum may be made with regard to excitation-energy, rotational state of the molecule, or by isotopic substitution of the nuclei. This predictive power is particularly useful when calculating spectra which are relevant to the study of planetary atmospheres.

A further theoretical adaptation leads to a particularly powerful aspect of coupled-channels modelling, the inclusion of unbound electronic states [40, 104, 117, 118]. By this means, the previously-discrete spectrum of theoretical energy levels is transformed into a dissociation continuum that is punctuated by broadened resonances which are representative of predissociated bound-states. These resonances exhibit linewidths which are directly related to their dissociative-decay lifetimes, and incorporate the effects of quantum interference between competing dissociation channels, i.e., have Fano lineshapes [36, 99]. Thus, not only is the full-width half-maximum of each resonance calculable, but so is an accurate representation of the background continuum between them, including for energies approaching and traversing a dissociation limit. Furthermore, by means of an appropriate transformation of the calculated wavefunction, from a molecular basis to one appropriate for the calculation of an asymptotic scattering matrix, the distribution of atomic states following molecular dissociation is deduced [118].

The inclusion of a ground-state model and set of electronic transition moments enables the calculation of a photoabsorption or photodissociation cross-section [49]. The mixing and quantum interference of the coupled transition amplitudes allows for the calculation of various intensity-interference effects which appear in the observed spectra [50, 155, 157]. Finally, the simulation of a thermal-distribution of ground-state rotational levels and the effects of Doppler broadening permits the generation of synthetic spectra which are directly

comparable to laboratory or field measurements, but with an effective resolution that is ideal.

One potential role of coupled-channels modelling is that of intelligent interpolator. For this, the fragmented information collected from laboratory studies is incorporated into the various model parameters. Its physically-explicit aspects then allow for the comprehensive generation of synthetic spectra without the burden of instrumental effects, and covering a wider range of conditions than could feasibly be studied in the laboratory. There are, in fact, a number of active fields of research, discussed below, which have an immediate need for accurate and comprehensive N_2 photoabsorption and photodissociation spectra. The direct use of experimental spectra or phenomenological line-by-line models are of little use here because they are inherently incomplete and distorted by instrumental limitations, or the scope of the assumed phenomenological model. Fortunately, the coupled-channels model presented in Chap. 6 is eminently suited to the applications at hand.

A further utility of the technique resides in the translation of a theoretical description of a molecule's quantum-states into a quantitative assessment of its multivariate, and frequently subtle, observable properties. In this way, new insights into the underlying physics may be made even where the supporting experimental evidence appears opaque when viewed in isolation. The theoretical description of N_2 dissociation is immature, and could certainly benefit from this methodology. Its further elucidation is a primary focus of the investigations detailed in Chap. 6. This has necessitated the modelling of triplet-multiplicity states of N_2, which are not observed frequently, so that guidance provided by the experimental record is limited, and often indirect. Because of this, the construction in Chap. 6 of a final, relatively complete, model of predissociation is approached in steps by a series of independent models of increasing complexity, building up from the most well-known states of N_2. In the culmination of Chap. 6, substantial progress has been made and the understanding of predissociation of $^1\Pi_u$ states, in particular, has been advanced significantly.

The objectives of the present modelling study have also prompted a series of collaborative experimental investigations. Some new laboratory studies of N_2 excitation are included in this thesis which extend the experimental record by means of technically-refined or entirely novel methods. Chapter 4 describes the analysis of new photoabsorption spectra recorded by means of a grating spectrometer and a synchrotron radiation source. The high resolution and low column density adopted for this experiment has permitted the first determinations of absolute oscillator-strength for a large number of transitions, as well as the direct measurement of broadened rotational-lines, betraying the presence of predissociation. This new data has been of critical importance to the specification of the coupled-channels model parameters governing predissociation and photoabsorption. Chapter 5 discusses the observation and analysis of further synchrotron-based photoabsorption spectra with even higher resolution. These were measured by means of a unique windowless XUV Fourier-transform spectrometer and extend the results of Chap. 4 to higher energies, lower temperatures, and a secondary isotopomer of N_2. Two further collaborative studies involve both laboratory and modelling work, and are detailed in Sec. 7.2 and 7.4. These are concerned, respectively, with the relative intensities of a series of N_2 emission bands to excited ground-state vibrational levels, and new measurements of electron energy loss spectra which are modelled following a generalisation of model transition moments.

Molecular nitrogen, N_2, is an important factor in the photochemistry of the Earth's atmosphere [37, 107, 116], as well as that of the Saturnian moons Titan [106, 126] and

Triton [161]. Nitrogen has also been observed in the interstellar medium [79] and its photodissociation in the Martian atmosphere has been studied [4]. There is currently a need among investigators of these various locations for an improved understanding of N_2 photoabsorption and photodissociation, as well as quantitatively accurate and comprehensive cross sections for input into their photochemical models. That is, the production of, possibly excited, nitrogen atoms following XUV absorption functions as a source of reactants for the production of further nitrogen-bearing molecules. Even where atomic fragments are not themselves of concern the predissociation of N_2 excited states is a critical factor in radiative-transfer models. Whereby, the suppression of emissive decay immediately alters any calculated radiation balance, particularly where the optical depth is sufficiently great that multiple cycles of absorption and emission occur. Furthermore, the predissociation broadening of absorption lines directly controls the important effect of self-shielding, and resultant isotopomer-selectivity. For the many reasons stated above, the coupled-channels model of N_2 that is the subject of this thesis comprises an ideal match to the current requirements of the atmospheric and astrophysical communities.

Two specific applications of the present coupled-channels model are presented in Chap. 7. A study of dayglow emission from the terrestrial atmosphere is discussed in Sec. 7.3, whereby, satellite observations of XUV flux can only be explained by an accurate model of the branching ratio of N_2 emissive and predissociative decay. Section 7.1 is concerned with explaining the relative populations of nitrogen isotopes in the atmosphere of Titan, observed by the Cassini-Huygens space probe. In this case, the narrowness of N_2 absorption features and the detailed differences between the absorption cross-section of different isotopomers is of critical importance.

Chapter 2

Spectroscopy of diatomic molecules

2.1 Basic symmetry properties

The subject of this thesis is an isolated N_2 diatom. Many properties of its molecular wavefunction may be deduced from physical symmetry considerations and without performing any calculations. Detailed discussions of the quantum-mechanical elements of diatomic molecules and their spectroscopic study are given by Hougen [56], Herzberg [54], and Lefebvre-Brion and Field [90].

The theoretical molecule does not interact with other particles, and is not subject to any external fields. Hence, the effects of a finite pressure and molecular-polarisation are not considered. These properties ensure spatial homogeneity and isotropy; the former of which allows for the immediate adoption of a centre-of-mass coordinate system for the molecular wavefunction.

The condition of spatial isotropy restricts the expectation values of any physically-observable quantity to angular-independence. This leads to the natural choice of a spherical geometry to represent the wavefunction; which may be at most phase dependent with respect to the angular coordinates. This property is common to all closed systems and leads to the conservation of angular-momentum; and the quantisation of its magnitude to values $\hbar\sqrt{J(J+1)}$, for $J = 0, 1, 2, \ldots$, with $2J+1$ degeneracy enumerated $M = -J, -J+1, \cdots, J$. Here, J is known as the *total angular-momentum quantum number*, and M is the *magnetic quantum number* and enumerates the possible values of total angular-momentum aligned along an arbitrary axis, originally provided experimentally by an external magnetic field. Isotropy also implies a second symmetry: invariance with respect to the exchange of left- and right-handed coordinates. This limits the wavefunction to, at most, a change in sign when all coordinate axes are inverted; this binary quantisation of *parity* is labelled $\Pi = +$ or $-$. In general, the sign of Π is a product of separate parities; that of the total angular-momentum related wavefunction, given by $(-1)^J$; and a combined parity arising from all other parts of the wavefunction. The even or oddness of the second factor is denoted by e or f, respectively.

Of primary interest are molecular stationary-states where energy, E, is conserved. Then, a sufficient set of rigorous quantum numbers that represents all possible states of the total molecular-wavefunction is given by

$$|iEJM\Pi\rangle\,. \tag{2.1}$$

Each of these states may be degenerate so that the index i is required to enumerate all

consistent internal configurations of the molecule.

Further insight into the molecular wavefunction may be achieved by considering a coordinate system with origin fixed at the centre-of-mass of the two nuclei, and with z-axis aligned with the internuclear axis. A detailed description of the transformation between external and molecule fixed coordinates is given by Pack and Hirschfelder [127].

In molecule fixed coordinates, the configuration of the nuclei is specified solely by the internuclear distance. Cylindrical symmetry is imposed on the motion of the electrons by the internuclear axis; resulting in a quantisation of the aligned component of electronic orbital-angular-momentum to values $\hbar\Lambda$, for $\Lambda = 0, 1, 2, \ldots$ (usually written $\Sigma, \Pi, \Delta, \ldots$). There arises a double degeneracy for states with $\Lambda > 0$ which corresponds physically to Λ aligned along or opposite to the positive-direction of the z-axis. Alternative linear combinations of these may be constructed which are either symmetric or antisymmetric with respect to an inversion of the centre-of-mass coordinates. These are labelled Λ^+ and Λ^-, respectively. When $\Lambda = 0$, only one state is possible but there still exists an innate inversion symmetry so that this too is superscripted, either as Σ^+ or Σ^-. The magnitude of the combined orbital angular-momenta of all electrons is sometimes assumed to be quantised according to $\hbar\sqrt{L(L+1)}$, where the quantum number L is similar to the spherically-symmetric atomic case. Additionally, the orbital angular-momentum of an individual electron, and its projection onto the internuclear axis, may be written $\hbar l$ and $\hbar\lambda$, respectively. Because of the electrostatic interactions between electrons and the nuclei; L, l, and λ are never good quantum-numbers.

Two distinctions arise at this point between heteronuclear (e.g., $^{14}N^{15}N$) and homonuclear (e.g., $^{14}N_2$ and $^{15}N_2$) diatomic molecules. These occur because the former have distinguishable nuclei and a well defined orientation with which to reference the z axis, while the similarity of the latter case limits the wavefunction to a phase change only when there is an exchange of nuclei. First, the wavefunctions of homonuclear molecules are required to be either symmetric or anti-symmetric with respect to inversion of the molecular coordinates, followed by an exchange of nuclei. This operation is equivalent to a reflection of all electronic-coordinates through a plane bisecting the internuclear axis. The resulting symmetric and antisymmetric states are labelled g (*gerade*) and u (*ungerade*), respectively, and correspond to united-atom wavefunctions (in the limit of co-located nuclei) that have even or odd total parity. Second, the nuclei of homonuclear molecules will be either Bosons or Fermions, and the total wavefunction will then be even or odd with respect to nuclear exchange and may be labelled s or a, respectively.

The effects of electron spin may be introduced by assuming the quantisation of the total electronic-spin angular-momentum to values $\hbar\sqrt{S(S+1)}$, with $S = 1/2, 1, 3/2, \ldots$. Then $\hbar\Sigma$; $\Sigma = -S, -S+1, \ldots, S$; is the component of total electronic-spin aligned with the internuclear-axis. Electromagnetic interaction between the electronic spin and orbital-angular-momenta prevents the rigorous quantisation of S and Σ. Instead, the molecular-axis projection of the total electronic-angular-momentum is quantised to values $\hbar\Omega = \hbar|\Lambda + \Sigma|$; and may be included in a set of good quantum numbers that describe stationary-states in the molecule fixed coordinate system,

$$|iEJM\Pi\Omega\rangle\,. \tag{2.2}$$

Such wavefunctions are often referred to as *Hund's case (c)* states [90, p. 101].

If the interaction between electronic spin and orbital-angular-momenta is weak then S and Σ are approximately good quantum numbers. In this case stationary states may be

referenced by the *Hund's case (a)* quantum numbers,

$$|iEJM\Pi\Lambda S\Sigma\Omega\rangle\,, \tag{2.3}$$

where only two of the three quantum numbers Λ, Σ, and Ω are independent. Even when the interaction between electronic spin and orbital-angular-momenta is not negligible, the non-rigorous set of Eq. (2.3) serves as a convenient labelling system for observed or calculated molecular states.

In the case of nuclei with nonzero rotational-angular-momentum, this new reference frame is noninertial; and wavefunctions expressed in the new coordinates must be transformed, via a rotation, to the laboratory frame before the evaluation of any physical properties. This breaks the cylindrical symmetry imposed by the internuclear axis and mixes wavefunctions of different Λ, eliminating this as a good quantum number; and introduces an interaction between the nuclear-rotational angular-momentum and electron spin, further breaking the rigorous definition of S and Σ. Such wavefunctions are once again defined solely by the quantum numbers of Eq. (2.1). Only states with the same g/u symmetry are mixed upon transformation to the laboratory frame of reference, and a further rigorous restriction prevents the mixing of e and f parity states. This latter constraint is observable where rotational mixing occurs between one state with $\Lambda = 0$, possessing definite e or f parity, and a pair of previously-degenerate e and f parity states with $\Lambda > 0$. This degeneracy is broken by parity selective mixing with the $\Lambda = 0$ state, and the resultant splitting of energy levels is termed Λ-doubling.

A quantisation of possible energy levels occurs when the total energy of a system is less than the potential energy of any separated subsystems at infinite range. That is, if ionisation and dissociation are both energetically inaccessible then the molecular wavefunction is strictly localised, and a vibrational quantum number, v, may act as a surrogate for an energy label of the total wavefunction,

$$|ivJM\Pi\Lambda S\Sigma\Omega\rangle\,. \tag{2.4}$$

The precise numbering of v depends on the separation of electronic and nuclear motions, discussed in the following sections.

A summary of the quantum numbers discussed above, and some others, is listed in Tab. 2.1; as well as the operators and eigenvalues they relate to.

2.2 Born-Oppenheimer solution of the Schrödinger equation

The usual Schrödinger equation of quantum mechanics provides an excellent description of a diatomic molecule. In what follows, the electrostatic force acting between all charged particles is explicitly represented by a Coulomb potential, but magnetic forces induced by charge currents and intrinsic particle spin are introduced as *a posteriori* perturbations.

The Schrödinger equation may be written in terms of the nonrelativistic Hamiltonian H, energy E, and wavefunction $\psi(\boldsymbol{r}_A, \boldsymbol{r}_B, \boldsymbol{r}_1, \ldots, \boldsymbol{r}_n)$, as

$$H\psi(\boldsymbol{r}_A, \boldsymbol{r}_B, \boldsymbol{r}_1, \ldots, \boldsymbol{r}_n) = E\psi(\boldsymbol{r}_A, \boldsymbol{r}_B, \boldsymbol{r}_1, \ldots, \boldsymbol{r}_n), \tag{2.5}$$

where $\boldsymbol{r}_i$ refers to the spatial coordinates of the two nuclei (subscripts A and B) and the

Operator	Eigenvalues	Description
H	E	Total energy.
I or σ_v	$\Pi = +, -$ or e, f	Total parity with respect to coordinate inversion.
$\boldsymbol{J}$	$\hbar\sqrt{J(J+1)},\ J = 0, 1, 2, \ldots$	Total angular-momentum.
$\boldsymbol{J}_Z$	$\hbar M,\ M = -J, -J+1, \ldots, J$	Component of $\boldsymbol{J}$ aligned with the laboratory Z-axis.
$\boldsymbol{L}$	$\hbar\sqrt{L(L+1)},\ L = 0, 1, 2, \ldots$	Total electronic-orbital angular-momentum.
$\boldsymbol{L}_z$	$\hbar\Lambda,\ \Lambda = 0, 1, 2, \ldots$ or $\Lambda = \Sigma, \Pi, \Delta, \ldots$	Component of $\boldsymbol{L}$ aligned with the internuclear axis.
$\boldsymbol{S}$	$\hbar\sqrt{S(S+1)},\ S = 0, 1, 2, \ldots$	Total electronic spin.
$\boldsymbol{S}_z$	$\hbar\Sigma,\ \Sigma = -S, -S+1, \ldots, S$	Component of $\boldsymbol{S}$ aligned with the internuclear axis.
$\boldsymbol{J}_e = \boldsymbol{S} + \boldsymbol{L}$	$\hbar\sqrt{J_e(J_e+1)},\ J_e = 0, 1, 2, \ldots$	Total electronic angular-momentum.
$\boldsymbol{J}_a = \boldsymbol{S}_z + \boldsymbol{L}_z$	$\hbar\Omega = \hbar\lvert\Lambda + \Sigma\rvert$	Component of $\boldsymbol{J}_e$ aligned with the internuclear axis.
$\boldsymbol{l}$	$\hbar\sqrt{l(l+1)},\ l = 0, 1, 2, \ldots$	One-electron orbital angular-momentum.
$\boldsymbol{l}_z$	$\hbar\lambda,\ \lambda = 0, 1, 2, \ldots$ or $\lambda = \sigma, \pi, \delta, \ldots$	Component of $\boldsymbol{l}$ aligned with the internuclear axis.
H^{Ryd}	$n = 0, 1, 2, \ldots$	One-electron principal quantum number.
$\boldsymbol{s}$	$\hbar/2$	One-electron spin angular-momentum.
$\boldsymbol{s}_z$	$\hbar\sigma,\ \sigma = 1/2, -1/2$ or α, β	Component of $\boldsymbol{s}$ aligned with the internuclear axis.
$\boldsymbol{R}$	$\hbar\sqrt{\mathcal{R}(\mathcal{R}+1)},\ \mathcal{R} = 0, 1, 2, \ldots$	Nuclear-rotational angular-momentum.
$\boldsymbol{N} = \boldsymbol{R} + \boldsymbol{L}$	$\hbar N(N+1),\ N = 0, 1, 2, \ldots$	Electronic-orbital plus nuclear-rotational angular-momentum.
$\boldsymbol{I} = \boldsymbol{i}_A + \boldsymbol{i}_B$	$\hbar\sqrt{I(I+1)},\ I = 0/2, 1/2, 2/2, \ldots$	Total nuclear-spin composed of individual spins $\boldsymbol{i}_{A/B}$.
I_e	$+1/-1$ or g/u	Coordinate inversion and reversal of the internuclear axis, only relevant to homonuclear molecules.
$\mathcal{P}_{AB}$	$+1/-1$ or s/a for Bosonic/Fermionic nuclei	Exchange of the nuclei, only relevant to homonuclear molecules.
	${}^{2S+1}\Lambda^{+/-}_{u/g,e/f,\Omega}$	Combined term symbol of an electronic state.
	$nl\lambda\ \left[{}^{2S+1}\Lambda^{+/-}_{u/g,e/f,\Omega}\right]^+$	Extended term symbol of a Rydberg electronic state.

Table 2.1: Some operators and quantum numbers relevant to the study of diatomic molecules. Subscripts Z and z indicate a component of angular momentum with regards to the laboratory and molecule fixed coordinates, respectively. The final two term symbols denote the conventional means of expressing the symmetry of an electronic state for a diatomic molecule. In the case of a Rydberg state, $nl\lambda$ refers to the Rydberg electron and the bracketed quantum numbers $[\ldots]^+$ refer to the parent ionic core in the absence of the Rydberg electron.

n electrons (subscripts $1 \ldots n$). For a diatomic molecule the Hamiltonian may be written

$$\begin{aligned} H &= \frac{-\hbar^2}{2}\left(\frac{1}{m_A}\nabla_A^2 + \frac{1}{m_B}\nabla_B^2 + \sum_{i=1}^{n}\frac{1}{m_e}\nabla_i^2\right) \\ &\quad + e^2\sum_{i=1}^{n}\left(\sum_{j=i+1}^{n}\frac{1}{|\boldsymbol{r}_i - \boldsymbol{r}_j|} - \frac{Z_A}{|\boldsymbol{r}_i - \boldsymbol{r}_A|} - \frac{Z_B}{|\boldsymbol{r}_i - \boldsymbol{r}_B|}\right) + \frac{e^2 Z_A Z_B}{|\boldsymbol{r}_A - \boldsymbol{r}_B|}, \end{aligned} \tag{2.6}$$

where the particle masses and proton numbers are given by m_i and Z_i, respectively, $\hbar = h/2\pi$ represents Planck's reduced constant, and e is the fundamental charge. In Eq. (2.6), the first pair of parentheses contain terms corresponding to the classical kinetic energy; the double summation enumerates terms describing the mutual electrostatic forces between electrons, and between electrons and nuclei; and the final term represents the electrostatic repulsion of the nuclei.

It is convenient to adopt a molecule centred coordinate system. First, bulk translation of the system is entirely neglected so that the centre of mass of the molecule is assumed stationary. Then, the electron coordinates, $\boldsymbol{r}_1 \ldots \boldsymbol{r}_n$, are defined to be cylindrical, with origin at the centre-of-mass of the two nuclei and z-axis aligned with the internuclear-axis,

from nucleus A to nucleus B. Then, the internuclear distance, R, and nuclear reduced mass, μ, are defined by

$$\begin{aligned} R &= |\boldsymbol{r}_A - \boldsymbol{r}_B|\,, \\ \mu &= \frac{m_A m_B}{m_A + m_B}. \end{aligned} \tag{2.7}$$

Finally, the orientation of the internuclear axis with respect to a laboratory Z-axis is described by angular coordinates θ and φ, the definition of which follow Pack and Hirschfelder [127]. Then, the total Hamiltonian of Eq. (2.6) may be conveniently partitioned into three parts representing the electronic, nuclear-rotational and nuclear-vibrational motions, according to

$$H = H^{el} + H^{rot} + H^{vib}, \tag{2.8}$$

where,

$$H^{el} = \frac{-\hbar^2}{2}\sum_{i=1}^{n}\frac{1}{m_e}\nabla_i^2 + e^2\sum_{i=1}^{n}\left(\frac{-Z_A}{|\boldsymbol{r}_i - \boldsymbol{r}_A|} - \frac{Z_B}{|\boldsymbol{r}_i - \boldsymbol{r}_B|} + \sum_{j=i+1}^{n}\frac{1}{|\boldsymbol{r}_i - \boldsymbol{r}_j|}\right), \tag{2.9}$$

$$H^{rot} = \frac{-\hbar^2}{2\mu R^2}\left[\frac{1}{\sin\theta}\frac{\partial}{\partial\theta}(\sin\theta\frac{\partial}{\partial\theta}) + \frac{1}{\sin^2\theta}\frac{\partial^2}{\partial\varphi^2}\right], \tag{2.10}$$

$$H^{vib} = \frac{-\hbar^2}{2\mu R^2}\frac{\partial}{\partial R}R^2\frac{\partial}{\partial R} + \frac{e^2 Z_A Z_B}{R}. \tag{2.11}$$

Here, the quantities $|\boldsymbol{r}_i - \boldsymbol{r}_A|$ and $|\boldsymbol{r}_i - \boldsymbol{r}_B|$ are implicitly dependent on R, and ∇_i^2 operates on coordinates relative to both the centre-of-mass and laboratory reference frames. The separation of $\frac{1}{m_A}\nabla_A^2 + \frac{1}{m_B}\nabla_B^2$ into the derivatives with respect to R, θ, and φ appearing in Eq. (2.10) and Eq. (2.11) is a standard result in spherical coordinates.

At this point we adopt the Born-Oppenheimer approximation, whereby it is assumed possible to formally separate the wavefunction into three factors,

$$\psi(\boldsymbol{r}, R, \theta, \varphi) = \phi(\boldsymbol{r}; R)\Theta(\theta, \varphi)\frac{\chi(R)}{R}, \tag{2.12}$$

representing electronic, rotational, and vibrational wavefunctions, respectively. Here, $\boldsymbol{r} = \boldsymbol{r}_1, \boldsymbol{r}_2, \ldots, \boldsymbol{r}_n$. Equation (2.5) may then be written,

$$\left(H^{el} + H^{vib} + H^{rot}\right)\phi(\boldsymbol{r}; R)\Theta(\theta, \varphi)\frac{\chi(R)}{R} = E\,\phi(\boldsymbol{r}; R)\Theta(\theta, \varphi)\frac{\chi(R)}{R}. \tag{2.13}$$

The internuclear-distance is transcribed as a mere parameter of the electronic wavefunction, $\phi(\boldsymbol{r}; R)$, because operating within the Born-Oppenheimer approximation it is assumed that

$$\frac{\partial}{\partial R}\phi(\boldsymbol{r}; R) \sim 0 \text{ and } \frac{\partial^2}{\partial R^2}\phi(\boldsymbol{r}; R) \sim 0. \tag{2.14}$$

Then, the R-dependence of the differential term in Eq. (2.9) may be neglected. This is equivalent to assuming that the orbital period of the electrons is significantly shorter than the vibrational period of the nuclei. Alternatively, it may be interpreted as meaning that the electronic wavefunction represents a dynamic steady-state, maintaining a near-equilibrium configuration as the nuclei slowly move. This approximation is supported by the large ratio of the nuclear reduced-mass to the electron mass. It is also assumed

that the rotational period of the nuclei is significantly greater than both the electronic and vibrational periods, such that the dependence of $\phi(\boldsymbol{r};R)$ on θ and φ may be ignored altogether.

Following these considerations, the following commutations are allowed,

$$H^{el}\phi(\boldsymbol{r};R)\Theta(\theta,\varphi)\frac{\chi(R)}{R} = \Theta(\theta,\varphi)\frac{\chi(R)}{R}H^{el}\phi(\boldsymbol{r};R), \tag{2.15}$$

$$H^{rot}\phi(\boldsymbol{r};R)\Theta(\theta,\varphi)\frac{\chi(R)}{R} = \phi(\boldsymbol{r};R)\frac{\chi(R)}{R}H^{rot}\Theta(\theta,\varphi), \tag{2.16}$$

$$H^{vib}\phi(\boldsymbol{r};R)\Theta(\theta,\varphi)\frac{\chi(R)}{R} = \phi(\boldsymbol{r};R)\Theta(\theta,\varphi)H^{vib}\frac{\chi(R)}{R}. \tag{2.17}$$

Substituting these three equations into Eq. (2.13), and dividing by $\phi(\boldsymbol{r};R)\Theta(\theta,\varphi)\frac{\chi(R)}{R}$ gives,

$$\frac{1}{\phi(\boldsymbol{r};R)}H^{el}\phi(\boldsymbol{r};R) + \frac{1}{\Theta(\theta,\varphi)}H^{rot}\Theta(\theta,\varphi) + \frac{R}{\chi(R)}H^{vib}\frac{\chi(R)}{R} = E. \tag{2.18}$$

Each term on the left hand side of this equation is a function of independent coordinates and so three separated equations are defined,

$$H^{el}\phi(\boldsymbol{r};R) = E^{el}(R)\phi(\boldsymbol{r};R), \tag{2.19}$$

$$H^{rot}\Theta(\theta,\varphi) = E^{rot}(R)\Theta(\theta,\varphi), \tag{2.20}$$

$$H^{vib}\frac{\chi(R)}{R} = E^{vib}(R)\frac{\chi(R)}{R}, \tag{2.21}$$

with the R-independent total-energy given by,

$$E = E^{el}(R) + E^{rot}(R) + E^{vib}(R). \tag{2.22}$$

The solution of Eq. (2.19) requires the calculation of both $E^{el}(R)$ and $\phi(\boldsymbol{r};R)$. The Born-Oppenheimer separation of variables reduces the contribution of the nuclei to that of a static potential and significantly reduces the complexity of the problem. The remaining electronic wavefunction in $3n$ spatial dimensions is regularly solved variationally, by minimising the total energy of a trial wavefunction composed of large linear-combination of basis functions. Independent solutions are calculated at discrete fixed-internuclear-distances, and the intervening solutions interpolated. Modern calculations employ basis sets with $\sim 10^6$ members but, for most molecules, are unable to calculate E^{el} to an accuracy comparable with experimental error. The solution of Eq. (2.19) is beyond the scope of this thesis and the basic theory may be found in many texts, e.g., Slater [142]. Some calculations of N_2 electronic wavefunctions are discussed in Sec. 3.5. Fortunately, knowledge of the electronic potential-energy, $E^{el}(R)$, alone is sufficient for the further calculation of eigenvalues of the total-energy; the precise functional form of $\phi(\boldsymbol{r};R)$ is not required. Then, the one-dimensional curve $E^{el}(R)$ may often be experimentally determinable.

Equation (2.20) is analogous to the standard problem of the rigid rotator, e.g., Herzberg [54, p. 66], with quantised energy eigenvalues given by

$$E^{rot}(R) = \frac{\hbar^2\mathcal{R}(\mathcal{R}+1)}{2\mu R^2}. \tag{2.23}$$

Here, $\mathcal{R} = 0, 1, 2, \ldots$ corresponds to the angular-momentum quantum-number of nu-

clear rotation. There are well-known analytical solutions for $\Theta(\theta, \varphi)$, given by spherical-harmonic functions.

Once $E^{el}(R)$ and $E^{rot}(R)$ are known we may proceed to solve Eq. (2.21). Substituting Eq. (2.11) into Eq. (2.21) gives

$$\frac{-\hbar^2}{2\mu}\frac{d^2}{dR^2}\chi(R) + V(R)\chi(R) = E\chi(R), \tag{2.24}$$

where the *potential-energy curve* is defined to be

$$V(R) = E^{el}(R) + E^{rot}(R) + \frac{e^2 Z_A Z_B}{R}. \tag{2.25}$$

The simplified differential term in Eq. (2.24), with respect to Eq. (2.11), is the result of choosing to represent the vibrational wavefunction by $\frac{\chi(R)}{R}$ instead of $\chi(R)$.

It is necessary to specify boundary conditions before the solutions of Eq. (2.24) may be determined. For the case of bound states, that is $E < V(0)$ and $E < \lim_{R\to\infty} V(R)$, the appropriate boundary conditions are,

$$\chi(0) = 0, \tag{2.26}$$

$$\lim_{R\to\infty} \chi(R) = 0, \tag{2.27}$$

$$\text{and} \quad \int_0^\infty \chi^\dagger(R)\chi(R)\, dR = 1. \tag{2.28}$$

The final condition (2.28) ensures unit normalisation of the total wavefunction, and presupposes similar conditions have been imposed on the electronic and rotational wavefunctions according to

$$\int_{\text{span of } \boldsymbol{r}} \phi^\dagger(\boldsymbol{r}; R)\phi(\boldsymbol{r}; R)\, d\boldsymbol{r} = 1 \quad \text{and} \quad \int_0^{2\pi}\int_{-0}^{\pi} \Theta^\dagger(\theta, \varphi)\Theta(\theta, \varphi)\sin\theta\, d\varphi\, d\theta = 1. \tag{2.29}$$

Following the imposition of Eqs. (2.26) and (2.27), only discrete values of E will permit the solution of Eq. (2.24). These represent the quantised internal-energy levels of the molecule.

The eigenvalues and eigenfunctions of Eq. (2.24) have been calculated numerically using many techniques [41, 66, 140]. The method of Johnson [66] is discussed further in Sec. 2.11.2. In some cases where the electronic-energies are not well known, $V(R)$ may be approximated analytically, and the solutions of Eq. (2.24) may also be analytic.

Born-Oppenheimer wavefunctions may not be constructed which represent unbound states, i.e., those with $E > \lim_{R\to\infty} V(R)$. Large internuclear distance will occur for such states, where the molecule is better represented as separated noninteracting atoms. In this case, the electronic R-dependence that was assumed negligible in Eq. (2.14) becomes a dominant term in Eq. (2.9).

2.3 Particle spin

A further product function representing electron spin may be appended to the Born-Oppenheimer wavefunction of Eq. (2.12), so that

$$\psi(\boldsymbol{r}, R, \theta, \varphi, S, \Sigma) = \phi(\boldsymbol{r}; R)\Theta(\theta, \varphi)\frac{\chi(R)}{R}\mathcal{S}(S, \Sigma). \tag{2.30}$$

Here, the quantum number S represents the combined intrinsic-spin of all electrons, and Σ is its projection onto the internuclear axis. There is no spatial representation of $\mathcal{S}(S, \Sigma)$ equivalent to a classical charge current. Instead, the equivalent quantum numbers $s = 1/2$ and $\sigma = \pm 1/2$ for a single electron are postulated as fundamental, and the combined spins of multiple electrons built up according to the regular quantum-mechanical rules governing the vector addition of angular momenta, e.g., [22, p. 54].

The nonrelativistic Hamiltonian of Eq. (2.6) contains no reference to particle spin, and so will be diagonal with respect to quantum states with differing S and Σ. Additionally, all possible spin states attached to a common spatial wavefunction will be degenerate. However, the addition of further spin dependent operators to this Hamiltonian, discussed in Sec. 2.6 and Sec. 2.5.2, introduces significant diagonal and off-diagonal matrix elements for the various spin functions. The diagonal terms result in large energy shifts for states of different S and smaller splittings for multiplet substates of the same S and different Σ. The diagonal effects may be mimicked by the nonrelativistic Hamiltonian following the addition of a phenomenological, possibly internuclear-distance dependent, potential-energy term to Eq. (2.6). Within the Born-Oppenheimer approximation this correction will propagate to be an extra term in $V(R)$ of Eq. (2.25). Commonly, these modifications are nearly R-independent and may be treated as simple vertical shifts in the potential energy.

A further novel manifestation of intrinsic spin occurs for homonuclear molecules. For the case where the intrinsic spins of the individual nuclei are nonzero (but necessarily equal, being homonuclear), the total nuclear-spin calculated by vector addition will depend on the relative alignment of the individual spins. The interaction energies of the various total-nuclear-spins with all other angular momenta is entirely negligible at room temperature, and they may be treated as degenerate. However, this vector addition does noticeably influence observed spectra as a consequence of the symmetry with respect to exchange of nuclei, required by their indistinguishability [54, p. 130].

The total wavefunction of a homonuclear diatom must be symmetric or antisymmetric with respect to the exchange of both spatial and spin coordinates between nuclei. The symmetric case occurs for nuclei of integer spin, i, and the antisymmetric case for nuclei of half-integer spin, known as Bosons or Fermions, respectively. This overall symmetry is confused somewhat by the partially molecule-fixed coordinates adopted for the wavefunctions developed in Sec. 2.2, where now three factors must be considered. First, a spin exchange factor of $(-1)^I$ arises, where $I = 0, 1, \ldots, 2i$ is the total nuclear-spin, and is degenerate with respect to its orientation with multiplicity $2I + 1$. Thus, for the case of $i = 1/2$, three states will occur with negative spin exchange factors, and one that is positive. Second, exchanging the spatial-coordinates of the nuclei operates on $\Theta(\theta, \varphi)$ such that $\theta \to (\pi - \theta)$ and $\varphi \to (\pi + \varphi)$. Considering the standard properties of spherical harmonics [54, p. 128], this transformation generates an additional rotational-factor of $(-1)^J$. Finally, exchanging the nuclei spatially reverses the molecule fixed z-axis, and introduces an additional factor depending on the symmetry of $\phi(\boldsymbol{r}; R)$ with respect to this

transformation. For the $^1\Sigma_g^+$ ground state of N_2 this factor is $+1$.

Preservation of the overall Bosonic or Fermionic character of nuclear exchange while considering the three factors described above leads to a modification of the thermal distribution of ground-state rotational levels (further properties of this distribution are discussed in Sec. 2.8.5). For the case of $^{15}N_2$, $i = 1/2$ and the total wavefunction is antisymmetric with respect to nuclear-exchange, requiring that valid wavefunctions may only be generated by combining symmetric spin exchange factors with antisymmetric rotational factors, or vice versa. Hence, because of the $1:3$ degeneracy ratio of symmetric to antisymmetric spin exchange factors there arises a reversed $3:1$ ratio in the rotational distribution of a thermally equilibriated ensemble of molecules. This is apparent in $^{15}N_2$ absorption spectra where transitions from $J = 0, 2, 4, \ldots$ ground-state levels appear three times stronger than those from $J = 1, 3, 5, \ldots$ levels.

A similar phenomenon occurs for $^{14}N_2$, with $i = 1$, where now the strength ratio of $J =$ even : odd transitions is given by $2:1$. The rotational levels of the heteronuclear molecule $^{14}N^{15}N$ are weighted uniformly.

2.4 Nonadiabatic and electronic perturbations

The observed energy levels of real diatomic molecules are imperfectly reproduced by calculations of the type described in Sec. 2.2. A large portion of the observed discrepancies arises from terms neglected by the Born-Oppenheimer approximation involving the operation of H^{vib} of Eq. (2.11) on the R-dependent electronic wavefunctions of Eq. (2.19).

The set of wavefunctions adopted in Eq. (2.19), henceforth written $\phi_i^{ad}(\boldsymbol{r}; R)$, definitively diagonalise the electronic Hamiltonian at each R, so that $\langle \phi_i^{ad} | H^{el} | \phi_j^{ad} \rangle_{\boldsymbol{r}} = \delta_{ij}$, with integration over $\boldsymbol{r}$ only. These are termed *adiabatic* because the electronic and nuclear motions are assumed to be uncoupled, so that no energy may be transferred between these modes. However, there actually exist *nonadiabatic* matrix elements $\langle \phi_i^{ad} | H^{vib} | \phi_j^{ad} \rangle_{\boldsymbol{r}} \neq 0$ arising from terms proportional to $\langle \phi_i^{ad} | \frac{d}{dR} | \phi_j^{ad} \rangle_{\boldsymbol{r}}$ and $\langle \phi_i^{ad} | \frac{d^2}{dR^2} | \phi_j^{ad} \rangle_{\boldsymbol{r}}$ [90, p. 92]. Of these matrix elements, the diagonal terms, with $i = j$, result in R-dependent shifts in potential energy. For the purposes of solving Eq. (2.21) these may be included as adjustments to $V^{el}(R)$. More problematic are the off-diagonal terms, with $i \neq j$. It is possible to reduce the magnitude of these terms by creating R-dependent linear-combinations of the $\phi_i^{ad}(\boldsymbol{r}; R)$ to form *diabatic* electronic wavefunctions, $\phi_i^{d}(\boldsymbol{r}; R)$.

Adiabatic electronic wavefunctions are universally constructed as a finite linear expansion of basis states $\varphi_j(\boldsymbol{r}; R)$,

$$\phi_i^{ad}(\boldsymbol{r}; R) = c_{i1}(R)\varphi_1(\boldsymbol{r}; R) + c_{i2}(R)\varphi_2(\boldsymbol{r}; R) + \cdots + c_{iN}(R)\varphi_N(\boldsymbol{r}; R). \tag{2.31}$$

In turn, each basis state is frequently represented by a configuration of single-electron molecular spin-orbitals arranged as an antisymmetrised product function [90, p. 148] [143],

$$\varphi_j(\boldsymbol{r}; R) = \det \left| \lambda_1(r_1, R)\sigma_1(1) \cdot \lambda_2(r_2, R)\sigma_2(2) \ldots \lambda_n(r_n, R)\sigma_n(n) \right|, \tag{2.32}$$

where $\lambda_i(r_i, R)$ and $\sigma_i(i)$ are spatial and spin functions, respectively, and $i = 1$ to n enumerates the individual electrons. Individual spin-orbitals, and consequently entire configurations, are constructed to be orthogonal and normalised.

The R-dependence of $\phi_i^{ad}(\boldsymbol{r}; R)$ arises from both the linear coefficients in Eq. (2.31) and the individual spin-orbitals in Eq. (2.32). The functional form and potential-energy of each

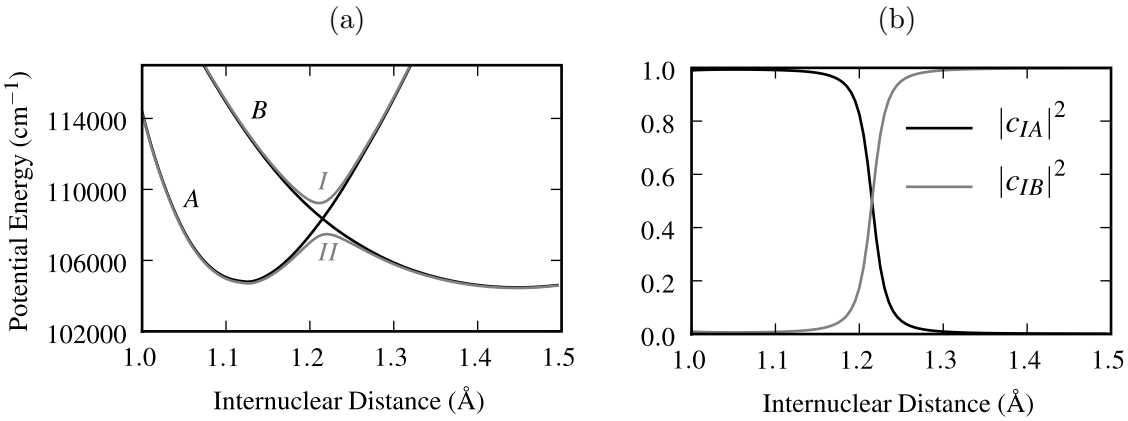

Figure 2.1: *(a):* An example of equivalent diabatic (*dark*) and adiabatic (*light*) potential-energy curves. The off-diagonal matrix element between diabatic states is $\langle A|H^{el}|B\rangle = 900\,\mathrm{cm}^{-1}$. *(b):* Fractional character of single-configuration diabatic states A and B into mixed-configuration adiabatic state I.

spin-orbital varies smoothly with internuclear distance and will not usually lead to large nonadiabatic matrix elements over the range of internuclear distance relevant to molecules in a bound state. However, it may occur that the R-dependent potential-energies of two configurations cross at some particular internuclear distance. Then, because it is necessary that the energy ordering of adiabatic states be R-independent, the expansion coefficients of Eq. (2.31) will change abruptly at the crossing point. Typically, the dominant expansion coefficient is exchanged from one configuration to the other. The resulting derivatives with respect to R may be responsible for large nonadiabatic matrix elements.

The exchange of configuration between two adiabatic electronic states appears as an avoided crossing in their potential-energy curves. An example of this is illustrated in Fig. 2.1. Here, potential-energy curves for two adiabatic states, labelled I and II, are well represented at small R by single-configuration diabatic wavefunctions corresponding to A and B, respectively. Near 1.2 Å the configurations of I and II become mixed, and for large R the two states are again independent but have exchanged configuration. The rapid change in configuration, shown in Fig. 2.1 (b), leads to a large value of $\langle I|H^{vib}|II\rangle$ near the crossing region.

The construction of a reasonable set of diabatic electronic states should principally seek to remove the effects of configuration mixing. The diabatic potential-energy curves following such a transformation, such as those of Fig. 2.1 (a), are simpler in form, have fewer extrema, and may cross at particular internuclear distances. There is no unique choice of transformation. However, any physical property may be expected to be sharply R-dependent where there is a rapid change in configuration; thus, many candidate operators may be used to diagonalise adiabatic states, generating similar diabatic representations. For example, Spelsberg and Meyer [145] adopted the matrix elements of $\langle\phi_i^{ad}|r^2|\phi_j^{ad}\rangle$ to diabaticise *ab initio*-calculated electronic wavefunctions for some nonadiabatically mixed $^1\Sigma_u^+$ and $^1\Pi_u$ states of N_2.

It is clear from Fig. 2.1 (a) that diabaticised potential-energy curves retain some R-dependence, due to the variation within individual configurations, and $\langle\phi_i^d|H^{vib}|\phi_j^d\rangle$ will not be completely diagonal. More significantly, forming adiabatic states into linear combinations renders the sum non-diagonal with respect to H^{el}. As a result, there are frequently large off-diagonal matrix elements of H^{el} between diabatic states, termed *electronic per-*

turbations. Diabaticisation does not remove the effect of state mixing, but merely shifts its origin from H^{vib} to H^{el}. This persistence arises because the approximations made during the definition of Born-Oppenheimer wavefunctions are inherently insufficient.

Either adiabatic or diabatic electronic wavefunctions and potential-energy curves may be chosen to provide a complete description of a diatomic molecule, but in either case must be accompanied by a specification of the state mixing. The more appropriate basis is that which has smaller and less broadly distributed off-diagonal matrix elements, and minimises the set of basis functions necessary to reproduce experimental data. Several studies [145, 167, 174] consider alternative treatments of a coupled state using diabatic and adiabatic representations.

Frequently, a diabatic representation proves simpler to implement, and more efficient to compute. Additionally, physical insight and qualitative predictions may be more easily achieved in the single-configuration picture because off-diagonal mixing terms are less likely to be R-dependent.

Some selection rules for the off-diagonal matrix elements of H^{el} may be determined without complex calculation. First, the rigorous quantum-numbers; representing total angular-momentum, parity and exchange of nuclei; may not be degraded by state mixing. Then, an electronic perturbation mixing states i and j, are limited to the following cases:

$$J_i = J_j; \tag{2.33}$$

$$e \sim e,\ f \sim f \text{ and } e \nsim f; \tag{2.34}$$

$$u \sim u,\ g \sim g \text{ and } u \nsim g. \tag{2.35}$$

Additionally, for a molecule well-represented by Hund's case (a) quantum numbers, some additional restrictions may be applied,

$$\Lambda_i = \Lambda_j,\ \Omega_i = \Omega_j,\ S_i = S_j \text{ and } \Sigma_i = \Sigma_j. \tag{2.36}$$

As can be seen from Eq. (2.32), H^{el} is composed of terms involving the coordinates of at most two electrons. Only one or two product functions of an electronic configuration in the form of Eq. (2.32) may then be modified by an individual term. This imposes a further restriction on the matrix elements of $\langle \phi_i^d | H^{el} | \phi_j^d \rangle$ if the diabatic states i and j are each represented by a single configuration. That is, all terms of this matrix element will certainly be zero if the configurations of i and j differ by more than two spin-orbitals.

Theoretical calculations of nonadiabatic or electronic perturbations requires detailed knowledge of the electronic wavefunctions involved. Alternatively, their magnitude, and possibly R-dependence, may be deduced from observed spectra by finding empirical parameters that correctly reproduce energy level shifts, transition intensity anomalies, or predissociation linewidths.

2.5 Rotational perturbations

Born-Oppenheimer wavefunctions, whether adiabatic or diabatic, are calculated assuming nonrotating nuclei, and will not be eigenfunctions of the total Hamiltonian once rotation is included. This results from the breaking of cylindrical symmetry, as discussed in Sec. 2.1. The off-diagonal mixing of electronic states may, however, be small enough to be treated perturbatively for sufficiently slow rotation.

If $\boldsymbol{R}$ is the quantum operator corresponding to the rotational angular-momentum vec-

tor; the rotational part of the Hamiltonian, defined in Eq. (2.16), may be written more succintly as

$$\begin{aligned} H^{rot}(R) &= \frac{1}{2\mu R^2} |\boldsymbol{R}|^2 \\ &= \frac{1}{2\mu R^2} |\boldsymbol{J} - \boldsymbol{L} - \boldsymbol{S}|^2 . \end{aligned} \tag{2.37}$$

The second equality in Eq. (2.37) may be expanded by making use of the following relation,

$$\begin{aligned} |\boldsymbol{J} - \boldsymbol{L} - \boldsymbol{S}|^2 = |\boldsymbol{J}|^2 + |\boldsymbol{L}|^2 + |\boldsymbol{S}|^2 - J_z^2 - L_z^2 - S_z^2 \\ - (J^+L^- + J^-L^+) - (J^+S^- + J^-S^+) + (L^+S^- + L^-S^+), \end{aligned} \tag{2.38}$$

where

$$X^{\pm} = X_x \pm iX_y \text{ for } X = J, L, \text{ or } S. \tag{2.39}$$

In deriving Eq. (2.38) it is necessary to recognise that nuclear rotation is necessarily orthogonal to the internuclear axis, so that $R_z = 0$.

In Eq. (2.39), *raising* and *lowering* operators are written X^+ and X^-, respectively, where $\hbar\sqrt{X(X+1)}$ is any quantised angular-momentum and its projection along the internuclear axis is given by $\hbar X_z$. Pure $|XX_z\rangle$ states are not eigenfunctions of $X^{\pm}$. Instead, they are transformed according to [90, p. 73],

$$X^{\pm} |XX_z\rangle = \begin{cases} \hbar \left[X(X+1) - X_z(X_z \pm 1)\right]^{1/2} |XX_z \pm 1\rangle ; & \text{normal} \\ \hbar \left[X(X+1) - X_z(X_z \mp 1)\right]^{1/2} |XX_z \mp 1\rangle ; & \text{anomalous.} \end{cases} \tag{2.40}$$

The normal case applies to $X = L$ or S but J is anomalous. This occurs because $\boldsymbol{J}$ and J_Z are properly defined in the laboratory frame of reference but the raising and lowering operators in Eq. (2.39) act on $J_z = \Omega$ in the molecular coordinate system.

Assuming that a Hund's case (a) basis is adopted for the electronic wavefunctions, and using Eqs. (2.37) to (2.40), then the diagonal elements of $H^{rot}(R)$ are given by,

$$\begin{aligned} E^{rot}(R) &= \langle JM\Omega\Lambda S\Sigma | H^{rot}(R) | JM\Omega\Lambda S\Sigma \rangle \\ &= B(R) \left[J(J+1) - \Omega^2 + S(S+1) - \Sigma^2 + L(L+1) - \Lambda^2 \right], \end{aligned} \tag{2.41}$$

where

$$B(R) = \frac{\hbar^2}{2\mu R^2}. \tag{2.42}$$

Generally, L is not a good quantum number because of the nonsphericity encouraged by the internuclear axis. Thus, neither of the nuclear-rotational and electronic-orbital angular momenta are quantised according to a single value of their respective quantum numbers. The nonquantised term that replaces $[L(L+1) - \Lambda^2]$ in Eq. (2.41) may be formally transferred from $E^{rot}(R)$ to $E^{el}(R)$. Alternatively, it may be treated as an arbitrary R-dependent fitting parameter which is distinct for each electronic state. The R-independent expectation value of $E^{rot}(R)$ may then be found by integrating over the internuclear distance, which, assuming a Born-Oppenheimer separation of the wavefunction, leads to the form

$$E^{rot} = B_v \left[J(J+1) - \Omega^2 + S(S+1) - \Sigma^2 \right], \tag{2.43}$$

where the *rotational constant* is given by,

$$B_v = \int_0^\infty \chi^\dagger(R) \frac{\hbar^2}{2\mu R^2} \chi(R)\, dR, \tag{2.44}$$

and is sometimes replaced with an approximate value calculated at the equilibrium internuclear distance, R_e, according to

$$B_v \simeq \frac{\hbar^2}{2\mu R_e^2}. \tag{2.45}$$

2.5.1 *L*-uncoupling

The three bracketed terms in Eq. (2.38) generate off-diagonal matrix elements of $H^{rot}(R)$, and are responsible for perturbations between different Hund's case (a) electronic states. The L-uncoupling operator arising from nuclear rotation is given by $-\frac{1}{2\mu R^2}\left(J^+L^- + J^-L^+\right)$, and mixes states with Λ and Ω differing by ± 1 and with common J, M, S, Σ, parity, and g/u symmetry.

Using the raising and lowering operators of Eq. (2.39), the effect of the second bracketed term of the L-uncoupling operator on a case (a) state is,

$$\begin{aligned} &J^-L^+ \left|JM\Omega\Lambda S\Sigma\right\rangle = \\ &\qquad \left[J(J+1) - \Omega(\Omega+1)\right]^{1/2} \left[L(L+1) - \Lambda(\Lambda+1)\right]^{1/2} \hbar^2 \left|JM\Omega+1\Lambda+1S\Sigma\right\rangle, \end{aligned} \tag{2.46}$$

with a similar result for the first term. Here, $L^\pm$ is responsible for the conversion $\Lambda \to \Lambda \pm 1$, and $J^\mp$ generates $\Omega \to \Omega \pm 1$. Then, the R-dependent off-diagonal matrix elements mixing pure case (a) electronic states are given by,

$$\begin{aligned} &\left\langle JM\Omega \pm 1\Lambda \pm 1S\Sigma\right| - \frac{1}{2\mu R^2} J^\pm L^\mp \left|\Omega\Lambda S\Sigma\right\rangle \\ &\qquad = -B(R) \left[J(J+1) - \Omega(\Omega \pm 1)\right]^{1/2} \left[L(L+1) - \Lambda(\Lambda \pm 1)\right]^{1/2}. \end{aligned} \tag{2.47}$$

Because L is rarely a good quantum number, the factor $\left[L(L+1) - \Lambda(\Lambda \pm 1)\right]^{1/2}$ must be calculated *ab initio* or treated as an adjustable parameter which may even be R-dependent.

If each relevant electronic state is well defined by a single configuration of single-electron spin-orbitals, only those differing by exactly one orbital may be mixed by the L-uncoupling operator. This is because, once written as a sum of single-electron operators,

$$L^\pm = \sum_i l_i^\pm,$$

it is clear that each term in the orbital angular-momentum raising and lowering operators will affect precisely one term of a configuration of single-electron spin-orbitals. Additionally, $J^\pm$ does not affect the electronic wavefunctions at all and so $J^\pm L^\mp$ is a single-electron operator.

2.5.2 *S*-uncoupling

The S-uncoupling operator comprises the part of $H^{rot}(R)$ given by $-\frac{1}{2\mu R^2}(J^+S^- + J^-S^+)$. This term results in off-diagonal matrix elements mixing consecutive Σ-substates of two

otherwise identical electronic states. The observed splitting of sublevels is similar to that caused by the spin-orbit operator discussed in Sec. 2.6, but is dependent on internuclear distance, R, and total angular-momentum, J.

Assuming the validity of the Born-Oppenheimer approximation, the off-diagonal matrix elements arising between Hund's case (a) electronic wavefunctions due to the S-uncoupling operator are

$$\left\langle JM\Omega \pm 1\Lambda S\Sigma \pm 1\right| - \frac{1}{2\mu R^2} J^{\pm} S^{\mp} \left| JM\Omega\Lambda S\Sigma\right\rangle = -B(R)\left[J(J+1) - \Omega(\Omega \pm 1)\right]^{1/2} \left[S(S+1) - \Sigma(\Sigma \pm 1)\right]^{1/2}. \quad (2.48)$$

2.5.3 Spin-electronic perturbations

The last parenthesised term in Eq. (2.38) is the spin electronic operator $(L^+S^- + L^-S^+)$, which generates off-diagonal matrix elements mixing Hund's case (a) stationary states with common Ω, according to

$$\left\langle JM\Omega\Lambda \pm 1S\Sigma \mp 1\right| \frac{1}{2\mu R^2} L^{\pm} S^{\mp} \left| JM\Omega\Lambda S\Sigma\right\rangle = B(R)\left[L(L+1) - \Lambda(\Lambda \pm 1)\right]^{1/2} \left[S(S+1) - \Sigma(\Sigma \mp 1)\right]^{1/2}. \quad (2.49)$$

Because these matrix elements have no J-dependence they may be absorbed into an effective electronic-potential energy.

2.6 Spin-orbit perturbations

Many theoretical molecular wavefunctions are characterised by the good quantum numbers S and Σ. These inherently assume that the intrinsic spin of the bound electrons is completely decoupled from their orbital motion. Because of the interacting magnetic moments generated by spinning and orbiting electrons, this is frequently an imperfect assumption and perturbations between states of different S and Σ result [90, p. 180].

The microscopic operator that is responsible for these perturbations is [8, 90, 175]

$$H^{SO} = \frac{\alpha^2\hbar^3}{2m_e^2 c}\left[\sum_i \left(\frac{Z_A}{r_i^3}\boldsymbol{l}_{iA}\cdot\boldsymbol{s}_i + \frac{Z_B}{r_i^3}\boldsymbol{l}_{iB}\cdot\boldsymbol{s}_i\right) - \sum_{i,j(i\neq j)}\left(\frac{\boldsymbol{r}_{ij}}{r_{ij}^3}\times\boldsymbol{p}_i\right)\cdot(\boldsymbol{s}_i + 2\boldsymbol{s}_j)\right], \quad (2.50)$$

where $\alpha = e^2/4\pi\epsilon_0\hbar c$ ($\alpha = 1/137.036$) is the fine structure constant, Z_A and Z_B are the proton numbers of the two nuclei, and i and j are indices over all electrons; so that $\boldsymbol{l}_{iA} = (1/\hbar)(\boldsymbol{r}_{iA}\times\boldsymbol{p}_i)$ is the dimensionless angular-momentum operator of the ith electron relative to nucleus A, and $\boldsymbol{r}_{ij}$ is the relative position vector for electrons i and j.

Classically, the first summation in Eq. (2.50) describes the energy of magnetic interaction arising between the electron spin vector, $\boldsymbol{s}_i$ and its instantaneous angular momentum with respect to the nuclei. The second summation considers the interaction of an electronic spin vector with the orbital motion of a different electron.

Veseth [175] achieves a simplification of Eq. (2.50) after considering the inherent cylin-

drical symmetry of a nonrotating diatomic molecule, so that,

$$H^{SO} = \sum_{i,j} \xi(i,j) \boldsymbol{l}_i \cdot \boldsymbol{s}_j, \tag{2.51}$$

where the operator $\xi(i,j)$ is a function of radial coordinates only, and $\boldsymbol{l}_i$ is the angular momentum of electron i referenced to the molecular centre of mass. An expansion of vector components, similar to Eq. (2.38), gives

$$H^{SO} = \sum_{i,j} \xi(i,j) \left[l_{iz} s_{jz} + \frac{1}{2} \left(l_i^+ s_j^+ + l_i^- s_j^- \right) \right]. \tag{2.52}$$

Considering further the case of wavefunctions described by the set of Hund's case (a) quantum numbers, $|ivJ\Lambda S\Sigma\Omega\rangle$, and well represented by a single configuration of single-electron spin-orbitals, some properties of H^{SO} may be deduced. Equation (2.52) describes a two-electron operator and so nonzero off-diagonal matrix elements may only arise between states differing by one or two single-electron spin-orbitals. Additionally, the net interaction-energy of paired electrons within a closed-shell will be zero, due to their opposing spins. Even for electronic states that are poorly represented by a single-configuration, approximate single-electron matrix elements may guide an experimental determination of H^{SO} [90].

The first bracketed term of Eq. (2.52) is responsible for diagonal matrix elements of H^{SO}, leading to the splitting of previously degenerate S and Σ isoconfigurational sublevels. These matrix elements are frequently expressed in terms of the spin-orbit splitting parameter, A, according to

$$\langle ivJ\Lambda S\Sigma\Omega | H^{SO} | ivJ\Lambda S\Sigma\Omega \rangle = A\Lambda\Sigma. \tag{2.53}$$

The energy separation of consecutive $\Sigma = -S, -S+1, \ldots, S$ multiplet components is then $A\Lambda$. The sign of A may be positive or negative.

There also exist off-diagonal matrix elements of H^{SO} which mix states with different configurations and Λ, i.e.,

$$\langle jv_j J_j \Lambda_j S_j \Sigma_j \Omega_j | H^{SO} | iv_i I_i \Lambda_i S_i \Sigma_i \Omega_i \rangle.$$

Some example H^{SO} off-diagonal matrix elements are evaluated in Lefebvre-Brion and Field [90, Sec. 3.4] from configurational principles, but the selection rules regarding such perturbations may be deduced simply from symmetry considerations. Because no terms involving nuclear rotation appear in the microscopic spin-orbit operator, both the total angular-momentum and its component along the internuclear axis are conserved in all cases, so that

$$J_j - J_i = 0 \text{ and } \Omega_j - \Omega_i = 0. \tag{2.54}$$

As well as the diagonal matrix elements mentioned above, the first term in Eq. (2.52) is responsible for homogeneous perturbations, governed by the selection rules

$$\Lambda_i = \Lambda_j, \ S_i = S_j, \text{ and } \Sigma_i = \Sigma_j. \tag{2.55}$$

The parenthetical terms lead to heterogeneous mixing restricted to cases where

$$S_i - S_j = 0, \pm 1 \text{ and } \Lambda_i - \Lambda_j = \Sigma_j - \Sigma_i = \pm 1. \tag{2.56}$$

As stated above, states differing by one or two spin-orbitals may be mixed by Eq. (2.51). However, the one-electron part of Eq. (2.51) is usually dominant, and perturbations between singly-differing configurations appear more frequently.

States of different parity or gerade/ungerade symmetry may not be mixed by the spin-orbit perturbations. Further symmetry arguments [90, p. 182] require that perturbations of the kind $\Sigma^{\pm} \sim \Sigma^{\pm}$ are forbidden, but $\Sigma^{\pm} \sim \Sigma^{\mp}$ mixing is allowed.

2.7 Parameterised energy levels

The success of the Born-Oppenheimer approximation is, in many cases, striking and is closely related to the appearance of simple patterns in observed spectra which may extend over many levels. Bound-state energy levels cannot be observed directly but may be determined relative to an arbitrary zero-point following the observation of a sufficient number of two-level transitions. The R-dependent partition of total energy given by Eq. (2.22) is not observable (except by means of ultrafast spectroscopy [90, chap. 9]); instead, the energy of each mode of Born-Oppenheimer motion is conveniently referenced to $R = R_e$, at the minimum of of $E^{el}(R)$, so that

$$E = E^{el} + E^{vib} + E^{rot}. \tag{2.57}$$

In general, no simple patterns appear in the energies, E^{el}, of the various electronic states of a diatomic molecule, although an estimate of the energy ordering of the possible configurations of single-electron spin-orbitals may be made. However, the progression of vibrational levels observed within an electronic state frequently have energies approximating those of a simple harmonic oscillator, given by

$$E^{vib} = \omega_e(v + 1/2) \text{ for } v = 0, 1, 2, \ldots. \tag{2.58}$$

This progression is equivalent to the eigenvalues arising from a parabolic potential-energy curve, and analytic forms for the corresponding harmonic vibrational-wavefunctions are also known [54]. For higher vibrational levels extending beyond the approximately parabolic potential-well near R_e, Eq. (2.58) may need to be augmented to include the effects of anharmonicity, according to

$$E^{vib} = \omega_e(v + 1/2) - \omega_e x_e(v + 1/2)^2 + \omega_e y_e(v + 1/2)^3 + \ldots. \tag{2.59}$$

Additional terms in $v + 1/2$ may be included to attain an improved fit to the experimental vibrational levels, but the physical significance and useful extrapolation of successively higher-order models is rapidly curtailed.

For a particular vibrational level within a harmonic potential-energy curve, the observed progression of rotational levels is frequently well-represented by the energy eigenvalues of the rigid rotator, given by Eq. (2.23) in terms of the nuclear-rotation quantum number $\mathcal{R}$. Normally, an equivalent expression is adopted in terms of the total angular-momentum quantum number J, given by Eq. (2.41), and employing the rotational constant of Eq. (2.44), B_v. That is,

$$E^{rot} = B_v J(J + 1). \tag{2.60}$$

The minimum physically-realisable value of E^{rot} occurs for $J = \Omega$, corresponding to no nuclear rotation.

Higher order parameterisations describing rotational level energies may be useful and are usually of the form,

$$E^{rot} = B_v J(J+1) - D_v \left[J(J+1)\right]^2 + H_v \left[J(J+1)\right]^3 + \ldots . \tag{2.61}$$

Here, the parameter D_v is frequently interpreted as arising from centrifugal distortion leading to third-order anharmonicity of the potential-energy curve, and is typically positive. The parameter H_v has no simple physical explanation, and a large value often indicates the presence of rotational or electronic perturbations. It may also be useful to extend the polynomial expansion of Eq. (2.61) to higher orders in terms of $J(J+1)$.

Fitted molecular parameters may be used to roughly define the shape of a potential energy curve. Large values of ω_e or B_v indicate a potential-energy curve with narrow sides or a small R_e, respectively. For example, comparing states 1 and 3 of Fig. 2.3(b), on page 36, it is immediately apparent that $\omega_{e1} < \omega_{e3}$ and $B_{v1} < B_{v3}$.

The previous sections describe the various physical effects neglected by the Born-Oppenheimer approximation which lead to poor agreement between observed energy levels and the patterns described above. These effects may be inculcated into the parameterisations discussed in this section following the inclusion of further terms of increasing complexity. The fitting of spectroscopic data to a low-order parameterisation is frequently useful, even when not all observations are perfectly reproduced, because the presence of non-conformers accentuates the existence of a local perturbation. Eventually however, it may become necessary to abandon such efforts and directly treat a higher-order version of the underlying Schrödinger equation, such as by solving a set of coupled equations.

A common type of perturbed energy level parameterisation includes two low-order polynomials of the form of Eq. (2.61), $E_i^{rot}(J)$ and $E_j^{rot}(J)$, representing the energy levels of two electronic states. If these states are mutually perturbing, the observed energy levels, $E_{i'}(J)$ and $E_{j'}(J)$, will deviate from any possible polynomial expansion. However, by introducing a local interaction-parameter, H_{ij}, the observed energy level may be reproduced by means of a matrix diagonalisation. This involves the solution of the following equation,

$$\begin{pmatrix} E_i(J) & H_{ij} \\ H_{ij}^{\dagger} & E_j(J) \end{pmatrix} = D^{\dagger}(J) \begin{pmatrix} E_{i'}(J) & 0 \\ 0 & E_{j'}(J) \end{pmatrix} D(J) \tag{2.62}$$

where

$$D(J) = \begin{pmatrix} c(J) & \sqrt{1-c(J)^2} \\ \sqrt{1-c(J)^2} & c(J) \end{pmatrix}. \tag{2.63}$$

Here, $c(J)$ and $\sqrt{1-c(J)^2}$ are coefficients describing the mixing of pure-states i and j into the perturbed-states i' and j'. Deperturbed energy levels and interaction parameters must be estimated iteratively until the eigenvalues of Eq. (2.62) agree with experiment. In the case of heterogeneous perturbations, H_{ij} may be replaced by $H_{ij}\sqrt{J(J+1)}$; and higher-dimension matrix diagonalisations may be used to reproduce the observed energy levels where more than two bands are mutually-perturbing.

2.7.1 Λ-doubling

As discussed in Sec. 2.1, electronic-rotational states may be labelled in terms of their e or f parity, with differing states being rigorously orthogonal with respect to all perturbations. Those states with $\Lambda \geq 1$ are doubly degenerate and have e- and f-parity levels which are otherwise identical, in the absence of perturbations. However, the presence of an inter-

acting non-degenerate $\Sigma^{\pm}$ state breaks this similarity, then e- and f-parity components of nearby $\Lambda \geq 1$ states appear doubled in observations of their spectrum.

One type of rotational interaction relevant to N_2 occurs between e-parity states of $^1\Sigma^+$ and $^1\Pi$ symmetry, by means of the L-uncoupling operator of Eq. (2.47). The e-parity $^1\Pi$ levels will then be perturbed relative to their unaffected f-parity analogues. The resultant Λ-doubling of e-parity rotational energy levels may be approximately parameterised according to the form

$$E_e^{rot}(J) = E_f^{rot}(J) + qJ(J+1). \tag{2.64}$$

Here, $E_f^{rot}(J)$ represents the f-parity $^1\Pi$ rotational levels, and the right hand side $J(J+1)$ term mirrors the J-dependence of the L-uncoupling operator. Sometimes higher-order terms in $J(J+1)$ may be appended to Eq. (2.64). Off-diagonal matrix elements of the spin-orbit operator may also lead to Λ-doubling.

2.8 Electric dipole transitions

2.8.1 Definitions

When a diatomic molecule is considered in conjunction with a photon, the Hamiltonian of the combined system is no longer diagonal with respect to the stationary states of an isolated molecule. The molecular states are mixed during the time of photonic interaction, and there is some probability an initial state will transit to a different final state.

The principal cases considered in this thesis are those where the incident photon is absorbed during the transition, involving an alteration of the molecular energy and angular momentum; and the largely symmetrical case of spontaneous emission of a photon. A similar excitation may occur following an inelastic collision with a free electron under some kinematic regimes; this situation is discussed in Sec. 2.9.

During an *electric-dipole* transition, electromagnetic radiation is treated as a spatially-homogeneous time oscillating electric field. Then, the interaction of photon and molecule may be treated using standard time dependent perturbation theory (for example Slater [143] p. 265). The significantly weaker magnetic-quadrupole interaction, and further higher-order effects, are not considered in this thesis.

In the following, the higher energy member of two electronic-rovibrational states will be labelled i, and the lower j. The energy difference between the two levels defines the transition wavenumber according to,

$$\nu_{ij} = \frac{E_i - E_j}{2\pi\hbar c}. \tag{2.65}$$

An alternative spectroscopic notation is commonly used whereby upper and lower states are superscripted with single and double primes, respectively.

The important off-diagonal matrix element governing electric-dipole transitions is the *transition moment*,

$$\mu_{ij} = \langle i|\boldsymbol{\mu}|j\rangle, \tag{2.66}$$

$$\boldsymbol{\mu} = e\sum_k^n \boldsymbol{r}_k, \tag{2.67}$$

where, the electric-dipole operator, $\boldsymbol{\mu}$, involves summation over all electrons, indexed by

k.

An absorbed or emitted photon will have a particular polarisation in the laboratory coordinate system, but the molecular wavefunction is usually expressed in the molecular frame of reference. Thus, the polarisation direction must be transformed into molecular coordinates before the transition moment can be calculated [56, 185]. Additionally, when neither radiation nor molecules have been prepared anisotropically, all directions are equivalent and it may be assumed that the electric vector of the electromagnetic field is aligned with the laboratory Z-axis. The necessary rotation of this onto an arbitrary direction in molecular-coordinates may be affected by the direction cosine operator, $\boldsymbol{\alpha}_Z$. The components, $(\alpha_{xZ}, \alpha_{yZ}, \alpha_{zZ})$, of this vector operator specify the three angles required to accomplish a three-dimensional rotation [56, 90]. Equation (2.66), applicable only to nonrotating molecules, must be replaced in the general case by,

$$\mu_{ij} = 3\langle i|\boldsymbol{\mu} \cdot \boldsymbol{\alpha}_Z|j\rangle, \tag{2.68}$$

where the factor of 3 arises due to the possible alternative assumptions of radiation polarised along the laboratory X or Y axes. The sign of μ_{ij} is not observable, instead an experimentally significant quantity is $|\mu_{ij}|^2$.

Several other quantities may be usefully derived from the transition moment. The *Einstein absorption coefficient* is defined according to

$$B_{ij} = \frac{|\mu_{ij}|^2}{6\hbar^2\epsilon_0 c}. \tag{2.69}$$

This describes the probability of a transition occurring in unit time for a molecule initially in its lower state and immersed in a radiation field of unit energy density, with respect to volume and wavenumber, and with frequency tuned to the resonant wavenumber.

The dimensionless *oscillator strength*, or f-value, is given by

$$f_{ij} = \frac{4\pi m_e c}{3\hbar e^2}\nu_{ij|}\mu_{ij}|^2, \tag{2.70}$$

and is defined to be the ratio of the transition probability in question to that of a $v = 0-1$ transition of an electron in a unit (a.u.) harmonic potential [54]. This is a convenient form when reporting experimental and theoretical transition intensities.

The transition *decay lifetime* is given by

$$\tau_{ij} = \frac{3\hbar\epsilon_0}{8\pi^2\nu_{ij}^3|\mu_{ij}|^2} \tag{2.71}$$

and encodes the rate of exponential population decrease for a sample of molecules prepared in state i, following exclusive decay via spontaneous emission into state j. Normally, state i may de-excite into multiple lower-energy states, and the observed *emission decay lifetime* of the excited level is given by a combination of all such pathways, according to

$$\tau_i^{-1} = \sum_j \tau_{ij}^{-1}. \tag{2.72}$$

For each emitting transition, the lifetime may be transformed simply into a corresponding decay rate according to

$$A_{ij} = \tau_{ij}^{-1}. \tag{2.73}$$

The *integrated absorption cross section*, denotes the expected rate of energy removed by an absorption transition from a resonantly-tuned radiation field of unit energy density. This quantity is given by,

$$\int \sigma_{ij} 2\pi\hbar c d\nu = 2\pi\hbar c \nu_{ij} B_{ij} \tag{2.74}$$

$$= \frac{e^2}{4\epsilon_0 m_e c} f_{ij}, \tag{2.75}$$

where the second form arises from the substitution of Eqs. (2.65), (2.69), and (2.70). The denoting of the integrated absorption cross section as an explicit integral is appropriate because of the finite energy spread observed for real transitions, which is discussed in the next section.

2.8.2 Electric dipole selection rules

In what follows some selection rules are discussed which immediately forbid many conceivable electric-dipole transitions. Further details of these results may be found in many publications [90, 143]. These rules are all rigorously true for transitions between pure Hund's case (a) states but some may be violated when either the initial or final state is perturbed.

The operators $\boldsymbol{\mu}$ and $\boldsymbol{\alpha}_Z$ contain no reference to spin variables and so the spin state of a transiting molecule will not be altered. Thus, transitions may only occur between similar multiplets of common total spin, that is

$$S_i - S_j = 0 \text{ and } \Sigma_i - \Sigma_j = 0. \tag{2.76}$$

The goodness of S and Σ is erased once the S-uncoupling or spin-orbit operators of Sec. 2.5.2 and Sec. 2.6, respectively, are considered. In this case, transitions between nominally different spin states may be observed.

The total energy of the system must be conserved so that,

$$E_i - E_j = 2\pi\hbar c \nu_{ij}. \tag{2.77}$$

The precision of this selection rule is relaxed somewhat in accordance with the Heisenberg uncertainty principle, and the finite lifetime of any excited state. Whereby, a short, or precisely known lifetime, τ_i, implies a poorly known level energy, E_i. For transitions connecting state i with an infinitely long-lived ground state, this uncertainty in E_i manifests as a range of allowed transition energies and a energy dependent distribution of oscillator strength with a Lorentzian functional form,

$$f_{ij}(\nu) = \frac{2m_e c}{3\hbar e^2} \frac{\nu_{ij} |\mu_{ij}|^2 \Gamma_i}{(\nu - \nu_{ij})^2 + \Gamma_i^2/4}. \tag{2.78}$$

This symmetric function is centred on the transition wavenumber, ν_{ij}, and has a full-width half-maximum, Γ_i, that is inversely proportional to the decay lifetime of i,

$$\Gamma_i = \hbar/\tau_i$$

$$= 5.309 \times 10^{-12}/\tau_i. \tag{2.79}$$

Here, the second form is appropriate for τ_i and Γ_i in units of s and cm^{-1}, respectively. For transitions between two excited states, the transition linewidth will be broadened by the finite lifetimes of both states.

A finite width resonance leads to a definition of the absorption cross section which is differential with respect to ν, which in accordance with Eq. (2.75) is given by

$$\sigma_{ij}(\nu) = \frac{e^2}{4\epsilon_0 m_e c} f_{ij}(\nu). \tag{2.80}$$

Photons possess one quantum of angular-momentum which must be added vectorially to the internal angular-momentum of the molecule, imposing the restrictions,

$$\Lambda_i - \Lambda_j = -1, 0, 1 \tag{2.81}$$

$$\text{and } J_i - J_j = \begin{cases} -1, 1; & \text{for } \Lambda_i - \Lambda_j = 0 \\ -1, 0, 1; & \text{for } \Lambda_i - \Lambda_j = \pm 1. \end{cases} \tag{2.82}$$

Observed transitions are divided into rotational branches labelled $P(J_j)$, $Q(J_j)$ and $R(J_j)$, corresponding to $J_i - J_j = -1$, 0 or $+1$; respectively. The invocation of Λ in Eqs. (2.81) and (2.82) assumes a Hund's case (a) representation for the molecular wavefunction, but if the effects of spin-orbit interactions cannot be ignored then these may be rewritten with Λ replaced by Ω.

The observable quantity μ_{ij} must be invariant with respect to any coordinate transformation; however, $\boldsymbol{\mu}$ is antisymmetric with respect to coordinate inversion. To compensate for this, one of states i and j in Eq. (2.66) must possess odd parity, and the other even parity. Otherwise μ_{ij} must be zero. The following electric-dipole transition selection rules are then imposed,

$$+ \leftrightarrow -, \; + \nleftrightarrow +, \text{ and } - \nleftrightarrow -. \tag{2.83}$$

Alternatively, if e/f parity labels are used to indicate parity,

$$\begin{aligned} e \leftrightarrow f, \; e \nleftrightarrow e, \; f \nleftrightarrow f \text{ for } J_i - J_j = 0, \\ \text{and } e \nleftrightarrow f, \; e \leftrightarrow e, \; f \leftrightarrow f \text{ for } J_i - J_j = \pm 1. \end{aligned} \tag{2.84}$$

For homonuclear molecules; such as $^{14}\mathrm{N}_2$ and $^{15}\mathrm{N}_2$, but not $^{14}\mathrm{N}^{15}\mathrm{N}$; similar arguments lead to an additional selection rule,

$$u \leftrightarrow g, \; g \leftrightarrow u, \; u \nleftrightarrow u, \text{ and } g \nleftrightarrow g. \tag{2.85}$$

2.8.3 Factorisation of the transition probability

Assuming that states i and j may be represented by uncoupled Born-Oppenheimer wavefunctions, as given by Eq. (2.12), then Eq. (2.68) may be factorised [56, 185] according to,

$$\mu_{ij} = \left(\int_0^\infty \int_{\boldsymbol{r}} \phi_i^\dagger(\boldsymbol{r}; R) \chi_i(R) \, \boldsymbol{\mu} \, \phi_j(\boldsymbol{r}; R) \chi_j(R) \, d\boldsymbol{r} \, dR \right) \cdot 3 \langle J_i M_i \Omega_i | \boldsymbol{\alpha}_Z | J_j M_j \Omega_j \rangle, \tag{2.86}$$

where the first factor is expressed in molecule centred coordinates and the second factor is known as the *rotational line strength*. This separation is possible because the electronic and vibrational wavefunctions are independent of the angular coordinates upon which

$\boldsymbol{\alpha}_Z$ operates; and the rotational wavefunction, expressed here with the vector $|JM\Omega\rangle$, is independent of the molecule fixed operator $\boldsymbol{\mu}$.

Equation (2.86) consists of a vector product generating three terms corresponding to,

$$\boldsymbol{\mu}\cdot\boldsymbol{\alpha}_Z = \mu_x\alpha_{xZ} + \mu_y\alpha_{yZ} + \mu_z\alpha_{zZ}, \tag{2.87}$$

where x, y, and z refer to the molecule fixed coordinate axes. This expansion may be alternatively written by employing the raising and lowering operators defined in Eq. (2.39) with normal commutation behaviour, so that

$$\begin{aligned}\boldsymbol{\mu}\cdot\boldsymbol{\alpha}_Z &= \frac{1}{2}\left(\mu_x - i\mu_y\right)\left(\alpha_{xZ} + i\alpha_{yZ}\right) + \frac{1}{2}\left(\mu_x + i\mu_y\right)\left(\alpha_{xZ} - i\alpha_{yZ}\right) + \mu_z\alpha_{zZ} \\ &= \frac{1}{2}\mu^-\alpha_Z^+ + \frac{1}{2}\mu^+\alpha_Z^- + \mu_z\alpha_{zZ}.\end{aligned} \tag{2.88}$$

It can be shown that for a particular transition only one term in Eq. (2.88) is nonzero [185]. For cases where the nonzero term involves either α_Z^+ or α_Z^-, the internuclear axis is perpendicular to the electric-field of the absorbed radiation, and parallel to the transferred photonic angular-momentum. This contribution of angular momentum will then act to increase, or decrease, the projection of orbital angular-momentum, such that $\Omega_i - \Omega_j = \pm 1$. Such transitions are termed *perpendicular*. Conversely, *parallel* transitions occur where $\alpha_{zZ} \neq 0$; in which case, $\Omega_i - \Omega_j = 0$. The transition moment for a parallel transition is given by,

$$\mu_{ij}^{\parallel} = 3\langle J_i M_i \Omega_i|\alpha_{zZ}|J_j M_j \Omega_j\rangle \int_0^\infty\int_{\boldsymbol{r}} \phi_i^\dagger(\boldsymbol{r};R)\chi_i^\dagger(R)\,\mu_z\,\phi_j(\boldsymbol{r};R)\chi_j(R)\,d\boldsymbol{r}\,dR, \tag{2.89}$$

with a similar expression for the perpendicular transition moment, $\mu_{ij}^{\perp}$.

It is convenient to define the parallel component of the *electronic transition moment* to be

$$R_{ij}^e(R) = \int_{\boldsymbol{r}} \phi_i^\dagger(\boldsymbol{r};R)\,\mu_z\,\phi_j(\boldsymbol{r};R)\,d\boldsymbol{r}. \tag{2.90}$$

Substituting this into Eq. (2.89) gives

$$\mu_{ij}^{\parallel} = 3\langle J_i M_i \Omega_i|\alpha_{zZ}|J_j M_j \Omega_j\rangle \int_0^\infty \chi_i^\dagger(R)R_{ij}^e(R)\chi_j(R)\,dR. \tag{2.91}$$

The transition rate defined by Eq. (2.69) is then given by

$$B_{ij} = \frac{\mu_{ij}^{\parallel}}{6\hbar^2\epsilon_0 c}\left|\int_0^\infty \chi_i^\dagger(R)R_{ij}^e(R)\chi_j(R)\,dR\right|^2 \underline{S}_{J_iJ_j\Omega_i\Omega_j}, \tag{2.92}$$

where the *Hönl-London factor* is a summation of line strength factors over all possible molecular orientations, given by

$$\underline{S}_{J_iJ_j\Omega_i\Omega_j} = \sum_{M_i,M_j} \left|3\langle J_i M_i \Omega_i|\alpha_{zZ}|J_j M_j \Omega_j\rangle\right|^2. \tag{2.93}$$

Explicit forms for the line strength factors are given in Hougen [56, Tab. 6] and the Hönl-London factors are listed here in Tab. 2.2. An identical form to Eq. (2.92) applies to perpendicular transitions, with $\mu_{ij}^{\perp}$ substituted for $\mu_{ij}^{\parallel}$.

	$\Omega_i = \Omega_j$	$\Omega_i = \Omega_j \pm 1$
$J_i = J_j + 1$	$\frac{(J_j+\Omega_j+1)(J_j-\Omega_j+1)}{J_j+1}$	$\frac{(J_j\pm\Omega_j+1)(J_j\pm\Omega_j+2)}{J_j+1}$
$J_i = J_j$	$\frac{2J_j+1}{J_j(J_j+1)}$	$\frac{(2J_j+1)(J_j\mp\Omega_j)(J_j\pm\Omega_j+1)}{J_j(J_j+1)}$
$J_i = J_j - 1$	$\frac{(J_j+\Omega_j)(J_j-\Omega_j)}{J_j}$	$\frac{(J_j\mp\Omega_j)(J_j\mp\Omega_j-1)}{J_j}$

Table 2.2: Hönl-London factors, $\underline{S}_{J_iJ_j\Omega_i\Omega_j}$, for single photon absorption and emission where the upper and lower states are indexed by i and j, respectively. The first column lists the summation $\sum_{M_iM_j}\left|3\langle J_iM_i\Omega_i|\alpha_{zZ}|J_jM_j\Omega_j\rangle\right|^2$, applicable to parallel transitions, and the second column lists $\sum_{M_iM_j}\left|3\langle J_iM_i\Omega_i|\alpha_Z^{\mp}|J_jM_j\Omega_j\rangle\right|^2$, relevant to perpendicular transitions. The rows refer to different angular-momentum transitions, and are applicable to the R, Q and P branches, in descending order.

For the case where $R^e_{ij}(R)$ varies little over the extent of the vibrational wavefunction, its value may be fixed at some average internuclear distance $\overline{R}$ and Eq. (2.92) further factorised according to,

$$B_{ij} = \frac{1}{6\hbar^2\epsilon_0 c}\left|R^e_{ij}(\overline{R})\right|^2 q_{ij}\underline{S}_{J_iJ_j\Omega_i\Omega_j}, \tag{2.94}$$

where the *Franck Condon factor* is defined to be

$$q_{ij} = \left|\int_0^\infty \chi_i^\dagger(R)\,\chi_j(R)\,dR\right|^2. \tag{2.95}$$

The separation of factors in Eq. (2.94) is convenient because the Hönl-London factors are completely specified by the upper- and lower-state symmetries, and the Franck Condon factors are straightforwardly calculable from theoretical potential-energy curves. The electronic transition moment may be determined from intensive *ab initio* calculations but is more commonly treated as a free parameter constrained by observed transition strengths.

2.8.4 Intensity interference effects

When diabatic electronic states are mixed perturbatively, the transition probability of the mixed levels may show the effects of quantum interference.

For the case of two-state mixing, the perturbed states may be written as linear combinations of pure states, $|i\rangle$ and $|k\rangle$,

$$\left|i'\right\rangle = c\,|i\rangle \pm (1-c^2)^{1/2}\,|k\rangle \tag{2.96}$$

$$\text{and } \left|k'\right\rangle = \mp(1-c^2)^{1/2}\,|i\rangle + c\,|k\rangle\,. \tag{2.97}$$

Here, the uncertainty in sign is decided by the sign of the perturbing off-diagonal matrix element, and it is assumed that $1/2 \le c^2 \le 1$, so that $|i'\rangle$ and $|j'\rangle$ consist mostly of $|i\rangle$ and $|j\rangle$ character, respectively.

The same coefficient, c, may be used to calculate the mixed transition moments, so

	$\Omega_i = \Omega_j$	$\Omega_i = \Omega_j \pm 1$
$J_i = J_j + 1$	$+$	$\pm$
$J_i = J_j$	$+$	$+$
$J_i = J_j - 1$	$+$	$\mp$

Table 2.3: Relative signs of M-independent rotational line strength factors, $\underline{S}^{1/2}_{J_i J_j \Omega_i \Omega_j} = \left(\sum_{M_i M_j} \left|\langle J_i M_i \Omega_i | \alpha_Z | J_j M_j \Omega_j \rangle\right|^2\right)^{1/2}$. Parallel and perpendicular transitions correspond to $\Omega_i = \Omega_j$ and $\Omega_i = \Omega_j \pm 1$, respectively. R, Q, and P rotational branches correspond to $J_i = J_j + 1$, $J_i = J_j$, and $J_i = J_j - 1$; respectively.

that,

$$|\mu_{i'j}|^2 = \left|c\mu_{ij} \pm (1-c^2)^{1/2}\mu_{kj}\right|^2 = c^2|\mu_{ij}|^2 + (1-c^2)|\mu_{kj}|^2 \mp 2c^2(1-c^2)\mu_{ij}\mu_{kj}, \tag{2.98}$$

and

$$|\mu_{k'j}|^2 = (1-c^2)|\mu_{ij}|^2 + c^2|\mu_{kj}|^2 \pm 2c^2(1-c^2)\mu_{ij}\mu_{kj}. \tag{2.99}$$

The transition probabilities and f-values of the mixed levels will be proportional to $|\mu_{i'j}|^2$ and $|\mu_{k'j}|^2$.

The first two terms in Eqs. (2.98) and (2.99) describe the sharing of transition probability according to the simple mixing fractions c^2 and $1 - c^2$. The final term introduces an interference phenomenon whereby extra strength is transferred from one mixed level to the other. The direction of this transfer depends on the signs of the interference terms, which are always opposite and given by the product of the signs of the perturbing matrix element, μ_{ij}, and μ_{kj}. The signs of μ_{ij} and μ_{kj} are, in turn, dictated by the signs of the diabatic electronic-transition moments, $R^e_{ij}(R)$ and $R^e_{kj}(R)$.

Total transition probability remains conserved when state mixing is introduced, so that

$$|\mu_{ij}|^2 + |\mu_{kj}|^2 = |\mu_{i'j}|^2 + |\mu_{k'j}|^2$$

. If more than two diabatic states are mixed together then the final set of mixed transition probabilities will depend on the relative signs of all perturbation matrix elements and electronic transition moments.

When the mixing of states discussed above occurs between electronic states of the same symmetry, as must be the case for all electronic perturbations, the preceding discussion is equally relevant to parallel and perpendicular transitions. However, rotational perturbations may mix excited states with Ω differing by ± 1. If both unperturbed states are electric-dipole accessible from a common lower state, then the perturbed transition moments are of mixed perpendicular and parallel character. This leads to an additional interference effect because of the mixing of perpendicular and parallel rotational line strength factors.

For unperturbed transitions, the signs of individual rotational line strength factors are irrelevant, with only the square of each factor appearing in the Hönl-London factors of Tab. 2.2. However, the sense of the interference term appearing in the perturbed transition moments of Eqs. (2.98) and (2.99) depends on the product of signs of individual rotational line strength factors. These factors are expressed as M-independent line strength factors, $\underline{S}^{1/2}_{J_i J_j \Omega_i \Omega_j}$, by Lefebvre-Brion and Field [90, Tab. 6.1] and Hougen [56, Tab. 6], and their

signs are summarised in Tab. 2.3. Critically, these signs are similar for P and R branch transitions of parallel transitions, but opposite in the perpendicular case. An interference effect is then observable when comparing the intensities of rotational lines arising from the P and R branches of the mixed transitions. The strength of rotational coupling increases according to $\sim J(J+1)$, and so will the magnitude of this effect. The observed P-branch f-values terminating on one of the mixed levels will increase with J while the other will decrease, and the reverse effect will occur in the R-branch. If the term series of the perturbed states cross at some particular J, the sign of the state mixing coefficient will be different on either side of the crossing point. In this case, the sense of the P/R intensity interference will dramatically reverse.

The most general case relevant to this thesis is that of an unmixed lower-state, and an upper state that combines multiple electronic states, possibly with different Ω. Then after generalising Eq. (2.98),

$$\left|i'\right\rangle = \sum_i \left|i\Omega_i\right\rangle \chi_i(R), \tag{2.100}$$

where the use of $\chi_i(R)$ as a mixing coefficient foreshadows the discussion in Sec. 2.11. The probability of a transition occurring between upper and lower states is then given by,

$$B_{ij} = \frac{1}{6\hbar^2\epsilon_0 c}\left|\sum_i\left(\int_0^\infty \chi_i^\dagger(R)R_{ij}^e(R)\chi_j(R)\,dR\cdot \underline{S}^{1/2}_{J_iJ_j\Omega_i\Omega_j}\right)\right|^2. \tag{2.101}$$

2.8.5 Experimental f-values

It is usually impossible to determine f-values from emission spectra because the distribution of excited levels from which the observed transitions initiate is likely to be unknown. Absorption experiments often involve excitation from an equilibrium ground state population and do not suffer from this difficulty.

An experimentally useful interpretation of the absorption cross section has this representing the probability of a photon with wavenumber ν being absorbed while attempting to traverse a unit length sample of gas of unit number density. The Beer Lambert law uses this definition to predict the reduction in intensity of a weak monochromatic photon beam passing through an absorbing gas, according to the equation

$$I(\nu) = I_0(\nu)e^{-\sigma(\nu)N}. \tag{2.102}$$

Here, $I_0(\nu)$ and $I(\nu)$ are the beam intensities before and after this traverse, respectively, and N is the *column density* of absorbing particles, given by the integral of absorber number density over the absorption path. The ν-dependent intensities are defined per unit area perpendicular to their propagation direction and per unit wavenumber.

The absorption cross section may be deduced from the *transmission cross section*, $I(\nu)/I_0(\nu)$, following the inversion of Eq. (2.102), according to

$$\sigma(\nu) = -\frac{1}{N}\ln\left(\frac{I(\nu)}{I_0(\nu)}\right). \tag{2.103}$$

Transitions are observed in ideal absorption experiments as finite width lines with the form of Eq. (2.78). The line strength of such a transition is proportional to the absorption cross section integrated over the entire line profile, $\int\sigma(\nu)d\nu$. Usually, reported

line strengths are listed as dimensionless f-values, given by,

$$f = \left(\frac{4\epsilon_0 m_e c^2}{e^2}\right)\frac{\int \sigma(\nu)d\nu}{\alpha}, \tag{2.104}$$

$$= 1.1296\times 10^{12}\frac{\int \sigma(\nu)d\nu}{\alpha}. \tag{2.105}$$

Here, Eq. (2.75) has been used to convert the integrated cross section to an f-value, and the second form is appropriate where the cross section and transition energy have units of cm^2 and cm^{-1}, respectively. The factor α is specific to each transition, and represents the fractional population of gas in the required initial state. This quantity will vary between experiments prepared in different ways.

In absorption experiments, the absorbing gas is usually held at a stable temperature and α is determined from the equilibrium thermal-distribution of ground-state rovibrational levels. Boltzmann statistics may be adopted for this purpose, so that

$$\alpha = \frac{(2J+1)I(J)}{\mathcal{N}}\exp\left(-\frac{E_{vJ}}{k_B T}\right). \tag{2.106}$$

Here, E_{vJ} is the energy of a particular ground-state rovibrational level, T is the ambient temperature, k_B is the Boltzmann constant, and $\mathcal{N}$ is the partition function,

$$\mathcal{N} = \sum_{v,J=0}^{\infty}(2J+1)I(J)\exp\left(-\frac{E_{vJ}}{k_B T}\right). \tag{2.107}$$

The factor $2J+1$ accounts for the degeneracy of the possible spatial-projections of total angular-momentum, and $I(J)$ accounts for the degeneracy of nuclear spin states, as discussed in Sec. 2.3. The latter appears only for homonuclear molecules and is restricted to a pair of values, constant for all odd and all even rotational levels. For the even-J levels of ground state $^{14}N_2$ and $^{15}N_2$, $I(J) = 2$ and 3, respectively, and in both cases the odd-parity levels are weighted by $I(J) = 1$.

In emission experiments, the distribution of initial-state levels will contain many rotational, vibrational and electronic states; and α will likely be unknown.

Oscillator strengths derived from Eq. (2.105) may be directly compared between experiments, and when combined with Eq. (2.70) provide the critical link between theoretically and experimentally determined transition strengths.

For a particular electronic-vibrational transition, the series of transitions between various lower and upper state rotational levels have strengths described by *line f-values*, $f_{J_i J_j}$. These quantities may be reduced further to *band f-values*, given by,

$$f_{J_i} = \frac{d_{J_j} f_{J_i J_j}}{\underline{S}_{J_i J_j \Omega_i \Omega_j}}. \tag{2.108}$$

Here, d_{J_j} represents the degeneracy of the initial-state rotational level J_j and $\underline{S}_{J_i J_j \Omega_i \Omega_j}$ are the Hönl-London factors of Table 2.2. Both of these quantities depend on the electronic symmetry of the upper or lower states. The Hönl-London factors include line strength contributions from each of the $J_j(J_j+1)$ projections of M_j. This factor is also included in the Boltzmann sum of Eq. (2.106) and so the factor d_{J_j} is necessary to compensate for this double counting. Table 2.4 lists degeneracy and Hönl-London factors that pertain to the N_2 transitions considered in this thesis.

Transition Type	Branch	d_{J_j}	$\underline{S}_{J_i J_j \Omega_i \Omega_j}$
$^1\Sigma \leftarrow {}^1\Sigma$	P	$2J_j + 1$	J_j
$^1\Sigma \leftarrow {}^1\Sigma$	R	$2J_j + 1$	$J_j + 1$
$^1\Pi \leftarrow {}^1\Sigma$	P	$2(2J_j + 1)$	$J_j - 1$
$^1\Pi \leftarrow {}^1\Sigma$	Q	$2(2J_j + 1)$	$2J_j + 1$
$^1\Pi \leftarrow {}^1\Sigma$	R	$2(2J_j + 1)$	$J_j + 2$

Table 2.4: Ground state degeneracy, d_{J_j}, and Hönl-London, $\underline{S}_{J_i J_j \Omega_i \Omega_j}$, factors relevant to the N_2 absorption transitions studied in this thesis. Indexed by upper-state J_i and lower-state J_j. The P, Q and R-branches correspond to $J_i - J_j = -1$, 0 and $+1$, respectively. In all cases the lower states is the ground state $X\,^1\Sigma_g^+$ and the upper-states have total symmetry of either $^1\Pi_u$ or $^1\Sigma_u^+$.

The utility of Eq. (2.108) arises because band f-values will show no rotational dependence for transitions between unperturbed electronic-vibrational states. Excepting, that is, for the effects of centrifugal distortion introduced by the contribution of E^{rot} of Eq. (2.23). Otherwise, any observed variation of band f-values within a rotational series immediately reveals the presence of perturbative mixing in either the upper or lower state. The ground state is completely unperturbed for the case of N_2, and such variations arise exclusively from perturbations among the excited states. Thus, for the purposes of this thesis the band f-values of Eq. (2.108) are usually indexed by excited-state J_i.

2.8.6 Instrument function and pressure dependence of *f*-values

A serious difficulty is frequently encountered in absorption experiments, induced by non-ideal instrumentation and appearing as an apparent pressure dependence of line f-values. The broadening of absorption features by a finite instrumental resolution leads to a systematic underestimate of f-values, even though the actual number of photons absorbed is independent of resolution. This phenomenon is discussed at length by Hudson and Carter [59] and Hudson [58], and briefly below.

Real spectrometers have a finite instrument resolution whereby the nominal beam intensity recorded at a particular energy actually contains spectral intensity from a range of energies,

$$I(\nu) = \int_{-\infty}^{\infty} I_{true}(\nu') F(\nu - \nu') d\nu'. \tag{2.109}$$

Here, the area normalised *instrument function*, $F(\nu')$, is narrowly peaked near $\nu' = 0$. The width of this peak defines the resolution of the instrument.

If the true cross section changes significantly over a spectral range smaller than the width of the instrument function then the application of Eq. (2.103) to a transmission spectrum will result in an artificially broadened cross section. More significantly, the integrated cross sectional area under a resonant feature observed in an instrument broadened spectrum will be underestimated because of the nonlinearity of Eq. (2.103). Line f-values determined from such spectra will then also be underestimated. This effect is greatest for deeply-absorbed lines, thus by sufficiently reducing the column density of absorbing gas (usually achieved by reducing the pressure) the true f-values may be approached. Unfortunately, in real experiments random noise appearing in the measurements of intensities will be to the detriment of f-value measurements of sparingly absorbed lines.

Even disregarding the effect of the instrument function, it is not possible to derive accurate f-values from saturated lines where $I(\nu)/I_0(\nu) \sim 0$. The worst case, however,

occurs when the blurring effect of a finite instrument function is combined with deeply absorbed narrow lines. In this case the observed transmission may not approach zero even for lines which are mortally saturated.

2.9 Electron excitation

Energy may be imparted to a molecule following its collision with a free electron. Assuming that the molecule is initially stationary, the energy transferred to it will be distributed as either translational kinetic-energy or an internal excitation. This internal excitation cannot normally be treated perturbatively, as is the case for collisions with a photon, because of complications arising from the slowness of the interaction, the indistinguishably of the colliding and target electrons, and because of the possibility of non-negligible momentum transfer.

In most experiments a beam of monochromatic electrons, with energy E_i, is directed at a low density sample of ground-state molecules. Those electrons that interact with the target molecules are detected with a range of residual energies, E_r, and scattered into a range of angles, θ, relative to the incoming beam. Knowledge of E_r, θ, and the electron energy loss, $W = E_i - E_r$, completely determines the kinematics of the scattering event. Additionally, the internal or kinetic energies of the excited molecule may be analysed, or that of any ejected particles where ionisation or dissociation occurs.

The excitation energy of the target molecule is simply equal to W and the momentum transferred to it, $\boldsymbol{K}$, is determined by the initial and residual momenta of the free electron, $\boldsymbol{k}_i$ and $\boldsymbol{k}_r$, respectively. The squared magnitude of the momentum transferred is then

$$K^2 = 4m_e \left[E_r + W/2 - \sqrt{E_r(W + E_r)} \cos\theta \right]. \tag{2.110}$$

An experimentally determined *differential energy loss cross section* is a measurement of the probability density of a scattered electron with a given initial energy and energy loss being detected at a particular scattering angle, and may be written

$$\frac{d^2\sigma(W,\theta,E_r)}{dW\,d\Omega} = \frac{2\pi I_r(W,\theta,E_r)\sin\theta}{I_i(E_i)}. \tag{2.111}$$

Here, I_i and I_r are the measured flux of impinging and scattered electrons, respectively, where the latter is detected over an infinitesimal element of solid angle, given by $d\Omega = 2\pi \sin\theta d\theta$, and energy loss, dW. When the flux of the incoming electron beam is not well known, the differential cross section of Eq. (2.111) may be established on a relative scale following normalisation by its sum over all angles, so that

$$\frac{d^2\sigma(W,\theta,E_r)}{dW\,d\Omega} = \frac{2\pi I_r(W,\theta,E_r)\sin\theta}{\int_0^\pi 2\pi I_r(W,\theta,Er)\sin\theta d\theta}. \tag{2.112}$$

The typical energy and angular resolutions of real electron detectors are insufficient to detect individual rotational transitions, although distinct vibrational bands are frequently observed. However, because the relation between detected beam flux and scattering cross section is linear, the summed strength of unresolved features will not be influenced by the resolution dependent effects discussed in Sec. 2.8.6.

None of the selection rules of Sec. 2.8.2 may be rigorously applied to electron induced transitions. Thus, many transitions may be observed that do not appear in optical spectra.

However, because of the introduced dependence on variables E_r and K, the interpretation of electron scattering cross sections is significantly more difficult than in the optical case.

2.9.1 Generalised oscillator strengths

A convergence between electron excitation and optical-absorption measurements occurs in the limit of very large electron energies and small scattering angles, i.e., with small K^2 [20, 61]. This similarity leads to electron excitations that obey the electric-dipole transition selection rules of Sec. 2.8.2 and possessing identical oscillator strengths to those determined from optical-absorption experiments.

For sufficiently high, but nonrelativistic, electron energies the first-order Born approximation provides a reasonable means of calculating the differential cross section governing excitation from a molecular electronic-rotational-vibrational state $\phi_0(\bar{\boldsymbol{r}})$, to a state $\phi_n(\bar{\boldsymbol{r}})$. This is given by

$$\frac{d\sigma_n(W,\theta)}{d\Omega} = \frac{m_e^2}{4\pi^2\hbar^4}\frac{k_r}{k_i}\left|\int e^{-i\boldsymbol{k}_r\cdot\boldsymbol{r}}\phi_n(\bar{\boldsymbol{r}})V\phi_0(\bar{\boldsymbol{r}})e^{i\boldsymbol{k}_i\cdot\boldsymbol{r}}d\boldsymbol{r}d\bar{\boldsymbol{r}}\right|^2, \tag{2.113}$$

where the molecular wavefunctions are written in molecular-frame coordinates and the free electron is represented before and after the scattering event by plane waves. This representation is appropriate for the case of negligible rotation and vibration of the molecule during the scattering event. The interaction operator in Eq. (2.113) includes electrostatic forces but not the effects of electron exchange, so that

$$V = \sum_{j=1}^{Z}\frac{e^2}{|\boldsymbol{r}-\boldsymbol{r}_j|} - \frac{Ze^2}{\boldsymbol{r}}, \tag{2.114}$$

where the summation is over all Z electrons orbiting the neutral target molecule. The summation in Eq. (2.114) denotes the repulsive force between scattered and target electrons, and the final term encodes the attraction between the positively-charged nuclei and the scattered electron.

A simplification of Eq. (2.113) is described in Inokuti [61] and leads to the alternative form,

$$\frac{d\sigma_n(W,\theta)}{d\Omega} = \frac{4m_e e^2}{\hbar^2}\frac{k_r}{k_i}K^{-2}\left|\mathcal{M}_n(\boldsymbol{K})\right|^2, \tag{2.115}$$

where all details of the molecular wavefunction are contained within the *Born generalised electronic transition moment*, defined to be

$$\mathcal{M}_n(\boldsymbol{K}) = \int\phi_n(\boldsymbol{r}_1\ldots\boldsymbol{r}_Z)K^{-1}\sum_{j=1}^{Z}e^{i\boldsymbol{K}\cdot\boldsymbol{r}_j}\phi_0(\boldsymbol{r}_1,\ldots\boldsymbol{r}_Z)d\boldsymbol{r}_1\ldots d\boldsymbol{r}_Z. \tag{2.116}$$

Writing this in ket notation, and expanding the exponential term in a power series, leads to the following limiting value for the case of small momentum transfer,

$$\lim_{K\to 0}\mathcal{M}_n(\boldsymbol{K}) = \left\langle n\middle|K^{-1}\sum_{j=1}^{Z}i\boldsymbol{K}\cdot\boldsymbol{r}_j\middle|0\right\rangle. \tag{2.117}$$

The transition matrix element in Eq. (2.117) is independent of the magnitude of $\boldsymbol{K}$, and is formally identically to the electric-dipole transition moment of Eq. (2.68). The

dimensionless *generalised electronic oscillator-strength* is defined in order to exploit this identity, and is given by

$$f_n(E_r,\theta) = \frac{K^2 W}{2}\frac{k_i}{k_r}\frac{d\sigma_n(W,\theta)}{d\Omega}. \tag{2.118}$$

All quantities in Eq. (2.118) may be determined experimentally, although real measurements of $d\sigma_n(W,\theta)/d\Omega$ will be hampered by finite energy and angular resolutions, and the presence of overlapping excitation channels. The generalised electronic oscillator strength may also be calculated theoretically by substituting Eq. (2.115) into Eq. (2.118), so that

$$f_n(K) = \frac{2m_e^2 e^2}{\hbar^2} W \left|\mathcal{M}_n(K)\right|^2. \tag{2.119}$$

Here, the argument of $\mathcal{M}_n$ is reduced to a scalar quantity following the assumption of randomly polarised target molecules, and the energy loss W coincides with the resonant energy of excitation into state n. A differential generalised electronic oscillator strength may be defined to incorporate the effects of continuum excitation.

In the limit of small momentum transfer the generalised oscillator strength is directly comparable to the optical oscillator strength,

$$\lim_{K\to 0} f_n(K) = f_n. \tag{2.120}$$

For a given incoming E_r and W, measurements are made as a function of scattering angle. However, Eq. (2.119) implies that K constitutes a more illustrative independent variable. That is, for sufficiently large electron energies and small scattering angles the observed generalised electronic oscillator strength will depend only on the momentum transferred, and be independent of all other scattering conditions.

The concept of the generalised electronic oscillator strength may be usefully extended to scattering energies which are too low to justify the use of Eq. (2.113). Lewis *et al.* [102] adopt a weaker assumption than the Born approximation, requiring only that the duration of scattering be significantly shorter than the rotational and vibrational periods of the target molecule. It is also assumed that the ground and excited states of the molecule are well described by Born-Oppenheimer wavefunctions in the form of Eq. (2.12), with lower and upper vibrational levels denoted by v'' and v', respectively. Then, the *adiabatic-nuclei generalised oscillator-strength* describing electronic excitation is defined to be,

$$f^{AN}_{nv',0v''}(K) = \frac{2m_e^2 e^2}{\hbar^2} W \left|\left\langle \chi_{nv'}(R)\middle|\mathcal{M}^{AN}_n(K;R)\middle|\chi_{0v''}(R)\right\rangle\right|^2. \tag{2.121}$$

Here, the generalised electronic transition moment $\mathcal{M}^{AN}_n(K;R)$ contains all reference to the electronic part of the molecular wavefunction. In many cases the R-dependence $\mathcal{M}^{AN}_n(K;R)$ will be slight over the extent of the radial wavefunctions $\chi_{0v''}(R)$ and $\chi_{nv'}(R)$. Then, the relative strengths of vibrational transitions to a common excited electronic state will be determined purely by their Frank Condon factor, calculated according to Eq. (2.95).

Equation (2.121) may be extended further to the case of an excited state which is perturbed and requires the provision of a coupled wavefunction in a form defined below by Eq. (2.127). In this case,

$$f^{AN}_{i,0v''}(K) = \frac{2m_e^2 e^2}{\hbar^2} W \left|\sum_{j=1}^{N_T}\left\langle \chi_{ij}(R)\middle|\mathcal{M}^{AN}_j(K;R)\middle|\chi_{0v''}(R)\right\rangle\right|^2, \tag{2.122}$$

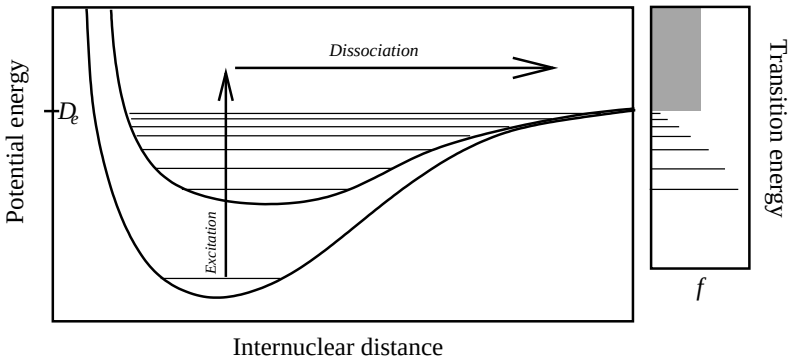

Figure 2.2: Potential-energy diagram representative of discrete and dissociative excitation. Transitions into a series of excited bound levels result in a discrete spectrum, f, terminating below the dissociation energy, D_e. Excitation above D_e leads to a continuous spectrum.

and the effects of quantum interference are included in the summation of $\mathcal{M}_j^{AN}$. The strength of a particular vibrational transition will be strongly dependent on the mixing of electronic character and the relative strengths of vibrational transitions arising from a particular nominal electronic transition will not exhibit a Frank Condon distribution.

2.10 Dissociation

Transitions between bound levels have been discussed above, but a diatomic molecule may also acquire sufficient energy, following excitation, to completely overcome the electromagnetic attachment between its constituent particles. In this case, an electron may be completely severed from the molecule in an ionisation event, or the nuclei may become dissociated and separated atoms formed.

Figure 2.2 depicts a dissociative excitation event as well as a qualitative absorption spectrum on either side of the minimum dissociation energy, D_e. The onset of a continuous spectrum is abrupt but there is a continuity of oscillator-strength density across the dissociation limit [2, 100]. That is, the quantities $f_{ij}/\Delta G_i$ and $df_j/d\nu$ join smoothly. Here, f_{ij} is the f-value of a particular bound–bound excitation from state j to state i, ΔG_i is the separation of state i from its neighbouring vibrational levels, and $df_j/d\nu$ is the oscillator-strength per unit spectral energy considering excitation from j into the dissociation continuum.

Predissociation [35, 54] may occur where, at a particular energy, two excited electronic states exist, one of which is bound and the other unbound. Then, if there is a perturbing matrix element mixing the two, a molecule initially excited into a bound level may irreversibly transit into the unbound state and dissociate. This decay will possess a characteristic lifetime, τ_d. Alternatively, the excited bound-level may decay via emission to one, or multiple, lower energy bound-levels; engendering a set of further decay lifetimes, $\tau_1, \tau_2, \ldots, \tau_n$. The total lifetime, τ, of the bound-level is then given by,

$$\tau^{-1} = \tau_d^{-1} + \sum_{i=1}^{n} \tau_i^{-1}, \tag{2.123}$$

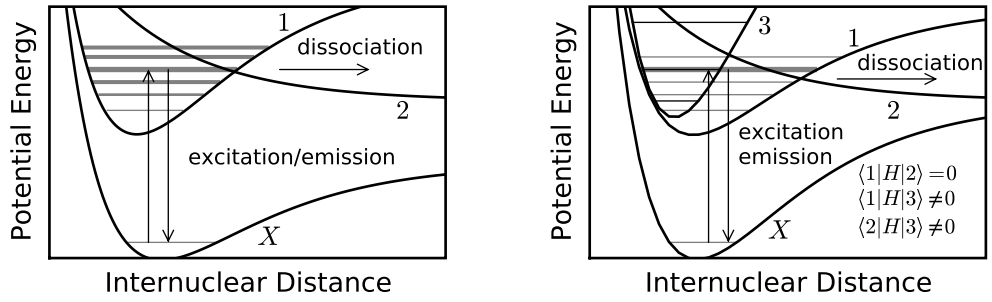

Figure 2.3: *(a):* A schematic example of perturbative mixing between states 1 and 2 following the excitation $1 \leftarrow X$. Predissociative decay competes with emission, apart from the first vibrational level of 1 which will be purely emissive because it lies below the dissociation energy of 2. *(b):* Depiction of an excitation to the fourth vibrational level of 1 which mixes perturbatively with the nearly degenerate bound-level of 3. An additional perturbation mixes 3 and 2. Thus indirect predissociation of 1 occurs, even though there is no direct coupling of 1 and 2. The other plotted vibrational levels of 2 will not be predissociated.

and the fraction of excited molecules that predissociate by,

$$\eta = \frac{\tau}{\tau_d}. \tag{2.124}$$

This *predissociation fraction* is a critical parameter in applications of atmospheric photochemistry where ongoing chemistry of the, possibly excited, atomic fragments is of concern.

The linewidth of a predissociated line is determined from its total lifetime according to Eq. (2.79). In many cases the predissociation process is sufficiently fast that emission is entirely suppressed, and the linewidth is inversely proportional to τ_d alone.

A sudden onset of predissociation may occur where a vibrational progression crosses the dissociation energy of a perturbing state, with all levels above this critical energy more or less affected. A schematic diagram of this scenario is depicted in Fig. 2.3. Photoemission from such a progression will dramatically decrease above the dissociation energy, or cease altogether if the predissociation fraction is ~ 1. Photoabsorption transitions terminating on the predissociated levels will not be weakened but will be broadened.

Indirect, or accidental, predissociation refers to the dissociative decay of a bound-level which is not directly perturbed by an unbound state; but instead decays via the mediation of a further, commonly-perturbing, bound level [3]. This situation is depicted in Fig. 2.3, where not all levels of state 1 are predissociated equally. In general this is a less common phenomena than direct predissociation, but has been observed, for example, in O_2 [99] and N_2 [111]. Indirect predissociation can be sensitive to isotopic substitution, which may affect the energy separation of the coupled bound-levels.

2.10.1 Fano lineshapes

It may occur that a particular dissociative state can be attained by multiple means beginning from a common initial state. For example, by direct excitation into an unbound continuum, or indirectly via predissociation mediated by an excited bound state. It also may occur that multiple bound or unbound states influence the appearance of a predissociative transition. The resulting quantum interference engenders resonances with *Fano*

line shapes [36, 99]. The energy dependence of an absorption cross section, $\sigma(\nu)$, corresponding to such a resonance may be written

$$\sigma(\nu) = \frac{2S}{\pi\Gamma\rho^2(1+q^2)}\left[1-\rho^2+\frac{\rho^2(q+x)^2}{1+x^2}\right], \quad x = 2(\nu-\nu_0)/\Gamma. \tag{2.125}$$

Here, ν_0, and Γ are the resonance energy and line width, respectively. The dimensionless parameters ρ and q describe the overlap and relative phases of the bound and continuum wavefunctions and control the shape of the resultant resonance. Accordingly, $0 \leq \rho \leq 1$ and q may take any value. Finally, S is related to the total strength of the resonance. The original derivation of Eq. (2.125) by Fano [35] concerns the competing processes of direct ionisation of atoms and preionisation via a bound level. In the present case, direct dissociation is discounted and competing absorption into multiple predissociative bound levels is responsible for the observed quantum interference.

Some depictions of Fano line shapes are shown in Fig. 2.4 for various values of ρ and q. A Lorentzian line shape is reproduced when $q \to \pm\infty$, in which case S is the

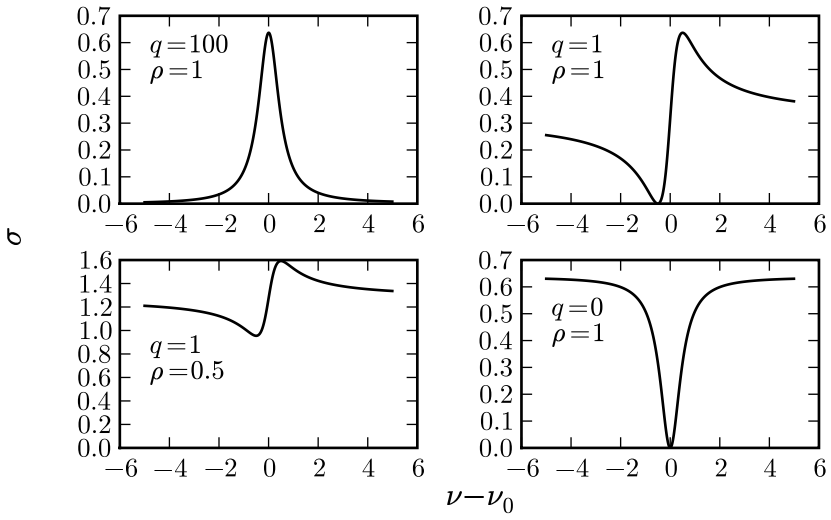

Figure 2.4: Some examples of Fano line shapes. In all cases $\Gamma = 1$ and $S = 1$. For $q < 0$ the resonance maximum occurs at lower energy than the minimum.

integrated cross sectional area of the resonance. For $q = 0$, a Lorentzian-shaped dip in the continuum background occurs, with the integrated reduction in cross section equal to S. For intermediate q the line shape is asymmetrical and the interpretation of S is less conveniently defined. Also, in this case the resonance centre will lie between the cross section extrema. For $\rho < 1$ the interference between bound and continuum levels is incomplete and the cross section does not decrease to zero.

Fano predissociation line shapes have been observed in vacuum ultraviolet photoabsorption spectra of molecular oxygen [99].

2.11 Solving the coupled Schrödinger equation

2.11.1 Basic formulation

Observable properties calculated from Born-Oppenheimer wavefunctions, Eq. (2.12), often do not agree with measured spectra within experimental uncertainty. The various perturbative terms discussed in Sec. 2.4 to Sec. 2.6 that are neglected by Born-Oppenheimer formulations are responsible for the majority of these discrepancies. Fundamentally, no set of electronic wavefunctions, whether adiabatic or diabatic, will simultaneously diagonalise all terms in the Hamiltonian of Eq. (2.8).

An improvement over the Born-Oppenheimer wavefunctions of Eq. (2.12) may be made by adopting a coupled representation,

$$\psi_i(\boldsymbol{r}, R, \theta, \varphi) = \sum_{j=1}^{N_T} \frac{1}{R}\chi_{ij}(R)\phi_j(\boldsymbol{r}; R)\Theta_j(\theta, \varphi). \tag{2.126}$$

Here $\psi_i(\boldsymbol{r}, R, \theta, \varphi)$ is the complete coupled-wavefunction and the pairs $\phi_j(\boldsymbol{r}; R)\Theta_j(\theta, \varphi)$ span a set of N_T diabatic (or adiabatic) electronic rotational-states that may be intermingled by perturbations. For convenience of notation, these pairs shall be henceforth combined into electronic-rotational states $\phi_j(\boldsymbol{r}; R)$, with the θ and φ coordinates subsumed into $\boldsymbol{r}$, so that

$$\psi_i(\boldsymbol{r}, R) = \sum_{j=1}^{N_T} \frac{1}{R}\chi_{ij}(R)\phi_j(\boldsymbol{r}; R). \tag{2.127}$$

Equation (2.127) represents a generalisation of the Born-Oppenheimer separation-of-variables, where now the total wavefunction is described by a linear combination of N_T product functions of electronic, rotational and nuclear-radial wavefunctions; instead of just one. The elements of $\chi_{ij}(R)$ no longer support the interpretation of vibrational wavefunctions, instead they have devolved to being R-dependent expansion coefficients of the $\phi_j(\boldsymbol{r}; R)$ basis set. The electronic-rotational basis is frequently described as a set of *coupled channels*, this terminology arising from analogous problems arising in scattering physics.

In principle, any complete set of $\phi_j(\boldsymbol{r}; R)$ may be used to represent $\psi_i(\boldsymbol{r}, R)$ to arbitrary precision, as long as a sufficiently large number of terms are included. However, the efficient calculation of $\psi_i(\boldsymbol{r}, R)$ will be greatly facilitated by an insightfully-chosen minimally-sized basis. Because the interaction energies of perturbations between Born-Oppenheimer states are significantly less than the energies of the states themselves, these form an excellent basis for $\phi_j(\boldsymbol{r}; R)$. When choosing between adiabatic or diabatic representations, whichever involves smaller perturbation matrix elements will likely prove more convenient. Here, a diabatic basis has been adopted, and so the $\phi_j(\boldsymbol{r}; R)$ are written with R listed as a parameter only.

The use of a Born-Oppenheimer basis will ensure the satisfaction of the orthonormality condition

$$\int \phi_i^\dagger(\boldsymbol{r}; R)\phi_j(\boldsymbol{r}; R)\, d\boldsymbol{r} = \delta_{ij}, \tag{2.128}$$

where all integrations from hereon span all electronic and nuclear rotational coordinates, $\boldsymbol{r}$.

Beginning from Eq. (2.127), and adopting the separated Hamiltonian of Eq. (2.8), the

Schrödinger equation may be written,

$$\sum_{j=1}^{N_T}\left(H^{el}+H^{rot}+H^{vib}\right)\frac{1}{R}\chi_{ij}\phi_j = E\sum_{j=1}^{N_T}\frac{1}{R}\chi_{ij}\phi_j, \tag{2.129}$$

where function arguments have been dropped for brevity. Then, multiplying by ϕ_k and integrating,

$$\sum_{j=1}^{N_T}\int\phi_k^\dagger\left(H^{el}+H^{rot}+H^{vib}\right)\phi_j\frac{1}{R}\chi_{ij}\,d\boldsymbol{r} = E\sum_{j=1}^{N_T}\frac{1}{R}\chi_{ij}\int\phi_k^\dagger\phi_j\,d\boldsymbol{r}. \tag{2.130}$$

Employing the commutation relations of Eq. (2.15) and Eq. (2.16) as well as the orthonormality expressed by Eq. (2.128), this expression becomes

$$\sum_{j=1}^{N_T}\left[\frac{1}{R}\chi_{ij}\int\phi_k^\dagger H^{el}\phi_j\,d\boldsymbol{r}+\frac{1}{R}\chi_{ij}\left(\frac{\hbar^2\mathcal{R}_k(\mathcal{R}_k+1)}{2\mu R^2}\delta_{jk}+H^{rot}(1-\delta_{jk})\right)\right.$$
$$\left.+\int\phi_k^\dagger H^{vib}\phi_j\frac{1}{R}\chi_{ij}\,d\boldsymbol{r}\right] = E\sum_{j=1}^{N_T}\frac{1}{R}\chi_{ij}\delta_{jk}. \tag{2.131}$$

The three bracketed terms in Eq. (2.131) require further explanation. Considering the first of these: when $k=j$ this represents the electronic potential-energy, $E_k^{el}(R)$, of Eq. (2.19). For $k\neq j$, this is the interaction energy between the diabatic states $\phi_k(\boldsymbol{r};R)$ and $\phi_j(\boldsymbol{r};R)$, and arises from terms neglected from the electronic part of the Hamiltonian as well as the spin-orbit operator. This term is precisely zero only if an adiabatic basis is adopted and for no nuclear rotation. The second term in brackets is the nuclear rotational energy of Eq. (2.23) with diagonal elements $\hbar^2\mathcal{R}_k(\mathcal{R}_k+1)/2\mu R^2$ as well as off-diagonal elements which mix different rotational-electronic states because of the L-uncoupling and S-uncoupling operators. Off-diagonal elements of the final term are set to zero by assuming a sufficiently weak R-dependence of diabatic electronic states.

Using the H^{vib} of Eq. (2.11), Eq. (2.131) may be simplified to

$$\frac{-\hbar^2}{2\mu}\frac{d^2}{dR^2}\chi_{ik}(R)+\sum_{j=1}^{N_T}\chi_{ij}(R)V_{jk}(R) = E\chi_{ik}(R), \tag{2.132}$$

where the *interaction parameters* are given by,

$$V_{jk}(R) = \begin{cases} E_j^{el}(R)+\frac{\hbar^2\mathcal{R}_k(\mathcal{R}_k+1)}{2\mu R^2} & j=k \\ \int\phi_j^\dagger(\boldsymbol{r};R)(H^{el}+H^{rot})\phi_k(\boldsymbol{r};R)\,d\boldsymbol{r} & j\neq k \end{cases} \tag{2.133}$$
$$= V_{kj}(R). \tag{2.134}$$

As discussed in Sec. 2.5, the nuclear rotational part of the diagonal elements in Eq. (2.133) are not strictly quantised to integer values of $\mathcal{R}_j$.

For each possible i there are $k=1\ldots N_T$ equations with the form of Eq. (2.132), and these must be solved simultaneously. There will be $i=1\ldots N_T$ linearly-independent solutions to Eq. (2.132), although it will be seen that many of these solutions are physically unreasonable once boundary conditions have been specified in Secs. 2.11.3 and 2.11.4.

By writing the members of $\psi_i(R)$ and $\phi_j(R)$ as the elements of $N_T \times 1$ vectors, and forming $\chi_{ij}(R)$ into a $N_T \times N_T$ matrix, all solutions to Eq. (2.127) may be simultaneously expressed in matrix form,

$$\boldsymbol{\psi}(\boldsymbol{r}, R) = \frac{1}{R}\boldsymbol{\chi}(R)\boldsymbol{\phi}(\boldsymbol{r}; R). \tag{2.135}$$

Similarly, Eq. (2.132) can be rewritten,

$$\frac{d^2}{dR^2}\boldsymbol{\chi}(R) = \frac{-2\mu}{\hbar^2}\boldsymbol{\chi}(R)\big[E\boldsymbol{I} - \boldsymbol{V}(R)\big], \tag{2.136}$$

where $\boldsymbol{I}$ is the identity matrix and elements of the *interaction matrix*, $\boldsymbol{V}(R)$, are given by Eq. (2.133).

Equation (2.136) is solved in the next section.

2.11.2 The renormalised Numerov method

The nuclear Schrödinger equation has been solved many times as an ordinary differential equation [Eq. (2.21)] [66, 140] or as a set of coupled-equations [Eq. (2.136)][41, 67]. This section describes the renormalised Numerov method [66, 67, 83, 167], an efficient integration scheme for solving the coupled equations, and appropriate where diabatic states are employed. The formalism below is also applicable to single channel problems following a trivial reduction from matrix to functional form.

For a problem coupling N_T channels, $\boldsymbol{\psi}(\boldsymbol{r}, R)$ and $\boldsymbol{\phi}(\mathbf{r}; R)$ of Eq. (2.135) are $N_T \times 1$ vectors; and $\boldsymbol{\chi}(R)$ and $\boldsymbol{V}(R)$ of Eq. (2.136) are $N_T \times N_T$ matrices. Each row of $\boldsymbol{\chi}(R)$ is an independent solution of Eq. (2.136). The diagonal elements of $\boldsymbol{V}(R)$ in Eq. (2.133) are the potential-energy curves representing the electronic and rotational energies of the ensemble of channels, and the significantly smaller off-diagonal elements are the various coupling terms between channels.

Following discretisation of the R coordinate into a series of points, R_n ($n = 1$ to N, with separation $R_n - R_{n-1} = h$) all quantities are referenced to a particular grid point by subscription.

First, some convenient matrices are defined,

$$\boldsymbol{T}_n = \frac{-h^2}{12}\frac{2\mu}{\hbar^2}(E\boldsymbol{I} - \boldsymbol{V}_n), \tag{2.137}$$

$$\boldsymbol{F}_n = (\boldsymbol{I} - \boldsymbol{T}_n)\boldsymbol{\chi}_n \tag{2.138}$$

$$\boldsymbol{U}_n = (\boldsymbol{I} - \boldsymbol{T}_n)^{-1}(2\boldsymbol{I} + 10\boldsymbol{T}_n). \tag{2.139}$$

It is then possible to write a 3-step recurrence formula, the solution of which converges to that of Eq. (2.136) for sufficiently small h, given by,

$$\boldsymbol{F}_{n+1} - \boldsymbol{U}_n\boldsymbol{F}_n + \boldsymbol{F}_{n-1} = 0. \tag{2.140}$$

This is the *Numerov method* and essentially consists of a finite-difference approximation of the second derivative term in Eq. (2.136), as well as a numerically stable approximation to the right hand side term. This can be further reduced to the *renormalised Numerov method* by defining the quantity $\boldsymbol{R}_n$ by the matrix equation,

$$\boldsymbol{F}_{n+1} = \boldsymbol{R}_n\boldsymbol{F}_n. \tag{2.141}$$

Then, substitution of the resulting expressions for $\boldsymbol{F}_{n+1}$ and $\boldsymbol{F}_n$ into equation Eq. (2.140) gives a 2-step recurrence formula,

$$\boldsymbol{R}_n = \boldsymbol{U}_n - \boldsymbol{R}_{n-1}^{-1}. \tag{2.142}$$

Physically, $\boldsymbol{F}_n$ is very similar in form to $\boldsymbol{\chi}_n$, being *renormalised* by $\boldsymbol{I} - \boldsymbol{T}_n$. $\boldsymbol{R}_n$ is then closely related to the ratio $\boldsymbol{\chi}_{n+1}/\boldsymbol{\chi}_n$. Iteration of Eq. (2.142) requires fewer matrix multiplications at each step than Eq. (2.140).

A recipe for obtaining coupled-channels solutions is as follows: specify $\boldsymbol{V}_n$ and E; calculate $\boldsymbol{T}_n$ and $\boldsymbol{U}_n$; specify a boundary condition at $n = 1$, in order to determine $\boldsymbol{R}_1$; iterate Eq. (2.142) from $n = 1$ to N; specify a further boundary condition defining $\boldsymbol{F}_1$; iterate $\boldsymbol{F}_n$ using Eq. (2.141) from $n = 1$ to N; determine $\boldsymbol{\chi}_n$ by inverting Eq. (2.138); and finally, normalise each row of $\boldsymbol{\chi}_n$.

During the iteration of Eq. (2.142), $\boldsymbol{R}_n \sim \boldsymbol{\chi}_n/\boldsymbol{\chi}_{n+1}$ may become excessively large at values of n where $\boldsymbol{\chi}_{n+1}$ approaches zero. In this case, Eq. (2.140) will remain finite and may be locally substituted for Eq. (2.142) in such regions.

The specification of boundary and normalisation-conditions depends upon the dissociation energies of the coupled potential-energy curves. Channels with $\lim_{R\to\infty} V(R) > E$ will support unbound radial wavefunctions, continuous with respect to E, and are termed *open channels*. *Closed channels* are those with $\lim_{R\to\infty} V(R) < E$, and in isolation will result in discrete bound wavefunctions. Further details of these two cases are given in Secs. 2.11.3, 2.11.4, and 2.11.5. In what follows the number of open and closed channels will be given by N_O and N_C, respectively, so that $N_T = N_O + N_C$.

2.11.3 All closed channels

For the case where all channels are closed, the radial wavefunction will be energetically constrained to a finite region and boundary conditions must be imposed requiring,

$$\boldsymbol{\chi}(R) = 0 \text{ and } \lim_{R\to\infty} \boldsymbol{\chi}(R) = 0. \tag{2.143}$$

Only particular values of E will result in solutions of Eq. (2.135) that satisfy these conditions. At each of these discrete energy eigenvalues, only one row of $\boldsymbol{\chi}(R)$ will represent a valid bound solution.

The first part of Eq. (2.143) may be inculcated into the renormalised Numerov method by setting $\boldsymbol{R}_1 = \boldsymbol{I}$; where R_1 is somewhere inside the innermost classical turning-point of the set of coupled channels, but need not be zero. This is equivalent to assuming that $\boldsymbol{\chi}(R_1) = 0$ and $\frac{d}{dR}\boldsymbol{\chi}(R_1) > 0$. The magnitude of $\boldsymbol{R}_1$ is not critical and will be revised during the eventual normalisation of $\boldsymbol{\chi}_n$.

A further recursion relation must be defined in order to encode a numerical form for the outer boundary condition of Eq. (2.143):

$$\boldsymbol{S}_n = \boldsymbol{U}_n - \boldsymbol{S}_{n+1}^{-1}, \tag{2.144}$$

where $\boldsymbol{S}_n$ is related to the ratio $\boldsymbol{\psi}_{n-1}/\boldsymbol{\psi}_n$, and defined by,

$$\boldsymbol{F}_{n-1} = \boldsymbol{S}_n \boldsymbol{F}_n. \tag{2.145}$$

It is possible to recursively iterate Eq. (2.144) inwards, from $n = N$ to 1, once a value of S_N has been specified. In perfect symmetry with the inner boundary condition, it is

sufficient to set $\boldsymbol{S}_N = \boldsymbol{I}$, for some R_N greater than the outermost classical turning-point.

Equations (2.142) and (2.144) are iterated outwards and inwards, respectively, for a trial energy, E, after adopting the above boundary specifications. Recursion is halted at some common point, R_M, intermediate to all classical turning-points and the radial wavefunctions, $\boldsymbol{\chi}_R(R)$ and $\boldsymbol{\chi}_S(R)$, calculated from the outwards and inwards recursion, respectively. These must be continuous, and have continuous first derivative, across the matching point R_M in order to satisfy the regular properties of a wavefunction. The trial energy is modified if these conditions cannot be satisfied following a simple rescaling of either $\boldsymbol{\chi}_R(R)$ or $\boldsymbol{\chi}_S(R)$, until a successful energy eigenvalue has been identified. It is not necessary to evaluate $\boldsymbol{\chi}_R(R)$ and $\boldsymbol{\chi}_S(R)$ at every trial; instead, the quantity

$$\det \left| \boldsymbol{R}_M - \boldsymbol{S}_M^{-1} \right|$$

will be zero at the correct energies. A scheme for rapid convergence to a spectrum of energy eigenvalues without skipping any members is discussed in Johnson [67].

Once an energy eigenvalue, E_i, has been resolved, the corresponding $N_T \times 1$ eigenvector, $(\boldsymbol{\chi}_n)_i$, may be calculated from the solutions to Eq. (2.141) and Eq. (2.145) for small and large R_n, respectively. This requires the initial specification of $\boldsymbol{F}_1 = 1$ and $\boldsymbol{F}_N = 1$ and the rescaling of either solution to achieve continuity at R_M. The consequent application of Eq. (2.138) will give the radial wavefunction $\boldsymbol{\chi}_{in}$. In accordance with the probability-density interpretation of the radial wavefunction, the following normalisation condition must also be imposed,

$$\int_0^\infty \boldsymbol{\chi}_i^\dagger(R) \boldsymbol{\chi}_i(R)\, dR = 1, \tag{2.146}$$

where the actual integral is approximated using the discrete values of $(\boldsymbol{\chi}_n)_i$.

2.11.4 Boundary conditions for open channel wavefunctions

This section considers the case where the total energy, E, is higher than the dissociation energy of at least one of the coupled electronic-rotational states, that is, at least one channel is open. Then, as long as $\boldsymbol{V}(R)$ cannot be blocked into any independent submatrices containing only closed-channels, all solutions vectors to Eq. (2.136), given by the rows of $\boldsymbol{\chi}(R)$, will contain an open-channel admixture. In this case, no bound radial-wavefunctions will be supported. Instead, the open channels provide a path to molecular dissociation so that the resultant radial-wavefunctions will extend to infinity and need not satisfy the previous outer boundary condition, $\lim_{R\to\infty} \boldsymbol{\chi}(R) = 0$. A new asymptotic boundary condition must then be imposed to correspond to the case of separated atoms. This scenario is reminiscent of a half-collision, and the formalism of scattering theory has been used by Mies (1980a, 1980b) [117, 118] to derive the correct asymptotic wavefunctions. The inner boundary condition, $\boldsymbol{\chi}(R) = 0$, is unaltered.

The two atomic products may be in the same or different, possibly excited, states and can be fully represented by the quantum numbers,

$$|iEJ\Pi\mathcal{R}\rangle\,.$$

Here, E is the combined internal-electronic and kinetic energies of the atoms; J is the total angular-momentum; Π is the total parity; $\mathcal{R}$ corresponds to the nuclear angular-momentum quantum number of Eq. (2.23) except at large R when the nuclei can no longer be considered a bound molecule, in this case $\mathcal{R}$ relates directly to the partial-waves

of scattering theory and is rigorously quantised; and i represents further degeneracies corresponding to all possible sublevels of orbital- and spin angular momenta internal to each atom, as well as the relative polarisation of these momenta between atoms. The various i correspond to different open-channels, and each results in a separate degenerate solution, enumerated by $i = 1$ to N_O.

Physical radial-wavefunctions exist for any total energy because the kinetic energy is not quantised, and solutions to Eq. (2.136) will be continuous with respect to E. The above set of quantum numbers corresponds to Hund's case (e) in molecular spectroscopy terms, which is the only Hund's case with quantum numbers that are all rigorously defined for separated atoms.

For the cases studied in this thesis, dissociation is a two-step process, photoabsorption followed by predissociation mediated by one or more open channels. Theoretical calculations of the absorption stage do not depend on the asymptotic wavefunction, but any experimentally observed dissociation products will require a theoretical description in terms of pure atomic states. This requirement restricts the form of the asymptotic interaction matrix in two ways: all off-diagonal elements must be zero, reflecting the non interaction of the remote atomic products; and the N_O diagonal elements corresponding to the dissociation energies of the open-channel potential-energy curves must equal the combined electronic-energies of a pair of pure atomic states, plus the nuclear-rotational kinetic-energy defined about the nuclear centre-of-mass. Then, neglecting contributions from terms of order R^{-3} and below, the asymptotic interaction matrix will have elements

$$\lim_{R\to\infty} V_{ij}(R) = \begin{cases} \lim_{R\to\infty} E_j^{el}(R) + \frac{\hbar^2\mathcal{R}_j(\mathcal{R}_j+1)}{2\mu R^2} & i = j, \\ 0 & i \neq j. \end{cases} \tag{2.147}$$

In this thesis, diabatic potential-energy curves and state interactions have been chosen which immediately conform to Eq. (2.147), otherwise, a diagonalisation of $\lim_{R\to\infty} \boldsymbol{V}(R)$ would be necessary.

The asymptotic wavefunctions approach the solutions of $N_T \times N_T$ uncoupled Schrödinger equations. After substituting Eq. (2.147) into Eq. (2.132) these asymptotic equations are of the form

$$\frac{-\hbar^2}{2\mu}\frac{d^2}{dR^2}\chi_{ij}(R) + \chi_{ij}(R)\left[\frac{\hbar^2\mathcal{R}_j(\mathcal{R}_j+1)}{2\mu R^2} - k_j^2\right] = 0, \tag{2.148}$$

where the asymptotic wavenumber, k_j, is real for open channels and imaginary for closed channels and is given by,

$$k_j^2 = \frac{2\mu}{\hbar^2}\left[E - \lim_{R\to\infty} E_j^{el}(R)\right]. \tag{2.149}$$

The general solution to Eq. (2.148) is of the form,

$$\lim_{R\to\infty} \chi_{ij}(R) = J_j(R)A_{ij} + N_j(R)B_{ij}, \tag{2.150}$$

where $J_j(R)$ and $N_j(R)$ are the well-known Bessel and Neumann functions [118] corresponding to spherical standing waves; the amplitudes A_{ij} and B_{ij} are dictated by the inner boundary condition and the structure of $\boldsymbol{V}(R)$ at small R. The inner boundary condition $\boldsymbol{\chi}(0) = 0$ is necessary but the choice of $\frac{d}{dR}\boldsymbol{\chi}(0)$ is arbitrary and each possible choice will result in a distinct set of A_{ij} and B_{ij}.

$J_j(R)$ and $N_j(R)$ converge to purely harmonic forms for sufficiently large R, so that

the asymptotic from of Eq. (2.150) is given by

$$\lim_{R\to\infty} \chi_{ij}(R) = k_j^{-\frac{1}{2}} \sin(k_j R - \pi\mathcal{R}/2) A_{ij} + k_j^{-\frac{1}{2}} \cos(k_j R - \pi\mathcal{R}/2) B_{ij}. \tag{2.151}$$

For convenience, the set of asymptotic solutions in Eq. (2.150) may be conveniently written in matrix form,

$$\lim_{R\to\infty} \boldsymbol{\chi}(R) = \boldsymbol{J}(R)\boldsymbol{A} + \boldsymbol{N}(R)\boldsymbol{B}, \tag{2.152}$$

where $\boldsymbol{J}(R)$ and $\boldsymbol{N}(R)$ are diagonal with nonzero elements $(\boldsymbol{J}(R))_{jj} = J_j(R)$, and similarly for $\boldsymbol{N}(R)$. Any linear recombination of the rows of $\chi_{ij}(R)$ will still solve the Eq. (2.132), and there is freedom to rearrange the calculated solutions with any unitary transformation, i.e., $\boldsymbol{\chi}^{\text{new}}(R) = \boldsymbol{\chi}(R)\boldsymbol{U}$.

For all closed channels, k_j is imaginary and Eq. (2.151) will contain only exponentially convergent and divergent terms. The latter are physically unacceptable so the following outer boundary condition must be wilfully imposed,

$$\lim_{R\to\infty} \chi_{ij}(R) = 0, \text{ if channel } j \text{ is closed.} \tag{2.153}$$

Then, N_C rows of $\boldsymbol{A}$ and $\boldsymbol{B}$ corresponding to closed channels will contain only zero elements and $\lim_{R\to\infty} \boldsymbol{\chi}(R)$ will only span N_O linearly-independent columns. It is then possible to further treat the asymptotic solutions given by Eq. (2.152) following the reduction of matrices to dimension $N_O \times N_O$ by temporarily discarding N_C rows and columns, and this is done hereafter. The rows corresponding to closed channels cannot be permanently discarded because they will contain nonzero elements inside their classical turning-points at small R. The influence of these is not directly expressed in the asymptotic solution but is still implied due to their interaction at small R.

The reduction of the asymptotic solutions of Eq. (2.148) to matrices $\boldsymbol{A}$ and $\boldsymbol{B}$ will prove to be convenient in Sec. 2.11.5, but the outer-boundary condition for open channels has yet to be specified. This problem is discussed in Mies [118] and Schinke [137, pp. 42, 69] and briefly covered here. The desired functional form for each of the asymptotic solutions is,

$$\lim_{R\to\infty} \chi^S_{ij}(R) = h^+_j(R)\delta_{ij} + h^-_j(R) S_{ij}, \tag{2.154}$$

where $h^-_j(R)$ and $h^+_j(R)$ are complex-valued linear-combinations of Bessel and Neumann functions,

$$h^+_j(R) = 2^{-\frac{1}{2}}\big[N_j(R) + iJ_j(R)\big], \tag{2.155}$$

$$\text{and } h^-_j(R) = 2^{-\frac{1}{2}}\big[N_j(R) - iJ_j(R)\big]. \tag{2.156}$$

Equation (2.154) will then have following the asymptotic form, after substitution of Eq. (2.151),

$$\lim_{R\to\infty} \chi^S_{ij}(R) = (2k_i)^{-\frac{1}{2}} e^{+i(k_i R - \pi\mathcal{R}/2)}\delta_{ij} + (2k_j)^{-\frac{1}{2}} e^{-i(k_j R - \pi\mathcal{R}/2)} S_{ij}. \tag{2.157}$$

Substituting Eq. (2.157) into Eq. (2.127), the asymptotic form of the total wavefunction

is given by,

$$\lim_{R\to\infty}\psi_i(\boldsymbol{r},R)=\mathcal{N}_i\left[\frac{1}{R}(2k_i)^{-\frac{1}{2}}e^{+i(k_iR-\pi\mathcal{R}/2)}\phi_i(\boldsymbol{r})+\sum_{j=1}^{N_O}\frac{1}{R}(2k_j)^{-\frac{1}{2}}e^{-i(k_jR-\pi\mathcal{R}/2)}\phi_j(\boldsymbol{r})S_{ij}\right]. \tag{2.158}$$

Equation (2.158) represents a physically-reasonable asymptotic solution and constitutes the necessary outer boundary condition. The first term is in the form of an outgoing spherical wave, with wavenumber k_i, and represents a pair of nuclei dissociating via the ith open channel. This form is then directly comparable with dissociation experiments, which observe atomic fragments in pure states. The remaining terms all have the form of incoming spherical waves and contain nonzero elements with $i\neq j$ because of the channel mixing that occurs at small R. The radial argument of the electronic wavefunctions, $\phi_i(\boldsymbol{r})$, has been dropped because any R-dependence at long range is purely the result of translation of the separated atoms, and it is simpler to consider the internal coordinates $\boldsymbol{r}$ of the electrons to be relative to their respective nuclear-centres. The normalisation constant, $\mathcal{N}_i$, has yet to be determined.

Molecular dissociation is an irreversible process, but it is being treated here by the time independent Schrödinger equation and therefore the calculated wavefunctions correspond to a steady-state. Thus, the presence of incoming waves in Eq. (2.158) is necessary to describe an inwards flux of particles that precisely balances the outwards flux represented by the single outwardly-propagating wave. As further illustration, a rearrangement of the dissociation wavefunctions of Eq. (2.158) leads to the similar form,

$$\lim_{R\to\infty}\psi_i(\boldsymbol{r},R)=\mathcal{N}_i\left[\sum_{j=1}^{N_O}\frac{(2k_j)^{-\frac{1}{2}}}{R}e^{+i(k_jR-\pi\mathcal{R}/2)}\overline{S}_{ij}\phi_j(\boldsymbol{r})+\frac{(2k_i)^{-\frac{1}{2}}}{R}e^{-i(k_iR-\pi\mathcal{R}/2)}\phi_i(\boldsymbol{r})\right], \tag{2.159}$$

which now describes incoming atoms in a pure state, and mixed-state outgoing atoms. This new formulation could be applied to studies of the elastic scattering of atoms.

It still remains to reshape the asymptotic radial solutions into the assumed form of Eq. (2.154). This may be done by adopting a matrix formulation in similar fashion to Eq. (2.152),

$$\lim_{R\to\infty}\boldsymbol{\chi}^S(R)=\boldsymbol{h}^+(R)+\boldsymbol{h}^-(R)\boldsymbol{S}, \tag{2.160}$$

then finding a unitary transformation matrix, $\boldsymbol{U}$, such that

$$\boldsymbol{\chi}^S(R)=\boldsymbol{\chi}(R)\boldsymbol{U}, \tag{2.161}$$

which, by substitution of Eq. (2.150) and Eq. (2.154) requires

$$\boldsymbol{h}^+(R)+\boldsymbol{h}^-(R)\boldsymbol{S}=\big[\boldsymbol{J}(R)\boldsymbol{A}+\boldsymbol{N}(R)\boldsymbol{B}\big]\boldsymbol{U}. \tag{2.162}$$

Whereupon, after writing $\boldsymbol{J}$ and $\boldsymbol{N}$ in terms of $\boldsymbol{h}^-$ and $\boldsymbol{h}^+$, according to Eq. (2.155) and Eq. (2.156),

$$\boldsymbol{h}^-(R)+\boldsymbol{h}^+(R)\boldsymbol{S}=2^{-\frac{1}{2}}\left[\boldsymbol{h}^+(R)(-i\boldsymbol{A}+\boldsymbol{B})+\boldsymbol{h}^-(R)(i\boldsymbol{A}+\boldsymbol{B})\right]\boldsymbol{U}. \tag{2.163}$$

Finally, equating the coefficients of $\boldsymbol{h}^-(R)$ and $\boldsymbol{h}^+(R)$ gives the desired unitary transfor-

mation,

$$\boldsymbol{U} = 2^{\frac{1}{2}}(-i\boldsymbol{A} + \boldsymbol{B})^{-1}, \tag{2.164}$$

as well as the $\boldsymbol{S}$ matrix,

$$\boldsymbol{S} = (i\boldsymbol{A} + \boldsymbol{B})(-i\boldsymbol{A} + \boldsymbol{B})^{-1}. \tag{2.165}$$

The total wavefunction of Eq. (2.127) must be spatially-normalised to unity. A normalisation procedure is described by Mies [118] in terms of the asymptotic wavefunction only. Then the correct value of the normalisation constant in Eq. (2.158) is

$$\mathcal{N}_i = \frac{\hbar^2\pi}{2\mu}. \tag{2.166}$$

2.11.5 Calculation of the open-channel wavefunctions

When solving the coupled-equations, with at least one open channel, the inward propagation of Numerov recursion is unnecessary. This is because the outer boundary condition of Eq. (2.143) is no longer applicable. Instead, the same inner boundary condition as for the case of uniformly closed channels, $\boldsymbol{R}_1 = \boldsymbol{I}$, is adopted as an initial value and Eq. (2.142) is iterated outwards from $n = 1$ to N. The value of R_N is selected to be sufficiently large that all of the coupled potential-energy curves will have approached their asymptotic values; in which case, further evaluation of $\boldsymbol{R}_n$ will result in $N_T \times N_T$ uncoupled solutions periodically oscillating in tune with their respective asymptotic wavenumbers. Equation. (2.141) may then be used to iteratively calculate $\boldsymbol{F}_n$ inwards from $n = N$. This step requires the specification of F_N and the following outer-boundary condition is chosen in order to suppress the nonphysical exponentially-increasing behaviour of the closed channels outside their classical turning points,

$$(\boldsymbol{F}_N)_{ij} = \begin{cases} 1 & i = j \text{ and channel } i \text{ is open,} \\ 0 & i = j \text{ and channel } i \text{ is closed,} \\ 0 & i \neq j. \end{cases} \tag{2.167}$$

At certain grid points $\boldsymbol{R}_n^{-1}$ may become poorly defined and Eq. (2.140) must be used to calculate $\boldsymbol{F}_n$, in place of Eq. (2.141). Finally, $\boldsymbol{\chi}_n$ is calculated from $n = 1$ to N by means of Eq. (2.138).

The outer boundary condition requires that each asymptotic channel corresponds to a particular pair of dissociated atomic states, and must now be enforced. First, the asymptotic wavefunctions, $\boldsymbol{\chi}_N$, are decomposed into spherical Bessel and Neumann functions. Then, if χ_N is one such wavefunction,

$$\chi_N = J_N A + N_N B. \tag{2.168}$$

Combining the expressions for χ_N and χ_{N-1}, A and B may be determined according to

$$A = \left(\frac{\chi_{N-1}}{N_{N-1}} - \frac{\chi_N}{N_N}\right)\left(\frac{J_{N-1}}{N_{N-1}} - \frac{J_N}{N_N}\right)^{-1}, \tag{2.169}$$

$$B = \left(\frac{\chi_{N-1}}{J_{N-1}} - \frac{\chi_N}{J_N}\right)\left(\frac{N_{N-1}}{J_{N-1}} - \frac{J_N}{N_N}\right)^{-1}. \tag{2.170}$$

The matrices $\boldsymbol{A}$ and $\boldsymbol{B}$ of Eq. (2.152) are composed of these elements.

The scattering matrix representation is not determined by directly applying Eq. (2.164). Instead the reactance matrix of scattering theory is first calculated, according to,

$$\boldsymbol{K} = \boldsymbol{B}\boldsymbol{A}^{-1}. \tag{2.171}$$

Using a standard linear-algebra diagonalisation technique, this is then decomposed into a product of two matrices according to

$$\boldsymbol{K} = \boldsymbol{M} \tan \boldsymbol{\xi} \boldsymbol{M}^{\dagger}. \tag{2.172}$$

Here, the columns of $\boldsymbol{M}$ are orthogonal and comprise the eigenvectors of $\boldsymbol{K}$, and the nonzero elements of the diagonal matrix $\tan \boldsymbol{\xi}$ are its corresponding eigenvalues. Furthermore, $\boldsymbol{\xi}$ are the phase shifts of scattering theory. An equivalent version of Eq. (2.164) in terms of the phase shift and eigenvectors of $\boldsymbol{K}$ is given by,

$$\boldsymbol{U} = \boldsymbol{A}^{-1} 2^{-\frac{1}{2}} i \boldsymbol{M} \cos \boldsymbol{\xi} e^{-i\boldsymbol{\xi}} \boldsymbol{M}^{\dagger}. \tag{2.173}$$

Finally, the coupled-channels solution must be transformed to the correct asymptotic form,

$$\boldsymbol{\chi}_n^S = \boldsymbol{\chi}_n \boldsymbol{U}. \tag{2.174}$$

2.12 Coupled channels cross sections

The numerical wavefunctions described in Sec. 2.11.3 and Sec. 2.11.5 must be combined with operators corresponding to observable quantities before they can be compared with an experiment. The cross section representing absorption from an unmixed lower-state to a coupled upper-state is one such observable, and may be computed by means of Eq. (2.101) and Eq. (2.74), according to

$$\sigma_{ij}(\nu) = \frac{\pi \nu}{3\hbar\epsilon_0} \left| \sum_k \left(\int_0^{\infty} \chi_{ik}^{\dagger}(R) R_{kj}^e(R) \chi_j(R)\, dR \cdot \underline{S}^{1/2}_{J_k J_j \Omega_k \Omega_j} \right) \right|^2 . \tag{2.175}$$

Here, R_{kj}^e is the R-dependent electric-dipole transition moment between the lower-state, j, and channel state k. Here, $\nu = (E_i - E_j)/2\pi\hbar c$ represents the wavenumber of an absorption transition, and E_i and E_j are the energies of state i and coupled-state j, respectively. Simpson's method is used to approximate the integral between model grid points once the various quantities appearing in Eq. (2.175) have been specified in numerical form.

If the set of coupled-channels are all closed, and $\chi_{ij}(R)$ has been calculated with E corresponding to a bound-state energy eigenvalue, then σ_{ij} and Eq. (2.75) may be used to calculate a discrete transition f-value. In an absorption experiment, this may be compared with the line f-value of an observed transition. If $\chi_{ij}(R)$ contains at least one open channel, and the asymptotic boundary conditions of Sec. 2.11.4 have been applied, then those i which correspond to open channels may be used to calculate an absorption cross-section, $\sigma_{ij}(\nu)$, which is continuous with respect to ν. In this case, transitions to closed-channel solutions are disregarded as nonphysical but nonetheless induce pseudo-resonant structure in the cross-sections calculated for open channels to which they are coupled. An example of a calculated cross section showing resonant behaviour is plotted in Fig. 2.5.

It is not necessary that all coupled states have nonzero transition moments, $R_{kj}^e(R)$.

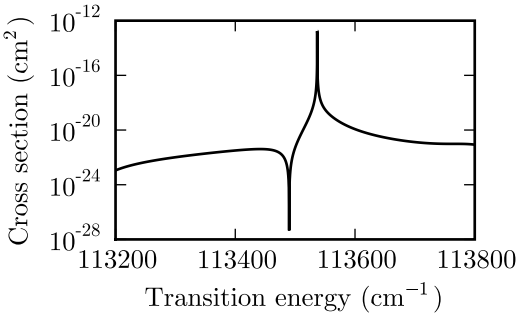

Figure 2.5: An example absorption cross section calculated by the coupled-channels method and showing a resonant feature with Fano lineshape and a varying background continuum.

Even nominally forbidden transitions may appear as resonances in the coupled-channels cross section if an inaccessible excited state obtains an admixture of nonzero transition moment because of off-diagonal elements in the interaction matrix.

Actual measurements of absorption are insensitive to the the final state of the dissociated atoms. The total absorption cross section is then found by summing over all open-channels, according to

$$\sigma_j(\nu) = \sum_{i=1}^{N_O} \sigma_{ij}(\nu). \tag{2.176}$$

The quantity $\sigma_{ij}(\nu)/\hbar\nu$ corresponds precisely to a partial photodissociation cross section. This is defined to be the rate of production of pairs of atomic dissociation products in state i, from a unit density sample of molecules in state j, exposed to a unit intensity photon beam of energy ν. This quantity may be directly compared with an experiment that detects the scattered atoms and analyses their kinetic energies. A dissociation cross section calculated in this way will only correspond to reality when the upper-state is certain to dissociate. If there exist alternative decay pathways, principally spontaneous emission, this calculation will overestimate the true photodissociation cross section; and the calculated pseudo-resonance lineshapes will not include the effects of emission broadening and appear narrower than reality.

The resonant feature in Fig. 2.5 dominates the surrounding continuum in terms of its peak cross section and the integrated cross section in its neighbourhood. Such resonances then comprise much of the useful information computed by the coupled-channels model. A calculated cross section may be summarised by parameterising the transition energies, strengths, and widths of the resonances that appear within it. In most cases a Lorentzian or Fano lineshape will be well-matched to the calculated resonances.

Regardless of the treatment of dissociative or emissive decay, the strength parameter of a Fano lineshape fitted to each model resonance is directly indicative of electric-dipole transition intensity and may be directly employed by Eq. (2.70) to calculate absorption f-values. These may be directly compared with experimental f-values. Additionally, the width of each resonance may be compared with experimental linewidths, or used to calculate the dissociative-decay lifetime according to Eq. (2.79).

2.12.1 Band models

In absorption experiments the predissociation rate of an excited state may be very fast and the observed rotational lines so broadened as to be indistinguishable. Alternatively,

individual rotational lines may be invisible due to poor experimental resolution. In these cases, a line-by-line comparison of experimental and model resonances will be fruitless and a model of an entire band must be considered instead. Such a band model would also suit those applications of synthetic spectra which are not interested in the properties of individual rotational lines. In what follows, quantities relating to the excited and ground states are labelled with single and double primes, respectively.

Total dissociation cross sections may be calculated for all possible rotational transitions according Eq. (2.176). These are combined into an absorption band model once each rotational transition has been weighted by its respective ground state fractional population. These weights, $\alpha_{J''}$, are calculated according to Eq. (2.106) and depend on the assumed temperature. For very high temperatures it may be necessary to consider multiple ground-state vibrational levels in Eq. (2.106). The combined cross section is then

$$\sigma(\nu) = \sum_{J'J''} \alpha_{J''} \sigma_{J'J''}(\nu), \tag{2.177}$$

where only rotational transitions that are permitted by the selection rules of Sec. 2.8.2 need be considered.

The cross section in Eq. (2.177) may be directly used by theoretical radiative-transfer models, or for comparison with an experimental transmission spectrum, in which case it must be further transformed according to

$$I(\nu) = I_0(\nu) \int_{-\infty}^{\infty} e^{-\sigma(\nu')N} F(\nu - \nu')\, 2\pi\hbar c d\nu'. \tag{2.178}$$

Here the column density, N; instrument function $F(\nu)$; and background intensity, $I_0(\nu)$ must be known *a priori* or determined as fitting parameters.

2.13 Rydberg states

A detailed discussion of electronic wavefunctions is beyond the scope of this thesis. However, in the case of *Rydberg states* a qualitative, and sometimes quantitative, understanding of the observed spectra may be obtained without any explicit electronic analysis. In regard to what follows, Mulliken [121] has written a review discussing many of the properties of Rydberg states and aspects of the theory of quantum defects are discussed in the collection edited by Jungen [71].

For a neutral molecule, Rydberg states may be approximated as the product of a positive ionic core, $\Psi^+(\boldsymbol{r})$, and a single Rydberg-electron with an orbital wavefunction, $\psi(\boldsymbol{r})$, with the majority of its radial extent beyond that of the core region. In comparison, the definition of a valence state requires all electrons to be near the molecular core, $R \lesssim 2\,\text{Å}$, so that all electrons in a valence state are spatially correlated.

The wavefunction of Rydberg state may be written, for some complete set of coordinates $\boldsymbol{r}$,

$$\Psi(\boldsymbol{r}) = \Psi^+(\boldsymbol{r})\psi(\boldsymbol{r}). \tag{2.179}$$

In this case the Rydberg electron will not be sensitive to the detailed structure of the ionic wavefunction and instead will move in a roughly-spherical attractive potential. Its properties will then resemble those of an electron bound to a hydrogen nucleus. The quality of this approximation will improve as the mean orbital radius of the Rydberg

electron increases, and its correlation with the core electrons is reduced. The function $\Psi^+(\boldsymbol{r})$ is expressed, as for a neutral molecule, in terms of molecular-frame coordinates and a rotation with respect to the laboratory frame; whereas, Rydberg orbitals are expressed in terms of non-rotating coordinates, as is done for atoms. Then Eq. (2.179) may be written

$$|EJ\rangle = \left|E^+ J^+ \Omega^+\right\rangle \left|E^R nl\lambda\right\rangle . \tag{2.180}$$

Here, the core state, with +-superscripts, is written in Hund's case (c) form, but may correspond to other limiting Hund's cases. The Rydberg electron is written in terms of principal and orbital angular-moment quantum numbers, n and l, as in the atomic case. The total energy and angular-momentum are divided between the core state and Rydberg electron, and E^+ is equivalent to the ionisation energy of the neutral molecule. Because there is always some correlation between the Rydberg electron and the non-sphericity of the core, the projection of Rydberg angular-momentum on the internuclear axis may be quantised according to the quantum number λ. The goodness' of l and λ are mutually exclusive and depend on the validity of the wavefunction separation expressed by Eq. (2.179). Frequently, an intermediate case occurs where neither l nor λ are strictly defined, but both form convenient labels and so are included in Eq. (2.180).

The energy levels of an experimental series of Rydberg states of increasing n, based on a common ionic core, and with common l, may be fit to the following form converging on the ionisation energy,

$$E_n = E^+ - Ry/(n - \delta_n)^2, \tag{2.181}$$

where Ry is the Rydberg constant and the *quantum defect*, δ, may be treated as a fitting parameter. The Rydberg constant is slightly mass dependent and in the case of $^{14}N_2$ has a value of $109\,735\,\mathrm{cm}^{-1}$.

The parameter δ_n is roughly analogous to the phase shift of scattering theory if the Rydberg electron is considered to be mostly remote from the ionic core, but periodically scattering from it. Alternatively, the inner part of the radial Rydberg-wavefunction will always deviate from that of a hydrogen orbital because of correlations with the core wavefunction, and the details of the interactions occurring in this region are encoded in δ_n. For Rydberg series with $l > 0$, δ_n is observed to approach a constant, nonzero, value for large n. This trend is consistent with the radial charge density distribution of analytic hydrogenic wavefunctions [143, p. 117] which are concentrated at increasing radius as n increases, apart from the case of $l = 0$ orbitals, for which there is no centrifugal repulsion.

The asymptotically stable value, $\delta_n \to \delta$, may be exploited during the extrapolation of Eq. (2.181) to unobserved energy levels. Further approximate properties of high Rydberg states may be predicted from δ alone [90, pp. 128, 570, 668; Chap. 8], and are discussed here briefly.

The increasing centrifugal barrier experienced by electrons of successively higher-l rapidly reduces their overlap with the core region. However, the shape of the core region wavefunction for constant l and increasing n remains largely unchanged, merely scaling in magnitude according to $\sim (n - \delta_n)^{-3/2}$.

If there is a perturbative matrix element operating between a Rydberg state and valence state, then an approximate factorisation may be made,

$$\langle \mathrm{core}^+ nl\lambda | H^{pert} | \mathrm{valence} \rangle = \langle \mathrm{core}^+ | H^{pert} | \mathrm{valence} \rangle \langle nl\lambda | H^{pert} | \mathrm{valence} \rangle. \tag{2.182}$$

The first factor describes any interaction between the Rydberg-core and valence states and will be constant with regard to the state of the Rydberg electron. The contribution of the Rydberg electronic wavefunction to the second factor will be zero except for the innermost part where it overlaps with the valence wavefunction. Then, in consideration of the above approximate scaling of the Rydberg radial wavefunctions,

$$\langle \mathrm{core}^+ nl\lambda | H^{pert} | \mathrm{valence} \rangle \approx (n - \delta_n)^{-3/2}. \tag{2.183}$$

An application of this relation may be made to the decrease in absorption strength with increasing n observed for many Rydberg series, in which case the electric-dipole operator of Eq. (2.67) must be substituted for H^{pert}.

Equation (2.183) may be extended to the case of two mutually-perturbing Rydberg states. When these are built upon different cores, or the same core with different l, their interaction energy scales as, approximately

$$\langle \mathrm{core}_i^+ n_i l_i \lambda_i | H^{pert} | \mathrm{core}_j^+ n_j l_j \lambda_j \rangle \approx (n_i - \delta_i)^{-3/2} (n_j - \delta_j)^{-3/2}. \tag{2.184}$$

Rydberg states built upon a common core, and with common l and λ, but having different values of n; are assumed to be completely noninteracting. For the case where both states have high principal quantum numbers, their wavefunctions will be hydrogenic and orthogonal, prohibiting electronic interactions; and the Rydberg electrons will be completely independent of the nuclear-coordinates and so these states will not be mixed by rotational or nonadiabatic perturbations.

An important case occurs for two Rydberg states, i and j, with common ion core, n, and l; but where $\lambda_i - \lambda_j = 1$. Under these circumstances it must be that $\Lambda_i - \Lambda_j = 1$ and the two states differ by only one electron orbital, namely the Rydberg electron. All conditions are then satisfied for the existence of a rotational perturbation between the two states and the magnitude of the interaction may be simply estimated by considering the *pure precession* approximation, with detailed discussions given by Hougen [56, Sec. 4.3] and Lefebvre-Brion and Field [90, p. 327]. The relevant off-diagonal matrix element may be derived from Eq. (2.47) where, because the configurations of the perturbed states differ only in the Rydberg electron, $L^{\pm}$ is equivalent to $l^{\pm}$. Then,

$$\langle i | H^{rot}(R) | j \rangle = \left\langle J(\Omega_i + 1)\mathrm{core}^+ nl(\lambda + 1) \right| - \frac{1}{2\mu R^2}(J^+ l^- + J^- l^+) \left| J\Omega_i \mathrm{core}^+ nl\lambda \right\rangle \tag{2.185}$$

$$= \frac{-\hbar^2}{2\mu R^2} \left[J(J+1) - \Omega(\Omega+1) \right]^{1/2} \left[l(l+1) - \lambda(\lambda+1) \right]^{1/2}. \tag{2.186}$$

Equation (2.185) may be applied to the important p-complex that is partially comprised of the $c_n\,{}^1\Pi_u$ and $c'_{n+1}\,{}^1\Sigma_u^+$ Rydberg states of N_2 [12]. These two states have the same ionic core complemented by the addition of an $np\pi$ and $np\sigma$ Rydberg electron, respectively. The $np\pi$ configuration is doubly degenerate, with alternative orbitals labelled $np\pi^+$ and $np\pi^-$, having orbital angular-momentum which is aligned and anti-aligned, respectively, with the internuclear axis. This degeneracy is similar to that discussed in Sec. 2.1 with respect to the doubling of states with $\Lambda > 0$. The orthogonal linear combinations $2^{-1/2}\,(np\pi^+ + np\pi^-)$ and $2^{-1/2}\,(np\pi^+ - np\pi^-)$ must be formed in order to generate states of definite e/f parity. According to the selection rules of rotational perturbations, nonzero matrix elements may only exist between these and a non-degenerate $np\sigma$ orbital

of the same parity.

For the case of $c_n\,{}^1\Pi_u$ and $c'_{n+1}\,{}^1\Sigma_u^+$, it is the e-parity levels that are affected and Eq. (2.185) may be expanded according to

$$\langle c_n\,{}^1\Pi_u|H^{rot}(R)|c'_{n+1}\,{}^1\Sigma_u^+\rangle = \left\langle J\,1\,\mathrm{core}^+ np\pi\right| - \frac{1}{2\mu R^2}(J^+l^- + J^-l^+)\left|J\,0\,\mathrm{core}^+ np\sigma\right\rangle \tag{2.187}$$

$$= \frac{-\hbar}{2\mu R^2}\sqrt{J(J+1)}\cdot 2^{-1/2}\left[\left\langle np\pi^+\right|l^+\left|np\sigma\right\rangle + \left\langle np\pi^-\right|l^-\left|np\sigma\right\rangle\right]. \tag{2.188}$$

Then, evaluating the remaining matrix elements by means of Eq. (2.40) ,

$$\langle c_n\,{}^1\Pi_u|H^{rot}(R)|c'_{n+1}\,{}^1\Sigma_u^+\rangle = \frac{-\hbar^2}{2\mu R^2}\sqrt{J(J+1)}\cdot 2. \tag{2.189}$$

Chapter 3

Spectroscopy of N_2

Good reviews of N_2 spectroscopy up to their publication are given in the exhaustive works of Lofthus and Krupenie [111] and K. P. Huber and G. Herzberg [72]. A further brief summary of the difficulties encountered in the study of those N_2 excited states observed in the XUV is given by Carroll and Hagim [15]. While the subsequent study of N_2 has been far from dormant, the overall picture of the ground and excited states remains largely unchanged. This chapter falls far short of an exhaustive review of the N_2 spectrum and the means by which it has been observed. Instead, an outline is provided here, in terms of a selection of experimental and theoretical investigations which have proved most useful to this thesis.

3.1 Overview of experimental techniques

Homonuclear N_2 has no permanent dipole-moment, which excludes the infrared detection of transitions between ground-state vibrational and rotational levels. The first electronically-excited level occurs $50\,000\,\mathrm{cm}^{-1}$ (6.2 eV) above the ground-state. However, neither this nor many other higher-lying states are accessible from the ground-state by electric-dipole transitions because of various symmetry selection rules, and the entire visible-range spectrum is suppressed. Nonetheless, the weak Lyman-Birge-Hopfield and Vegard-Kaplan band systems involving excited states $a\,^1\Pi_g$ and $A\,^3\Sigma_u^+$, respectively, have been observed in absorption from the ground state [111, 163, 166]. Further electronic states have been accessed by electron spectra [68, 76], and in some cases [75, 183], laser-based excitation of higher-lying states is facilitated by a preliminary excitation to the metastable state $a''\,^1\Sigma_g^+$, which is located $98\,840\,\mathrm{cm}^{-1}$ above the ground state.

Significant absorption is finally observed for energies of $100\,000\,\mathrm{cm}^{-1}$ (12.40 eV) and above, in the XUV region. The dipole-accessible excited-states are discussed in Sec. 3.3 and are plotted with low resolution in Fig. 3.1. This shows an electron energy-loss cross-section of N_2 between 96 780 and $177\,440\,\mathrm{cm}^{-1}$, measured with sufficiently high scattering-energy so as to approach an equivalent optical spectrum. This spectrum shows the onset of the dipole-allowed transitions, and resolves a progression of vibrational bands with erratically variable oscillator-strengths up to the beginning of the ionisation continuum.

Direct dissociation following an electric-dipole transition may occur $116\,300\,\mathrm{cm}^{-1}$ (14.42 eV) above the ground state, although predissociation occurs for even the lowest dipole-allowed excited states. The mechanism leading to predissociation requires the simultaneous perturbation of multiple zeroth-order electronic-states, discussed in Sec. 3.4, and is accidental in nature and highly erratic. The first ionisation limit is reached at $126\,200\,\mathrm{cm}^{-1}$ (15.65 eV) and resonance structure of the ion has been observed [78], as well as super-excited neutral

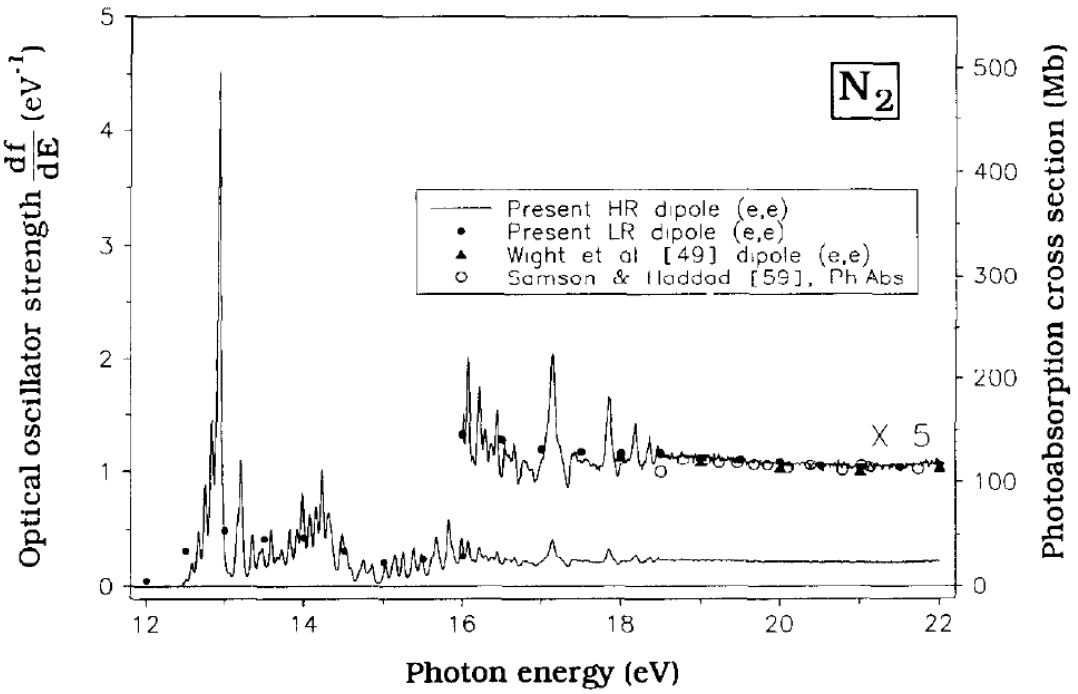

Figure 3.1: Oscillator strengths of N_2 determined from measurement of $\sim 0°$ scattering of 8 keV electrons. The resolution of the instrument is 0.01 eV FWHM (490 cm^{-1} FWHM). After Chan *et al.* [21].

levels which are significantly autoionised.

Despite the ubiquity of predissociation, the majority of rotational lines in the extreme ultra-violet have Doppler limited lineshapes. The room temperature Doppler width of $^{14}N_2$ is 0.23 cm^{-1} FWHM at 100 000 cm^{-1} (2.9×10^{-5} eV FWHM at 12.4 eV), an example of a Doppler limited observed absorption cross section is shown in Fig. 3.2. This width may be reduced by cooling the N_2 target gas by means of liquid nitrogen or supersonic expansion. Such cooling will also suppress the appearance of high-rotation transitions, leading to decongested absorption spectra and simplifying the assignment of rotational lines.

Molecular nitrogen's three isotopomers $^{14}N_2$, $^{14}N^{15}N$ and $^{15}N_2$ exist in the ratio 1 : 0.0073 : 0.000013 in the Earth's atmosphere. The natural abundance of $^{14}N^{15}N$ is sufficiently high that it is sometimes observed simultaneously with $^{14}N_2$ in high-pressure experiments, and studies have also been conducted with enriched $^{15}N_2$. A purified sample of $^{14}N^{15}N$ will rapidly gain an admixture of $^{14}N_2$ and $^{15}N_2$ when exposed to XUV radiation because of its high dissociativity and the resultant association of nitrogen atoms.

The majority of experimental data concerning the dipole-allowed spectrum of N_2 have arisen from the direct measurement of photoabsorption and emission. All such experiments are seriously hampered by the need to generate and manipulate radiation in the XUV range, for which there is no known transparent medium suitable for constructing windows and beam splitters. For the strongest bands, low pressures of N_2 are required in order to avoid the saturation of absorption spectra, in which case the radiation source, target gas, and detector must be contained inside a common vacuum system.

The earliest measurements of N_2 XUV spectra, beginning in 1930, obtained the nec-

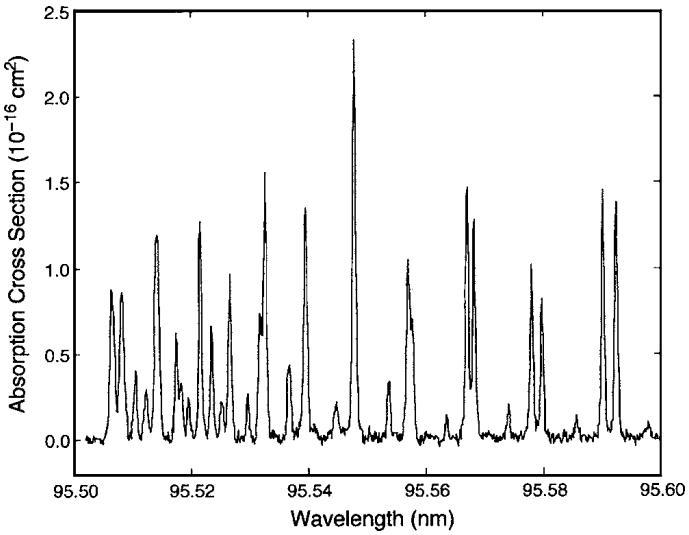

Figure 3.2: Photoabsorption cross section showing the $b\,^1\Pi_u(v'=5) \leftarrow X\,^1\Sigma_g^+(v''=0)$ bandhead region. Measured in absorption during the KEK series of experiments, discussed in Chap. 4. The observed rotational lines have negligible natural width with respect to room temperature Doppler broadening of $0.23\,\mathrm{cm}^{-1}$ FWHM, and the instrumental resolution, $0.65\,\mathrm{cm}^{-1}$ FWHM. After Stark *et al.* [155].

essary ultraviolet radiation from classical discharge lamps, most frequently employing the helium emission continuum, spanning $60-100\,\mathrm{nm}$. Dispersion of this continuum was achieved by means of gratings, and its detection made photographically. Many of these experiments were capable of resolving individual rotational-transitions, and allowed for the qualitative observation of line strength and predissociation broadening. The utilisation of synchrotron radiation in the mid 20^{th} century provided a source of radiation with significantly improved brightness and spectral profile. Also, the photographic detection of ultraviolet light has been completely replaced by photosensitive electronics, enabling the quantitative determination of the strength and lineshapes of individual rotational lines. The spectral resolution of functioning grating spectrometers has remained largely static, or perhaps decreased, but has recently been surpassed by XUV Fourier-transform spectrometry. This new technique also allows for an absolute wavelength calibration and rapid data acquisition.

Recently, frequency multiplied lasers have been developed that are capable of generating XUV radiation with a very narrow frequency profile. When combined with a source of nitrogen cooled by supersonic expansion, these experiments have enabled the most precise measurement of natural linewidths. Laser-based radiation sources are frequently unstable so careful monitoring of the beam brightness must be made simultaneously with absorption measurements. More seriously, these experiments may not be scanned over large wavelength ranges due to the complexity of the various optical elements.

Multi-photon excitation may preclude the need for XUV radiation by accessing high energy levels via an intermediary excitation. Additionally, these allow for the probing of optically-forbidden transitions and the attainment of sub-Doppler resolution.

Electron scattering experiments employing low or threshold collision energies are freed from the optical-dipole transition selection rules, and so allow the probing of transitions that are optically invisible. High-energy small-angle electron scattering, however, closely approximates the direct absorption of radiation and allows for simpler measurements of

equivalent photoabsorption cross sections. The principal disadvantage of electron scattering techniques lies in the poor energy discrimination of electron sources and analysers when compared with optical methods. However, the magnitude of electron excitation cross sections may be fairly reliably determined at low resolution; whereas, absolute absorption cross sections may only be determined from optical spectra if all resonant features are completely resolved, as discussed in Sec. 2.8.6.

Additional information regarding the decay mechanism of excited N_2 has been obtained from photoabsorption and electron excitation experiments after detecting the subsequent fluorescence, or any ionisation and dissociation fragments.

3.2 The ground state

The ground state of N_2 (labelled X) has total symmetry $^1\Sigma_g^+$, has e-type parity, and is principally represented by the closed shell configuration of single-electron molecular-orbitals

$$(1\sigma_g)^2(1\sigma_u)^2(2\sigma_g)^2(2\sigma_u)^2(1\pi_u)^4(3\sigma_g)^2. \tag{3.1}$$

No perturbations have been observed among the energy levels of the ground state, nor any perturbing candidates proposed, and a reliable reduction of its known vibrational and rotational energy levels to molecular parameters can be found in Edwards *et al.* [31], expressed as Dunham coefficients. These are the result of a least-squares fitting procedure constrained by measurements of nearly $\sim 13\,000$ electronic transitions observed in emission, and involving ground-state vibrational levels up to $v = 15$. All but 6% of the energy levels calculated from the resultant molecular constants fall within experimental error. The deduced rotational energy levels of the first vibrational level of $^{14}N_2$ are summarised (to an accuracy of $0.0001\,\mathrm{cm}^{-1}$), by the expression

$$1175.9495 + 1.98957 \times J(J+1) - 5.7418 \times 10^{-6} \times [J(J+1)]^2 \ \mathrm{cm}^{-1}. \tag{3.2}$$

A more recent reduction to spectroscopic parameters has been performed by Le Roy *et al.* [84]. This study extends the work of Edwards *et al.* [31] to higher vibrational levels and also includes data from the isotopomers $^{14}N^{15}N$, and $^{15}N_2$. Additional measurements obtained by means of Raman and magnetic-quadrupole spectroscopy contribute to this analysis. Additionally, Le Roy *et al.* [84] directly constructed an analytic potential-energy curve optimised to best reproduce the known energy levels. The differences between the studies of Edwards *et al.* [31] and Le Roy *et al.* [84] are negligible over the range of ground-state vibrational levels relevant to this thesis.

For the case of a sample of thermally-equilibriated gas at room temperature, or below, there is no significant population of N_2 above the first vibrational level, or with rotational levels having $J \gtrsim 30$. The ground-state potential-energy curve and a calculation of the radial-wavefunction of its first vibrational level are shown in Fig. 3.3.

3.3 $^1\Sigma_u^+$ and $^1\Pi_u$ states

According to the selection rules discussed in Sec. 2.8.2, electric-dipole transitions involving the N_2 ground-state are restricted to two cases,

$$^1\Sigma_u^+ \leftrightarrow X\,^1\Sigma_g^+ \text{ and } ^1\Pi_u \leftrightarrow X\,^1\Sigma_g^+.$$

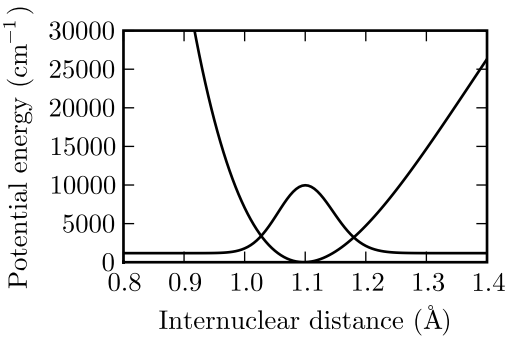

Figure 3.3: The potential-energy curve of the N_2 ground-state, as determined by Edwards *et al.* [31]. Also plotted is the internuclear-distance dependence of a theoretical wavefunction representing the first vibrational level.

Term Symbol	Configuration	
$X\,^1\Sigma_g^+$	$\ldots(2\sigma_u)^2(1\pi_u)^4(3\sigma_g)^2(1\pi_g)^0$	Ground state.
$b\,^1\Pi_u$	$\ldots(2\sigma_u)^1(1\pi_u)^4(3\sigma_g)^2(1\pi_g)^1$	$R \lesssim 1.2$ Å
	$\ldots(2\sigma_u)^2(1\pi_u)^3(3\sigma_g)^1(1\pi_g)^2$	$R \gtrsim 1.2$ Å
$c_n\,^1\Pi_u$	$\ldots(2\sigma_u)^2(1\pi_u)^4(3\sigma_g)^1(1\pi_g)^0 + np\pi_u$	Converging on $N_2^+\left[X\,^2\Sigma_g^+\right]$.
$o_n\,^1\Pi_u$	$\ldots(2\sigma_u)^2(1\pi_u)^3(3\sigma_g)^2(1\pi_g)^0 + ns\sigma_g$	Converging on $N_2^+\left[A\,^2\Pi_u\right]$.
$b'\,^1\Sigma_u^+$	$\ldots(2\sigma_u)^1(1\pi_u)^4(3\sigma_g)^2(1\pi_g)^0(4\sigma_g)^1$	$R \lesssim 1.1$ Å
	$\ldots(2\sigma_u)^2(1\pi_u)^3(3\sigma_g)^2(1\pi_g)^1$	$R \gtrsim 1.1$ Å
$c'_{n+1}\,^1\Sigma_u^+$	$\ldots(2\sigma_u)^2(1\pi_u)^4(3\sigma_g)^1(1\pi_g)^0 + np\sigma_u$	Converging on $N_2^+\left[X\,^2\Sigma_g^+\right]$.
$C\,^3\Pi_u$	$\ldots(2\sigma_u)^1(1\pi_u)^4(3\sigma_g)^2(1\pi_g)^1$	$R \lesssim 1.4$ Å
$C\,^3\Pi_u$	$\ldots(2\sigma_u)^2(1\pi_u)^3(3\sigma_g)^1(1\pi_g)^2$	$R \gtrsim 1.4$ Å
$C'\,^3\Pi_u$	$\ldots(2\sigma_u)^2(1\pi_u)^3(3\sigma_g)^1(1\pi_g)^2$	
$G_3\,^3\Pi_u$	$\ldots(2\sigma_u)^2(1\pi_u)^4(3\sigma_g)^1(1\pi_g)^0 + np\pi_u$	Converging on $N_2^+\left[X\,^2\Sigma_g^+\right]$.
$F_3\,^3\Pi_u$	$\ldots(2\sigma_u)^2(1\pi_u)^3(3\sigma_g)^2(1\pi_g)^0 + ns\sigma_g$	Converging on $N_2^+\left[A\,^2\Pi_u\right]$.

Table 3.1: Configurations of some electronic states of N_2, where "..." represents the closed-shell core orbitals $(1\sigma_g)^2(1\sigma_u)^2(2\sigma_g)^2$. Some additional notes describe the internuclear-distance, R, dependence of the configurationally mixed valence states, as well as the ionic core that Rydberg states are built upon.

No electronically-excited states below 100 000 cm^{-1} are of the correct symmetry to satisfy these restrictions and so do not feature prominently in most photochemical circumstances.

The lowest-energy dipole-allowed transition from the ground state terminates on the first vibrational level of $b\,^1\Pi_u$, located 100 820 cm^{-1} above the ground-state potential-energy minimum. The majority of the N_2 neutral-transition dipole-oscillator-strength is expended on transitions to $b\,^1\Pi_u$ as well as the further states $c_3\,^1\Pi_u$, $o_3\,^1\Pi_u$, $b'\,^1\Sigma_u^+$, and $c'_4\,^1\Sigma_u^+$; with potential-energy curves represented diabatically in Fig. 3.4. The principal configurations of these dipole-accessible states are listed in Tab. 3.1. Note that a number of $^3\Pi_u$ states are also shown in Fig. 3.4, some of which are plotted adiabatically.

Significant electronic perturbations mix these states, such that the schematic diabatic representation of Fig. 3.4 was not realised until the combined efforts of Lefebvre-Brion [89], Dressler [30], and Carroll and Collins [13]. Prior to this, the observed levels were distributed over 12 suspected states. Diabatic potential-energy curves for the deperturbed singlet states have been determined experimentally [30, 89, 104, 153], and have been calculated *ab initio* [33, 34, 145].

The $c'_4\,^1\Sigma_u^+$ and $c_3\,^1\Pi_u$ states are the first members of the np Rydberg series converg-

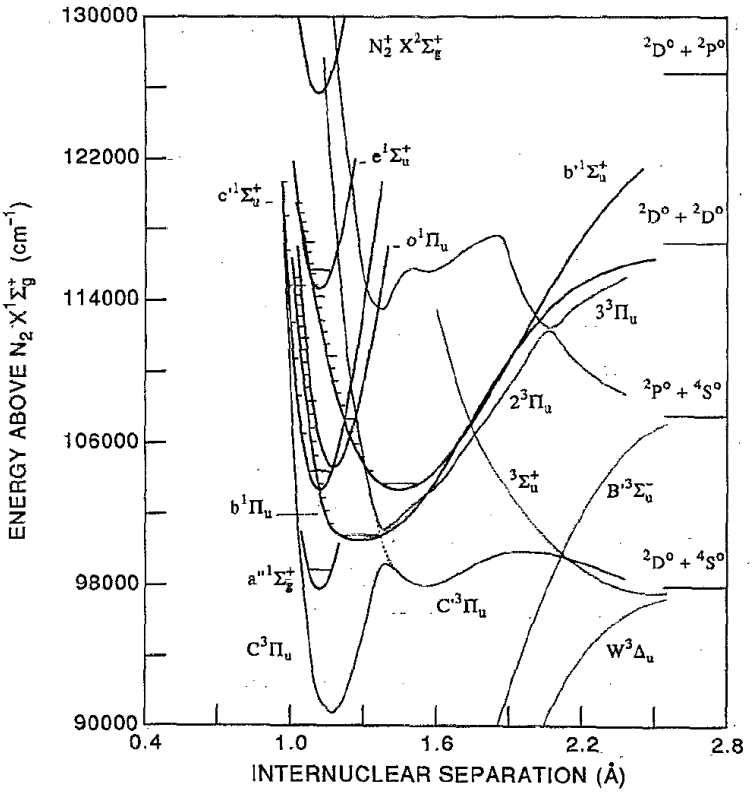

Figure 3.4: Some states of N_2 relevant to observed ultraviolet and XUV transitions. After Walter *et al.* [181]. A further state, $c_3\,{}^1\Pi_u$, is unlabelled but is virtually coincident with $c_4'\,{}^1\Sigma_u^+$.

ing on the ionic ground state, $N_2^+\left[X\,^2\Sigma_g^+\right]$, with Rydberg electrons in σ and π orbitals, respectively, and with principal quantum number $n = 3$. Accordingly, the potential-energy curves of these states are very similar. These have a small equilibrium internuclear-separation and are similar in shape to the limiting ion core. The effect of the alternative alignments of Rydberg-electron orbital-angular-momentum with respect to the internuclear axis leads to a slight increase in energy and equilibrium internuclear-distance of $c_4'\,^1\Sigma_u^+$ relative to $c_3\,^1\Pi_u$. Higher-n members of these series are labelled c_{n+1}' and c_n, and have been observed up to $n = 38$ [17, 18, 57].

There is a further Rydberg series beginning at slightly higher energy, labelled $o_n\,^1\Pi_u$. These states consist of an outermost electron in an $np\pi_u$ orbital, building upon a core corresponding to the first excited-state of the ion, $N_2^+\left[A\,^2\Pi_u\right]$. The lowest member of this series, with $n = 3$, crosses the outer limb of $c_n\,^1\Pi_u$ near 1.17 Å and a strong electronic perturbation occurs with an interaction energy of around $580\,\mathrm{cm}^{-1}$ [145].

The two valence states, $b\,^1\Pi_u$ and $b'\,^1\Sigma_u^+$, have double entries in Tab. 3.1 corresponding to internuclear-distance-dependent configurations. Their mixed configurations are revealed by oddly shaped potential-energy curves, particularly with regard to the flattened potential-well of $b\,^1\Pi_u$. A further diabaticisation of these into single-configuration states is, in principle, possible but would likely introduce larger purely-electronic perturbations than the electronic + nonadiabatic perturbations arising from a mixed specification. The *ab initio* calculations of Spelsberg and Meyer [145, Fig. 7] provide an estimate of the R-dependence of the b and b' configurations including, in either case, more than the two dominant configurations listed in Tab. 3.1. As discussed in Sec. 2.4, a change in configuration implies the possibility of strongly R-dependent electronic transition moments and perturbation matrix elements. The rate of configurational-change is greatest near an internuclear-distance of approximately 1.2 Å and 1.1 Å for $b\,^1\Pi_u$ and $b'\,^1\Sigma_u^+$, respectively.

There are large homogeneous electronic-perturbations mixing $b\,^1\Pi_u \sim c_3\,^1\Pi_u$ and $b\,^1\Pi_u \sim o_3\,^1\Pi_u$ which have been deduced from experimental data by Stahel *et al.* [153] and Spelsberg and Meyer [145]. The latter authors also calculated the magnitude and R-dependence of these off-diagonal matrix elements by *ab initio* means. The interaction energy of the $b \sim c_3$ perturbation was found to be $-853\,\mathrm{cm}^{-1}$ at their crossing point near 1.12 Å, where the negative sign is relevant when multiple electronic perturbations are present. There is no potential crossing between b and o_3, but near the o_3 potential-minimum the interaction energy perturbing these states was found to be $260\,\mathrm{cm}^{-1}$. Similarly, $b'\,^1\Sigma_u^+$ and $c_4'\,^1\Sigma_u^+$ are mutually perturbing with an interaction energy of $-880\,\mathrm{cm}^{-1}$ at the potential crossing near 1.22 Å [145]. Figure 3.5 demonstrates the large term value shifts induced by this perturbation.

These large-magnitude homogeneous perturbations mix the various states so thoroughly that sudden crossings between perturbing rotational-series are rare. Instead, strongly-avoided level crossings induce unusual progressions of rotational energy levels; as well as an uneven spacing of some vibrational levels.

In a reasonable first approximation, the selection rule forbidding the mixing of states of different Λ may be regarded with confidence, and the $^1\Pi_u$ and $^1\Sigma_u^+$ states treated separately, as has been done theoretically several times [89, 104, 145, 153]. However, the L-uncoupling operator of Sec. 2.5.1 introduces rotational perturbations which break this rule. The resultant interaction energies are of the form $\left(b\hbar^2/2\mu R^2\right)\left[J(J+1) - \Omega(\Omega+1)\right]$ and will increase rapidly with nuclear-rotation. The L-uncoupling operator may only act between states with configurations that differ by a single spin-orbital, in which case b is of order 1. Candidates for rotational perturbations may then be deduced from Tab. 3.1.

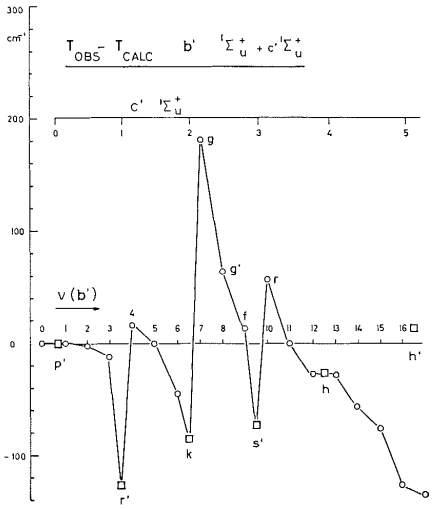

Figure 3.5: Difference between observed and deperturbed term energies for the vibrational progressions of $b'\,^1\Sigma_u^+$ and $c_4'\,^1\Sigma_u^+$. After Dressler [30].

First, $c'_{n+1}\,^1\Sigma_u^+$ and $c_n\,^1\Pi_u$ are known to form a Rydberg p-complex [12, 18], whereby vibrational levels of common n and v are nearly degenerate and rotationally coupled. Several theoretical models consider this interaction [12, 32, 53, 183] with regard to $n = 3$, and adopt a value of $b = 2$ which is estimated according to the assumption of pure-precession, discussed in Sec. 2.13.

A second rotational-mixing is configurationally permitted between $o_3\,^1\Pi_u$ and the large-R configuration of $b'\,^1\Sigma_u^+$. Because of their wildly different equilibrium internuclear-distances, the rotational constants of these two states are significantly different, and several crossings of their rotational series occur [151, 176].

3.3.1 Line assignments

K. Yoshino, P. K. Carroll, and coworkers performed a comprehensive survey of the XUV absorption spectrum at room and liquid-nitrogen temperatures. They employed Helium lamps and synchrotron radiation, combined with dispersion gratings and XUV sensitive photographic emulsion to measure spectra of $^{14}N_2$, $^{14}N^{15}N$, and $^{15}N_2$ between 100 000 and 124 000 cm^{-1} [13, 14, 18, 186, 188, 189]. A further exhaustive survey was made of emission bands arising from many excited states between 100 000 and 117 000 cm^{-1} by the group of Roncin et al. [130, 131, 132, 133, 134, 135]. These experiments dispersed and photographically-recorded the fluorescence of a low-pressure N_2 discharge lamp. The results of Yoshino et al. and Roncin et al. comprise the core set of transition energies and deduced term energies employed as references in this thesis. These have been supplanted in some cases by more recent experiments boasting greater resolution or a more rigorous wavelength calibration, but never improved thoroughness. A database of this spectroscopic information may be found on the world-wide-web [47].

A large set of absolute absorption cross sections, for transition energies between 100 000 and 117 000 cm^{-1}, were measured by G. Stark and collaborators using synchrotron radiation impinging on a 6 metre grating spectrometer [50, 154, 155, 157, 159]. The dispersed radiation was recorded by a translating, linearly-responsive, photoelectric detector. Theoretical line profiles were fitted to the observed spectra, allowing for the deconvolution of blended features and occasional improvement upon the transition energies and line assign-

	f-parity			*e*-parity		
	$^{14}N_2$	$^{14}N^{15}N$	$^{15}N_2$	$^{14}N_2$	$^{14}N^{15}N$	$^{15}N_2$
$b\,^1\Pi_u$	$0-20,\,22-24$	$5-7$	$0-16$	$0-20, 22-24$	$5-7$	$0-16$
$c_3\,^1\Pi_u$	$0-5$	$0-2$	$0-2$	$0-5$	$0-2$	$0-2$
$c_4\,^1\Pi_u$	$0-1$			$0-2$		
$c_5\,^1\Pi_u$	$0-1$			$0-1$		
$c_6\,^1\Pi_u$	0			0		
$c_8\,^1\Pi_u$	0			0		
$o_3\,^1\Pi_u$	$0-5$		$0-4$	$0-5$		$0-4$
$o_4\,^1\Pi_u$	0			0		
$b'\,^1\Sigma_u^+$				$0-28, 30-34$	$1, 7$	$0-21, 24, 25$
$c_4'\,^1\Sigma_u^+$				$0-8$	0	$0-6$
$c_5'\,^1\Sigma_u^+$				$0-2$		
$c_6'\,^1\Sigma_u^+$				$0-1$		0
$c_7'\,^1\Sigma_u^+$				0		
$c_8'\,^1\Sigma_u^+$				0		
$c_9'\,^1\Sigma_u^+$				0		

Table 3.2: The vibrational levels of $^1\Pi_u$ and $^1\Sigma_u^+$ states that have been rotationally analysed following their experimental observation. This list has been compiled from multiple sources discussed in the text

.

ments of earlier studies. The experimental method of Stark et al. is discussed further in Chap. 4.

The highest experimental resolution of any N_2 measurements have been achieved by the frequency sextupled XUV laser of W. Ubachs and coworkers [46, 94, 129, 146, 147, 148, 149, 150, 151, 152, 168, 169, 170, 172, 177, 179]. In this series of experiments, the observed linewidths were further reduced by inducing a supersonic expansion of the target gas, lowering the Doppler width to below $0.002\,\mathrm{cm}^{-1}$ FWHM and the overall experimental resolution to $0.01\,\mathrm{cm}^{-1}$ FWHM. The large background of ultraviolet radiation that passes through the frequency multiplier inevitably ionises the XUV-excited N_2. The detection of these ions traces the excitation rate of N_2 as the laser frequency is scanned. Experiments have been performed by Ubachs et al. upon all of the isotopomers of N_2 for selected bands between $102\,500$ and $111\,500\,\mathrm{cm}^{-1}$.

New photoabsorption measurements of $^{14}N_2$ and $^{15}N_2$ between $115\,000$ and $125\,000\,\mathrm{cm}^{-1}$ are discussed in Chap. 5. These employ a window- and beam-splitter-free Fourier-transform spectrometer attached to a synchrotron source with enhanced brightness in the XUV wavelength range, achieved by means of an undulator insertion-element. The wavelength calibration of these measurement is inherently accurate and the achievable resolution exceeds that of previous synchrotron-based experiments.

The group of P. Cosby has performed a number of experiments where N_2 is prepared in the excited state $a''\,^1\Sigma_g^+$ and then further excited by a low-bandwidth ultraviolet laser into dipole-allowed states [23, 52, 53, 181, 182, 183]. Detection is achieved by observing the presence of dissociation products. The high resolution and stability of this experiment allow for the precise measurement of individual rotational levels.

Table 3.2 summarises the excited vibrational-levels of $^1\Pi_u$ and $^1\Sigma_u^+$ symmetry which have been rotationally analysed.

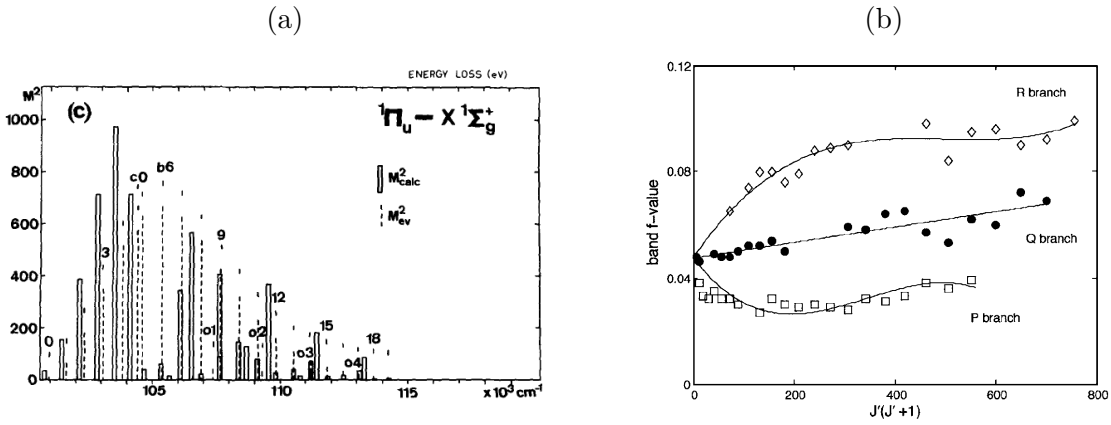

Figure 3.6: *(a):* The relative dipole-strengths calculated by Stahel *et al.* [153] for the vibrational progressions: $b\,^1\Pi_u(v'=v) \leftarrow X\,^1\Sigma_g^+(v''=0)$, $c_3\,^1\Pi_u(v'=v) \leftarrow X\,^1\Sigma_g^+(v''=0)$, and $o_3\,^1\Pi_u(v'=v) \leftarrow X\,^1\Sigma_g^+(v''=0)$. These are plotted against the energy location of each band. Calculations which include, and disregard, the homogeneous interactions between excited states are plotted as *dashed lines* and *boxes*, respectively. After Stahel *et al.* [153]. *(b):* Heterogeneously perturbed band oscillator-strengths of $c_3\,^1\Pi_u(v'=0) \leftarrow X\,^1\Sigma_g^+(v''=0)$. After Stark *et al.* [155].

3.3.2 Oscillator strengths

The earliest measurements of N_2 absorption oscillator-strengths [19, 82] were limited by the nonlinear response of photographic detection, a dearth of bright radiation sources, and the dispersion achievable. More serious still is the effect of poor resolution upon the integrated line strengths of sharp resonances measured in absorption, as discussed in Sec. 2.8.6. Stark *et al.* [155] attempted to address these problems and determined absolute f-values for a large number of rotational-transitions for many $^1\Pi_u - X$ and $^1\Sigma_u - X$ vibrational bands. This data set, along with new results in Chap. 4, comprises the primary calibration reference for coupled-channels-modelled electronic transition moments deduced in this thesis.

The measurements discussed in Chap. 5, made with the aid of a Fourier-transform spectrometer, will allow for the determination of f-values of a similar quality to the previous measurements of Stark et al. once they have been completely analysed. Some preliminary analysis of this data above the upper energy limit investigated by Stark et al. has been performed for the purpose of calibrating the coupled-channels model.

There have also been measurements of N_2 oscillator-strengths which employ electron-excitation techniques. Geiger and Schröder [38] scattered mono-energetic electrons from N_2 and analysed their residual energy. The resultant spectrum, covering energy losses of 100 800 to 120 200 cm^{-1} (12.5 to 14.9 eV), was of insufficient resolution (0.01 eV, 80 cm^{-1}) to observe individual rotational transitions. However, the experimental conditions resulted in sufficiently small momentum transfer such that the observed relative band intensities were directly proportional to optical oscillator-strengths. A similar experiment was performed by Chan *et al.* [21] at a similar resolution but extended to a maximum energy loss of 200 eV. This extension allowed for the sum-rule normalisation of the entire spectrum and an estimate of optical oscillator-strength was determined for many vibrational bands which is independent of any calibration.

Homogeneous mixing of states with common symmetry, either $^1\Pi_u$ or $^1\Sigma_u$, grossly perturbs the Franck-Condon distribution of oscillator-strength from the vibrational en-

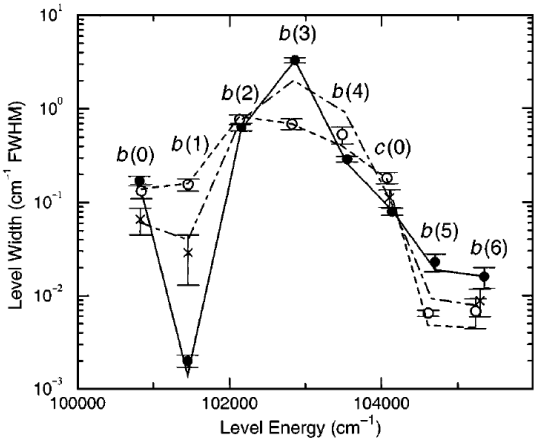

Figure 3.7: Predissociation linewidths of the lowest $^1\Pi_u$ of N_2 determined experimentally (*points with error bars*) and by means of a coupled-channels model (*lines*). Results are shown for $^{14}N_2$ (*solid line, filled circles*), $^{14}N^{15}N$ (*dot-dashed line, crosses*), and $^{15}N_2$ (*dashed lines, open circles*). After Lewis *et al.* [103].

velope expected for unperturbed states. Figure 3.6 (a) shows oscillator-strengths for $b\,^1\Pi_u - X\,^1\Sigma_g^+$, $c_3\,^1\Pi_u - X\,^1\Sigma_g^+$, and $o_3\,^1\Pi_u - X\,^1\Sigma_g^+$, calculated in a previous coupled-channels study of N_2 [153]. Alternative calculations are shown including, and excluding, the effects of homogeneous mixing.

A divergence in the f-values of P- and R-branch transitions which link the same excited rovibrational-level to different ground-state levels may occur where heterogeneous perturbations exist, as discussed in Sec. 2.8.4. Figure 3.6 (b) shows an example of such branching in the optical f-values of $c_3\,^1\Pi_u(v'=0) \leftarrow X\,^1\Sigma_g^+(v''=0)$ [155]. Many similar effects have been observed throughout the XUV spectrum of N_2.

Rotationally-resolved measurements of oscillator strength in connection with the ground-state have been made for the following excited levels: $b\,^1\Pi_u(v = 0-14, 16-19, 23)$, $c_3\,^1\Pi_u(v = 0-3)$, $o_3\,^1\Pi_u(v = 0-5)$, $c_4\,^1\Pi_u(v = 0-1)$, $b'\,^1\Sigma_u^+(v = 1, 3-18)$, $c_4'\,^1\Sigma_u^+(v = 0-5)$, and $c_5'\,^1\Sigma_u^+(v = 0)$. This list excludes a few $^1\Pi_u$ levels for which measurements of the oscillator strength of isolated rotational levels have been made, but only as the result of rotational perturbations with levels of $^1\Sigma_u^+$ symmetry. Such levels indicate the strength and sign of the perturbing matrix elements but do not provide new information regarding any electric-dipole transition moments.

3.3.3 Linewidths and lifetimes

All $^1\Pi_u$ and $^1\Sigma_u^+$ levels lie above the dissociation energies of at least two electronic states, as listed in Tab. 3.3, and may predissociate. The observed linewidths of these levels, or equivalent lifetimes, show significant and haphazard vibrational, rotational and isotopomeric dependence; suggesting the widespread presence of indirect predissociation. The variation of measured linewidths for $^1\Pi_u$ levels below $105\,000\,\mathrm{cm}^{-1}$ is plotted in Fig. 3.7. This wanders over more then three orders of magnitude as well as demonstrating isotopomeric dependence.

Many experimentalists have attended to the study of N_2 predissociation because of its curious nature. The quantitative observation of predissociating levels is usually accomplished by one of three techniques: the measurement of predissociative broadening

Atomic Products	D_e	Ref.	Progenitors
$^4S+^4S$	79844	[134]	$X\,^1\Sigma_g^+$
$^4S+^2D$	99113.5	[111]	$C'\,^3\Pi_u$
$^4S+^2P$	108729.1	[111]	
$^2D+^2D$	118294	[134]	$C\,^3\Pi_u$, $b\,^1\Pi_u$, $2\,^3\Sigma_u$
$^2D+^2P$	128652.5	[111]	$b'\,^1\Sigma_u^+$

Table 3.3: Asymptotic energies, D_e, of the lowest four dissociation channels, relative to the bottom of the N_2 $X\,^1\Sigma_g^+$ potential-energy curve. Dissociation limits, D_0, for $^{14}N_2$, $^{14}N^{15}N$, and $^{15}N_2$ may be found by subtracting the energy of $X(v=0, J=0)$; 1175.7, 1156.1, and 1136.1 cm^{-1}; respectively. The first ionisation limit occurs at 125 667.5 cm^{-1} above the neutral ground state. Also listed are some of the molecular electronic-states that dissociate to a particular limit.

absorption resonances, the detection of dissociation products, or in time resolved measurement of a decaying excited state. The first and last methods are directly related by Eq. (2.79), and all must allow for the component of the observed linewidths (lifetimes) that arises from radiative decay. Because of the variable nature of N_2 predissociation, the probability of dissociative decay varies across the spectrum, from completely dominating to entirely negligible.

Photographic recording of spectra has permitted the qualitative assessment of N_2 predissociation by noting the appearance of diffuse absorption features, along with an absence of corresponding emission [13, 111]. In particular, it was noted by Carroll and Collins [13] that features corresponding to $b\,^1\Pi_u(v'=0,2,3,4) \leftarrow X\,^1\Sigma_g^+(v''=0)$ appeared diffusely in their absorption measurements of $^{14}N_2$, in line with the lack of observed emission from these excited levels. In most cases, linewidths may not be determined precisely from photographic spectra because of the nonlinear response of photographic emulsion. Lewis *et al.* [104] did, however, deduce the 3.3 cm^{-1} FWHM broadening evident in absorption spectra pertaining to the excited level $b\,^1\Pi_u(v=3)$.

The photoelectrically-detected absorption-spectra of Stark *et al.* [155], and new measurements discussed in Chap. 4, allow for the quantitative measurement of resonance linewidths for several $^{14}N_2$ bands between 100 000 and 118 000 cm^{-1}. The experimental resolution of these experiments permit the detection of broadening greater than 0.1 cm^{-1} FWHM. Similar synchrotron-based measurements are discussed in Chap. 5 which have been made at higher energies, and slightly higher resolution, using a Fourier transform spectrometer.

The group of Ubachs et al. examined the predissociative properties of $^{14}N_2$, $^{14}N^{15}N$, and $^{15}N_2$ by employing two methods [46, 129, 147, 150, 152, 169, 170, 171, 172, 177, 179]. First, when examining the most predissociated levels the low-bandwidth of the frequency-multiplied laser used by this group, combined with supersonic cooling of the target N_2, enabled the measurement of absorption linewidths as narrow as 0.01 cm^{-1} FWHM. In a second experiment, rotational levels of a particular excited-state were pumped by a pulse of XUV radiation, then subsequently ionised by a precisely delayed ultraviolet pulse, and the ionisation products detected. In this way, a decay time constant was observed directly. This method is suitable for the most weakly predissociated, and longest lived, excited levels; in which case, the de-excitation will occur by a mixture of dissociation and fluorescence. The two experimental techniques employed by Ubachs et al. are complementary and exclusive; short-lived states decay too quickly to be measured by the pump-probe technique, and long-lived states are too narrow to be deconvoluted from the instrumental bandwidth.

A series of experiments performed by Sommavilla [144] also employed an XUV laser.

	$^{14}N_2$	$^{14}N^{15}N$	$^{15}N_2$
$b\,^1\Pi_u$	$v = 0-14$	$0,1,5,6,$	$0-9$
$c_3\,^1\Pi_u$	$0-5$	0	$0,1$
$o_3\,^1\Pi_u$	$0-3,5$		$0,1$
$b'\,^1\Sigma_u^+$	$1,4-9,11-22$		$1,5,6$
$c_4'\,^1\Sigma_u^+$	$0-2,4-6$	1	$0,1$
$c_5'\,^1\Sigma_u^+$	1		

Table 3.4: Excited vibrational levels of N_2 $^1\Pi_u$ and $^1\Sigma_u^+$ states for which some linewidth information is available. This data originates from many sources which are listed in the text.

In this case, observation of N_2 photoabsorption was achieved by direct measurement of the absorption-attenuated laser intensity, measured relative to a reference intensity furnished by a beam splitter. The achieved laser bandwidth was $0.01\,cm^{-1}$ FWHM and the target was cooled by supersonic expansion. Natural linewidths of the excited levels $b'\,^1\Sigma_u^+(v = 8, 11)$, $o_3\,^1\Pi_u(v = 2, 3)$, and $b\,^1\Pi_u(v = 12)$ were observed. The narrowest of these, $b\,^1\Pi_u(v = 12)$, was found to have a linewidth of only $0.06\,cm^{-1}$ FWHM.

Shemansky and coworkers [1, 64, 108, 109, 139] have observed the dispersed emission from a number of electronically-excited levels of N_2. These rotationally-resolved measurements of line strength provide an estimate of the branching ratio between emissive and dissociative decay pathways, once combined with a detailed knowledge of the optical oscillator-strengths and electronic-excitation rates of the observed levels.

The distribution of atomic products following the dissociation of a particular excited level is also of interest. In most cases a single predissociation channel dominates, but near the dissociation energies listed in Tab. 3.3 significant branching may occur to multiple channels. The work of Cosby et al. [23, 52, 53, 181, 182, 183] includes measurements of rotationally-resolved predissociation branching-ratios for a number of $^1\Pi_u$ and $^1\Sigma_u^+$ states excited from an intermediate electronic-state, $a''\,^1\Sigma_g^+$.

Several other experiments have determined predissociation linewidths for particular excited-levels by using optical [125] or electron scattering [55, 73, 173, 191] techniques.

Table 3.4 lists all levels for which knowledge of linewidths has been obtained. The precision of this information, and the rotational levels to which it applies, vary widely according to the particular experimental source. Many further levels have upper bounds on their linewidths, imposed by the instrumental resolutions of various measurements in which no broadening was detected.

3.4 $^3\Pi_u$ states

Identities for the electronic states responsible for the predissociation of N_2 singlet levels were first considered by Dressler [30] and Carroll and Collins [13]. Both works cited the states $C\,^3\Pi_u$ and $C'\,^3\Pi_u$, with potential-energy curves for these plotted in Fig. 3.8 using a diabatic representation.

At all energies relevant to N_2 electric-dipole-allowed transitions, $C'\,^3\Pi_u$ is unbound and provides the most likely ultimate dissociation channel for the predissociation of $^1\Pi_u$ states. The $C\,^3\Pi_u$ state is strongly electronically-coupled to $C'\,^3\Pi_u$ [16] and a second spin-orbit coupling to the isoconfigurational $b\,^1\Pi_u$ could explain the observed variability of $^1\Pi_u$ predissociation. That is, those $^1\Pi_u$ levels which are accidentally degenerate with $C\,^3\Pi_u$ levels will be indirectly coupled to the unbound $C'\,^3\Pi_u$ and appear broadened, or with reduced lifetimes, in observed spectra. Lewis *et al.* [104] successfully confirmed the

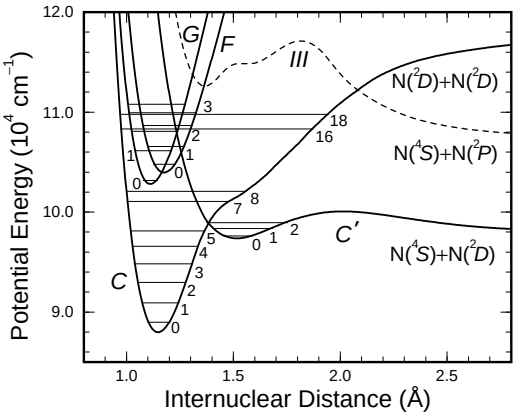

Figure 3.8: Some $^3\Pi_u$ states of N_2, after Lewis *et al.* [105]. *Dashed:* Adiabatic potential-energy curve of $III\,^3\Pi_u$ calculated *ab initio* by Partridge [128]. *Solid:* Diabatic potential-energy curves of $C\,^3\Pi_u$, $C'\,^3\Pi_u$, $F_3\,^3\Pi_u$, and $G_3\,^3\Pi_u$, deduced by Lewis *et al.* [105]. Term energies of all known vibrational levels for these states are plotted as horizontal lines.

mechanism postulated by Dressler [30] and Carroll and Collins [13] by reproducing the observed predissociation of $b\,^1\Pi_u(v=0-6)$ and $c_3\,^1\Pi_u(v=0)$ levels for $^{14}N_2$, $^{14}N^{15}N$, and $^{15}N_2$ by means of a coupled-channels model that included $C\,^3\Pi_u$ and $C'\,^3\Pi_u$. This analysis deduced values for the matrix elements governing electronic-coupling between $^3\Pi_u$ states, and the spin-orbit interactions that mixes these with the $^1\Pi_u$ states.

Several *ab initio* investigations have been made of the valence states $C\,^3\Pi_u$ and $C'\,^3\Pi_u$ [9, 25, 33, 42, 122, 128], including the calculation of adiabatic potential-energy curves. The electronic configuration of the diabatic $C\,^3\Pi_u$ is strongly R-dependent, as can be seen from the unusual kink in its potential-energy curve near 1.4 Å in Fig. 3.8. Below this point, the principal configuration listed in Tab. 3.1 is strongly bound, whereas for large-R the configuration changes, and is associated with a much larger equilibrium internuclear-distance. A diabatic formulation of $C\,^3\Pi_u$ where it is separated into two strongly-coupled states would likely remove most effects of configuration interaction. Similarly, the maximum in the potential-energy of $C'\,^3\Pi_u$, near 2 Å in Fig. 3.8, suggests that this state could alternatively be devolved into two diabatic states, one of which is purely dissociative.

The direct detection of $^3\Pi_u$ levels is hindered by the electric-dipole selection rule regarding multiplicity, which suppresses their optical accessibility from the ground state. Additionally, the considerable predissociation linewidths of many $^3\Pi_u$ levels would prevent their discrimination in spectra. Those vibrational-levels that have nonetheless been observed are plotted in Fig. 3.8. Some of these measurements [45, 69, 76, 77, 112, 113, 173] were achieved following electron excitation, in which case the electric-dipole selection rules do not apply; and further levels have been observed at high-resolution following forbidden photoabsorption from the ground-state [98, 146, 148, 166]. Observation of the latter is made possible by the presence of spin-orbit perturbations with singlet levels. Certain optical transitions between mutually excited triplet states are allowed and have been observed in emission and absorption [11, 16, 48, 86, 87, 98, 136].

In some cases, the presence of triplet levels may be deduced indirectly where perturbations in the energy levels or linewidths of singlet states indicate the presence of an invisible perturber [98, 151]. An example of this is shown in Fig. 3.9, whereby the reduced term values of $^{15}N_2$ $c_3\,^1\Pi_u(v=1)$ indicate three perturbing states, with level crossings apparent

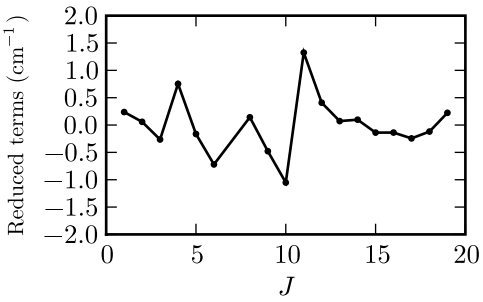

Figure 3.9: Reduced term values of $^{15}N_2$ $c_3\,{}^1\Pi_u(v=1)$, as measured by Sprengers *et al.* [151]. A third order polynomial has been subtracted from the deduced term values in order to highlight a of series level crossings with $C\,{}^3\Pi_u(v=14)$.

between the pairs of rotational-levels, $J = 3-4$, $6-8$, and $10-11$. These are, in fact, due to the $\Omega = 0$, 1, and 2 sublevels of $C\,{}^3\Pi_u(v=14)$ [98]. Similarly structured perturbations occur elsewhere in the N_2 spectrum, appearing in some cases as multiple peaks in the rotational dependence of observed linewidths.

Further triplet states, $F_3\,{}^3\Pi_u$, and $G_3\,{}^3\Pi_u$, are known to exist with energies similar to the observable $^1\Pi_u$ and $^1\Sigma_u^+$ levels, and may be characterised as Rydberg states. Specifically, $F_3\,{}^3\Pi_u$ is a configurational analogue of $o_3\,{}^1\Pi_u$, which differs only in the relative sign of the spin functions of the open-shell orbitals $3\sigma_g$ and $3p\pi_u$. Consequently, the potential energy curve of $F_3\,{}^3\Pi_u$, plotted in Fig. 3.8, is very similar to that of $o_3\,{}^1\Pi_u$, differing principally by an $\sim$880 cm^{-1} R-independent energy shift of the former relative to the latter. Similarly related are the configurational analogues $G_3\,{}^3\Pi_u$ and $c_3\,{}^1\Pi_u$, with an energetic separation of $\sim$630 cm^{-1}. *Ab initio* calculations of the Rydberg $^3\Pi_u$ states have been performed [24, 92].

Electronic interactions are configurationally permitted between all combinations of $F_3\,{}^3\Pi_u$, $G_3\,{}^3\Pi_u$, $C\,{}^3\Pi_u$, and $C'\,{}^3\Pi_u$; and are likely to be large given the strength of coupling between isoconfigurational $^1\Pi_u$ states. New determinations of the Rydberg–Rydberg interaction between $F_3\,{}^3\Pi_u$ and $G_3\,{}^3\Pi_u$ and Rydberg–valence couplings mixing these with $C'\,{}^3\Pi_u$ are discussed in Sec. 6.6.1.

The $\Omega = 0$ and 2 $^3\Pi_u$-substates are forbidden to interact with the $\Omega = 1$ $^1\Pi_u$ states in the case of a nonrotating molecule. However, the triplet substates become mixed with increasing J by the S-uncoupling operator of Sec. 2.5.2, and are then universally free to induce perturbations.

The predissociation of $^1\Sigma_u^+$ levels has also been attributed to the $^3\Pi_u$ states [98, 183]. This effect is even less direct than previously, and involves the $^1\Sigma_u^+ \sim {}^1\Pi_u$ rotational-interaction discussed above as a further intermediate step towards dissociation.

Less is known of the $^3\Sigma_u^+$ states of N_2 situated above 100 000 cm^{-1} than for the $^3\Pi_u$ case, but with regard to the perturbation of optically-observable levels, the Rydberg state $D\,{}^3\Sigma_u^+$ is probably the most significant of the lowest energies. This is the configurational analogue of $c_4'\,{}^1\Sigma_u^+$ and there likely exists a significant off-diagonal matrix element of the spin-orbit operator which mixes these levels. Additionally, $D\,{}^3\Sigma_u^+$ and $G_3\,{}^3\Pi_u$ form the lowest-n members of a Rydberg p-complex convergent on the ground state of the N_2 ion, along with $c_4'\,{}^1\Sigma_u^+$ and $c_3\,{}^1\Pi_u$. Significant rotational coupling of these two states is then likely.

Various low-resolution observations of $D\,{}^3\Sigma_u^+$ transitions have furnished information

on its $v = 0 - 3$ levels [45, 77, 173], including a determination of an extended $D\,^3\Sigma_u^+(v = 0)$ lifetime [81]. High-resolution measurements [39, 69, 74, 146] have led to molecular parameters for $v = 0$ and 1 in $^{14}N_2$, and $v = 1$ for $^{15}N_2$. Kanamori *et al.* [74] observed line broadening of $D\,^3\Sigma_u^+(v = 1) \leftarrow E\,^3\Sigma_g^+[1]$ $^{14}N_2$ transitions with a quadratic dependence on J. They attributed this to predissociation of $D\,^3\Sigma_u^+(v = 1)$ mediated by a heterogeneous coupling. A new study of $D\,^3\Sigma_u^+$ and its interactions with the $^3\Pi_u$ states is discussed in Sec. 6.6.4.

The first unbound state of $^3\Sigma_u^+$ symmetry, labelled "2" in Tab. 3.3, has a sufficiently low dissociation energy that it may influence the predissociation of all $^1\Pi_u$ and $^1\Sigma_u^+$ levels. This is particularly likely where the potential-energy curve of $2\,^3\Sigma_u$ crosses those of $b\,^1\Pi_u$ and $b'\,^1\Sigma_u^+$ near 1.7 Å [173, Fig. 1].

3.5 Some previous quantitative models of N_2

3.5.1 Local perturbation models

Many N_2 bands possess rotational series exhibiting perturbations as localised level-crossings, Λ doubling of term values, or as intensity anomalies. These phenomena have frequently been studied, to high accuracy, by means of local-perturbation models [26, 30, 94, 109, 177, 179, 186, 188, 189], where the expansive study of Dressler [30] is of particular note. Such models empirically represent a minimal set of perturbed bands and their interactions by a small set of parameters. A simple example of such a model is presented in Sec. 2.7. The interaction parameters thus deduced are the product of an off-diagonal matrix element arising from the electronic, spin-orbit, rotational, or some other part of the molecular Hamiltonian; and a vibrational overlap. Because these factors may not be separated the derived parameters may not be extrapolated beyond the data used to derive them.

3.5.2 Lefebvre-Brion

The valence-Rydberg electronic interaction between $b'\,^1\Sigma_u^+$ and $c_4'\,^1\Sigma_u^+$ was treated quantitatively for the first time by Lefebvre-Brion [89], who globally deperturbed the levels $b'(v = 0 - 14)$ and $c_4'(v = 0 - 4)$. In this study, diabatic potential-energy curves were constructed for both states as polynomial functions, and then used to calculate a set of deperturbed vibrational energy levels and wavefunctions. A large interaction matrix was then constructed with diagonal elements consisting of deperturbed energies, and off-diagonal elements constructed as products of Franck-Condon factors and an assumed electronic-interaction energy. Diagonalising this matrix rendered a set of perturbed energy eigenvalues which could be directly compared with experiment.

An iterative refinement of the defining potential-energy polynomial coefficients and interaction energy permitted Lefebvre-Brion to calculate a set of vibrational bands with term origins and rotational constants in agreement with the entire set of experimental values to within $20\,\mathrm{cm}^{-1}$ and $0.07\,\mathrm{cm}^{-1}$, respectively.

3.5.3 Stahel *et al.*

Stahel *et al.* [153] used the coupled-channels technique to perform a simultaneous deperturbation of the levels $b'\,^1\Sigma_u^+(v = 0 - 28)$, $c_4'\,^1\Sigma_u^+(v = 0 - 8)$, $c_5'\,^1\Sigma_u^+(v = 0 - 2)$, $b\,^1\Pi_u(v = 0 - 19)$, $c_3\,^1\Pi_u(v = 0 - 4)$, and $o_3\,^1\Pi_u(v = 0 - 4)$. Independent models were constructed for the two symmetry classes, consisting of diabatic potential-energy curves

and all possible combinations of homogeneous electronic-interactions. Additionally, diabatic electronic-transition-moments were adopted in order that the observed N_2 relative oscillator-strengths might also be studied.

The modelled diabatic potential-energy curves were defined according to the Rydberg-Klein-Rees algorithm, and beginning from a set of assumed Dunham coefficients representing the deperturbed vibrational term origins and rotational constants [54]. Initially, a matrix diagonalisation similar to that of Lefebvre-Brion [89] was iteratively performed in order to determine a set of optimal Dunham coefficients and electronic interaction-energies. Once a satisfactory convergence had been achieved, a coupled-channels calculation of term origins and rotational constructed was undertaken, with the remaining experimental discrepancies found to be below $15\,\mathrm{cm}^{-1}$ and $0.1\,\mathrm{cm}^{-1}$, respectively. A simple vertical shift of the diabatic potential-energy curves during the coupled-channels calculations was required to reach this level of agreement because of the finite set of vibrational levels explicitly represented in the matrix diagonalisation phase.

No high-resolution optical oscillator-strength measurements were available in the time of Stahel et al.. Instead, the low-resolution electron-energy-loss measurements of Geiger and Schröder [38] were used to determine appropriate model electronic transition moments, and were limited to a relative scale. The calculated oscillator-strengths are applicable to $J = 0$ transitions only because of the neglect of rotational coupling between the $^1\Sigma_u^+$ and $^1\Pi_u$ manifolds, whereas the validating data is averaged over many rotational levels. Despite this limitation, as well as possible errors in the partition of experimental oscillator-strength between bands, most calculated band strengths agreed with experiment to within 30%, despite ranging over several orders of magnitude.

The model of Stahel *et al.* was extended by Carroll and Hagim [15] to consider the case of $^{15}N_2$ for $J = 0$ and $^{14}N_2$ for $J > 0$. In the latter case, heterogeneous coupling between $^1\Pi_u$ and $^1\Sigma_u^+$ states was not considered.

3.5.4 Spelsberg and Meyer

Spelsberg and Meyer [145] conducted a further comprehensive modelling study of the N_2 singlet states with energies in the range of 100 000 to 122 000 cm^{-1}. These authors performed *ab initio* calculations of adiabatic electronic-wavefunctions for the same six electronic states considered by Stahel *et al.* [153]. The effect of heterogeneous rotational-coupling was not considered, and $^1\Sigma_u^+$ and $^1\Pi_u$ manifolds were studied independently.

For each symmetry class, large quantum chemical calculations were repeated at a range of internuclear distances; yielding sampled versions of *ab initio* adiabatic potential-energy curves. The internuclear-distance-dependent nonadiabatic mixing of adiabatic states was not calculated. Instead, a diagonalisation of these states was performed at each internuclear distance with respect to a proxy operator, with matrix elements $\langle\phi_i|r^2|\phi_j\rangle$, where ϕ_i and ϕ_j are adiabatic electronic-wavefunctions and r is the radial coordinate. This procedure yielded a set of diabatic states which were assumed to have negligible off-diagonal nonadiabatic coupling and simultaneously provided internuclear-distance-dependent electronic coupling functions in the diabatic basis. The same transformation was also applied to the *ab initio*-calculated adiabatic electronic transition moments, in order to render diabatic transition moments.

The diabatic potential-energy curves were reduced to polynomial Morse-like curves, and the diabatic couplings represented by Gaussian forms, for the purposes of interpolating between the sampled internuclear-distances. Diabatic vibrational-wavefunctions and

energy levels were calculated from the parameterised potential-energy curves and used, along with the diabatic interaction terms, to diagonalise a large matrix of vibrational energy levels. The resultant vibrational term origins and rotational constants were then compared to the experimental data set collated by Stahel *et al.* [153].

Further empirical refinements were made to the *ab initio*-derived model. The parameters governing the shape of the various potential-energy curves and coupling moments were iteratively adjusted in order to best match the available observations. This optimised model agreed with the experimental energy levels and rotational constants to within $6.6\,\mathrm{cm}^{-1}$ and $0.291\,\mathrm{cm}^{-1}$, respectively, with a significantly smaller root-mean-square error and with the $^1\Pi_u$ levels showing better agreement than the $^1\Sigma_u^+$ levels.

Transition moments for each vibrational level were calculated from the *ab initio* diabatic electronic transition moments and qualitatively compared with the experimental electron energy-loss spectra of Geiger and Schröder [38].

3.5.5 Heterogeneous models

Only a few N_2 models exist which include non-local heterogeneous mixing between states of $^1\Sigma_u^+$ and $^1\Pi_u$ symmetry. The L-uncoupling operator is responsible for such interactions and is proportional to $\sqrt{J(J+1)}$; so must be included in any model considering molecular states with $J > 0$.

The model constructed by Helm *et al.* [53] represented three $^1\Sigma_u^+$ and three $^1\Pi_u$ diabatic electronic-states with the same potential-energy curves as determined by Stahel *et al.* [153]. A large matrix was then constructed consisting of diabatic vibrational energy levels; the homogeneous interactions of Stahel *et al.*; and a heterogeneous-interaction term mixing $c_4'\,^1\Sigma_u^+$ and $c_3\,^1\Pi_u$, and equivalent to the term defined in Eq. (2.23). Diagonalisation of this matrix gave rovibrational energy levels and electronic-state mixing-coefficients for $J \geq 0$.

Edwards *et al.* [32] constructed a similar model which solved the coupled Schrödinger equation, rather than performing a matrix diagonalisation. The calculated rovibrational term energies were in agreement with the experimental values to within $\sim 15\,\mathrm{cm}^{-1}$ for the levels analysed in this work, $b'\,^1\Sigma_u^+(v = 3, 9, 17)$, $c_4'\,^1\Sigma_u^+(v = 0, 3-4)$, $b\,^1\Pi_u(v = 1, 5)$, and $c_3\,^1\Pi_u(v = 1)$, up to $J = 30$. The model formulation of Edwards *et al.* [32] was further utilised by Ubachs *et al.* [170] in an attempt to explain their experimentally-observed rotationally-dependent excited state lifetimes for some $^{14}N_2$ levels, as well as by Sprengers *et al.* [151] for comparison with a large number of $^{14}N^{15}N$ and $^{15}N_2$ level energies they observed at high resolution.

The combined experimental and theoretical study of Walter *et al.* [183] observed a flux of dissociation fragments following the two-photon excitation of $c_4'\,^1\Sigma_u^+(v = 3, 4)$, $b'\,^1\Sigma_u^+(v = 10, 12, 13, 15)$, and $c_3\,^1\Pi_u(v = 3, 4)$; with $a''\,^1\Sigma_g^+(v = 0)$ acting as an intermediary state. Similar to those discussed above, this study was adapted from the work of Stahel *et al.* [153] by the inclusion of $c_4'\,^1\Sigma_u^+ \sim c_3\,^1\Pi_u$ rotational coupling and solved the coupled Schrödinger equation. Furthermore, the electronic transition moments of Stahel *et al.* were also adopted in order to explain the rotational dependence of the measured photofragment intensity. This model explained much of the observed J-dependence but requires the uncertain assumption that the transition moments connecting excited states with $X\,^1\Sigma_g^+$ were comparable with those describing excitation from $a''\,^1\Sigma_g^+$.

3.5.6 Australian National University models

Using similar methodology to that discussed in Chap. 6, Lewis *et al.* [104] constructed a coupled-channels model incorporating $C\,^3\Pi_u$, $C'\,^3\Pi_u$, $b\,^1\Pi_u$, $c_3\,^1\Pi_u$, and $o_3\,^1\Pi_u$; all possible homogeneous interactions between states of like symmetry; and spin-orbit interaction parameters perturbing the $^3\Pi_u$ and $^1\Pi_u$ states. This model successfully explained the variable line broadening observed for the $b(v = 0 - 6)$ and $c_3(v = 0)$ levels in $^{14}N_2$, $^{14}N^{15}N$, and $^{15}N_2$ as the result of accidental predissociation to the $N(^4S) + N(^2D)$ limit of $C'\,^3\Pi_u$. This work included only the $\Omega = 1$ $^3\Pi_u$-substates, that is, those that may directly perturb states of $^1\Pi_u$ symmetry. The model constructed thus provided an experimental derivation of the $C\,^3\Pi_u$ and $C'\,^3\Pi_u$ potential-energy curves, as well as the following off-diagonal matrix elements, assumed to be independent of internuclear-distance:

$$\begin{aligned} \langle C\,^3\Pi_u|H^{el}|C'\,^3\Pi_u\rangle &= 810 \pm 20, \\ \langle b\,^1\Pi_u|H^{SO}|C\,^3\Pi_u\rangle &= 46 \pm 2, \\ \text{and } \langle b\,^1\Pi_u|H^{SO}|C'\,^3\Pi_u\rangle &= -1.3 \pm 0.5\,\text{cm}^{-1}. \end{aligned}$$

The $b\,^1\Pi_u$, $c_3\,^1\Pi_u$, and $o_3\,^1\Pi_u$ potential-energy curves used by Lewis *et al.* were modified forms of those constructed by Spelsberg and Meyer [145], with the alterations made in light of an improved set of experimental term values. The same coupled-channels model was used by Lewis *et al.* [103] to compute rotation-dependent predissociation linewidths for $b\,^1\Pi_u(v = 1)$ in $^{14}N_2$. These calculations explained a discrepancy between measurements of the $b\,^1\Pi_u(v = 1)$ lifetime observed in emission from an N_2 sample prepared with differing rotational temperatures [125, 152].

The coupled-channels model of Haverd *et al.* [49] extended that of Lewis et al. by the inclusion of channels representing the $\Omega = 0$ and 2 substates of $C\,^3\Pi_u$ and $C'\,^3\Pi_u$. The potential-energy curves corresponding to these new states are assumed identical in shape to their $\Omega = 1$ analogues, merely shifted vertically by equal and opposite amounts. This specification is equivalent to the assumption of R-independent spin-orbit splittings. Haverd *et al.* [49] also included interactions of the form of Eq. (2.48) in order to represent the effect of S-uncoupling.

Also added were new R-dependent electronic transition moments for $b\,^1\Pi_u - X\,^1\Sigma_g^+$, $c_3\,^1\Pi_u - X\,^1\Sigma_g^+$, and $o_3\,^1\Pi_u - X\,^1\Sigma_g^+$. Their final model successfully reproduced the predissociation linewidths and Λ-doubling of $b\,^1\Pi_u(v = 3)$; as well as the absorption oscillator-strengths of $b\,^1\Pi_u(v' = 0 - 6) \leftarrow X\,^1\Sigma_g^+(v'' = 0)$, $c_3\,^1\Pi_u(v' = 0 - 1) \leftarrow X\,^1\Sigma_g^+(v'' = 0)$, and $o_3\,^1\Pi_u(v' = 0) \leftarrow X\,^1\Sigma_g^+(v'' = 0)$; including the rotational dependence shown by many of these quantities.

Chapter 4

KEK absorption measurements

A series of experiments involving N_2 was conducted between 1997 and 1999 at the 2.5 GeV storage ring of the Photon Factory, a synchrotron radiation facility at the High Energy Accelerator Research Organization (KEK) in Tsukuba, Japan. The intention was to make comprehensive high-resolution oscillator-strength and linewidth measurements of absorption spectra between 100 000 and 116 000 cm^{-1} (99.5 to 86.0 nm). These experiments are described in a series of articles, Stark *et al.* [154, 155, 157], and Heays *et al.* [50]; I have contributed to the last two of these.

The principal motivation for acquiring such comprehensive absolute cross section measurements was in order to inform the ANU coupled-channels model of N_2; and eventually generate precise synthetic absorption and dissociation spectra for astrophysical purposes. Accurate measurements and assignments of N_2 line energies already exist, due to the previous photographic experiments described in Sec. 3.3.1. This new experiment, having photoelectric detection, has permitted the direct measurement of resonance lineshapes, allowing for some new assignments of blended and perturbed lines. However, the principal strengths of the KEK experiments are the measurements of absolute oscillator-strengths and predissociation linewidths.

4.1 Experimental design and procedure

I did not participate in the collection of data and only a brief description of the experimental procedure will be given here. A detailed account of the apparatus has been given by its constructors [62, 63] and further details of the experimental conditions adopted may be found in earlier publications [154, 155].

No materials exist which are transparent in the range of photon energies relevant to N_2 absorption. Accordingly, a common vacuum chamber contained all components of the spectrometer and differential pumping was required to prevent a flow of N_2 into the synchrotron storage ring. A schematic of the apparatus is shown in Fig. 4.1. After entering the spectrometer, a broadband beam of synchrotron radiation encounters a predisperser, consisting of a grating and slit assembly that separates the incoming radiation and filters all but a single dispersion order, reducing the bandpass to approximately 3 nm. A second grating recombines the radiation, rendering the entire element nondispersive. This reduction in bandpass prevented contamination of the principal spectrum by extraneous dispersion orders arising from the main grating.

The spectrometer cell was 6.65 m in length, and filled with a monitored pressure of flowing room temperature N_2, with natural isotopic abundance (99.3% $^{14}N_2$, 0.7% $^{14}N^{15}N$). The radiation traverses the cell almost twice, resulting in a total absorption path length

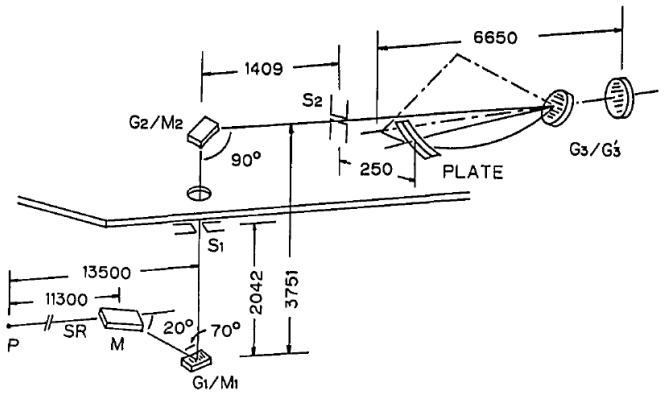

Figure 4.1: Schematic of the extreme-ultraviolet spectrometer at KEK. The beam enters at the lower left. In order to decrease the source bandpass, the beam is diffracted by grating G_1, and then a single dispersion order is recombined at G_2. The entrance slit and primary grating of the spectrometer are labelled S_2 and G_3, respectively. The photographic plate in this schematic was replaced by a translating photoelectric detector masked by a second slit. After Ito *et al.* [63].

of 12.49 m.

The primary dispersive element was a 1200 grooves/mm grating, blazed at 550 nm in order to direct more light into the observed diffraction order. A reciprocal dispersion of approximately 0.02 nm/mm (90 cm^{-1} /mm at 111 000 cm^{-1}) was achieved in the detection plane; and entrance and exit slits of approximately 10 μm width resulted in an instrumental resolution of 0.7 cm^{-1} FWHM (6×10^{-4} nm FWHM). The resolution was determined experimentally, by the analysis of narrow resonances in the spectra.

A translating photoelectric detector recorded the spectra with signal rates of $\sim 50\,000\ \mathrm{s}^{-1}$ and signal integration times of 1 s resulting in a signal-to-noise ratio of ~ 250 during measurements of the background continuum. Data points were recorded at 1.06×10^{-4} nm ($\sim 0.13\ \mathrm{cm}^{-1}$) intervals.

Multiple scans were made of each band, and at a range of gas pressures so that accurate f-values could be determined for all observed rotational lines. That is, low column density scans were necessary to avoid the effects of saturation near band heads, as discussed in Sec. 2.8.6, and lines from weak bands or high rotational levels of strong bands were observable only at high column density. The maximum achievable column density was limited by the amount of gas outflow permissible before risking contamination of the synchrotron ring. Each scan extended over approximately 200 cm^{-1}.

The main goal of the experiment was to measure absolute f-values, for which an absolute determination of column density was required. This was achieved by expanding a known amount of N_2 into the known volume of the tank, and observing the equilibrium pressure registered by an attached gauge. Following this calibration, the pressure readout was converted into a measurement of gas density, and the column density determined from the beam path length. Spectra were recorded at column densities ranging from 4.1×10^{13} to $4.9 \times 10^{15}\ \mathrm{cm}^{-2}$. This calibration procedure was complicated by leakage occurring at the spectrometer entrance and exit slits, and the overall 10% estimated uncertainty in column density is the primary source of error afflicting the measured f-values [154].

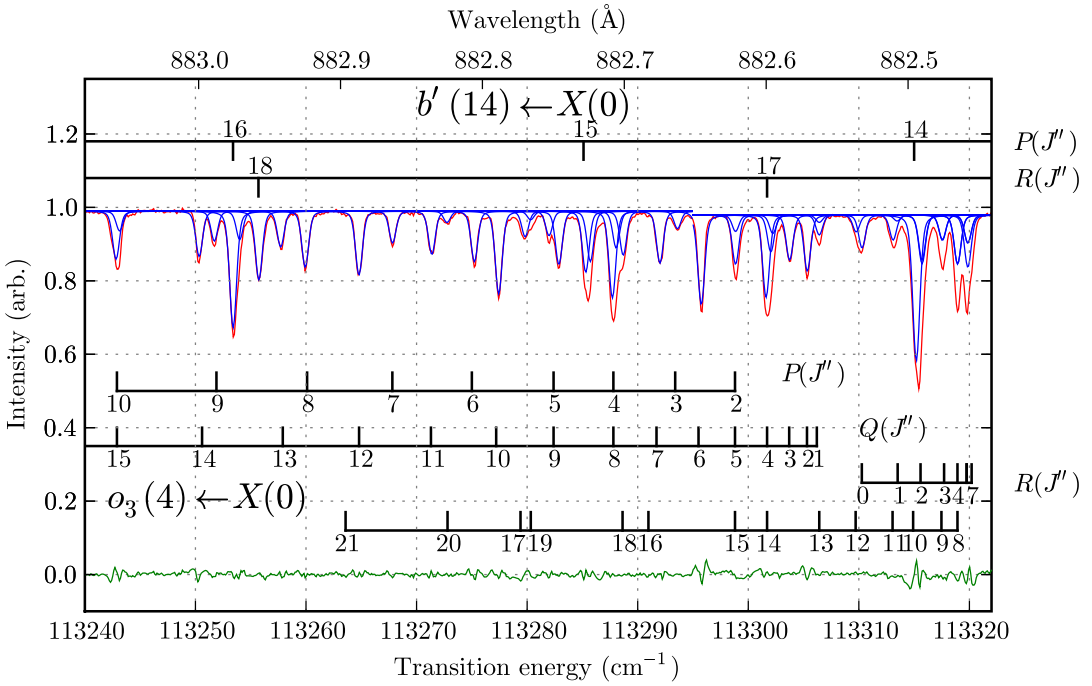

Figure 4.2: Partial spectrum of the overlapping bands $b'\,^1\Sigma_u^+(v'=14) \leftarrow X\,^1\Sigma_g^+(v''=0)$ and $o_3\,^1\Pi_u(v'=4) \leftarrow X\,^1\Sigma_g^+(v''=0)$. *Red trace:* KEK transmission scan recorded with a column density of $2.28 \times 10^{15}\,\mathrm{cm}^{-2}$. *Blue traces:* Contribution to model transmission cross section from individual rotational lines. *Green trace:* The difference between the KEK and modelled cross sections.

4.2 Analysis of the spectra

The raw KEK measurements are photon counts, binned in time as the photoelectric detector is translated. The intensity dips in these scans were compared with the database of known N_2 transition energies discussed in Sec. 3.3.1, in order to determine a suitable energy scale calibration. A linear calibration was sufficiently accurate over the range of each scan. An example of an experimental spectrum is plotted in Fig. 4.2.

An accurate knowledge of the experimental instrument function is necessary before the strengths and widths of any observed lines can be fit to the absorption spectra, as discussed in Sec. 2.8.6. In the case of the KEK experiment, the finite widths of the entrance and exit slits of the spectrometer are primarily responsible for the instrumental resolution. Their combination is equivalent to an ideal measurement being convolved by a triangular function, of FWHM which is the product of reciprocal-dispersion and slit width. Instrumental effects other than slit width were found to contribute to the instrument function, so a more general form than a simple triangle is necessary. A Voigt profile was adopted, consisting of a roughly-triangular Gaussian line shape convolved with a Lorentzian function, the latter allowing for the possibility of broad wings in the instrument function. Voigt functions were not evaluated by direct convolution, but instead approximated by the formula of Whiting [184]. The widths of the Gaussian and Lorentzian functions constitute free parameters which were adjusted to provide a best-fit to the intensity transmission function of several tens of spectral lines for which the natural line width was assumed to be zero.

Three batches of measurements were made at KEK, over several years, and each resulted in a different fitted instrument function. The three pairs of Gaussian and Lorentzian

widths are: 0.56 and 0.25 cm^{-1} FWHM; 0.62 and 0.21 cm^{-1} FWHM; and 0.65 and 0 cm^{-1} FWHM. The uncertainty in the total instrumental width was estimated to be 0.1 cm^{-1}, and constitutes a component of the uncertainty in the final fitted linewidths. Those lines with widths below 0.1 cm^{-1} FWHM were unable to be determined.

An additional contribution to the instrument function was observed for KEK data recorded in 1998 (relevant to Stark *et al.* [157]). In some transmission scans, but not all, the observed absorption lines were doubled, with a second line appearing in the transmission spectra. These had the same shape as the original, were shifted to higher energy by approximately 1 cm^{-1}, and with up to 0.15× the absorption strength of the primary line. The cause of this phenomenon is not known, but may have arisen from an internal reflection somewhere in the beam line which generates a secondary off-axis incident beam at the entrance of the spectrometer. The appearance of these extra lines was modelled by convolving the Voigt instrument function described above by two δ-functions, the separation and relative strengths of which were adjusted to best fit the observed spectra.

A FORTRAN program was used to least-squares fit parameters defining the experimental instrument function and the observed absorption lines. This program was originally written by the authors of Stark *et al.* [155] and somewhat altered by myself. The relevant variables governing each resonance are its central energy, k_0, integrated strength, σ_0, and natural FWHM, Γ. Together, these define a Lorentzian natural lineshape of the form,

$$\sigma_n(\nu) = \frac{\sigma_0 \Gamma/2\pi}{(\nu - \nu_0)^2 + \Gamma^2/4}. \tag{4.1}$$

Each resonance is also Doppler broadened by a Gaussian function,

$$\sigma_d(\nu) = \frac{4\ln 2}{\pi \Gamma_d} \exp\left(\frac{-4\ln 2}{\Gamma_d^2}\nu\right), \tag{4.2}$$

where the Doppler FWHM is given by,

$$\Gamma_d = \nu_0 \sqrt{\frac{8 k_b T \ln 2}{mc^2}}, \tag{4.3}$$

$$= 2.34 \times 10^{-6}\, \nu_0. \tag{4.4}$$

Here, k_b is the Boltzmann constant, T is the temperature, c is the speed of light and m the mass of the molecule. The form given by Eq. (4.4) is relevant for $^{14}N_2$ at 300 K, with Γ_d and ν_0 in units of cm^{-1}. Over the wavelength range covered by the KEK experiments $\Gamma_d = 0.235 - 0.272\,\mathrm{cm}^{-1}$. Each Doppler broadened absorption line was then modelled by the convolution of its natural and Doppler lineshapes, equivalent to a Voigt profile, and calculated by means of an approximate numerical form [184].

The background intensity, $I_0(\nu)$, recorded by the KEK spectrometer was unstable and it was necessary to frequently recalibrate a linear form for the local background by assuming zero absorption in the windows between spectral lines. This made it impossible to measure continuum or very broad absorption features where these vary less rapidly than does the background intensity.

A model cross section was constructed by summing a linear background term (parameters A and B) with however many Doppler broadened absorption lines are apparent,

labelled $i = 1 \ldots n$, such that

$$\sigma(\nu) = A + B\nu + \sum_{i=1}^{n} \sigma_i(\nu). \tag{4.5}$$

A modelled transmission intensity was then calculated using Eq. (2.102)) and degraded by convolution with the experimental instrument function, according to Eq. (2.109). The spectrum thus generated was directly compared with the experimental transmission scans and a point-wise residual calculated. In all cases, iterative adjustment of the various parameters led to a rapid convergence to randomly distributed residuals, with standard deviation indicative of the magnitude of experimental noise. This inversion was sufficiently sensitive that overlapped lines could frequently be parameterised individually.

Sometimes it was necessary to fix either the strengths or widths of overlapped lines to an assumed value, in order that the converse parameter might be more accurately determined. Often, natural linewidths were assumed negligible with respect to the Doppler and instrument widths, based on previous measurements of excited state widths or decay lifetimes. Fitted line strengths were converted to band f-values using Eqs. (2.105) and (2.108) which, for most vibrational bands, vary slowly with rotation. For those bands which are not perturbed heterogeneously, consistent band f-values were observed for lines of common excited-stated J arising from different rotational transitions. It was sometimes possible to take advantage of these continuities and assume interpolated values for the line strengths of blended features.

Of further aid to the fitting procedure were the reliable transition energy combination differences between P- and R-branch lines terminating on common excited-state rotational levels, these could be calculated from the well-known ground-state energy levels [31, 84].

In a few cases, it was possible to newly assign (or reassign) the observed absorption lines. Most of these lines have been previously observed photographically, but the innovation of reliably fitted lineshapes and f-values enabled these new assignments.

4.3 Results

Results are presented here of the reduction of KEK spectra to rotationally-resolved line energies, f-values, and linewidths for 44 vibrational bands between 107 300 and 116 200 cm^{-1}. Electronic transitions from the ground-state, $X\,{}^1\Sigma_g^+(v=0)$, were observed terminating on the excited vibrational-levels $b\,{}^1\Pi_u(v = 9-20, 22-23)$, $c_3\,{}^1\Pi_u(v = 2-5)$, $c_4\,{}^1\Pi_u(v=0)$, $o_3\,{}^1\Pi_u(v = 1-5)$, $b'\,{}^1\Sigma_u^+(v = 3, 5-18)$, $c_4'\,{}^1\Sigma_u^+(v = 2-5)$, and $c_5'\,{}^1\Sigma_u^+(v=0)$. That is, nearly all singlet $\leftarrow X\,{}^1\Sigma_g^+(v=0)$ bands present in the observed spectral region, the exception being $b\,{}^1\Pi_u(v'=21) \leftarrow X\,{}^1\Sigma_g^+(v''=0)$ which was too weak to be observed at the maximum permissible KEK column density.

For brevity, the band designation $b\,{}^1\Pi_u(v') \leftarrow X\,{}^1\Sigma_g^+(v''=0)$ will be henceforth abbreviated to $b(v') \leftarrow X(0)$, and similarly for transitions to other electronic states. Rotational transitions are expressed below in terms of the ground-state rotational angular-momentum quantum number; and notated $P(J'')$, $R(J'')$, or $Q(J'')$. Term energies, f-values, and linewidths are indexed by the excited-state quantum number, J or J', with the conventional prime frequently neglected for convenience.

As an example of a fitted spectrum, some of the rotational lines arising from the transitions $b'(14) \leftarrow X(0)$ and $o_3(4) \leftarrow X(0)$ are plotted in Fig. 4.2. The term series of the excited states responsible for these two bands cross between $J = 18$ and 19. This

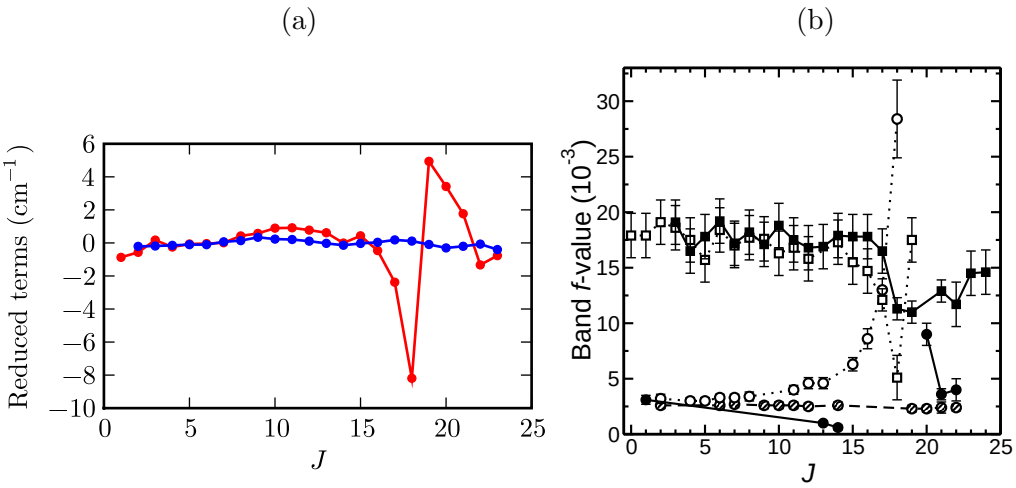

Figure 4.3: *(a):* Term values of $o_3\,{}^1\Pi_u(v=4)$ for its e-parity (*red*) and f-parity (*blue*) levels. These have been reduced by the subtraction of a 3$^{\rm rd}$ order polynomial in terms of $J(J+1)$. *(b):* Band f-values for rotational transitions of $o_3\,{}^1\Pi_u(v'=4) \leftarrow X\,{}^1\Sigma_g^+(v''=0)$ (*circles*), and $b'\,{}^1\Sigma_u^+(v'=14) \leftarrow X\,{}^1\Sigma_g^+(v''=0)$ (*squares*). *Open symbols, dotted lines:* P-branch f-values. *Closed symbols, solid lines:* R-branch f-values. *Hashed symbols, dashed lines:* Q-branch f-values. After Heays *et al.* [50].

is evident in the perturbed energy levels of the $o_3(4) \leftarrow X(0)$ R-branch, with the $R(17)$ line shifted to lower energy than would be expected given the energy separation of its neighbours. This perturbation is more explicitly resolved in Fig. 4.3(a) where the reduced term values of $o_3(4)$ clearly indicate that this perturbation occurs only for the e-parity levels. This is consistent with a ${}^1\Pi_u \sim {}^1\Sigma_u^+$ e-parity only rotational interaction between $o_3\,{}^1\Pi_u(v=4)$ and $b'\,{}^1\Sigma_u^+(v=14)$. The most dramatic consequence of this perturbation is the modification of P- and R-branch f-values of both $o_3(4) \leftarrow X(0)$ and $b'(14) \leftarrow X(0)$ from constancy, plotted in Fig. 4.3(b). Here, the ${}^1\Sigma_u^+$ character acquired by $o_3\,{}^1\Pi_u(v=4)$ from the interaction leads to strength borrowing which is complicated by the intensity interference effect discussed in Sec. 2.8.4. The strengthened $o_3(4) \leftarrow X(0)$ P branch, and weakened R branch, below $J=18$ are accompanied by conversely affected $b'(14) \leftarrow X(0)$ transitions. For $J > 18$ the sense of the P/R strength branching is suddenly reversed, because of a change in sign of the mixing coefficient induced by the ${}^1\Pi \sim {}^1\Sigma$ perturbation. This reversal occurs across the point of minimum energy degeneracy between $o_3(4)$ and $b'(14)$.

Term value and f-value perturbations of the type observed for $o_3(4)$ and $b'(14)$ occur for a large number of the bands observed at KEK. A different variety of perturbation manifests as rotationally-dependent predissociation linewidths, with an example plotted in Fig. 4.4(a). Below $J=10$, the linewidths of $o_3(2) \leftarrow X(0)$ transitions are observed to have a constant value with a mean of 0.26 ± 0.05 cm^{-1} FWHM. For higher rotational levels, the widths are erratically enhanced with a maximum value of $2.3\pm0.4\,$cm^{-1} FWHM at $J=18$. Two more linewidth maxima are observed at $J=14$ and 16. This triple perturbation is apparent in both e and f linewidths and is consistent with a level crossing by an interacting predissociated triplet state with $\Lambda \geq 1$. This perturber was determined to be the $v=18$ level of $C\,{}^3\Pi_u$, which has not been directly observed but Lewis *et al.* [98]

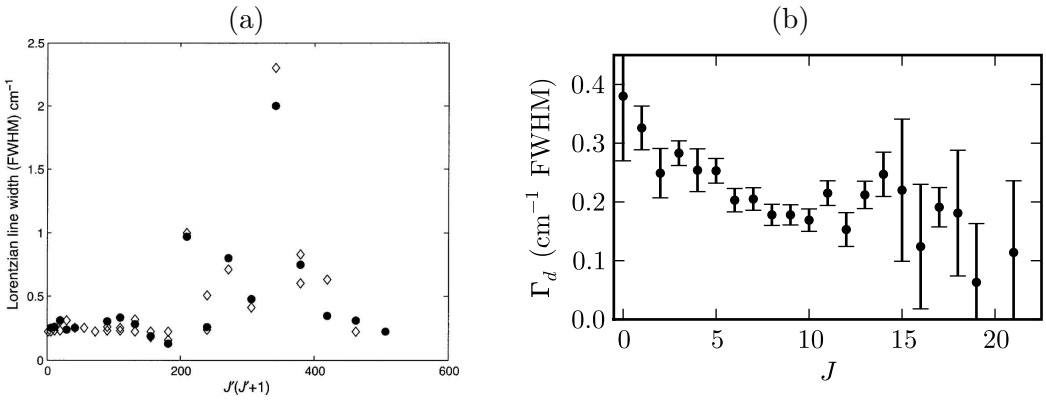

Figure 4.4: *(a):* Measured predissociation linewidths of $o_3\,{}^1\Pi_u(v=2)$. *Open points:* e-parity widths measured from P- and R-branch transitions. *Closed points:* f-parity widths measured from Q-branch transitions. After Stark *et al.* [157]. *(b):* Predissociation linewidths, Γ_d, of $b'\,{}^1\Sigma_u^+(v=17)$.

have deduced its spectroscopic parameters from the $o_3(2)$ perturbation.

Several $^1\Pi_u$ levels exhibit J-dependent line broadening similar to that of $o_3(2)$. Additionally, some $^1\Sigma_u^+$ levels show evidence of line broadening. Figure 4.4(b) plots the observed predissociation linewidths of $b'\,{}^1\Sigma_u^+(v=17)$, which are seen to gradually decrease, and have a value of $0.23\pm0.02\,\mathrm{cm}^{-1}$ FWHM when extrapolated to $J=0$. The $J=0$ broadening of this vibrational level is likely due to a spin-orbit interaction with an unknown and predissociated state of $^3\Pi_u$ or $^3\Sigma_u^+$ symmetry. An additional peak in linewidth coincides with a level crossing with $o_3(5)$ between $J=15$ and 16. The observed linewidths of $o_3(5)$ ($0.8\pm2\,\mathrm{cm}^{-1}$ FWHM at $J=8$) indicate this state is short-lived relative to $b'(17)$. In this case, rotational mixing between the two levels will decrease the lifetime of $b'(17)$ and locally increase its predissociation linewidth.

A band by band discussion of the KEK spectra and an exhaustive tabulation of the deduced spectroscopic data are publised in the open literature[50, 51, 157, 158]. Here, only summaries of the observed predissociation linewidths and f-values are listed, in Tabs. 4.1 and 4.2, respectively.

Two kinds of band f-values are summarised in Tab. 4.2. For each band, an extrapolation of the measured f-values to $J=0$ is listed under the column labelled f_0. For the purposes of determining this limiting value, low-order polynomials are defined in terms of $J(J+1)$ and fitted to the observations. The $P(1)$ lines occurring for $^1\Sigma_u^+ \leftarrow X$ bands provide a direct measurement of f_0, but usually appear only weakly amidst a much stronger bandhead. No $J=0$ levels exist for electronic states with $\Omega>0$, so that f_0 is not physically realisable in the case of the $^1\Pi_u$ states. However, many theoretical models simulate an effective $J=0$ level and may be usefully compared with f_0 for these.

Also listed in Tab. 4.2 are the polynomial coefficients fitted to the J dependence of band f-values, $f(J)$. For unperturbed bands, or those which are homogeneously perturbed by states which are remote in energy, $f(J)$ will be constant and equal to f_0. In the case of N_2 however, few such bands exist. For bands which are perturbed heterogeneously, separate $f(J)$ listings are necessary to describe the P, R, and Q branches. The former two are affected oppositely, and the latter not at all, by the interference term encountered where $^1\Pi_u - X$ and $^1\Sigma_u^+ - X$ transition amplitudes are mixed. In an extreme case, the P and R branches of $c_3(4) \leftarrow X(0)$ are measurable only because of strength borrowed from

Level	Γ_0 cm^{-1} FWHM	$\Gamma(J)$ cm^{-1} FWHM	Obs. J	$\Gamma_{lit.}$ cm^{-1} FWHM
$o_3(1)$	0.27(5)	$0.27 - 3 \times 10^{-4} J(J+1)$	$1-26$	0.050(6) [179]
$b(9)$	0.21(5)		$1-20$	0.23(1) [179]
$c_3(2)$	0.13(5)		$1-26$	0.09(1) [150]
$b(11)$	0.35(5)		$1-19$	0.33(3) [169]
$o_3(2)$	0.26(5)		$1-24$	0.018(3) [125]
$b(13)$	0.23(5)		$1-22$	
$c_3(3)$	0.35(5)		$1-22$	
$b(14)$	0.21(5)	$0.21 - 2.3 \times 10^{-4} J(J+1)$	$1-21$	
$o_3(3)$	~ 0.1		$1-22$	
$b'(14)$	0.19(5)		$0-24$	
$b'(15)$	0.17(3)	$0.17 - 2.8 \times 10^{-4} J(J+1)$	$1-16$	
$c_3(5)$	0.4(1)	Complex variation.	$3-13$	
$c'_4(5)$		Complex variation.	$7, 9, 13-19$	
$o_3(5)$		Complex variation.	$11-15$	
$b'(17)$	0.23(2)	Complex variation.	$0-15$	

Table 4.1: Summary of predissociation linewidths determined from the KEK spectra, listed in order of increasing state energy. Rotationless linewidths, Γ_0, are determined for each vibrational level following an extrapolation of the observed widths to $J = 0$. Where possible, rotationally-dependent linewidths are parameterised by linear functions, according to $\Gamma(J) = \Gamma_0 + \Gamma_J J(J+1)$. Also listed is the range of J for which linewidths were observed. Previous measurements are given under $\Gamma_{lit.}$ with bracketed references. Uncertainties in units of the least-significant digit are given in parentheses.

the stronger $b'(13) \leftarrow X(0)$ transition by means of rotational interaction. This strictly e-parity interaction does not affect the Q branch of $c_3(4) \leftarrow X(0)$, which does not appear in the KEK spectra at all.

For comparison, previously measured and calculated f-values are also listed in Tab. 4.2. The relative f-values deduced by Geiger and Schröder [38] agree quite well with those observed here, for the most part, but with some significant exceptions. These experimenters scattered 25 keV electrons from ground-state N_2 and observed the resultant spectrum of electron energy-loss at small scattering angles. The kinematic conditions employed may be reliably expected to simulate optical absorption conditions. Their energy-loss spectrum has been fixed to an absolute scale by calibrating the integrated strength of the well-resolved $b(3) \leftarrow X(0)$ band against the absolute optical f-values of Stark *et al.* [155]. The remaining discrepancies are attributed to two causes related to the relatively poor instrumental resolution of Geiger and Schröder, with a FWHM of $80\,cm^{-1}$. First, individual rotational-transitions will not be resolved and their band averaged f-values will not always agree with the KEK extrapolations to $J = 0$, particularly for those bands experiencing significant rotational strength variation. Second, entire bands are sometimes overlapped in the spectrum of Geiger and Schröder [38], and in some cases the observed strength may have been incorrectly apportioned between them. An example of this occurs for the overlapped bands $o_3(3) \leftarrow X(0)$ and $b'(11) \leftarrow X(0)$ which, when combined, have newly-measured f-values in agreement with those of Geiger and Schröder, but which deviate individually.

Poorer agreement is found between the KEK f-values and electron energy loss derived values of Chan *et al.* [21], also calibrated with respect to $b(3) \leftarrow X(0)$. Generally, the latter are greater in magnitude and for some bands exceed the present measurements by a factor of three. The $400\,cm^{-1}$ FWHM instrumental resolution of Chan *et al.* [21] certainly makes the band by band comparison of their results with the present high-resolution rotationless f-values somewhat precarious. However, the sum of energy loss f-values for all bands

also disagrees with the current measurement, exceeding it by 52%. The origin of this discrepancy is unknown and may reside in the sum rule normalisation adopted by Chan *et al.* [21] in order to fix their f-values to an absolute scale.

The theoretical models of Stahel *et al.* [153] and Spelsberg and Meyer [145] do not account for rotational interactions and so may be directly compared with the measured rotationless f-values of Tab. 4.2. In general, the relative band f-values calculated by these sophisticated models are in excellent agreement with the KEK values. The f-values of Stahel *et al.* are calculated from experimentally determined transition moments and have been rescaled here to best match the $b(3) \leftarrow X(0)$ transition, which has a well-known f-value determined by Stark *et al.* [155]. Particularly large disagreements are evident for bands terminating on $o_3(v)$ levels and their immediate neighbours. This has since been established to be due to an incorrect sign assigned to the $o_3 - X$ transition moment in their model formulation [104]. The correct sign was calculated by Spelsberg and Meyer [145] and largely corrects the observed discrepancies. The f-values of Spelsberg and Meyer were calculated *ab initio* but were found to consistently overestimate the KEK-derived values, and the results in Tab. 4.2 have been uniformly reduced by a factor of 0.75, to best match $b(3) \leftarrow X(0)$.

Most observed bands did not present linewidths above the $0.1\,\mathrm{cm}^{-1}$ FWHM measurable limit imposed by the KEK instrument function. Those that did have rotationless linewidths listed in Tab. 4.1. These are determined in the same fashion as the rotationless f-values discussed above. Several bands were found to have haphazardly J-dependent linewidths, with values listed in the appendices. A further set of bands presented J-dependencies which are approximated in Tab. 4.1 by linear functions in terms of $J(J+1)$. A few linewidths have been measured previously, and these comparative values are also listed.

The previously observed linewidths of $b(9)$, $c_3(2)$, and $b(11)$ agree well with the current measurements. Significant discrepancies exist however for $o_3(1)$, and $o_3(2)$. The former disagreement is explained simply. The experiment of Vieitez *et al.* [179] directly resolves the $o_3(1)$ low-J rotational levels by means of high resolution XUV laser spectroscopy. The mean linewidth measured by their apparatus for rotational-lines with $J < 4$, $0.050 \pm 0.006\,\mathrm{cm}^{-1}$ FWHM, is beyond reproach. In the KEK spectra, however, all $o_3(1)$ levels with $J < 5$ appear only weakly and could not be parameterised. A perturbation mixing $o_3(1)$ and $b(9)$ is discussed at length in Vieitez *et al.* [179] and leads to a sudden increase in $o_3(1)$ linewidths at $J = 5$, an effect which is critically missing in the extrapolation of KEK linewidths to $J = 0$.

There is a significant disagreement between the presently observed $o_3(2)$ linewidth and that determined from the time resolved fluorescence spectroscopy of Oertel *et al.* [125]. This is likely due to an incorrect partition of fluorescence between bands in the low resolution experiment of Oertel *et al.* [125].

Table 4.2: Summary of $^{14}N_2$ band f-values measured at KEK and comparable values measured elsewhere. All f-values are in units of 10^{-3} and have uncertainties listed parenthetically in units of the least-significant digit. KEK measurements for bands with $T_0 < 111\,872\,\mathrm{cm}^{-1}$ are published in Stark *et al.* [157], apart from $b'(3) \leftarrow X(0)$; and all other bands are published in Heays *et al.* [50]. Band origins, T_0, are taken from an on-line database [47], apart from those of $b(20)$, $c_3(5)$, $c_4'(7)$, and $o_3(5)$ which have KEK-derived values. Rotationless f-values, f_0, are extrapolated to $J = 0$ and band-averaged f-values, f_{band}, correspond to a rotational temperature of 300 K. Rotationally-dependent f-values, $f(J)$, are approximately represented as polynomials in terms of $J(J+1)$. The number and J-range of observed rotational lines are listed for each band. Previous determinations of comparable f-values are either experimental and band-averaged, or theoretical and rotationless. Of these, the results of Geiger and Schröder [38], Stahel *et al.* [153], and Spelsberg and Meyer [145] have been normalised to the well-known $b(3) \leftarrow X(0)$ f-value of 0.043×10^{-3}.

Upper level	T_0 (cm^{-1})	No. obs. lines	Obs. J	f_0 This work	f_{band} Ref. [38]	f_{band} Ref. [21]	f_0 Ref. [153]	f_0 Ref. [145]	$f(J)$ $x = J(J+1)$
$b'(3)$	105 869	3	5, 7, 9	0.09(1)	0.92		0.12	0.12	
$b'(5)$	107 326	34	0 − 19	1.1(1)	0.92		0.94	1.2	$P:\ 1.12 + 0.0014x$
									$R:\ 1.12 - 0.0012x$
$o_3(1)$	107 636	58	1 − 26	3.0(3)			26	7.3	
$b(9)$	107 648	43	1 − 20	14(2)	21	26	5.6	16	
$b'(6)$	107 999	33	1 − 19	1.7(2)	1.9	2.2	1.4	1.9	$1.74 - 0.0025x + 9.4 \times 10^{-6}x^2$
$b(10)$	108 372	51	1 − 19	11(1)	11	14.7	9.2	15	$10.9 - 0.0060x$
$c_4'(2)$	108 544	29	0 − 19	1.2(1)			1.2	1.4	$P:\ 1.20 - 0.0038x + 1.2 \times 10^{-5}x^2$
									$R:\ 1.20 + 0.011x - 1.9 \times 10^{-5}x^2$
$c_3(2)$	108 693	60	1 − 26	11(1)	13	15.5	8.2	14	$Q:\ 10.6 + 2.9 \times 10^{-3}x + 3.2 \times 10^{-5}x^2$
									$P:\ 10.6 + 0.028x - 2.5 \times 10^{-5}x^2$
									$R:\ 10.6 - 0.023x + 8.8 \times 10^{-5}x^2$
$b'(7)$	108 952	27	1 − 19	0.51(5)			0.19	0.45	$P:\ 0.51 - 9.5 \times 10^{-3}x + 5.0 \times 10^{-5}x^2$
									$R:\ 0.51 + 6.8 \times 10^{-4}x - 2.3 \times 10^{-6}x^2 + 1.1 \times 10^{-8}x^3$
$b(11)$	109 120	52	1 − 19	4.4(4)	3.7	4.8	5.1	6.8	$4.44 - 7.1 \times 10^{-3}x$
$b'(8)$	109 544	31	1 − 20	4.0(4)			2.7	4.4	$4.02 - 4.0 \times 10^{-3}x$
$o_3(2)$	109 560	57	1 − 24	14(2)	21	28	24	19	$14.2 + 1.01 \times 10^{-2}x$
$b(12)$	109 831	48	1 − 24	3.0(3)	0.72	1.8	1.7	4.3	$3.03 - 1.6 \times 10^{-4}x - 1.6 \times 10^{-5}x^2$
$b'(9)$	110 197	47	1 − 27	8.7(9)	5.9	12.8	6.5	10.4	$8.68 + 3.4 \times 10^{-3}x - 4.5 \times 10^{-5}x^2 + 5.9 \times 10^{-8}x^3$
$b(13)$	110 529	47	1 − 22	3.1(3)			2.5	4.5	3.06
$c_4'(3)$	110 656	48	0 − 28	7.8(8)	1.2	19	6.5	9.6	$P:\ 7.81 + 6.7 \times 10^{-3}x$
									$R:\ 7.81 + 3.0 \times 10^{-2}x - 6.5 \times 10^{-5}x^2 + 4.5 \times 10^{-8}x^3$
$c_3(3)$	110 796	37	1 − 20	1.0(1)			0.97	1.7	$Q:\ 1.02 + 1.7 \times 10^{-4}x$
									$P:\ 1.02 + 9.2 \times 10^{-2}x - 9.4 \times 10^{-4}x^2 + 5.0 \times 10^{-6}x^3 - 9.7 \times 10^{-9}x^4$
									$R:\ 1.02 - 6.9 \times 10^{-2}x + 1.7 \times 10^{-3}x^2$
$b'(10)$	110 943	26	1 − 21	4.2(4)	1.0		3.4	5.2	$4.18 - 2.8 \times 10^{-2}x + 5.6 \times 10^{-5}x^2$
$b(14)$	111 210	51	1 − 21	3.0(3)	0.73	5.1	4.6	4.6	$2.97 - 6.0 \times 10^{-4}x$
$o_3(3)$	111 448	43	1 − 22	8.8(9)	19	24	12	10.2	$Q:\ 8.75 + 1.5 \times 10^{-3}x$
$b'(11)$	111 581	46	0 − 27	13(1)	18	6.5	11	16	$13.4 - 4.5 \times 10^{-3}x - 8.7 \times 10^{-6}x^2$

Continued on Next Page...

Table 4.2 – Continued

Upper level	T_0 (cm^{-1})	No. obs. lines	Obs. J	f_0 This work	f_{band} Ref. [38]	f_{band} Ref. [21]	f_0 Ref. [153]	f_0 Ref. [145]	$f(J)$ $0 \leq J \leq J_{\max}$
$b(15)$	111 872	4	$15-20$	<1	0.52		0.85	1.6	1.9
$b'(12)$	112 238	38	$0-21$	16(2)	18	30.3	18	19	$16-4.6\times10^{-3}x$
$b(16)$	112 509	6	$2-9$	1.1(2)	0.45		1.1	1.3	1.1
$c_4'(4)$	112 768	35	$1-23$	18(2)	34	49.6	20	22	$18+6.0\times10^{-2}x-1.1\times10^{-4}x^2$
$c_3(4)$	112 851	15	$3-15$	<0.3	3.1	2.10	0	0.025	$P,R:\ 0+4.1\times10^{-3}x+2.2\times10^{-3}x^2$ for $J<8$
$b'(13)$	112 908	22	$1-19$	10(1)	2.6		11	12	$10.0-1.3\times10^{-1}x+4.2\times10^{-4}x^2$ for $J<13$
$b(17)$	113 127	18	$1-9, 17-18$	0.51(5)			2.3	0.83	0.51 for $J<9$
$o_3(4)$	113 307	32	$1-22$	2.5(3)	2.9	6.20	5.8	3.3	$Q:\ 2.5$
									$P:\ 2.5+1.1\times10^{-2}x+1.62\times10^{-5}x^2$ for $J<15$
$b'(14)$	113 540	40	$0-24$	18(2)	25	34.1	23	24	$P:\ 18.0-9.1\times10^{-3}x$ for $J<15$
									$R:\ 18.0-2.5\times10^{-3}x$ for $J<15$
$b(18)$	113 707	7	$4-11$	0.51(6)			0.27	0.67	0.51
$b'(15)$	114 169	41	$1-22$	24(3)	29	40.9	28	29	$24-1.0\times10^{-2}x$
$b(19)$	114 255	2	$2, 8$	0.36(6)			0.4	0.50	0.36
$b(20)$	114 746	6	$2-9$						$P:\ 5.8-3.6\times10^{-2}x$
$b'(16)$	114 754	40	$0-24$	34(4)		62.6	38	41	$34-2.5\times10^{-2}x$
$c_3(5)$	114 825	8	$3, 7-13, 17$	<0.5					$P:\ 0+2.1\times10^{-2}x$ for $J<13$
									$R:\ 0+7.7\times10^{-3}x$ for $J<17$
$c_4'(5)$	114 833	15	$5-25$	0.18		0.6	0.4	0.15	$P:\ 0+1.6\times10^{-2}x$ for $J<17$
									$R:\ 0+2.7\times10^{-2}x$ for $J<18$
$o_3(5)$	115 259	21	$3-17$	0.71(8)		1.55			$Q:\ 0.71$
									$P:\ 0.71-8.1\times10^{-3}x+2.1\times10^{-4}x^2$ for $J<14$
$b'(17)$	115 369	38	$0-23$	16(2)	21	31.8	20	21	16 for $J<13$
$c_4(0)$	115 566	38	$1-22$	8.7(9)	12				$Q:\ 8.7$
									$P,R:\ 8.7$ for $J<8$
$b(22)$	115 663	1	9	<0.5					
$c_5'(0)$	115 850	27	$5-22$	5.2(6)	5.2		6.5	7.6	$P:\ 5.2+3.7\times10^{-2}x$ for $J<15$
									$R:\ 5.2+1.5\times10^{-2}x$ for $J<15$
$b(23)$	116 029	4	$4-8$	0.08(2)					
$b'(18)$	116 206	25	$0-23$	2.4(3)	1.9	3.26	3.6	2.9	$2.4-1.2\times10^{-2}x$ for $J<14$
Sum				278	259	423	313	341	

Chapter 5

SOLEIL absorption measurements

A high-resolution absorption experiment was conducted at the SOLEIL synchrotron facility.[a] The objective was to make new measurements of the energies, oscillator strengths and widths of many absorption lines of N_2 and CO in the extreme-ultraviolet spectral region. The simultaneously high-resolution and broadband measurements were made possible by the use of the unique extreme-ultraviolet Fourier-transform spectrometer attached to the DESIRS beam line at SOLEIL.

The N_2 measurements were intended to extend those measured with the KEK grating spectrometer, discussed in Chap. 4, by operating at shorter wavelengths and including both of the isotopomers $^{14}N_2$ and $^{15}N_2$. No detailed analysis has yet been made of the $^{15}N_2$ measurements and they will not be discussed further. The CO measurements were intended as a first, somewhat exploratory, attempt to determine oscillator strengths of several bands of importance to astrophysical applications, and are beyond the scope of this thesis.

The beam line and Fourier-transform spectrometer were built and are maintained by the resident scientists Laurent Nahon, Denis Joyeux, and Nelson de Oliveira. The visiting group of spectroscopists consisted of Glenn Stark,[b] Peter Smith,[c] Jim Lyons,[d] Lucy Archer,[b] Douglas Blackie,[e] and myself.

5.1 Fourier-transform spectroscopy

Fourier-transform spectroscopy is a dominant tool in various applications involving infrared frequencies, and is also widely used in the visible range, and its general principles are described by Thorne [164]. Extension of the technique to the ultraviolet [164, 187] has been slow because of the difficulty of machining optical elements to the required precision, of the order of the incident wavelength. Additionally, there is a dearth of transparent materials at high energies from which beam splitters may be constructed. The furthest-extending material is crystalline LiF, which will (partially) transmit photons with energies up to $95\,000\,\mathrm{cm}^{-1}$ (105 nm).

Essentially, traditional grating spectrometers work by combining temporally coherent wavefronts (scattered from individual rulings of the grating) in a detection plane. There

[a] Source Optimisée de Lumière d'Energie Intermédiaire du LURE, L'Orme des Merisiers Saint-Aubin - BP 48 91192 Gif-sur-Yvette CEDEX, France.

[b] Department of Physics, Wellesley College, Wellesley, Massachusetts 02481, USA.

[c] Harvard-Smithsonian Center for Astrophysics, Cambridge, Massachusetts 02138, USA.

[d] Institute of Geophysics and Planetary Physics, Department of Earth and Space Sciences, University of California, Los Angeles, California 90095, USA.

[e] Department of Physics, Imperial College, London SW7 2AZ, UK.

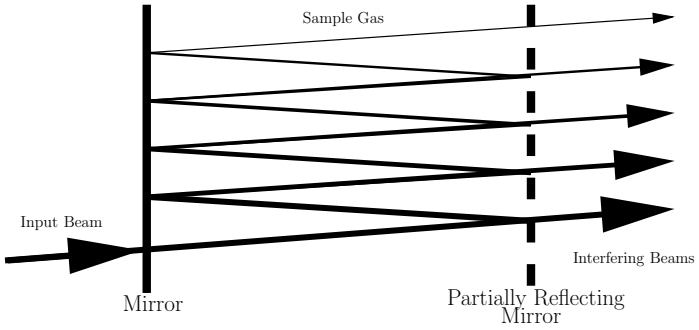

Figure 5.1: Schematic of a Fabry-Perot interferometer. An input beam is multiply reflected between two mirrors and partially transmitted at each reflection into a series of spatially overlapping, interfering beams. Translating one of the mirrors adjusts the path difference of the interfering beams.

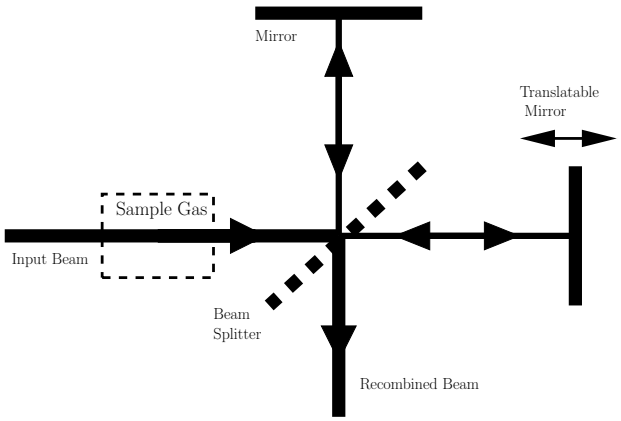

Figure 5.2: Schematic of a Michelson interferometer. A broad-band input beam is passed through an absorption cell and divided at a beam splitter, reflected, and recombined to form an interferogram. Translating one of the mirrors alters the path difference between the two trajectories and, hence, the phase difference of the interfering beams.

are usually several thousand ruled lines to a grating, and accordingly several thousand wavefronts are combined to produce an interference pattern which is spatially-modulated perpendicular to the beam's propagation.

Interferometric spectrometers work by adding wavefronts such that spatial modulation is achieved parallel to the beam propagation direction. Two examples of apparatuses that achieve this are the Fabry-Perot etalon and the Michelson interferometer. The former is shown schematically in Fig. 5.1 and operates by repeatedly splitting a beam by means of two reflecting surfaces, one of which is partially transmitting. The increasing path travelled by beams transmitted on the first, second and higher-order traversals of the cavity results in an output beam with recombined intensity dependent on the separation between the two mirrors, the wavelength of the light, and also the angle of incidence of the incoming beam. In this case, several tens of wavefronts with successively decreasing intensity are recombined into an axially symmetric interference pattern.

The Michelson interferometer depicted in Fig. 5.2 splits a beam into two at a partially-reflecting surface, manipulates these, and finally recombines them. The recombined intensity will be dependent on the relative phase of the two interfering beams, which is in turn dependent on the relative distances they have travelled. The intensity pattern observed

as a function of path difference, x, for light of a particular wavenumber, ν, and spectral intensity, $I(\nu)$, is given by the equation

$$I(\nu, x) = I(\nu)\big[1 + \cos(2\pi\nu x)\big]. \tag{5.1}$$

If the separated beams are of different intensities, perhaps because the beam splitter is not exactly 50% reflecting, or background radiation is contaminating the experiment, then this expression must be replaced by

$$I(\nu, x) = I(\nu)\big[1 + C\cos(2\pi\nu x)\big], \tag{5.2}$$

where $0 \leq C \leq 1$ represents the *contrast* of the apparatus.

A simple photoelectric detector at the interferometer's exit aperture will not discriminate between radiation of different wavenumbers and will instead record the quantity

$$I(x) = \int_0^\infty I(\nu)d\nu + C\int_0^\infty I(\nu)\cos(2\pi\nu x)d\nu. \tag{5.3}$$

The path difference, x, may be scanned by means of a translating mirror on one of the interferometer arms and an interferogram, $I(x)$, obtained.

The first integral in Eq. (5.3) is independent of x and is immediately subtracted from the experimental interferogram, and the second integral is formally equivalent to the cosine Fourier-transform of $I(\nu)$. Then, it is immediately possible to reconstruct the intensity spectrum by performing an inverse Fourier-transform, according to

$$I(\nu) = \frac{2}{\pi}\int_0^\infty I(x)\cos(2\pi\nu x)dx. \tag{5.4}$$

In principle, a complete spectrum may be calculated from a single perfect interferogram, but limiting factors arise in practice. First, it is not feasible to scan the path difference of the interfering beams to infinity, as is required by the integral in Eq. (5.4). Instead, the measurement is halted at some maximum path difference, L (that is, the maximum translation of the movable arm of a Michelson interferometer is $L/2$). The Fourier transform represented by $I(x)$ has been, effectively, multiplied by a step function with the form

$$F(x) = \begin{cases} 1, & 0 \leq x \leq L \\ 0, & x > L. \end{cases}$$

Such a multiplication is equivalent to the convolution of $I(\nu)$ by an instrument function

$$F(\nu) = \mathrm{sinc}(2\pi\nu L), \tag{5.5}$$

which is just the inverse Fourier-transform of $F(x)$. By recording an interferogram with greater maximum path difference, the full-width half-maximum (FWHM) of the central peak of $F(\nu)$ may be reduced, according to the relation

$$\Gamma_{\mathrm{instr}} = \frac{1}{0.6L}. \tag{5.6}$$

Aside from the central peak of $F(\nu)$, several subsidiary peaks may be visible in measurements of $I(\nu)$ and the negative minima of $F(\nu)$ may even induce the appearance in absorption spectra of transmission *above* the background intensity.

A second design compromise must be considered when selecting the sampling interval, Δx, of $I(x)$; that is, the period at which the integrated intensity is discretised as a function of path difference. The imposition of sampling is equivalent to multiplying the true intensity profile by a series of Dirac δ-functions,

$$\sum_{n=0}^{\infty} \delta(x - n\Delta x).$$

The instrument function of Eq. (5.5) must now be rewritten to include this effect,

$$F(\nu) = \mathrm{sinc}(2\pi\nu L) \sum_{n=0}^{\infty} \delta\left(\nu - \frac{n}{\Delta x}\right), \tag{5.7}$$

where the separation of δ-functions in the ν-coordinate is inversely proportional to that in the x-coordinate. The instrument function now acts to periodically repeat the entire spectrum, with a free spectral range given by $1/(2\Delta x)$. This quantity may be increased by sampling an interferogram measurement more frequently.

The benefits of measuring an interferogram with greater maximum path difference or smaller sampling steps must be weighed against a commensurate increase in acquisition time, or a poorer signal to noise ratio in the inverted spectrum.

The way that experimental noise arises in Fourier-transform spectroscopy is also peculiar. Because the detection of photons is highly efficient, random error in ultraviolet spectrometry principally arises from the photon noise of the radiation source, which is proportional to the square root of the detected intensity. Then, the observed noise observed in an interferogram, in addition to the true signal, is given by

$$n(x) = \sqrt{I(x)}\epsilon(x), \tag{5.8}$$

where $\epsilon(x)$ is a unit random variable; with Fourier transform, $\epsilon(\nu)$, also given by a unit random variable. Linearity of the inverse Fourier-transform transfers this noise to the inverted spectrum with the form

$$n(\nu) = \int_{-\infty}^{\infty} \sqrt{I(\nu')}\epsilon(\nu - \nu')d\nu' \tag{5.9}$$

Finally, the expectation value of $n(\nu)$ is given by

$$\langle n(\nu) \rangle = \int_{-\infty}^{\infty} \sqrt{I(\nu')}d\nu'. \tag{5.10}$$

Thus, spectral noise is independent of wavenumber, and proportional to the integrated square root intensity of the entire spectrum. Then, in absorption experiments, resonance dips appear as noisily as does the continuum background. This is in contrast to grating spectrometry where the signal-to-noise ratio (SNR) is independent of wavenumber.

To obtain an improved SNR, in absorption experiments it is desirable to limit the radiation source to a bandpass covering the region of interest, thereby reducing the total detected intensity. Alternatively, lower-resolution measurements have a much improved SNR, because of the reduced length of scanning. Emission spectra show significantly lower SNR than for the case of absorption when measured by Fourier-transform spectrometry, because the total flux of detected radiation is significantly less.

A principal advantage of interferometry, with respect to dispersion techniques, arises from the highly accurate wavenumber calibration attainable. The inverted spectrum is guaranteed to vary linearly with wavenumber; and because it is recorded at once in its entirety, may be calibrated by a single reference standard.

Other experimental effects not encountered in grating spectrometry can arise due to various mechanical deficiencies which may occur in the construction of Fourier-transform spectrometers. Further details regarding the causes and characteristics of several types of periodic and ghosting artifacts that may appear due to such deficiencies are discussed in Learner *et al.* [85]. One type of experimental effect relevant to the SOLEIL spectrometer arises from an intensity modulation on the interferogram, occurring periodically as the split-beam path difference is scanned. This affect may arise, for example, from a slight angular variation of the translating mirror as a motivating screw is turned. Then, assuming the true interferogram to by sinusoidally modulated, according to

$$I'(x) = I(x)\left[1 + A\sin\left(2\pi Bx + C\right)\right], \tag{5.11}$$

the true spectrum will appear convolved by three δ-functions,

$$\delta(\nu) + A\delta(\nu \pm B) - A\delta(\nu \mp B) \tag{5.12}$$

Thus, the true spectrum is observed combined with two oppositely displaced ghost spectra with alternative signs controlled by the modulation phase, C.

5.2 Experimental design and procedure

Many details concerning the design and construction of the SOLEIL Fourier-transform spectrometer are discussed by de Oliveira *et al.* [27] and on the beam line website [28]. The nonexistence of a transparent material capable of forming a beam splitter for extreme-ultraviolet radiation prohibits a design based on a Michelson interferometer. Instead, the spectrometer contains a Fresnel interferometer, whereby the spatially coherent synchrotron beam is divided by two angularly-offset retro-reflecting mirror's. The divided beam forms an interference pattern at a recombination point focused onto a photoelectric detector. The phase of the interference fringes is adjusted by translating one of the mirrors, scanning the path difference between the two beams. A schematic is shown in Fig. 5.3.

The translation and tilt of the movable mirror is monitored and actively controlled by analysing the output of a HeNe laser, with a separate visible-wavelength interferometer attached to the mirrors reverse. Additionally, the HeNe 633 nm line appears in the main spectrum and provides a convenient standard for wavelength calibration of the extreme-ultraviolet region. The width of this line is instrument limited and enables a direct measurement of the instrument function, as plotted in Fig. 5.4. The sinc functional form of the observed HeNe line in Fig. 5.4(b) was found to be in perfect agreement with Eq. (5.5) and Eq. (5.6). Weak features appearing $\pm 1000\,\mathrm{cm}^{-1}$ above and below the HeNe line in Fig. 5.4(a) belie an experimental instrument function containing a factor like that in Eq. (5.12). These ghost features have an intensity which varies from spectrum to spectrum, and may cause weak bands observed in the spectra to be contaminated by very strong features displaced by $\pm 1000\,\mathrm{cm}^{-1}$.

The maximum path difference attainable in the instrument is 10.3 cm, corresponding to a spectral resolution of $0.1625\,\mathrm{cm}^{-1}$ FWHM (1.625×10^{-4} nm FWHM at 100 nm) and

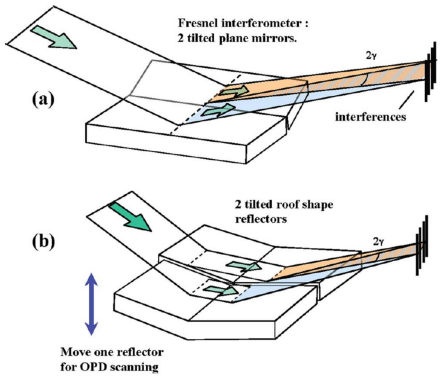

Figure 5.3: Schematic of a Fresnel interferometer. *(a):* Two fixed and tilted mirrors cause different parts of a single spatially-coherent beam to overlap and interfere. *(b):* Roof shaped mirrors, one of which may be translated, enable the continuous scanning of beam path difference and interference at a fixed point. The SOLEIL mirrors are angled at 90°, forming retro reflectors. After de Oliveira *et al.* [27].

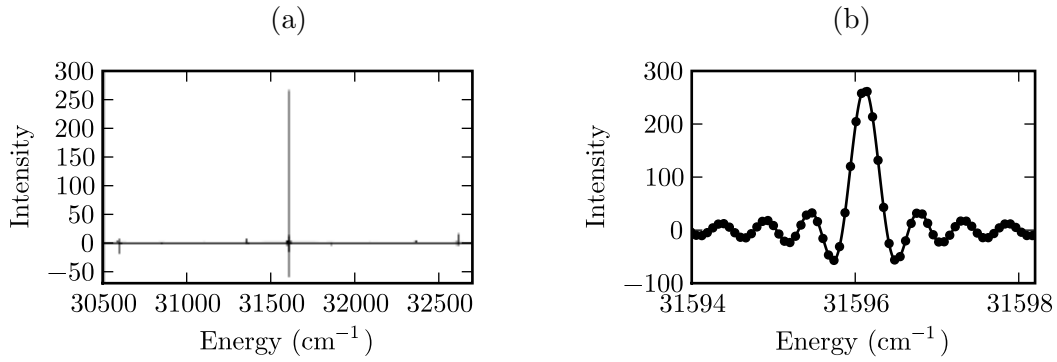

Figure 5.4: *(a):* The HeNe laser line in the SOLEIL spectra which has a profile equivalent to the experimental instrument function. Weak features at $\pm 1000\,\mathrm{cm}^{-1}$ are artefactual copies of the main line, one of which is inverted. *(b):* Measured HeNe line *(points)* fitted to a sinc function *(curve)* with centre at $31\,596.18\,\mathrm{cm}^{-1}$ ($2 \times 633\,\mathrm{nm}$) and a FWHM of $0.325\,\mathrm{cm}^{-1}$.

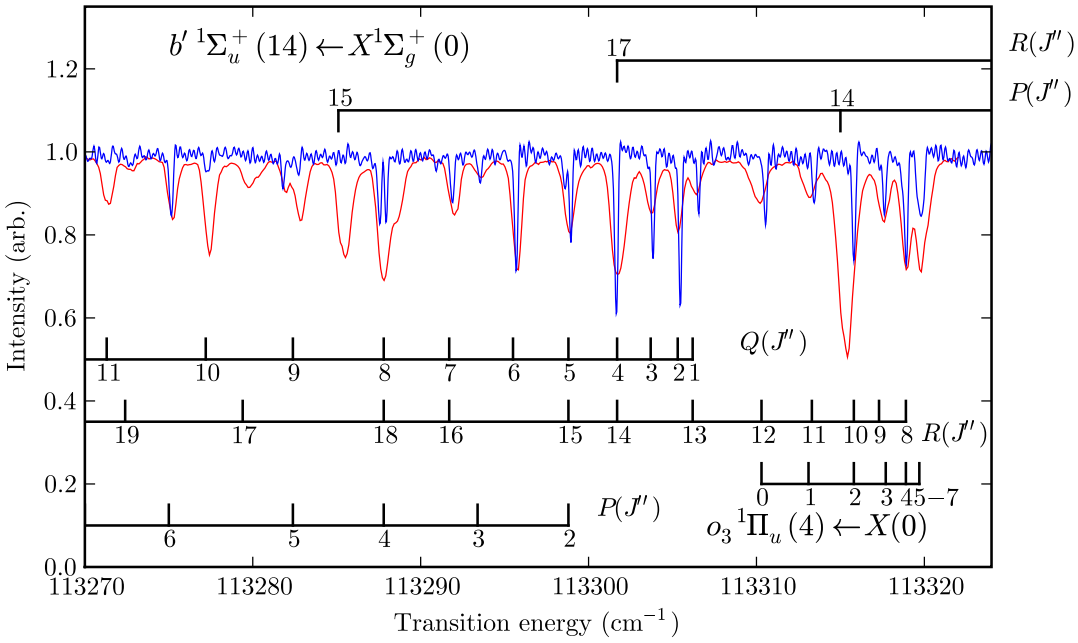

Figure 5.5: Transmission spectra showing the bandhead of $o_3\,^1\Pi_u(v'=4) \leftarrow X\,^1\Sigma_g^+(v''=0)$ and overlapping lines of $b'\,^1\Sigma_u^+(v'=14) \leftarrow X\,^1\Sigma_g^+(v''=0)$. *Blue:* liquid-nitrogen cooled spectrum (temperature of $\sim 100\,\mathrm{K}$) measured at SOLEIL with Doppler width and instrumental resolution of 0.15 and $0.1625\,\mathrm{cm}^{-1}$ FWHM, respectively. *Red:* Room temperature scan from the KEK series of experiments, discussed in Sec. 4. The observed lines are Doppler and instrumentally broadened by 0.26 and $0.65\,\mathrm{cm}^{-1}$ FWHM, respectively.

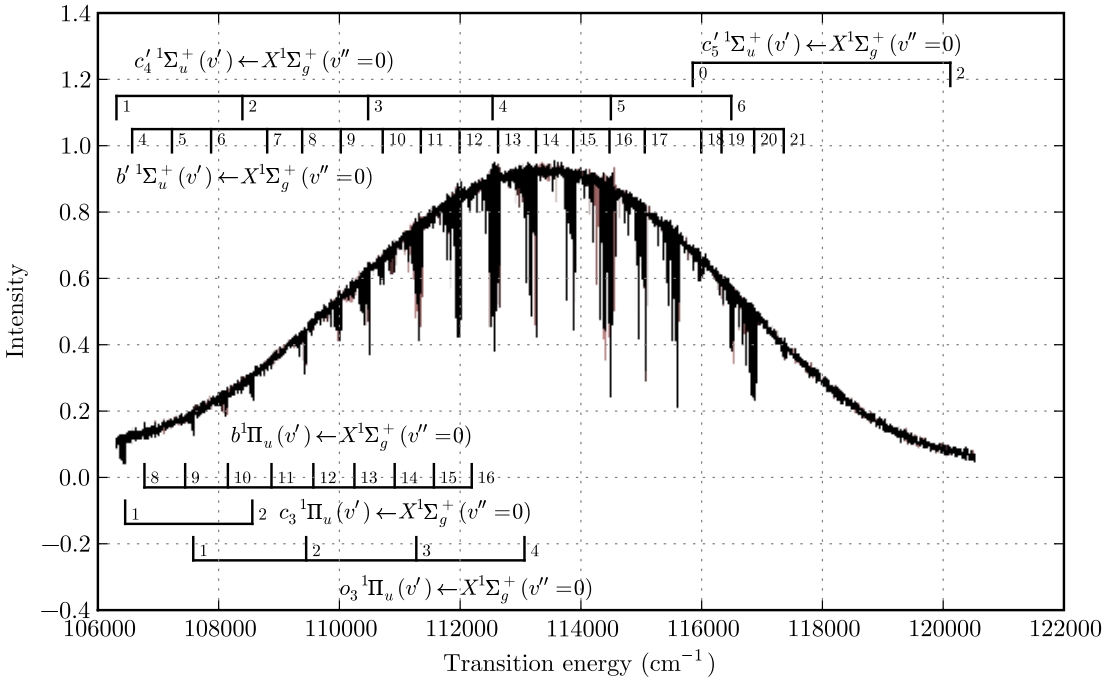

Figure 5.6: An example transmission spectrum showing $^{15}N_2$ absorption. The FWHM of the synchrotron beam bandpass is approximately 7700 cm^{-1} (5 nm). Transition energies are labelled for the known vibrational bands terminating on excited electronic-states with symmetry $^1\Pi_u$ or $^1\Sigma_u^+$ symmetry.

a resolving power of 600 000 at 100 000 cm^{-1} (100 nm). A spectrum demonstrating the maximum resolution of the instrument is shown in Fig. 5.5. For this measurement, the temperature of the N_2 sample has been reduced to approximately 100 K by a liquid-nitrogen evaporative-cooling system, and the resultant Doppler width is approximately 0.14 cm^{-1} FWHM. The natural linewidths of $b(14) \leftarrow X(0)$ transitions are determined in Chap. 4 to be $\sim 0.2\,\mathrm{cm}^{-1}$ FWHM, whereas the widths of $o_3(4) \leftarrow X(0)$ lines in Fig. 5.5 are instrument limited.

The interferogram sampling period is variable, and a single scan may consist of up to 10^6 points and have a maximum free spectral range of 172 000 cm^{-1} (that is, down to 58 nm). Aliasing of short-wavelength radiation onto the principal spectrum is limited by an undulator insertion device. This focuses the synchrotron beam energy into a tunable bandpass with a FWHM of 7000 cm^{-1} at 115 000 cm^{-1} (5 nm at 87 nm); this bandpass is shown in Fig. 5.6. Additionally, an argon-gas filter may be inserted into the synchrotron beam to further reduce short-wavelength aliases contaminating the observed spectra.

The observed beam brightness and fringe contrast varied considerably during the 1.5 years of the experimental campaign. Changes in the synchrotron beam alignment and hydrocarbon contamination on various optical elements of the spectrometer were responsible for the majority of the observed changes. At no time was the SNR of a single interferogram sufficiently high to result in a useful spectrum. Instead, between 20 and 200 independent spectra recorded under identical conditions were necessary to obtain a spectrum with an SNR of 50 to 100, once averaged. For example, the spectrum in Fig. 5.6 resulted from the average of 80 interferograms, has a SNR of 100 at the peak of the undulator band pass, and a lower value elsewhere. Helpfully, limiting the beam bandwidth by means of

the undulator improves the SNR in two ways: by increasing the signal strength in the region of interest; and by decreasing the overall beam intensity so that the noise level of the inverted spectrum is reduced.

The choice of resolution and the number of interferograms recorded for each setting of undulator band pass and N_2 column density were limited according to the available measurement time. Most measurements were recorded with a resolution of $0.325\,\mathrm{cm}^{-1}$ FWHM, and a few with alternative resolutions of 0.1625, 0.650, or $1.3\,\mathrm{cm}^{-1}$ FWHM.

The sample N_2 pressure was adjusted between 10^{-3} and 1 mb, as recorded by a Pirani pressure gauge located inside the absorption cell. This pressure certainly varied in the capillary tubes through which the synchrotron beam enters and exits the differentially pumped absorption cell, and the relative accuracy of the pressure gauge is doubtful at the low end of experimental pressures. Thus, the column density of N_2 could not be directly measured and must be determined in a post-analysis calibration, relative to the absolute f-values determined from the KEK experiment analysed in Chap. 4.

The spectrometer is controlled by a convenient computer interface, and visiting beam line users may setup and initialise scans almost immediately. During the various $3-6$ day experimental periods of continuous beam time, the apparatus was functional and operating $\sim$80% of the time, with the remainder dedicated to tuning and maintenance by the resident scientists.

5.3 Analysis of the spectra

A line by line analysis of the SOLEIL $^{14}N_2$ spectra was conducted which was similar in method to that applied to the KEK data set of Sec. 4.2. A new FORTRAN program was written which fits individual line energies, strengths, and natural widths to the SOLEIL transmission spectra.

A model absorption cross section was constructed as the sum of individual rotational lines. Each of these was assigned a Voigt lineshape consisting of a Lorentzian component, arising from the assumed natural linewidth, and a Gaussian component resulting from Doppler broadening. Each Voigt profile was positioned and scaled to best match the energy, ν_0, and strength of an observed line. The majority of measurements were made at room temperature and an energy dependent Doppler width could immediately be accorded a value of $2.34\times10^{-6}\times\nu_0$ cm^{-1} FWHM, where ν_0 has units of cm^{-1}. For those measurements where liquid-nitrogen cooling was used, an appropriate temperature was deduced from observations of the distribution of f-values between the various rotational transitions of several unperturbed bands. This estimate was verified by fitting the Doppler width to observed lines with negligible natural linewidth.

The effects of pressure broadening were not apparent over the range of N_2 pressures adopted for this study. That is, multiple recordings were made at different column densities for some absorption lines, with the same fitted natural linewidths resulting in each case.

The model cross section was then converted to an ideal transmission spectrum by the application of Eq. (2.102), and scaled by the energy dependent background intensity of the synchrotron beam, assumed to have a polynomial form.

Finally, convolution of the ideal transmission spectrum with an assumed instrument function resulted in a complete model of the experiment which was compared point by point with the measured spectra. A series of least-squares optimisations resulted in a set of best-fitting line parameters and an estimate of the statistical uncertainty in each.

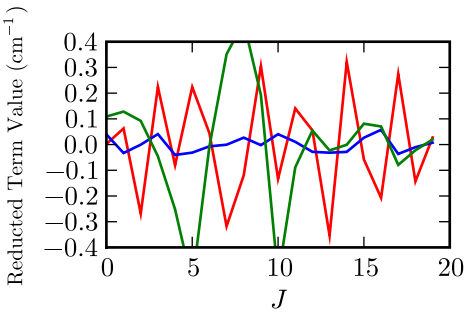

Figure 5.7: Experimental term values of $^{14}N_2$ $c_5'\,{}^1\Sigma_u^+(v''=0)$ following the subtraction of a 5^{th}-order polynomial of best fit. The measurements are from three sources: KEK (*red*); SOLEIL (*blue*); and Carroll and Yoshino [18] (*green*).

The synchrotron beam band pass was not stable with time and a background intensity could not usefully be obtained from a direct measurement of the synchrotron beam with the target gas removed. Instead, the spectrum was fitted in contiguous blocks spanning less than $200\,\text{cm}^{-1}$, over which the background intensity may be treated as varying linearly. Where the spectral lines are sparsely distributed, the background could be reliably determined from the regions of negligible absorption between lines. Otherwise, the background must first be estimated over a larger spectral range and set to a fixed value during the least-squares determination of line parameters.

The SOLEIL spectra have a worse SNR than those recorded during the KEK experiments, and so the fitting of slightly-absorbed lines is relatively unreliable. However, the SOLEIL column densities are generally higher than those adopted at KEK, so that all lines are more deeply absorbed. High-rotational transitions are therefore more distinct and measurable, but the strongest rotational lines (occurring with J'' in the range of 4 to 12) are more likely to be over-absorbed, increasing the likelihood of underestimating their oscillator strengths. This latter problem is partially offset by a precise knowledge of the instrument function, whereas determination of the KEK instrument function was treated simultaneously to the fitting of spectral lines and was accompanied by a degree of uncertainty. Blended lines could be observed and parameterised with a greater degree of confidence than in the case of the KEK measurements, also due to a precise knowledge of the SOLEIL instrument function.

An accurate absolute calibration of the SOLEIL spectra is a natural result of Fourier-transform spectroscopy, although not a critical feature with regard to the expected application of these new N_2 spectra. More significant is the high precision with which the relative transition energies of individual lines could be observed. This feature is demonstrated in Fig. 5.7, which compares the scatter of $c_5'\,{}^1\Sigma_u^+(v=0)$ term energies about a polynomial parameterisation, deduced alternatively from a SOLEIL spectrum, the KEK experiment, and the photographically recorded spectra of Carroll and Yoshino [18]. Clearly, much weaker perturbations may be discerned by analysis of the SOLEIL energy levels than otherwise.

An example fit of the bandhead of $b'(21) \leftarrow X(0)$ is shown in Fig. 5.8. Also appearing in this figure are significantly narrower lines attributed to $c_4(1) \leftarrow X(0)$. For this spectrum, the model fitting process was aided by an additional series of constraints. That is, the $b'(21) \leftarrow X(0)$ P- and R-branch transitions to common excited-state rotational-levels are guaranteed to have identical natural linewidth and be separated in energy by a com-

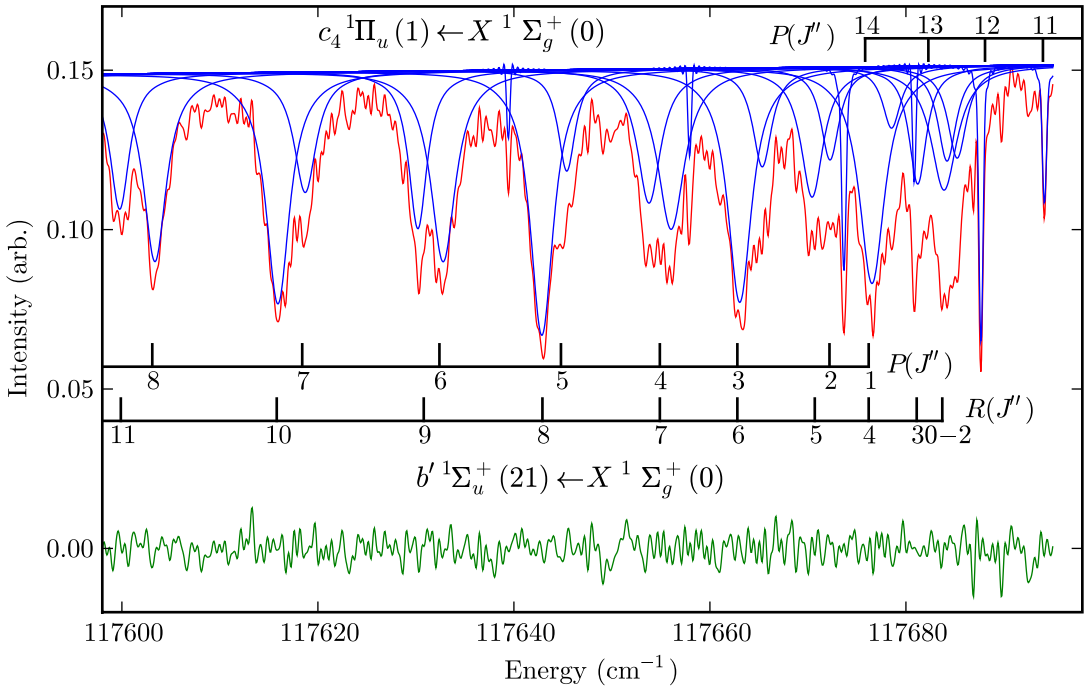

Figure 5.8: *Red:* SOLEIL transmission scan showing the bandhead of $b'\,{}^1\Sigma_u^+(v' = 21) \leftarrow X\,{}^1\Sigma_g^+(v'' = 0)$. Narrow overlapping lines are attributed to $c_4\,{}^1\Pi_u(v' = 1) \leftarrow X\,{}^1\Sigma_g^+(v'' = 0)$. *Blue:* Model lines. *Green:* The difference between experimental and modelled transmission, showing residual evidence of weak unmodelled lines near $117\,690\,\mathrm{cm}^{-1}$.

bination difference that is precisely calculable from ground-state energy levels. This extra information enabled the fitting of the band head R-branch levels, despite a high degree of blendedness. Also indicated in the residual trace are neglected lines near $117\,690\,\mathrm{cm}^{-1}$ and possible another feature near $117\,650\,\mathrm{cm}^{-1}$ which is broader.

The least-squares fitting routine used to determine the various model parameters also produces estimates of their uncertainties, as discussed in Sec. 6.2. In order to determine the reliability of these estimates, a large number of synthetic single-line model transmission cross sections were degraded with random noise and then least-squares fitted. A series of ensembles covered all experimentally encountered line strengths, linewidths, and background SNRs; and each consisted of 500 trials. The estimated uncertainty in the fitting parameters of each trial was recorded as well as the actual fitting errors, and this data is summarised in Fig. 5.9.

One conclusion that may be drawn from Fig. 5.9 is that fitted line energies with uncertainty estimated by the least-squares program to be below $0.05\,\mathrm{cm}^{-1}$ may adopt that uncertainty as a useful standard error. Similarly, the least-squares estimated uncertainty may be adopted as a standard error of fitted line strengths where it does not exceed 15% of the line strength. Estimated uncertainties up to 30% of a fitted linewidth may likewise be regarded with confidence.

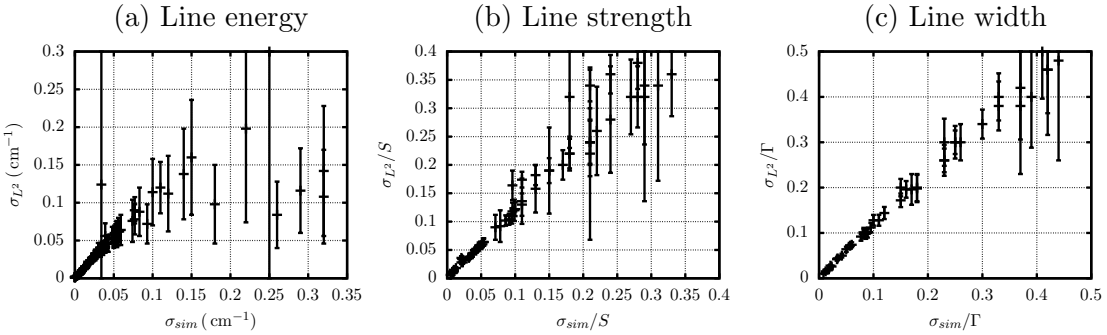

Figure 5.9: *(a):* Estimated uncertainty versus actual fitting error of line energies for synthetic data. Each error bar represents an ensemble of 500 fitted residuals, where $\sigma_{\rm sim}$ is the standard deviation of these residuals; and the σ_{L^2} error bars show the range of uncertainties estimated by the least-squares program. *(b):* Residual standard deviations and estimated uncertainty in fitted line strengths. These have been scaled by line strength. *(c):* Residual standard deviations and estimated uncertainty in fitted linewidths. These have been scaled by linewidth.

5.4 Column density calibration

Absorption lines arising from the absorption band $c_5'\,{}^1\Sigma_u^+(v'=0) \leftarrow X\,{}^1\Sigma_g^+(v''=0)$ have been observed in both the KEK and SOLEIL data sets. This red degraded band has its head at $115\,850\,\mathrm{cm}^{-1}$ and is not overlapped by any other strong bands down to $115\,600\,\mathrm{cm}^{-1}$, whereupon the similarly-intense $c_4\,{}^1\Pi_u(v'=0) \leftarrow X\,{}^1\Sigma_g^+(v''=0)$ is found. Absorption lines in both the P and R branches of $c_5'(0) \leftarrow X(0)$ are well resolved up to $P(16)$ and $R(18)$, show a large range of line strengths, and were not found to have measurable natural linewidths. These properties make this band a suitable subject for comparing the KEK and SOLEIL data sets, to check for consistency in their analysis and in order to calibrate the column densities of the SOLEIL spectra, thus putting the SOLEIL derived f-values on an absolute scale.

Figure 5.10 shows example transmission scans from KEK and SOLEIL. In either case, scans at multiple column densities cover this region and the plotted examples are those which were found to provide the best f-value measurements. From the KEK data set, this was the spectrum measured with the second-highest column density, $N = 4.1 \times 10^{14}\,\mathrm{cm}^{-2}$, and a maximum absorption of $\sim 25\%$. The lower column density KEK scans did not resolve the weakest lines and the f-values of the stronger lines were underestimated by the fitting routine when using the highest-pressure scan.

Excessive absorption is not such a concern when analysing the SOLEIL data set because of the well-known and narrow instrument function, and accurate f-value measurements were possible for lines with up to 90% peak absorption. The resilience of the SOLEIL fitted line strength to deep absorption is fortuitous because it compensates somewhat for a SNR which is poorer than that of the KEK spectra.

The $c_5'(0) \leftarrow X(0)$ lines appearing in three different SOLEIL spectra were analysed and the resultant line strengths converted to band f-values. These are plotted in Fig. 5.11 along with KEK derived band f-values. The three sets of SOLEIL measurements were made under different experimental conditions, with the following nominal pressure readings associated with each subplot of Fig. 5.11: (b) $1.5 \times 10^{-3}\,\mathrm{mb}$, (c) $4.9 \times 10^{-3}\,\mathrm{mb}$, and (d) $1.3 \times 10^{-1}\,\mathrm{mb}$. The KEK measurements in (a) are an amalgamation of several scans at different N_2 pressures but with absolutely calibrated column densities. An instrumental resolution of $0.325\,\mathrm{cm}^{-1}$ FWHM was used in (a) and (b), but increased to

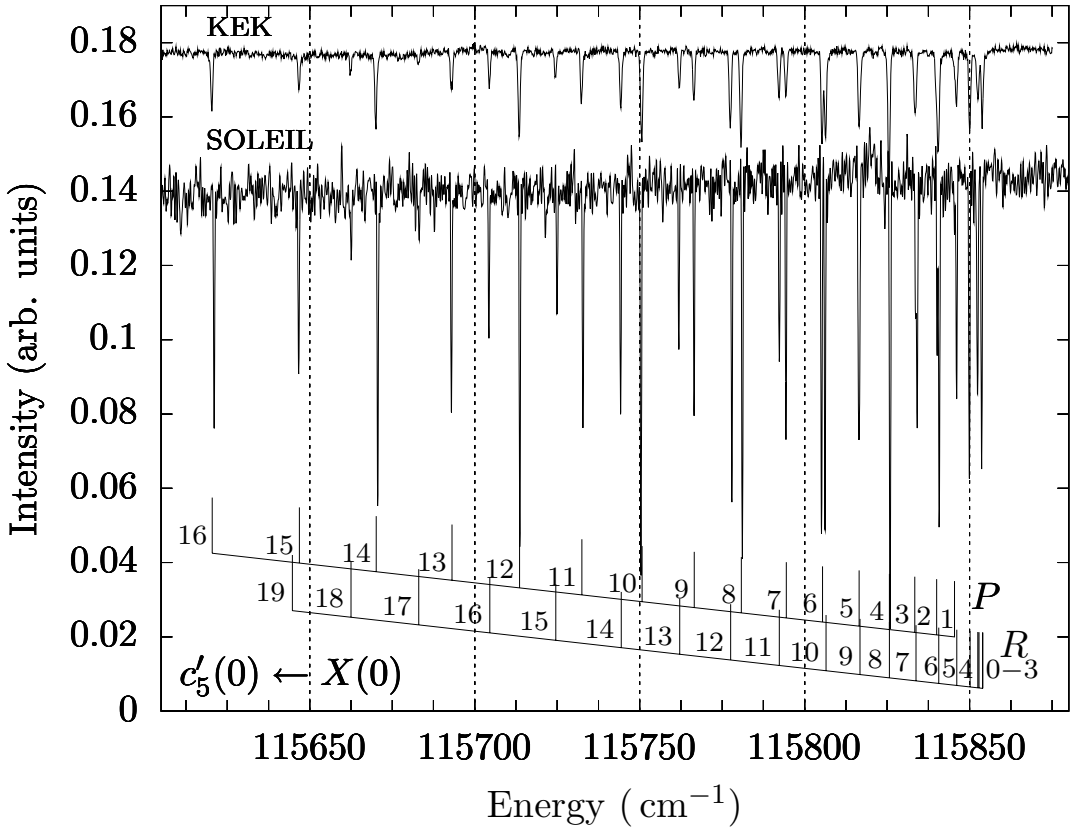

Figure 5.10: Experimental transmission spectra of $c_5'\,{}^1\Sigma_u^+(v'=0) \leftarrow X\,{}^1\Sigma_g^+(v''=0)$ as measured at the KEK and SOLEIL synchrotrons.

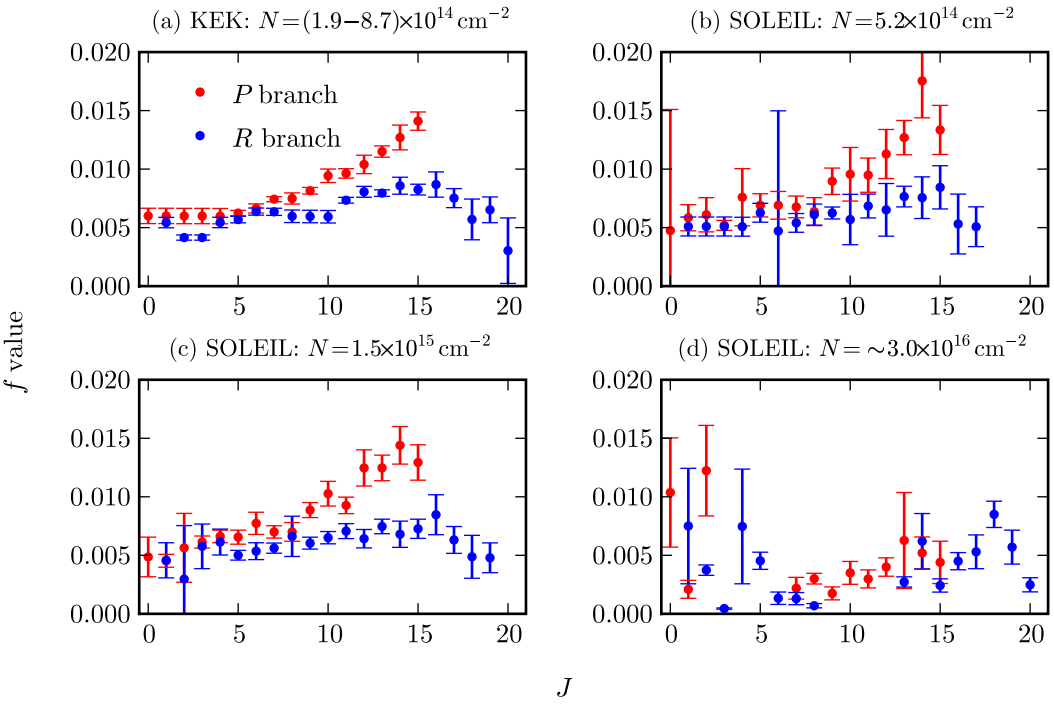

Figure 5.11: Experimental band f-values of $c_5'(0) - X(0)$ from two data sets, and for several column densities N. The KEK results were derived from spectra discussed in Chap. 4 and are a composite of measurements made over a range of column densities. Column densities have been assigned to the SOLEIL spectra that lead to the best agreement between band f-values of the two experiments.

$0.65\,\mathrm{cm}^{-1}$ FWHM for (d) because of time constraints.

It is clear that the higher SNR of the KEK data set leads to less scattered f-value measurements, an effect somewhat compensated for in Fig. 5.11 (c) where a more deeply absorbed SOLEIL spectra has been analysed. The band f-values in Fig. 5.11 (d) are determined from the most deeply absorbed spectrum and are clearly distorted by saturation. Particularly affected are the strongest lines of $c'_5(0) \leftarrow X(0)$, those with $4 \lesssim J \lesssim 12$, which are apparently underestimated.

The relative f-values plotted in Fig. 5.11 (a), (b), and (c) are in excellent agreement, and column densities for (b) and (c) have been adopted that provided a best fit to the absolute f-values of (a). These calibrated column densities may be now be used to analyse further lines appearing in the SOLEIL spectra for which no KEK measurements exist. It was not possible to calibrate the column density of the spectrum corresponding to Fig. 5.11 (d) because of the distorting saturation.

The ratios of calibrated column density to the nominal pressure measurement in the absorption cell are 2.9×10^{-18} and $3.3 \times 10^{-18}\,\mathrm{mb/cm}^{-2}$ for spectra corresponding to Fig. 5.11 (b) and (c), respectively. The 13% difference between these two ratios reinforces the suspicion that a relative calibration of SOLEIL column densities between spectra based on their recorded N_2 pressure may not be regarded with much confidence.

The uncertainty in the calibrated column densities here is approximately the same as that of the original KEK standard, that is 10% [154]. The additional uncertainty introduced by the cross-experiment comparison of line strengths is quite negligible when so many well resolved lines are used.

The procedure described here was repeated for other SOLEIL spectra, and other absorption bands, recorded at higher and lower pressures in order to determine their column densities. The complete series of $^{14}N_2$ measurements have column densities falling in the range of 3.6×10^{14} to $1.8 \times 10^{18}\,\mathrm{cm}^{-2}$.

5.5 Temperature calibration

Some measurements of $^{14}N_2$ were made whilst cooling the absorption chamber by the evaporation of liquid-nitrogen in a surrounding jacket. The efficiency of this cooling process is unknown and the equilibrium temperature of the N_2 sample was estimated directly from the observed spectra by two methods.

The Doppler broadening of the observed lines is proportional to the square root of temperature according to Eq. (4.3). By least-squares fitting widths to a collection of spectral lines that are expected to have negligible natural linewidth the Doppler component of broadening, and hence the temperature, may be determined directly. The liquid-nitrogen cooled experiments were also conducted at the best resolution of the instrument, $0.1625\,\mathrm{cm}^{-1}$ FWHM, making this determination easier, and the deduced temperature was $130 \pm 50\,\mathrm{K}$.

A more accurate determination of temperature was made by examining the distribution of oscillator strength over the rotational lines of a single vibrational band, determined by the thermal distribution of ground-state levels according to the Boltzmann statistics of Eq. (2.106). The distribution of ground-levels and the sample temperature may be determined by measuring the rotational distribution of oscillator strength while taking into account the Hönl-London factors of Tab. 2.2. This analysis was repeated for three unperturbed bands which are known from KEK measurements to have line strengths well described by Hönl-London factors, and a temperature of $90 \pm 5\,\mathrm{K}$ was deduced.

Upper level	T_0 (cm^{-1})	Obs. Lines	Obs. J	f_0	$f_{\mathrm{av.}}$	f_{EEL}	$f(J)$ $x = J(J+1)$
$b(15)$	111 870	12	$1-7$	0.0014(2)	0.0014	0.0004	0.0014
$b'(19)$	116 682	45	$0-25$	0.0088(9)	0.007	0.0084	See Fig. 5.13
$c'_4(6)$	116 806	22	$0-19$	0.008(1)	0.0072	0.0071	*P,R:* $0.0073 - 1.6\times10^{-5}x$ for $J<13$
$b'(20)$	117 205	39	$0-21$	0.010(2)	0.014	0.0071	*P,R:* $0.010 + 6.7\times10^{-6}x$
$b'(21)$	117 680	44	$0-23$	0.0039(5)	0.0063		*P:* $0.0039 + 5.3\times10^{-6}x$ for $J<20$
							R: $0.0039 + 8.9\times10^{-6}x$ for $J<20$
$c_4(1)$	117 751	33	$1-18$	0.00071(8)	0.0010	0.0034	*Q:* 0.00071
							P,R: See Fig. 5.17
$c'_5(1)$	118 069	32	$2-25$	0.00016(5)	0.000084		See Fig. 5.18
$b'(22)$	118 483	37	$0-17$	0.0036(4)	0.0033	0.0020	*P,R:* $0.0036 - 4.2\times10^{-6}x$

Table 5.1: Summary of experimental f-values deduced from the SOLEIL data set, listed in order of increasing term origin, T_0. Rotationless f-values, f_0, are extrapolated to $J=0$, where J is the excited state angular-momentum quantum number. Rotationally-dependent f-values, $f(J)$, are approximated by linear functions in terms of $J(J+1)$. Also listed is the total number of observed lines and the span of observed J. The linearised $f(J)$ are not always applicable to the entire range of observed J. A previous measurement of band integrated oscillator strengths, determined from the electron energy loss spectra of Geiger and Schröder [38], are listed under f_{EEL}. These have been normalised to the well-known band $b(3) \leftarrow X(0)$ with $f_0 = 0.043$ [155]. To provide a more direct comparison with f_{EEL}, band averaged f-values have been calculated from the observed SOLEIL lines and are listed as $f_{\mathrm{av.}}$.

5.6 Results

A total of 15 $^{14}N_2$ bands were analysed, corresponding to transitions from $X\,^1\Sigma_g^+(v=0)$ to the excited levels $b'\,^1\Sigma_u^+(v=12-22)$, $c'_4\,^1\Sigma_u^+(v=6)$, $c'_5\,^1\Sigma_u^+(v=1)$, $b\,^1\Pi_u(v=15)$, and $c_4\,^1\Pi_u(v=1)$. Line parameters for all those rotational transitions that could be accurately least-squares fitted are listed in Appendix A.2. Summary descriptions of band f-values and linewidths for each vibrational band are given in Tab. 5.1 and Tab. 5.2, respectively. Individual discussions of each band are presented below. Rotational transitions are discussed in terms of the ground-state angular-momentum quantum number using the regular symbols $P(J'')$, $R(J'')$, and $Q(J'')$. Deduced line parameters are labelled according to the excited-state angular-momentum quantum number, J.

Table 5.1 includes all deduced band f-values except those pertaining to the transitions $b'(v'=12-18) \leftarrow X(0)$, which were used in conjunction with KEK absolute f-values for the purpose of column density calibration and do not constitute new information. The rotationless f-values, f_0, are an extrapolation of these observations to $J=0$. In the case of $^1\Sigma - {}^1\Sigma$ transitions, this quantity may be determined directly from the $P(1)$ line; for those bands of type $^1\Pi_u - {}^1\Sigma$, no excited-state $J=0$ level exists and the rotationless f-value is nonphysical. In either case, f_0 may be most accurately determined by fitting a polynomial in terms of $J(J+1)$ to many known low-J f-values, even where a $P(1)$ line is directly measured. The rotationless f-value may be usefully compared to theoretical models where the effects of rotational interactions have been neglected.

The band averaged f-values, $f_{\mathrm{av.}}$, are calculated as the weighted mean of band f-values for all observed rotational lines, where the weights are proportional to the strength of each line at a temperature of 300 K. A simple summation of the observed line strengths is not possible, because for some bands not all strongly contributing lines were reliably parameterised, due to blendedness. A comparison of $f_{\mathrm{av.}}$ and the relative electron energy loss intensities of Geiger and Schröder [38], f_{EEL}, provides an experimental corroboration

Level	Obs. J	Γ_0 (cm^{-1} FWHM)	Γ_{prev} (cm^{-1} FWHM)	$\Gamma(J)$ $x = J(J+1)$
$b(15)$	$1-7$	0.09(3)		0.09
$b'(12)$	$0-15$	0.07(2)	0.021(3) [125]	0.07
$b'(13)$	$1-7$	0.11(2)	0.07(3) [53]	0.11
$b'(14)$	$0-16$	0.25(2)	0.19(5) [50]	0.25
$b'(15)$	$0-21$	0.27(2)	0.17(3) [50]	$0.27 - 3 \times 10^{-4}x$
$b'(16)$	$1-21$	0.09(2)		0.09
$b'(17)$	$0-21$	0.29(2)	0.23(2) [50]	$0.29 - 1.3 \times 10^{-3}x$, for $J < 11$
$b'(18)$	$0-15$	0.08(2)		0.08
$b'(19)$	$0-25$	0.10(2)		$0.09 + 3.4 \times 10^{-4}x$, for $J < 15$
$c'_4(6)$	$0-19$	0.05(2)		See text.
$b'(20)$	$0-21$	0.16(3)		See text.
$b'(21)$	$0-23$	2.58(7)		$2.58 - 2.7 \times 10^{-3}x$
$c_4(1)$	$1-18$	0.18(2)		e-parity: $0.18 + 3 \times 10^{-4}x$
				f-parity: $0.18 - 2 \times 10^{-4}x$
$c'_5(1)$	$2-25$	2.8(5)		See text.
$b'(22)$	$0-17$	1.41(3)		$1.41 - 6.4 \times 10^{-4}x + 1.6 \times 10^{-5}x^2$

Table 5.2: Summary of natural linewidths deduced from the SOLEIL data set. Rotationless linewidths, Γ_0, are extrapolated to $J = 0$; and rotationally-dependent f-values, $\Gamma(J)$, are approximated by linear or quadratic functions in terms of $J(J+1)$, where possible. Also listed is the span of observed J. Not all listed $\Gamma(J)$ are applicable over the entire range of observed J. Previously determined linewidths are listed under Γ_{prev}. Experimental uncertainties in units of the least-significant digit are listed in parentheses, and references to previous measurements are bracketed.

of the present measurements. The calibration of f_{EEL} to an absolute scale has been made by considering the well-resolved band $b(3) \leftarrow X(0)$, with a known absolute oscillator strength of 0.043 [155].

A comparison of $f_{\mathrm{av.}}$ with f_{EEL} relies on the equivalence of electron excited generalised oscillator-strengths to optical f-values at small momentum transfer. The measurements of Geiger and Schröder [38] employed 25 keV electron impact energies and small scattering angles and certainly fulfil this criterion. More serious is the low-resolution of $80\,\mathrm{cm}^{-1}$ FWHM achieved in this experiment. Although the integrated intensity over a large energy range will not be degraded at low resolution in an electron scattering experiment, the partitioning of intensity between individual bands is less certain, and impossible where bands are overlapped. For this reason, the agreement between f_{EEL} and $f_{\mathrm{av.}}$ for individual bands is not very good. More concerning is the disparity in summed oscillator-strength over all bands in Tab. 5.1, with the summed values of $f_{\mathrm{av.}}$ and f_{EEL} given by 0.039 and 0.028, respectively.

Table 5.2 summarises the natural linewidths observed for each band in the SOLEIL experiment. Extrapolations to $J = 0$ have been made for each band, listed under Γ_0, which may be usefully compared with theoretical models that do not include the effects of rotational perturbations. A simple parameterisation of linewidths to higher J is also given, although for some bands this variation was too complex to be constrained by a polynomial. Some previous experimental measurements exist for these bands, listed under Γ_{prev}.

$b\,^1\Pi_u(v'=15) \leftarrow X\,^1\Sigma_g^+(v''=0)$

This weak band was observed in the KEK series of experiments but its measurement coincided inconveniently with a period of poor beam stability, so that line parameters

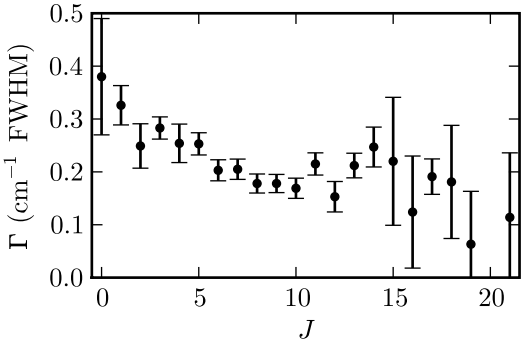

Figure 5.12: Natural linewidths, Γ, of $b'(17) \leftarrow X(0)$, plotted as a function of excited-state J.

could not be deduced reliably. New measurements here are free of this problem and are also made with greater column density and liquid-nitrogen cooling. The resulting f-values and linewidths are significantly scattered and have large uncertainties but since no rotational dependencies were observed an overall mean provides a good estimate of a band-averaged f-value and linewidth.

$b'\,^1\Sigma_u^+(v'=12-18) \leftarrow X\,^1\Sigma_g^+(v''=0)$

These bands were observed during the KEK series of experiments and their well-characterised f-values were used to calibrate SOLEIL column densities. New measurements of the linewidths of these bands have been deduced from the higher-resolution SOLEIL spectra.

No rotational dependence was observed in the predissociation linewidths of $b'(12-14,16,18) \leftarrow X(0)$, and a mean value for each band has been calculated from all observed rotational levels and listed in Tab. 5.2. Transitions to $b'(15) \leftarrow X(0)$ become gradually more narrow as J increases, and a linear fit to this dependence has been used to determine a rotationless linewidth. A linear fit was also made to the negative J dependence of $b'(17) \leftarrow X(0)$ linewidths, plotted in Fig. 5.12, but only as far as $J = 10$, after which the decrease appears to be arrested.

Several of the newly-determined linewidths disagree with earlier observations. A previous measurement of the $b'(12)$ lifetime was made by Oertel *et al.* [125], who performed a time resolved measurement of dispersed fluorescence. The equivalent natural-linewidth, $0.02 \pm 0.003\,\mathrm{cm}^{-1}$ FWHM, does not agree with the present measurement within their combined uncertainties. This difference is likely attributable to an incorrect partition of the observed fluorescence to particular states in the low-resolution spectrum of Oertel *et al.*.

The rotationless linewidths of $b(14,15,17) \leftarrow X(0)$ were previously deduced from the KEK spectra, and lie below the present measurements by 27%, 45%, and 23%; respectively. The absolute differences are similar, $0.06-0.1\,\mathrm{cm}^{-1}$ FWHM, suggesting that the empirical instrument function adopted for the KEK measurements may have utilised a Gaussian of too great width ($0.65 \pm 0.1\,\mathrm{cm}^{-1}$ FWHM).

The measured linewidth of $b'(13)$ marginally agrees with a previous measurement by Helm *et al.* [53]. This employed a low-bandwidth ultraviolet laser to directly observe the widths of individual rotational lines arising from the transition $b'(13) \leftarrow a''\,^1\Sigma_g^+(v''=0)$.

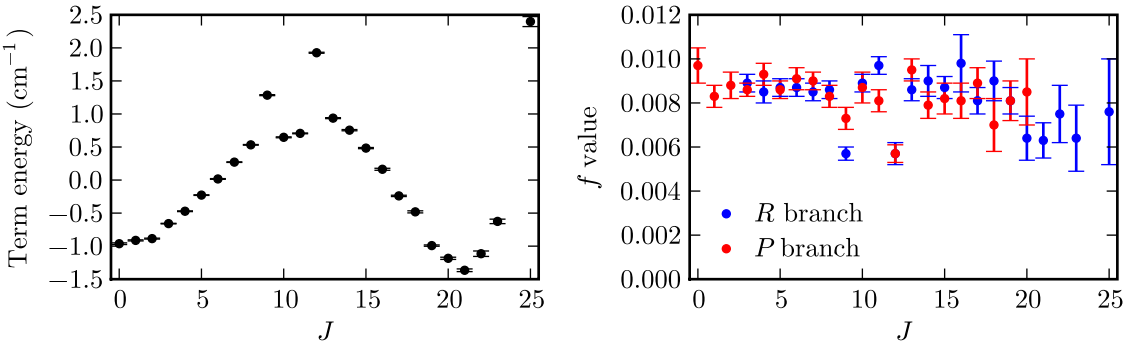

Figure 5.13: Fitted term energies of $b'(19)$ and band f-values of $b'(19) \leftarrow X(0)$, plotted as a function of excited-state J. Term energies have been reduced by the removal of a second-order polynomial of best fit, calculated in terms of $J(J+1)$. The plotted error bars represent the estimated statistical uncertainty of the fitting procedure only.

$b'\,^1\Sigma_u^+(v'=19) \leftarrow X\,^1\Sigma_g^+(v''=0)$

The reduced term values of $b'(19)$ are plotted in Fig. 5.13 and appear doubly perturbed, at $J = 9$ and 12, by level crossings. Extra lines appear near both perturbations and have been assigned to the following transitions which satisfy P- and R-branch combination differences: $R(8)$ at 116 636.31 cm^{-1}, $P(10)$ at 116 560.47 cm^{-1}, $R(11)$ at 115 690.78 cm^{-1}, and $P(13)$ at 116 490.08 cm^{-1}. The strength borrowed by these from $b'(19) \leftarrow X(0)$ is evident in the locally-decreased f-values plotted in Fig. 5.13.

Upon extrapolating the known vibrational levels of $b\,^1\Pi_u$ and $c_3\,^1\Pi_u$ to higher energies, transitions to their respective $v = 25$ and 6 levels should appear somewhere in the region of the observed extra lines. Examining the sense of the energy shifts, it is likely that the low-J perturber has a greater rotational-constant than $b'(19)$, and the upper perturber a lesser rotational-constant, these conditions are fulfilled by $c_3(6)$ and $b(25)$, respectively.

Aside from the above level crossings, the $b'(19) \leftarrow X(0)$ f-values show no prominent rotational dependence, and the observed linewidths increase gradually. There is an apparent decrease in both f-values and linewidths for $J > 19$. However, the corresponding transitions appear only weakly in the spectra and are less reliably parameterised than those for lower J.

$c_4'\,^1\Sigma_u^+(v'=6) \leftarrow X\,^1\Sigma_g^+(v''=0)$

The fitted line parameters of $c_4'(6) \leftarrow X(0)$ are plotted in Fig. 5.14 and show several perturbations.

The apparently enhanced linewidth of $J = 0$ may not be viewed with confidence due to the weakness of this line in the available spectra. However, the increased width for $J = 3$ relative to its neighbours is determined from both the $P(4)$ and $R(2)$ lines, both of which are well resolved. The $J = 3$ rotational lines do not show corresponding perturbations in their term energies or f-values.

A deflection of the $J = 8$ and 9 term values indicates a level crossing with a perturbing state of lower rotational constant. Extra lines are also visible in the spectra corresponding to perturbing $R(8)$ and $P(10)$ transitions, located at 116 812.2 and 116 736.63 cm^{-1}, respectively. These extra lines have 10% of the strength of the $c_4'(6)$ main lines, and their

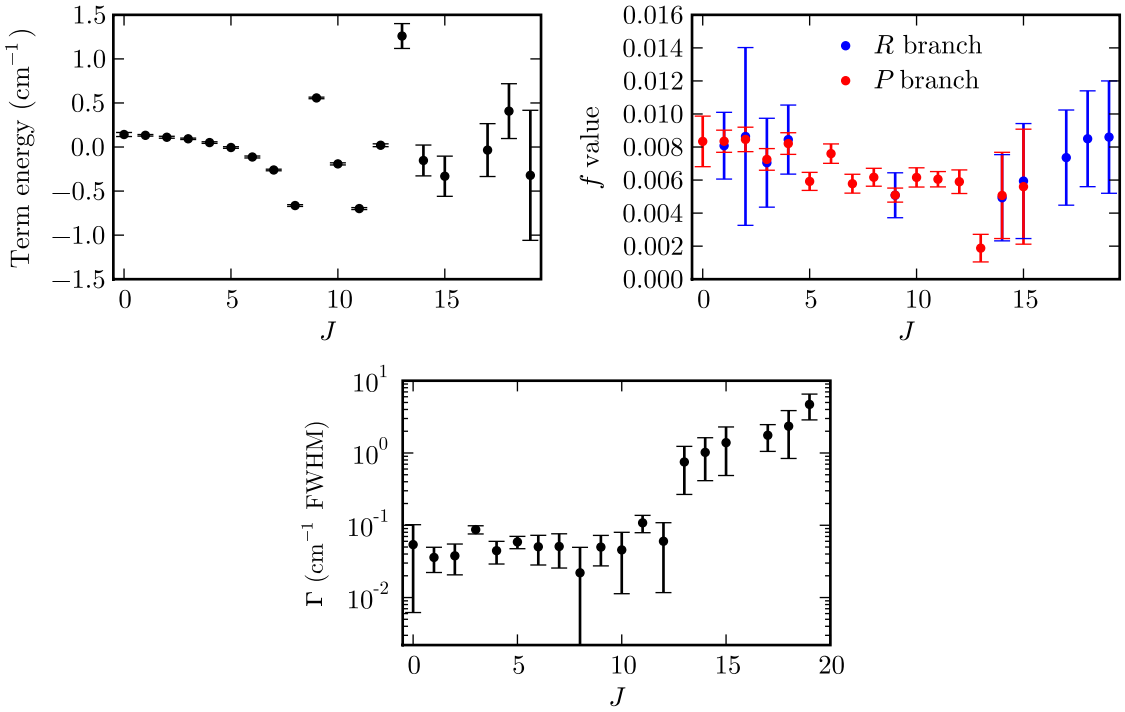

Figure 5.14: Fitted term energies, band f-values, and linewidths, Γ, of $c_4'(6) \leftarrow X(0)$, plotted as a function of excited-state J. Term energies have been reduced by the removal of a second-order polynomial of best fit, calculated in terms of $J(J+1)$. The plotted error bars represent the estimated statistical uncertainty of the fitting procedure only.

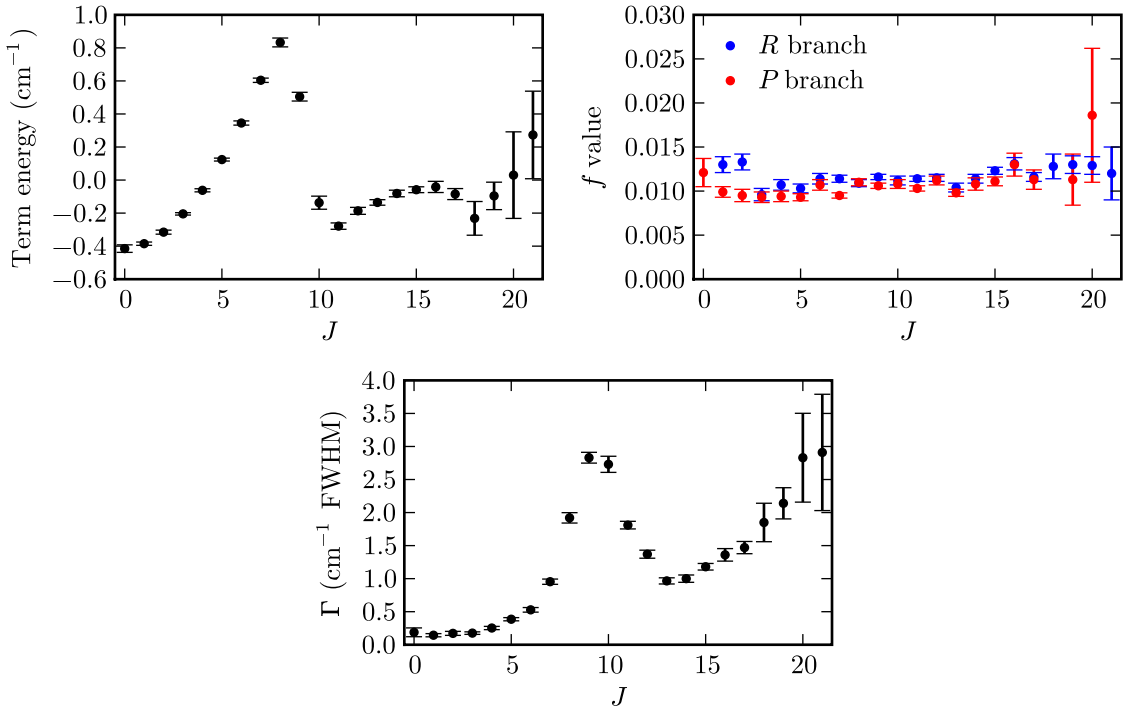

Figure 5.15: Fitted term energies, band f-values, and linewidths, Γ, of $b'(20) \leftarrow X(0)$, plotted as a function of excited-state J. Term energies have been reduced by the removal of a second-order polynomial of best fit, calculated in terms of $J(J+1)$. The plotted error bars represent the estimated statistical uncertainty of the fitting procedure only.

combination difference rigorously asserts their assignment, even though the perturbing state is otherwise unknown.

There is another level crossing between $J = 13$ and 14, also accompanied by the appearance of extra lines assigned as perturbing $R(12)$ and $P(14)$ transitions, appearing at 116 817.75 and 116 710.43 cm^{-1}, respectively. These extra lines have approximately 70% of the strength of the main lines, which are significantly weakened, as shown in Fig. 5.14. Three more extra lines appear near the $c'_4(6) \leftarrow X(0)$ $P(14)$ line which may be related to this perturbation, but these do not have clear analogues amongst the R-branch of $c'_4(6) \leftarrow X(0)$ which is, however, heavily blended. The sum of integrated cross sections observed for $c'_4(6) \leftarrow X(0)$ $P(14)$ and all four extra lines is, within error, equal to the expected value of an unperturbed $c'_4(6) \leftarrow X(0)$ $P(14)$ line.

Finally, there is rapid increase in the observed $c'_4(6)$ linewidths for $J > 12$. The onset of this effect corresponds to the $c'_4(6)$ term series crossing the $b\,^1\Pi_u$ dissociation energy of 117 118 cm^{-1}, relative to $X\,^1\Sigma_g^+(v = 0, J = 0)$, and is attributable to predissociation into the $b\,^1\Pi_u$ continuum. It may be that the $c'_4(6)$ perturbations for levels below this dissociation energy are the result of interactions with high vibrational levels of $b\,^1\Pi_u$.

$b'\,^1\Sigma_u^+(v' = 20) \leftarrow X\,^1\Sigma_g^+(v'' = 0)$

Three important effects are evident in the strongly J-dependent linewidths of $b'(20)$ plotted in Fig. 5.15. First, the $J = 0$ width of 0.16±0.03 cm^{-1} FWHM likely results from

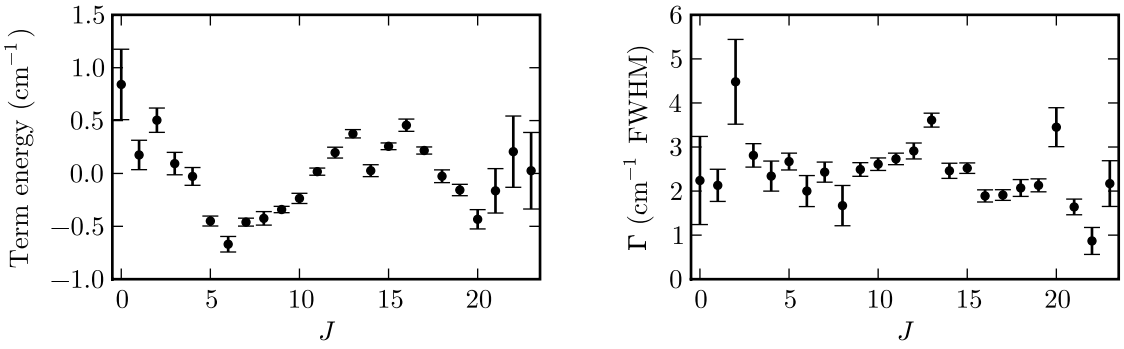

Figure 5.16: Fitted term energies and linewidths, Γ, of $b'(21) \leftarrow X(0)$, plotted as a function of excited-state J. Term energies have been reduced by the removal of a second-order polynomial of best fit, calculated in terms of $J(J+1)$. The plotted error bars represent the estimated statistical uncertainty of the fitting procedure only.

predissociation following a spin-orbit interaction with the $\Omega = 0$ component of an unknown $^3\Sigma$ or $^3\Pi$ state. Measurable $J = 0$ linewidths have been noted for the other $^1\Sigma_u^+$ states, with the same general explanation applying.

The peak in linewidth around $J = 9$ has a more concrete explanation. Since $b'(20)$ lies above the dissociation energy of $b\,^1\Pi_u$, all $^1\Pi_u$ levels in the region will be strongly predissociated by mutual electrostatic interactions. In turn, a rotational interaction with $b'(20)$ will transmit this predissociativity. The $J = 9$ width peak apparently arises from such a rotational interaction with $o_3\,^1\Pi_u(v = 6)$. No lines attributable to $o_3(6) \leftarrow X(0)$ are visible in the experimental spectra. These are likely to have large widths, evidenced by the large span of broadened $b'(20)$ rotational levels, as well as the slowness of the accompanying term energy deflection.

Finally, the linewidths of $b'(20)$ continue to increase for rotational-levels above those perturbed by $o_3(6)$. This phenomenon is likely due to perturbations with the $\Omega = 0$ components of states of $^3\Pi_u$ symmetry which are themselves predissociated. Such perturbations are rigorously forbidden for $J = 0$ but may increase in strength approximately proportionately to $J(J+1)$ if there are nonzero matrix elements of the L-uncoupling or spin-rotation operators. A precise explanation of the observed $J > 0$ linewidths for $b'(20)$ and the other $^1\Sigma_u^+$ levels is usually difficult to arrive at because of the large number of invisible but perturbing $^3\Pi_u$ and $^1\Pi_u$ states present at such high energies.

$b'\,^1\Sigma_u^+(v'=21) \leftarrow X\,^1\Sigma_g^+(v''=0)$

All of the observed levels of $b'(21)$ are significantly broadened by predissociation, with fitted linewidths plotted in Fig. 5.16. All rotational lines with $J \leq 4$ are severely blended and likely determined with less confidence than represented by the fitting uncertainties plotted in Fig. 5.16, as indicated by the increased scatter of these levels for the various fitted parameters.

No rotational-dependence of linewidths can be concluded for $J \leq 10$. However the increased width of $J = 13$ relative to its neighbours may be regarded with confidence due to the appearance of this unblended line in one SOLEIL spectrum with moderate absorption. Accompanying this increased width, there is a slight distortion of the $b'(21)$

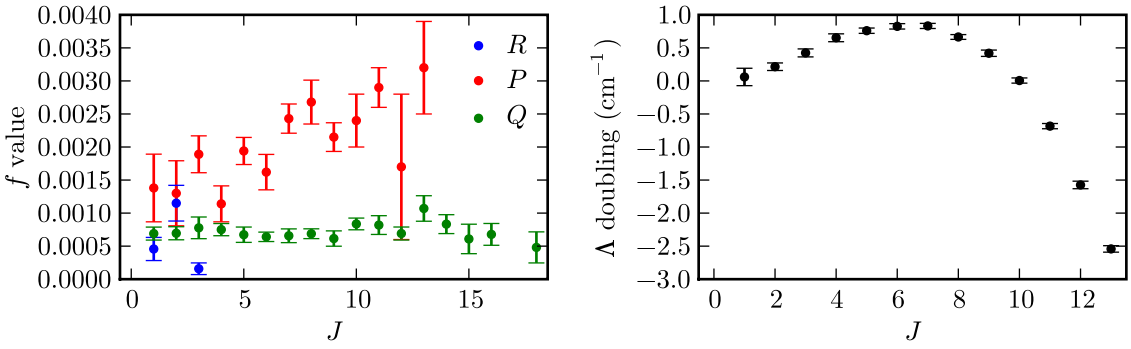

Figure 5.17: Fitted band f-values of $c_4(1) \leftarrow X(0)$ and the difference between e-parity, T_e, and f-parity, T_e, term values of $c_4(1) \leftarrow X(0)$, plotted as a function of excited-state J. The plotted error bars represent the estimated statistical uncertainty of the fitting procedure only.

term series from a simple polynomial dependence, with the $J = 13$ and 14 levels shifted to higher and lower energies, respectively, by $\sim 0.2\,\mathrm{cm}^{-1}$. This is visible in Fig. 5.16 as a slight discontinuity in the reduced term energies. The sense of the observed deflection indicates a level crossing from below; that is, by a perturbing state with greater rotational constant than $b'(21)$. The various $^1\Pi_u$ and $^1\Sigma_u^+$ Rydberg states of N_2 satisfy this condition but no known or likely levels of these will intersect $b'\,^1\Sigma_u^+(v = 2)$. Thus, the perturbing state in this case is unknown.

The $b'(21) \leftarrow X(0)$ f-values increase approximately linearly with J, with the R branch increasing marginally more rapidly than the P branch.

$c_4\,^1\Pi_u(v'=1) \leftarrow X\,^1\Sigma_g^+(v''=0)$

The Q-branch of $c_4(1) \leftarrow X(0)$ appears completely unperturbed in the SOLEIL spectra, with no rotational dependence apparent in its f-values or linewidths. However, the P and R branches, terminating on e-parity levels of $c_4(1)$, are perturbed, as indicated by the Λ doubling of e-parity term values in Fig. 5.17. This initially increases with J but subsequently reverses and changes sign, indicating that $c_4(1)$ is rotationally-coupled to multiple e-parity levels of $^1\Sigma_u^+$ symmetry. Additionally, the P-branch f-values increase with rotation and the R branch rapidly becomes unmeasurable due to its weakness. This variation between branches arises from an interference effect which is common among N_2 transitions of mixed $^1\Pi \leftarrow {}^1\Sigma$ and $^1\Sigma \leftarrow {}^1\Sigma$ character, and is described in detail in Sec. 2.8.4.

$c_5'\,^1\Sigma_u^+(v'=1) \leftarrow X\,^1\Sigma_g^+(v''=0)$

The observed f-values and linewidths of $c_5'(1) \leftarrow X(0)$ are plotted in Fig. 5.18 and show strong rotational dependence. The P-branch f-values decrease rapidly with rotation below $J = 11$ with $P(10)$ and $P(11)$ entirely missing from the recorded spectra. Unfortunately no spectra were measured at a column density suitable for the analysis of the heavily blended R-branch lines for $J < 8$. The $R(7)$, $R(8)$, and $R(9)$ lines have band f-values which are greater than those P-branch lines with the same J. For $J > 11$ the observed f-values increase rapidly, with the P-branch lines now lying slightly above the R branch.

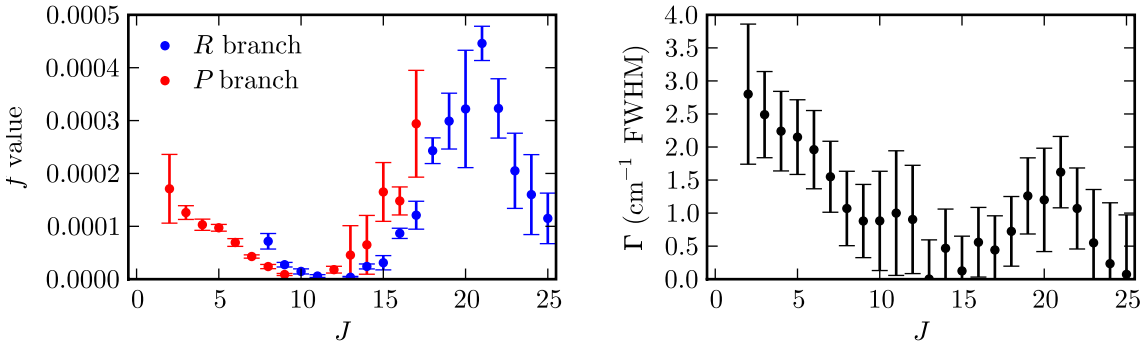

Figure 5.18: Fitted f-values and linewidths, Γ, of $c'_5(1) \leftarrow X(0)$, plotted as a function of excited-state J. The plotted error bars represent the estimated statistical uncertainty plus an extra uncertainty, due to the imprecision of the column density determination for spectra in which this band appears.

Finally, the R-branch f-values decrease for $J > 21$ with no comparative observations of the P branch.

A similar rotational dependence is apparent in the $c'_5(1)$ linewidths as for the f-values. A linewidth minimum occurs at approximately $J = 13$ and a subsidiary maximum at $J = 21$, as shown in Fig. 5.18.

Systematic errors in the analysis of $c'_5(1) \leftarrow X(0)$ are greater than for the other bands. The only spectrum in which this weak band is resolved was recorded with a very high column density, $N = (1.8 \pm 0.6) \times 10^{18}\,\mathrm{cm}^{-2}$, and at relatively poor resolution, defined by a FWHM of $1.3\,\mathrm{cm}^{-1}$. The large column density uncertainty is due to the lack of suitable calibration bands. This problem arises because almost the entire spectrum is somewhat absorbed at such high column density, so that a background intensity may only be estimated in a few locations. Despite the large error incurred in absolute terms, the relative f-value features discussed above are reliably inferred, particularly with respect to the complete annihilation of oscillator strength at $J = 11$.

$b'\,{}^1\Sigma_u^+(v'=22) \leftarrow X\,{}^1\Sigma_g^+(v''=0)$

No rotationally-localised perturbations are evident in the observed line parameters of $b'(22) \leftarrow X(0)$. Both the observed linewidths and f-values decrease with rotation, and the linewidths are seen to increase again for $J > 14$, as shown in Fig. 5.19.

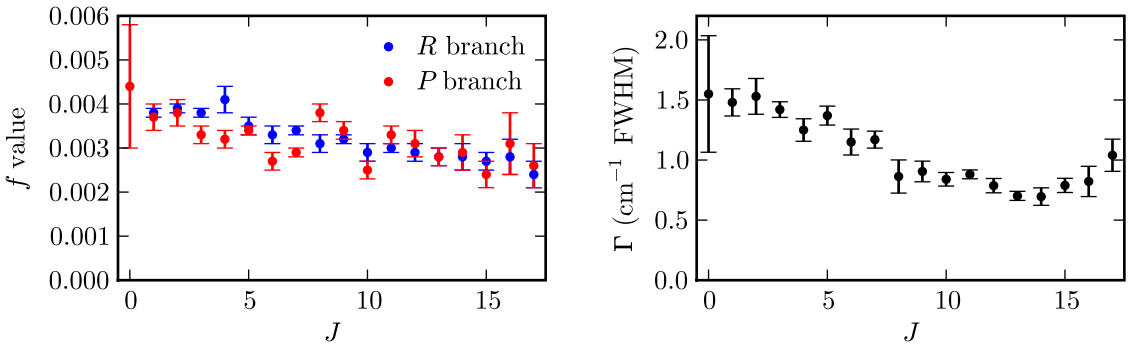

Figure 5.19: Fitted f-values and linewidths, Γ, of $b'(22) \leftarrow X(0)$, plotted as a function of excited-state J. The plotted error bars represent the estimated statistical uncertainty of the fitting procedure only.

Chapter 6

Coupled-channels model of N_2

A computer program has been developed at the Australian National University which solves the coupled Schrödinger-equation for diatomic nuclear-motion using the methods detailed in Sec. 2.11. This code has been used to study molecular oxygen [40, 80, 95, 96, 99], and has since been adapted to the case of N_2. Several modelling studies of N_2 photoabsorption and dissociation from before my arrival to the research group have employed this code [49, 103, 104, 105]. Since then I have been involved in extending this modelling to encompass further aspects of the N_2 spectrum. Details of this new work are given in this chapter.

The coupled-channels technique adopted here is semi-empirical and does not explicitly represent an electronic wavefunction, so that its properties must be construed from external information. Fortunately, the N_2 experimental record contains an enormous number of precisely-measured transition energies, as well as smaller quantities of optical oscillator-strengths and excited-state linewidths, with the most important data sets detailed in Chap. 3. Unfortunately, it is not possible to deduce the various free-parameters required by the coupled-channels code from a direct inversion of this data. Instead, an iterative approach is necessary where these parameters are adjusted until a best-fit to the experimental data is achieved.

My role as an investigator attempting to construct a coupled-channels of N_2 may be divided into three parts. First, it is necessary to define which parts of the spectrum are to be studied. Second, all available experimental information concerning this spectrum must be collected and evaluated. In some cases this data may need to be deperturbed in order to remove the effects of neglected electronic states. Finally, the iterative optimisation of the model must be guided so as to prevent a nonphysical convergence.

Sections 6.4 to 6.6 discuss separate models of N_2 which progressively include a more complete set of excited-state symmetry classes. By increasing the complexity of the model gradually, the largest state interactions may be estimated first and neglected higher-order effects will be illustrated.

6.1 Model parameters

6.1.1 The ground state

A representation of the N_2 ground state must be specified in order to treat photoabsorption or photoemission. A numerical potential-energy curve has been constructed from the molecular constants of Edwards *et al.* [31] by means of the Rydberg-Klein-Rees (RKR) method. The Numerov method, discussed in Sec. 2.11.2, has been used to perform a single-channel calculation of ground-state energy levels and vibrational wavefunctions from this

curve. These energy levels are found to correctly reproduce those of Edwards *et al.* [31].

Solving the Schrödinger equation with the same ground-state potential-energy curve, but adjusted reduced mass, reproduces the spectra of all isotopomers. Single-channel calculations of the $v = 0$ rotational energy levels of $^{14}N^{15}N$ and $^{15}N_2$ agrees with those calculated from the rotational constants of Bendtsen [6] to within $0.01\,\mathrm{cm}^{-1}$.

No improvements to the shape of the ground-state potential-energy curve have been found necessary.

6.1.2 Excited state potential-energy curves

The coupled-channels model includes 20 excited electronic-states at its most complex. Each of these is represented numerically by an R-dependent potential-energy curve. These are represented on a uniformly discretised R-grid spanning 0 to 10 Å in 0.005 Å steps. This outer limit is chosen sufficiently large that the nuclei are completely dissociated. Then, the calculated large-R wavefunctions are those of free particles, and suitable for the calculation of an asymptotic scattering matrix. The potential-energy curves of all dissociating states in the model are within $0.3\,\mathrm{cm}^{-1}$ of their asymptotic values at $R = 7.5$ Å.

While optimising each potential curve, it is not necessary to consider the energy at each grid point as a free parameter. Moreover, in order to present a well-posed optimisation problem, the permissible number of free parameters governing the shape of a potential-energy curve is limited by the quantity of experimental data. This implies that each potential should be described by a model with fewer parameters than, approximately, twice the number of known vibrational levels. That is, the principal contributions from each vibrational level to the set of experimental constraints are two molecular-parameters: a term origin and a rotational constant.

Polynomial forms, such as Morse functions [54] or the constructions of Spelsberg and Meyer [145], describe low-order potential-energy curve parameterisations. These are designed to be versatile near the critical potential-well region, as well as preserve the generic features of a small-R centrifugal barrier and a large-R approach to the correct dissociation limit. Spelsberg and Meyer model the $b'\,^1\Sigma_u^+$, $c_4'\,^1\Sigma_u^+$ and $c_5'\,^1\Sigma_u^+$ states of N_2, including potential-energy curves and the necessary state interactions, with only 25 parameters. Nonetheless, this model successfully reproduces 80 experimental data; specifically, 40 pairs of vibrational term values and rotational constants, accurate to within 7 and $0.3\,\mathrm{cm}^{-1}$, respectively.

The coupled-channels optimisation program has been written so as to allow for convenient experimentation with alternative forms of potential-energy curve parameterisation. Various schemes were trialled, including high-order polynomial expansions and piecewise functions of R. Ultimately, the preferred parameterisation form was the direct specification of each potential energy at a set of radial distances covering the span of the potential well relevant to the observed vibrational levels. A cubic-spline interpolation is used to transform these specified coordinates onto the required 0.005 Å grid. The inner and outer limbs of the model potential-energy curves are unconstrained above the energy of the highest observed vibrational level. In the hope of engendering a reasonable extrapolation into unknown levels, and a tidy appearance, the outer limbs have been assumed to have simple functional forms. The inner part is joined to the potential well with continuous first derivative, achieved by correctly selecting the parameters C_0 and C_1, and accorded the form

$$V(R) = C_0 + C_1 R^{-1}. \tag{6.1}$$

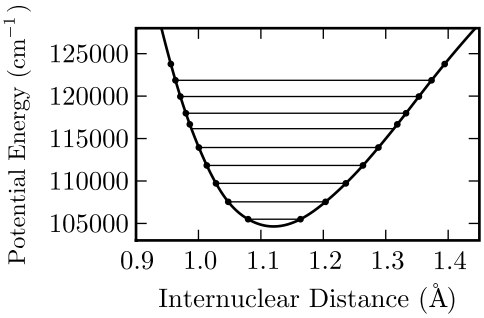

Figure 6.1: Spline interpolated potential-energy curve representing $c_4'\,{}^1\Sigma_u^+$. The markers indicate those points used to parameterise the curve. Intervening points are determined by spline interpolation. Analytic forms for the inner and outer limbs have been joined to the spline interpolation above 122 500 cm^{-1}. Horizontal lines represent the known $^{14}N_2$ vibrational-levels of $c_4'\,{}^1\Sigma_u^+$.

The outer limb is represented by a polynomial expansion,

$$V(R) = C_0 + C_1\mathscr{R} + C_2\mathscr{R}^2 + \ldots, \text{ where } \mathscr{R} = 1 - e^{-\beta R}. \tag{6.2}$$

Here, the Morse coordinate [145], $\mathscr{R}$, ensures that the outer limb rapidly converges to a constant dissociation energy. The parameters β, C_0, and C_1 are selected so as to control the rate of this convergence, and form a connection to the potential which maintains a continuous first derivative. Higher order term in Eq. (6.2) may be adopted to achieve a continuous second derivative.

Figure 6.1 provides an example of a cubic-spline parameterisation of the model potential curve representing the diabatic state $c_4'\,{}^1\Sigma_u^+$. The explicitly specified points are not uniformly distributed. For each known vibrational level two points are specified; one each near the inner and outer classical turning-points. The (V, R) coordinate of each specified point may be adjusted during the optimisation phase of model construction.

To a first approximation, the term origin of each vibrational level is insensitive to any small horizontal shift of the potential-energy curve; and the rotational constant will not be greatly affected by any slight broadening or narrowing of the curve, as long as the equilibrium internuclear distance is unaltered. Because of this approximate independence, it is beneficial to jointly specify pairs of points on each potential-energy curve, with a common energy but located on either side of the potential minimum. The R coordinates of these points are then given by $\overline{R} \pm \Delta R$, where $\overline{R}$ is their mean position and ΔR their separation. These latter quantities comprise more useful independent variables than the R-coordinates themselves.

The same potential-energy curves are applicable to all N_2 isotopomers because all significant mass dependent terms in the molecular Hamiltonian are explicitly calculated. The addition of a centrifugal potential of the form given by Eq. (2.41) results in a potential-energy curve applicable to rotational levels with $J > \Omega$.

6.1.3 State interactions and electronic transition moments

There is a maximum of 41 state interactions included in the coupled-channels models detailed here, and most of these are treated independently of R. This simplistic treatment is frequently obligatory where there is little experimental data available to constrain an interaction, but its reasonableness is supported by the single-configuration basis preferen-

tially adopted in the model. There is particularly little information regarding electronic and spin-orbit couplings involving triplet states which, being forbidden to optical excitation, do not often appear in spectra. Instead, these couplings are largely known through isolated perturbations or predissociative broadening of the observable singlet-states. In a few cases where the available information supports such a treatment, simple 2 or 3 parameter R-dependences have been used, with polynomial or Gaussian form.

The coupled-channels model is used to calculate absorption cross sections according to Eq. (2.176) and Eq. (2.175). Then, electronic transition moments must be specified for all electronic states that are not forbidden by the electric-dipole selection rules to undergo excitation from the ground state. These are represented in the model by polynomial forms or *ab initio*-calculated numerical functions of internuclear distance.

6.2 Optimisation procedure

The iterative adjustment of model parameters is achieved using the *leastsq* program included in the *SciPy* software package, available from `www.scipy.org`. This software employs the Levenberg-Marquadt algorithm [114] which seeks to minimise the least-squares measure of fit

$$L^2 = \sum_{i=1}^{m} w_i^2 d_i(p_1, p_2, \ldots, p_n)^2. \tag{6.3}$$

Here, each element d_i is the experimental residual of one model-calculated energy, out of a total of m; and each of these is dependent on the set of varied model parameters, $p_1 \ldots p_n$.

Three kinds of experimental data are input into the optimisation routine as model constraints: term values, in order to define the potential-energy curves and coupling terms of the $^1\Pi_u$ and $^1\Sigma_u^+$ states; f-values, to constrain the model electric-dipole transition moments; and linewidths, to define the predissociating $^3\Pi_u$ and $^3\Sigma_u^+$ states as well as their coupling to the singlet manifold. At least as many data must be specified as there are model parameters in order for the optimisation problem to be well-posed. In effect, more than this minimum is usually required because of the presence of correlations in the dependence of constraining data on the model parameters, and in order to avoid becoming stuck in local minima of the L^2 norm. However, the necessary computation time scales with the amount of experimental data, so redundant constraints should be avoided.

The minimisation of Eq. (6.3) will tend to evenly distribute the residual error across the set of d_i. Because of this, when experimental data of varying magnitude are being simultaneously optimised (i.e., a mixture of term origins and rotational constants, or linewidths of varying scale) it is beneficial to weight the residuals by factors, w_i, that are proportional to the magnitude of each datum. Similarly, data that have been ascribed varied experimental uncertainties should be weighted proportionately to their inverse. A perfect model convergence will result when $L^2 = 0$, but experimental inaccuracies and omissions in the model formulation prevent this.

Estimates of the uncertainties of each fitted model parameter, p_j, are also calculated by the least-squares program and are inversely proportional to $\frac{\partial^2 L^2}{(\partial p_j)^2}$. A large value of this derivative implies that the model fit is highly sensitive to variations in p_j and it is well determined although correlations between the model parameters degrade this simple interpretation and likely lead to underestimates of the true uncertainty. For example, the alteration of an interaction energy may, in many cases, be compensated for by a modification of potential-energy curves, a subtlety which may not be fully expressed in

the calculated uncertainties. Furthermore, imperfections in the model formulation may introduce additional unknown errors. As such the various numerical uncertainties should be considered relative only.

The coupled-channels model of N_2 expounded in the following sections is very complex. The selection of included electronic states and state couplings which may lead to a satisfactory reproduction of the constraining observations is not necessarily unique, and neither is their precise formulation in terms of numerical parameters. A slight difference in model formulations may lead to a large difference in optimised parameters, even where there is no change in the quality of fit. One cause of such instability arises where the observational data is of insufficient quantity or precision to constrain a complex model, and care has been made to avoid overextending the N_2 model in this way. However, the diabatic representation of electronic states is also inherently nonunique and alternative model formulations are equally valid as long as their constituent states and interactions are treated together and not quoted in isolation.

6.2.1 Optimisation of energy levels

During each iteration of the optimisation process, a trial model is used to calculate term values for a set of levels which are also known from the experimental record. This requires an evaluation of model cross sections at many energies covering those regions where resonances are expected to appear. Some resonances are extremely narrow, with full-width half-maxima below $10^{-5}\,\mathrm{cm}^{-1}$, and may shift in location by as much as $10\,\mathrm{cm}^{-1}$ between optimisation iterations. A strategy has been devised to minimise the number of model evaluations required to characterise each resonance given this broad range of scales.

By examining the second derivative $\frac{d^2\sigma}{d\nu^2}$, an approximate position for each resonance may be identified in a cross section sampled at energy intervals much greater than the resonance linewidth, even where no local maximum is evident. This quantity will change sign at least once across the line profile of any of the resonance types shown in Fig. 2.4 but is unlikely to do so within any reasonably-small range of ν because of variations in the background continuum. A resonance location estimated in this way may be further refined by bisecting the adjacent sampled energy-intervals with new model evaluations, and recalculating $\frac{d^2\sigma}{d\nu^2}$. Eventually, a maximum will appear in the modelled cross section and its location taken as the resonance centre. This may be found more precisely by further bisecting the neighbouring energy intervals.

Knowledge of the term origins, T_{0v}, and rotational constants, B_v, for a progression of vibrational states indexed by v, is sufficient to determine the shape of an uncoupled potential-well up to the highest-known energy T_{0v}. Such a determination may even be achieved analytically, such as by means of the RKR method [138, 190]. This technique exploits a useful physical interpretation which suggests that a large value of $T_{0v+1} - T_{0v}$ indicates a small separation between the classical turning-points of level v, and a small value of B_v indicates the mean internuclear-distance of these turning points is large. This interpretation routinely fails for the strongly-coupled states of N_2, but RKR curves provide suitable starting points for the further refinement of numerical potential-energy curves. Some N_2 states have been studied *ab initio*, providing another source of starting-point potential-energy curves.

In practice, rotational constants are not calculated by directly evaluating Eq. 2.44. Instead, an effective rotational-constant is calculated for some low value of J, typically 5,

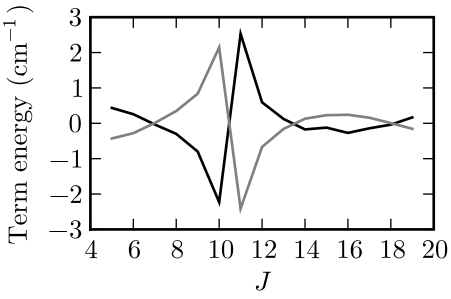

Figure 6.2: Experimental term values reduced by the subtraction of a third-order polynomial of best fit in terms of $J(J+1)$. *Dark:* $c_4'\,{}^1\Sigma_u^+(v=0)$. *Light:* $b'\,{}^1\Sigma_u^+(v=1)$.

according to

$$B_v^{\text{eff}} \simeq \frac{T_v(J) - T_{0v}}{J(J+1)}. \tag{6.4}$$

The residual elements arising from each vibrational level that contribute to the minimisation of Eq. (6.3) are then,

$$d_{vT} = w_T \Delta T_{0v}, \tag{6.5}$$

$$\text{and } d_{vB} = w_B \frac{\Delta T_v(J) - \Delta T_{0v}}{J(J+1)}, \tag{6.6}$$

where Δ indicates the difference between experimental and model values, and the adopted weighting factors are $w_T = 1$ and $w_B = 100$.

For many vibrational levels exhibiting the effects of anharmonicity and perturbations between electronic states, T_{0v} and B_v^{eff} do not fully describe the observed rotational series. Thus further model constraints must be defined according to $d_v = \Delta T_v(J) - \Delta T_{0v}$ for as many values of J as are required to complete this description. These additional residuals are referenced to the term-origin residual, ΔT_{0v}, in order to reduced the correlation of multiple residuals to a single model parameter.

Where their term series cross, perturbations between valence and Rydberg states materialise as a localised deflection of rotational level energies. An important example is the crossing in $^{14}N_2$ of $c_4'\,{}^1\Sigma_u^+(v=0)$ and $b'\,{}^1\Sigma_u^+(v=1)$ between $J = 11$ and 12, with corresponding reduced term-values plotted in Fig. 6.2. The total amplitude of the deflection at the crossing point is approximately $5\,\text{cm}^{-1}$, and is strongly sensitive to the $\langle b'\,{}^1\Sigma_u^+|H^{el}|c_4'\,{}^1\Sigma_u^+\rangle$ perturbing matrix-element. Good model constraints on this coupling parameter are the term-value differences $\Delta T_{c_4'(0)}(12) - \Delta T_{c_4'(0)}(11)$ and $\Delta T_{b'(1)}(12) - \Delta T_{b'(1)}(11)$. These are insensitive to any small error in the shape of the $b'\,{}^1\Sigma_u^+$ and $c_4'\,{}^1\Sigma_u^+$ potential-energy curves which might induce a common model error for $J = 11$ and 12. Similar relative-difference constraints are adopted for other level crossings arising in the N_2 spectrum.

Because Schrödinger's equation contains second-order derivatives in R, all potential-energy curves must be continuous and possess continuous first-derivatives. Furthermore, diabaticised potential-energy curves frequently appear smoother once adiabatic avoided-crossings have been removed; this is clear, for example, when comparing Fig. 1 and Fig. 5 of Spelsberg and Meyer [145]. However, the optimisation of a spline-parameterised potential-energy curve will frequently result in the appearance of excessively sharp potential-energy

variation. This nonphysical behaviour may arise following convergence to a local minimum in the L^2 norm, or because of errors in the constraining experimental data. An improved convergence may be possible by improving the initial estimate of model parameters or by increasing the amount of constraining data. However, where these solutions are unfeasible or computationally inefficient, it is possible to guide the optimisation routine around local convergence minima and smooth out the effects of experimental error by appending a measure of smoothness to the set of d_i in Eq. (6.3).

At each discretised element of the potential-energy curve, a numerical measure of smoothness is calculated according to the form,

$$d_{m+k} = N \frac{d^2}{dR^2} \left[\frac{V_k''}{\left(1 + V_k'^2\right)^{3/2}} \right] . \tag{6.7}$$

Here, V_k is the potential-energy at the kth discretisation, and V_k' and V_k'' are the corresponding numerically-approximated first and second derivatives with respect to R. The bracketed quantity in Eq. (6.7) is a measure of curvature and is sensitive to the units of V and R; which are selected to be 500 eV and Å, respectively. This choice reduces the undesired contribution of the natural curvature of each potential well to d_{m+k}. The overall scaling parameter, N, must be large enough that the smoothness requirement influences the optimisation procedure, without preventing convergence to the experimental data. Values between 10^{-5} and 10^{-4} were adopted for N.

If the deduced potential-energy curves and interaction parameters are nearly correct following the successful convergence of an initial optimisation, a further optimisation is less likely to converge to an incorrect local-solution. Then, the potential-energy curves may be refitted to a spline-numerical form with more degrees of freedom or with a lessened requirement of smoothness.

Many perturbations observed in the spectrum of N_2 arise from multiple state interactions which interfere quantum mechanically. When modelling these cases, the relative signs of the interfering coupling parameters is of critical importance, and several trial optimisations may be required before the correct combination of signs is struck. Also because of the highly mixed nature of N_2, when a previously-neglected electronic state or interaction is appended to a converged model it is usually necessary to refit all model parameters, even those concerning states which are not directly affected by the new additions.

In some cases, perturbing states or state couplings may be excluded during the optimisation of a preliminary coupled-channels model. Consequently, it may happen that some local perturbations and level crossings cannot be represented by such a model. Constraining the optimisation by experimental levels affected by these perturbations will then introduce nonphysical distortions in the fitted model parameters. The effects of such omissions are usually obvious and the perturbed experimental data may be neglected or deperturbed manually prior to their inclusion. If an excluded perturbing state is sufficiently remote in energy then its effect on the optimised energy levels will be nearly uniform. This type of omission, even when the levels shifts are large, may be redressed by a smooth adjustment of the model potential-energy curves. The subsequent optimisation of a more comprehensive model will remove this compensating distortion.

Following the successful convergence of an optimisation, it is essential to verify the quality-of-fit of all experimentally known energy levels. Any poorly reproduced rovibrational levels that cannot be classified as resulting from experimental error or perturbative

effects not included in the model must be added to the list of constraints, and a new optimisation initiated.

Using the method discussed in Sec. 2.11.3, it is possible to calculate coupled-channels bound levels without including any open channels. The coupled-channels code was written specifically to study photodissociation and cannot conveniently be applied to the case of no open channels. In those cases where no unbound states are required to reproduce the observed level energies it is necessary to include a weakly-coupled unbound pseudo-state. In this way, bound levels still appear as narrow resonances amidst a continuous model cross section.

6.2.2 Optimisation of f-values and linewidths

A realistic ground state and set of electronic transition moments is not required for the calculation of excited-state energy levels, because any approximation to these will result in identifiable resonances in the modelled cross section. However, in order to reproduce experimental absorption f-values these parameters must be correctly specified.

When determining the quality of a trial set of electronic transition moments, Fano lineshapes are fitted to a series of calculated resonances corresponding to transitions for which experimental absorption f-values are known. This is done as is described in Sec. 2.10.1, and it is necessary that the coupled-channels cross section be calculated at sufficiently many energies such that the shape of each resonance is well represented. The parameterised line strengths are then converted to f-values according to Eqs. (2.105) and (2.108), and may be compared directly with experiment.

Because the strength of N_2 absorption varies by several orders of magnitude across its spectrum, the residual disagreement between coupled-channels and experimental f-values ($f_{\rm mod}$ and $f_{\rm exp}$, respectively) are transformed during optimisation to the form

$$d_f = \log\left(\frac{f_{\rm mod}}{f_{\rm exp}}\right). \tag{6.8}$$

This representation reflects an assumption that the uncertainties of the measured f-values are proportional to their magnitude. This is frequently the case because experimental conditions, such as column-density, may themselves be varied over several orders-of-magnitude in order to compensate for the range of observed line strengths.

The magnitude, or R-dependence, of each electronic transition moment may be adjusted until optimal agreement is found between calculated and observed f-values. It may also be necessary to trial alternative signs for the various transition moments, in order to explain the quantum interference that is frequently observed for transitions involving electronically-mixed levels.

Some N_2 states of symmetry $^3\Pi_u$ and $^3\Sigma_u^+$ have not been directly observed but are known from the predissociative broadening they induce in observed singled levels. The potential-energy curves of these perturbing states and the accompanying state interactions must then be adjusted to best fit the observed singlet linewidths. As is the case for observed f-values these widths, Γ, may span several orders of magnitude and are best incorporated into the optimisation program in logarithmic form, according to

$$d_\Gamma = \log\left(\frac{\Gamma_{\rm mod}}{\Gamma_{\rm exp}}\right). \tag{6.9}$$

6.3 Validation of the coupled-channels technique

The coupled-channels code has been successfully applied to previous problems and its results verified by experimental observations. For the purpose of further validation of its efficacy, the spectroscopic model of N_2 derived by Spelsberg and Meyer [145], discussed in Sec. 3.5.4, has been recreated here and their calculations repeated.

Spelsberg and Meyer approximately interpolated their *ab initio* potential-energy curves by means of polynomial functions, and their electronic-coupling functions by Gaussians. These quantities have been evaluated on our coupled-channels model grid as numerical functions. Their *ab initio* electronic transition moments are expressed directly in a numerical form following the digitisation of figures appearing in Spelsberg and Meyer [145].

Separate coupled-channels models have been constructed describing states with $^1\Sigma_u^+$ and $^1\Pi_u$ symmetry, which aim to reproduce the spectroscopic term origins and rotational constants for 41 and 30 vibrational levels, respectively. For each level, the coupled-channels calculated resonant-energies with total angular-momentum $J = 0$ are directly comparable to the experimental term origins, T_0 (G_v in Spelsberg and Meyer); and the term energy $T(J)$, for $J = 1$, may then be used to fix the rotational constant according to

$$B \simeq [T(1) - T_0]/2. \tag{6.10}$$

This method of calculating B differs slightly from that of Spelsberg and Meyer who evaluated Eq. (2.44) directly. Oscillator strengths have been calculated for each vibrational level by fitting Fano profiles to the T_0 resonances.

Figure 6.3 compares the $^1\Pi_u$ term origin and rotational-constant residuals calculated by Spelsberg and Meyer and the present coupled-channels model. The previous and new modelled transition moments for each level are also plotted. The residuals calculated from the coupled-channels model are identical to those achieved by Spelsberg and Meyer, except in the case of $v = 12$ and 13 where the coupled-channels rotational-constant residuals are $\sim 2\times$ smaller. These two levels correspond to $o_3\,^1\Pi_u(v = 1)$ and $b\,^1\Pi_u(v = 9)$, which are nearly degenerate and highly mixed at $J = 0$. The degree of admixture changes rapidly with J and so the rotational-constant of each state is not well represented by Eq. (6.10). Nonetheless, it is clear that the coupled-channels code is functioning correctly.

It was found necessary to reverse the sign of Spelsberg and Meyer's published $^1\Pi_u$ residuals in order to show the agreement plotted in Fig. 6.3 (a) and (b). The $^1\Sigma_u^+$ residuals did not require this modification and show a similar level of agreement between alternative models as that depicted in Fig. 6.3.

The matrix diagonalisation of diabatic vibrational-levels conducted by Spelsberg and Meyer in order to determine the spectroscopic parameters of mixed levels is likely to be more computationally efficient than the direct solution of the coupled Schrödinger equation. However, the coupled-channels method implicitly include the effects of all bound vibrational levels as well as the unbound continuum, whereas the matrix diagonalisation of Spelsberg and Meyer includes only a limited number of bound levels and none of the continuum. Because of this, it was necessary to shift the potential-energy curves of Spelsberg and Meyer vertically in order to achieve the level of agreement shown in Fig. 6.3. The degree of consensus following this shift demonstrates that the matrix diagonalisation method is entirely appropriate for the application of Spelsberg and Meyer; although this assessment cannot be automatically expected to extend to energies approaching, or above, the $b\,^1\Pi_u$ dissociation energy. Also, the matrix diagonalisation method is inher-

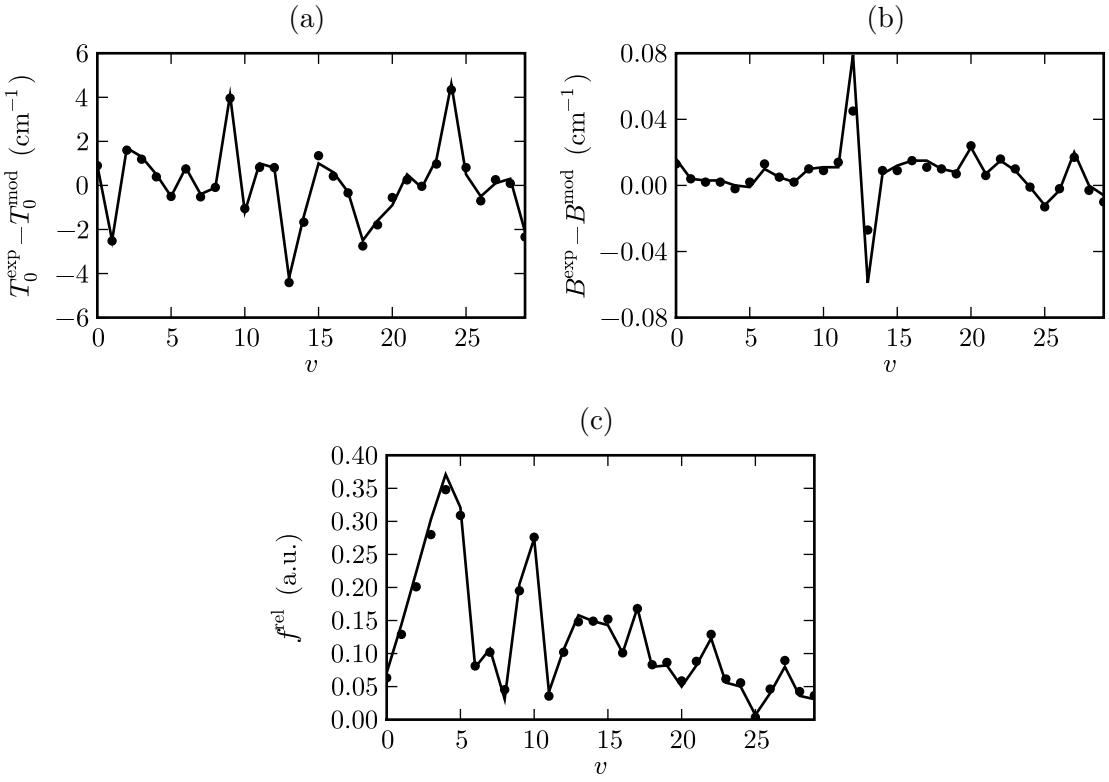

Figure 6.3: *(a):* The difference between experimental and modelled term origins for the $^1\Pi_u$ levels of Spelsberg and Meyer [145] (*lines*) and the present model (*points*). The abscissae refer to their vibrational numbering, which spans all coupled states. *(b):* The difference between experimental and modelled rotational constants. *(c):* Calculated transition moments.

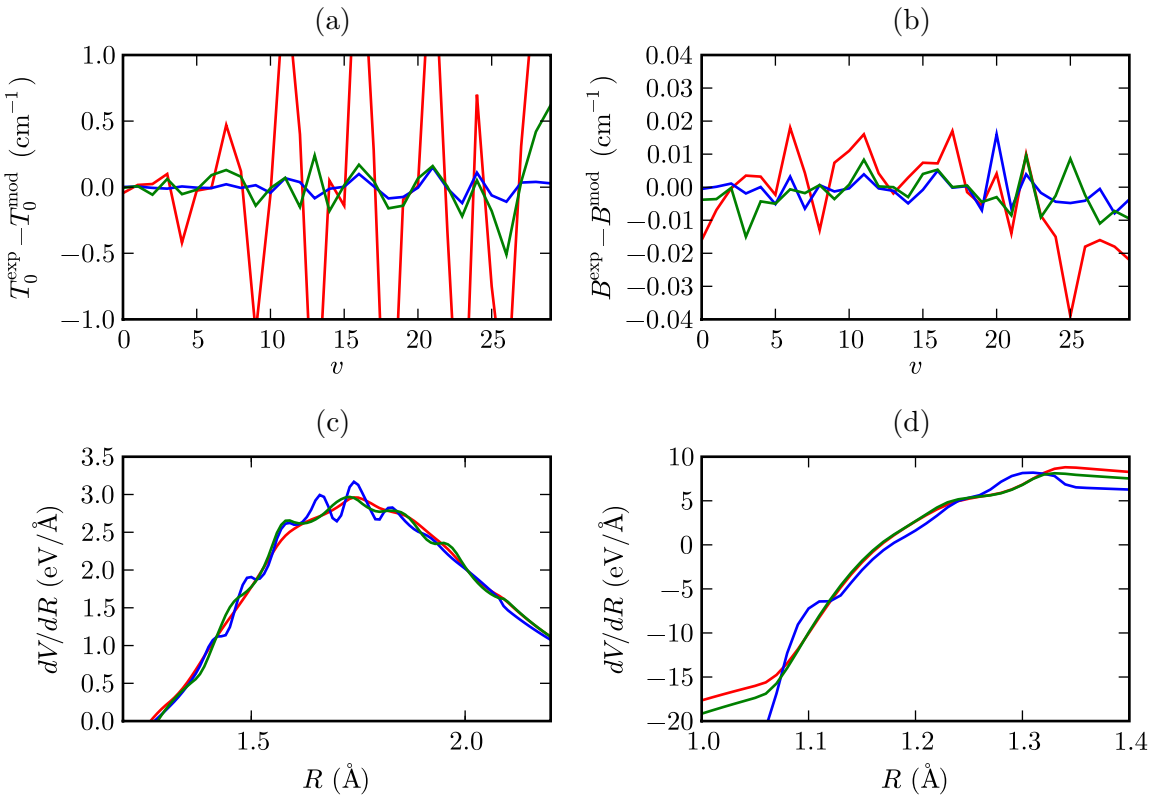

Figure 6.4: *Red curves:* Results of a reoptimisation of the $^1\Pi_u$ model of Spelsberg and Meyer [145] with a high requirement of potential-energy curve smoothness. *Blue curves:* Results of a reoptimisation with a low requirement of potential-energy curve smoothness. *Green curves:* Results of a reoptimisation with a medium requirement of potential-energy curve smoothness and updated experimental data. *(a):* Residual term origins. The abscissae refer to the vibrational numbering of Spelsberg and Meyer. *(b):* Residual rotational-constants. *(c):* First derivative of the potential-energy curve of $o_3\,^1\Pi_u$. *(d):* First derivative of the potential-energy curve of $b\,^1\Pi_u$.

ently incapable of reproducing the finite predissociation linewidths of the discrete levels it calculates.

It should be possible to achieve improved agreement between the coupled-channels model and the observed energy levels by adopting the numerical-spline potential-energy curves discussed in Sec. 6.1.2. To test this hypothesis, numerical-spline versions of Spelsberg and Meyer's polynomial $^1\Pi_u$ potential-energy curves were constructed. A least-squares optimisation was then performed adjusting the parameters describing the shape of these potentials as well as simultaneously refitting the electronic-coupling functions. This led to a total of 85 varied parameters, whereas the formulation of Spelsberg and Meyer adopted only 25 free parameters. Because this number now exceeds the amount of constraining data, the smoothness constraint described in Sec. 6.2.1 was imposed on the optimised potential-energy curves. Several trial optimisations were performed with varying weight attached to the smoothness requirement. The best performing optimisation results in remarkably small T_0 and B residuals, depicted in Fig. 6.4(a) and (b), which are certainly below the confidence limit of the experimental data. However, in order to achieve this unrealistic convergence, the corresponding potential-energy curves

exhibit disturbing oscillations in their first derivatives; as shown in Fig. 6.4(c) and (d) for the curves of $o_3\,{}^1\Pi_u$ and $b\,{}^1\Pi_u$, respectively. The smoothness of the $c_3\,{}^1\Pi_u$ first-derivative is approximately equivalent to that of $o_3\,{}^1\Pi_u$.

The poorest model convergence shown in Fig. 6.4 demonstrates acceptably smooth potential-energy curves but significantly greater T_0 and B residuals. The root-mean-square residual average of term origins and rotational constants for this coupled-channels model are $0.43\,\mathrm{cm}^{-1}$ and $0.008\,\mathrm{cm}^{-1}$, respectively; and the corresponding averages for the model of Spelsberg and Meyer are $1.62\,\mathrm{cm}^{-1}$ and $0.01\,\mathrm{cm}^{-1}$. Apparently, some improvement has been achieved by adopting spline-potentials in the fitting of term origins but relatively-little with regards to the rotational constants.

The experimental data used to constrain the model of Spelsberg and Meyer was compiled in 1983 [153]. A new data set, arising from a reanalysis of the experimental record of ${}^1\Pi_u$ levels, may lead to an improved model agreement. To test this, a further optimisation has been conducted, constrained by the same vibrational levels as the original work of Spelsberg and Meyer, but with updated term origins and rotational constants. These have been obtained from a database of N_2 term energies [47], from which T_0 and B level have been calculated for each vibrational by fitting its term series to Eq. (2.61). The resultant residuals, and derivatives of the optimised $b\,{}^1\Pi_u$ and $o_3\,{}^1\Pi_u$ potential-energy curves are plotted in Fig. 6.4 The updated data set has allowed for a significantly improved fit of model term origins, and an equivalent fit of rotational-constants, with root-mean-square average residuals given by 0.2 and $0.006\,\mathrm{cm}^{-1}$, respectively. Additionally, the potential-energy curves fitted to the new data are somewhat smoother than previously. This suggests that some experimental errors that were previously compensated for by potential-energy distortions have been corrected.

6.4 *f*-parity ${}^1\Pi_u$ model

A large portion of the observed N_2 absorption spectrum between 100 000 and $120\,000\,\mathrm{cm}^{-1}$ arises from ${}^1\Pi_u \leftarrow X\ Q$-branch transitions. These terminate on f-parity upper-state levels that are completely decoupled from the co-energetic ${}^1\Pi_u$ and ${}^1\Sigma_u^+$ levels with e-type parity. A model consisting only of ${}^1\Pi_u$ excited states will then be sufficient to reproduce transition energies and f-values for this part of the spectrum.

The ${}^1\Pi_u$ model constructed by Spelsberg and Meyer [145], while not spectroscopically accurate, is an excellent starting point for further optimisation. I have sought to improve upon their analysis in three ways: by considering a larger and more recent body of experimental energy levels, including those of the additional Rydberg state $c_4\,{}^1\Pi_u$; by adopting a more general numerical form for the potential-energy curves; and by optimising the diabatic ${}^1\Pi_u - X\,{}^1\Sigma_g^+$ electronic transition moments in order to best fit a broad range of observed oscillator-strengths. The model constructed may also be considered an extension to those developed by Lewis *et al.* [104] and Haverd *et al.* [49], which adopt a similar methodology to study f-parity ${}^1\Pi_u$ states between 100 000 and $105\,000\,\mathrm{cm}^{-1}$.

There are four ${}^1\Pi_u$ diabatic states represented in the model, the valence state $b\,{}^1\Pi_u$ and the Rydberg states $c_3\,{}^1\Pi_u$, $c_4\,{}^1\Pi_u$, and $o_3\,{}^1\Pi_u$. Figure 6.5 shows the final configuration of optimised potential-energy curves for these diabatic states, as well as the energies of their known ${}^{14}N_2$ vibrational levels. The effects of electronic coupling between the different states is immediately evident in the uneven energy-spacing between $b\,{}^1\Pi_u$ vibrational levels, particularly with regards to $b(v = 4)$ and $b(5)$. The large gap above $b(20)$ occurs because $b(21)$ has not been observed.

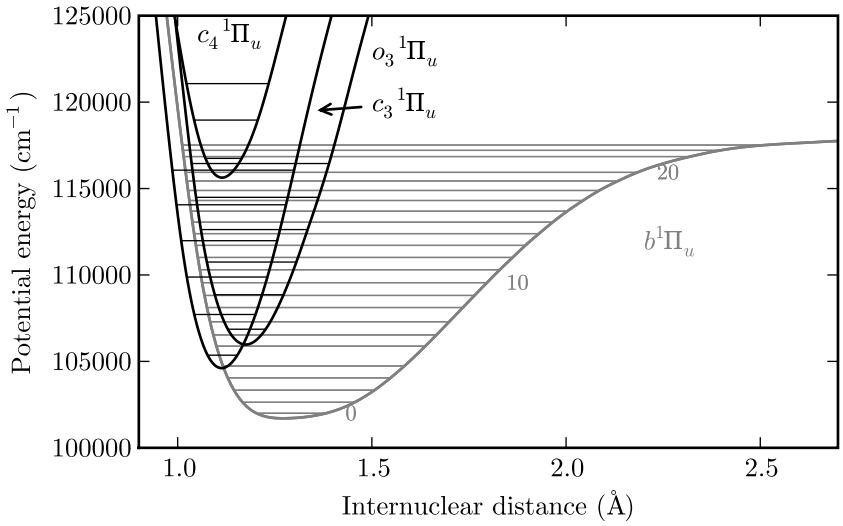

Figure 6.5: Optimised $^1\Pi_u$ potential-energy curves. Horizontal lines indicate the known $^{14}N_2$ vibrational levels. A few representative labels are attached to the $b\,^1\Pi_u$ vibrational levels, and $b\,^1\Pi_u(v = 21)$ has not been observed.

The potential-energy curves of all states are represented by a spline-interpolated form, in a similar fashion to those of Sec. 6.3. The inner and outer limbs of each potential curve are represented by the analytical forms of Eq. (6.1) and Eq. (6.2), and have been smoothly connected to the spline-interpolated potential well. The asymptotic outer-limit of all states have been adjusted to agree with their respective dissociation energies. However, for all singlet states apart from $b\,^1\Pi_u$, the energy range considered lies well below dissociation and the precise way in which the potential-energy outer limbs tend to their asymptotic limits is not experimentally constrained.

6.4.1 $^1\Pi_u \sim {}^1\Pi_u$ electronic perturbations

There are five electronic-coupling matrix-elements included in the model, mixing the following pairs of states: $b \sim c_3$, $b \sim o_3$, $c_3 \sim o_3$, $b \sim c_4$, and $o_3 \sim c_4$. These have been treated separately in two different models; one with R-independent electronic-coupling and one with R-dependences given by the Gaussian forms of Spelsberg and Meyer [145]. In all cases, the electronic couplings were scaled uniformly with respect to internuclear distance during optimisation of the model. The coupling between c_3 and c_4 has been assumed to be zero, as is appropriate for a diabatic representation of states belonging to the same Rydberg series.

Fitted electronic-couplings are listed in Tab. 6.1 and plotted in Fig. 6.6 for alternative models. The R-dependent coupling functions for $b \sim c_3$, $b \sim o_3$, and $c_3 \sim o_3$ have been scaled relative to the original forms of Spelsberg and Meyer by factors of 1.02, 0.77, and 0.96; respectively. However, the model is only sensitive to each electronic coupling function over an R-extent limited to the classically accessible regions of the Rydberg states concerned. For the range of energies considered here, these all lie within 0.95 to 1.45 Å.

The crossing points between R-dependent and R-independent coupling functions mixing the pairs of states $b \sim c_3$ and $c_3 \sim o_3$ correspond very nearly to the crossing points between the corresponding potential-energy curves. This is consistent with the expected pref-

	R-independent	R-dependent, $ae^{-(R-b)^2/c}$		
		a	b	c
$\langle b\|H^{el}(R)\|c_3\rangle$	−845(1)	−1261(1)	0.906	0.355
$\langle b\|H^{el}(R)\|o_3\rangle$	+351(1)	+368(2)	0.968	0.276
$\langle b\|H^{el}(R)\|c_4\rangle$	−187(1)	−166(4)	0.906	0.355
$\langle c_3\|H^{el}(R)\|o_3\rangle$	+634(2)	3149(3)	0.670	0.383
$\langle c_3\|H^{el}(R)\|c_4\rangle$	0	0		
$\langle o_3\|H^{el}(R)\|c_4\rangle$	+140(2)	414(11)	0.670	0.383

Table 6.1: Optimised electronic-coupling matrix elements mixing $^1\Pi_u$ diabatic states. Matrix elements are listed in units of cm^{-1} and R-dependent parameters (b and c) are given in units of Å. Statistical uncertainties calculated by the least-squares fitting program are given parenthetically in terms of the least-significant digit. The matrix element $\langle c_3|H^{el}|c_4\rangle$ was explicitly set to zero.

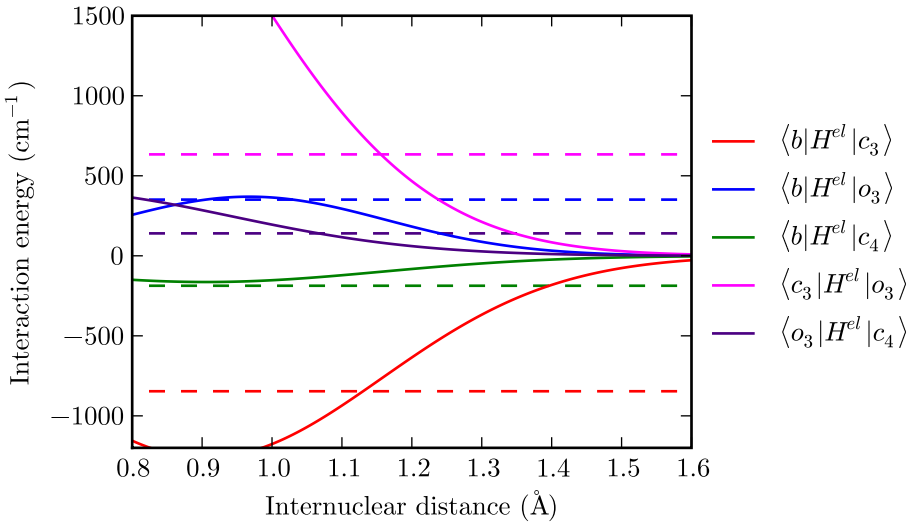

Figure 6.6: Optimised electronic-coupling matrix elements mixing $^1\Pi_u$ diabatic states with alternative internuclear-distance dependences. *Dashed lines:* R-independent. *Solid lines:* Gaussian R-dependence.

erential overlap of diabatic wavefunctions at potential-energy crossing points [54, p. 285].

The listed fitting uncertainties in Tab. 6.1 are calculated by the least-squares program and do not include the implicit uncertainties regarding the R-dependence of coupling functions. Furthermore, these uncertainties may underestimate the correlation of diagonal and off-diagonal matrix elements, where the alteration of an interaction energy may be compensated for by a modification of potential-energy curves. As such the uncertainties listed in Tab.6.1, and those that follow, should be considered relative only.

The c_3 potential-energy curve optimised with R-dependent electronic-coupling is shifted in energy relative to the R-independent case by $+200\,\mathrm{cm}^{-1}$. Similarly, the o_3 and b potential-energy curves are shifted by -85 and $-62\,\mathrm{cm}^{-1}$, respectively. Further modifications to the shape of each potential-energy curve were found to be necessary to compensate for the different R-dependence of electronic-coupling, but in all cases the curves appear smooth and physically reasonable.

The model formulations with alternative coupling R-dependencies resulted in a virtually identical level of agreement when compared with experimental level energies. This insensitivity to the nature of the electronic-coupling does not provide extra evidence supporting the *ab initio* electronic-coupling calculated by Spelsberg and Meyer [145]. However, out of respect for the first-principles nature of *ab initio* calculations, the R-dependent coupling functions of Tab. 6.1 are adopted herein.

6.4.2 Inclusion of $c_4\,^1\Pi_u$

It is clear from Fig. 6.5 that the consideration of $b\,^1\Pi_u$ levels with $v > 19$ requires the inclusion of at least the first vibrational level of $c_4\,^1\Pi_u$. Experimental observations of $c_4(0-2)$ have been rotationally analysed and all three levels are included among the optimisation constraints. No Q-branch optical transitions have been observed terminating on $c_4(2)$ and an extrapolation of e-parity term values to $J = 0$ has been adopted as an effective f-parity term origin for this level.

Three schemes for constructing a potential-energy curve for c_4 were considered. The R-dependence of the c_3 and c_4 potential-energy will be broadly similar because they are members of the same Rydberg series, and a shifted copy of the c_3 curve may be sufficient to represent c_4. Alternatively, high-n members of the c_n Rydberg series will have potential-energy curves that are similar in shape to that of the ionic ground state, $\mathrm{N}_2^+\left[X\,^2\Sigma_g^+\right]$. An ionic potential-energy curve has been constructed from the molecular constants given by Lofthus and Krupenie [111, Tab. 1], and a shifted version of this may provide a better fit to the observed c_4 levels. Quantum defects of the $c_n\,^1\Pi_u$ Rydberg series are listed in Tab. 6.2 and are calculated from the known $v = 0$ levels of the observed n-members [111]. Also listed are the vibrational constant, ω_e, and anharmonicity, $\omega_e x_e$, for $n = 3$ and 4, as well as the limiting ionic state. Considering these parameters, c_4 appears to be intermediately situated between c_3 and $\mathrm{N}_2^+\left[X\,^2\Sigma_g^+\right]$, suggesting that the c_4 potential-energy curve will likely differ significantly from both possible precursors. Alternatively, a completely novel potential-energy curve may be defined by a spline-interpolated numerical curve. In this case, a good fit of to the observed levels is assured but less may be deduced about the patterns arising from the c_n Rydberg series and any perturbations which may be occurring.

The electronic-coupling matrix elements connecting $c_4 \sim b$ and $c_4 \sim o_3$ are likely to be related to the equivalent matrix elements of interactions involving $c_3\,^1\Pi_u$. Specifically, the approximate Rydberg scaling of Eq. (2.183) predicts matrix elements involving c_4 with

	δ	ω_e	$\omega_e x_e$
$c_3\,{}^1\Pi_u$	0.742	2429	52
$c_4\,{}^1\Pi_u$	0.704	2222	21
$c_5\,{}^1\Pi_u$	0.698		
$c_6\,{}^1\Pi_u$	0.694		
$c_8\,{}^1\Pi_u$	0.686		
$N_2^+\left[X\,{}^2\Sigma_g^+\right]$		2207	16.1

Table 6.2: Quantum defects, δ, of some members of the $c_n\,{}^1\Pi_u$ Rydberg series converging on $N_2^+\left[X\,{}^2\Sigma_g^+\right]$. These are calculated from the energy levels listed by Lofthus and Krupenie [111, Tabs. 14,15,17]. Also listed for some states are the vibrational constants and anharmonicity parameters, ω_e and $\omega_e x_e$, respectively. These have been calculated from the term origins of the known $c_3\,{}^1\Pi_u$ and $c_4\,{}^1\Pi_u$ vibrational levels [47]. The equivalent molecular constants for $N_2^+\left[X\,{}^2\Sigma_g^+\right]$ are those deduced by Klynning and Pages [78].

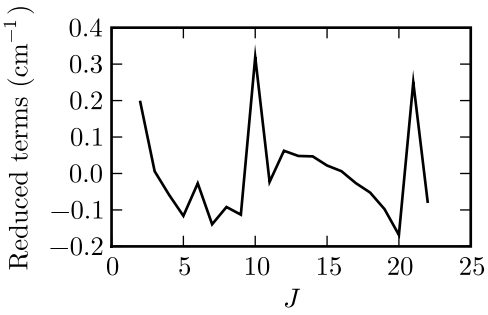

Figure 6.7: Term energies of $^{14}N_2$ $c_4\,{}^1\Pi_u(v=0)$ f-parity levels. These have been reduced by the subtraction of a 5^{th} order polynomial of best-fit in terms of $J(J+1)$.

the same R-dependence as for c_3, but scaled according to

$$\langle c_4|H^{el}(R)|b\rangle = \left(\frac{3-\delta_{c_3}}{4-\delta_{c_4}}\right)^{3/2}\langle c_3|H^{el}(R)|b\rangle, \tag{6.11}$$

$$\langle c_4|H^{el}(R)|o_3\rangle = \left(\frac{3-\delta_{c_3}}{4-\delta_{c_4}}\right)^{3/2}\langle c_3|H^{el}(R)|o_3\rangle, \tag{6.12}$$

where the quantum-defects listed in Tab. 6.2 predict a scaling factor of 0.56.

There are two localised perturbations occurring in the rotational series of $c_4(0)$. These are demonstrated in Fig. 6.7, where slight level shifts at $J=9$ and 20 have been attributed to level crossings with $b(22)$ and $b(23)$, respectively. Extra lines appearing in the experimental spectra of Chap. 4 have been assigned to the $J=9$ levels of $b(22)$, in both the e and f parities. No rotational levels of $b(23)$ are known above $J=11$, but the extrapolation to the crossing point at $J=20$ is feasible and there are no other reasonable perturber candidates. The term origins and rotational constants of the three known vibrational levels of c_4 are unlikely to constitute sufficient information to simultaneously fix the form of the c_4 potential-energy curve as well as the magnitude of electronic coupling to b and o_3. In this case, the local perturbations with b provide particularly useful model constraints.

Several optimisations were performed, trialling various forms of the c_4 potential-energy curve and different combinations of electronic-coupling magnitudes. When considering a shifted version of the $N_2^+\left[X\,{}^2\Sigma_g^+\right]$ potential-energy curve it was possible to reproduce the f-parity term values of $c_4(0)$ to within $0.1\,\text{cm}^{-1}$. The rotational constant of $c_4(1)$ was also

well fitted but the $c_4(1)$ and $c_4(2)$ term origins were overestimated by 0.5 and 3.0 cm^{-1}, respectively. Alternatively, a modified version of the c_3 curve lead to respective term origin overestimates of 16 and 30 cm^{-1}. In both cases the shifted curves had equilibrium internuclear-distances intermediate to c_3 and $\mathrm{N}_2^+\left[X\,^2\Sigma_g^+\right]$. Unsurprisingly, a numerical spline potential-energy curve for c_4 was capable of reproducing all c_4 term values to high precision, and this form was adopted for further development of the coupled-channels model.

It was found that the modelled level shifts at $J = 9$ and 20 were equally sensitive to the magnitude of $c_4 \sim b$ and $c_4 \sim o_3$ coupling, and adopting a 0.56× scaling of these relative to the respective coupling elements of c_3 grossly overestimates the observed shifts. Instead, the observations could be reproduced by alternatively setting the magnitude of one c_4 coupling to zero and scaling the other by a factor of ~ 0.2, or else assigning them both somewhat smaller magnitudes. Thus, it proved impossible to independently determine the size of both couplings and, ultimately, a common scaling of 0.13 was adopted for $c_4 \sim b$ and $c_4 \sim o_3$ relative to $c_3 \sim b$ and $c_3 \sim o_3$, respectively. This is significantly less than the prediction of quantum-defect theory and suggests that the spatial correlation of $c_3\,^1\Pi_u$ Rydberg and core electrons is too great to warrant a simple extrapolation of its properties to $c_4\,^1\Pi_u$.

6.4.3 Optimisation of energy levels

Many trials were necessary in order to determine the best combination of variable model parameters and constraining experimental data. Finally, 231 rotational energy levels were included in the optimisation routine, and 161 model parameters. The experimental data have various sources, discussed in Sec. 3.3.1, and include 64 vibrational levels: $b\,^1\Pi_u(v = 0-20, 22-24)$, $c_3\,^1\Pi_u(v = 0-5)$, $c_4\,^1\Pi_u(v = 0-2)$, and $o_3\,^1\Pi_u(v = 0-5)$ in $^{14}\mathrm{N}_2$; and $b\,^1\Pi_u(v = 0-16)$, $c_3\,^1\Pi_u(v = 0-2)$, and $o_3\,^1\Pi_u(v = 0-4)$ for $^{15}\mathrm{N}_2$. The forms of the potential-energy curves were additionally constrained by the smoothness requirement discussed in Sec. 6.4.3, and the final curves are plotted in Fig. 6.5.

The quality of the final coupled-channels model was judged in comparison with the complete *f*-parity $^1\Pi_u$ data set of 1244 rotational levels. This set includes the $^{14}\mathrm{N}^{15}\mathrm{N}$ vibrational levels $b(5-7)$ and $c_3(0,2)$ which were not referenced during optimisation. There is too much reference data to be listed exhaustively. Instead, a summary of the model agreement with experimental term values is plotted in Fig. 6.8(a). This histogram shows the distribution of model residual errors for all known *f*-parity term-energies. The model residuals have a standard-deviation of 0.54 cm^{-1} and are not normally distributed, with more outliers than can be expected from random measurement errors alone. This indicates that there may be problems with the experimental data set, such as might arise from an incorrect energy calibration of observed spectra; or that there are omissions in the model formulation, such as excluded states or insufficient variability of potential-energy curves and coupling functions.

A second histogram, Fig. 6.8(b), summarises the residual errors of an extended model which includes further *f*-parity states with symmetries $^3\Pi_u$ and $^3\Sigma_u^+$, and with a reduced standard deviation of 0.44 cm^{-1}. The inclusion of these improves the reproduction of $^1\Pi_u$ energy levels because of the existence of spin-orbit coupling between singlet and triplet states. Despite the disorder incurred, all further results presented regarding $^1\Pi_u$ and $^1\Sigma_u^+$ levels include the influence of the triplet states, but a proper discussion of these states is deferred until Sec. 6.6.

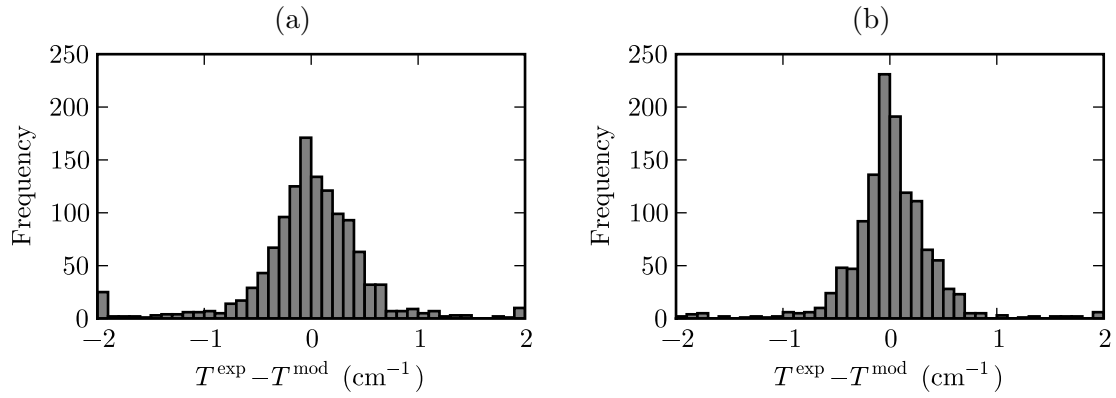

Figure 6.8: *(a):* Histograms of f-parity term value residual errors, $T^{\rm exp} - T^{\rm mod}$, for all known rotational-vibrational levels and all isotopomers of N_2. Calculated from an optimised model of $^1\Pi_u$ states. The mean and standard-deviation of the residuals are -0.01 and 0.54 cm^{-1}, respectively, and outliers have been accumulated in the extreme bins. *(b):* Calculated from an optimised model of $^1\Pi_u + {}^3\Pi_u + {}^3\Sigma_u^+$ states, and with mean and standard-deviation 0.01 and 0.44 cm^{-1}, respectively.

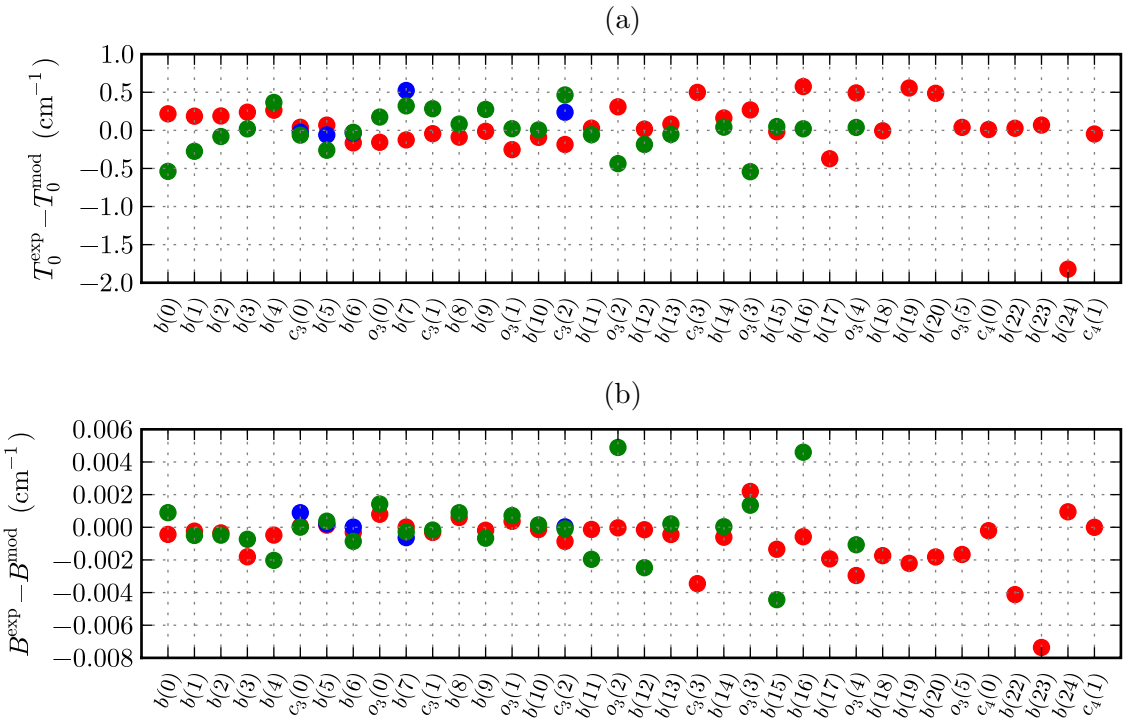

Figure 6.9: Residual error of modelled term origins ($T_0^{\rm exp} - T_0^{\rm mod}$) and rotational constants ($B^{\rm exp} - B^{\rm mod}$) for the known f-parity $^1\Pi_u$ levels of $^{14}N_2$ (*red*), $^{14}N^{15}N$ (*blue*), and $^{15}N_2$ (*green*). These are plotted in order of increasing energy.

Further details of the residual errors are plotted in Fig. 6.9. which shows the residual errors for model term origins and rotational constants, for each isotopomer of N_2. Many of the observed transitions corresponding to low-rotation term values are obscured by band heads and, frequently, there is some uncertainty in the extrapolation of an experimental term series to its term origin. Additionally perturbations occur for many levels, and lead to large centrifugal distortions in their rotational series, or large shifts in the energy of isolated rotational lines. The plotted data has been approximately deperturbed by neglecting obviously inaccurate and perturbed term values. It is not intended that this reduced data set provides a complete specification of experimental knowledge, instead, the same trimmed set of rotational levels has been used to calculate the modelled term origins and rotational constants so that a direct comparison with experiment may be made. For most levels, the residual term origins and rotational constants are approximately within ± 0.5 and $\pm 0.002\,\mathrm{cm}^{-1}$, respectively, with some exceptions discussed below.

The largest term origin residual occurs for $^{14}N_2$ $b(24)$, with a model energy which is overestimated by $2\,\mathrm{cm}^{-1}$. Better agreement was achieved during the preliminary optimisation of the model which excluded all triplet states, suggesting that the cause of the $b(24)$ scatter is a nonphysical perturbation induced by an incorrectly located and unknown $^3\Pi_u$ level. The distortion induced in the b potential-energy curve as compensation for this perturbation has also noticeably degraded the fitted rotational-constants of $b(22)$ and $b(23)$.

There is not enough data to assess the f-parity term origins and rotational-constants of $c_3(4)$, $c_3(5)$, and $c_4(2)$, instead the evaluation of these is deferred until the discussion of an e-parity model is Sec. 6.5.

6.4.4 Optimisation of f-values

All absorption intensity between 100 000 and 116 000 cm^{-1} arising from transitions terminating on f-parity levels of $^1\Pi_u$ states may be explained by the four electronic transition moments governing transitions between $X\,^1\Sigma_g^+$ and the excited diabatic states $b\,^1\Pi_u$, $c_3\,^1\Pi_u$, $o_3\,^1\Pi_u$, and $c_4\,^1\Pi_u$. For greater energies, higher members of the $c_n\,^1\Pi_u$ and $o_n\,^1\Pi_u$ Rydberg series are manifest.

Homogeneous mixing between electronic states leads to a non Franck-Condon distribution of oscillator strength between the vibrational levels of each nominal electronic transition. Furthermore, the rotational line strengths within many vibrational bands do not follow a simple Hönl-London distribution. However, this complex spectrum may be reproduced in its entirety by the coupled-channels model once the correct diabatic electronic transition moments are specified.

Several alternative formulations of the $b - X$, $c_3 - X$, $c_4 - X$, and $o_3 - X$ transition moments have been trialled. Each of these involved an optimisation phase with constraint provided by a set of experimental f-values, weighted according to Eq. (6.8). The f-values used were measured during the KEK series of optical absorption experiments, discussed in Chap. 4. A single value extrapolated to zero rotation was chosen to represent each vibrational band.

Spelsberg and Meyer [145] calculated R-dependent transition moments *ab initio* for $b - X$, $c_3 - X$, and $o_3 - X$. One set of optimised model f-values were calculated by uniformly rescaling these transition moments, with a different factor used for each diabatic transition. The scaling factors thus deduced were 0.82, 0.82, and 0.85 for $b - X$, $c_3 - X$, and $o_3 - X$, respectively. The similarity of these factors supports the internal consistency

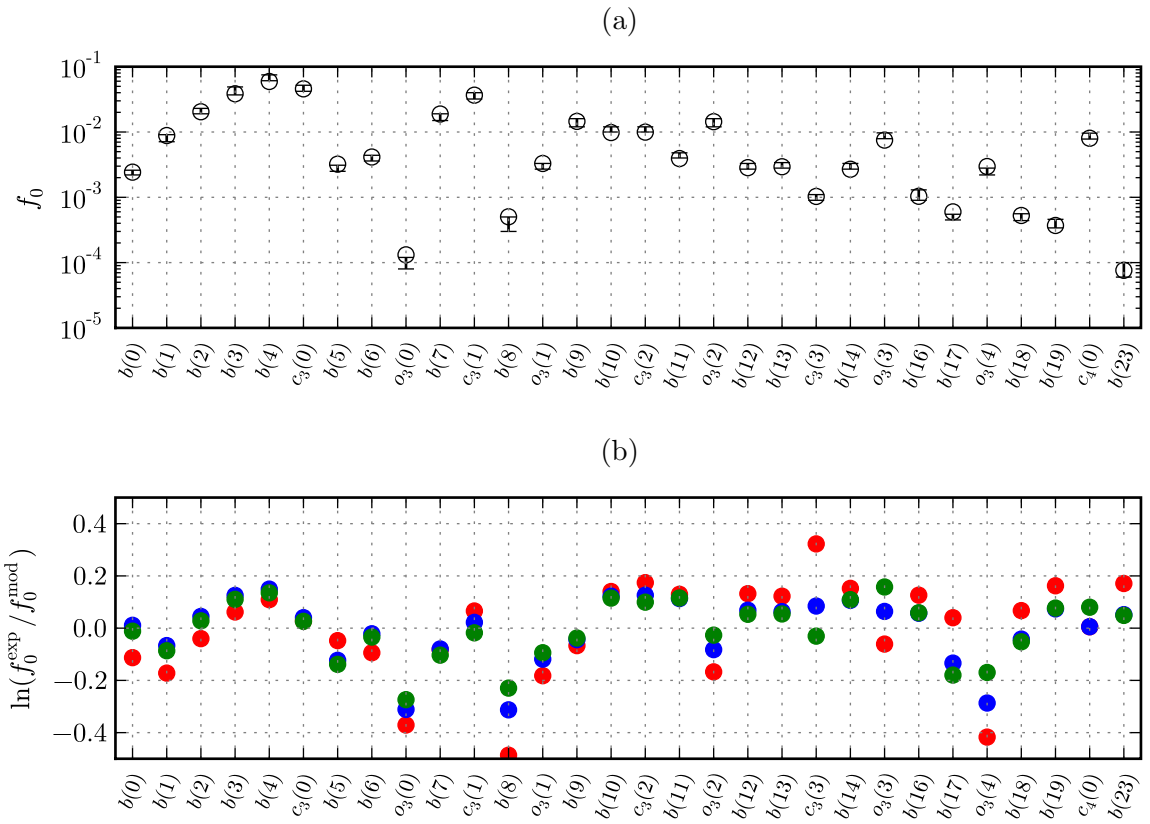

Figure 6.10: *(a):* Experimental (*error bars*) and modelled (*points*) f-values for the known f-parity $^1\Pi_u$ states of $^{14}N_2$, extrapolated to $J = 0$. The model values are calculated with electronic transition moments possessing a linear R-dependence. *(b):* Residual model error of f-values, with electronic transition moments possessing an R-dependence that is constant (*red*), the *ab initio* form of Spelsberg and Meyer [145] (*blue*), and linear (*green*).

of the calculations of Spelsberg and Meyer [145].

In light of the similarity expected within a Rydberg series, the same R-dependence was adopted for $c_4 - X$ as for $c_3 - X$, but with its magnitude reduced by a best-fit factor of 0.55. Unlike the homogeneous interaction matrix elements discussed in Sec. 6.4.2, this reduction is in good agreement with that predicted by quantum defect theory, requiring a factor of 0.56.

Novel R-dependences were also trialled. Coefficients dictating constant, linear, and quadratic forms were optimised with regard to the same set of experimental f-values. The model residuals produced by some of the alternative models are plotted in Fig. 6.10(a). It is clear that the R-dependence of Spelsberg and Meyer performs better than where the transition moments are constants, and a linear dependence is better still. Hereon, the linear form is adopted as the preferred transition-moment because of this improved agreement.

The forms of some fitted transition moments are shown in Fig. 6.11 and demonstrate a high degree of similarity between the R-dependence of Spelsberg and Meyer and the optimised linear form, the latter being an incremental improvement only. The largest

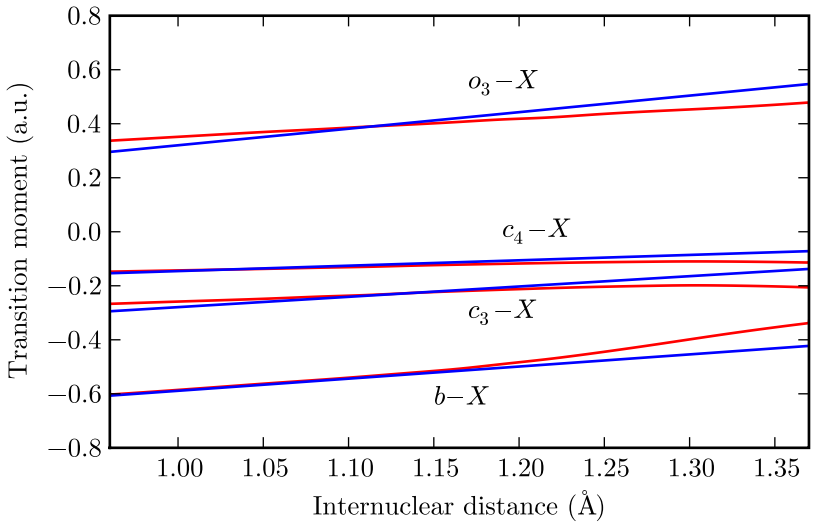

Figure 6.11: Model electronic transition moments optimised to agree with $^1\Pi_u - X\,{}^1\Sigma_g^+$ f-parity optical transitions. *Red:* A rescaled version of the *ab initio* R-dependence deduced by Spelsberg and Meyer [145]. *Blue:* Linear R-dependence.

	$R^e = a + b(R - 1.15)$	
Transition	a	b
$b - X$	−0.520(11)	+0.51(11)
$c_3 - X$	−0.220(9)	+0.39(9)
$c_4 - X$	−0.117(5)	+0.27(6)
$o_3 - X$	+0.411(7)	+0.61(13)

Table 6.3: Fitted linear diabatic electronic transition moments, R^e, for $^1\Pi_u - X\,{}^1\Sigma_g^+$ transitions, in units of a.u.. Internuclear distance, R, has units of Å, and statistical uncertainties extracted from the least-squares fitting program are given parenthetically in terms of the least-significant digit.

discrepancies occur for R above 1.25 Å. However, the present set of experimental f-values are all derived from transitions connected to the $v = 0$ ground state level, which has a wavefunction appreciably different from zero over a limited range of R, between 0.95 and 1.25 Å. Thus, the correctness of the linear transition-moments beyond 1.25 Å cannot be confirmed.

The set of linear coefficients defining optimised transition moments are listed in Tab. 6.3, and Fig. 6.10(b) compares the model calculated f-values with the constraining experimental measurements, demonstrating good agreement over nearly three orders of magnitude. An additional optimisation was performed to determine best-fit quadratically-dependent transition-moments. This resulted in slightly reduced fitted residuals relative to the linear case, but this improvement was deemed insufficient to warrant the increase in complexity.

6.5 *e*-parity $^1\Pi_u + {}^1\Sigma_u^+$ model

In addition to the Q-branch transitions appearing in N_2 absorption-spectra, are many branches comprised of P and R lines which are ascribable to transitions of parity-type $e \leftarrow e$. The excited states responsible for these are rigorously decoupled from the f-parity

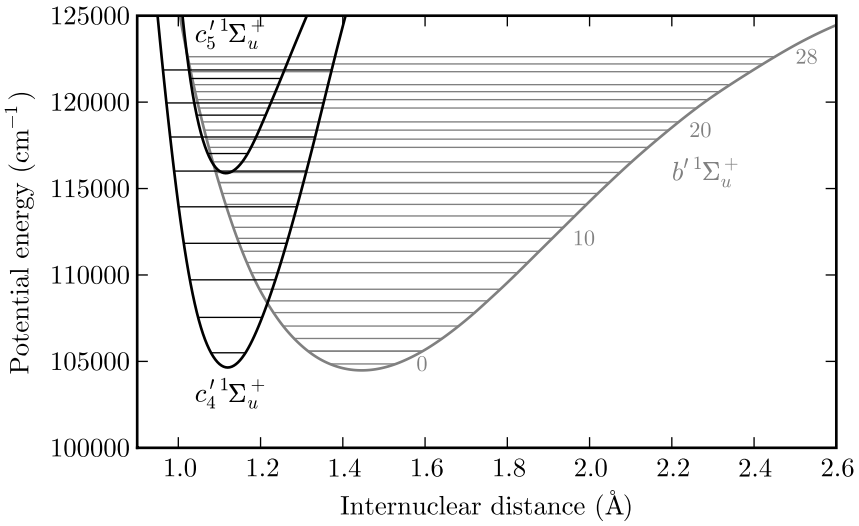

Figure 6.12: Potential-energy curves of the three $^1\Sigma_u^+$ states incorporated into the e-parity coupled-channels model. Also shown are the term origins of the known vibrational levels.

levels which terminate Q-branch transitions, and are treated here by a coupled-channels model which is a distinct extension to that discussed in Sec. 6.4.

The objective of the present model is to correctly reproduce the known e-parity level energies between 100 000 and 122 000 cm^{-1} arising from states of symmetry $^1\Pi_u$ and $^1\Sigma_u^+$, as well as the observed absorption oscillator-strengths. To these ends, it is necessary to consider seven electronic states: the $^1\Pi_u$ states b, c_3, o_3, and c_4; and the $^1\Sigma_u^+$ states b', c_4', and c_5'. All of these states are accessible from the ground state following electric-dipole excitation, and each requires the specification of an electronic transition moment.

Additionally, this model seeks to partially explain the predissociation observed for some $^1\Sigma_u^+$ levels. All such levels that lie above the dissociation energy of $b\,^1\Pi_u$ may have reduced lifetimes, and broadened lineshapes, because of rotational coupling into the $b\,^1\Pi_u$ continuum. Additionally, further predissociation occurs into the continua of the $C'\,^3\Pi_u$ and $C\,^3\Pi_u$ states; the consequences of this effect are modelled in Sec. 6.6.3.

The $^1\Pi_u$ potential-energy curves and homogeneous interactions determined in Sec. 6.4 were constructed with reference to f-parity term energies only, but have here been extended to the e-parity case without modification. Excepting, that is, for a small high-energy extension discussed in Sec. 6.5.3.

The $^1\Sigma_u^+$ potential-energy curves calculated by Spelsberg and Meyer [145] are adopted as a beginning point for further refinement. These were originally defined by polynomial functions with as many as seven terms, but are represented here by the more general form described in Sec. 6.1.2. A total of 100 model parameters were varied in order to optimise the shape of the $^1\Sigma_u^+$ potential-energy curves, and the smoothness constraint of Sec. 6.2.1 was needed to condition each curve and prevent the appearance of nonphysical potential-energy oscillations. Fig. 6.12 shows the optimised $^1\Sigma_u^+$ potential-energy curves as well as the locations of all known vibrational-levels within the energy range of interest.

6.5.1 $^1\Sigma_u^+ \sim {}^1\Sigma_u^+$ electronic interactions

There are strong homogeneous electronic-couplings between the pairs of states $b'\,^1\Sigma_u^+ \sim c_4'\,^1\Sigma_u^+$ and $b'\,^1\Sigma_u^+ \sim c_5'\,^1\Sigma_u^+$. These are apparent in the uneven spacing of $b'\,^1\Sigma_u^+$ levels plotted in Fig. 6.12. An additional coupling, $c_4'\,^1\Sigma_u^+ \sim c_5'\,^1\Sigma_u^+$, was included in the model of Spelsberg and Meyer [145] but has here been assumed to be zero. In principle, either assumption is legitimate given the nonuniqueness of the diabatic formalism, and the present choice has been made with regard to the expected orthogonality of states within the $c_{n+1}'\,^1\Sigma_u^+$ Rydberg series. The shape of the R-dependent electronic coupling determined by Spelsberg and Meyer [145] for the interaction of $b'\,^1\Sigma_u^+ \sim c_4'\,^1\Sigma_u^+$ has been adopted here for both $b'\,^1\Sigma_u^+ \sim c_4'\,^1\Sigma_u^+$ and $b'\,^1\Sigma_u^+ \sim c_5'\,^1\Sigma_u^+$; each separately scaled during model optimisation. The fitted R-dependent homogeneous electronic perturbation matrix elements are:

$$\langle b'\,^1\Sigma_u^+|H^{el}|c_4'\,^1\Sigma_u^+\rangle = (-1730 \pm 1) \times e^{-(R-1.003)^2/0.258}, \tag{6.13}$$

$$\langle b'\,^1\Sigma_u^+|H^{el}|c_5'\,^1\Sigma_u^+\rangle = (-1066 \pm 1) \times e^{-(R-1.003)^2/0.258}, \tag{6.14}$$

$$\text{and } \langle c_4'\,^1\Sigma_u^+|H^{el}|c_5'\,^1\Sigma_u^+\rangle = 0\,\text{cm}^{-1}. \tag{6.15}$$

The best-fit $b'\,^1\Sigma_u^+ \sim c_5'\,^1\Sigma_u^+$ coupling has $0.61\times$ the magnitude of $b'\,^1\Sigma_u^+ \sim c_4'\,^1\Sigma_u^+$, slightly larger than the $0.56\times$ scaling predicted by quantum defect theory. The uncertainty in these fitted interaction energies, and subsequently listed model parameters, are estimated by the least-squares fitting program. As an aside, R-independent electronic coupling was considered, and a similar degree of agreement between modelled and experimental level energies emerged.

6.5.2 $^1\Sigma_u^+ \sim {}^1\Pi_u$ rotational interactions

Levels with $J = 0$ only occur for $^1\Sigma$ states, and the observed $P(1)$ spectral lines arising from these levels are completely independent of the $^1\Pi_u$ manifold. However, the L-uncoupling operator discussed in Sec. 2.5.1 generates perturbations of the type $^1\Pi \sim {}^1\Sigma$, with a magnitude that scales as $\sqrt{J(J+1)}$. That is, all levels with $J > 0$ may contain an admixture of both symmetries. Such heterogeneous rotational-coupling is represented within the coupled-channels model by several R-independent off-diagonal matrix-elements possessing the form of Eq. (2.47).

In the present model, rotational coupling is permitted between the pairs of states $c_3\,^1\Pi_u \sim c_4'\,^1\Sigma_u^+$, $c_4\,^1\Pi_u \sim c_5'\,^1\Sigma_u^+$, $b\,^1\Pi_u \sim b'\,^1\Sigma_u^+$, and $o_3\,^1\Pi_u \sim b'\,^1\Sigma_u^+$. Nonzero coupling between all other combinations of $^1\Sigma_u^+$ and $^1\Pi_u$ diabatic states is precluded by electronic configurations that differ by more than one molecular orbital. The mixed configurations of the adopted $b'\,^1\Sigma_u^+$ and $b\,^1\Pi_u$ diabatic states may result in significant R-dependent $b'\,^1\Sigma_u^+ \sim b\,^1\Pi_u$ and $b'\,^1\Sigma_u^+ \sim o_3\,^1\Pi_u$ rotational coupling, but this could not be definitively confirmed during the model optimisation.

An estimated interaction energy for the diabatic Rydberg states $c_{n+1}'\,^1\Sigma_u^+$ and $c_n\,^1\Pi_u$ is discussed in Sec. 2.13 according to pure-precession assumption, and leads to a prediction of $\langle c_n\,^1\Pi_u|H^{rot}|c_{n+1}'\,^1\Sigma_u^+\rangle = B(R)\sqrt{J(J+1)}\dot{2}$. A prior estimate of the magnitude of heterogeneous coupling between $b\,^1\Pi_u$, $o_3\,^1\Pi_u$, and $b'\,^1\Sigma_u^+$ may not be obtained in this way, and zero was assumed.

After optimisation, the best-fitting rotational-perturbation matrix elements were found

to be:

$$\langle c_3\,{}^1\Pi_u|H^{rot}|c_4'\,{}^1\Sigma_u^+\rangle = B(R)\sqrt{J(J+1)} \times (+2.01 \pm 0.01), \tag{6.16}$$

$$\langle c_4\,{}^1\Pi_u|H^{rot}|c_5'\,{}^1\Sigma_u^+\rangle = B(R)\sqrt{J(J+1)} \times (+1.96 \pm 0.03), \tag{6.17}$$

$$\langle b\,{}^1\Pi_u|H^{rot}|b'\,{}^1\Sigma_u^+\rangle = B(R)\sqrt{J(J+1)} \times (-0.13 \pm 0.03), \tag{6.18}$$

$$\text{and } \langle o_3\,{}^1\Pi_u|H^{rot}|b'\,{}^1\Sigma_u^+\rangle = B(R)\sqrt{J(J+1)} \times (-0.65 \pm 0.05). \tag{6.19}$$

Here, the dimensionless fitted quantities are bracketed along with an estimated uncertainty calculated by the least-squares fitting routine.

All e-parity $c_n\,{}^1\Pi_u$ and $c_{n+1}'\,{}^1\Sigma_u^+$ vibrational levels are strongly perturbed by the $c_n \sim c_{n+1}'$ interactions, with the resultant Λ-doubling of e- and f-parity $c_3\,{}^1\Pi_u$ and $c_4\,{}^1\Pi_u$ levels plotted in Fig. 6.13. The excellent agreement between modelled and experimental Λ-doubling suggests that the optimised $\langle c_3\,{}^1\Pi_u|H^{rot}|c_4'\,{}^1\Sigma_u^+\rangle$ and $\langle c_4\,{}^1\Pi_u|H^{rot}|c_5'\,{}^1\Sigma_u^+\rangle$ matrix elements have been determined with confidence, and the validity of the pure-precession approximation is strongly supported.

The potential-energy curves of $b\,{}^1\Pi_u$ and $b'\,{}^1\Sigma_u^+$ have roughly similar radial extent and thus have vibrational levels with likewise similar rotational constants. Few level crossings then occur between these two states and the model $b \sim b'$ rotational interaction is primarily constrained by a single perturbation, occurring for $b'(0)$ and $b(4)$ between $J = 21$ and 22. Figure 6.14(a) shows model residuals for $b\,{}^1\Pi_u(v = 4)$ term values which have been calculated with, and without, the presence of $b \sim b'$ coupling. Evidently, this coupling is necessary in order to explain the perturbed term value at $J = 22$. The fitted magnitude of this coupling is small, as expected for the interaction of two valence states, and is likely to be less well-known than estimated by the least-squares program because of the lack of constraining information.

The $o_3\,{}^1\Pi_u$ and $b'\,{}^1\Sigma_u^+$ states have quite different rotational constants and several crossings between pairs of their vibrational levels have been observed. Figure 6.15 plots the Λ-doubling and model residuals of those $o_3\,{}^1\Pi_u$ levels that are most sensitive to the $o_3 \sim b'$ rotational interaction. Term value distortions as large as $15\,\mathrm{cm}^{-1}$ occur near the observed level crossings, but all local perturbations are correctly reproduced by the model to within $\pm 1\,\mathrm{cm}^{-1}$.

The fitted matrix-element $\langle o_3\,{}^1\Pi_u|H^{\mathrm{rot}}|b'\,{}^1\Sigma_u^+\rangle = 0.65\,\mathrm{cm}^{-1}$, is surprisingly large given that it occurs between a valence and Rydberg state, and is configurationally forbidden for small-R, with configurations listed in Tab. 3.1. The large-R configuration of $b'\,{}^1\Sigma_u^+$, however, only differs from $o_3\,{}^1\Pi_u$ by one molecular orbital and must be responsible for the observed coupling. This coupling must then have significant R-dependence, with the fitted R-independent magnitude likely to be close to the true value near the crossing point of $o_3\,{}^1\Pi_u$ and $b'\,{}^1\Sigma_u^+$ potential-energy curves, at $R = 1.24\,\text{Å}$.

There is an apparent perturbation of $^{15}N_2$ $o_3\,{}^1\Pi_u(v = 0)$ term values between $J = 3$ and 4 which is not reproduced by the model. This is due to a level crossing with the $v = 1$ level of $D\,{}^3\Sigma_u^+$ [97], which is not included in the coupled-channels model, and is discussed further in Sec. 6.6.3.

6.5.3 A perturbation between $o_3\,{}^1\Pi_u(v = 6)$ and $b'\,{}^1\Sigma_u^+(v = 20)$

An approximate energy may be deduced for the $^{14}N_2$ $v = 6$, e-parity level of $o_3\,{}^1\Pi_u$ by examining the $b'\,{}^1\Sigma_u^+(v = 20)$ linewidths, with experimental measurements discussed in Chap. 5. As depicted in Fig. 5.15, there is a clear perturbation in the linewidths and term

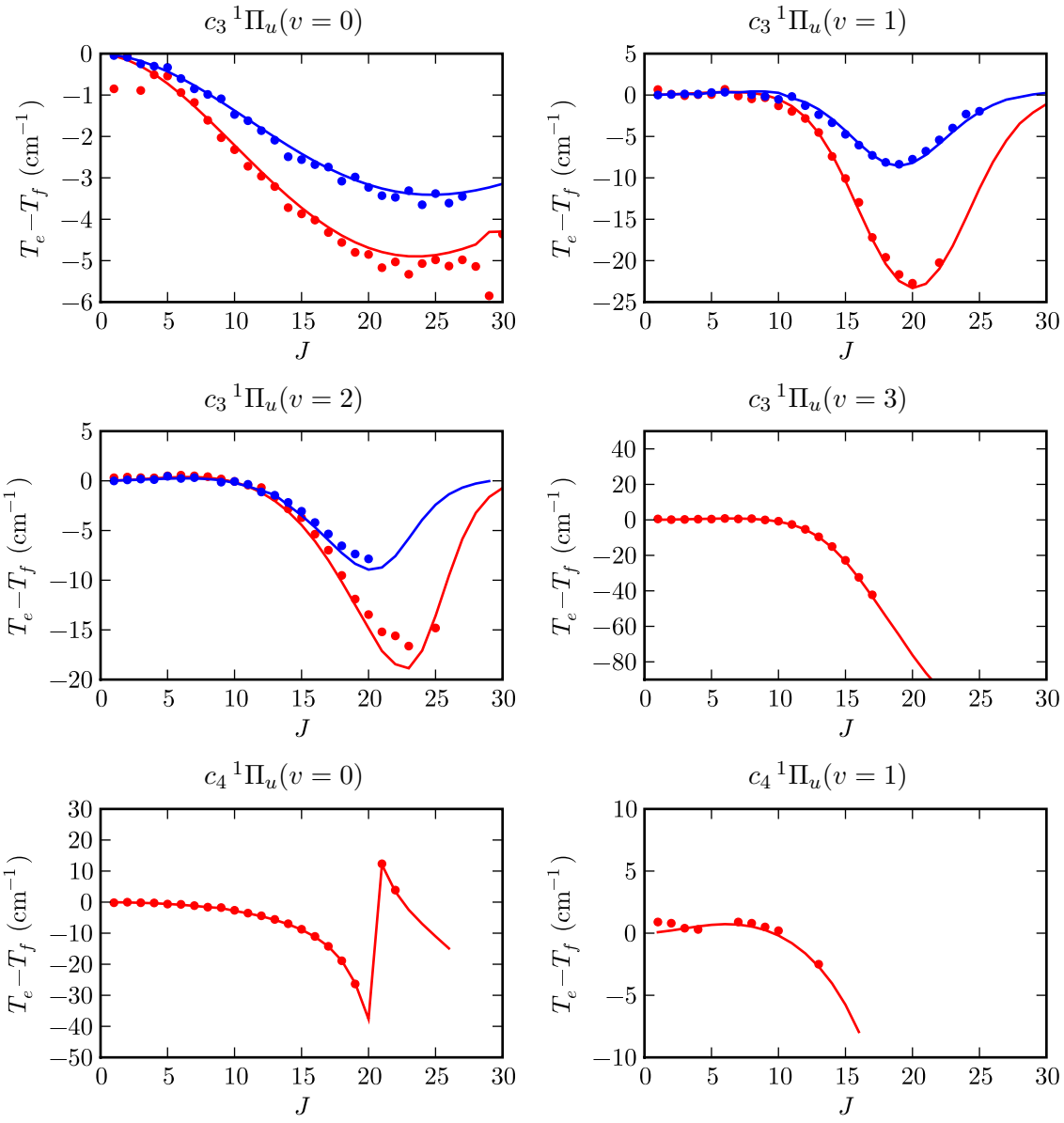

Figure 6.13: Modelled (*curves*) and experimental (*points*) Λ-doubling of $c_3\,{}^1\Pi_u(v=0-3)$ for $^{14}N_2$ (*red*) and $^{15}N_2$ (*blue*). Here, T_e and T_f are *e*- and *f*-parity term values, respectively.

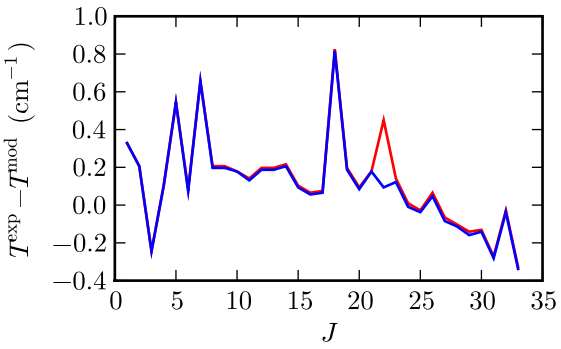

Figure 6.14: Difference between modelled ($T^{\rm mod}$) and experimental ($T^{\rm exp}$) term values of $^{14}N_2$ $b\,^1\Pi_u(v=4)$, for the case of no $b \sim b'$ rotational coupling (*red*), and with the optimised coupling (*blue*). The large model residual generated for $J = 3-7$ and $J = 17$ are due to level crossings with the spin-orbit-coupled states $D\,^3\Sigma_u^+(v=0)$ and $G_3\,^3\Pi_u(v=0)$, respectively. These perturbations are discussed further in Sec. 6.6.3.

values near the $J = 10$ level of $b'(20)$, which has an energy of 117 322 cm^{-1}. A simple extrapolation of lower vibrational levels of $o_3\,^1\Pi_u$ suggests that $o_3(6)$ will occur near this energy, and is likely to be strongly predissociated because it lies above the dissociation energy of $b\,^1\Pi_u$. Upon experimentation, a small adjustment of the coupled-channels model $o_3\,^1\Pi_u$ potential-energy curve incurs a large J-shift of the $b'(20)$ linewidth peak, supporting the assignment of this perturbation.

A coarse adjustment of the vertical displacement of the o_3 potential-energy curve succeeded in optimising the agreement between model and experimental $b'(20)$ linewidths. Because of their weakness and breadth, the perturbing e-parity $o_3(6)$ resonances were overwhelmed by $b'(20)$ in the model cross section and not discernible. However, $o_3(6)$ level energies were calculable after applying the same shift to the f-parity model. These new levels lie above all others known for $b\,^1\Pi_u$, $c_3\,^1\Pi_u$, and $o_3\,^1\Pi_u$; and were incorporated into a modified version of the f-parity coupled-channels model of Sec. 6.4 by a slight adjustment of the upper limbs of all $^1\Pi_u$ potential energy curves. This was achieved without degrading the model residuals of lower $^1\Pi_u$ levels, or $c_4\,^1\Pi_u(v=1)$ which lies above $o_3(6)$. This modification required alterations to the potential-energy curves of both $o_3\,^1\Pi_u$ and $c_3\,^1\Pi_u$, because of the strong electrostatic interaction between these states.

A reproduction of the $b'(20)$ linewidth maximum is shown in Fig. 6.16(a) and there is good agreement between experimental and theoretical values. Figure 6.16(b) demonstrates the successful reproduction of experimental $b'(20)$ term values over the level crossing with $o_3(6)$. The deduced f-parity term-energies of $o_3(6)$ for $J = 9$, 10 and 11 are 117 295, 117 331, and 117 371 cm^{-1}; respectively. The estimated uncertainty of these energies is ± 5 cm^{-1} and was determined by shifting all of the $^1\Pi_u$ potential-energy curves uniformly and observing the effect upon $b'(20)$. The width of the modelled $o_3(6)$ resonances was 47 cm^{-1} FWHM. This quantity is also experimentally constrained by the $b'(20)$ linewidths but has an unknown uncertainty because of the large number of model parameters upon which it depends.

6.5.4 Optimisation of energy levels

The fitting of e-parity energy levels is more complicated, and slightly less successful, than for the f-parity model of Sec. 6.4.3 because of the increased number of states and state

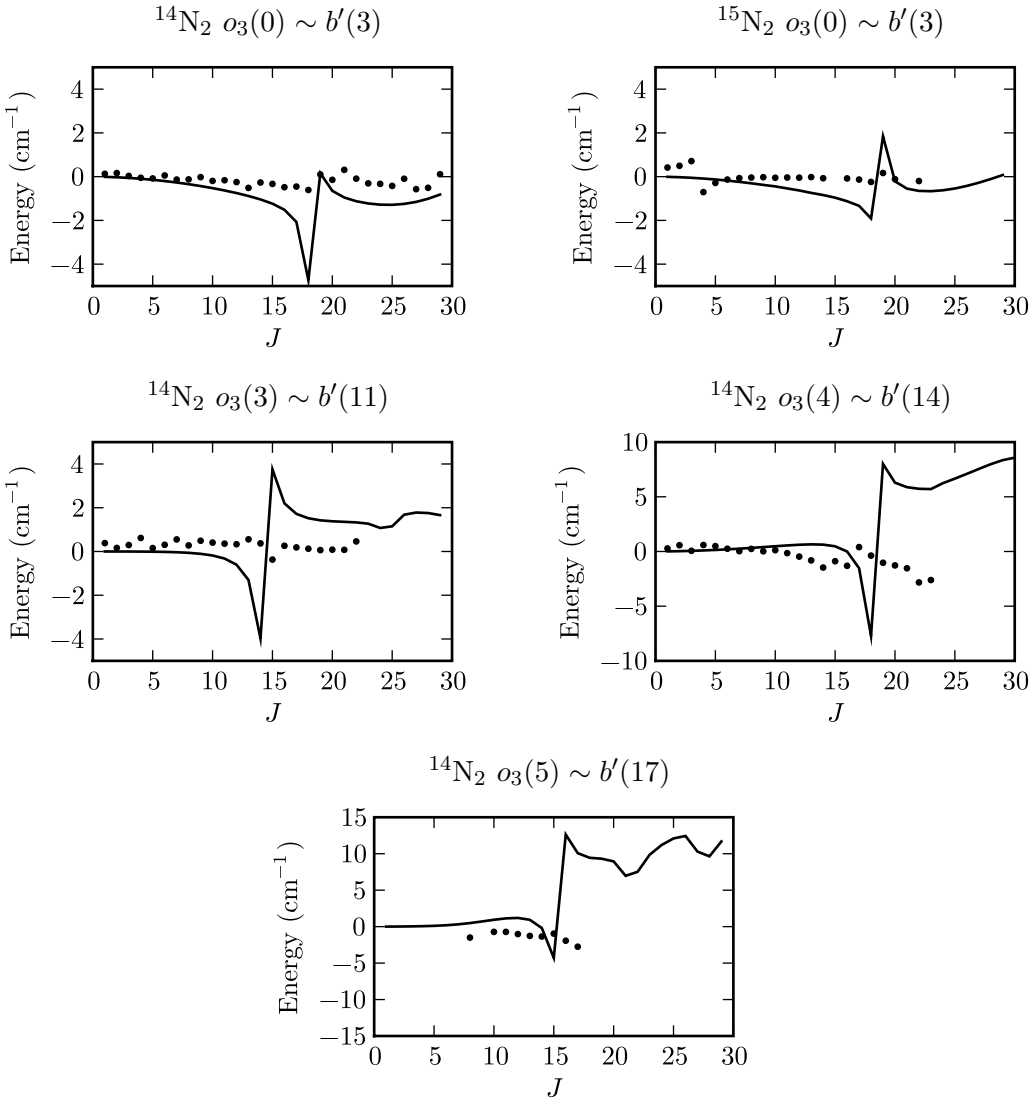

Figure 6.15: *Curves:* Difference between e- and f-parity term values for several vibrational levels of $o_3\,{}^1\Pi_u$ which are perturbed by crossing vibrational levels of $b'\,{}^1\Sigma_u^+$. *Points:* Difference between model and experimental term values of the $o_3\,{}^1\Pi_u$ levels. Each subfigure is labelled by the $o_3\,{}^1\Pi_u$ level plotted and the perturbing $b'\,{}^1\Sigma_u^+$ level.

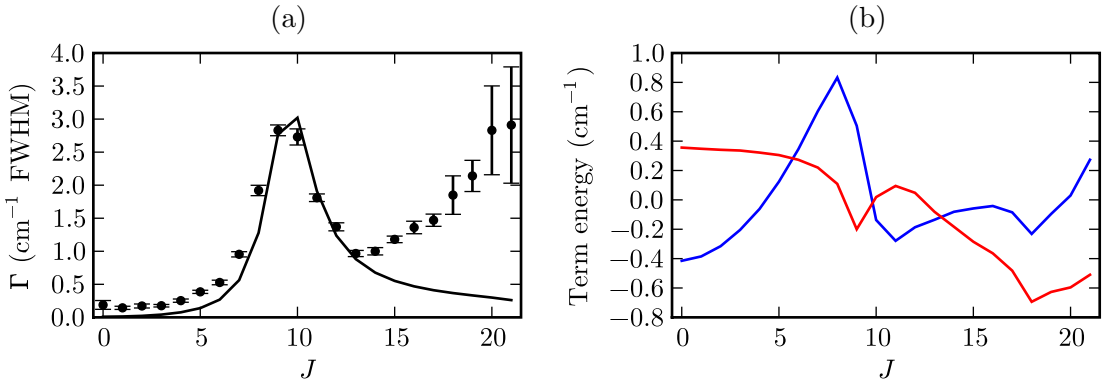

Figure 6.16: *(a):* Predissociation linewidths, Γ, of $b'\,^1\Sigma_u^+(v=20)$ for $^{14}N_2$, which is perturbed by $o_3\,^1\Pi_u(v=6)$. *Error bars:* Values deduced from the SOLEIL photoabsorption spectra of Chap. 5. *Curve:* Calculated by the coupled-channels model. *(b):* Experimental reduced term values (*blue*) and residual errors of model term values for $b'\,^1\Sigma_u^+(v=20)$. A third order polynomial has been subtracted from the reduced values.

interactions involved. Many trial optimisations were required before a set of parameters and constraints were found that provided a satisfactory convergence of model residuals. The eventual set of reference experimental data considers 327 rotational term-energies arising from 99 vibrational levels: that is $^{14}N_2$ $b\,^1\Pi_u(v=4-7,9,11,12)$, $c_3\,^1\Pi_u(v=0-4)$, $o_3\,^1\Pi_u(v=0-5)$, $c_4\,^1\Pi_u(v=0-1)$, $b'\,^1\Sigma_u^+(v=0-28)$, $c_4'\,^1\Sigma_u^+(v=0-8)$, and $c_5'\,^1\Sigma_u^+(v=0-2)$; $^{15}N_2$ $b\,^1\Pi_u(v=5,7,8)$, $c_3\,^1\Pi_u(v=0-1)$, $b'\,^1\Sigma_u^+(v=0-21,24-25)$, and $c_4'\,^1\Sigma_u^+(v=0,3-6)$; and $^{14}N^{15}N$ $b'\,^1\Sigma_u^+(v=7)$. Each vibrational level was represented by at least three rotational term energies, and for perturbed levels as many as nine were required.

The majority of levels are affected by rotational coupling and the observed Λ-doubling of $^1\Pi_u$ states provides a direct constraint on the various heterogeneous interaction parameters. Consequently, those *e*-parity $^1\Pi_u$ levels that are significantly Λ-doubled were included as model constraints even though the $^1\Pi_u$ potential-energy curves were not manipulated. Consideration was made for all of the $c_3\,^1\Pi_u$, $c_4\,^1\Pi_u$, and $o_3\,^1\Pi_u$ levels plotted in Figs. 6.13 and 6.15, as well as a number of $b\,^1\Pi_u$ levels.

The least-squares optimisation was finally compared with a complete set of *e*-parity $^1\Sigma_u^+$ and $^1\Pi_u$ term values, consisting of 2269 members. A histogram showing the resultant collection of model residuals is plotted in Fig. 6.17.

Figure 6.18 summarises the quality of fit of $^1\Sigma_u^+$ vibrational levels and Fig. 6.19 summarises a few *e*-parity $^1\Pi_u$ levels for which comparable *f*-parity levels are not well known and could not be analysed in Sec. 6.6. For each vibrational level, arranged in order of increasing energy, an experimental and modelled term origin and rotational-constant has been calculated and the difference plotted. Because of the centrifugal distortion and perturbations present for virtually all levels, a subset of low-J levels were used to produce this two parameter summary of quality of fit. Consequently, these figures to do not completely represent the quality-of-fit for each vibrational level.

The majority of levels show absolute agreement between experimental term origins and rotational-constants below 1 and $0.005\,\mathrm{cm}^{-1}$, respectively, but with some notable exceptions. The largest disagreement occurs for the term origins of $c_4'\,^1\Sigma_u^+(v=5)$ in

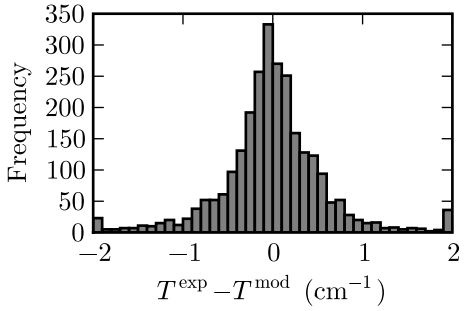

Figure 6.17: Histogram of *e*-parity modelled term value residual errors for all known rotational-vibrational levels and all isotopomers of N_2. Residuals with magnitudes greater than $2\,\mathrm{cm}^{-1}$ have been plotted in the extreme bins. The mean and standard deviations of the residuals are 0.018 and $0.70\,\mathrm{cm}^{-1}$, respectively.

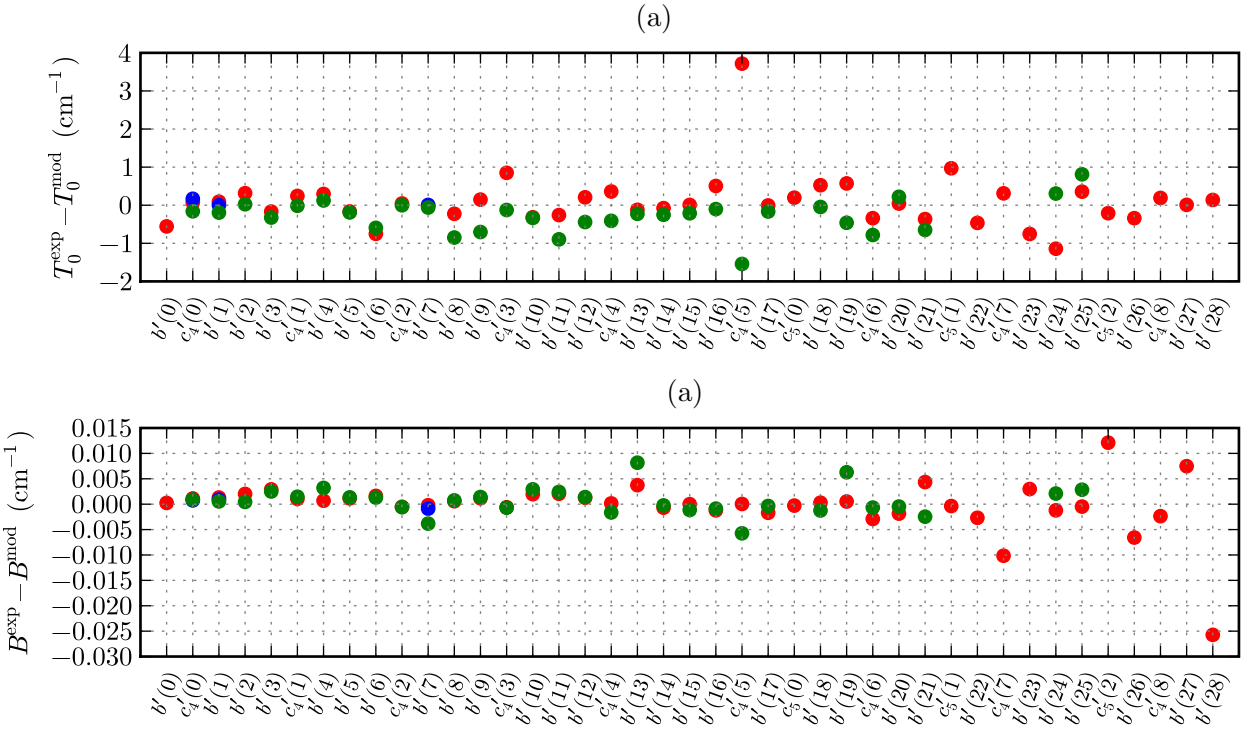

Figure 6.18: Residual error of modelled term origins ($T_0^{\mathrm{exp}} - T_0^{\mathrm{mod}}$) and rotational constants ($B^{\mathrm{exp}} - B^{\mathrm{mod}}$) for the known $^1\Sigma_u^+$ levels of $^{14}N_2$ (*red*), $^{14}N^{15}N$ (*blue*), and $^{15}N_2$ (*green*).

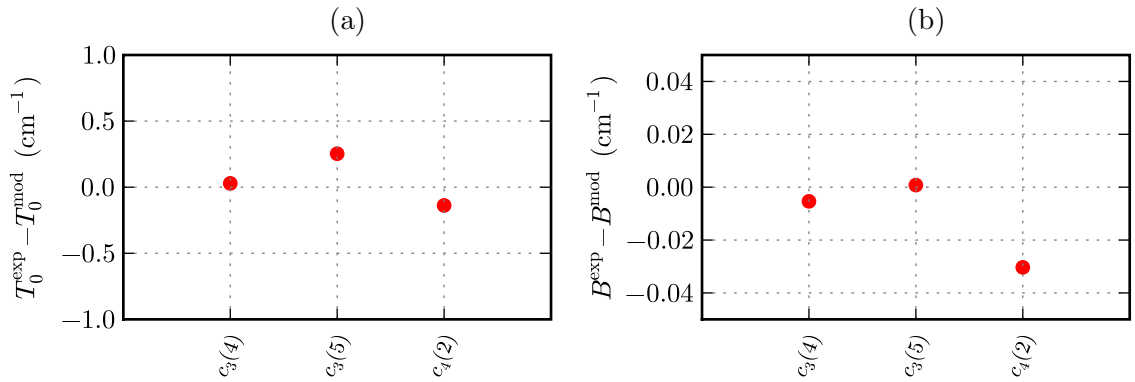

Figure 6.19: Residual error of modelled term origins ($T_0^{\rm exp} - T_0^{\rm mod}$) and rotational constants ($B^{\rm exp} - B^{\rm mod}$) for some e-parity $^1\Pi_u$ levels of $^{14}N_2$.

$^{14}N_2$ and $^{15}N_2$, which are mislocated in the model by approximately -4 and $+1.5\,\mathrm{cm}^{-1}$, respectively. A definitive explanation of this discrepancy is difficult to ascertain. In $^{14}N_2$, the $J = 0$ levels $c_4'(5)$ and $c_3(5)$ are separated in energy by $\sim 10\,\mathrm{cm}^{-1}$. This closeness leads to strong rotational mixing for $J > 0$, as well as a highly congested spectrum. An error in the rotational assignment of either level could be responsible for the inability of the coupled-channels to simultaneously treat $c_4'(5)$ in $^{14}N_2$ and $^{15}N_2$.

The poor agreement of modelled and experimental rotational-constants for $c_4'(7)$ in $^{14}N_2$ may be the result of a poorly known experimental value. Only a few rotational term values have been determined [47] for this level, and several of these are surprisingly scattered. Several further $^{14}N_2$ levels lying higher in energy than $b'(25)$ also have poorly fitted rotational constants. For these cases, the likely cause is the omission of $c_n\,^1\Pi_u$ and $c'_{n+1}\,^1\Sigma_u^+$ states with $n > 4$.

6.5.5 Optimisation of f-values

In order to reproduce the absorption spectrum of e-parity excited levels from the ground state, an extension was made to the $^1\Pi_u$-only absorption model of Sec. 6.4.4 by the further addition of three diabatic electronic-transition moments, i.e., those governing the transitions $b'\,^1\Sigma_u^+ - X$, $c_4'\,^1\Sigma_u^+ - X$, and $c_5'\,^1\Sigma_u^+ - X$.

Several versions of these transition moments were considered, having alternative R-dependences, and optimised with respect to a set of $^1\Sigma_u^+ - X$ oscillator strengths obtained from the KEK series of experiments, discussed in Chap. 4. Despite the significant rotational dependence of oscillator strengths observed in Chap. 4, a single f-value extrapolated to $J = 0$ was sufficient to constrain each of the 24 excited levels considered, that is $b'\,^1\Sigma_u^+(v = 1, 3-18)$, $c_4'\,^1\Sigma_u^+(v = 0-5)$, and $c_5'\,^1\Sigma_u^+(v = 0)$, all for $^{14}N_2$. The various $^1\Pi_u - X$ transition moments optimised in Sec. 6.4.4 with respect to f-parity excited levels were adopted here unaltered.

Figure 6.20(a) demonstrates the level of agreement between modelled and experimental f-values with optimised transition moments constrained by several alternative R-dependences. In the first case, the $b' - X$ and $c_4' - X$ moments calculated *ab initio* by Spelsberg and Meyer [145] were rescaled to best fit the present observations. The $c_4' - X$ R-dependence was also used to represent $c_5' - X$, although Spelsberg and Meyer [145] cal-

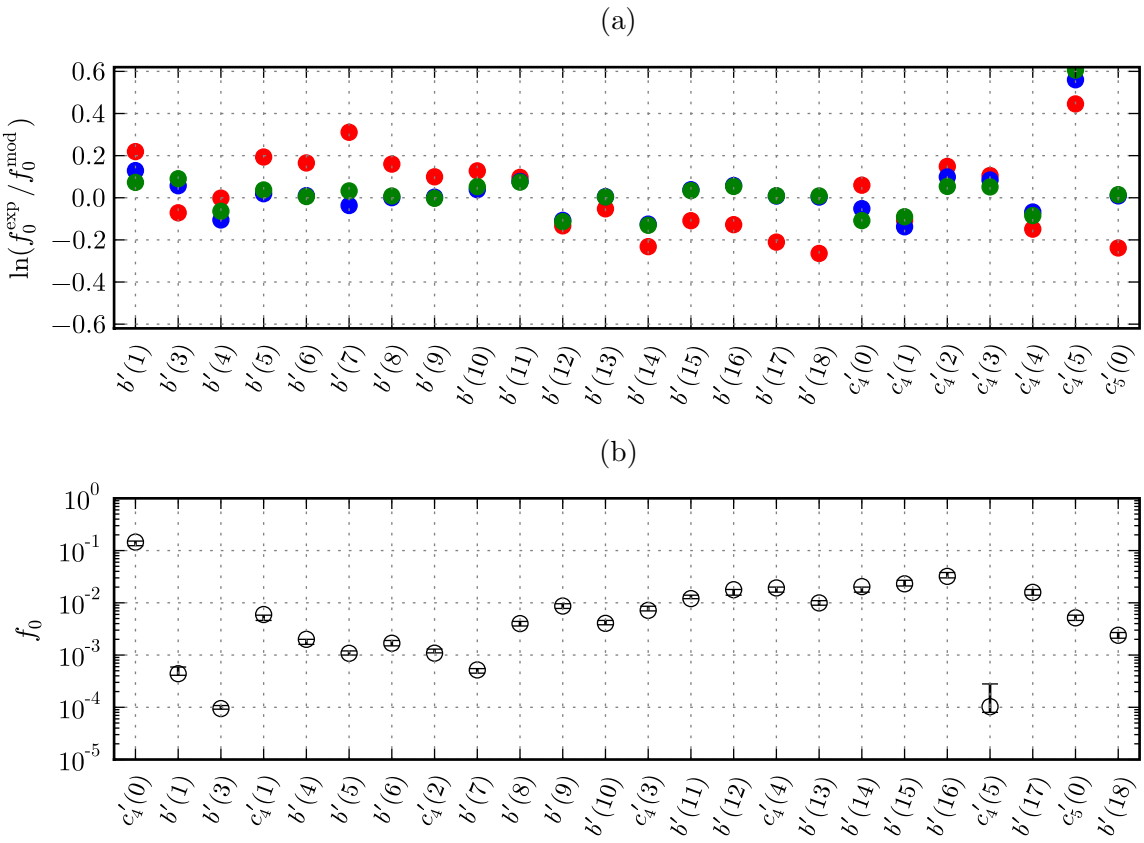

Figure 6.20: *(a):* Residual model errors of f-values, calculated with electronic-transition moments possessing R-dependences that are: the *ab initio* form of Spelsberg and Meyer [145] (*red*); linear (*blue*); and quadratic (*green*). *(b):* Experimental (*error bars*) and modelled (*points*) f-values for $^1\Sigma_u^+ - X\,^1\Sigma_g^+$ transitions of $^{14}N_2$, extrapolated to $J = 0$. The model values are calculated with electronic-transition moments possessing a linear R-dependence.

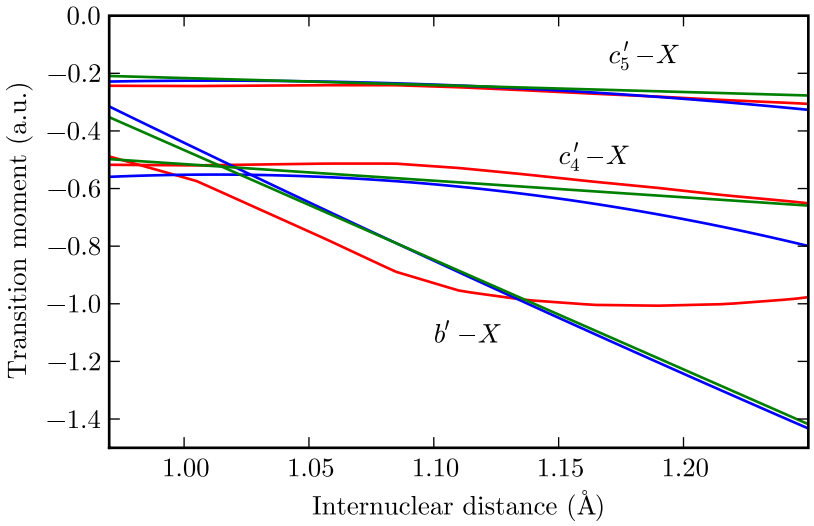

Figure 6.21: Model electronic-transition moments optimised to agree with the database of $^1\Sigma_u^+ - X\,^1\Sigma_g^+$ *e*-parity optical transitions. *Red:* A rescaled version of the *ab initio* R-dependences deduced by Spelsberg and Meyer [145]. *Blue:* Linear R-dependences. *Green:* Quadratic R-dependences.

Transition	$R^e = a + b(R-1)$ a	b
$b' - X$	−0.47(5)	−3.8(4)
$c_4' - X$	−0.52(2)	−0.58(16)
$c_5' - X$	−0.21(1)	−0.58(16)

Table 6.4: Fitted linear diabatic electronic transition moments, R^e, for $^1\Sigma_u^+ - X\,^1\Sigma_g^+$ transitions in units of a.u.. Internuclear distance, R, has units of Å, and statistical uncertainties extracted from the least-squares fitting program are given parenthetically in terms of the least-significant digit.

culated this separately. This decision was made with respect to the commonality expected within the $c_{n+1}'\,^1\Sigma_u^+$ Rydberg series. The distinction is likely to be negligible given the similarity of the *ab initio* $c_4' - X$ and $c_5' - X$ transition moments. Ultimately, the $b' - X$ and $c_4' - X$ transition moments were reduced by factors of 0.82 and 0.91, respectively, and the $c_5' - X$ transition moment was found to require 0.47× the magnitude of $c_4' - X$.

A significantly improved fit to the experimental f-values was achieved when fitting coefficients to linear transition-moments, with $c_4' - X$ and $c_5' - X$ constrained to have a common gradient. Figure 6.21 shows only small differences between the forms of linear and *ab initio* transition moments for $c_4' - X$ and $c_5' - X$, but a more significant difference with regards to $b' - X$. The very large deviation at large internuclear distance of the latter is somewhat uncertain because the magnitude of the ground state wavefunction decreases rapidly as R approaches 1.25 Å. Consequently, the modelled f-values are not as sensitive to this region as elsewhere.

The best-fit linear $^1\Sigma_u^+ - X\,^1\Sigma_g^+$ transition moments are listed in Tab. 6.4. Upon experimentation, a further reduction in model residuals resulted from assuming transition moments with quadratic forms, and these are also plotted in Fig. 6.20. However, these do not deviate significantly from the linear case and it was judged that the slight benefit of a quadratic R-dependence does not justify the extra complexity involved.

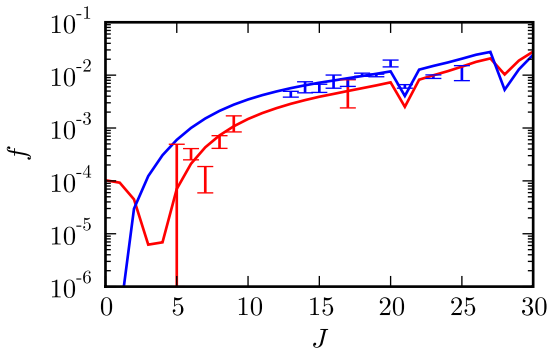

Figure 6.22: Experimental (*error bars*) and modelled (*curves*) f-values of $c_4'\,{}^1\Sigma_u^+(v'=5) \leftarrow X\,{}^1\Sigma_g^+(v''=0)$. The P and R branches are plotted in red and blue, respectively.

A comparison of experimental and optimised model f-values is plotted in Fig. 6.20(b). For each band an f-value corresponding to $J = 0$ has been presented and the overall fit is quite satisfactory across three orders of magnitude. The largest discrepancy occurs for $c_4'(5) \leftarrow X(0)$, which is apparently underestimated by 75%. However, because of the congested nature of this band's appearance in absorption spectra, mentioned above, no f-values have been experimentally determined for $J < 5$. Furthermore, the nonlinear mixing of electronic transition amplitudes results in a rapid variation of $c_4'(5) \leftarrow X(0)$ line strengths with J, as shown by Fig. 6.22. An extrapolation of f-values by the coupled-channels model to rotational levels lower than what has been observed actually predicts the occurrence of a minimum. Given these complications, the disagreement between observed and calculated $J = 0$ f-values is unsurprising.

6.6 $^3\Pi_u + {}^3\Sigma_u^+$ model

As discussed in Sec. 3.4, the observed predissociativity of $^1\Pi_u$ levels is attributable to their spin-orbit coupling to a complex of electronic states with $^3\Pi_u$ symmetry. A model representation of these states is necessary to explain N_2 dissociation as well as various local perturbations apparent among the $^1\Pi_u$ and $^1\Sigma_u^+$ term energies. Additionally, further elucidation of the N_2 triplet states is itself of interest.

6.6.1 $^3\Pi_{u,\Omega=1}$ states

A new coupled-channels model is presented here which builds upon the work of Lewis *et al.* [104] and includes the $\Omega = 1$ substates of $C'\,{}^3\Pi_u$, $C\,{}^3\Pi_u$, $F_3\,{}^3\Pi_u$, and $G_3\,{}^3\Pi_u$. Further details may be found in the published version of this work [105].

The construction of this type of coupled-channels model is reliant on constraining experimental information. The experimental observation of N_2 triplet levels is discussed in Sec. 3.4, and summarised as term origins, rotational constants, and dissociation linewidths in Tab. 6.5. This is the same data set as collated by Lewis *et al.* [98] from the experimental record and new observations.

A diabatic basis was adopted and the optimised potential-energy curves are plotted in Fig. 3.8. The known vibrational levels of the various $^3\Pi_u$ states are also plotted in this figure. These curves have a numerical form and are adjusted during optimisation by vertical shifts at particular internuclear distances, and the intervening points modified according

Iso.	Level	$T_{\rm exp}$ [a]	Refs.	$T_{\rm CSE}$ [a]	ΔT [a]	$B_{\rm exp}$ [b]	$B_{\rm CSE}$ [b]	ΔB [b]	$\Gamma_{\rm exp}$ [c]	$\Gamma_{\rm CSE}$ [c]
$^{14}N_2$	$C(0)$	88 980.0	[136, 165]	88 980.1	−0.1	1.815	1.815	0.000		0.000
	$C(1)$	90 974.4	[136, 165]	90 974.2	0.2	1.793	1.793	0.000		0.000
	$C(2)$	92 915.1	[136, 165]	92 915.3	−0.2	1.769	1.769	0.000		0.000
	$C(3)$	94 789.1	[136, 165]	94 788.9	0.2	1.740	1.740	0.000		0.000
	$C(4)$	96 570.3	[136, 165]	96 570.2	0.1	1.701	1.701	0.000		0.000
	$C'(0)$	97 563.7	[11]	97 563.7	0.0	1.049	1.049	0.000		0.000
	$C(5)$	98 133.	[86]	98 133.	0.	1.407	1.407	0.000		0.000
	$C'(1)$	98 359.7	[87]	98 359.9	−0.2	1.218	1.218	0.000		0.000
	$C'(2)$	98 943.(5)	[162]	98 944.	−1.		1.028			0.000
	$C(7)$	101 069.(2)	[98]	101 069.	0.	1.38(2)	1.41	−0.03	16.(3)	15.
	$C(8)$	102 054.(3)	[98]	102 052.	2.		1.30		18.(4)	17.
	$G(0)$	103 317.4	[48]	103 317.4	0.0	1.885	1.884	0.001	0.11(1) [d]	0.09
	$F(0)$	104 730.6(1)	[148]	104 730.6	0.0	1.805(1)	1.806	−0.001	0.45(3)	0.46
	$G(1)$	106 167.(1)	[98]	106 167.	0.		1.839		9.6(12)	9.6
	$F(1)$	106 579.(2)	[98]	106 579.	0.	1.75(3)	1.75	0.00	16.(3)	16.
	$G(2)$	108 030.(50)	[173]	108 032	−2		1.78			89.
	$C(16)$	108 293.0(3)	[98]	108 293.0	0.0	1.153(2)	1.154	−0.001	$\lesssim 0.5$	0.01
	$C(18)$	109 727.(6)	[98]	109 724.	3.	1.08(2)	1.10	−0.02	5.0(17)	4.0
	$F(2)$	108 640.(50)	[173]	108 649	−9		1.70			148.
	$F(3)$	109 980.(50)	[173]	109 972	8		1.73			138.
	$G(3)$	110 800.(80)	[173]	110 831	−31		1.8			254.
$^{15}N_2$	$C(7)$	100 893.(2)	[98]	100 892.	1.	1.31(2)	1.33	−0.02	15.(3)	13.
	$C(13)$	105 727.(3)	[98]	105 728.	−1.	1.11(2)	1.11	0.00	2.3(13) [e]	1.6
	$C(14)$	106 477.3(3)	[98]	106 478.3	−1.0	1.12(1)	1.14	−0.02	~ 0.05 [f]	0.02
	$F(1)$	106 537.(3)	[98]	106 538.	−1.	1.61(4)	1.58	0.03	18.(2)	16.

[a] Term origin, in $\rm cm^{-1}$. $\Delta T = T_{\rm exp} - T_{\rm CSE}$.
[b] Effective e-level rotational constant for $J \leq 5$, in $\rm cm^{-1}$. $\Delta B = B_{\rm exp} - B_{\rm CSE}$.
[c] Low-J predissociation width, in $\rm cm^{-1}$ FWHM.
[d] Estimated value for $J \approx 11$, from Fig. 2 of Ref. [48].
[e] Width for $J \approx 13$.
[f] Estimated value for $\Omega = 2, J \approx 4$.

Table 6.5: Comparison between experimental and modelled spectroscopic parameters and predissociation widths for the $^3\Pi_u$ levels of N_2.

	Lewis *et al.* [103][a]	Sec. 6.6.1[b]	Sec. 6.6.2[c]	Sec. 6.6.3[d]
$\langle C\,^3\Pi_u \vert H^{el} \vert C'\,^3\Pi_u\rangle$	810(20)	798(15)	789(13)	789(13)
$\langle F_3\,^3\Pi_u \vert H^{el} \vert C'\,^3\Pi_u\rangle$	–	315(60)	302(56)	302(56)
$\langle G_3\,^3\Pi_u \vert H^{el} \vert C'\,^3\Pi_u\rangle$	–	1175(200)	1331(30)	1331(30)
$\langle F_3\,^3\Pi_u \vert H^{el} \vert G_3\,^3\Pi_u\rangle$	–	1115(15))	1102(40)	1102(40)
$\langle C\,^3\Pi_u \vert H^{SO} \vert C\,^3\Pi_u\rangle$	–	–	–	R-dependent
$\langle C'\,^3\Pi_u \vert H^{SO} \vert C'\,^3\Pi_u\rangle$	–	–	–	0
$\langle F_3\,^3\Pi_u \vert H^{SO} \vert F_3\,^3\Pi_u\rangle$	–	–	–	-38
$\langle G_3\,^3\Pi_u \vert H^{SO} \vert G_3\,^3\Pi_u\rangle$	–	–	–	2
$\langle C'\,^3\Pi_{u\Omega=1} \vert H^{SO} \vert b\,^1\Pi_u\rangle$	-1.3(5)	–	-2.0(2)	-2.0(2)
$\langle C\,^3\Pi_{u\Omega=1} \vert H^{SO} \vert b\,^1\Pi_u\rangle$	46(2)	–	46(2)	46(2)
$\langle F_3\,^3\Pi_{u\Omega=1} \vert H^{SO} \vert o_3\,^1\Pi_u\rangle$	–	–	-38	-38
$\langle G_3\,^3\Pi_{u\Omega=1} \vert H^{SO} \vert c_3\,^1\Pi_u\rangle$	–	–	-4.1(7)	-4.1(7)
$\langle 2\,^3\Sigma_{u\Omega=1} \vert H^{SO} \vert b\,^1\Pi_u\rangle$	–	–	11(1)	11(1)

[a]Includes $^1\Pi_u$ states b, c_3, and o_3; and $^3\Pi_{u,\Omega=1}$ states C and C'.
[b]Includes $^3\Pi_{u,\Omega=1}$ states C, C', F_3, and G_3.
[c]Includes $^1\Pi_u$ states b, c_3, c_4, and o_3; $^3\Pi_{u,\Omega=1}$ states C, C', F_3, and G_3; and $2\,^3\Sigma_{u,\Omega=1}$.
[d]Includes $^1\Pi_u$ states b, c_3, c_4, and o_3; $^1\Sigma_u^+$ states b', c_4', and c_5'; $^3\Pi_{u,\Omega=0,1,2}$ states C, C', F_3, and G_3; and $2\,^3\Sigma_{u,\Omega=1}$. Both e- and f-parity states are included.

Table 6.6: Modelled interactions involving $^3\Pi_u$ states, in units of cm^{-1}, and for several different coupled-channels models. The R-dependent quantity $\langle C\,^3\Pi_u \vert H^{SO} \vert C\,^3\Pi_u\rangle$ is discussed in Sec. 6.6.3 and plotted in Fig. 6.27(a).

to a spline-interpolation. The forms of $C\,^3\Pi_u$ and $C'\,^3\Pi_u$ curves prior to optimisation were derived from the adiabatic *ab initio* calculations of Partridge [128], following their conversion to a diabatic form. The $F_3\,^3\Pi_u$ and $G_3\,^3\Pi_u$ states were initially assumed to have the same form as the isoconfigurational singlet states $c_3\,^1\Pi_u$ and $o_3\,^1\Pi_u$, respectively, but with bulk horizontal and vertical shifts applied, as well as a final spline-interpolated adjustment.

An *ab initio*-calculated potential-energy curve [128] is also shown in Fig. 3.8 for an unmodelled state, $III\,^3\Pi_u$. The magnitudes of possible electrostatic interactions mixing this state and those it crosses are unknown but potentially significant. Thus, the exclusion of $III\,^3\Pi_u$ prevents any extrapolation of the present model to levels above $G_3\,^3\Pi_u(v=3)$.

Electronic-coupling matrix elements between $^3\Pi_u$ states are all assumed to be R-independent, and have fitted values listed in Tab. 6.6. An R-dependence of the $C\,^3\Pi_u \sim C'\,^3\Pi_u$ interaction is, however, quite likely given the configurational change of $C\,^3\Pi_u$ occurring around $R = 1.5\,\text{Å}$, and which is discussed further in Sec. 6.6.3. The available experimental information was deemed insufficient for the task of determining any such R-dependence. Instead, the deduced interaction energy of $798\pm15\,\mathrm{cm}^{-1}$ is likely representative of the internuclear distance where the $C\,^3\Pi_u$ and $C'\,^3\Pi_u$ curves cross, near $R = 1.39\,\text{Å}$. This fitted interaction energy is in agreement with the value determined by Lewis *et al.* [104], $810\pm20\,\mathrm{cm}^{-1}$; and somewhat exceeds the semi-empirical estimate of Ledbetter and Dressler [87], $\sim 700\,\mathrm{cm}^{-1}$.

A large interaction energy, $1115\pm15\,\mathrm{cm}^{-1}$, was determined for the Rydberg–Rydberg coupling between $G_3\,^3\Pi_u$ and $F_3\,^3\Pi_u$, and with quite small uncertainty. This magnitude is unsurprising given the similarly large interaction between $c_3\,^1\Pi_u$ and $o_3\,^1\Pi_u$, treated in Sec. 6.4. The magnitudes of the $G_3\,^3\Pi_u \sim C'\,^3\Pi_u$ and $F_3\,^3\Pi_u \sim C'\,^3\Pi_u$ interactions are less certain, and determined to be $1175\pm200\,\mathrm{cm}^{-1}$ and $315\pm60\,\mathrm{cm}^{-1}$, respectively. This deduction was limited by the dearth of experimental constraint and the strong coupling between $G_3\,^3\Pi_u$ and $F_3\,^3\Pi_u$; whereby, their respective interactions with $C'\,^3\Pi_u$ are highly

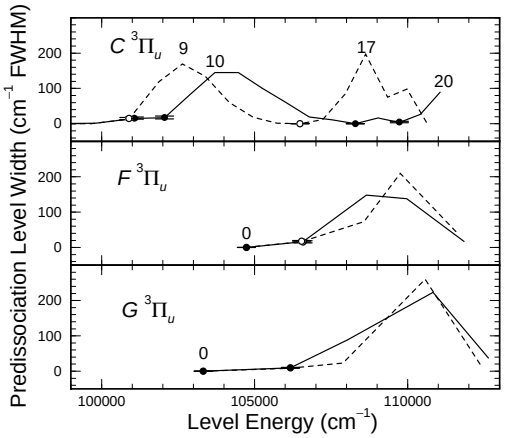

Figure 6.23: Modelled (*line vertices*) and experimental (*error bars and points*) coupled-channels predissociation widths of $C\,^3\Pi_u$, $F_3\,^3\Pi_u$, and $G_3\,^3\Pi_u$. Results are shown for $^{14}N_2$ (*solid lines, closed circles*) and $^{15}N_2$ (*dashed lines, open circles*). Vibrational numbering is attached to a few levels for reference.

correlated and difficult to analyse independently. However, it is clear from the model fitting that the three electronic interactions $F_3 \sim G_3$, $F_3 \sim C'$, and $G_3 \sim C'$ are collectively responsible for the variable linewidths of $F_3\,^3\Pi_u$ and $G_3\,^3\Pi_u$. Furthermore, the product of signs for the associated matrix elements is evidently positive, although the sign of individual terms has not been determined.

The electronic couplings of $C\,^3\Pi_u$ with $F_3\,^3\Pi_u$ and $G_3\,^3\Pi_u$ could not be fixed because of a lack of experimental data sensitive to these interactions. Nonetheless, they are likely to be significant given the importance of the equivalent coupling between singlet configurational analogues, $b\,^1\Pi_u$, $o_3\,^1\Pi_u$, and $c_3\,^1\Pi_u$, respectively; which are discussed in Sec. 6.4. The neglect of these interactions in the present model has likely been accommodated as a smooth deformation of the fitted potential-energy curves from their true diabatic forms.

The shapes of all potential-energy curves, and the various non-zero electronic interactions, were iteratively adjusted in order to best fit the experimental term origins, rotational-constants, and predissociation linewidths listed in Tab. 6.5. Comparable quantities calculated by the optimised model are listed in this table, and observed and computed linewidths are also plotted in Fig. 6.23. Overall, the experimental data are reproduced very will with respect to their various measurement uncertainties.

A complete listing of calculated spectroscopic parameters and predissociation linewidths for all $^3\Pi_u$ levels between 99 000 and 113 000 cm^{-1} is given in Tab. 6.7. Some of these calculated quantities are generated by the coupled-channels treatment of a collaborator, R. Lefebvre,[a] which operates differently to the scheme espoused elsewhere in this thesis. Very briefly, the usual resonance energies are generalised to a complex form, and space normalised inward and outward solutions of the Schrödinger equation may be calculated, even where open channels are included [88, 105, 123, 141]. As part of these calculations, the complex part of the generalised energy is proportional to an equivalent predissociation width and the mixing of diabatic basis electronic states is automatically computed. The parameters determined by this method and the computational technique discussed in Sec. 2.11 give identical results in almost all cases. The exceptions occur for a few very broad and electronically-mixed resonances which are more accurately characterised by the

[a]Laboratoire de Photophysique Moléculaire, Bâtiment 213, Université de Paris-Sud

Iso.	Level	$T_{\rm calc}$ [a]	$B_{\rm calc}$ [b]	$\Gamma_{\rm calc}$ [c]	$\%C$	$\%F$	$\%G$
$^{14}N_2$	$C(v=6)$	99 800.7	1.120	1.7	100	0	0
	$C(v=7)$	101 068.9	1.407	15.2	100	0	0
	$C(v=8)$	102 052.3	1.301	17.2	100	0	0
	$C(v=9)$	102 900.8	1.307	83.3	100	0	0
	$C(v=10)$	103 699.	1.33	145.	99	0	1
	$C(v=11)$	104 464.	1.31	145.	99	0	1
	$C(v=12)$	105 241.1	1.26	101.	100	0	0
	$C(v=13)$	106 017.4	1.199	60.4	98	1	1
	$C(v=14)$	106 785.1	1.159	19.2	99	1	0
	$C(v=15)$	107 537.8	1.140	10.8	98	1	1
	$C(v=16)$	108 293.0	1.154	0.01	93	5	2
	$C(v=17)$	109 034.2	1.109	16.5	96	2	2
	$C(v=18)$	109 724.3	1.096	4.0	94	2	4
	$C(v=19)$	110 412.6	1.060	26.7	95	5	0
	$C(v=20)$	111 060.1	1.00	89.	92	3	5
	$F(v=0)$	104 730.6	1.806	0.46	0	58	42
	$F(v=1)$	106 579.4	1.745	16.2	1	78	21
	$F(v=2)$	108 649.	1.70	148.	10	64	26
	$F(v=3)$	109 972.	1.73	138.	10	45	45
	$F(v=4)$	111 844.5	1.736	17.1	2	56	42
	$G(v=0)$	103 317.4	1.884	0.09	0	23	77
	$G(v=1)$	106 166.8	1.839	9.6	2	27	71
	$G(v=2)$	108 032.0	1.780	89.	6	30	64
	$G(v=3)$	110 831.	1.8	223.	21	38	41
	$G(v=4)$	112 641.0	1.757	37.4	2	46	52
$^{15}N_2$	$C(v=6)$	99 665.6	1.052	0.06	100	0	0
	$C(v=7)$	100 892.5	1.327	12.8	100	0	0
	$C(v=8)$	101 877.	1.27	119.	99	0	1
	$C(v=9)$	102 642.	1.31	169.	96	0	4
	$C(v=10)$	103 389.	1.27	134.	99	0	1
	$C(v=11)$	104 166.6	1.169	60.7	100	0	0
	$C(v=12)$	104 950.4	1.136	18.2	100	0	0
	$C(v=13)$	105 728.0	1.105	1.6	100	0	0
	$C(v=14)$	106 478.3	1.138	0.02	86	10	4
	$C(v=15)$	107 220.2	1.069	11.6	99	0	1
	$C(v=16)$	107 964.	1.23	85.	64	14	22
	$C(v=17)$	108 626.	1.0	197.	57	28	15
	$C(v=18)$	109 342.8	1.021	75.	96	1	3
	$C(v=19)$	109 976.4	0.96	98.	90	8	2
	$C(v=20)$	110 635.6	1.116	0.08	77	12	11
	$F(v=0)$	104 703.9	1.688	0.41	0	57	43
	$F(v=1)$	106 538.0	1.577	16.5	13	68	19
	$F(v=2)$	108 575.7	1.38	73.	45	39	16
	$F(v=3)$	109 776.	1.7	210.	24	36	40
	$F(v=4)$	111 607.3	1.622	42.2	3	55	42
	$G(v=0)$	103 324.3	1.759	0.08	0	23	77
	$G(v=1)$	106 110.6	1.719	8.1	1	29	70
	$G(v=2)$	107 881.3	1.445	23.0	35	21	44
	$G(v=3)$	110 530.	1.6	260.	41	34	25
	$G(v=4)$	112 397.0	1.641	15.4	7	44	49

[a] T_{v0}, in $\rm cm^{-1}$.
[b] Effective rotational constant for $J \leq 5$, in $\rm cm^{-1}$.
[c] Predissociation level width for $J = 0$, in $\rm cm^{-1}$ FWHM.

Table 6.7: Computed spectroscopic parameters, predissociation level widths, and electronic parentage for the coupled $^3\Pi_u$ states of $^{14}N_2$ and $^{15}N_2$.

complex-resonance technique. This is because there may be some difficulty in fitting Fano profiles to a real cross section consisting of broad and overlapping resonances.

The highly mixed nature of $^3\Pi_u$ states is apparent in several of the computed quantities. If unperturbed, the rotational constants of the various levels of $F_3\,^3\Pi_u$ and $G_3\,^3\Pi_u$ will be very to close those of their respective ionic limits, $N_2^+\left[A\,^2\Pi_u\right]$ and $N_2^+\left[X\,^2\Sigma_g^+\right]$, given by 1.735 and 1.922 cm^{-1} [72, p. 426], respectively. However, $F_3\,^3\Pi_u(v=0)$ is observed, and calculated, to have a higher rotational-constant, 1.806 cm^{-1}; and, to a lesser degree, $G_3\,^3\Pi_u(v=0)$ is lower than expected, 1.885 cm^{-1}. These differences can be explained by the significant mixing between states listed in Tab. 6.7, such that the computed electronic-character of $F_3\,^3\Pi_u(v=0)$ is 42% $G_3\,^3\Pi_u$, but $G_3\,^3\Pi_u(v=0)$ is somewhat less mixed, with 23% $F_3\,^3\Pi_u$ composition. A similar pattern of perturbed rotational-constants and mixed F_3/G_3 character is apparent for $v>1$ and in $^{15}N_2$.

Figure 6.23 shows the predissociation linewidths predicted by the model for $C\,^3\Pi_u$, $F_3\,^3\Pi_u$, and $G_3\,^3\Pi_u$ levels. Unsurprisingly, there are no observations corresponding to the broadest levels. The pattern of $C\,^3\Pi_u$ widths is approximately oscillatory with a period of $\sim 7000\,cm^{-1}$, in line with the general behaviour of an outer-limb crossing with the dissociative $C'\,^3\Pi_u$ [90, p. 509-519]. However, coupling to $F_3\,^3\Pi_u$ and $G_3\,^3\Pi_u$ introduces further width structure for $v \gtrsim 15$.

6.6.2 $^3\Pi_{u,\Omega=1} + {}^3\Sigma^+_{u\,,\Omega=1} + {}^1\Pi_u$

The $^3\Pi_{u,\Omega=1}$ model described in the previous section has been combined with the $^1\Pi_u$ model of Sec. 6.4 in order to reproduce the observed predissociation of the latter. This model neglects all $^3\Pi_{u,\Omega=0}$ and $^3\Pi_{u,\Omega=2}$ states, which are mixed with the $\Omega=1$ levels by the S-uncoupling operator, proportionately to $\sqrt{J(J+1)}$. Thus, only the linewidths of $^1\Pi_u$ levels with low J are considered.

Spin-orbit interactions have been assumed to mix several pairs of isoconfigurational diabatic $^3\Pi_u$ and $^1\Pi_u$ states; that is, $b\,^1\Pi_u \sim C\,^3\Pi_u$, $b\,^1\Pi_u \sim C'\,^3\Pi_u$, $c_3\,^1\Pi_u \sim G_3\,^3\Pi_u$, and $o_3\,^1\Pi_u \sim F_3\,^3\Pi_u$. Further mixing is permissible between combinations of $^1\Pi_u$ and $^3\Pi_u$ states with configurations that differ by a single electronic spin-orbital, but are expected to be significantly weaker than the above isoconfigurational interactions, and are neglected. The first two couplings were investigated thoroughly with respect to the predissociation of $^1\Pi_u$ levels below 105 000 cm^{-1} by Lewis *et al.* [104]; and their R-independent interaction energies, listed in Tab. 6.6, are adopted as initial estimates for the present optimisation.

Lefebvre-Brion and Field [90, pp. 184–190] discuss a means of estimating the magnitude of the spin-orbit constant, $A = \langle F_3\,^3\Pi_u|H^{SO}|F_3\,^3\Pi_u\rangle$, of the Rydberg state $F_3\,^3\Pi_u$ in terms of the experimentally known A of its limiting ionic state [29, 78], according to

$$\langle F_3\,^3\Pi_u|H^{SO}|F_3\,^3\Pi_u\rangle \simeq -\frac{1}{2}\langle N_2^+\left[A\,^2\Pi_u\right]|H^{SO}|N_2^+\left[A\,^2\Pi_u\right]\rangle \tag{6.20}$$

$$\simeq -38\,cm^{-1}. \tag{6.21}$$

A further estimate of $\langle G_3\,^3\Pi_u|H^{SO}|c_3\,^1\Pi_u\rangle \simeq 2\,cm^{-1}$ is given in Lewis *et al.* [104]. This slightness of this matrix element is reasonable given that the only contribution to it arises from a diffuse $3p\pi$ Rydberg orbital, and that the spin-orbit operator [90, pp. 181-185] is proportional to $1/r^3$, where r is the orbital radius.

The values of these diagonal spin-orbit matrix may also be adopted as estimates of the off-diagonal matrix elements $\langle F_3\,^3\Pi_u|H^{SO}|o_3\,^1\Pi_u\rangle$ and $\langle G_3\,^3\Pi_u|H^{SO}|c_3\,^1\Pi_u\rangle$. This is

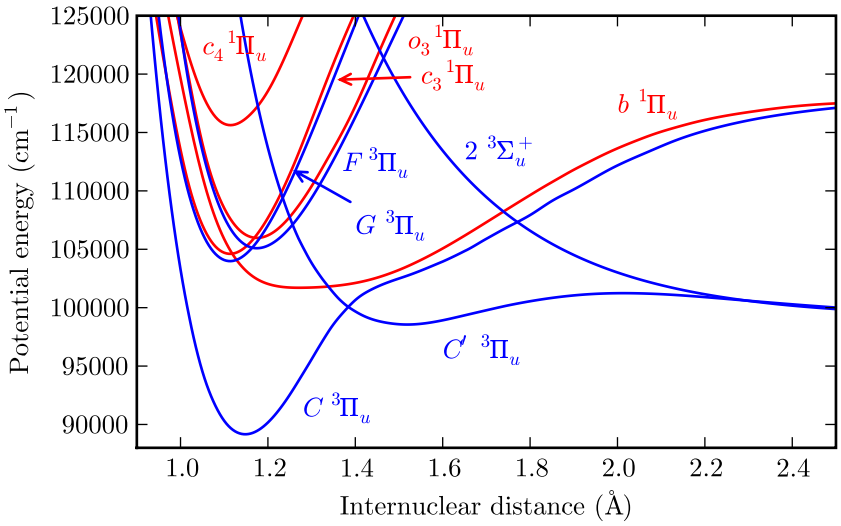

Figure 6.24: Optimised $^1\Pi_u$, $^3\Pi_u$, and $^3\Sigma_u^+$ potential-energy curves in a diabatic representation. The $^3\Sigma_u^+$ state is labelled "2" in accordance with van der Kamp *et al.* [173].

reasonable because the pairs of states $F_3\,{}^3\Pi_u \sim o_3\,{}^1\Pi_u$ and $G_3\,{}^3\Pi_u \sim c_3\,{}^1\Pi_u$ are isoconfigurational, and will have very similar electronic wavefunctions.

Following the introduction of coupling between them, the $^1\Pi_u$ and $^3\Pi_u$ states studied separately in Secs. 6.4 and 6.6.1 will require an adjustment of their potential-energy curves and homogeneous electronic-interactions. That is, during previous attempts to reproduce the $^1\Pi_u$ and $^3\Pi_u$ experimental data, the neglected influence of spin-orbit coupling was counterfeited by slightly distorting the various model parameters. Now, a diabatic model that deperturbs the effects of spin-orbit coupling is sought, and these distortions can be removed.

An optimisation of potential-energy curves and state interactions was performed while being constrained by the previously-discussed experimental energy levels, and $^3\Pi_u$ energy levels and linewidths. A new compilation of $^1\Pi_u$ predissociation linewidths, listed in Tab. 6.8, was also included. This has been collected from a variety of sources with references given in Sec. 3.3.3.

The final potential-energy curves for $^3\Pi_u$, $^3\Sigma_u^+$, and $^1\Pi_u$ states are plotted in Fig. 6.24 and do not differ greatly from those determined during the optimisation of the previous less-complete models. The various fitted electronic and spin-orbit interaction energies concerning $^3\Pi_u$ states are listed in Tab. 6.6 alongside previous estimates. The parameters governing the homogeneous electronic interactions of $^1\Pi_u$ states were not altered from those values determined in Sec. 6.4.

The quality of fit for the various $^3\Pi_u$ molecular-parameters and predissociation linewidths following optimisation is essentially the same as was achieved whilst uncoupled from the $^1\Pi_u$ states in Sec. 6.6.1. The principal effect of the inclusion of triplet states on the $^1\Pi_u$ energy levels was a downward shift of $1-2\,\mathrm{cm}^{-1}$. This was corrected by a modification of the $b\,{}^1\Pi_u$ potential-energy curve that saw the potential well raised by $\sim 5\,\mathrm{cm}^{-1}$ and the right-hand limb shifted outwards slightly. These effects might be considered, somewhat grossly, as compensating for repulsion by the Rydberg $^3\Pi_u$ states and $C\,{}^3\Pi_u$, respectively. Similar alterations were required of the $c_n\,{}^1\Pi_u$ and $o_3\,{}^1\Pi_u$ potential-energy curves.

Level	T_0	$\Gamma_{\rm mod}$	$\Gamma_{\rm exp}$	Refs.
		$^{14}N_2$		
$b(0)$	100 817	0.151	0.17(2)	[149]
$b(1)$	101 451	0.00036	0.0006(3)	[152]
$b(2)$	102 152	0.571	0.53(11)	[171]
$b(3)$	102 861	3.18	3.31(62)	[171]
$b(4)$	103 548	0.301	0.307(10)	[172]
$c_3(0)$	104 138	0.0694	0.080(7)	[149]
$b(5)$	104 700	0.0268	0.023(4)	[149]
$b(6)$	105 346	0.0165	0.016(3)	[149]
$o_3(0)$	105 683	0.0155	0.0221(46)	[172]
$b(7)$	106 109	0.015	0.0096(23)	[147]
$c_3(1)$	106 528	0.0254	0.0342(66)	[150]
$b(8)$	106 933	0.0732	0.056(24)	[147]
$b(9)$	107 629	0.0364	0.0500(58)	[179]
$o_3(1)$	107 652	0.25	0.234(13)	[179]
$b(10)$	108 372	0.0474	0.0530(79)	[150]
$c_3(2)$	108 694	0.10	0.085(14)	[150]
$b(11)$	109 119	0.265	0.35(5)	[157]
$o_3(2)$	109 561	0.212	0.26(5)	[157]
$b(12)$	109 831	0.0409	0.06(1)	[144]
$b(13)$	110 529	0.183	0.23(5)	[157]
$c_3(3)$	110 796	0.365	0.36(5)	[157]
$b(14)$	111 209	0.233	0.21(5)	[157]
$o_3(3)$	111 447	0.165	0.13(4)	[144]
$c_3(4)$	112 849	0.00353	0.009(2)	[53]
$c_3(5)$	114 827	0.0972	0.4(1)	[50]
		$^{14}N^{15}N$		
$b(0)$	100 831	0.0681	0.066(21)	[149]
$b(1)$	101 454	0.0301	0.029(16)	[149]
$c_3(0)$	104 105	0.0936	0.113(24)	[149]
$b(5)$	104 657	0.0101	$<$ 0.006	[149]
$b(6)$	105 291	0.00852	0.0088(29)	[149]
		$^{15}N_2$		
$b(0)$	100 844	0.128	0.132(23)	[149]
$b(1)$	101 456	0.137	0.156(23)	[149]
$b(2)$	102 129	0.765	0.768(89)	[149]
$b(3)$	102 818	0.81	0.688(89)	[149]
$b(4)$	103 485	0.534	0.53(11)	[149]
$c_3(0)$	104 070	0.167	0.183(25)	[149]
$b(5)$	104 613	0.00449	0.0064(4)	[147]
$b(6)$	105 235	0.00468	0.0068(24)	[149]
$o_3(0)$	105 648	0.0139	0.0189(44)	[149]
$b(7)$	105 978	0.00772	0.0080(26)	[149]
$c_3(1)$	106 449	0.00161	0.0049(15)	[98]
$o_3(1)$	107 577	0.216	0.196(44)	[150]
$b(9)$	107 444	0.0816	0.115(18)	[150]

Table 6.8: Modelled ($\Gamma_{\rm mod}$) and experimental ($\Gamma_{\rm exp}$) predissociation linewidths of $^1\Pi_u$ levels. Also listed are term origins (T_o) for each level and the relevant experimental references. All quantities are in units of $\rm cm^{-1}$ and uncertainties in $\Gamma_{\rm exp}$ are given parenthetically in units of the least-significant digit.

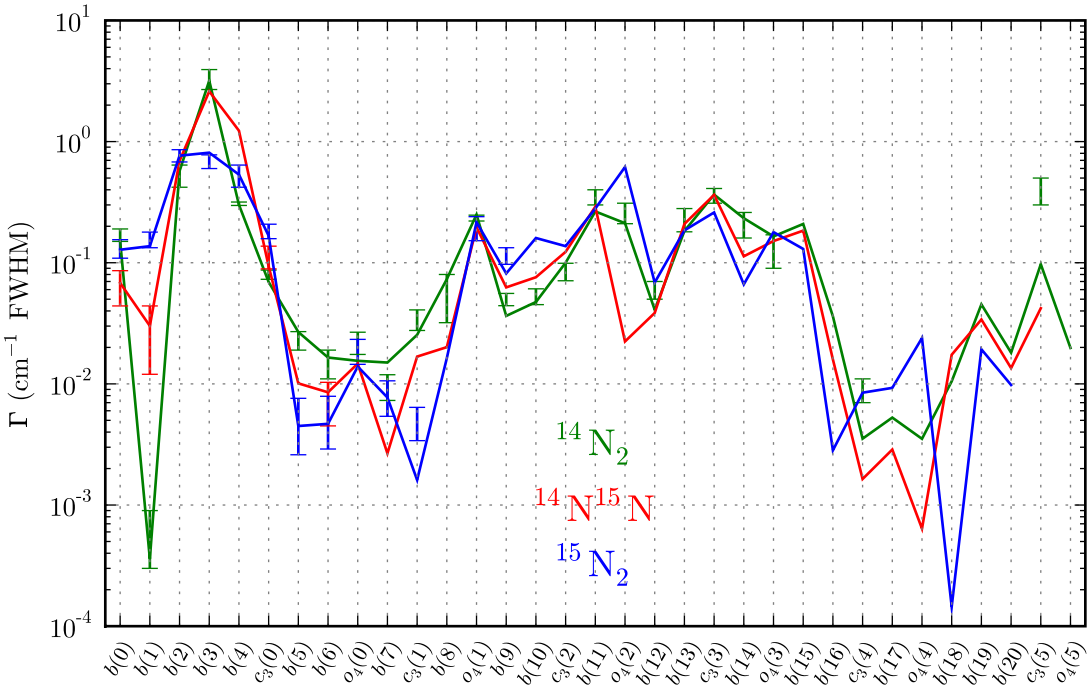

Figure 6.25: Experimental (*error bars*) and modelled (*lines*) predissociation linewidths of $^1\Pi_u$ levels for three isotopomers.

A summary of calculated and experimental $^1\Pi_u$ predissociation linewidths is plotted in Fig. 6.25 and listed in Tab. 6.8. The model values have been calculated for zero nuclear-rotation so that the effects of rotational coupling to $^1\Sigma_u^+$ and $^3\Pi_{u,\Omega=0,2}$ states is neglected. Where sufficient information exists, the experimental linewidths have also been extrapolated to zero rotation and reduced by an experimental predissociation fraction. The latter conversion eliminates the contribution of radiative decay which is not represented within the coupled-channels model.

Overall, the agreement between modelled and experiment widths is very good. Only one width, for $c_3\,{}^1\Pi_u(v=5)$ in $^{14}N_2$, shows disagreement approaching 3× the experimental uncertainty. This discrepancy is likely due to an unreliable extrapolation of the observed $c_3\,{}^1\Pi_u(v=5)$ linewidths to zero rotation, due to their small number and large uncertainties [50]. The range of correctly modelled widths extends over nearly 4 orders of magnitude, and includes isotopomeric effects of up to 2 orders of magnitude.

In order to achieve the agreement of experiment and model listed in Tab. 6.8 it was found necessary to make a further addition to the coupled states. The potential-energy curve of the dissociative state $2\,{}^3\Sigma_u$ is plotted in Fig. 6.24 and is the second highest-energy $^3\Sigma_u^+$ state of N_2. The necessity of this inclusion is demonstrated in Fig. 6.26, where it is clear that $C'\,{}^3\Pi_u$ alone fails to provide a sufficiently probable predissociation pathway for $b\,{}^1\Pi_u(v=9,10,12)$. The addition of a fitted coupling $\langle 2\,{}^3\Sigma_{u\Omega=1}|H^{SO}|b\,{}^1\Pi_u\rangle = 11\pm1\,\mathrm{cm}^{-1}$ corrects this deficiency, in agreement with the $10\,\mathrm{cm}^{-1}$ predicted interaction energy of Dateo [25]. The *ab initio* calculations of Dateo [25] also furnished a potential-energy curve for $2\,{}^3\Sigma_u$, which has been adjusted here by a uniform inwards shift of 0.024 Å in order to best fit the observed widths. The levels in Fig. 6.26 which are most strongly affected by $2\,{}^3\Sigma_u \sim b\,{}^1\Pi_u$ coupling have energies adjacent to the potential-energy crossing

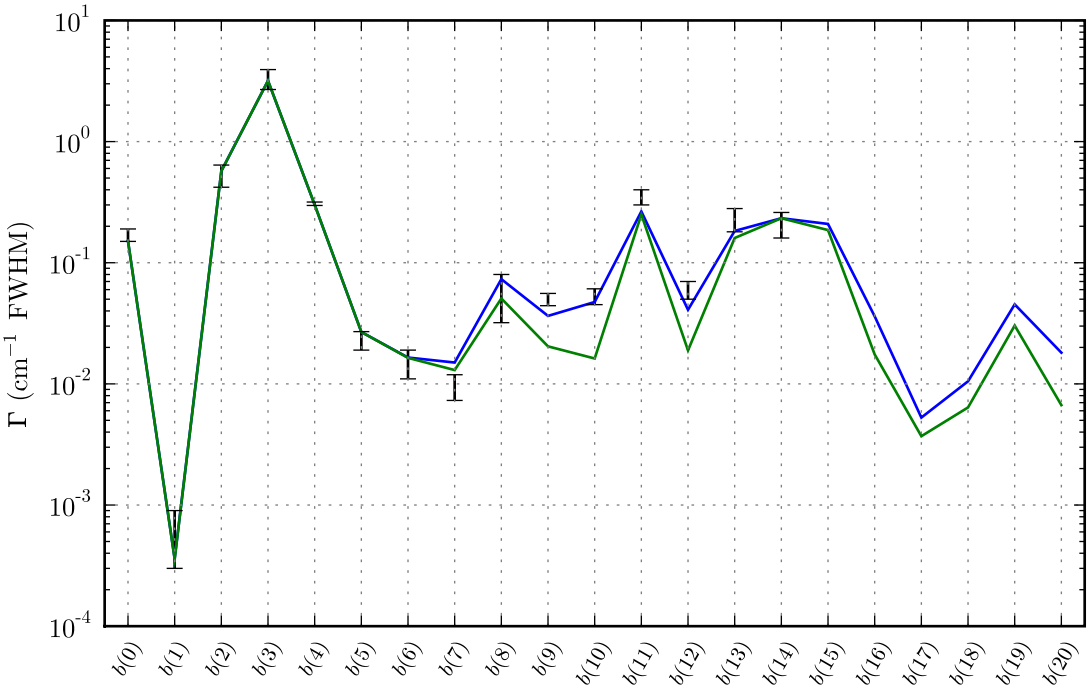

Figure 6.26: Experimental (*error bars*) and modelled (*lines*) linewidths of $b\,^1\Pi_u$ levels. Calculations are made including (*blue*) and excluding (*green*) the unbound state $2\,^3\Sigma_u^+$.

point of these two states, near 1.7 Å.

6.6.3 $^3\Pi_{u,\Omega=0,1,2} + {}^3\Sigma_{u,1}^+ + {}^1\Pi_u + {}^1\Sigma_u^+$

A complete model of $^1\Pi_u$ predissociation requires the consideration of $^3\Pi_u$ levels with $\Omega = 0$, 1, and 2. In principle, the spin-orbit perturbations discussed in Sec. 2.6 only affect states with common Ω; in the case of Sec. 6.6.2, those with $\Omega = 1$. However, for a rotating molecule, the S-uncoupling operator discussed in Sec. 2.5.2 mixes $\Omega = 0$, 1, and 2 substates so that the selection rule governing $^3\Pi_{u\Omega=0,2} \sim {}^1\Pi_u$ spin-orbit perturbations is relaxed.

In this section, a new model consisting of triplet and singlet states has been constructed which includes all Ω-substates of $C\,^3\Pi_u$, $C'\,^3\Pi_u$, $F_3\,^3\Pi_u$, and $G_3\,^3\Pi_u$; and builds upon the models developed in Secs. 6.4, 6.5 and 6.6.2. The various calculated quantities in Tabs. 6.5 and 6.8 will not be altered by this extension because they pertain to the limit of zero rotation, and so are decoupled from the $\Omega = 0$ and 2 substates introduced here. New experimental information is then necessary to validate this new model. This arises from those $^3\Pi_u$ levels for which $\Omega = 0$ and 2 levels have been directly observed, or where these perturb singlet levels with sufficiently large molecular rotation that the effects of S-uncoupling become noticeable. Because none of the available experimental information is sufficiently sensitive to the splitting of $2\,^3\Sigma_u$ substates the potential-energy curve determined in the previous section for $\Omega = 1$ is adopted here for both e and f parities, and the $^3\Sigma_{u,\Omega=0}^+$ f-parity state is neglected entirely.

The various potential-energy curves and interaction terms determined in Sec. 6.6.2 do not need to be modified here. However, a spin-orbit splitting parameter, $A(R)$ of Sec. 2.6, remains to be determined for each $^3\Pi_u$ state. That is, the potential-energy curves of the

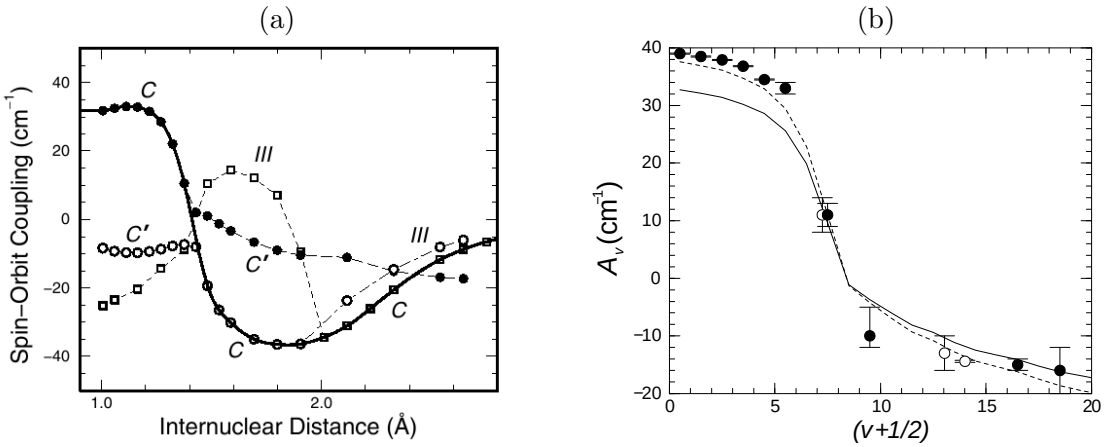

Figure 6.27: *(a):* Calculated *ab initio* diagonal spin-orbit function for the lowest three non-Rydberg states of $^3\Pi_u$ symmetry, labelled diabatically. *(b):* The spin-orbit constant of $C\,^3\Pi_u$ as a function of vibrational quantum number, A_v. *Error bars, closed points:* Experimental determination from $^{14}N_2$. *Error bars, open points:* Experimental determination from $^{15}N_2$. *Solid line: Ab initio* calculated. *Dashed line: Ab initio* calculated curve multiplied by a factor of 1.15 to best match the experimental data.

$\Omega = 0$ and 2 sublevels are assumed to have a similar form to the $\Omega = 1$ curves, but modified according to

$$V_{\Omega=0}(R) = V_{\Omega=1}(R) - A(R) \tag{6.22}$$

$$\text{and } V_{\Omega=2}(R) = V_{\Omega=1}(R) + A(R). \tag{6.23}$$

A new combined experimental and *ab initio* study of the $C\,^3\Pi_u$ spin-orbit parameter forms part of my body of work, with further details given in its published version [122]. Spin-orbit splitting parameters are known experimentally for a comprehensive set of $C\,^3\Pi_u$ vibrational levels, and plotted in Fig. 6.27(b). The lowest vibrational levels have well-characterised spin-orbit constants [10, 87] which are positive and decrease for increasing v. The higher levels on the other hand, are predissociation broadened and coincident with many singlet levels, making their detection and analysis more difficult. Thus, the spin-orbit parameters that have been deduced for $v > 5$ [49, 98] often involve relatively large uncertainties. Additionally, experimentally fixing the sign of A relies on the correct assignment of observed sub-bands to either $\Omega = 0$ or $\Omega = 2$ levels. This discrimination is impossible to confirm unless levels corresponding to $J = 0$ and 1, for which no $\Omega = 2$ levels are possible, are clearly observed. The quality of available information has prevented the determination of this sign for higher vibrational levels of $C\,^3\Pi_u$, such that the expected reversal of sign predicted by the qualitative arguments of Lewis *et al.* [98] has not been confirmed. In order to end this ambiguity, sophisticated multi-configurational calculations have been made of the non-Rydberg $^3\Pi_u$ states of N_2 by collaborators H. Ndome and M. Hochlaf.[b]

A principal result of this work are new *ab initio* potential-energy curves and diagonal matrix elements of the spin-orbit operator for $C\,^3\Pi_u$, $C'\,^3\Pi_u$, and the next-highest energy $^3\Pi_u$ valence state, labelled III. The calculated spin-orbit coupling is plotted in

[b] Laboratoire de Modélisation et Simulation Multi Echelle, Université Paris-Est

Level	$A_{\rm exp}$	Ref.	$A_{\rm est}$	$\%C$	$\%F$	$\%G$
$^{14}N_2$ $F_3\,^3\Pi_u(v=1)$	-28(3)	[98]	-30.8	1	78	21
$^{15}N_2$ $F_3\,^3\Pi_u(v=1)$	-32(2)	[98]	-28.7	13	68	19
$^{14}N_2$ $G_3\,^3\Pi_u(v=0)$	-8.35(8)	[48, 98]	-7.7	0	23	77

Table 6.9: The known experimental, $A_{\rm exp}$, and estimated, $A_{\rm est}$, spin-orbit parameters of $F_3\,^3\Pi_u$ and $G_3\,^3\Pi_u$, in units of $\rm cm^{-1}$. Estimates are made assuming diabatic spin-orbit matrix elements $\langle F_3\,^3\Pi_u|H^{SO}|F_3\,^3\Pi_u\rangle = -38\,\rm cm^{-1}$ and $\langle G_3\,^3\Pi_u|H^{SO}|G_3\,^3\Pi_u\rangle = 2\,\rm cm^{-1}$, and the coupled-channels calculated mixing fractions listed under $\%F$ and $\%G$. The significant fraction $\%C$ for $^{15}N_2$ $F_3\,^3\Pi_u(v=1)$ has been incorporated by adopting an affective spin-orbit splitting of $\langle C\,^3\Pi_u|H^{SO}|C\,^3\Pi_u\rangle = -14.4\,\rm cm^{-1}$, corresponding to the experimentally determined value for $C\,^3\Pi_u(v=14)$ in Fig. 6.27.

Fig. 6.27(a), where the various adiabatically calculated line segments have been joined according to the same diabatic representation as adopted in Fig. 6.24. The spin-orbit coupling of $C\,^3\Pi_u$ confirms the expected R-dependence, with a change of sign at 1.41 Å. The majority of this variation may be explained by the change of principal configuration in the diabatic representation adopted here for $C\,^3\Pi_u$, and as discussed in Sec. 3.4.

Figure 6.27(b) shows experimental and calculated spin-orbit constants for particular vibrational levels of $C\,^3\Pi_u$. The computed values have been determined by means of three single-channel calculations of $C\,^3\Pi_u$ vibrational levels, for $\Omega = 0$, 1, and 2. A potential-energy curve for the $\Omega = 1$ case has been adopted from the coupled-channels model of Sec. 6.6.1; $\Omega = 0$ and 2 curves are derived from this using the $A(R)$ of Fig. 6.27(a) and Eqs. (6.22) and (6.23). Spin-orbit splittings are then calculated from the Ω-dependent energy shifts for each triplet of calculated vibrational levels. The neglect of $F_3\,^3\Pi_u$ and $G_3\,^3\Pi_u$ in this analysis is unlikely to be serious given the low admixture of these states into the majority of $C\,^3\Pi_u$ levels, as listed in Tab. 6.7.

Also plotted in Fig. 6.27(b) are the results of a separate series of spin-orbit constants, which are calculated from a modified version of the *ab initio* spin-orbit coupling function of Fig. 6.27(a). This curve achieves an improved agreement with the experimental values by uniformly increasing the magnitude of the *ab initio* coupling by a factor of 1.15. It is this modified coupling that is adopted below as a best estimate of the R-dependent matrix-element $\langle C\,^3\Pi_u|H^{SO}|C\,^3\Pi_u\rangle$.

A zero spin-orbit splitting was assumed for $C'\,^3\Pi_u$, in line with the $< 1\,\rm cm^{-1}$ splitting of triplet components experimentally determined by Carroll [11] for its $v = 3$ and 4 levels.

Diagonal matrix elements of the spin-orbit operator for $F_3\,^3\Pi_u$ and $G_3\,^3\Pi_u$ are assumed to be R-independent, which is justified by the adoption of a diabatic single-configuration representation for these states. In principle, if a larger quantity of experimental information was available, some R-dependence might still become apparent. Spin-orbit splitting parameters have been determined experimentally for a few vibrational levels of $F_3\,^3\Pi_u$ and $G_3\,^3\Pi_u$ [48, 98], listed in Tab. 6.9. However, because of the large electronic interaction mixing $G_3\,^3\Pi_u$ and $F_3\,^3\Pi_u$, these vibrational-level specific spin-orbit parameters are not equivalent to diabatic deperturbed values.

An estimate was already derived in Sec. 6.6.2 of $-38\,\rm cm^{-1}$ for the $F_3\,^3\Pi_u$ spin-orbit parameter, citing similarity to the experimentally well-characterised $N_2^+\left[A\,^2\Pi_u\right]$ ionic state. Additionally, a value of $\langle G_3\,^3\Pi_u|H^{SO}|G_3\,^3\Pi_u\rangle = 2\,\rm cm^{-1}$ was furnished for $G_3\,^3\Pi_u$. The spin-orbit splittings of particular vibrational levels may be calculated by weighting the diabatic A according to the electronic-mixing fractions determined in Sec. 6.6.1 and listed

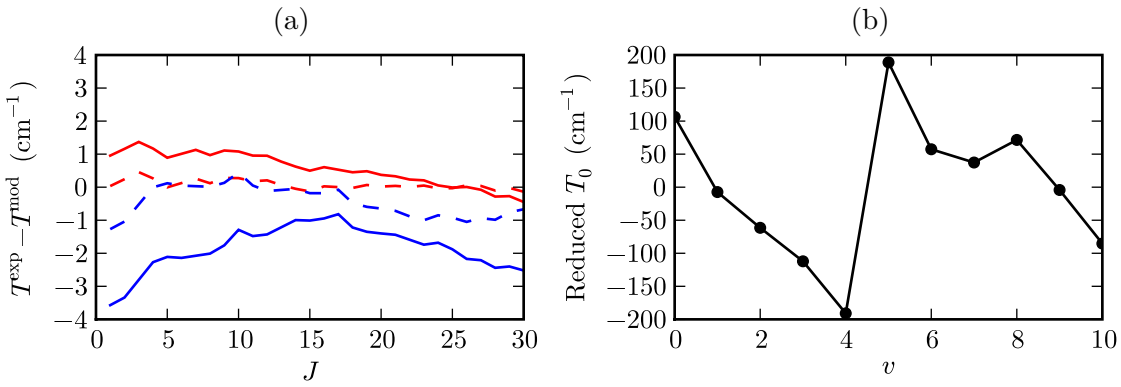

Figure 6.28: *(a):* Difference between experimental, $T^{\rm exp}$ and modelled, $T^{\rm mod}$, term values of $b\,^1\Pi_u$ levels with $v = 2$ (*red*) and $v = 3$ (*blue*) in $^{14}N_2$. Residuals are shown for a coupled-channels model of $^1\Pi_u$ states only (*solid lines*) and including $^3\Pi_u$ states (*dashed lines*). *(b):* Term origins of $b\,^1\Pi_u(v = 0 - 10)$ reduced by a 3$^{\rm rd}$ order polynomial in terms of $v + 1/2$.

in Tab. 6.7. Results of these calculations are listed in Tab. 6.9 and show good agreement with the experimental values, considering their uncertainties. There proved to be insufficient experimental information to further refine the spin-orbit parameters of $F_3\,^3\Pi_u$ and $G_3\,^3\Pi_u$ and the estimates described above have been adopted.

There also occurs rotationally-dependent S-uncoupling which mixes isoconfigurational triplet substates. In all cases, these latter interactions increase rapidly with J and may be estimated from Eq. (2.48). The relevant matrix elements are given by

$$\langle \Omega = 1|H^{\rm rot}|\Omega = 0\rangle = -B(R)\,[J(J+1)]^{1/2} \cdot \sqrt{2}, \tag{6.24}$$

$$\langle \Omega = 1|H^{\rm rot}|\Omega = 2\rangle = -B(R)\,[J(J+1) - 2]^{1/2} \cdot \sqrt{2}, \tag{6.25}$$

$$\text{and } \langle \Omega = 0|H^{\rm rot}|\Omega = 2\rangle = 0. \tag{6.26}$$

A number of level crossings and close degeneracies of $^3\Pi_u$ states and $^1\Pi_u/^1\Sigma_u^+$ levels have been observed. These lead to strongly J-dependent predissociation broadening and energy level deflections of the singlet partner, and in some cases the perturbing $^3\Pi_u$ levels have been observed themselves. These perturbations are discussed individually below and generally show good qualitative agreement. The precise mechanism of each perturbation has been investigated as well as the reasons for any errors in the reproduction of their finer details.

$b\,^1\Pi_u(v = 3) \sim C\,^3\Pi_u(v = 9)$ in $^{14}N_2$

Aside from the introduction of predissociative broadening and the bulk energy shift of $^1\Pi_u$ levels discussed in Sec. 6.6.2, the introduction of $^3\Pi_u$ states also results in a local shift of $b\,^1\Pi_u(v = 3)$ in $^{14}N_2$. This level is perturbed downwards $\sim 2\,\text{cm}^{-1}$ because of a mutual repulsion with the overlying $C\,^3\Pi_u(v = 9)$. The term origin offset of the unobserved $C\,^3\Pi_u(v = 9)$ is modelled in Sec. 6.6.1 to be $38\,\text{cm}^{-1}$, and its predicted predissociation width of $83\,\text{cm}^{-1}$ FWHM (Tab. 6.7) results in the $> 3\,\text{cm}^{-1}$ FWHM broadening deduced experimentally for $b\,^1\Pi_u(v = 3)$ [155, 171].

The influence of $C\,^3\Pi_u(v = 9)$ is also evident in the residual errors of modelled

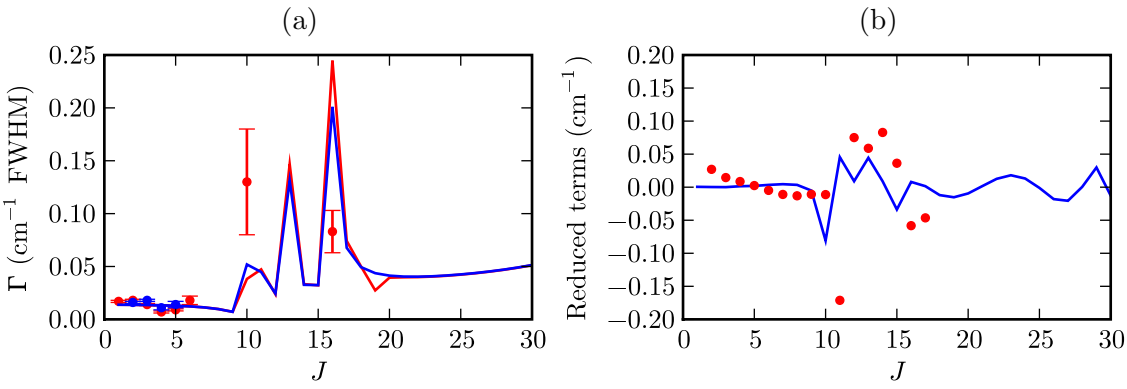

Figure 6.29: *(a):* Modelled (*lines*) and experimental (*error bars*) predissociation linewidths of $^{15}N_2$ $o_3\,^1\Pi_u(v = 0)$ which is perturbed by $C\,^3\Pi_u(v = 13)$. Linewidths are plotted for *e*-parity (*purple*) and *f*-parity (*orange*) levels. *(b):* Modelled (*lines*) and experimental (*points*) term values of $o_3\,^1\Pi_u(v = 0)$, reduced by the subtraction of a 2^{nd} order polynomial in terms of $J(J + 1)$.

$b\,^1\Pi_u(v = 3)$ term values, plotted in Fig. 6.28(a). A coupled-channels model excluding the $^3\Pi_u$ states significantly overestimates these energies, and a compensatory distortion is induced in the potential-energy curve of $b\,^1\Pi_u$ during an attempted model optimisation. This in turn leads to an underestimate for the $b\,^1\Pi_u(v = 2)$ term origin, also shown in Fig. 6.28(a). Both levels are corrected by the inclusion of $C\,^3\Pi_u(v = 9)$ and a $C\,^3\Pi_u \sim b\,^1\Pi_u$ interaction, and a smooth $b\,^1\Pi_u$ potential-energy curve also results.

The perturbing effect of $C\,^3\Pi_u(v = 9)$ is not discernible among the $b\,^1\Pi_u$ term origins plotted in Fig. 6.28(b) because it is dwarfed by the heterogeneously-interacting $c_3\,^1\Pi_u(v = 0)$, situated between $v = 4$ and 5. Part of the value of the coupled-channels technique lies in identifying small, but informative perturbations such as this.

$o_3\,^1\Pi_u(v = 0) \sim C\,^3\Pi_u(v = 13)$ in $^{15}N_2$

Perturbations in the term values of $o_3\,^1\Pi_u(v = 0)$ in $^{15}N_2$ have been observed which are coincident with increased predissociation broadening, as shown in Fig. 6.29(a). These irregularities have been attributed to an interaction with $C\,^3\Pi_u(v = 13)$ [98] and are qualitatively reproduced by the coupled-channels model.

In Fig. 6.29(a), the modelled low-rotation linewidths are in good agreement with experiment but the widths for $J = 10$ and 16 are over- and under-estimated, respectively. The $C\,^3\Pi_u(v = 13)$ also appear to be slightly misplaced in energy in Fig. 6.29(b), where the modelled crossing from above of $o_3\,^1\Pi_u(v = 0)$ by $C^3\Pi_{u,\Omega=0}(v = 13)$ occurs between $J = 11$ and 12, whereas the observed term values indicate a crossing between $J = 10$ and 11.

$c_3\,^1\Pi_u(v = 1) \sim C\,^3\Pi_u(v = 14)$ in $^{15}N_2$

A series of perturbations have been observed amongst the term values of $c_3\,^1\Pi_u(v = 1)$ for $J < 15$ [151] and are plotted in Fig. 6.30(a). This perturbation has been analysed in detail [98], along with extra lines observed near the $c_3\,^1\Pi_u(v = 1)$ transitions, and is attributed to $C\,^3\Pi_u(v = 14)$. The three level crossings of $c_3\,^1\Pi_u(v = 1)$ and $C\,^3\Pi_u(v = 14)$; attributable to $\Omega = 0$, 1 and 2 triplet substates, in order of increasing J; have magnitudes which are

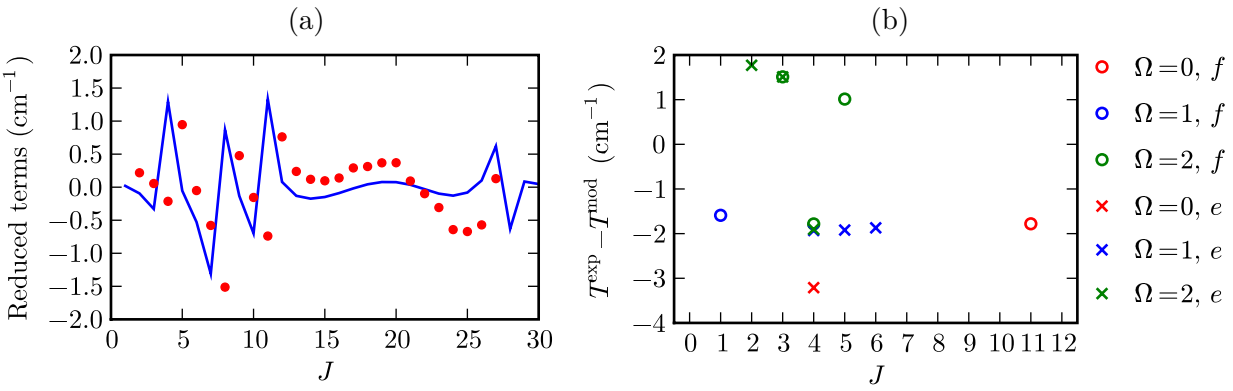

Figure 6.30: *(a):* Calculated (*blue*) and experimental (*red*) reduced term-values of $c_3\,{}^1\Pi_u(v=1)$ for $^{15}N_2$, which is perturbed by $C\,{}^3\Pi_u(v=14)$. *(b):* Residual term values of $C\,{}^3\Pi_u(v=14)$.

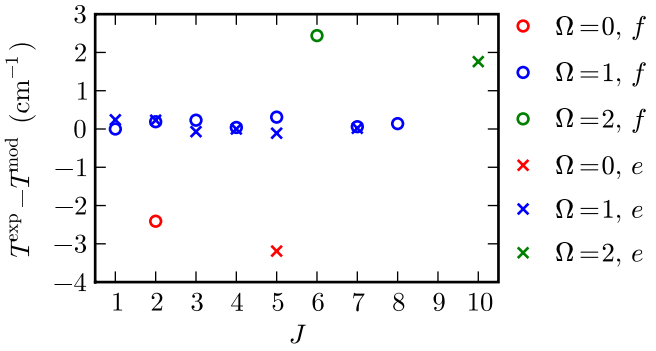

Figure 6.31: Difference between experimental, $T^{\rm exp}$, and modelled, $T^{\rm mod}$, term values of $C\,{}^3\Pi_u(v=16)$.

quite well reproduced by the model, as shown in Fig. 6.30(a). However, the calculations are in error by one rotational unit with respect to the location of each crossing, as a result of slight errors in the location of $C\,{}^3\Pi_u(v=14)$ levels, as plotted in Fig. 6.30(b).

$C\,{}^3\Pi_u(v=16)$ in $^{14}N_2$

Lewis *et al.* [98] analysed a $^{14}N_2$ absorption spectrum recorded at sufficiently high pressure that an apparent triplet $\leftarrow X\,{}^1\Sigma_g^+$ band is directly observable. They assigned the excited state to be $C\,{}^3\Pi_u(v=16)$ and determined a large number of term values with $J \leq 11$ arising from sublevels with all possible values of Ω and e/f-parity.

The residual errors of modelled $C\,{}^3\Pi_u(v=16)$ term values are plotted in Fig. 6.31 and shows particularly good agreement for the $\Omega = 1$ levels. This is unsurprising given that the $C\,{}^3\Pi_u(v=16)$ potential-energy curve was optimised in Sec. 6.6.2 with reference to $\Omega = 1$ levels only.

The divergence of $\Omega = 0$ and 2 term residuals, apparent in Fig. 6.31, can be removed by replacing the R-dependent diagonal spin-orbit constant of $C\,{}^3\Pi_u$ by a constant value of $-15.5\,\mathrm{cm}^{-1}$, which is in agreement with the experimental value, $-16\pm4\,\mathrm{cm}^{-1}$.

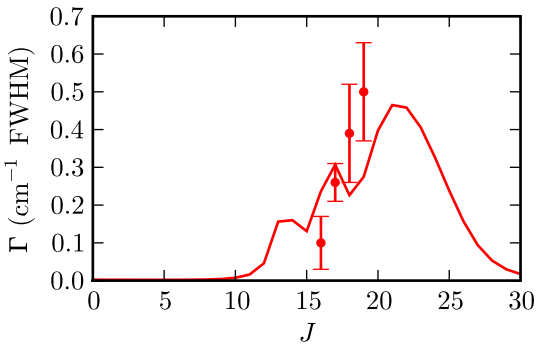

Figure 6.32: Modelled (*curve*) and experimental (*error bars*) predissociation linewidths of $^{14}N_2$ $b'\,^1\Sigma_u^+(v=7)$, which is perturbed by $C\,^3\Pi_u(v=17)$.

$b'\,^1\Sigma_u^+(v=7) \sim C\,^3\Pi_u(v=17)$ in $^{14}N_2$

During the KEK series of experiments, discussed in Chap 4, the linewidths of four transitions terminating on $b'\,^1\Sigma_u^+(v=7)$ were measured for levels with J between 16 and 19. Upon examining the coupled-channels cross sections for a range of J, it is apparent that this broadening is attributable to a level crossing between $b'\,^1\Sigma_u^+(v=7)$ and $C\,^3\Pi_u(v=17)$. This triplet level has never been observed, but is predicted by the model to have a term origin $\sim 80\,\mathrm{cm}^{-1}$ above $b'\,^1\Sigma_u^+(v=7)$, but with a lesser rotational constant. Thus, the observed broadening is due to a decreasing energy separation between $b'\,^1\Sigma_u^+(v=7)$ and $C\,^3\Pi_u(v=17)$ with increasing J.

Figure 6.32 shows the observed and calculated linewidths of $b'\,^1\Sigma_u^+(v=7)$ with are in rough agreement as far as they are comparable.

$c_3\,^1\Pi_u(v=2) \sim C\,^3\Pi_u(v=17)$ in $^{14}N_2$, $^{14}N^{15}N$, and $^{15}N_2$

New observations of excitation to $c_3\,^1\Pi_u(v=2)$ from the ground state have been made at high resolution for $^{14}N_2$, $^{14}N^{15}N$, and $^{15}N_2$. This was done using the XUV + UV double-photon ionisation apparatus at Vrije Universiteit in The Netherlands.[c] In this experiment, ground-state N_2 is excited by a frequency tripled XUV laser, and then ionised by the overlapping ultraviolet radiation.

The results of this study have been published [178]. Part of this work is dedicated to a joint experimental and coupled-channels study of the interaction of $c_3\,^1\Pi_u(v=2)$ with $C\,^3\Pi_u(v=17)$, and the modelling involved forms part of my published body of work. These states exhibit level crossings in all isotopomers, with term values summarised in Fig. 6.33. The theoretical levels of $C\,^3\Pi_u(v=17)$ for $\Omega = 0$, 1, and 2 plotted in this figure are calculated from a previous version of the coupled-channels model which was optimised to represent this particular vibrational level of $C\,^3\Pi_u$, whereas, the current model under discussion comprises a global $^3\Pi_u$ model. Because of this, the calculated quantities discussed below show slightly less agreement with experiment than the published results [178].

The level crossing of $c_3\,^1\Pi_u(v=2)$ and $C\,^3\Pi_u(v=17)$ occurs with $J \simeq 25$, 18, and 8 for the case of $^{14}N_2$, $^{14}N^{15}N$, and $^{15}N_2$; respectively. Their interaction is evident in the

[c]Department of Physics and Astronomy, Laser Center, Vrije Universiteit, De Boelelaan 1081, 1080 HV Amsterdam, The Netherlands

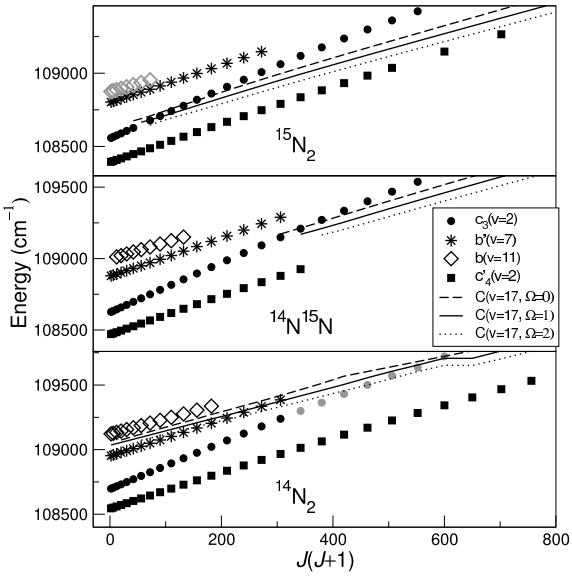

Figure 6.33: Experimental term values of $b\,^1\Pi_u(v = 11)$, $b'\,^1\Sigma_u^+(v = 7)$, $c_3\,^1\Pi_u(v = 2)$, and $c_4'\,^1\Sigma_u^+(v = 2)$, and modelled term values of $C\,^3\Pi_u(v = 17)$ for $\Omega = 0$, 1, and 2. The results of the double-photon ionisation experiment are plotted as points, apart from the gray circles which are previously published measurements [47]. Results are shown for $^{14}N_2$, $^{14}N^{15}N$, and $^{15}N_2$. After Vieitez *et al.* [178].

experimental linewidths for each isotopomer, plotted in Fig. 6.34. The resolution of the experimental apparatus is $\sim 0.4\,\mathrm{cm}^{-1}$ FWHM, which includes a contribution due to Doppler broadening. The measured linewidths in Fig. 6.34 were determined directly, by fitting variable-width theoretical line-profiles to the observed ionisation spectra. Additionally, the observed ionisation signal integrated over each line is dependent on the predissociation lifetime of the excited state, because of the competition between decay through predissociation, emission, and photoionisation. Thus those rotational levels which exhibit enhanced broadening in Fig. 6.34 appear more weakly in the spectra, corroborating the measured linewidths.

Overall, good qualitative agreement is evident in the modelled and experimental widths of Fig. 6.34, although, some discrepancies are apparent. The $^{14}N_2$ width peak results from a conjoined perturbation of all Ω sublevels, and its centre, predominantly attributable to $\Omega = 1$, is overestimated by the model. The width maximum in both $^{14}N^{15}N$ and $^{15}N_2$ are computed to occur 1 or 2 rotational levels above what the experimental values suggest. Finally, the secondary width peak observable at $J = 12$ for $^{15}N_2$ is significantly underestimated by the model.

Further understanding of the calculated J-dependence of linewidths may be elicited following inspection of the coupled-channels cross section, which is plotted for several values of J in Fig. 6.35 for the case of $^{15}N_2$. The plotted narrow resonances are ascribable to $c_3\,^1\Pi_u(v = 2)$, and $C\,^3\Pi_u(v = 17)$ appears as (sometimes inseparable) triplets of broad features, which correspond to $\Omega = 2$, 1, and 0; in order of increasing energy. It is apparent in Fig. 6.34 that the initial increase of $c_3\,^1\Pi_u(v = 2)$ widths with J is due to its close degeneracy with the $\Omega = 2$ substate of $C\,^3\Pi_u(v = 17)$ whereas the dominant width calculated at $J = 9$ is the result of a level crossing with the $\Omega = 1$ component.

It is also apparent in Fig. 6.35 that the width of $C\,^3\Pi_u(v = 17)$ become narrower with increasing J, decreasing from 16.5 to $5.4\,\mathrm{cm}^{-1}$ FWHM by $J = 11$. This offers an

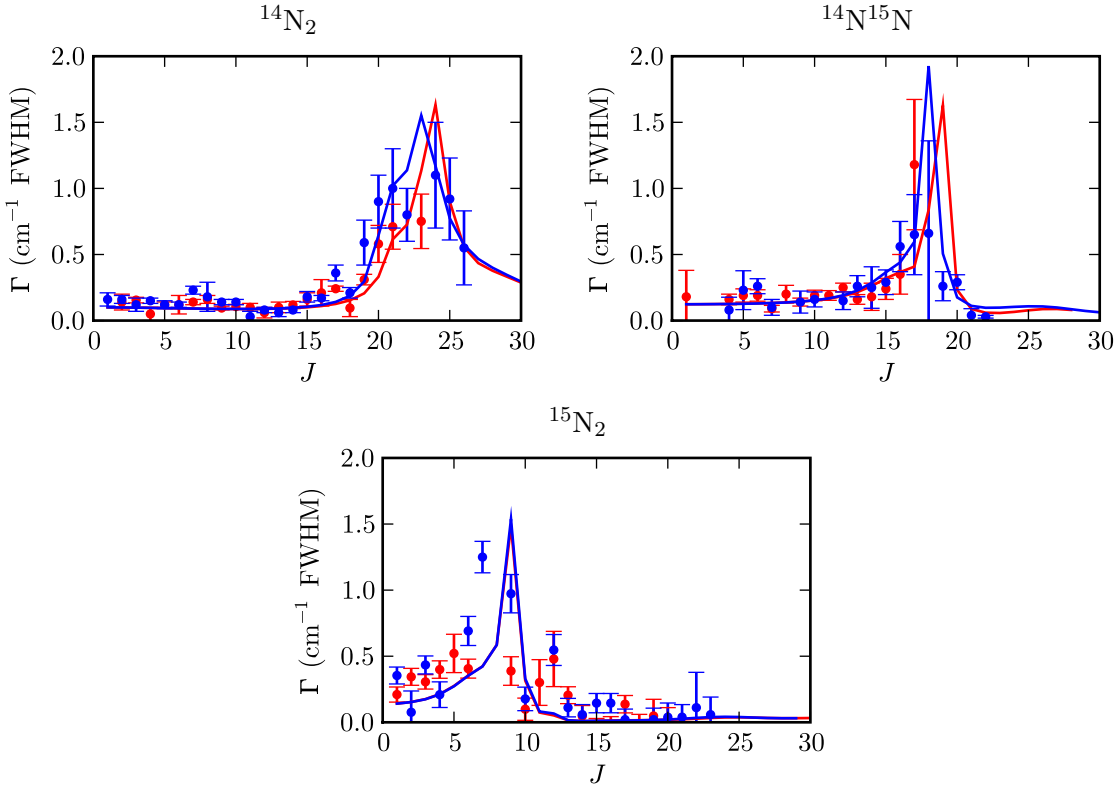

Figure 6.34: Modelled (*lines*) and experimental (*error bars*) predissociation linewidths for $c_3\,{}^1\Pi_u(v=2)$, perturbed by $C\,{}^3\Pi_u(v=17)$, for $^{14}N_2$, $^{14}N^{15}N$, and $^{15}N_2$. Linewidths are plotted for e-parity (*purple*) and f-parity (*orange*) levels.

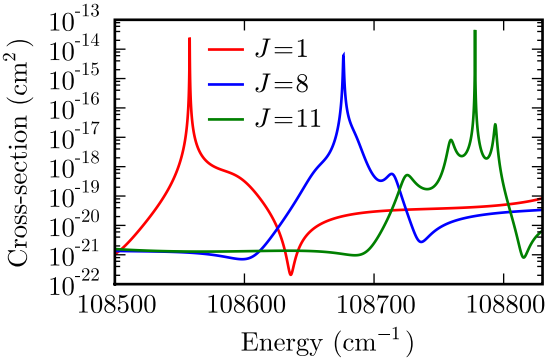

Figure 6.35: Coupled-channels photodissociation cross section showing the $J = 1$, 8, and 11 levels of $c_3\,{}^1\Pi_u(v=2)$ (narrow resonances) and $C\,{}^3\Pi_u(v=17)$ (triplets of broad features). The energy scale is relative to the ground state zero-point.

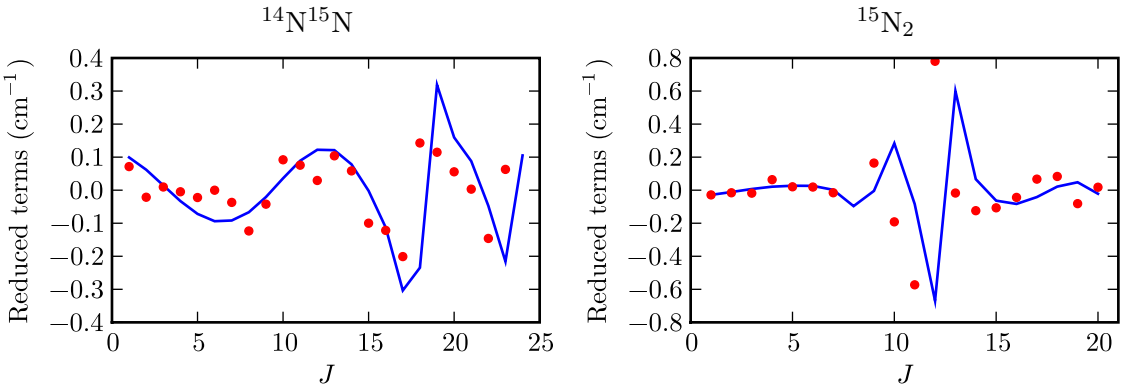

Figure 6.36: Modelled (*lines*) and experimental (*points*) f-parity term values of $c_3\,{}^1\Pi_u(v=2)$ reduced by the subtraction of a 5$^{\text{th}}$ order polynomial in terms of $J(J+1)$.

explanation why the observed broadening of $c_3\,{}^1\Pi_u(v=2)$ near $J=12$, attributable to the $C^3\Pi_{u,\Omega=2}$ substate, is less severe than where it is crossed by $C^3\Pi_{u,\Omega=1}$.

The localised deflections observed for the term values of $c_3\,{}^1\Pi_u(v=2)$ in $^{14}N^{15}N$ and $^{15}N_2$ are a further ramification of their perturbations with $C\,{}^3\Pi_u(v=17)$. These are plotted in Fig. 6.36 and the magnitude of the observed level shifts are reasonably well reproduced by the model. The dominant perturbation occurs for the $J=11$ and 12 for the $^{15}N_2$ term values and are evidently the result of the level crossing with the $\Omega=1$ substate of $C\,{}^3\Pi_u(v=17)$. This crossing is mislocated by the model, as is also the case of the $^{14}N^{15}N$ crossing, appearing at too high a value of J.

$o_3\,{}^1\Pi_u(v=2) \sim C\,{}^3\Pi_u(v=18)$ in $^{14}N_2$

Stark *et al.* [155] observed a dramatic variation of $o_3\,{}^1\Pi_u(v=2)$ natural linewidths as a function of J, which is plotted in Fig. 6.37(a). Lewis *et al.* [98] analysed these widths and the accompanying term energy perturbations, shown in Fig. 6.37(b), and attributed them to an interaction with $C\,{}^3\Pi_u(v=18)$. The coupled-channels model reproduces this interaction, with the width maxima recreated at the correct value of J, but with incorrect magnitudes. Neither are the detailed deflections of $o_3\,{}^1\Pi_u(v=2)$ term values correctly modelled. $C\,{}^3\Pi_u(v=18)$ has the lesser rotational constant so will exhibit three crossings of the $o_3\,{}^1\Pi_u(v=2)$ term series from above, with observed crossings appearing to occur between $J=13-14$, $J=15-16$, and $J=17-18$. The model, however, locates these crossings one rotational unit higher.

$b'\,{}^1\Sigma_u^+(v=4) \sim F_3\,{}^3\Pi_u(v=1)$ in $^{14}N_2$ and $^{15}N_2$

Lewis *et al.* [98] observed and analysed level crossings between $b'\,{}^1\Sigma_u^+(v=4)$ and $F_3\,{}^3\Pi_u(v=1)$ in $^{14}N_2$ and $^{15}N_2$. These crossing manifest as multiply-peaked J-dependent line broadening of $b'\,{}^1\Sigma_u^+(v=4)$, as plotted in Fig. 6.38(a).

In the case of $^{14}N_2$, three linewidth peaks are resolved experimentally and are approximately centred on $J=7$, 12 and 16; corresponding to level crossings with the $\Omega=0$, 1, and 2 substates of $F_3\,{}^3\Pi_u$; respectively. The coupled-channels model correctly locates these width peaks, but with incorrect magnitudes, so that the $\Omega=1$ peak is barely dis-

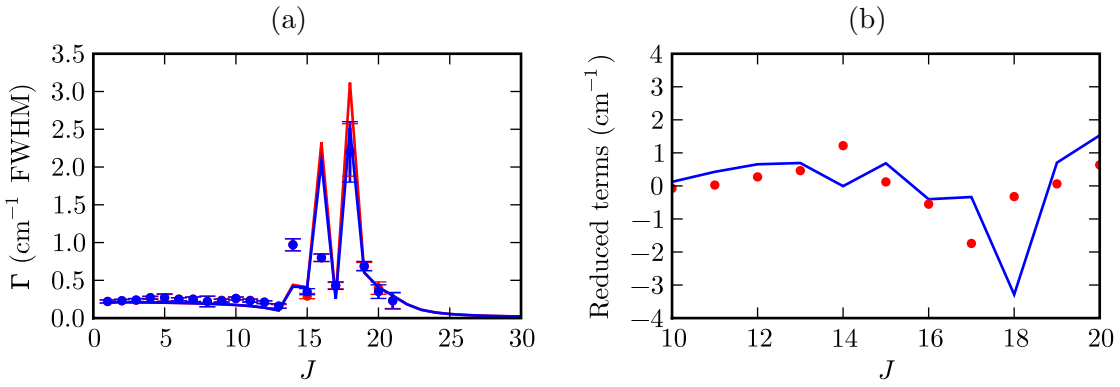

Figure 6.37: *(a):* Modelled (*lines*) and experimental (*error bars*) predissociation linewidths of $^{14}N_2$ $o_3\,{}^1\Pi_u(v = 2)$ which is perturbed by $C\,{}^3\Pi_u(v = 18)$. Linewidths are plotted for e-parity (*purple*) and f-parity (*orange*) levels. *(b):* Model (*red*) and experimental (*blue*) f-parity term values of $^{14}N_2$ $o_3\,{}^1\Pi_u(v = 2)$ reduced by the subtraction of a third-order polynomial in terms of $J(J + 1)$.

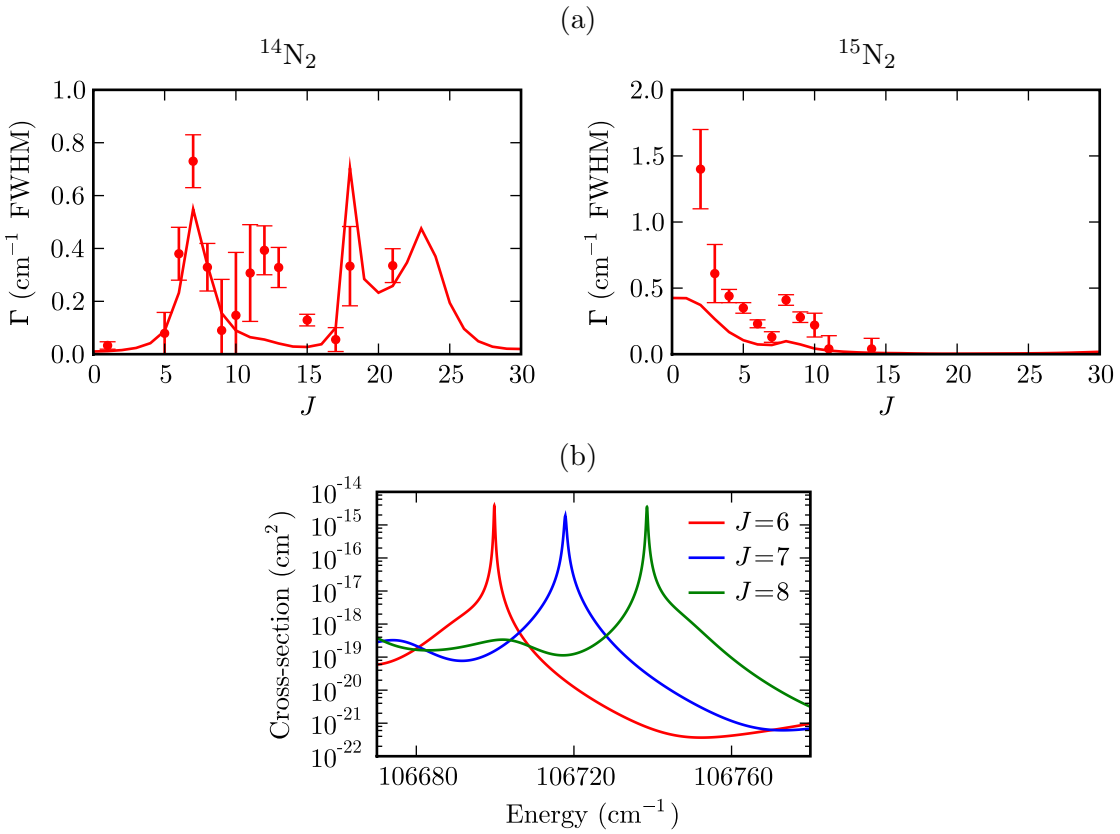

Figure 6.38: *(a):* Modelled (*lines*) and experimental (*error bars*) predissociation linewidths of $^{14}N_2$ and $^{15}N_2$ $b'\,{}^1\Sigma_u^+(v = 4)$, which are perturbed by $F_3\,{}^3\Pi_u(v = 1)$. *(b):* Coupled-channels cross section showing the region around $^{14}N_2$ $b'\,{}^1\Sigma_u^+(v = 4)$ for $J = 6$, 7, and 8.

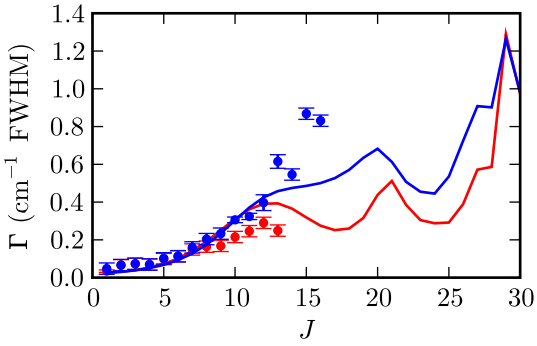

Figure 6.39: Modelled (*lines*) and experimental (*error bars*) predissociation linewidths of $^{14}N_2$ $c_3\,{}^1\Pi_u(v=1)$ which is perturbed by $F_3\,{}^3\Pi_u(v=1)$. Linewidths are plotted for e-parity (*purple*) and f-parity (*orange*) levels.

cernible, and the $\Omega = 0$ peak is somewhat overestimated. The fourth modelled peak at $J = 23$ is due to a predicted crossing of $b'\,{}^1\Sigma_u^+(v=4)$ with $C\,{}^3\Pi_u(v=14)$ which has not been observed. A similar pattern occurs in the linewidths of $^{15}N_2$, where the maxima at $J = 0$ and 8 result from the $\Omega = 1$ and 2 components of $F_3\,{}^3\Pi_u(v=1)$, respectively. Once again, these are correctly located by the model, but with incorrect magnitudes.

Because of their large width, the $F_3\,{}^3\Pi_u(v=1)$ levels are not easily discernible in the model cross section, plotted in Fig. 6.38(b). This shows the $\Omega = 0$ level of $F_3\,{}^3\Pi_u(v=1)$ passing under sharp resonances corresponding to levels of $b'\,{}^1\Sigma_u^+(v=4)$. At the point of greatest degeneracy, $b'\,{}^1\Sigma_u^+(v=4, J=7)$ is noticeably broadened.

$c_3\,{}^1\Pi_u(v=1) \sim F_3\,{}^3\Pi_u(v=1)$ in $^{14}N_2$

The experimental linewidths of $c_3\,{}^1\Pi_u(v=1)$, plotted in Fig. 6.39, are derived from two sources. Stark *et al.* [155] observed a J-dependent broadening of f-parity levels corresponding to $J = 11 - 20$ and Hashimoto and Kanamori [48] observed e- and f-parity linewidths up to $J = 16$. The latter absorption experiment was performed at very high resolution, but involved target gas of an unknown temperature and error bars for this data correspond to the $0.03\,\mathrm{cm}^{-1}$ FWHM Doppler broadening estimated by the authors.

The term origin of $c_3\,{}^1\Pi_u(v=1)$ lies $50\,\mathrm{cm}^{-1}$ below $F_3\,{}^3\Pi_u(v=1)$, which has an observed experimentally deduced linewidth of $16\,\mathrm{cm}^{-1}$ FWHM [98]. The initial increase of $c_3\,{}^1\Pi_u(v=1)$ width with respect to J results from a decrease in the separation of states, and the subsequent multi-peaked structure is due to level crossings with the $\Omega = 2$, 1, and 0 components of $F_3\,{}^3\Pi_u(v=1)$, in order of increasing J.

The coupled-channels model successfully models the increase of f-parity predissociation for $J \leq 12$ but underestimates subsequent values, whereas, the lesser e-parity widths are progressively overestimated by the coupled-channels model. A significant contribution to the e/f parity dependence of $c_3\,{}^1\Pi_u(v=1)$ linewidths arises from the e-parity only repulsion of $c_3\,{}^1\Pi_u(v=1)$ levels by the overlying $b'\,{}^1\Sigma_u^+(v=4)$, such that the effective rotational constant of $c_3\,{}^1\Pi_u(v=1)$ is decreased and its level crossings with $F_3\,{}^3\Pi_u(v=1)$ occur at higher-J than the f-parity crossings.

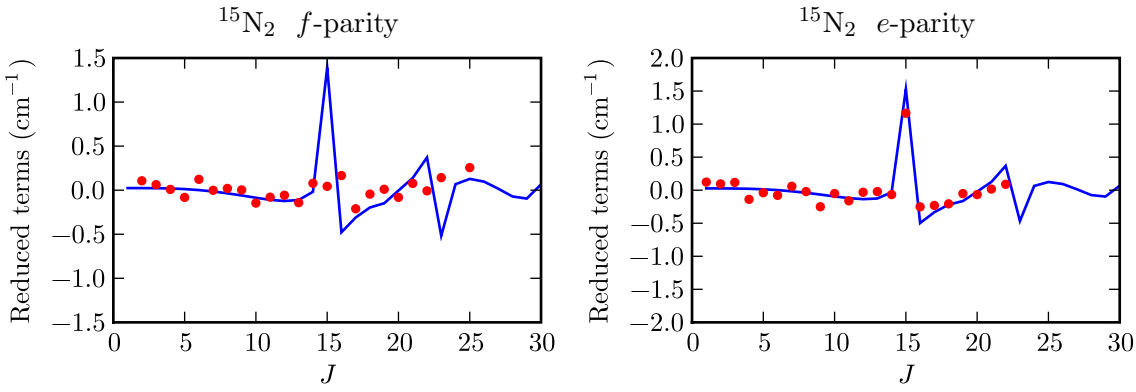

Figure 6.40: Modelled (*blue*) and experimental (*red*) term-values of $^{15}N_2$ $b\,^1\Pi_u(v=4)$. These have been reduced by the subtraction of a 2$^{\text{nd}}$ order polynomial in terms of $J(J+1)$ in order to highlight perturbations with $G_3\,^3\Pi_u(v=0)$.

$b\,^1\Pi_u(v=4) \sim G_3\,^3\Pi_u(v=0)$ in $^{14}N_2$ and $^{15}N_2$

The $G_3\,^3\Pi_u(v=0)$ level has been observed directly in absorption for both $^{14}N_2$ and $^{15}N_2$ [98, 151, 155]. This forbidden transition becomes visible because of strength borrowed from transitions involving the nearby $b\,^1\Pi_u(v=4)$. The interaction with $G_3\,^3\Pi_u(v=0)$ also leads to term-value perturbations of $b\,^1\Pi_u(v=4)$, which are plotted in Fig. 6.40 for the case of $^{15}N_2$. Model calculated reduced term-values are also shown and reveal the separate interactions of $G_3\,^3\Pi_u$ $\Omega=0$, 1, and 2 sublevels at $J=15$, 18, and 22; respectively.

The strongest $b\,^1\Pi_u(v=4)$ level shifts occurs due to $G^3\Pi_{u,\Omega=0}$ and are approximately reproduced by the model for the case of e-parity term values, but are significantly overestimated for the f-parity. This e/f discrepancy follows from the omission of an additional perturbing state from the coupled-channels model, $D\,^3\Sigma_u^+$. This Rydberg state is the triplet analogue of $c_4'\,^1\Sigma_u^+$, and possesses a significant off-diagonal matrix element of the L-uncoupling operator, $\langle D\,^3\Sigma_u^+|H^{\text{rot}}|G_3\,^3\Pi_u\rangle$, in analogy with the similar interaction of $c_4'\,^1\Sigma_u^+$ and $c_3\,^1\Pi_u$, except now both e- and f-parity levels of $G_3\,^3\Pi_u$ may be perturbed by the various sublevels of $D\,^3\Sigma_u^+$. An analysis of this interaction is presented in Sec. 6.6.4.

A series of perturbations in the term series of $b\,^1\Pi_u(v=4)$ in $^{14}N_2$ for $J<8$ are also the direct result of a level crossing with $D\,^3\Sigma_u^+(v=0)$, and are evident in Fig. 6.14.

$b\,^1\Pi_u(v=10) \sim G_3\,^3\Pi_u(v=2)$ in $^{14}N_2$

Stark *et al.* [157] observed broadening of both e- and f-parity levels of $b\,^1\Pi_u(v=10)$, and Lewis *et al.* [105] observed weak and broad features lines overlapping $b\,^1\Pi_u(v'=10) \leftarrow X\,^1\Sigma_g^+(v''=0)$ photoabsorption spectra. These were analysed and assigned to transitions involving $C\,^3\Pi_u(v=16)$ levels with $J \leq 11$. Experimental and calculated linewidths for $b\,^1\Pi_u(v=10)$ are plotted in Fig. 6.41(a), where the model successfully predicts the onset of broadening near $J=17$ but fails to reproduce the more rapid onset of f-parity broadening, relative to the e-parity levels. The lack of a e/f branching in the model widths is likely due to the omission of $D\,^3\Sigma_u^+$ from the coupled-channels.

After examining the model output in some detail, it is evident that the J-dependent broadening of $b\,^1\Pi_u(v=10)$ involves both $C\,^3\Pi_u(v=16)$ and $G_3\,^3\Pi_u(v=2)$. The latter

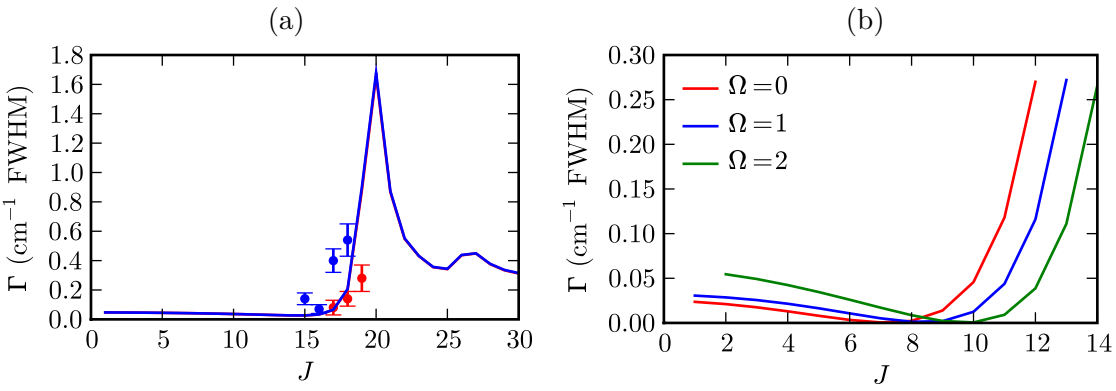

Figure 6.41: *(a):* Modelled (*lines*) and experimental (*error bars*) predissociation linewidths of $^{14}N_2$ $b\,^1\Pi_u(v = 10)$ which is perturbed by $C\,^3\Pi_u(v = 16)$. Linewidths are plotted for *e*-parity (*purple*) and *f*-parity (*orange*) levels. *(b):* Modelled predissociation linewidths of $C\,^3\Pi_u(v = 16)$.

state has not been rotationally analysed but has been observed at low resolution [173] at an energy below $C\,^3\Pi_u(v = 16)$ and $b\,^1\Pi_u(v = 10)$. Model calculations, listed in Tab. 6.7, predict a significant width for $G_3\,^3\Pi_u(v = 2)$ and a rotational constant larger than that of $b\,^1\Pi_u(v = 10)$ and $C\,^3\Pi_u(v = 16)$, which have similar magnitudes. Thus, the broadening of $b\,^1\Pi_u(v = 10)$ is due to increased mixing with $G_3\,^3\Pi_u(v = 2)$ as the two states approach a level crossing.

The detailed form of $b\,^1\Pi_u(v = 10)$ J-dependent broadening also involves $C\,^3\Pi_u(v = 16)$, which is itself significantly affected by $G_3\,^3\Pi_u(v = 2)$, as shown in Fig. 6.41. The calculations predict a minimum width occurring for $C\,^3\Pi_u(v = 16)$ and $b\,^1\Pi_u(v = 10)$ near $J = 9$ and 14, respectively. This is the result of quantum interference occurring between alternative predissociation pathways, via $C\,^3\Pi_u$ or $G_3\,^3\Pi_u$, with both ultimately leading to the dissociative state $C'\,^3\Pi_u$.

6.6.4 Predissociation of $D\,^3\Sigma_u^+$

A further coupled-channels model has been constructed for the purpose of explaining the observed predissociation of the Rydberg state $D\,^3\Sigma_u^+$. This work has been done as part of a joint experimental and theoretical investigation and has been published [97]. My contribution was to its modelling aspects.

Previous observations of $D\,^3\Sigma_u^+$ are summarised in Sec. 3.4 including apparent predissociation of its $v = 1$ level in $^{14}N_2$. Two types of new measurements have been made: direct absorption of $D\,^3\Sigma_u^+$ and its perturbation partners from the ground state by means of extreme-ultraviolet (XUV) laser excitation; and its excitation from the metastable state $E\,^3\Sigma_g^+$ by means of near-infrared (NIR) spectroscopy. Details of the experimental setups are deferred to the published version of this work [97], but the XUV and NIR experiments enjoy Doppler-limited instrumental resolutions of 0.01 and 0.024 cm^{-1} FWHM, respectively; as well as absolute energy calibrations accurate to 0.2 and 0.002 cm^{-1}, respectively.

Measurements have been made of $D\,^3\Sigma_u^+(v = 0-3)$ in $^{14}N_2$ and for $v = 1$ in $^{15}N_2$, with a complete listing of transition energies and linewidths provided in the publication [97]. The experimental quantities necessary to constrain the empirical elements of the following coupled-channels model may be reduced to a set of term origin and rotational-constants,

Iso.	v	$T_{\rm exp}$	$T_{\rm dia}$	$T_{\rm CSE}$	ΔT	$B_{\rm exp}$	$B_{\rm dia}$	$B_{\rm CSE}$	ΔB
$^{14}N_2$	0	103 572.7	103 572.43	103 572.46	0.03	1.961	1.921	1.961	0.040
	1	105 709.5	105 709.28	109 709.27	−0.01	1.883	1.899	1.882	−0.017
	2	107 805	107 805.42	107 805.40	−0.02	1.842	1.885	1.846	−0.039
	3	109 859	109 858.42	109 858.40	−0.02	1.843	1.874	1.839	−0.035
$^{15}N_2$	1	105 641.8	105 641.83	105 641.82	−0.01	1.760	1.774	1.760	−0.014

Table 6.10: Comparison of experimental and calculated spectroscopic parameters for levels of the $D\,^3\Sigma_u^+$ state of N_2, all in cm^{-1}. Calculations by the full coupled-channels model including $^3\Pi_u$ states are subscripted "CSE", and to highlight the importance of the coupling between states, alternative single-channels calculation consisting only of a diabatic $D\,^3\Sigma_u^+$ state are also listed, labelled "dia".

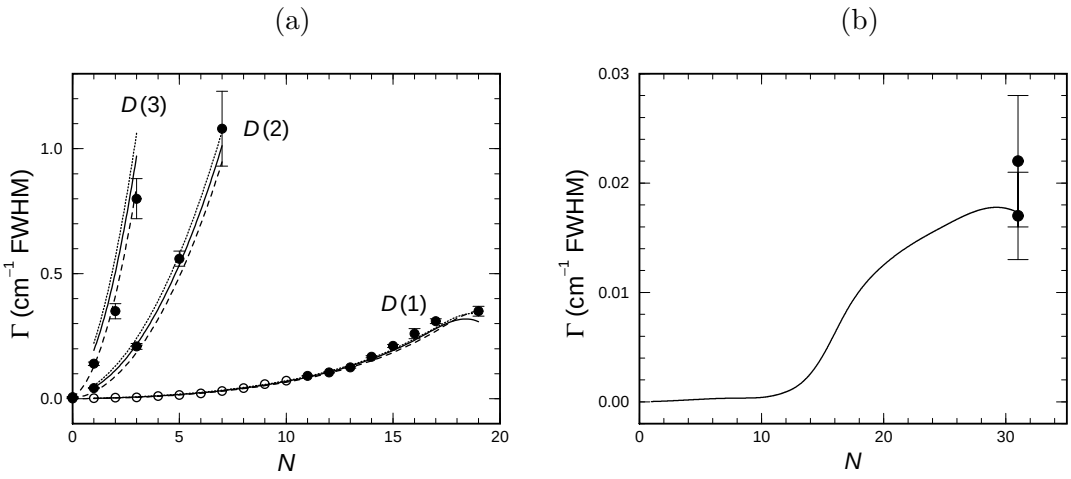

Figure 6.42: *(a):* Experimental (*error bars*) and modelled (*curves*) predissociation linewidths of, Γ, of $D\,^3\Sigma_u^+(v = 1 - 3)$ for $^{14}N_2$. These are plotted in terms of the conventional Hund's case (b) independent angular-momentum N [54, 70], defined in Tab. 2.1, and the dashed, solid, and dotted lines refer to $J = N - 1$, $J = N$, and $J = N + 1$ triplet substates, respectively. *(b):* Experimental and modelled predissociation linewidths of $D\,^3\Sigma_u^+(v = 0)$.

and a summary of the observed predissociation linewidths. These are summarised in Tab. 6.10 and Fig. 6.42, respectively.

The vibrational and rotational dependence of the experimental linewidths portrayed in Fig. 6.42 is striking, and its rapid increase with J is indicative of a heterogeneous rotational-interaction of some kind. A likely candidate perturber is $G_3\,{}^3\Pi_u$ which, together with $D\,{}^3\Sigma_u^+$, forms part of a Rydberg p-complex [12] along with two isoconfigurational singlet states, $c_3\,{}^1\Pi_u$ and $c_4'\,{}^1\Sigma_u^+$.

According to the selection rules discussed in Secs. 2.5 and 2.6, $D\,{}^3\Sigma_u^+$ and $G_3\,{}^3\Pi_u$ may be perturbed by both the spin-orbit operator and the rotational part of the molecular Hamiltonian. Matrix elements describing these interactions must be evaluated in an e/f-parity basis because the presence of a Σ state permits the occurrence of Λ-doubling. In total, there are 9 states which must be considered [65, 70, 90, 101], represented here by Hund's case (a) wavefunctions $|\Lambda, \Sigma, \Omega\rangle$:

$$^3\Sigma^+_{\Omega=0,f} = |\Lambda = 0, \Sigma = 0, \Omega = 0\rangle\,, \tag{6.27}$$

$$^3\Sigma^+_{1,\,\substack{e\\f}} = 2^{-\frac{1}{2}}\Big[|0,1,1\rangle \mp |0,-1,-1\rangle\Big], \tag{6.28}$$

$$^3\Pi_{0,\,\substack{e\\f}} = 2^{-\frac{1}{2}}\Big[|1,-1,0\rangle \mp |-1,1,0\rangle\Big], \tag{6.29}$$

$$^3\Pi_{1,\,\substack{e\\f}} = 2^{-\frac{1}{2}}\Big[|1,0,1\rangle \mp |-1,0,-1\rangle\Big], \tag{6.30}$$

$$\text{and } ^3\Pi_{2,\,\substack{e\\f}} = 2^{-\frac{1}{2}}\Big[|1,1,2\rangle \mp |-1,-1,-2\rangle\Big]. \tag{6.31}$$

Here, $\substack{e\\f}$ indicates two states of opposite parity, and all states have been decomposed into a basis consisting of projected angular-momenta with definite sign.

States with signed angular momenta are convenient for the specification of two critical off-diagonal matrix elements, which may be calculated *ab initio*, but are determined experimentally here. These dictate the magnitude of the spin-orbit interaction, by means of the parameter

$$\begin{aligned}\xi &= \langle 0,0,0|H^{\mathrm{SO}}|\pm 1, \mp 1, 0\rangle \\ &= \langle 0, \pm 1, \pm 1|H^{\mathrm{SO}}|\pm 1, 0, \pm 1\rangle,\end{aligned} \tag{6.32}$$

and rotational interactions, according to

$$\eta = \frac{\hbar}{2\mu R}\langle \Lambda = 0|L^{\pm}|\Lambda = \mp 1\rangle. \tag{6.33}$$

The matrix element in Eq. (6.33) occurs as part of both the L-uncoupling and spin-electronic operators given by Eqs. (2.47) and (2.49), respectively. The remaining parts of these operators may be evaluated exactly, in terms of S, Σ, J, and Ω.

Then, combining the wavefunctions given by Eqs. (6.27) to (6.31) with the spin-orbit and L-uncoupling operators results in the following nonzero $^3\Sigma^+ \sim {}^3\Pi$ off-diagonal matrix

elements:

$$\left\langle {}^3\Sigma^+_{0,f}\middle|H^{\rm rot}+H^{\rm SO}\middle|{}^3\Pi_{0,f}\right\rangle = \sqrt{2}\xi + 2\eta, \tag{6.34}$$

$$\left\langle {}^3\Sigma^+_{0,f}\middle|H^{\rm rot}+H^{\rm SO}\middle|{}^3\Pi_{1,f}\right\rangle = -\eta\sqrt{2J(J+1)}, \tag{6.35}$$

$$\left\langle {}^3\Sigma^+_{1,\,f}{}^{e}\middle|H^{\rm rot}+H^{\rm SO}\middle|{}^3\Pi_{0,\,f}{}^{e}\right\rangle = \pm\eta\sqrt{J(J+1)}, \tag{6.36}$$

$$\left\langle {}^3\Sigma^+_{1,\,f}{}^{e}\middle|H^{\rm rot}+H^{\rm SO}\middle|{}^3\Pi_{1,\,f}{}^{e}\right\rangle = \xi + \sqrt{2}\eta, \tag{6.37}$$

$$\text{and } \left\langle {}^3\Sigma^+_{1,\,f}{}^{e}\middle|H^{\rm rot}+H^{\rm SO}\middle|{}^3\Pi_{2,\,f}{}^{e}\right\rangle = -\eta\sqrt{J(J+1)-2}. \tag{6.38}$$

The parameter ξ is not associated with any J-dependence, and give the apparent extrapolation of $D\,{}^3\Sigma^+_u$ linewidths in Fig. 6.42(a) to $J=0$, must have a small value. The lowest-J measured width is for $^{14}N_2$ $D\,{}^3\Sigma^+_u(v=1, J=1)$ and its value, $0.0065\pm0.0007\,\mathrm{cm}^{-1}$, is the primary constraint in the following optimisation of ξ.

A simplification may be made for η as was done in Sec. 2.13 with regard to L-uncoupling of the singlet members of the present $3p$ Rydberg complex. By assuming the Rydberg electronic-orbital is well decoupled from the remaining Σ^+ molecular core, then Eq. (6.33) may be reduced to an approximate form, given by

$$\eta \simeq \frac{\hbar}{2\mu R}\langle p\sigma|l^-|p\pi\rangle \tag{6.39}$$

$$\simeq \frac{\hbar}{2\mu R}\sqrt{2}. \tag{6.40}$$

A coupled channels model of $D\,{}^3\Sigma^+_u$ and ${}^3\Pi_u$ states has been constructed in order to explain the observed predissociation in Fig. 6.42. The ${}^3\Pi_u$ model of the previous sections has been adopted here unaltered. An initial potential-energy curve for $D\,{}^3\Sigma^+_u$ was constructed by adopting the shape of the isoconfigurational $c_3\,{}^1\Pi_u$ curve. This was shifted and linearly-scaled horizontally and vertically in order to best reproduce the spectroscopic constants of Tab. 6.10, with its final form shown in Fig. 6.43.

Fitted parameters of $\xi = 1.0\pm0.3\,\mathrm{cm}^{-1}$ and $\eta = \frac{\hbar}{2\mu R}(1.40\pm0.02\,\mathrm{cm}^{-1})$ were found to reproduce the observed linewidths very well, as shown in Fig. 6.42. This finding confirms the hypothesis that the observed predissociation of $D\,{}^3\Sigma^+_u$ is controlled by its interaction with $G_3\,{}^3\Pi_u$. Furthermore the fitted value of η confirms the legitimacy of the approximations leading to Eq. (6.40). Because $D\,{}^3\Sigma^+_u$ and $G_3\,{}^3\Pi_u$ are isoconfigurational, the form of their electronic wavefunctions will be similar, leading to the approximate equality

$$\xi = \langle D\,{}^3\Sigma^+_u|H^{\rm SO}|G_3\,{}^3\Pi_u\rangle \tag{6.41}$$

$$\simeq \langle G_3\,{}^3\Pi_u|H^{\rm SO}|G_3\,{}^3\Pi_u\rangle. \tag{6.42}$$

The latter matrix element was attributed an estimated value of $2\,\mathrm{cm}^{-1}$ in Sec. 6.6.2, in approximate agreement with the present value of ξ.

The approximately quadratic linewidth dependence on J in Fig. 6.42 results from the L-uncoupling matrix elements appearing in Eq. (6.35), (6.36), and (6.38). The increase of width with v, as well as the apparent overturning of $D\,{}^3\Sigma^+_u(v=1)$ widths for high rotation, are multichannel effects, related to the increasing predissociation of $G_3\,{}^3\Pi_u$ itself (Sec. 6.6.1) and an approaching level crossing with $C\,{}^3\Pi_u(v=10)$, respectively.

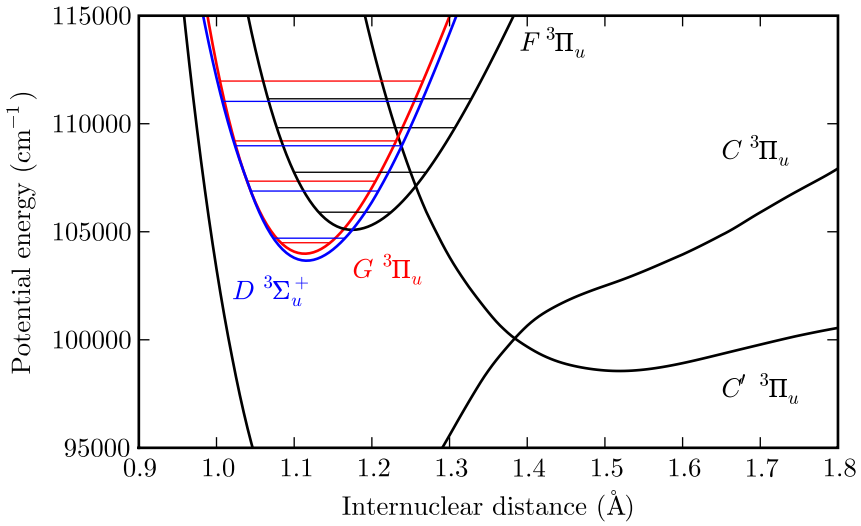

Figure 6.43: Model potential-energy curves of the coupled $^3\Pi_u$ states and $D\,^3\Sigma_u^+$. The known vibrational levels of $D\,^3\Sigma_u^+$, $G_3\,^3\Pi_u$, and $F_3\,^3\Pi_u$ for $^{14}N_2$ are also indicated.

6.7 Closer analysis of some model results

A complete presentation of spectral information contained within the modelled range of energies would surely exceed the patience of any reader. Here, several excited vibrational levels are discussed in finer detail as an example. Appendix A.3 comprises a summary of the critical parameters of many further modelled levels.

All $c_3\,^1\Pi_u(v)$ and $c_4'\,^1\Sigma_u^+(v)$ e-parity levels with common v are strongly mixed by the L-uncoupling operator. As an example of this phenomenon, the complex of bands around the pair of levels with $v = 0$ are examined in some detail, including two arising from interacting valence states, $b\,^1\Pi_u(v = 5)$ and $b'\,^1\Sigma_u^+(v = 1)$. These levels embody many effects which are well suited to a coupled-channels treatment, they are strongly mutually perturbing but are also subject to the influence of yet more levels, rendering any local-deperturbation model inherently incomplete. The $c_4'\,^1\Sigma_u^+(v'=0) \leftarrow X\,^1\Sigma_g^+(v''=0)$ transition is actually the strongest of the N_2 spectrum and is particularly important with regards to atmospheric applications [7, 160].

Figure 6.44 depicts the e-parity rotational term series of these four strongly-interacting vibrational levels. In principle, the line segments joining discrete rotational levels are subjectively assigned, but are chosen here to render the smoothest possible progressions, and labelled according to their principal diabatic character at $J = 0$. The plotted levels are generated using the e-parity coupled-channels model described in Sec. 6.5. Additional calculations were also made using the model of Sec. 6.4 in order to model the excitation of f-parity $^1\Pi_u$ levels by Q-branch transitions. Both e- and f-parity models were integrated with the model of triplet states described in Sec. 6.6.3.

Separate term series are plotted for the three isotopomers of N_2, and all show the same qualitative behaviour. That is, the energies of each band are similar for all isotopomers because of the low vibrational numbers involved. For higher vibrational levels the isotopic shifts are larger.

Simulated dissociation cross sections are plotted in Fig. 6.45 showing $c_4'\,^1\Sigma_u^+(v'=0) \leftarrow X\,^1\Sigma_g^+(v''=0)$, and parts of $c_3\,^1\Pi_u(v'=0) \leftarrow X\,^1\Sigma_g^+(v''=0)$, $b'\,^1\Sigma_u^+(v'=1) \leftarrow X\,^1\Sigma_g^+(v''=0)$

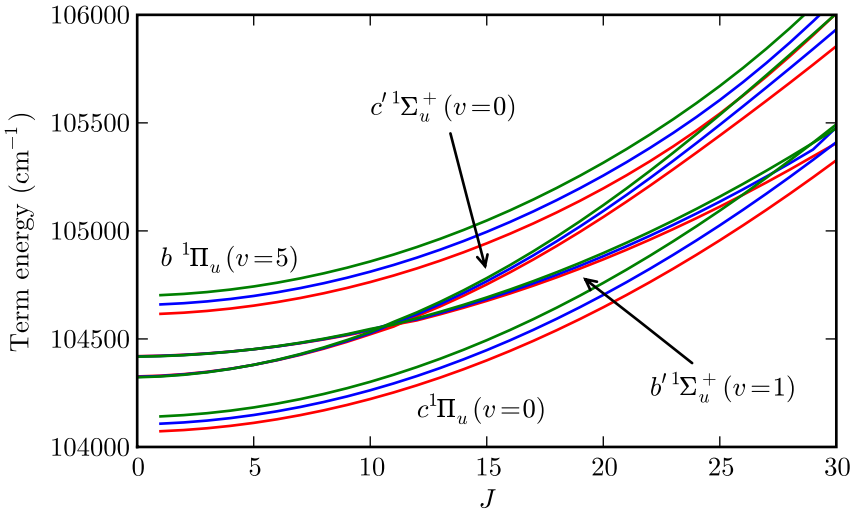

Figure 6.44: Model e-parity term values of $c_4'\,^1\Sigma_u^+(v=0)$, $b'\,^1\Sigma_u^+(v=1)$, $c_3\,^1\Pi_u(v=0)$, and $b\,^1\Pi_u(v=5)$ for three isotopomers: $^{14}N_2$ (*green*); $^{14}N^{15}N$ (*blue*); and $^{15}N_2$ (*red*).

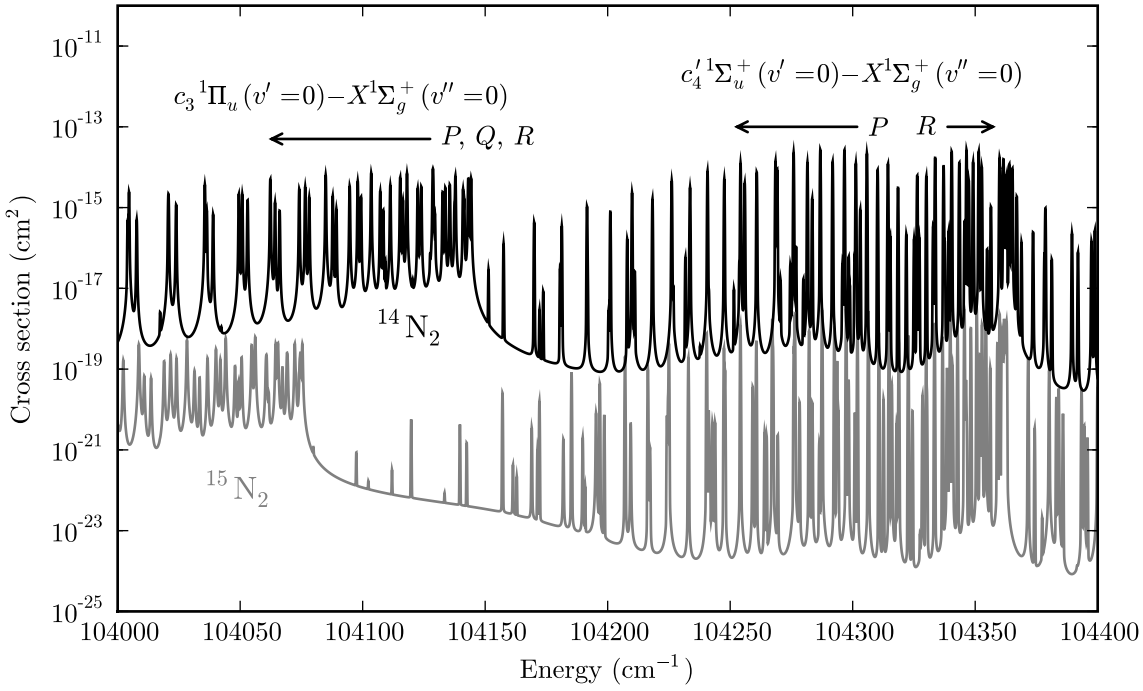

Figure 6.45: Model cross section showing two bands of $^{14}N_2$ and $^{15}N_2$ ($\times 10^{-4}$), with lines from further unlabelled bands visible in the plotted energy range.

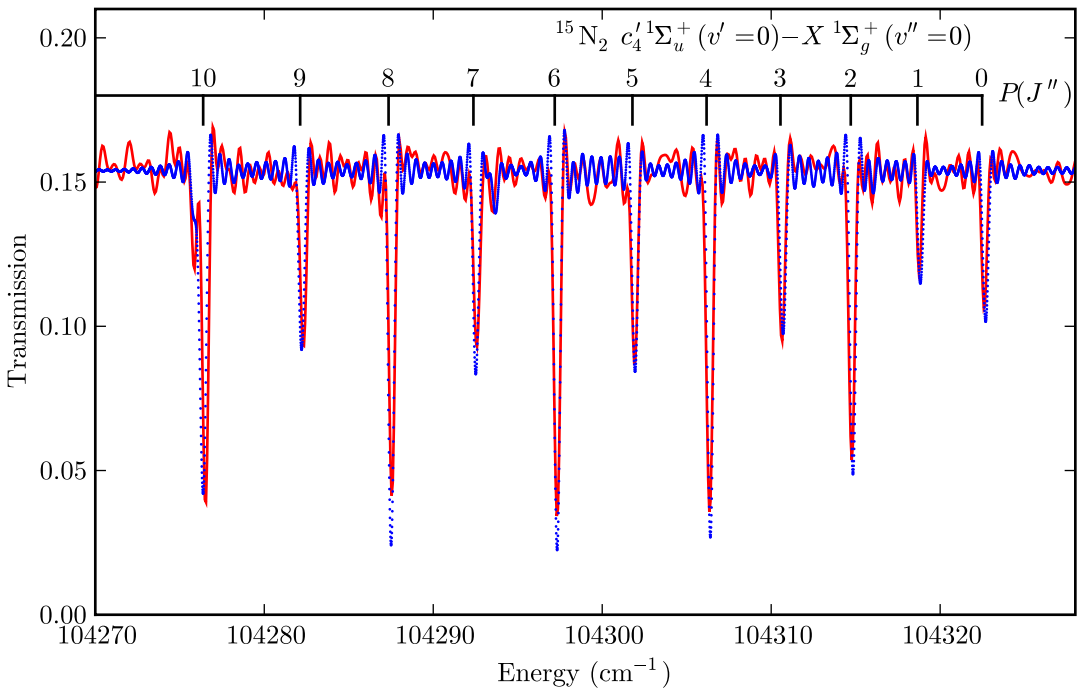

Figure 6.46: Simulated (*blue points*) and experimental (*red curve*) transmission spectrum showing the P branch of $c_4'\,^1\Sigma_u^+(v'=0) \leftarrow X\,^1\Sigma_g^+(v''=0)$ for $^{15}N_2$. The experimental spectrum was measured during the SOLEIL series of experiments, discussed in Chap. 5, and corresponds to an instrumental resolution of $0.325\,\mathrm{cm}^{-1}$ FWHM and a column density of $8\times10^{13}\,\mathrm{cm}^{-2}$. The simulation alters the coupled-channels cross section to match these parameters. An extra line is apparent in both the modelled and experimental spectra at $104\,276\,\mathrm{cm}^{-1}$, and is attributed to the $P(12)$ transition of $b'\,^1\Sigma_u^+(v'=1) \leftarrow X\,^1\Sigma_g^+(v''=0)$.

and $b\,^1\Pi_u(v'=5) \leftarrow X\,^1\Sigma_g^+(v''=0)$, for the isotopomers $^{14}N_2$ and $^{15}N_2$. Each of these is generated by summing the coupled-channels model output for all possible rotational transitions with excited-state $J \leq 30$, after weighting each by a Boltzmann distribution of ground-state rotational levels corresponding to an assumed temperature of 300 K. This combination is then artificially Doppler broadened by convolution with a Gaussian profile with an energy-dependent width of $\sim 0.23\,\mathrm{cm}^{-1}$ FWHM, corresponding to a temperature of 300 K. The predissociation linewidths of the levels discussed here do not exceed $0.1\,\mathrm{cm}^{-1}$ FWHM.

Figure 6.46 shows a smaller section of the $^{15}N_2$ cross section which has been converted into a simulated transmission spectrum. This is achieved by the application of Eq. (2.102), and further broadening by convolution with a sinc function whose central peak has a width of $0.325\,\mathrm{cm}^{-1}$ FWHM. This final step was intended to mimic the instrumental resolution of the SOLEIL Fourier transform spectrometer discussed in Chap. 5. A direct comparison with a SOLEIL absorption spectrum is then possible in Fig. 6.46, showing good agreement.

Three perturbation matrix elements dominate the interaction of levels in Fig. 6.44. The electronic mixing of $b'\,^1\Sigma_u^+$ and $c_4'\,^1\Sigma_u^+$ is evident in a distortion of the $^{14}N_2$ rotational levels, plotted in Fig. 6.47(a), where a level crossing occurs between $J = 10$ and 11. Here, the $b'(1)$ and $c_4'(0)$ term values with $J = 10$ are deflected upwards and downwards, respectively, by $\sim 2.5\,\mathrm{cm}^{-1}$; and in the reverse sense for $J = 11$. The slightness of

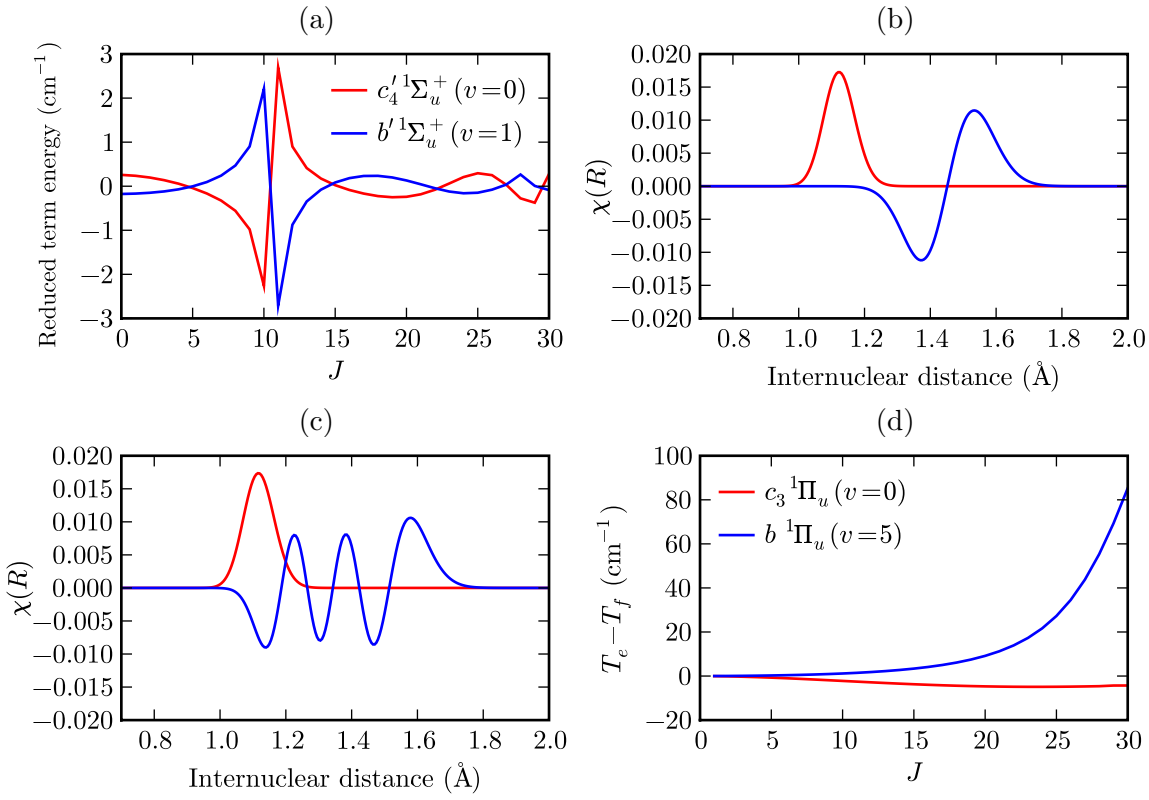

Figure 6.47: *(a):* Model term values of $^{14}N_2$ $c_4'\,^1\Sigma_u^+(v=0)$ and $b'\,^1\Sigma_u^+(v=1)$ reduced by the subtraction of a 5^{th} order polynomial of best-fit in terms of $J(J+1)$. *(b):* A single-channels calculation of wavefunctions, $\chi(R)$, for $^{14}N_2$ $c_4'\,^1\Sigma_u^+(v=0)$ (*red*) and $b'\,^1\Sigma_u^+(v=1)$ (*blue*). *(c):* Single-channel wavefunctions of $^{14}N_2$ $c_3\,^1\Pi_u(v=0)$ (*red*) and $b\,^1\Pi_u(v=5)$ (*blue*). *(d):* Model Λ-doubling of $^{14}N_2$ $c_3\,^1\Pi_u(v=0)$ and $b\,^1\Pi_u(v=5)$, where T_e and T_f are e- and f-parity term values, respectively.

this perturbation is remarkable given the magnitude of the $b' \sim c'_4$ electronic coupling, $\sim 1000\,\mathrm{cm}^{-1}$, but is understandable in view of the poor radial-overlap of $c'_4(0)$ and $b'(1)$ single-channel wavefunctions, plotted in Fig. 6.47(b). These wavefunctions were calculated by solving the Schrödinger equation for uncoupled $b'\,^1\Sigma_u^+$ and $c'_4\,^1\Sigma_u^+$ potential energy curves.

The electronic coupling that mixes $b\,^1\Pi_u$ and $c_3\,^1\Pi_u$ is of similar magnitude to that perturbing $b'\,^1\Sigma_u^+$ and $c'_4\,^1\Sigma_u^+$, but leads to a significantly larger interaction between the $b(5)$ and $c_3(4)$ vibrational levels than occurs for $b'(1)$ and $c'_4(0)$. This is demonstrated in Fig. 6.44, where these levels are sufficiently mixed that the normal difference between valence and Rydberg state rotational constants is not evident. Instead the $b(5)$ and $c_3(0)$ terms values show a similar rate of increase with J. Furthermore, the large isotopomer-dependence of $c_3(0)$ term values, despite its nominal $v = 0$ label, is evidence of mixing with a higher vibrational level. An explanation for the strength of the $c_3(0) \sim b(5)$ interaction relative to the co-energetic $^1\Sigma_u^+$ levels is offered by the significantly more advantageous overlap of $b(5)$ and $c_3(0)$ diabatic wavefunctions, plotted in Fig. 6.47(c).

A third perturbing matrix element which is significant to this energy region results from rotational coupling between $c_3\,^1\Pi_u$ and $c'_4\,^1\Sigma_u^+$. The e-parity only selectivity of this interaction is evident in the Λ-doubling of $c_3(0)$ and $b(5)$ term values, plotted in Fig. 6.47(d). The maximum experimentally observed Λ-doubling of $b(5)$ is $11.9\,\mathrm{cm}^{-1}$, occurring for $J = 21$, and a further splitting is predicted by the coupled-channels model for larger J. In a first-order approximation, this effect is attributable to an energy level repulsion with the underlying $c'_4(0)$, and the reversed splitting of e- and f-parity term values for $c_3(0)$ may be explained by the overlying $b'(1)$. A more complete description of state mixing would invoke further vibrational levels which are not plotted in Fig. 6.44, because of the large homogeneous electronic interactions affecting all states.

The perturbations mixing $c_3(0)$, $b(5)$, $c'_4(0)$, and $b'(1)$ are also evident in the observed and modelled oscillator-strengths of their transitions from $X\,^1\Sigma_g^+(v = 0)$, the rotational dependences of which are plotted in Fig. 6.48. Because the potential-energy curves of $c'_4\,^1\Sigma_u^+$ and $X\,^1\Sigma_g^+$ are very similar in shape and equilibrium internuclear-distance, the vibrational overlap of $c'_4(0)$ and $X(0)$ diabatic radial-wavefunctions is large; and the unperturbed $c'_4(0) \leftarrow X(0)$ f-value is accordingly great. The rotational dependences of f-values in Fig. 6.48 are primarily dictated by the borrowing of strength from $c'_4(0)$ by the other excited levels.

The energy separation of $c'_4(0)$ and $b'(1)$ is minimal near $J = 10$, and the $b'(1) \leftarrow X(0)$ f-values are greatly enhanced, while those of $c'_4(0) \leftarrow X(0)$ f-values concordantly reduced. These effects as well as the $b'(1)$ and $c'_4(0)$ term value deflections in Fig. 6.47 provide a direct constraint on the $b'\,^1\Sigma_u^+ \sim c'_4\,^1\Sigma_u^+$ electronic-coupling, and are well reproduced by the model. A further $b'(1) \leftarrow X(0)$ f-value enhancement is predicted at $J = 29$, where a level crossing between $b'(1)$ and $c_3(0)$ occurs.

Because $c_3(0)$ and $b(5)$ are highly mixed, their effect on the f-values of $c'_4(0) \leftarrow X(0)$ cannot be separated. As discussed in Sec. 2.8.4, the rotational interaction of $^1\Sigma$ and $^1\Pi$ excited states will lead to an intensity transfer between the resultant two bands which has an opposite sense for P- and R-branch transitions. This is evident in the $c'_4(0) \leftarrow X(0)$ f-values of Fig. 6.48 where, below $J = 22$, the P branch is enhanced and the R branch diminished. The reverse effect is observed for $c_3(0) \leftarrow X(0)$ and, in either case, no branching occurs as J tends to zero because of the $\sqrt{J(J+1)}$ dependence of rotational coupling. The P and R branches of $b(5) \leftarrow X(0)$ are also perturbed, but with f-values affected oppositely to $c_3(0) \leftarrow X(0)$. This difference results from the combined signs of

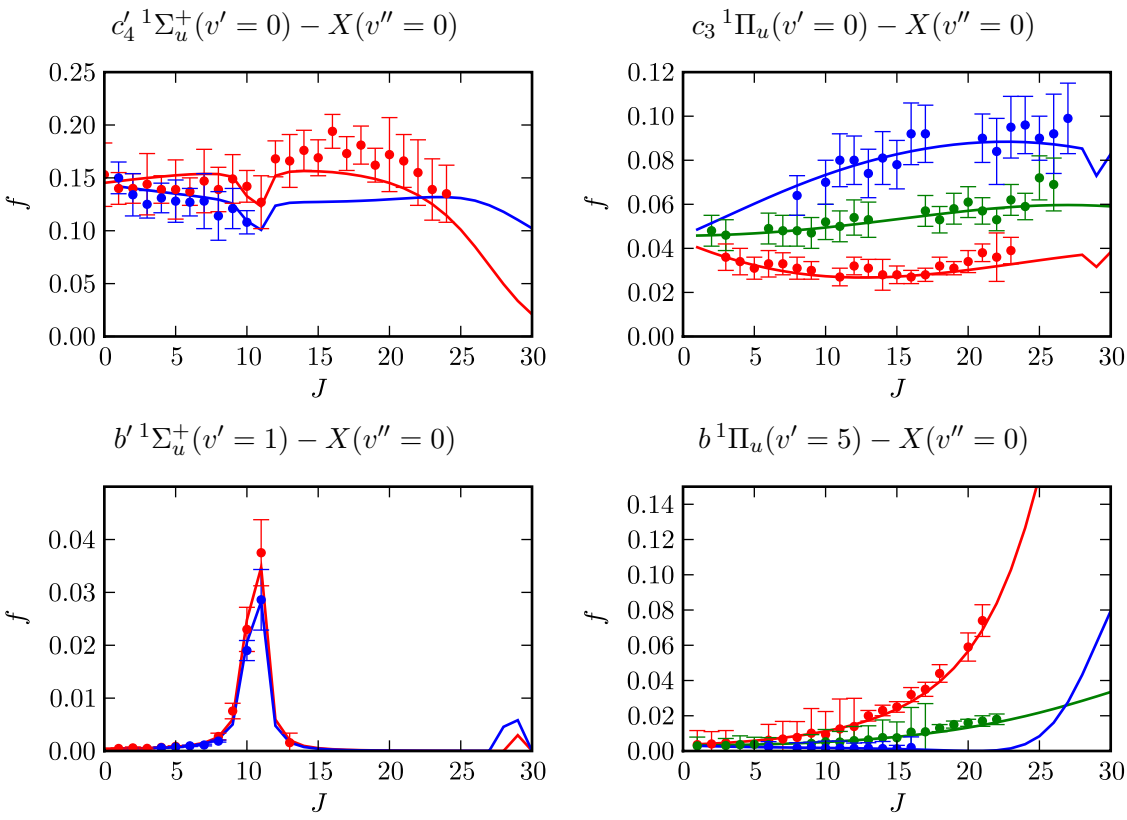

Figure 6.48: Experimental (*error bars*) and modelled (*curves*) f-values of $c_4' \, ^1\Sigma_u^+(v'=0)-$, $c_3 \, ^1\Pi_u(v'=0)-$, $b' \, ^1\Sigma_u^+(v'=1)-$, and $b \, ^1\Pi_u(v'=5) - X \, ^1\Sigma_g^+(v''=0)$. The P, Q, and R branches are plotted in red, green, and blue; respectively.

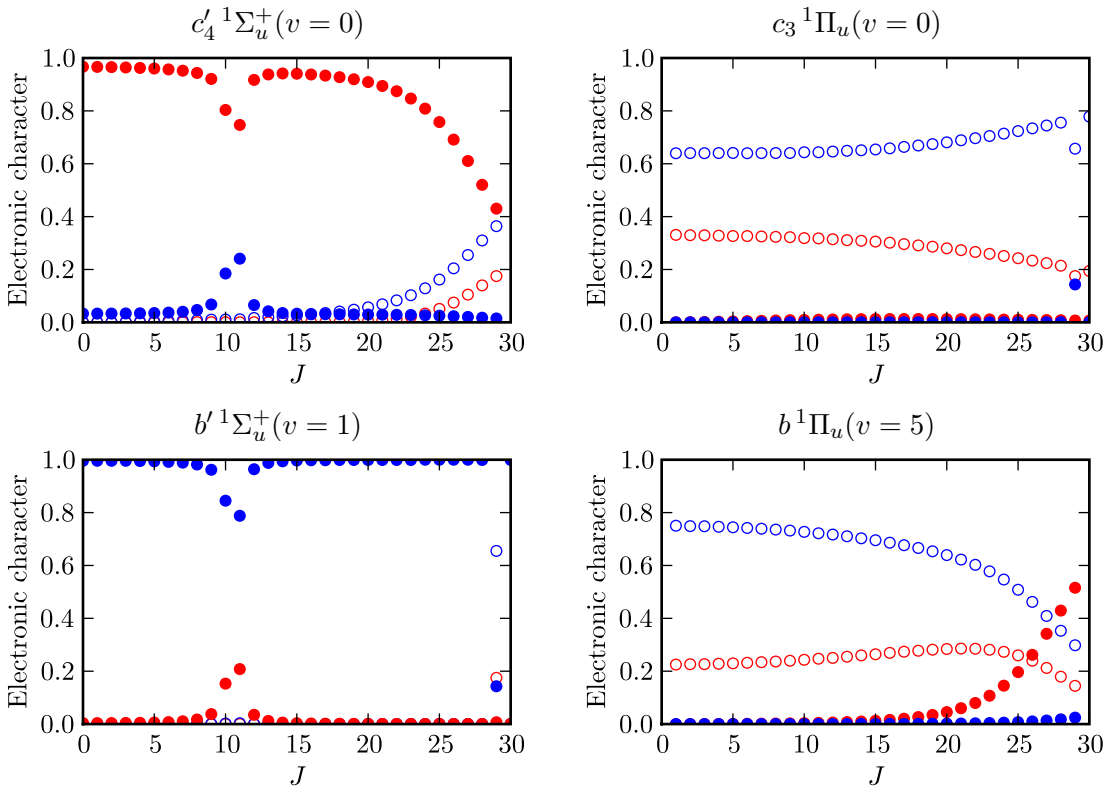

Figure 6.49: Calculated fractional electronic-character of several excited vibrational levels for the e-parity electronic states $c_4'\,^1\Sigma_u^+$ (*red, filled*), $c_3\,^1\Pi_u$ (*red, empty*), $b'\,^1\Sigma_u^+$ (*blue, filled*), and $b\,^1\Pi_u$ (*blue, empty*).

$c_4' \leftarrow X$, $c_3 \leftarrow X$, and $b \leftarrow X$ electronic transition moments; as well as the fact that $b(5)$ lies below $c_4'(0)$, and $c_3(0)$ above.

A further instructive quantity may be extracted from the coupled radial wavefunction, the vector quantity $\chi(\mathbf{R})$ of Eq. (2.136). That is, by integrating its components with respect to internuclear distance, according to

$$c_i = \frac{1}{\mathcal{N}} \int_0^\infty [\chi(\mathbf{R})]_i dR, \tag{6.43}$$

where i spans all bound electronic states, the resultant quantities, c_i, describe the contribution of each diabatic electronic state to the calculated wavefunction. The normalisation constant $\mathcal{N}$ is chosen so that $\sum_i c_i = 1$. Figure 6.49 shows this fractional electronic-character for the $c_4'(0)$, $c_3(0)$, $b'(1)$, and $b(5)$ levels. The mixed nature of these states is in line with the discussion of the preceding paragraphs. That is, the $c_4'(0)$ and $b'(1)$ levels are not greatly mixed apart from close to the level crossing near $J = 11$; and $c_3(0)$ and $b(5)$ are significantly mixed, even so that $c_3(0)$ has more $b\,^1\Pi_u$ character than $c_3\,^1\Pi_u$. This latter phenomenon arises because $c_3(0)$ is also perturbed by $b\,^1\Pi_u$ levels with $v \neq 5$, so that the apparent shortfall of c_3 diabatic character has merely been distributed to other mixed levels not plotted in Fig. 6.49. The rotational mixing of $^1\Pi_u$ and $^1\Sigma_u^+$ states is also evident for large J.

Chapter 7

Applications of the N_2 Model

A series of collaborative studies are presented in this chapter which incorporate the coupled-channels model of N_2 and form part of my doctoral research. An integration of theoretical analysis and laboratory measurement is essential to the refinement of both, and two examples of complementary studies are presented in Secs. 7.2 and 7.4. The ultimate practical application of the coupled-channels model is to photochemistry, and Secs. 7.1 and 7.3 discuss two important modelling studies of real-world N_2.

7.1 Source of nitrogen isotope anomaly in HCN in the atmosphere of Titan

Molecular nitrogen is the primary constituent of the atmosphere of the Saturnine moon Titan, and has a major effect on the photochemistry there. The isotopomeric ratio of $HC^{14}N/HC^{15}N$ within the Titanic atmosphere has been measured and falls in the range 60−110 [44, 115]. More recently, mass spectroscopy performed aboard the Cassini-Huygens probe has determined the isotopic ratio of $^{14}N/^{15}N$ in the form of N_2 to be 183±5 [124, 180]. The large difference between the isotopic compositions of HCN and N_2 is indicative of photochemical enrichment.

A modelling study is presented here which incorporates a radiative transfer model with the necessary photochemistry in order explain the observed isotope dependent production of HCN. My contribution to this paper are calculations of isotopomeric-dependent photodissociation cross sections of N_2, from which the altitude dependent production rates of atomic nitrogen are calculated. The high-precision of the N_2 coupled-channels model over a large wavelength range comprises a critical quantity in this study, as does its ability to generate equally reliable spectra for all isotopomers. My contribution to the published version of this work [106] lies in a simulation of N_2 photodissociation.

A necessary step in the formation of HCN is the production of atomic nitrogen, via the excitation and subsequent dissociation of N_2. Excitation may be engendered by solar radiation; or else following collisions with cosmic rays, free electrons, and ions. Both processes were found to be significant. Furthermore, the wavelength dependence of N_2 photoexcitation is sensitive to isotopic composition, whereas the chemical pathways from atomic nitrogen to HCN are not. Thus, selection prior to dissociation must explain the disparity in N_2 and HCN isotopic ratios.

A critical quantity is the *photodissociation rate*, defined to be the number of molecules dissociated per unit volume and per unit time, at a particular altitude, and integrated over all possible energies of the product atoms. Writing this mathematically, as a sum of transitions from all ground-state thermally-populated levels, j, with energy E_j, to all

electric-dipole accessible dissociation channels, i, with an excited energy $\nu + E_j$,

$$\text{photodissoc. rate} = \sum_{i,j} N_j(z) \int_{D_e - E_j}^{\infty} F(\nu, z)\sigma_{ij}(\nu)\eta_i(\nu + E_j)d\nu. \qquad (7.1)$$

The contribution from each transition $i \leftarrow j$ is calculated by integrating over all photon energies sufficient to exceed the dissociation energy, D_e, and scaling this by the number density of each ground-state level, $N_j(z)$. Here, z denotes depth from the top of the atmosphere. The integrand in Eq. (7.1) is a product of the ambient radiation flux, $F(\nu)$; $i \leftarrow j$ absorption cross section, $\sigma_{ij}(\nu)$; and the predissociation fraction of the excited state, $\eta_i(\nu + E_j)$.

At the top of the atmosphere, $F(\nu, 0)$ is proportional to a solar spectrum. At greater depth, $F(\nu, z)$ has been depleted by prior absorption; and decays approximately exponentially with respect to the column density, $\int_0^z N(z)dz$, where $N(z)$ is the altitude dependent N_2 density. The depth of radiation penetration gains wavelength dependence through the absorption cross section, which in the case of N_2 consists of many predissociation- and Doppler-broadened lines. The flux of photons corresponding to the central energies of these lines decay most rapidly with depth. Similarly, photon energies corresponding to transitions from ground-state levels with low populations, $N_j(z)$, will proceed deeper into the atmosphere. Mirroring the changing profile of radiation flux, the dominant contribution to photodissociation will be made by the strongest absorption features at high altitude, shifting towards the weaker at greater depth.

When calculating the rate of photodissociation arising from the transitions of $^{14}N^{15}N$, $N_j(z)$ will be lower than for the corresponding transitions in $^{14}N_2$, in approximate proportion to the relative isotopomeric abundances. Because of this, radiation sympathetic with the resonant energies of $^{14}N^{15}N$ which are not overlapped by $^{14}N_2$ will, on average, penetrate deeper than for $^{14}N_2$. Thus, the ratio of $^{14}N^{15}N/^{14}N_2$ absorption, and succeeding dissociation, will increase with atmospheric depth. The relative abundances of $^{15}N/^{14}N$ available for chemical reactions will then be greater at lower altitudes. This process is known as *photolytic fractionation*.

The coupled-channels model of N_2 is suitable for generating absorption cross sections for this application. Particularly, the isotopomeric independence of the model parameters ensures that the cross sections calculated for $^{14}N_2$ and $^{14}N^{15}N$ may be regarded with equal confidence. Modelled cross sections were generated for the two isotopomers, for energies between 100 000 and 124 000 cm^{-1}, for rotational transitions with $J \leq 30$, and at temperatures of 100, 150, 200 and 300 K.

Over a sufficiently large spectral range the integrated model cross sections for $^{14}N_2$ and $^{14}N^{15}N$ converge, despite the significant differences that occur for particular bands. This implies that spectroscopic accuracy, $< 1\,\text{cm}^{-1}$, is not required for this application and the extrapolation of the coupled-channels model to energies above the limit of its optimisation range is reasonable. The isotopomer dependent shifts of vibrational band heads for excited levels with $v > 0$, and reduced-mass dependent rotational-constants for all levels, are such that many $^{14}N^{15}N$ lines appear in the windows of the $^{14}N_2$ spectrum. This property permits a depth-dependent ratio of $^{14}N^{15}N/^{14}N_2$ dissociation rates as described above.

Figure 7.1 shows the modelled $^{14}N_2$ photodissociation cross section and also the ratio of $^{14}N^{15}N/^{14}N_2$ cross sections; rotational detail is not perceptible on such a broad scale. Deviations of this ratio from unity are widespread but, once a reduced resolution version is calculated, it is seen to consist of a series of dips, corresponding to vibrational band

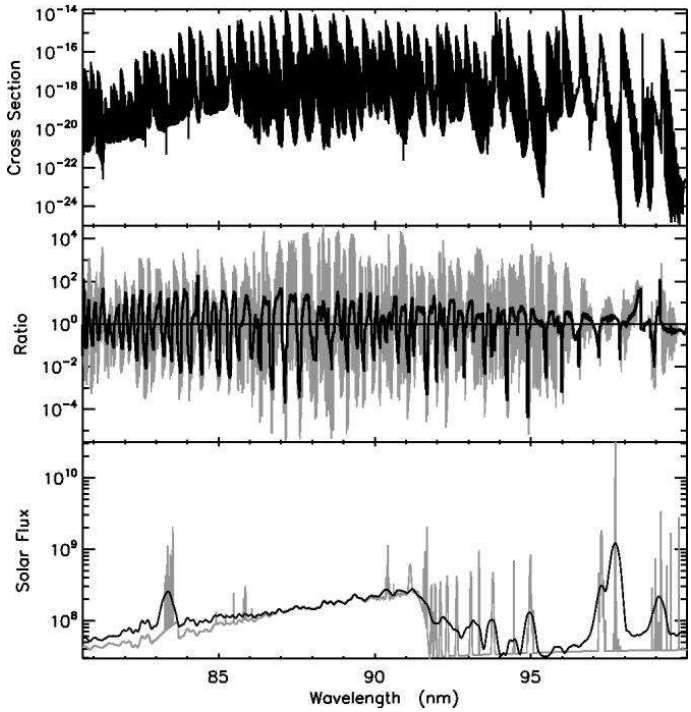

Figure 7.1: After Liang *et al.* [106]. *Top*: Modelled coupled-channels photodissociation cross section (cm^2) for $^{14}N_2$ at 150 K. *Middle*: Ratio of $^{14}N^{15}N/^{14}N_2$ photodissociation cross sections at 150 K, the light and dark curves have been smoothed to reduced resolutions of 0.003 nm and 0.1 nm, respectively. *Bottom*: Observed (low resolution, *dark curve*) and synthetic (high resolution, *light curve*) solar spectra (photons $\mathrm{cm}^{-2}\,\mathrm{s}^{-1}\,\mathrm{Å}^{-1}$), scaled at 1 AU (the mean Earth-Sun separation).

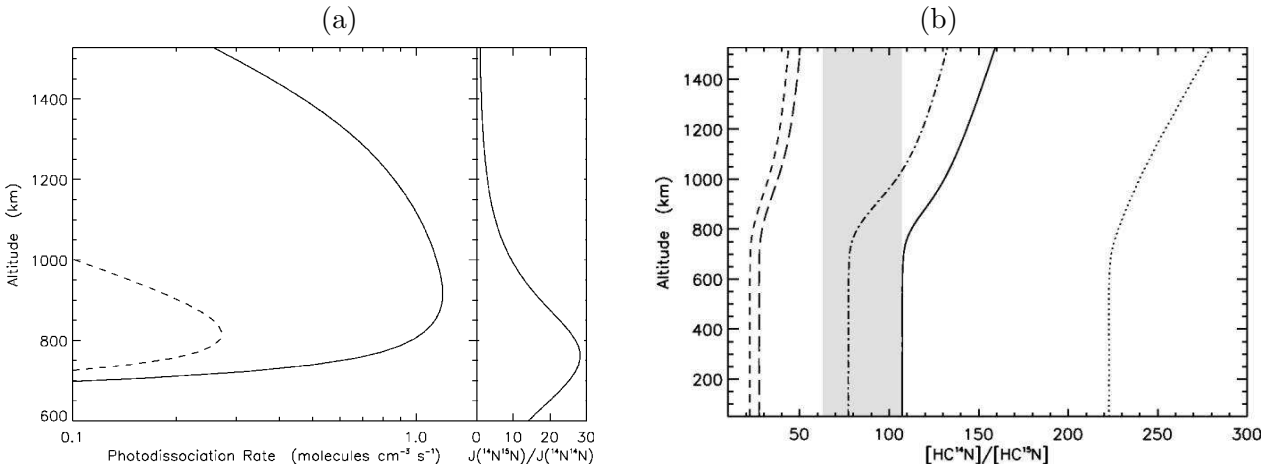

Figure 7.2: After Liang *et al.* [106]. *(a) Left:* Calculated photodissociation rates of $^{14}N_2$ (*solid curve*) and $^{14}N^{15}N$ (*dashed curve*) in Titan's atmosphere. *(a) Right:* Ratio of $^{14}N^{15}N/^{14}N_2$ photodissociation coefficients. That is, the product of radiation flux and absorption cross section, but not the isotopomeric abundances. *(b):* Ratio of $HC^{14}N$ to $HC^{15}N$ abundances calculated by alternative photochemical models: without N_2 photolytic fractionation (*dotted*); with photolytic fractionation determined from the coupled-channels cross sections (*short dashed*); with photolytic fractionation determined from zero-point-energy shifted cross sections (*long dashed*); and with additional atomic nitrogen flux (*solid and dashed-dotted*). The observational constraint on the relative abundance is shown by shading.

heads, and intervening broad peaks. The N_2 bands are predominantly red degraded and the $^{14}N^{15}N$ vibrational levels are shifted to lower energy, relative to $^{14}N_2$. Thus, on average, the $^{14}N^{15}N$ band heads are overlapped with the tail of $^{14}N_2$ bands, and the $^{14}N_2$ band heads are unobstructed; explaining the features observed in Fig. 7.1.

As discussed in Sec. 2.12, the coupled-channels cross sections do not immediately provided an estimate of the predissociation fraction, necessary for the calculation of the photodissociation rate in Eq. (7.1). The majority of N_2 levels excitable by extreme-ultraviolet radiation predissociate completely. Two exceptions to this are $b\,^1\Pi_u(v=1)$ and $c_4'\,^1\Sigma_u^+(v=0)$. For these levels, the coupled-channels photodissociation cross section was corrected in a line by line manner for the nonzero emission fraction. Emission rates were calculated for decay to all significant ground-state vibrational levels, as well as the predissociation rate for each excited level, and these were combined into a branching fraction using Eqs. (2.124) and (2.73).

Details of the chemical and radiative-transfer model are deferred to the published version of this work Liang *et al.* [106]. Here, the main conclusions are summarised. Figure 7.2(a) shows the photolytically-engendered enhancement of $^{14}N^{15}N$ photodissociation that occurs at large atmospheric depth relative to $^{14}N_2$, as predicted by the photochemical model. The principle result of this work is plotted in Fig. 7.2(b) which shows the altitude dependent fractional abundance of $HC^{14}N$ to $HC^{15}N$, for several variants of the photochemical model. Also plotted are the bounds of the observed fraction. Ignoring the effects of photolytic fractionation, the $HC^{14}N/HC^{15}N$ ratio lies well above the observations and even above the measured isotopic ratio of $^{14}N/^{15}N$ itself. The latter effect is induced by diffusive fractionation, whereby the abundance of the lighter N_2 isotopomer is enhanced above 800 km, which is also where the majority of HCN formation occurs. The inclusion of coupled-channels-modelled isotopomer dependent photodissociation reduces

the $HC^{14}N/HC^{15}N$ ratio to below the observed value. Thus, it was found necessary to include an additional N_2 dissociation pathway, that is, collisions with a flux of electrons and ions stemming from the Saturnian magnetosphere. This process is certainly isotopomer independent and its magnitude constitutes a free model parameter. Thus, the formation of a final photochemical model that agrees with the observed $HC^{14}N/HC^{15}N$ ratio also constrains the rate of collisional dissociation.

7.2 Radiative properties of $N_2\, c_4'\, {}^1\Sigma_u^+ - X\, {}^1\Sigma_g^+$

This section discusses new high-resolution laboratory measurements of N_2 emission following electron impact excitation, as well as a coupled-channels analysis of these results. There is a published version of this work [110] and my contribution resides in its modelling aspects.

The observed transitions were from $c_4'\, {}^1\Sigma_u^+$ to the ground state, $X\, {}^1\Sigma_g^+$; for the vibrational series $c_4'(v_i = 0) \rightarrow X(v_j = 0 - 3)$. In order to model the observed cross sections, overlapping bands arising from $b'\, {}^1\Sigma_u^+ \rightarrow$, $b\, {}^1\Pi_u \rightarrow$, $c_3\, {}^1\Pi_u \rightarrow$, and $o_3\, {}^1\Pi_u \rightarrow X\, {}^1\Sigma_g^+$ were considered. A few additional atomic-nitrogen lines were also accounted for.

A detailed description of the experimental setup is deferred to the appendix. Briefly, magnetically collimated electrons are accelerated to 20 or 100 eV and excite N_2, either flowing from a capillary array, or present as a constant pressure background gas. The resulting XUV fluorescence is dispersed by a grating and detected photoelectrically. Most spectra were recorded with a resolution of 300 Å FWHM (30 cm^{-1} FWHM)at 1000 Å (100 000 cm^{-1}). Additional measurements were made of $c_4'(v_i = 0) \rightarrow X(v_j = 0 - 3)$ with a resolution of 16 Å FWHM (1.6 cm^{-1} FWHM) by decreasing the spectrometers entrance and exit slit widths and operating the grating in its second order. Great care was taken to ensure that the spectra were recorded at sufficiently low column density that the re-absorption of emitted radiation was negligible.

The volumetric emission rate arising from decay from state i, to state j; occurring with transition energy ν_{ij}; is given by,

$$I_{ij} = g_i \eta_{ij}, \tag{7.2}$$

where g_i is the production rate of excited N_2 in state $|i\rangle$ following electron impact, and η_{ij} is the fraction of excited molecules that decay via emission to $|j\rangle$. If F is the flux of electrons, N_j the population density of ground-state level $|j\rangle$, and σ_{ij} the $i \leftarrow j$ electron excitation cross section then,

$$g_i = F \sum_j N_j \sigma_{ij}^e. \tag{7.3}$$

A functional form, corresponding to the modified Born approximation [108], was adopted for the electron excitation cross section, σ_{ij}^e. An appropriate set of parameters describing cross sections for the electronic transitions $c_4'\, {}^1\Sigma_u^+ - X\, {}^1\Sigma_g^+$ and $b\, {}^1\Pi_u - X\, {}^1\Sigma_g^+$ as a function of electron energy have been determined previously [1, 64]. Individual rovibrational transitions are excited in proportion to their optical oscillator strengths (f-values).

For a given total decay rate including predissociation, A_i, and particular $i \rightarrow j$ decay rate, A_{ij}, the $i \rightarrow j$ emission branching fraction is given by

$$\eta_{ij} = \frac{A_{ij}}{A_i^d + \sum_k A_{ik}}. \tag{7.4}$$

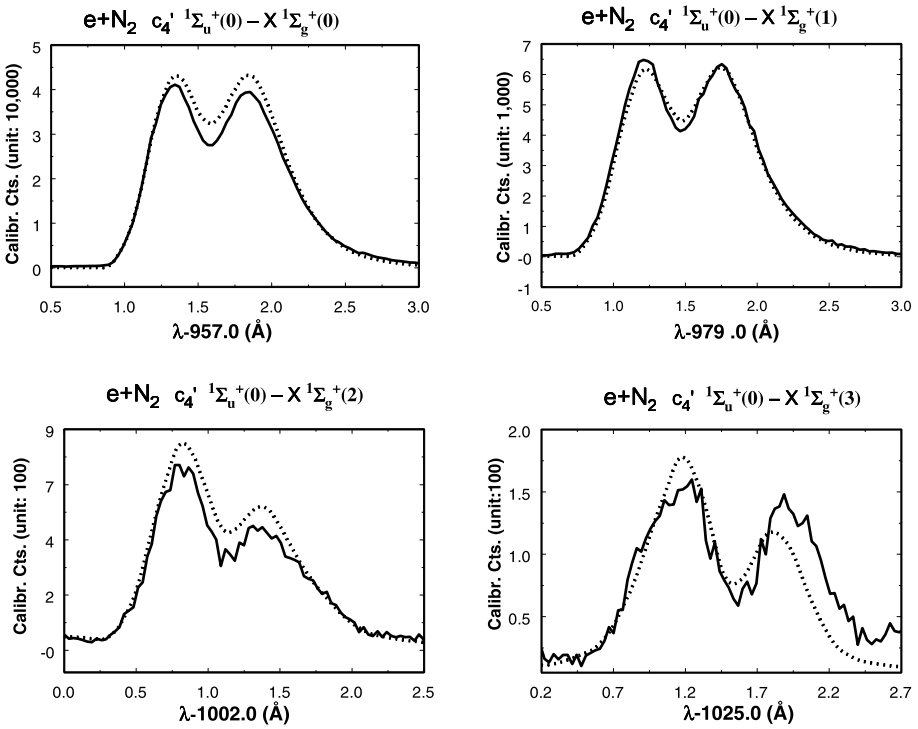

Figure 7.3: After Liu *et al.* [110]. *Solid curves:* Measured emission spectra of four N_2 emission bands. *Dotted curves:* Modelled spectra, these have been scaled by a single parameter to give a best fit for the integrated intensity of $c_4'(v_i = 0) \rightarrow X(v_j = 1)$.

The emission rate, A_{ij}, is related to the transition f-value, f_{ij}, by

$$A_{ij} = 0.667 \left(\frac{2J_j + 1}{2J_i + 1} \right) \nu_{ij}^2 f_{ij}. \tag{7.5}$$

Model values for f_{ij} may be determined for each rovibrational transition by fitting line parameters to the resonances that appear in the coupled-channels cross sections, as described in Sec. 2.12. Model f-values were calculated for transitions to ground-state levels with vibrational quantum number $v_j \leq 9$. The dissociation rate is also determined from the coupled-channels parameterised linewidths, Γ, according to the relations,

$$A_d = \hbar\Gamma. \tag{7.6}$$

The model electronic transition moments have magnitudes that are calibrated against the absolute f-values of Stark *et al.* [155] and those presented in Chap. 4. These room temperature absorption experiments involve transitions from $X(v_j = 0)$ only. The R dependencies of the transition moments are those of Spelsberg and Meyer [145]. Extending the coupled-channels model to calculations of f-values for transitions with $v_j > 0$ is valid only if the adopted R-dependencies are realistic over the radial extent of the ground-state wavefunction with largest v_j. As discussed below, sufficient new information has been obtained in the present study to experimentally determine a new R dependence for the $c_4' - X$ transition moment. This has a similar form to the *ab initio* calculations of Spelsberg and Meyer [145] and is valid over a larger range of R than the linear transition moment deduced in Sec. 6.5.5.

Once g_i and η_{ij} have been computed from Eq. (7.3) and Eq. (7.4), the intensity of each

$v_i \to v_j$	Exp.	CSE	CSE-noR	Reference
		Relative emission intensity		
$0 \to 0$	6.3(4)	6.8	7.8	Present work.
$0 \to 1$	1.0	1.0	1.0	Present work.
$0 \to 2$	0.099(9)	0.113	0.087	Present work.
$0 \to 3$	0.019(4)	0.018	0.016	Present work.
		Absorption f-value		
$0 \leftarrow 0$	0.138(14)	0.138	0.138	Stark *et al.* [155]
$1 \leftarrow 0$	0.0052(6)	0.0054	0.0063	Stark *et al.* [155]
$2 \leftarrow 0$	0.0012(1)	0.0011	0.0011	Stark *et al.* [157]
$3 \leftarrow 0$	0.0076(7)	0.0081	0.0080	Stark *et al.* [157]

Table 7.1: Emission intensities derived from the present work for bands $c'_4\, {}^1\Sigma_u^+(0) \to X\, {}^1\Sigma_g^+(v_j)$, relative to $v_j = 1$. These are compared with the coupled-channels model. Two calculations are shown, for a $c'_4 - X$ electronic transition moment with no internuclear-distance dependence, CSE-noR; and an optimised quadratic dependence, CSE. Also shown are similar comparisons with the absolute absorption f-values of Stark *et al.* [155] and Stark *et al.* [157].

emission line is computed from Eq. (7.2). A synthetic spectrum is constructed from these and coupled-channels calculated transition energies, which is then degraded according to the instrument resolution and compared with the experimental spectra. An overall scaling must be made to the experimental intensities because of the unknown detector sensitivity, electron flux, and N_2 column density. Thus, only the relative emission intensities of the measured transitions have been determined.

Individual rotational lines were not observed in the low-resolution measurements of $c'_4(0) \to X(0-3)$ reproduced in Fig. 7.3. All of the experimental spectra were scaled by a single factor, chosen to match the integrated intensity of $c'_4(0) \to X(1)$ to the model value. The relative emission intensities decrease rapidly with v_j. This is because $c'_4\, {}^1\Sigma_u^+$ and $X\, {}^1\Sigma_g^+$ have very similar potential-energy curves leading to a very small overlap of their radial-wavefunctions when $v_i \neq v_j$. The $\sim 250\times$ reduction in intensity for increasing v_j, and changes in the band profile are anticipated by the model spectra. The intensity of the $c'_4(0) \to X(3)$ P-branch, with wavelength $\geq 1026.6\,\text{Å}$, is underestimated by the coupled-channels model; as discussed in the article, this is probably due to overlapping atomic nitrogen transitions that are not included in the model cross sections.

High-resolution measurements have been made of two emission bands, $c'_4(0) \to X(1,2)$. The coupled-channels model shows good agreement with these, as well as those lines arising from $b'\, {}^1\Sigma_u^+(1) \to X(1,2)$. The overlapping of $c'_4(0) \to X(v_j)$ and $b'(1) \to X(v_j)$ for common v_j is not simply additive; the upper-states of these transitions have mixed electronic-wavefunctions, as discussed in Sec. 6.7.

By combining the known absolute absorption f-values of $c'_4(0-3) \leftarrow X(0)$ [155, 157] with the new relative f-values, there is sufficient information to experimentally determine the R dependence of the $c'_4 - X$ electronic transition moment. Each measured vibrational-transition constitutes a projection of the electronic transition moment, $R^e_{ij}(R)$, onto the vibrational overlap $\langle v_i | R^e_{ij}(R) | v_j \rangle$. A sufficiently large set of measured transition strengths can then be inverted to give the functional form of $R^e_{ij}(R)$. Here, the inversion is not performed directly, instead a quadratic form is assumed for $R^e_{ij}(R)$ with coefficients optimised to best match the available data, summarised in Tab. 7.1. Values of R between 1 and 1.27 Å are sampled by this data set. This range is limited by the lack of measurements for transitions with excited and ground states that are both vibrationally excited. The optimised

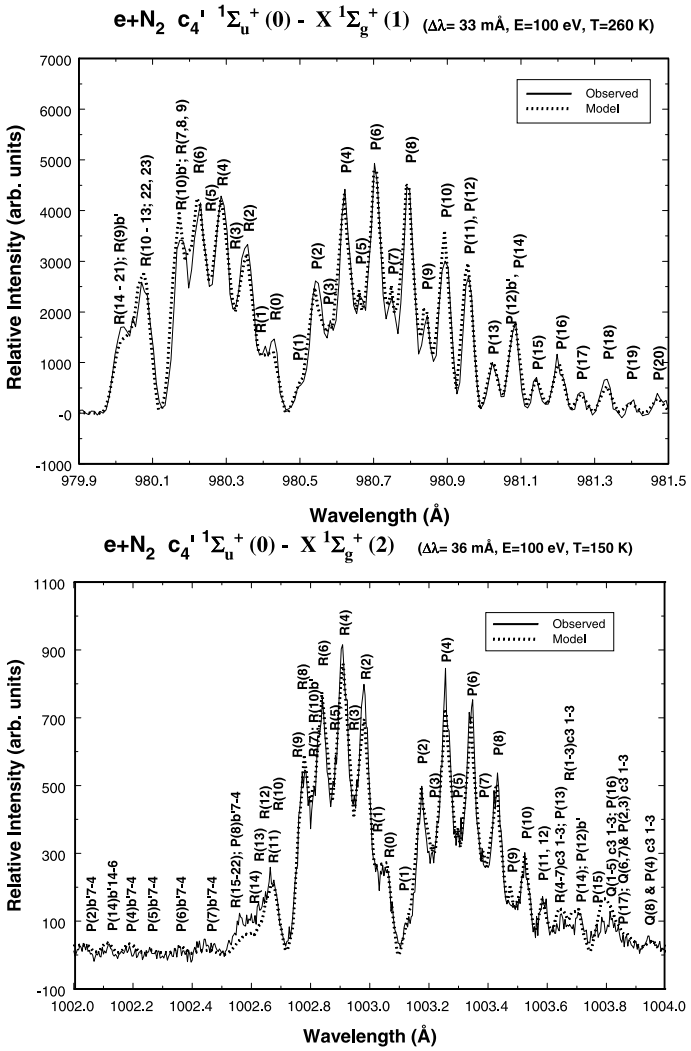

Figure 7.4: After Liu *et al.* [110]. *Solid curves:* High resolution measurements of two N_2 emission bands. *Dotted curves:* Model spectra. Lines arising from $b'\,{}^1\Sigma_u^+(v_i = 1) \rightarrow X(v_j = 1, 2)$ are labelled "b'". The modelled spectra have been scaled uniformly, and a rotational temperature of 260 K was found to best fit the experimental data.

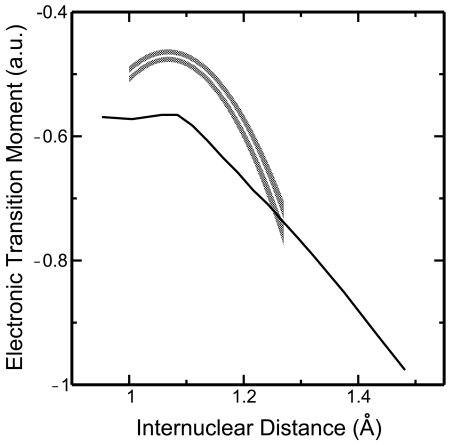

Figure 7.5: After Liu *et al.* [110]. *Shaded curve:* Experimentally determined diabatic $c_4' \, ^1\Sigma_u^+ - X \, ^1\Sigma_g^+$ electronic transition moment, the shading denotes the uncertainty in the fitted quadratic coefficients. *Solid curve:* The *ab initio* transition moment of Spelsberg and Meyer [145].

$c_4' - X$ electronic transition moment is,

$$R_{ij}^e(R) = -0.4702 - 6.620(R - 1.068)^2 \text{ for } 1 < R < 1.27, \tag{7.7}$$

where R has units of Å, and $R_{ij}^e(R)$ is in atomic units. This result is plotted Fig. 7.5 and has a similar shape to the *ab initio* calculation of Spelsberg and Meyer [145] but a lesser overall magnitude.

7.3 Analysis of terrestrial N_2 dayglow

The *Far Ultraviolet Spectroscopic Explorer* (FUSE) satellite was designed, primarily, to detect the presence of extrasolar deuterium. It has also made observations of the Earth's atmospheric airglow [37]. The primary (78%) constituent of the terrestrial upper-atmosphere is N_2. Ionisation of this by solar radiation generates large quantities of photoelectrons, which proceed to excite further N_2 into high-lying neutral states. The resultant emission of extreme-ultraviolet radiation is observed by FUSE, and is the subject of a new study presented here, and in a refereed form elsewhere [107]. My contribution to this work was in the calculation of N_2 absorption, emission, and predissociation rates.

The present analysis seeks to study the vibrational series $c_4' \, ^1\Sigma_u^+(v_i = 0) \rightarrow X \, ^1\Sigma_g^+(v_j = 0 - 9)$, employing FUSE measurements covering $904 - 994$, $987 - 1083$, and $1094 - 1188$ Å; with a spectral resolution of ~ 0.4 Å FWHM ($\sim 40\,\text{cm}^{-1}$ FWHM at 1000 Å). This resolution is not sufficient to identify N_2 rotational lines; although, the individual profiles of the separated $c_4'(0) \rightarrow X(v_j)$ P and R branches are resolved. These measurements have been previously analysed by Bishop *et al.* [7], but an improved calibration of the data set and the availability of the N_2 coupled-channels model warrant further analysis.

The present analysis methodology is similar to the laboratory study of Liu *et al.* [110], discussed in Sec. 7.2. A simulated coupled-channels emission spectrum of the $c_4'(0) \rightarrow X(v_j)$ bands is calculated and used to identify their relative intensities in the observed spectrum, as well as the presence of any overlapping spectral features. For each modelled transition, the volumetric production rate of emitted photons is calculated using Eqs. (7.2−7.6). The same coupled-channels-calculated transition energies, f-values, and

v_j	Model	FUSE	v_j	CSE
0	2115.4	24±7	12	5.63
1	314.6	100±9	13	2.53
2	35.6	35.3±3.6	14	0.619
3	6.39		15	0.023
4	3.36		16	0.218
5	3.63		17	0.403
6	5.73	5.2	18	0.227
7	8.56	7.3	19	0.019
8	10.8	11.1	20	0.037
9	11.8	11.6	$\sum(v_j > 20)$	~ 0.8
10	11.2		$\sum(v_j \geq 2)$	116.6
11	9.0		$\sum(v_j \geq 0)$	2547

Table 7.2: Observed (FUSE) emission brightness ($\mathrm{R\AA}^{-1}$) for the combined bands $c_4'\,{}^1\Sigma_u^+(v_i = 0) \rightarrow X\,{}^1\Sigma_g^+(v_j)$ and $b'\,{}^1\Sigma_u^+(v_i = 1) \rightarrow X\,{}^1\Sigma_g^+(v_j)$ for $v_j = 0 - 20$. Coupled-channels calculated (CSE) brightnesses have been scaled to best match the FUSE data for $v_j = 2, 8, 9$ and do not account for the effects of self absorption.

linewidths were input into these equations as employed in Sec. 7.2. Absolute agreement between model and spectra is not attainable due to the large number of uncalibrated atmospheric parameters, so the model spectra are scaled by a uniform factor in order to best match the observed brightness, measured in Rayleighs [60] per Angstrom ($\mathrm{R\AA}^{-1}$). However, when compared to the ideal laboratory conditions of Sec. 7.2, additional complications arise in the analysis of the FUSE spectra; these are discussed below.

The electron excitation cross section of Eq. (7.3) is dependent on the electronic-state of the excited molecule and the energy distribution of exciting electrons [108]. The necessary parameters governing the excitations $c_4'\,{}^1\Sigma_u^+ \leftarrow X\,{}^1\Sigma_g^+$ and $b\,{}^1\Pi_u \leftarrow X\,{}^1\Sigma_g^+$ have been previously determined [1, 64], and are assumed extensible to other electronic transitions of the same symmetry, i.e., $b'\,{}^1\Sigma_u^+ \leftarrow X\,{}^1\Sigma_g^+$ and $c_3\,{}^1\Pi_u \leftarrow X\,{}^1\Sigma_g^+$. The correctness of this assumption, and the energy distribution of exciting electrons could, in principle, be determined from the relative strengths of bands observed in the FUSE data set. However, the spectra analysed here are dominated by $c_4'(0) - X(v_j)$ and $b'(1) \rightarrow X(v_j)$ emission, and no definitive assessment of the electron energy distribution could be made from this restricted set of transitions. The temperature distribution of the emitting part of the atmosphere is not known, and a single value of $500 \pm 50\,\mathrm{K}$ was adopted in order to achieve the best agreement of model and experimental spectra.

There are many spectral features overlapping the $c_4'(0) \rightarrow X(v_j)$ transitions. Most significant is emission arising from $b'\,{}^1\Sigma_u^+(v_i = 1)$, which is rotationally mixed with $c_4'\,{}^1\Sigma_u^+(v_i = 0)$ and largely indistinguishable in the spectra studied here, leading to the designation below of a common band, $c_4'\,{}^1\Sigma_u^+(0) \sim b'\,{}^1\Sigma_u^+(1) - X\,{}^1\Sigma_g^+(v_j)$. Band models were also included for N_2 emission arising from $b'\,{}^1\Sigma_u^+(v_i = 0 - 14)$, $b\,{}^1\Pi_u(v_i = 0 - 14)$, $c_4'\,{}^1\Sigma_u^+(v_i = 0 - 4)$, and $c_3\,{}^1\Pi_u(v_i = 0 - 1)$. Rotational levels up to $J_i = 30$ and ground-state vibrational levels up to $v_j = 20$ were considered. Additionally, many unmodelled transition features appear in the spectra which are identified as attributable to atomic oxygen, nitrogen, and argon, as well as emission from carbon monoxide.

In Figs. 7.6 and 7.7, $c_4'(0) \rightarrow X(v_j = 2, 8, 9)$ and the P-branch of $c_4'(0) \rightarrow X(6)$ are free of overlapping features. The modelled spectra have been uniformly scaled to best match these bands and good agreement is observed even though the integrated band strengths vary by an order of magnitude. This calibration provides an estimate of the column integrated electron excitation rates to $c_4'\,{}^1\Sigma_u^+(v_i = 0)$ and $b'\,{}^1\Sigma_u^+(v_i = 1)$. Tab. 7.2 lists the

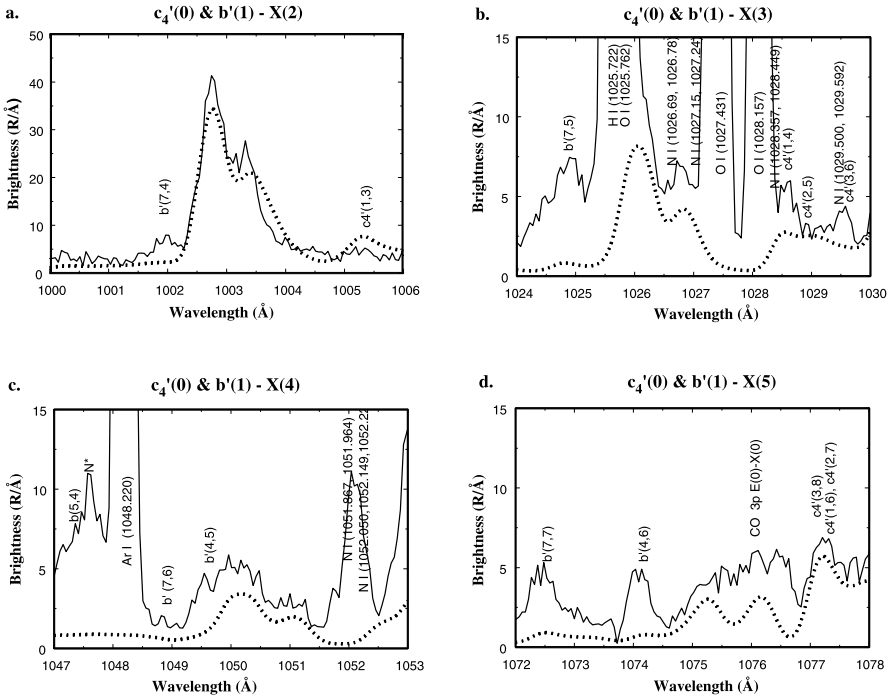

Figure 7.6: *Solid:* FUSE observations in the neighbourhood of the $c'_4(v_i = 0) \rightarrow X(v_j = 2 - 5)$ emission bands. *Dotted:* Coupled-channels spectra. After Liu *et al.* [107].

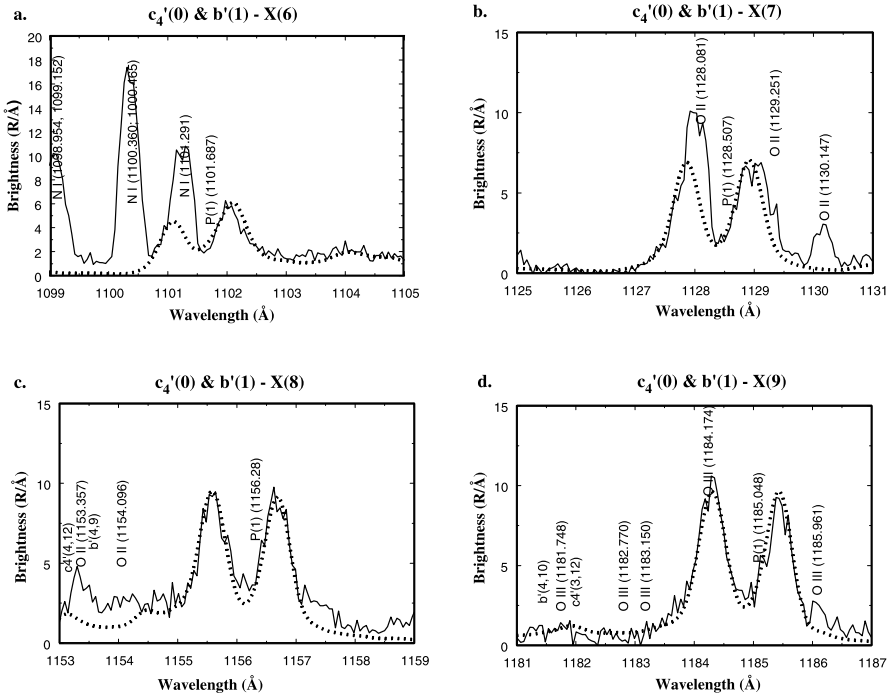

Figure 7.7: *Solid:* FUSE observations in the neighbourhood of the $c'_4(v_i = 0) \rightarrow X(v_j = 6 - 9)$ emission bands. *Dotted:* Coupled-channels spectra. After Liu *et al.* [107].

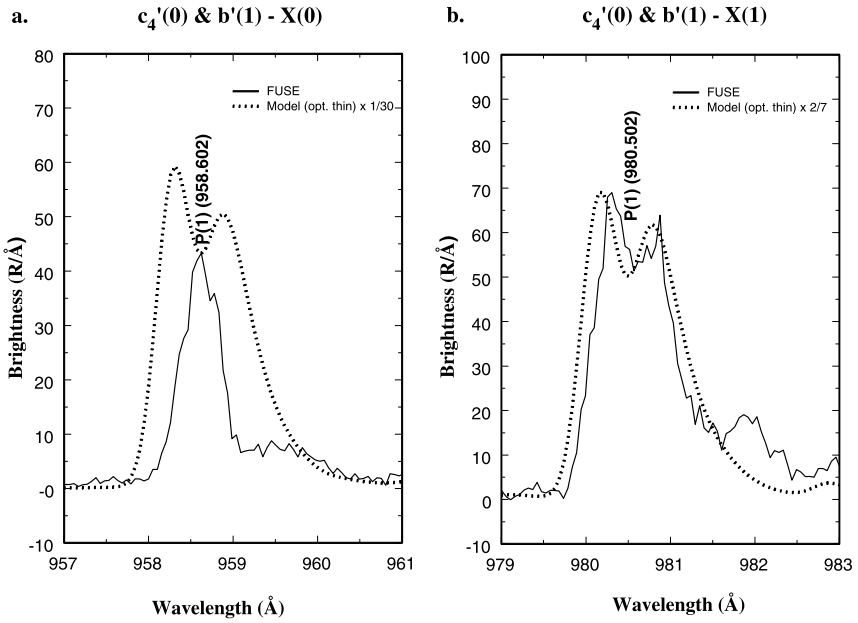

Figure 7.8: *Solid:* FUSE observations in the neighbourhood of the $c'_4(v_i = 0) \rightarrow X(v_j = 0 - 1)$ emission bands. *Dotted:* Model spectra. After Liu *et al.* [107].

integrated band intensities of the combined emission $c'_4\,{}^1\Sigma_u^+(0) \sim b'\,{}^1\Sigma_u^+(1) \rightarrow X\,{}^1\Sigma_g^+(v_j)$; also listed are the corresponding simulated quantities for $v_j \leq 20$. Emission to $v_j > 20$ is assumed negligible. The large discrepancy for $v_j = 0$ and 1 is accounted for below and the, otherwise, good agreement suggests that the modelled intensity of unmeasured emission channels are reliable.

In the laboratory study of Sec. 7.2, the effects of self absorption were avoided by adopting a low N_2 column density. In the atmosphere, self absorption of $c'_4(0) \rightarrow X(0)$ is unavoidable and leads to a significant decrease in observed emission via this channel [7, 116]. The large electronic transition moment for $c'_4\,{}^1\Sigma_u^+ - X\,{}^1\Sigma_g^+$, combined with a near-perfect overlap of the $v_i = 0$ and $v_j = 0$ vibrational wavefunctions, leads to $c'_4(v_i = 0) \rightarrow X(0)$ being the strongest absorption feature in the entire N_2 spectrum, and similarly dominant in low column density laboratory emission measurements. However, within the atmosphere, the same high transition strength also leads to significant re-absorption of the emitted radiation, exciting N_2 back into $c'_4(0)$ and, consequently, causing secondary emission. Multiple repetitions of the emission and absorption cycle will occur before any radiation attains the altitude of the FUSE spectrometer.

Three modifications will be made to the observed spectra by self absorption. First, if nonradiative decay processes are present, such as predissociation, then some energy will be lost during each re-absorption cycle and the observed emission intensity will be decreased. Second, some secondary emission will be to ground-state levels with $v_j > 0$, increasing the observed emission via these channels. Finally, the shape of the self absorbed band will be adjusted, depending on the f-values and predissociation fractions of the individual rotational levels. In the case of $c'_4(0)$, predissociation occurs because of rotational mixing with the $^1\Pi_u$ manifold (discussed in Sec. 3.4). The predissociation rate of $c'_4(0)$ then mirrors the $J_i(J_i + 1)$ dependence of rotational coupling, and the higher J_i transitions within the $c'_4(0) \rightarrow X(v_j)$ series will be less attenuated by self absorption.

Figure 7.8 demonstrates this effect of self absorption on $c'_4(0) \rightarrow X(0)$ and $c'_4(0) \rightarrow$

$X(1)$. The measured band profiles are narrower than the model predicts because the outer wings of high-rotational transitions have been attenuated. It is possible that $c'_4(0) \rightarrow X(2)$ shows a similar effect in Fig. 7.6. In the case of $c'_4(0) \rightarrow X(0)$ all rotational lines have disappeared aside from the $P(1)$ line, which corresponds to the least predissociated $c'_4(0)$ rotational-level, with $J_i = 0$. Because of self absorption, the integrated strength of $c'_4(0) \rightarrow X(0)$ is only 11% of the model prediction, when the latter is calibrated by the FUSE measurements of $c'_4(0) \rightarrow X(v_j = 2, 8, 9)$. Similarly, $c'_4(0) \rightarrow X(1)$ presents only 31% of the expected strength.

7.4 Tuning out vibrational levels in molecular electron energy-loss spectra

The coupled-channels model of N_2 described by this thesis was constructed in order to reproduce optical absorption and emission spectra. However, the excited- and ground-state wavefunctions calculated by the coupled-channels model are quite general and, in principle, the optical-specific part of the model is restricted to the electronic transition moment. Here, the coupled-channels wavefunctions and modified transition moments are used to explain new electron energy-loss spectra. A similar coupled-channels model has been constructed by Lewis *et al.* [95], concerned with the electron-impact excitation of O_2.

Details of the experimental apparatus used to measure the electron energy-loss spectra are given in Lewis *et al.* [95] and Khakoo *et al.* [77]. Briefly, a monochromatic beam of electrons impinges on a low-density room temperature beam of N_2, and subsequently a movable hemispherical electron analyser determines the energy distribution of scattered electrons at a range of scattering angles. The measurements utilised here were made with incident energies of $E_0 = 30$, 50 and 100 eV (242 000, 403 000 and 807 000 cm^{-1}; respectively) and at multiple scattering angles from 1° to 90°. The intensity of scattered electrons with energy losses from $E = 12.0 - 13.82$ eV (96 800 − 111 500 cm^{-1}) were detected by scanning the acceptance energy of the electron analyser. The energy lost by the scattered electron is transferred to the N_2 target and leads to a combination of electronic, vibrational, and rotational excitation.

The resolution of the spectrometer was 40 meV FWHM (320 cm^{-1} FWHM), and was sufficient to resolve some bands individually as well as determine their integrated cross sections. For overlapping features, it was necessary to fit a model spectrum to the experimental scans by adjusting the strengths of uniformly shaped peaks fixed at the known energies of the observed bands. The strengths of individual rotational excitations were not considered because the resolution FWHM of the instrument is significantly greater than the extent of the rotational distribution of each band. The experimental instrument function defines the shape of each model band and was determined by fitting an analytical form to the isolated feature arising from excitation to $a''\,^1\Sigma_g^+(v = 0)$. In the range of measured energy loss, dipole-allowed transitions are present terminating on $b\,^1\Pi_u(v = 0 - 13)$, $c_3\,^1\Pi_u(0 - 3)$, $o_3\,^1\Pi_u(0 - 2)$, $b'\,^1\Sigma_u^+(0 - 10)$, and $c'_4\,^1\Sigma_u^+(0 - 3)$; as well as dipole-forbidden bands involving $a''\,^1\Sigma_g^+(0 - 1)$, $G_3\,^3\Pi_u(0 - 3)$, $F_3\,^3\Pi_u(0 - 3)$, and $D\,^3\Sigma_u^+(1 - 4)$. The confidence with which the observed cross sections can be distributed over these bands is variable. Figure 7.9 shows example energy-loss spectra for two different scattering angles.

The N_2 coupled-channels model has been used to calculate generalised vibrational oscillator-strengths (GVOSs) that reproduce those deduced from the electron energy-loss spectra. The theory of GVOS and its critical governing-parameter, the momentum trans-

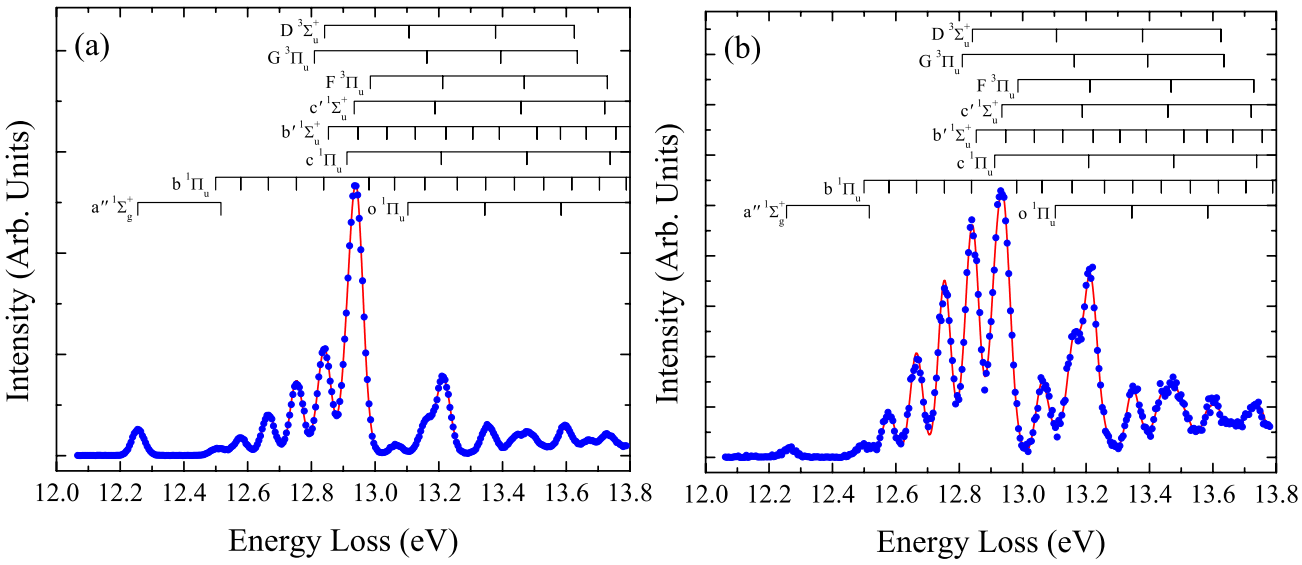

Figure 7.9: After Khakoo *et al.* [77]. *(a):* Electron energy-loss spectrum arising from incident electrons with $E_0 = 50\,\text{eV}$ scattered at 3°. *(b):* Scattered at 20°. The locations of N_2 bands in this region are also plotted.

ferred during scattering, are outlined in Sec. 2.9.1. The adiabatic generalised electronic transition moment (GETM) of Sec. 2.9.1, $\mathcal{M}_j^{AN}(K;R)$, has been substituted in the present application by a set of diabatic transition moments, $\mathcal{M}_j^{d}(K;R)$, in line with the diabatic formulation of the coupled-channels model. This set includes excitation from the ground state to all excited levels, j, which are electric-dipole accessible and of $^1\Pi_u$ symmetry. That is, the valence state $b\,^1\Pi_u$, and Rydberg states $c_3\,^1\Pi_u$ and $o_3\,^1\Pi_u$.

Each GETM has been derived from the corresponding optical transition moment and subsequently altered by means of a single adjustable parameter, the relative scaling of Rydberg–valence GETMs. In this way the experimental relative intensities of many observed $^1\Pi_u \leftarrow X$ bands are reproduced, for a range of nonzero momentum transfer.

7.4.1 Experimental generalised oscillator-strengths

Some of the $^1\Pi_u \leftarrow X\,^1\Sigma_g^+(v=0)$ bands present have been singled out for a detailed appraisal of the $E_0 = 100\,\text{eV}$ spectra. These occur between 12.5 and 13.7 eV and terminate on the excited levels $b(0-13)$, $c_3(0-2)$, and $o_3(0-1)$. Under the assumption that the energy-loss intensity contribution from $^3\Pi_u$ and $^3\Sigma_u^+$ states is suppressed at this high value of E_0, the respective GVOS of the $^1\Pi_u$ bands have all been individually determined from the energy loss spectrum, apart from $b(9)$ and $o_3(1)$, which are treated as an integrated pair.

Figure 7.10 shows the measured GVOS of these bands for $K^2 < 1.5$, normalised to the subsequently modelled GVOS of $b(2)$. Also plotted are the $J = 0$ optical oscillator-strengths of Stark *et al.* [155] and the electron energy-loss measurements of Geiger and Schröder [38]. The former definitively corresponds to $K^2 = 0$ and the kinematic conditions of the latter lead to $K^2 \simeq 4\times10^{-3}$ a.u., which is effectively equivalent to optical conditions. The measurements of Stark *et al.* [155] are at high resolution and there is no confusion between the partition of oscillator strength between bands. However, the $J = 0$ character

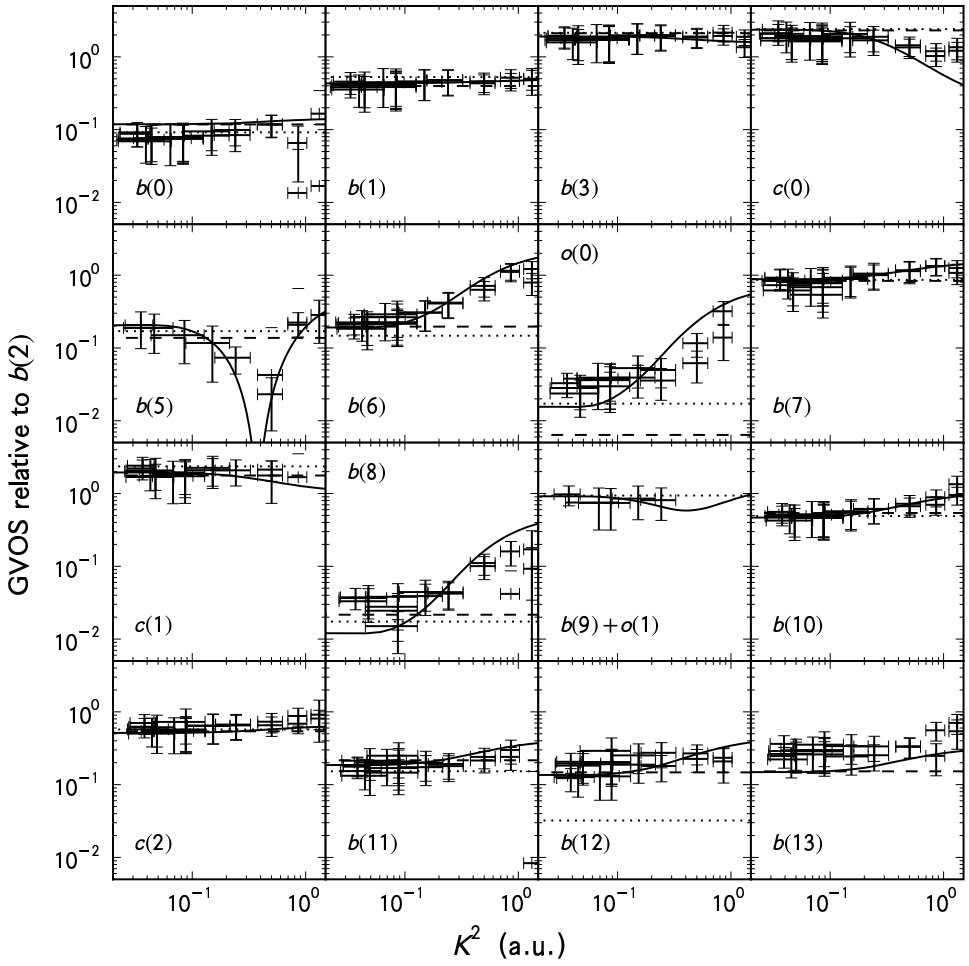

Figure 7.10: *Error bars:* GVOS derived from the experimental energy loss spectra. *Solid line:* GVOS calculated by the optimised coupled-channels model. *Dashed line:* Optical oscillator-strengths of Stark *et al.* [155]. *Dotted line:* Electron-scattering-derived optical oscillator-strengths of Geiger and Schröder [38]. All quantities are plotted relative to the modelled GVOS of $b(2)$.

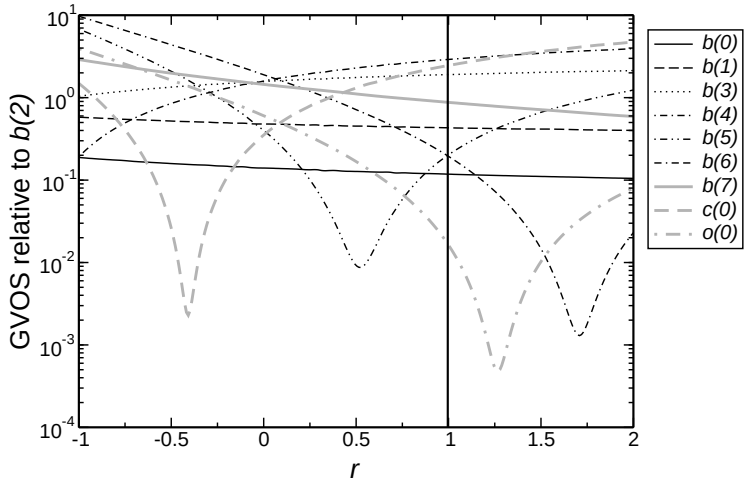

Figure 7.11: Calculated GVOSs of selected bands, relative to $b(2)$. The independent variable, r, is scanned by modifying the GETMs of the Rydberg c_3- and o_3-states by a common factor. The vertical line corresponds to optical conditions.

of this data set is not strictly comparable with the band averaged values of the present measurements or those of Geiger and Schröder [38]. Thus, the inconsistency between electronic and optical measurements of the $K^2 = 0$ GVOS of $o_3(0)$ may be explained by a rapid increase in oscillator strength with J, observed by Stark *et al.* [155], but not reflected in their $J = 0$ oscillator strength. The anomalously low relative GVOS accorded to $b(12)$ by Geiger and Schröder [38] cannot be explained in this way and may be due to an incorrect partitioning of the energy-loss cross section between bands.

The current measurements of the $b(2)$ GVOS span values of K^2 from 0.034 to 3.2 a.u., and show a decrease over this range, from 0.017 ± 0.006 to 0.0011 ± 0.0006. The removal of this order-of-magnitude variation from the data plotted in Fig. 7.10 allows for the observation of more subtle effects.

7.4.2 Coupled-channels generalised oscillator-strengths

The f-parity N_2 coupled-channels model constructed in Sec. 6.4 was adapted for the present application, and required the modification of two defining parameters during extension to the case of finite momentum transfer. These parameters uniformly scale the $b - X$, $c_3 - X$, and $o_3 - X$ optical electronic transition moments to give the GETMs $\mathcal{M}^d_b(K;R)$, $\mathcal{M}^d_{c_3}(K;R)$, and $\mathcal{M}^d_{o_3}(K;R)$. Ultimately it was found to be impossible to uniquely determine scaling factors for the $c_3 - X$ and $o_3 - X$ GETMs because of the poor discrimination of o_3 levels in the energy-loss spectra; instead, these were scaled by a common factor. This assumption is defended on the grounds that both are Rydberg states with one particularly-reactive electron at large radial distance, and will share common electron scattering behaviour at sufficiently small momentum transfer relative to the valence b-state, with no remote electron. An instructive parameter, r, is the scaling ratio of Rydberg to valence GETMs, relative to their precursor optical transition moments.

Figure 7.11 shows calculated GVOSs for a range of r and a selection of $^1\Pi_u$ bands, and plotted relative to the GVOS of $b(2)$. A value of $r = 1$ corresponds to an unmodified coupled-channels model and relates to optical conditions. A normalisation was adopted relative to $b(2)$ because this level is of relatively pure b-state valence electronic character, and removing this dependence serves to further emphasise the occurrence of quantum

interference between GETMs.

Several of the bands plotted in Fig. 7.11 possess rotationally-dependent oscillator strengths. In particular, the strength of $o_3(0) \leftarrow X(0)$ increases by an order of magnitude between $J = 1$ and 22, as does $b(5) \leftarrow X(0)$ between $J = 1$ and 20 [155]. In order to calculate strengths that are comparable to the band averaged energy-loss measurements, separate model line strengths are calculated for the $Q(4)$, $Q(6)$, $Q(8)$, $Q(10)$, and $Q(12)$ rotational transitions. Averaging these gives an oscillator strength that is directly comparable with the experiment. For this averaging, a Boltzmann distribution of ground-state levels is adopted, assuming a temperature of 300 K.

The contributions of P- and R-branch transitions are neglected in these calculations, even though Stark *et al.* [155] have observed significant perturbations in the oscillator strengths of these branches, which are also reproduced by the full e-parity coupled-channels model. This omission is made feasible by the fortuitous occurrence of nearly equal, but opposite, perturbations in the P- and R-branch oscillator-strengths relative to the Q. This is a common feature of ${}^1\Pi_u \sim {}^1\Sigma_u^+$ rotational perturbations, and lead to a band averaged oscillator strength which is largely independent of the observed P- and R-branch differences.

The modelled GVOSs of Fig. 7.11 reveal transitions involving $b(0-4)$ and $b(7)$ which only gradually vary with r, whereas those to $b(5)$, $b(6)$, $c_3(0)$ and $o_3(0)$ display deep minima where the $b - X$ and $c_3 - X$ GETMs approach complete cancellation. It is not expected that the GETM of either state will change sign as K^2 is increased, so the interference minimum of $c_3(0)$ is unlikely to be observed. Furthermore, it is expected that the Rydberg state GETMs will falloff more rapidly with increasing K^2 than for the valence states, disinclining the observation of minima for $b(6)$ and $o_3(0)$. The latter expectation arises because the large orbital-radius of the outermost single-electron molecular orbital from a Rydberg state makes these particularly sensitive to the spatially-inhomogeneous electric field induced by a scattering electron.

A minimum is actually observed in the $b(5)$ experimental relative-GVOS plotted in Fig. 7.10, as well as under $E_0 = 50$ and 30 eV scattering conditions. Effectively, the excitation of $b(5)$ have been *tuned out*, simply by adjusting the momentum transfer parameter. The presence, and sense, of the variation in the other observed relative-GVOSs in Fig. 7.10 are also in qualitative agreement with Fig. 7.11, assuming r is anti-dependent on K^2.

7.4.3 Optimised generalised electronic transition moments

There is sufficient experimental information to attempt a quantitative assessment of the variation of model GETMs with increasing momentum transfer. To this end, the $b - X$, $c_3 - X$, and $o_3 - X$ electronic transition moments were scaled to best fit the observed GVOSs of $b(2)$ and $b(5)$ for a range of K^2, and $E_0 = 100$ eV. The $c_3 - X$, and $o_3 - X$ GETMs were scaled by a common factor during this optimisation.

The isolated $b(2)$ level was selected as a constraint because it provides a reliable measure of the $b - X$ GETM, independent of the Rydberg states; whereas the pronounced interference observed for the $b(5)$ level provides a constraint on the Rydberg$-X$ GETMs. The optimised scaling factors were then smoothly interpolated in order to reduce the effect of experimental noise. The optimised GETMs plotted in Fig. 7.12(a) decrease monotonically with increasing K^2, and more quickly for the Rydberg states. The smoothness of the optimised GETMs is deceptive, an absolute error of approximately ± 0.1 is estimated for the scaling factors plotted in Fig. 7.12(a). This uncertainty arises from experimen-

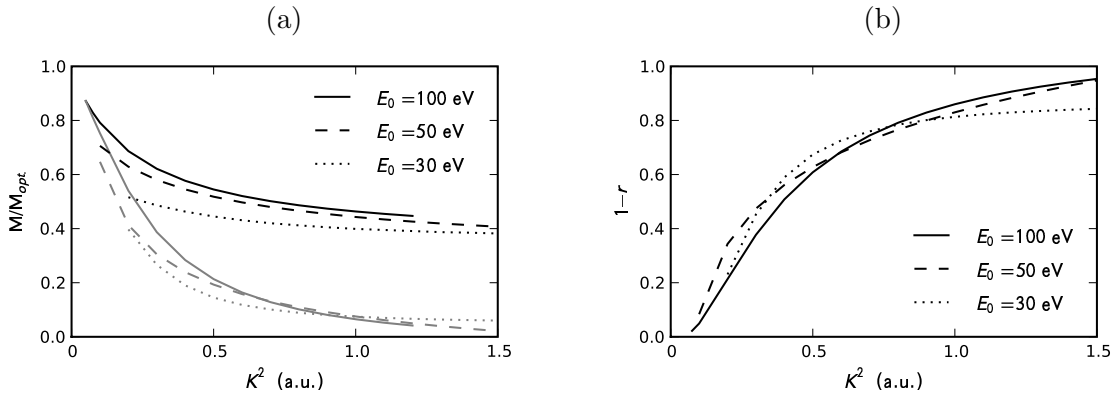

Figure 7.12: *(a):* Scaling of optical transition moments necessary to reproduce the observed GVOS of $b(2)-X$ and $b(5)-X$. For the three cases of $E_0 = 100$, 50, and 30 eV; the scaling of $\mathcal{M}_b^d$ relative to the optical case is plotted in black, and the common scaling of $\mathcal{M}_{c_3}^d$ and $\mathcal{M}_{o_3}^d$ is plotted in grey. *(b):* Relationship between $1-r$ and momentum transfer for the scattering of $E_0 = 100$, 50 and 30 eV electrons. Here, r is the ratio of Rydberg to valence state GETMs, relative to optical conditions.

tal noise, an imperfect division of spectral intensity between bands, and the neglect of rotationally-perturbing $^1\Sigma_u^+$ states in the f-parity model.

Figure 7.10 shows a high level of agreement between the experimental and modelled GETMs for $E_0 = 100$ eV. Particularly encouraging is the large and correctly-modelled variation in relative GVOS observed for $b(6)$ and $b(8)$, which can only be effected by quantum interference induced by a mixed electronic-character. Furthermore, the calculated and observed relative GVOS of $o_3(0)$ is seen to increase with K^2 despite the rapidly decreasing o_3-state GETM, also indicating the presence of quantum interference. None of these effects were referenced during the optimisation procedure.

Theoretical GETMs were also determined from the GVOS measurements with $E_0 =$ 50 and 30 eV, and a similar level of model-experiment agreement was found as for the $E_0 = 100$ eV case. The functional decreases with increasing momentum transfer of these optimised GETM scaling factors are also plotted in Fig. 7.12(a). It was not possible to perform measurements for the lowest values of K^2 with scattering energies of $E_0 = 50$ and 30 eV.

In all cases the GETMs of the Rydberg states decrease faster than for the valence state, and the lower intensities observed for decreasing E_0 subsequently appear as weaker model GETMs. The latter trend points to an inapplicability of the Born approximation, which would require that the GVOS be independent of all scattering parameters apart from the momentum transfer. It remains true, however, that the GVOS will approach optical conditions in the limit of small K^2 for all cases [102].

Finally, Fig. 7.12(b) shows the ratio of the optimised scaling of Rydberg to valence GETMs. The estimated uncertainty in r stands at ± 0.14. The three curves in Fig. 7.12(b) show a similar rate of fall-off in r with respect to K^2. This similarity arises despite the poor fulfilment's of the Born approximation, and reflects the particularly strong interaction occurring between the scattered electron and the large-orbital-radius outermost electron of the Rydberg states. These curves fall slightly below those determined from mixed Rydberg/valence bands observed in the O_2 energy-loss spectra of Lewis *et al.* [102], but otherwise appear very similar.

Conclusions

The major achievement of this thesis has been the construction of a new model of the N_2 excited (and ground) states, the final product of which is a photodissociation cross section applicable to the XUV excitation of $^{14}N_2$, $^{14}N^{15}N$, and $^{15}N_2$ at any temperature. The motivations for this undertaking were twofold: an elucidation of the quantum physics governing the N_2 molecule, particularly with regard to its electric-dipole-forbidden states and the phenomenon of predissociation; and to produce synthetic spectra capable of fulfilling a particular demand from photochemical modellers, once and for all.

Beyond the rigorously conserved quantities of energy, angular-momentum, and parity, the raw output of the coupled-channels model is indivisible. That is, the concept of the Born-Oppenheimer electronic state and its accompanying potential-energy curve has been superseded, and the Schrödinger equation solved in its coupled form. There is an element of the "black box" to the resulting model output, and calculated resonances must be assigned approximate electronic-vibrational identities, largely using the same pattern-matching as is done for experimental spectra. Rather than representing a limitation, this aspect of the coupled-channels technique reflects the physical realism of its formulation, and is key to its predictive power.

It is convenient to reduce resonances appearing in the modelled cross section to a parameterisation of transition energy, oscillator strength, and predissociation linewidth; and these quantities have been used to guide the formulation of the model and validate its efficacy. Various quantified measures of model accuracy are listed in Chap. 6, and plotted exhaustively in App. A.3. However, an ultimate test of the model's veracity is a direct pointwise comparison of the calculated photodissociation cross section with an equivalent experimental laboratory measurement, or its success in explaining natural phenomena in the field. That is, the precise lineshapes of calculated resonances are frequently significant, as well as the elaborate complexes formed by overlapping lines and the background continuum itself.

The vast majority of the observed absorption lines appearing in the XUV spectrum of N_2 are attributed to two excited valence states and three series of Rydberg states, distributed over the $^1\Pi_u$ and $^1\Sigma_u^+$ symmetries. The potential-energy curves and homogeneous interactions of these critical states have been determined previously to very-high accuracy [145]. These have been improved upon here, following a reassessment guided by an updated data base of experimental information. Two N_2 Rydberg series, $c_n\,^1\Pi_u$ and $c'_{n+1}\,^1\Sigma_u^+$, are part of an np-complex and their resultant heterogeneous interaction has been previously treated [32, 53, 183]. However, a substantially improved treatment of $^1\Pi_u \sim {}^1\Sigma_u^+$ coupling has been achieved here, due to the simultaneous analysis of many interactions over a broad range of levels, and the inclusion of heterogeneous interactions other than those mixing $c_n\,^1\Pi_u$ and $c'_{n+1}\,^1\Sigma_u^+$.

One of the more surprising findings reported here arises from the large magnitude determined for the $o_3\,{}^1\Pi_u \sim b'\,{}^1\Sigma_u^+$ interaction, assumed to be R-independent. However, the chosen model representation of $b'\,{}^1\Sigma_u^+$ is of mixed and R-dependent configuration, as is likely to be the matrix element governing its mixing with $o_3\,{}^1\Pi_u$. Accordingly, this interaction warrants further study, whether by coupled-channels, *ab initio*, or experimental means.

A further novelty of this work has been the inclusion of the $n = 4$ level of the $c_n\,{}^1\Pi_u$ Rydberg series, and its heterogeneous interaction with $c'_{n+1}\,{}^1\Sigma_u^+$. With this addition, all singlet dipole-allowed states are included in the model up to an energy of $119\,800\,\mathrm{cm}^{-1}$, where the $n = 5$ members occur. An extrapolation above this energy is reasonable given that the various interactions of Rydberg states with the ground state and other excited levels progressively reduce in magnitude for increasing n. Nevertheless the truncation of the Rydberg series makes it impossible for the model to reproduce some perturbations in which higher-n levels participate, and their oscillator strength is inevitably neglected. An expansion of the coupled-channels basis set to include higher Rydberg states would then be of value. Such an endeavour would be aided by the increasing similarity of Rydberg potential-energy curves for increasing n, and a simplification of their interactions with other states. However, the ultimate model would require an infinite progression of Rydberg states, and is inherently unattainable by means of the coupled-channels technique. Another formalism, the multi-channel quantum-defect theory [119, 120], provides rigorous closure when modelling an infinite Rydberg series, and may be applicable to the N_2 problem.

The dissociative states and Rydberg series' studied here are also relevant to the dissociative recombination [5, 42, 43] of N_2^+. In this case a highly-excited and shortlived N_2 molecule is formed following the attachment of a free electron. If predissociation successfully competes with preionisation then neutral atoms will be generated. The coupled-channels formulism adopted here could be used to model this phenomenon and lead to potentially useful results concerning its isotopomeric branching ratio and the distribution of final atomic states. However, the highly-excited states involved are not reproduced by the current model formulation.

Overall, the vast majority of ${}^1\Pi_u$ and ${}^1\Sigma_u^+$ electronic-vibrational-rotational term values with energies between 100 000 and $122\,000\,\mathrm{cm}^{-1}$ are reproduced by the N_2 model to within $1\,\mathrm{cm}^{-1}$ of their known values. That is, the dominant portion of excited states accessible by XUV photoabsorption are now reproducible to spectroscopic accuracy. Alternative theoretical techniques, or a more specific coupled-channels model, are capable of still-higher precision when limited to a smaller set of levels, but the objective of this thesis has been a comprehensive model with broad applicability. Furthermore, the specification of some of the more subtle state interactions requires the assessment of multiple perturbations throughout the spectrum. These can only be analysed by a model that is, at once, global and accurate.

Electronic-transition moments governing ${}^1\Pi_u - X$ and ${}^1\Sigma_u^+ - X$ transitions are deduced here, and extend the model to the study of optical absorption and emission. Previous *ab initio* and empirical transition moments [49, 145] are improved upon by the inclusion of heterogeneous interactions and the guidance of an enhanced data base of experimental f-values. The final model convincingly reproduces the strengths of all transitions for which measurements exist, that is, covering almost all vibrational bands between 100 000 and $118\,500\,\mathrm{cm}^{-1}$; including the dramatic vibrational and rotational variation of f-values therein, and for emission to excited ground-states vibrational levels. A fascinating exten-

sion of the photoabsorption model has been to the electron-impact excitation of N_2, where an alteration of the transition moments is sufficient to reproduce excitation strengths under kinematic conditions which are far from optical. This has been possible because the coupled excited-state wavefunctions are physically realistic stationary-states of the molecule, and therefore quite general.

The model of $^3\Pi_u$ states presented here was initially studied separately from the singlet levels. Far fewer observations have been made of these states than for the singlet case, and the established picture of their interaction is less certain. It was necessary to simultaneously utilise all known $^3\Pi_u$ term origins, rotational constants, and predissociation linewidths to guide the general formulation of a $^3\Pi_u$ model and, finally, its specific parameters. Eventually, two valence and two Rydberg states were included, and all experimental data concerning them, covering energies from 88 000 to 111 000 cm^{-1}, is well reproduced by the final model. However, there remains scope to more accurately ascertain the magnitudes of some of the critical interactions, as well as include further $^3\Pi_u$ states at higher energies. Further progress in this direction would benefit from new data regarding these states.

A precise reproduction of transition energies and line strengths is of significant value, but the fusion of singlet and dissociative triplet states is the critical feature which allows the coupled-channels model to make a real contribution to the efforts of photochemical modellers. This has been accomplished, and the overall picture of $^1\Pi_u$ predissociation induced by $^3\Pi_u$ states, and including its dramatic vibrational dependence, is now essentially complete for energies up to 111 000 cm^{-1}. The observed predissociation has been shown to be reliant on a coupled treatment of $^1\Pi_u$ and $^3\Pi_u$ states involving multiple spin-orbit interactions which mix the symmetries. It would likely have been impossible to deduce values for all of the necessary interactions without the analytical power of the coupled-channels model. One unexpected result arises from a peculiarity of $b\,^1\Pi_u(v = 9, 10)$ linewidths, which has been explained here by the inclusion of an alternative predissociation channel, via the unbound state $^3\Sigma_u^+$, which has now been incorporated into the coupled-channels model.

The finer details of rotationally-dependent $^1\Pi_u$ predissociation are qualitatively reproduced by the model. The discrepancies that occur are attributable to $^1\Pi_u \sim {}^3\Pi_u$ level crossings where the sensitivity to the $^3\Pi_u$ model parameters is heightened. A future joint-optimisation of $^1\Pi_u$ and $^3\Pi_u$ states will hopefully allow a more precise specification of critical parameters, and remove these remaining inconsistencies.

An important project for the future is an elucidation of the predissociation mechanism of $^1\Sigma_u^+$ states. The current model works well where the heterogeneous interactions of $^1\Pi_u$ states dominates this mechanism, but $^1\Sigma_u^+ \sim {}^3\Pi_u$ spin-orbit coupling, and the effects of unmodelled $^3\Sigma_u^+$ states play a dominant role elsewhere. The determination of these factors awaits new experimental measurements of $^1\Sigma_u^+$ predissociation linewidths. A beginning of this work is included here where the level energies and predissociation of $D\,^3\Sigma_u^+$ have been studied. The continued study of this state would be of value, particularly with regard to its interactions with $^1\Pi_u$ and $^1\Sigma_u^+$ levels.

The present modelling formulation allows for the calculation of dissociative branching to different atomic states. This feature has not been exploited in the work presented here but its application to photochemical applications is intended. Experimental branching ratio are also known [52, 173, 181], and their analysis by coupled-channels means is already underway.

The final coupled-channels model presented here is suitable for the calculation of pho-

toabsorption/photodissociation cross sections with all the characteristics required by photochemical modellers. For the transmission of this data, a website has been established[a] which provides synthesised XUV spectra at a range of temperatures and will be updated as further improvements are made to the model formulation. Already, use has been made of this information by a number of studies in which I have collaborated, and which are presented in this thesis. The various applications therein are of significant interest and novelty but are likely only the first recruitment of the coupled-channels model.

The continuing expansion of the N_2 spectroscopic data base potentially allow for various other model improvements. Immediately promising, are the absorption spectra recorded at the SOLEIL synchrotron, which have only begun to be analysed. The data already compiled in this thesis includes new absolute oscillator strengths, natural linewidths, and observations of entirely new levels for a number of $^1\Sigma_u^+$ and $^1\Pi_u$ states. Once complete, the SOLEIL analysis will complement results of the KEK series of experiments, now fully-analysed and also detailed in this thesis, and a complete survey of the XUV spectrum up to the ionisation limit will have been established for $^{14}N_2$ and $^{15}N_2$. This data will facilitate many of the possible extensions to the N_2 coupled-channels modelling which are discussed above.

There is no clear limit to how sophisticated and inclusive a model such as this can be, although the work presented here represents a decent portion of what is likely feasible. Certainly, more Rydberg and forbidden states can, and should, be added; but an N_2 model of ultimate complexity is limited by the experimental data base and the patience of its investigators, even though the coupled-channels technique itself remains generally applicable. There are also other diatomic molecules which could be studied by means of the methodology adopted here. For example, the spectrum of carbon monoxide is quite similar in outline to N_2, it has an active XUV absorption spectrum, is predissociated, and is of interest to the astrophysical community. Furthermore, because the two molecules have the same electronic configuration many of the states which influence the N_2 spectrum have approximate analogues in CO [91].

[a] `http://www.wellesley.edu/Physics/gstark/N2_ANU_cross_sections`

Appendices

A.1 Abstracts of publications

The following abstracts are for refereed journal articles which I have authored. For all works listed here concerning laboratory and astrophysical measurements, I contributed to the analysis of experimental data but was not involved in its collection. For those papers concerning photochemical modelling, I was responsible for aspects of these calculations to do with the radiative and dissociation properties of N_2.

THE ASTROPHYSICAL JOURNAL, 664: L115–L118, 2007 August 1

SOURCE OF NITROGEN ISOTOPE ANOMALY IN HCN IN THE ATMOSPHERE OF TITAN

MAO-CHANG LIANG,[1,2] ALAN N. HEAYS,[3] BRENTON R. LEWIS,[3] STEPHEN T. GIBSON,[3] AND YUK L. YUNG[2]
Received 2007 May 7; accepted 2007 June 15; published 2007 July 12

ABSTRACT

The $^{14}N/^{15}N$ ratio for N_2 in the atmosphere of Titan was recently measured to be a factor of 2 higher than the corresponding ratio for HCN. Using a one-dimensional photochemical model with transport, we incorporate new isotopic photoabsorption and photodissociation cross sections of N_2, computed quantum-mechanically, and show that the difference in the ratio of $^{14}N/^{15}N$ between N_2 and HCN can be explained primarily by the photolytic fractionation of $^{14}N^{14}N$ and $^{14}N\,^{15}N$. The $[HC^{14}N]/[HC^{15}N]$ ratio produced by N_2 photolysis alone is 23. This value, together with the observed ratio, constrains the flux of atomic nitrogen input from the top of the atmosphere to be in the range (1–2) × 10^9 atoms cm^{-2} s^{-1}.

Subject headings: atmospheric effects — methods: numerical — molecular processes — planetary systems — planets and satellites: individual (Titan) — radiative transfer

THE JOURNAL OF CHEMICAL PHYSICS **128**, 114302 (2008)

Oscillator strengths and line widths of dipole-allowed transitions in $^{14}N_2$ between 89.7 and 93.5 nm

G. Stark,[1,a)] B. R. Lewis,[2] A. N. Heays,[2] K. Yoshino,[3] P. L. Smith,[3] and K. Ito[4]
[1]*Department of Physics, Wellesley College, Wellesley, Massachusetts 02481, USA*
[2]*Research School of Physical Sciences and Engineering, The Australian National University, Canberra, ACT 0200, Australia*
[3]*Harvard-Smithsonian Center for Astrophysics, Cambridge, Massachusetts 02138, USA*
[4]*Photon Factory, Institute for Materials Structure Science, High Energy Accelerator Research Organization, 1-1 Oho, Tsukuba, Ibaraki 305-0801, Japan*

(Received 20 November 2007; accepted 21 December 2007; published online 17 March 2008)

Line oscillator strengths in the 20 electric dipole-allowed bands of $^{14}N_2$ in the 89.7–93.5 nm (111480–106950 cm^{-1}) region are reported from photoabsorption measurements at an instrumental resolution of ~6 mÅ (0.7 cm^{-1}) full width at half maximum. The absorption spectrum comprises transitions to vibrational levels of the $3p\sigma_u$ c_4' $^1\Sigma_u^+$, $3p\pi_u$ c_3 $^1\Pi_u$, and $3s\sigma_g$ o_3 $^1\Pi_u$ Rydberg states and of the b' $^1\Sigma_u^+$ and b $^1\Pi_u$ valence states. The J dependences of band f values derived from the experimental line f values are reported as polynomials in $J'(J'+1)$ and are extrapolated to $J'=0$ in order to facilitate comparisons with results of coupled Schrödinger-equation calculations. Most bands in this study are characterized by a strong J dependence of the band f values and display anomalous P-, Q-, and R-branch intensity patterns. Predissociation line widths, which are reported for 11 bands, also exhibit strong J dependences. The f value and line width patterns can inform current efforts to develop comprehensive spectroscopic models that incorporate rotational effects and predissociation mechanisms, and they are critical for the construction of realistic atmospheric radiative-transfer models. © *2008 American Institute of Physics*. [DOI: 10.1063/1.2834933]

Experimental and coupled-channels investigation of the radiative properties of the N_2 $c_4' {}^1\Sigma_u^+ - X {}^1\Sigma_g^+$ band system

Xianming Liu,[1] Donald E. Shemansky,[1] Charles P. Malone,[2] Paul V. Johnson,[2] Joseph M. Ajello,[2] Isik Kanik,[2] Alan N. Heays,[3] Brenton R. Lewis,[3] Stephen T. Gibson,[3] and Glenn Stark[4]

Received 31 August 2007; revised 28 September 2007; accepted 6 November 2007; published 14 February 2008.

[1] The emission properties of the N_2 $c_4' {}^1\Sigma_u^+ - X {}^1\Sigma_g^+$ band system have been investigated in a joint experimental and coupled-channels theoretical study. Relative intensities of the $c_4' {}^1\Sigma_u^+(0) - X {}^1\Sigma_g^+(v_i)$ transitions, measured via electron-impact-induced emission spectroscopy, are combined with a coupled-channel Schrödinger equation (CSE) model of the N_2 molecule, enabling determination of the diabatic electronic transition moment for the $c_4' {}^1\Sigma_u^+ - X {}^1\Sigma_g^+$ system as a function of internuclear distance. The CSE rotational transition probabilities are further verified by comparison with a high-resolution experimental spectrum. Spontaneous transition probabilities of the $c_4' {}^1\Sigma_u^+ - X {}^1\Sigma_g^+$ band system, required for modeling atmospheric emission, can now be calculated reliably.

Citation: Liu, X., D. E. Shemansky, C. P. Malone, P. V. Johnson, J. M. Ajello, I. Kanik, A. N. Heays, B. R. Lewis, S. T. Gibson, and G. Stark (2008), Experimental and coupled-channels investigation of the radiative properties of the N_2 $c_4' {}^1\Sigma_u^+ - X {}^1\Sigma_g^+$ band system, *J. Geophys. Res.*, *113*, A02304, doi:10.1029/2007JA012787.

THE JOURNAL OF CHEMICAL PHYSICS **129**, 164306 (2008)

A coupled-channel model of the $^3\Pi_u$ states of N_2: Structure and interactions of the $3s\sigma_g F_3$ $^3\Pi_u$ and $3p\pi_u G_3$ $^3\Pi_u$ Rydberg states

B. R. Lewis,[1,a)] A. N. Heays,[1] S. T. Gibson,[1] H. Lefebvre-Brion, and R. Lefebvre
[1]*Research School of Physical Sciences and Engineering, The Australian National University, Canberra, Australian Capital Territory 0200, Australia*
[2]*Laboratoire de Photophysique Moléculaire, Bâtiment 213, Université de Paris-Sud, 91405 Orsay Cedex, France*

(Received 23 June 2008; accepted 4 September 2008; published online 24 October 2008)

New and existing spectroscopic data on N_2, obtained using a wide variety of experimental techniques, are interpreted using a coupled-channel Schrödinger-equation (CSE) model of the structure and predissociation dynamics for the interacting Rydberg and valence states of $^3\Pi_u$ symmetry. As a result, $v>0$ levels of the $3p\pi_u G_3$ $^3\Pi_u$ Rydberg state are assigned correctly for the first time, leading to the identification of very strong perturbations in the G_3-state vibrational structure. A four-channel CSE model, which includes the $3s\sigma_g F_3$ $^3\Pi_u$ and $3p\pi_u G_3$ $^3\Pi_u$ Rydberg states and the C' $^3\Pi_u$ and C $^3\Pi_u$ valence states, indicates strong Rydberg–Rydberg coupling between the F_3 and G_3 states, strong Rydberg-valence coupling between the G_3 and C' states, and weaker coupling between the F_3 and C' states. © *2008 American Institute of Physics.*
[DOI: 10.1063/1.2990656]

THE JOURNAL OF CHEMICAL PHYSICS **129**, 164307 (2008)

Sign reversal of the spin-orbit constant for the $C\,^3\Pi_u$ state of N_2

H. Ndome,[1] M. Hochlaf,[1] B. R. Lewis,[2,a)] A. N. Heays,[2] S. T. Gibson,[2] and H. Lefebvre-Brion[3]
[1]*Laboratoire de Modélisation et Simulation Multi Echelle, Université Paris-Est, MSME FRE 3160 CNRS, 5 Boulevard Descartes, 77454 Marne-La-Vallée, France*
[2]*Research School of Physical Sciences and Engineering, The Australian National University, Canberra, Australian Capital Territory 0200, Australia*
[3]*Laboratoire de Photophysique Moléculaire, Université de Paris-Sud, Bâtiment 213, 91405 Orsay Cedex, France*

(Received 23 June 2008; accepted 4 September 2008; published online 24 October 2008)

Ab initio calculations are performed at the multireference configuration-interaction level of theory on the diagonal spin-orbit functions for the lowest non-Rydberg states of $^3\Pi_u$ symmetry in molecular nitrogen. Spin-orbit constants deduced from the *ab initio* results confirm the recent suggestion, based on new experimental results, that the $C\,^3\Pi_u$ state of N_2, long known to be *regular* in the region of its potential-energy curve minimum, becomes *inverted* at higher energies. By removing the effects of the crossing $C'\,^3\Pi_u$ state, it is shown that A_v for the C state changes sign from positive to negative near $v=8$, corresponding to a change in principal molecular-orbital configuration from $(1\sigma_g)^2(1\sigma_u)^2(2\sigma_g)^2(2\sigma_u)(3\sigma_g)^2(1\pi_u)^4(1\pi_g)$ to $(1\sigma_g)^2(1\sigma_u)^2(2\sigma_g)^2(2\sigma_u)^2(3\sigma_g)\times(1\pi_u)^3(1\pi_g)^2$ at an internuclear distance near 1.4 Å. © *2008 American Institute of Physics*.
[DOI: 10.1063/1.2990658]

THE JOURNAL OF CHEMICAL PHYSICS **128**, 134313 (2008)

Interactions of the $3p\pi_u\ c^1\Pi_u(v=2)$ Rydberg-complex member in isotopic N_2

M. O. Vieitez,[1] T. I. Ivanov,[1] C. A. de Lange,[1] W. Ubachs,[1,a)] A. N. Heays,[2] B. R. Lewis,[2] and G. Stark[3]
[1]*Department of Physics and Astronomy, Laser Centre, Vrije Universiteit, De Boelelaan 1081, 1081 HV Amsterdam, The Netherlands*
[2]*Research School of Physical Sciences and Engineering, The Australian National University, Canberra, ACT 0200, Australia*
[3]*Department of Physics, Wellesley College, Wellesley, Massachusetts 02481, USA*

(Received 3 January 2008; accepted 28 January 2008; published online 7 April 2008)

The $3p\pi_u\ c^1\Pi_u - X\,^1\Sigma_g^+(2,0)$ Rydberg and $b'\,^1\Sigma_u^+ - X\,^1\Sigma_g^+(7,0)$ valence transitions of $^{14}N_2$, $^{14}N^{15}N$, and $^{15}N_2$ are studied using laser-based 1 extreme ultraviolet (XUV)+1′ UV two-photon-ionization spectroscopy, supplemented by synchrotron-based photoabsorption measurements in the case of $^{14}N_2$. For each isotopomer, effective rotational interactions between the $c(v=2)$ and $b'(v=7)$ levels are found to cause strong Λ-doubling in $c(v=2)$ and dramatic P/R-branch intensity anomalies in the $b'-X(7,0)$ band due to the effects of quantum interference. Local perturbations in energy and predissociation line width for the $c(v=2)$ Rydberg level are observed and attributed to a spin-orbit interaction with the crossing, short-lived $C\,^3\Pi_u(v=17)$ valence level. © *2008 American Institute of Physics*. [DOI: 10.1063/1.2883955]

THE JOURNAL OF CHEMICAL PHYSICS **129**, 204303 (2008)

Structure and predissociation of the $3p\sigma_u D\ ^3\Sigma_u^+$ Rydberg state of N_2: First extreme-ultraviolet and new near-infrared observations, with coupled-channels analysis

B. R. Lewis,[1,a)] K. G. H. Baldwin,[1] A. N. Heays,[1] S. T. Gibson,[1] J. P. Sprengers,[2] W. Ubachs,[2] and M. Fujitake[3]
[1]*Research School of Physical Sciences and Engineering, The Australian National University, Canberra, Australian Capital Territory 0200, Australia*
[2]*Department of Physics and Astronomy, Laser Centre, Vrije Universiteit, De Boelelaan 1081, 1081 HV Amsterdam, The Netherlands*
[3]*Department of Physics, Kanazawa University, Kakuma, Kanazawa 920-11, Japan*

(Received 21 September 2008; accepted 22 October 2008; published online 24 November 2008)

The $3p\sigma_u D\ ^3\Sigma_u^+$ Rydberg state of N_2 is studied experimentally using two high-resolution spectroscopic techniques. First, the forbidden $D\ ^3\Sigma_u^+ - X\ ^1\Sigma_g^+$ transition is observed for the first time via the (0,0) band of $^{14}N_2$ and the (1,0) band of $^{15}N_2$, using 1 extreme-ultraviolet +1 ultraviolet two-photon-ionization laser spectroscopy. Second, the Rydberg–Rydberg transition $D\ ^3\Sigma_u^+ - E\ ^3\Sigma_g^+$ is studied using near-infrared diode-laser photoabsorption spectroscopy, thus extending the previous measurements of Kanamori *et al.* [J. Chem. Phys. **95**, 80 (1991)], to higher transition energies, and thereby revealing the (2,2) and (3,3) bands. The combined results show that the $D(v=0-3)$ levels exhibit rapidly increasing rotational predissociation as v increases, spanning nearly four orders of magnitude. The D-state level structure and rotational predissociation signature are explained by means of a coupled-channels model which considers the electrostatically coupled $^3\Pi_u$ Rydberg-valence manifold, together with a pure-precession **L**-uncoupling rotational interaction between the $3p\sigma_u D\ ^3\Sigma_u^+$ and $3p\pi_u G\ ^3\Pi_u$ Rydberg p-complex components. © *2008 American Institute of Physics*. [DOI: 10.1063/1.3023034]

Analysis of terrestrial thermospheric $N_2\ c_4'\ ^1\Sigma_u^+(0) \sim b'\ ^1\Sigma_u^+(1) - X\ ^1\Sigma_g^+$ dayglow emission observed by the Far Ultraviolet Spectroscopic Explorer

Xianming Liu,[1] Alan N. Heays,[2] Donald E. Shemansky,[1] Brenton R. Lewis,[2] and Paul D. Feldman[3]

Received 12 May 2008; revised 14 January 2009; accepted 2 February 2009; published 10 April 2009.

[1] Terrestrial thermospheric dayglow emission from the coupled and overlapping $c_4'\ ^1\Sigma_u^+(0)$ and $b'\ ^1\Sigma_u^+(1)$ levels of molecular nitrogen, observed by the Far Ultraviolet Spectroscopic Explorer, is analyzed with the aid of a coupled channels quantum mechanical model of N_2 spectroscopy and predissociation dynamics. Model emission spectra for the mixed $c_4'\ ^1\Sigma_u^+(0) \sim b'\ ^1\Sigma_u^+(1) - X\ ^1\Sigma_g^+(v_i = 2, 6-9)$ transitions, calculated for the case of excitation by photoelectron impact, are in excellent agreement with the observations. While the principal excitation mechanism for N_2 in the thermosphere is photoelectron impact, evidence is also found in other transitions of resonant fluorescence, induced by lines in the solar atomic hydrogen Lyman series, atomic oxygen transitions, and other N_2 bands. The observed emission rate of the $c_4'\ ^1\Sigma_u^+(0) \sim b'\ ^1\Sigma_u^+(1) - X\ ^1\Sigma_g^+(0)$ band is ~1% of that inferred from the emission rates to $X\ ^1\Sigma_g^+(v_i > 2)$ levels. A qualitative explanation is given for the drastically reduced intensity and band shape distortion observed in the $c_4'\ ^1\Sigma_u^+(0) - X\ ^1\Sigma_g^+(0)$ emission band. Estimates of the total electron excitation rates for the nominal $b'\ ^1\Sigma_u^+(1)$ and $c_4'\ ^1\Sigma_u^+(0)$ levels are determined from the spectrum by extrapolating the model through regions containing unmeasured and/or resonantly absorbed bands.

Citation: Liu, X., A. N. Heays, D. E. Shemansky, B. R. Lewis, and P. D. Feldman (2009), Analysis of terrestrial thermospheric $N_2\ c_4'\ ^1\Sigma_u^+(0) \sim b'\ ^1\Sigma_u^+(1) - X\ ^1\Sigma_g^+$ dayglow emission observed by the Far Ultraviolet Spectroscopic Explorer, *J. Geophys. Res.*, *114*, D07304, doi:10.1029/2008JD010403.

THE JOURNAL OF CHEMICAL PHYSICS **131**, 194308 (2009)

Oscillator strengths and line widths of dipole-allowed transitions in $^{14}N_2$ between 86.0 and 89.7 nm

A. N. Heays,[1,a)] B. R. Lewis,[1] G. Stark,[2] K. Yoshino,[3] Peter L. Smith,[3] K. P. Huber,[4] and K. Ito[5]

[1]*Research School of Physical Sciences and Engineering, The Australian National University, Canberra, Australian Capital Territory 0200, Australia*
[2]*Department of Physics, Wellesley College, Wellesley, Massachusetts 02481, USA*
[3]*Harvard-Smithsonian Center for Astrophysics, Cambridge, Massachusetts 02138, USA*
[4]*Steacie Institute for Molecular Sciences, National Research Council of Canada, Ottawa, Ontario K1A 0R6, Canada*
[5]*Photon Factory, Institute for Materials Structure Science, High Energy Accelerator Research Organization, 1-1 Oho, Tsukuba, Ibaraki 305-0801, Japan*

(Received 18 August 2009; accepted 10 October 2009; published online 20 November 2009)

Oscillator strengths of 23 electric-dipole-allowed bands of $^{14}N_2$ in the 86.0–89.7 nm (111 480–116 280 cm^{-1}) region are reported from synchrotron-based photoabsorption measurements at an instrumental resolution of 6.5×10^{-4} nm (0.7 cm^{-1}) full width at half maximum. The absorption spectrum comprises transitions to vibrational levels of the $c_n\ ^1\Pi_u$ (n=3,4), $o_3\ ^1\Pi_u$, and $c'_{n+1}\ ^1\Sigma^+_u$(n=3,4) Rydberg states as well as the $b\ ^1\Pi_u$ and $b'\ ^1\Sigma^+_u$ valence states. The J dependences of band f-values derived from the experimental line f-values are reported as polynomials in $J(J+1)$ and are extrapolated to zero nuclear rotation in order to facilitate comparisons with the results of coupled Schrödinger equation calculations. Many bands in this study are characterized by a strong J dependence of the band f-values and display anomalous P-, Q-, and R-branch intensity patterns. Predissociation line widths are reported for six bands. The experimental f-value and line-width patterns inform current efforts to develop comprehensive spectroscopic models for N_2 that incorporate rotational effects and predissociation mechanisms, and are critical for the construction of realistic atmospheric radiative-transfer models. [doi:10.1063/1.3257690]

A.2 Results of analysis of the SOLEIL spectra

This appendix contains a complete listing of all $^{14}N_2$ $^1\Pi_u \leftarrow X\,^1\Sigma_g^+(v''=0)$ and $^1\Sigma_u^+ \leftarrow X\,^1\Sigma_g^+(v''=0)$ bands appearing in the SOLEIL spectra which were rotationally analysed for this thesis. Further details of the experiment are discussed in Chap. 5.

There are eight bands included which appear between 111 800 and 116 700 cm^{-1}, and which have been previously studied at slightly lower resolution during the KEK series of experiments, described in Chap. 4. Seven further bands, between 116 700 and 119 000 cm^{-1}, have been observed previously in the photographic absorption measurements discussed in Sec. 3.3.1, and the absolute f-values and linewidths listed here are completely new. Also, some new assignments of lines within previously observed bands have been made possible by the fitting of accurate lineshapes.

Some excessively blended or weak transitions were analysed but not included in these listings. This analysis was done in order to confirm the overall plausibility of the analysis, even where new information could not be confidently obtained.

For each $^1\Sigma_u^+ \leftarrow X$ band listed, P- and R-branch transition-energies are indexed by the excited-state angular-momentum quantum number, J; and term energies are calculated from these using the known $^{14}N_2$ ground-state energy-levels discussed in Sec. 3.2. P- and R-branch band f-values are also listed, as well as the observed linewidths. Because all observable broadening originates from the finite lifetime of the excited states, lines of common J in either branch share a common linewidth. The two $^1\Pi_u \leftarrow X$ bands observed have been given separate listings for their $e \leftarrow e$ and $f \leftarrow e$ parity transitions. The former are equivalent to the $^1\Sigma_u^+ \leftarrow X$ case excepting that no $J=0$ level exists, and the excited state f-parity levels are accessed through the observed Q-branch only.

Uncertainty in the listed f-values and linewidths is given parenthetically in units of the least-significant digit of each value. This includes both statistical uncertainty estimated by the fitting routine and the assumed systematic uncertainties of the experiment. All transition and term energies are estimated to have combined statistical and systematic uncertainties below 0.1 cm^{-1}.

$b^1\Pi_u(v'=15) \leftarrow X^1\Sigma_g^+(v''=0),\ e \leftarrow e$

	Transition energy (cm^{-1})		Term energy	Band f-value		Linewidth
J	$P(J+1)$	$R(J-1)$	(cm^{-1})	$P(J+1)$	$R(J-1)$	(cm^{-1} FWHM)
3	111 845.40	111 873.25	111 885.19	0.0015(7)	0.0015(3)	0.09(5)
4		111 869.83	111 893.71		0.0014(6)	0.1(1)
5		111 864.59	111 904.38		0.0016(4)	0.12(6)
6		111 857.48	111 917.16		0.0013(8)	0.1(2)
7		111 848.49	111 932.04		0.0014(5)	0.05(7)

$b^1\Pi_u(v'=15) \leftarrow X^1\Sigma_g^+(v''=0),\ f \leftarrow e$

	Transition energy (cm^{-1})	Term energy	Band f-value	Linewidth
J	$Q(J)$	(cm^{-1})	$Q(J)$	(cm^{-1} FWHM)
1	111 870.56	111 874.54	0.0015(8)	0.1(1)
2	111 866.86	111 878.80	0.0013(3)	0.05(4)
3	111 861.32	111 885.19	0.0015(4)	0.09(8)
4	111 853.92	111 893.71	0.0014(3)	0.08(4)
5	111 844.70	111 904.38	0.0018(6)	0.1(1)
6	111 833.62	111 917.17	0.0013(4)	0.11(8)

$b'^1\Sigma_u^+(v'=12) \leftarrow X^1\Sigma_g^+(v''=0)$

	Transition energy (cm^{-1})		Term energy	Band f-value		Linewidth
J	$P(J+1)$	$R(J-1)$	(cm^{-1})	$P(J+1)$	$R(J-1)$	(cm^{-1} FWHM)
0	112 234.42		112 238.40	0.014(7)		0.06(2)
1	112 228.64	112 240.55	112 240.57	0.017(4)	0.018(4)	0.06(2)
2	112 221.00	112 240.95	112 244.89	0.020(5)	0.018(4)	0.06(2)
3	112 211.53	112 239.36	112 251.31	0.018(4)	0.016(4)	0.06(2)
4	112 200.16	112 235.98	112 259.85	0.013(3)	0.014(3)	0.06(2)
5	112 187.02	112 230.80	112 270.58	0.017(4)	0.013(3)	0.07(2)
6	112 172.02	112 223.77	112 283.43	0.017(4)	0.013(3)	0.07(2)
7	112 155.27	112 214.89	112 298.47	0.018(4)	0.013(3)	0.06(2)
8	112 136.52	112 204.19	112 315.56	0.017(4)	0.013(3)	0.06(2)
9	112 116.06	112 191.61	112 334.84	0.015(4)	0.016(4)	0.06(2)
10	112 093.67	112 177.22	112 356.22	0.020(5)	0.015(4)	0.07(2)
11	112 069.56	112 161.00	112 379.79	0.016(4)	0.012(3)	0.08(2)
12		112 143.03	112 405.55		0.017(4)	0.08(5)
13		112 123.07	112 433.30		0.014(3)	0.08(4)
14		112 101.28	112 463.19		0.016(5)	0.08(4)
15		112 077.73	112 495.29		0.015(4)	0.08(4)

$b'^1\Sigma_u^+(v'=13) \leftarrow X^1\Sigma_g^+(v''=0)$

	Transition energy (cm^{-1})		Term energy	Band f-value		Linewidth
J	$P(J+1)$	$R(J-1)$	(cm^{-1})	$P(J+1)$	$R(J-1)$	(cm^{-1} FWHM)
1	112 898.37	112 910.13	112 910.26	0.010(2)	0.020(6)	0.10(2)
2	112 891.13	112 910.95	112 914.97	0.009(2)	0.012(3)	0.12(2)
3		112 910.30	112 922.24		0.004(1)	0.11(2)
4		112 907.78	112 931.65		0.008(2)	0.11(2)
5		112 904.09	112 943.88		0.007(1)	0.11(2)
6		112 899.43	112 959.11		0.007(1)	0.11(2)
7		112 894.27	112 977.82		0.0042(8)	0.07(2)

$b'^1\Sigma_u^+(v'=14) \leftarrow X^1\Sigma_g^+(v''=0)$

	Transition energy (cm^{-1})		Term energy	Band f-value		Linewidth
J	$P(J+1)$	$R(J-1)$	(cm^{-1})	$P(J+1)$	$R(J-1)$	(cm^{-1} FWHM)
0	113 536.42		113 540.40	0.015(5)		0.24(2)
1	113 530.67	113 542.54	113 542.59	0.016(2)	0.020(3)	0.24(2)
2	113 522.90	113 542.86	113 546.80	0.019(3)	0.020(3)	0.27(2)
3	113 513.35	113 541.19	113 553.13	0.018(2)	0.020(3)	0.25(2)
4	113 501.96	113 537.72	113 561.62	0.021(3)	0.019(3)	0.26(2)
5	113 488.63	113 532.38	113 572.18	0.019(2)	0.019(2)	0.25(2)
6	113 473.46	113 525.18	113 584.86	0.019(3)	0.016(2)	0.26(2)
7	113 456.43	113 516.10	113 599.65	0.018(2)	0.019(2)	0.25(2)
8	113 437.55	113 505.17	113 616.57	0.021(3)	0.018(2)	0.26(2)
9	113 416.84	113 492.38	113 635.61	0.017(2)	0.019(2)	0.23(2)
10	113 394.24	113 477.73	113 656.75	0.018(3)	0.018(2)	0.24(4)
11	113 369.75	113 461.25	113 680.01	0.019(3)	0.018(2)	0.29(3)
12	113 343.50	113 442.89	113 705.41	0.021(3)	0.017(3)	0.2(1)
13		113 422.73	113 732.96		0.018(2)	0.30(2)
14		113 400.75	113 762.66		0.021(3)	0.30(2)
15		113 377.08	113 794.64		0.018(3)	0.30(2)
16		113 351.93	113 829.10		0.020(4)	0.30(2)

$b'^1\Sigma_u^+(v'=15) \leftarrow X^1\Sigma_g^+(v''=0)$

J	Transition energy (cm^{-1}) $P(J+1)$	$R(J-1)$	Term energy (cm^{-1})	Band f-value $P(J+1)$	$R(J-1)$	Linewidth (cm^{-1} FWHM)
0	114 165.79		114 169.77	0.021(5)		0.1(1)
1	114 159.92	114 171.86	114 171.86	0.024(3)	0.024(3)	0.27(4)
2	114 152.19	114 172.05	114 176.06	0.017(3)	0.024(3)	0.25(5)
3	114 142.58	114 170.39	114 182.35	0.024(3)	0.022(3)	0.26(2)
4	114 131.05	114 166.84	114 190.72	0.024(3)	0.022(3)	0.24(3)
5	114 117.67	114 161.42	114 201.22	0.023(3)	0.021(2)	0.28(2)
6	114 102.40	114 154.12	114 213.80	0.023(3)	0.023(3)	0.24(3)
7	114 085.24	114 144.91	114 228.46	0.020(3)	0.022(3)	0.26(2)
8	114 066.21	114 133.81	114 245.22	0.023(3)	0.022(3)	0.24(3)
9	114 045.27	114 120.86	114 264.07	0.021(3)	0.021(2)	0.22(2)
10	114 022.46	114 105.97	114 284.98	0.020(3)	0.020(3)	0.22(3)
11	113 997.74	114 089.18	114 307.97	0.019(2)	0.021(3)	0.20(2)
12	113 971.14	114 070.55	114 333.07	0.022(3)	0.022(3)	0.18(4)
13	113 942.66	114 049.95	114 360.20	0.018(2)	0.021(3)	0.20(3)
14	113 912.22	114 027.48	114 389.39	0.025(5)	0.022(3)	0.21(5)
15	113 879.93	114 003.08	114 420.65	0.021(3)	0.020(3)	0.21(4)
16	113 845.69	113 976.79	114 453.96	0.024(5)	0.021(4)	0.19(7)
17	113 809.54	113 948.58	114 489.32	0.023(7)	0.021(3)	0.16(5)
18		113 918.50	114 526.77		0.025(6)	0.2(1)
19		113 886.45	114 566.21		0.021(4)	0.14(8)
20		113 852.45	114 607.66		0.018(8)	0.1(2)
21		113 816.57	114 651.18		0.016(6)	0.1(1)

$b'^1\Sigma_u^+(v'=16) \leftarrow X^1\Sigma_g^+(v''=0)$

J	Transition energy (cm^{-1}) $P(J+1)$	$R(J-1)$	Term energy (cm^{-1})	Band f-value $P(J+1)$	$R(J-1)$	Linewidth (cm^{-1} FWHM)
1	114 744.75	114 756.64	114 756.69	0.029(3)	0.031(4)	0.09(2)
2	114 738.32	114 758.17	114 762.19	0.030(4)	0.031(4)	0.08(2)
3	114 730.42	114 758.28	114 770.21	0.028(4)	0.031(4)	0.09(3)
4		114 756.78	114 780.65		0.028(3)	0.10(2)
5	114 709.76	114 753.48	114 793.29	0.031(4)	0.030(4)	0.10(2)
6	114 696.70	114 748.43	114 808.10	0.027(3)	0.033(4)	0.08(2)
7	114 681.73	114 741.39	114 824.95	0.031(4)	0.026(3)	0.08(2)
8	114 664.75	114 732.36	114 843.76	0.029(3)	0.028(3)	0.08(2)
9	114 645.70		114 864.48	0.025(3)		0.07(3)
10	114 624.60	114 708.10	114 887.12	0.027(4)	0.028(4)	0.11(2)
11	114 601.35	114 692.80	114 911.58	0.029(4)	0.028(4)	0.08(2)
12	114 576.03	114 675.42	114 937.94	0.025(3)	0.029(3)	0.08(2)
13	114 548.58	114 655.93	114 966.16	0.029(4)	0.026(4)	0.06(3)
14	114 519.12	114 634.38	114 996.29	0.025(4)	0.028(4)	0.09(3)
15	114 487.58	114 610.75	115 028.31	0.025(3)	0.027(4)	0.09(3)
16	114 453.98	114 585.08	115 062.25	0.029(6)	0.025(4)	0.08(4)
17	114 418.34	114 557.38	115 098.12	0.026(5)	0.019(3)	0.10(3)
18		114 527.61	115 135.88		0.034(6)	0.12(6)
19	114 341.03	114 495.88	115 175.64	0.022(6)	0.027(4)	0.13(5)
20		114 462.12	115 217.33		0.025(9)	0.1(1)
21		114 426.29	115 260.90		0.024(6)	0.1(1)

$b'^1\Sigma_u^+(v'=17) \leftarrow X^1\Sigma_g^+(v''=0)$

J	Transition energy (cm^{-1}) $P(J+1)$	$R(J-1)$	Term energy (cm^{-1})	Band f-value $P(J+1)$	$R(J-1)$	Linewidth (cm^{-1} FWHM)
0	115 365.42		115 369.40	0.020(4)		0.4(1)
1	115 359.72		115 371.66	0.016(2)		0.33(4)
2	115 352.20		115 376.07	0.015(2)		0.25(4)
3	115 342.90	115 370.76	115 382.69	0.015(2)	0.017(2)	0.28(2)
4	115 331.84		115 391.52	0.016(2)		0.25(4)
5	115 318.98	115 362.75	115 402.53	0.015(2)	0.018(2)	0.25(2)
6	115 304.35	115 356.07	115 415.75	0.014(2)	0.017(2)	0.20(2)
7	115 287.91	115 347.55	115 431.12	0.016(2)	0.018(2)	0.21(2)
8	115 269.71	115 337.31	115 448.72	0.014(2)	0.017(2)	0.18(2)
9	115 249.71	115 325.25	115 468.49	0.016(2)	0.018(2)	0.18(2)
10	115 227.91	115 311.42	115 490.43	0.015(2)	0.017(2)	0.17(2)
11	115 204.37	115 295.79	115 514.60	0.014(2)	0.018(2)	0.22(2)
12		115 278.49	115 541.01		0.017(2)	0.15(3)
13	115 152.30	115 259.62	115 569.85	0.013(3)	0.017(2)	0.21(2)
14	115 124.44	115 239.66	115 601.58	0.013(2)	0.016(2)	0.25(4)
15		115 220.46	115 638.02		0.011(2)	0.2(1)
16	115 048.32		115 656.59	0.013(2)		0.1(1)
17	115 016.65	115 155.69	115 696.42	0.016(2)	0.015(2)	0.19(3)
18		115 127.95	115 736.22		0.012(2)	0.2(1)
19	114 942.87		115 777.48	0.016(3)		0.1(1)
21		115 030.94	115 865.55		0.012(4)	0.1(1)

$b'^1\Sigma_u^+(v'=18) \leftarrow X^1\Sigma_g^+(v''=0)$

J	Transition energy (cm^{-1}) $P(J+1)$	$R(J-1)$	Term energy (cm^{-1})	Band f-value $P(J+1)$	$R(J-1)$	Linewidth (cm^{-1} FWHM)
0	116 202.77		116 206.75	0.0025(7)		0.1(1)
1	116 197.32	116 209.26	116 209.26	0.0022(3)	0.0036(6)	0.07(2)
2	116 190.57	116 210.51	116 214.45	0.0022(4)	0.0031(4)	0.08(3)
3	116 182.42	116 210.24	116 222.20	0.0027(3)	0.0031(4)	0.10(2)
4	116 172.91	116 208.70	116 232.58	0.0026(4)	0.0028(4)	0.09(3)
5	116 162.03	116 205.81	116 245.60	0.0024(7)	0.0019(3)	0.07(2)
6	116 149.88	116 201.59	116 261.27	0.0019(3)	0.0024(3)	0.07(2)
7	116 136.42	116 196.07	116 279.63	0.0016(2)	0.0019(3)	0.09(2)
8	116 121.74	116 189.36	116 300.76	0.0009(1)	0.0018(3)	0.03(2)
9	116 105.88	116 181.42	116 324.65	0.0012(2)	0.0012(2)	0.05(2)
10	116 088.86	116 172.35	116 351.37	0.0010(2)	0.0014(2)	0.08(5)
11	116 070.71		116 380.94	0.0007(1)		0.12(5)
12	116 051.56	116 150.91	116 413.44	0.0004(2)	0.0009(1)	0.1(2)
13	116 031.22	116 138.65	116 448.86	0.0003(1)	0.00040(8)	na(2)
15		116 111.33	116 528.89		0.0002(1)	na(2)

$b'^1\Sigma_u^+(v'=19) \leftarrow X^1\Sigma_g^+(v''=0)$

J	Transition energy (cm^{-1}) $P(J+1)$	$R(J-1)$	Term energy (cm^{-1})	Band f-value $P(J+1)$	$R(J-1)$	Linewidth (cm^{-1} FWHM)
0	116 678.64		116 682.62	0.010(1)		0.13(3)
1	116 672.85		116 684.79	0.008(1)		0.10(2)
2	116 665.27		116 689.06	0.009(1)		0.10(2)
3	116 655.88	116 683.72	116 695.66	0.0086(9)	0.009(1)	0.12(2)
4	116 644.69	116 680.48	116 704.36	0.009(1)	0.009(1)	0.10(2)
5	116 631.71	116 675.48	116 715.27	0.0086(9)	0.009(1)	0.10(2)
6	116 616.96	116 668.66	116 728.35	0.009(1)	0.009(1)	0.13(2)
7	116 600.41	116 660.07	116 743.63	0.009(1)	0.0085(9)	0.10(2)
8	116 582.12	116 649.73	116 761.13	0.008(1)	0.0086(9)	0.09(2)
9	116 562.58	116 638.14	116 781.36	0.0073(9)	0.0057(6)	0.17(2)
10	116 539.93	116 623.46	116 802.47	0.009(1)	0.009(1)	0.14(2)
11	116 516.36	116 607.79	116 826.58	0.008(1)	0.010(1)	0.15(2)
12	116 492.28	116 591.66	116 854.19	0.0057(7)	0.0057(8)	0.10(2)
13	116 464.41	116 571.75	116 881.97	0.010(1)	0.009(1)	0.19(2)
14	116 435.83	116 551.05	116 912.98	0.008(1)	0.009(1)	0.16(3)
15	116 405.64	116 528.81	116 946.37	0.008(1)	0.009(1)	0.19(2)
16	116 373.97	116 505.05	116 982.23	0.008(1)	0.010(2)	0.21(4)
17	116 340.84	116 479.82	117 020.58	0.009(1)	0.008(1)	0.19(3)
18	116 306.52	116 453.45	117 061.72	0.007(1)	0.009(1)	0.18(4)
19	116 270.67	116 425.52	117 105.28	0.008(1)	0.008(1)	0.13(3)
20	116 234.06	116 396.68	117 151.91	0.009(2)	0.006(1)	0.04(5)
21		116 366.76	117 201.37		0.006(1)	0.12(6)
22		116 336.19	117 254.15		0.008(2)	0.1(1)
23		116 304.88	117 310.13		0.006(2)	0.1(1)
25		116 241.65	117 433.33		0.008(3)	0.2(2)

$c_4'^1\Sigma_u^+(v'=6) \leftarrow X^1\Sigma_g^+(v''=0)$

J	Transition energy (cm^{-1}) $P(J+1)$	$R(J-1)$	Term energy (cm^{-1})	Band f-value $P(J+1)$	$R(J-1)$	Linewidth (cm^{-1} FWHM)
0	116 803.01		116 806.99	0.008(2)		0.05(5)
1	116 798.59	116 810.52	116 810.52	0.008(1)	0.008(2)	0.04(2)
2	116 793.72	116 813.61	116 817.59	0.008(1)	0.009(5)	0.04(2)
3	116 788.42	116 816.27	116 828.21	0.007(1)	0.007(3)	0.09(2)
4	116 782.66	116 818.47	116 842.34	0.008(1)	0.008(2)	0.04(2)
5	116 776.45	116 820.21	116 860.00	0.0059(8)		0.06(2)
6	116 769.75	116 821.47	116 881.15	0.008(1)		0.05(2)
7	116 762.57	116 822.23	116 905.79	0.0058(8)		0.05(3)
8	116 754.69	116 822.30	116 933.71	0.0062(8)		0.02(3)
9	116 747.99	116 823.55	116 966.77	0.0051(7)	0.005(1)	0.05(2)
10	116 738.87	116 822.38	117 001.39	0.0062(8)		0.05(3)
11	116 729.54	116 820.99	117 039.77	0.0060(8)		0.11(3)
12	116 720.98	116 820.37	117 082.89	0.0059(9)		0.06(5)
13	116 712.48	116 819.79	117 130.04	0.0019(9)		0.8(5)
14	116 700.86	116 816.13	117 178.03	0.005(3)	0.005(3)	1.0(6)
15	116 690.01	116 813.19	117 230.75	0.006(4)	0.006(4)	1.4(9)
17	116 665.01	116 806.55	117 347.29		0.007(3)	1.8(7)
18		116 802.79	117 411.06		0.009(3)	2(2)
19		116 797.36	117 477.12		0.009(4)	5(2)

$b'^1\Sigma_u^+(v'=20) \leftarrow X^1\Sigma_g^+(v''=0)$

J	Transition energy (cm^{-1}) $P(J+1)$	$R(J-1)$	Term energy (cm^{-1})	Band f-value $P(J+1)$	$R(J-1)$	Linewidth (cm^{-1} FWHM)
0	117 200.86		117 204.84	0.012(2)		0.19(7)
1	117 195.05	117 207.15	117 206.99	0.010(1)	0.013(2)	0.14(2)
2	117 187.43	117 207.15	117 211.30	0.010(1)	0.013(2)	0.17(3)
3	117 177.98	117 205.83	117 217.77	0.009(1)	0.010(1)	0.18(2)
4	117 166.71	117 202.51	117 226.39	0.009(1)	0.011(1)	0.25(2)
5	117 153.61	117 197.38	117 237.17	0.009(1)	0.010(1)	0.39(2)
6	117 138.70	117 190.41	117 250.10	0.011(1)	0.011(1)	0.53(3)
7	117 121.96	117 181.63	117 265.18	0.010(1)	0.011(1)	0.95(4)
8	117 103.29	117 170.99	117 282.34	0.011(1)	0.011(1)	1.92(8)
9	117 082.20	117 157.87	117 301.05	0.011(1)	0.012(1)	2.83(8)
10	117 059.03	117 142.53	117 321.55	0.011(1)	0.011(1)	2.7(1)
11	117 034.43	117 125.85	117 344.65	0.010(1)	0.011(1)	1.81(6)
12	117 008.15	117 107.57	117 370.08	0.011(1)	0.012(1)	1.37(6)
13	116 980.02	117 087.30	117 397.56	0.010(1)	0.010(1)	0.97(5)
14	116 949.93	117 065.23	117 427.13	0.011(1)	0.011(1)	1.00(6)
15	116 918.02	117 041.19	117 458.75	0.011(1)	0.012(1)	1.18(5)
16	116 884.09	117 015.29	117 492.44	0.013(2)	0.013(1)	1.36(9)
17	116 848.46	116 987.38	117 528.14	0.011(2)	0.012(1)	1.47(9)
18		116 957.53	117 565.80		0.013(2)	1.9(3)
19	116 771.36	116 926.01	117 605.80	0.011(3)	0.013(2)	2.1(2)
20	116 729.99	116 892.59	117 647.84	0.019(8)	0.013(2)	2.8(7)
21		116 857.43	117 692.04		0.012(3)	2.9(9)

$b'^1\Sigma_u^+(v'=21) \leftarrow X^1\Sigma_g^+(v''=0)$

J	Transition energy (cm^{-1}) $P(J+1)$	$R(J-1)$	Term energy (cm^{-1})	Band f-value $P(J+1)$	$R(J-1)$	Linewidth (cm^{-1} FWHM)
0	117 678.60		117 682.58	0.007(3)		2(1)
1	117 672.32	117 684.26	117 684.26	0.0029(9)	0.006(1)	2.1(4)
2	117 665.41	117 685.30	117 689.28	0.005(1)	0.006(1)	4(1)
3	117 656.11	117 683.96	117 695.90	0.0044(8)	0.0037(8)	2.8(3)
4	117 645.46	117 681.27	117 705.14	0.0030(6)	0.0037(8)	2.3(3)
5	117 632.85	117 676.61	117 716.40	0.0040(5)	0.0046(6)	2.7(2)
6	117 618.77	117 670.49	117 730.17	0.0043(7)	0.0042(8)	2.0(4)
7	117 603.44	117 663.11	117 746.66	0.0037(4)	0.0042(5)	2.4(2)
8	117 586.23	117 653.85	117 765.25	0.0050(6)	0.0044(9)	1.7(5)
9	117 567.36	117 642.92	117 786.14	0.0042(5)	0.0049(6)	2.5(2)
10	117 546.76	117 630.27	117 809.28	0.0040(5)	0.0046(7)	2.6(1)
11	117 524.54	117 615.99	117 834.77	0.0051(5)	0.0050(6)	2.7(1)
12	117 500.45	117 599.84	117 862.36	0.0051(7)	0.0051(7)	2.9(2)
13	117 474.53	117 581.85	117 892.09	0.0043(5)	0.0054(6)	3.6(2)
14	117 446.24	117 561.49	117 923.40	0.0043(7)	0.0063(8)	2.5(2)
15	117 416.62	117 539.80	117 957.36	0.0059(7)	0.0063(7)	2.5(1)
16	117 385.05	117 516.15	117 993.32	0.005(1)	0.008(1)	1.9(1)
17	117 351.07	117 490.09	118 030.83	0.0055(8)	0.0068(8)	1.9(1)
18	117 315.07	117 462.01	118 070.28	0.006(2)	0.0043(9)	2.1(2)
19	117 277.13	117 431.98	118 111.74	0.006(1)	0.008(1)	2.1(1)
20	117 236.94	117 399.69	118 154.90	0.010(3)	0.010(2)	3.5(4)
21		117 365.79	118 200.40		0.005(1)	1.6(2)
22		117 329.78	118 247.74		0.011(4)	0.9(3)
23		117 290.96	118 296.21		0.006(3)	2.2(5)

$c_4{}^1\Pi_u(v'=1) \leftarrow X^1\Sigma_g^+(v''=0),\ e \leftarrow e$

J	Transition energy (cm^{-1}) $P(J+1)$	$R(J-1)$	Term energy (cm^{-1})	Band f-value $P(J+1)$	$R(J-1)$	Linewidth (cm^{-1} FWHM)
1	117 739.11	117 751.05	117 751.05	0.0014(5)	0.0005(2)	0.20(7)
2	117 734.92	117 754.81	117 758.79	0.0013(5)	0.0012(3)	0.21(8)
3	117 730.62	117 758.47	117 770.41	0.0019(3)	0.00016(9)	0.20(4)
4	117 726.17		117 785.85	0.0011(3)		0.15(5)
5	117 721.50		117 805.05	0.0019(3)		0.20(4)
6	117 716.59		117 827.99	0.0016(3)		0.2(1)
7	117 711.47		117 854.69	0.0024(3)		0.32(9)
8	117 706.00		117 885.01	0.0027(4)		0.23(4)
9	117 700.27		117 919.05	0.0022(3)		0.23(4)
10	117 694.20		117 956.72	0.0024(5)		0.3(1)
11	117 687.73		117 997.96	0.0029(4)		0.22(5)
12	117 680.91		118 042.82	0.002(1)		0.1(2)
13	117 673.74		118 091.30	0.0032(8)		0.3(1)

$c_4{}^1\Pi_u(v'=1) \leftarrow X^1\Sigma_g^+(v''=0),\ f \leftarrow e$

J	Transition energy (cm^{-1}) $Q(J)$	Term energy (cm^{-1})	Band f-value $Q(J)$	Linewidth (cm^{-1} FWHM)
1	117 747.01	117 750.99	0.0007(1)	0.1(1)
2	117 746.64	117 758.58	0.0007(1)	0.26(6)
3	117 746.11	117 769.98	0.0008(2)	0.13(6)
4	117 745.41	117 785.20	0.0008(1)	0.15(3)
5	117 744.61	117 804.29	0.0007(1)	0.16(6)
6	117 743.61	117 827.16	0.0006(1)	0.15(4)
7	117 742.46	117 853.86	0.0007(1)	0.3(1)
8	117 741.13	117 884.35	0.0007(1)	0.12(8)
9	117 739.62	117 918.63	0.0006(1)	0.15(4)
10	117 737.93	117 956.71	0.0008(1)	0.15(4)
11	117 736.12	117 998.64	0.0008(2)	0.14(5)
12	117 734.16	118 044.39	0.0007(1)	0.14(5)
13	117 731.93	118 093.84	0.0011(2)	0.14(5)
14	117 729.61	118 147.17	0.0008(2)	0.11(7)
15	117 727.04	118 204.21	0.0006(2)	0.11(7)
16	117 724.41	118 265.15	0.0007(2)	0.11(7)
18	117 718.60	118 398.36	0.0005(2)	0.11(7)

$c_5'^1\Sigma_u^+(v'=1) \leftarrow X^1\Sigma_g^+(v''=0)$

J	Transition energy (cm^{-1}) $P(J+1)$	$R(J-1)$	Term energy (cm^{-1})	Band f-value $P(J+1)$	$R(J-1)$	Linewidth (cm^{-1} FWHM)
2	118 055.72		118 079.59	0.00017(8)		3(1)
3	118 047.57		118 087.36	0.00013(4)		2.5(7)
4	118 037.84		118 097.52	0.00010(3)		2.2(6)
5	118 026.72		118 110.27	0.00010(3)		2.1(6)
6	118 014.25		118 125.65	0.00007(2)		2.0(6)
7	118 000.33		118 143.55	0.00004(1)		1.6(5)
8	117 985.06	118 052.68	118 164.08	0.000024(8)	0.00007(3)	1.1(6)
9	117 968.38	118 043.95	118 187.17	0.000009(3)	0.000027(9)	0.9(6)
10		118 033.96	118 212.98		0.000015(7)	0.9(8)
11		118 022.38	118 241.16		0.000006(3)	1.0(9)
12	117 910.44		118 272.35	0.000018(8)		0.9(8)
13	117 888.38	117 995.71	118 305.94	0.00005(6)	0.000004(2)	0.0(6)
14	117 865.04	117 980.29	118 342.20	0.00006(6)	0.000024(9)	0.5(6)
15	117 840.48	117 963.67	118 381.22	0.00017(7)	0.00003(2)	0.1(5)
16	117 814.76	117 945.87	118 423.04	0.00015(5)	0.00009(3)	0.6(5)
17	117 787.92	117 926.94	118 467.68	0.0003(1)	0.00012(4)	0.4(5)
18		117 907.10	118 515.37		0.00024(8)	0.7(5)
19		117 886.74	118 566.50		0.0003(1)	1.3(6)
20		117 866.37	118 621.58		0.0003(1)	1.2(8)
21		117 847.08	118 681.69		0.0004(1)	1.6(5)
22		117 830.20	118 748.16		0.0003(1)	1.1(6)
23		117 816.72	118 821.97		0.00020(9)	0.6(8)
24		117 805.95	118 902.45		0.00016(9)	0.2(9)
25		117 796.87	118 988.55		0.00012(6)	0.1(9)

$b'^1\Sigma_u^+(v'=22) \leftarrow X^1\Sigma_g^+(v''=0)$

J	Transition energy (cm^{-1}) $P(J+1)$	$R(J-1)$	Term energy (cm^{-1})	Band f-value $P(J+1)$	$R(J-1)$	Linewidth (cm^{-1} FWHM)
0	118 481.40		118 485.38	0.004(1)		1.6(5)
1	118 475.65	118 487.59	118 487.59	0.0037(5)	0.0038(4)	1.5(1)
2	118 468.14	118 488.03	118 492.01	0.0038(5)	0.0039(4)	1.5(1)
3	118 458.81	118 486.66	118 498.60	0.0033(4)	0.0038(4)	1.42(7)
4	118 447.74	118 483.55	118 507.42	0.0032(4)	0.0041(5)	1.25(9)
5	118 434.97	118 478.73	118 518.52	0.0034(4)	0.0035(4)	1.37(8)
6	118 420.47	118 472.19	118 531.87	0.0027(3)	0.0033(4)	1.1(1)
7	118 404.15	118 463.82	118 547.37	0.0029(3)	0.0034(4)	1.17(7)
8	118 386.18	118 453.80	118 565.20	0.0038(4)	0.0031(4)	0.9(1)
9	118 366.59	118 442.15	118 585.37	0.0034(4)	0.0032(3)	0.91(9)
10	118 345.21	118 428.72	118 607.73	0.0025(3)	0.0029(4)	0.84(6)
11	118 322.31	118 413.76	118 632.54	0.0033(4)	0.0030(3)	0.88(4)
12	118 297.80	118 397.19	118 659.71	0.0031(4)	0.0029(4)	0.79(6)
13	118 271.78	118 379.10	118 689.34	0.0028(3)	0.0028(3)	0.70(4)
14	118 244.25	118 359.50	118 721.41	0.0029(5)	0.0028(4)	0.70(7)
15	118 215.35	118 338.53	118 756.09	0.0024(4)	0.0027(3)	0.79(6)
16	118 185.07	118 316.17	118 793.34	0.0031(8)	0.0028(5)	0.8(1)
17	118 153.61	118 292.63	118 833.37	0.0026(6)	0.0024(4)	1.0(1)

A.3 Results of the coupled-channels model

This appendix contains summarised data generated by the coupled-channels model for many excited electronic-vibrational levels of $^1\Pi_u$ or $^1\Sigma_u^+$ symmetry, as well as properties of their optical excitation from the ground state. This information is presented graphically and also includes a comparison with relevant experimental data. Calculations have been made for both e- and f-parity levels, so two models are required. These are the final products of Chap. 6 and have the same formulations as described in Sec. 6.6.3.

Photodissociation cross sections have been calculated which include all transitions of $^{14}N_2$, $^{14}N^{15}N$, and $^{15}N_2$ from the $v = 0$ ground-state to excited levels with energies in the range of $100\,000 - 125\,000\,\mathrm{cm}^{-1}$ $(80 - 100\,\mathrm{nm})$, and with total angular-momentum $J \leq 30$. Resonances are identifiable in these spectra and have been grouped into rotational series. Some of these resonances correspond to experimentally known transitions but many have not been observed. A Fano lineshape was fitted to each resonance profile, and values representing its line centre, full-width half-maximum, and integrated strength extracted. Line strengths were converted into dimensionless band f-values by the division of Hönl-London factors according to Eq. (2.108) and the line centre of each transition converted into a term value by the addition of a rotation- and isotopomer-dependent ground-state energy.

Given the highly perturbed nature of N_2 excited states, the assignment of calculated resonances to particular electronic-vibrational levels is somewhat arbitrary and an attempt has been made here to choose assignments that reflect the principal electronic character of the calculated levels. In accordance with this convention, diabatic assignments have been made where the term series of interacting states cross. In a few cases where strong interactions of multiple bands are evident, it is simpler to make adiabatic non-crossing assignments.

Pages 215 to 223 summarise the assignment of term values with plots of energy versus J. A series of figures following these reproduces the calculated spectroscopic data of individual vibrational levels, as well as comparable experimental quantities.

Plots labelled "reduced terms" reproduce term values which have been modified by the subtraction of the function $T_{0v}+B_vJ(J+1)-D_vJ^2(J+1)^2$, with coefficients selected to best fit each term series. Plots of the difference between e- and f-parity levels for $^1\Pi_u$ states are labelled "$T_e - T_f$". Calculated term values are plotted as curves and experimental values as points. Uncertainties in the experimental data vary according to their origin, but all have a random component with standard deviation $\leq 0.1\,\mathrm{cm}^{-1}$, and absolute calibration errors are $\leq 0.5\,\mathrm{cm}^{-1}$. Residual errors of the model are also instructive and the difference between experimental and modelled term values are plotted as "$T^{\mathrm{exp}} - T^{\mathrm{mod}}$". All term value related quantities are in units of cm^{-1}.

Calculated linewidths, Γ, and f-values, f, are plotted as curves on both linear and logarithmic scales, because of their frequent variation across multiple orders of magnitude, and are in units of $\mathrm{cm}^{-1}\,\mathrm{FWHM}$ and cm^{-1}, respectively. Error bars indicate the experimentally known linewidths and f-values as well as their uncertainties. The various sources of experimental $^1\Pi_u$ and $^1\Sigma_u^+$ linewidths are listed in Tabs. 6.3 and A.1, respectively. All experimental f-values are the published results of the KEK and SOLEIL photoabsorption experiments [50, 51, 155, 156, 157, 158], discussed in Chaps. 4 and 5.

Finally, the model-determined diabatic electronic characters of all e-parity levels are shown in plots labelled "e parity elec. char.". These are calculated by integrating the coupled-channels mixed radial wavefunctions over R, at an energy corresponding to the

Level	Γ cm^{-1}	Reference
	$^{14}N_2$	
$b'(1)$	0.0167(17)	[172]
$b'(4)$	0.033(14)	[150]
$b'(5)$	0.0070(8)	[129]
$b'(6)$	0.088(15)	[150]
$b'(7)$	0.00570(85)	[125]
$b'(8)$	0.044(9)	[144]
$b'(9)$	0.0075(11)	[125]
$b'(11)$	0.057(5)	[144]
$b'(12)$	0.0212(32)	[125]
$b'(13)$	0.0692(29)	[53]
$b'(14)$	0.19(5)	[50]
$b'(15)$	0.17(3)	[50]
$b'(16)$	0.084(9)	Chap. 5
$b'(17)$	0.23(2)	[50]
$b'(18)$	0.081(13)	Chap. 5
$b'(19)$	0.11(2)	Chap. 5
$b'(20)$	0.142(23)	Chap. 5
$b'(21)$	2.46(9)	Chap. 5
$b'(22)$	1.35(2)	Chap. 5
$c'_4(0)$	0.0193(17)	[172]
$c'_4(1)$	0.0196(51)	[150]
$c'_4(2)$	0.0100(28)	[150]
$c'_4(4)$	0.014(2)	[53]
$c'_4(5)$	0.7(1)	[50]
$c'_4(6)$	0.049(8)	Chap. 5
$c'_5(1)$	2.79(44)	Chap. 5
	$^{14}N^{15}N$	
$c'_4(1)$	0.0221(32)	[170]
	$^{15}N_2$	
$b'(1)$	0.0082(10)	[168]
$b'(5)$	0.0212(68)	[150]
$b'(6)$	0.096(18)	[150]
$c'_4(0)$	0.0099(6)	[147]
$c'_4(1)$	0.0171(44)	[150]

Table A.1: Experimentally determined natural linewidths, Γ, of $^1\Sigma_u^+$ states. The listed widths are extrapolated to $J = 0$ and many bands have variable widths for higher J. In the case of $c'_4\,{}^1\Sigma_u^+(v = 7)$, the lowest observed width was for $J = 7$.

centre of each resonance, and are normalised by the sum of characters for all $^1\Sigma_u^+$ and $^1\Pi_u$ levels.

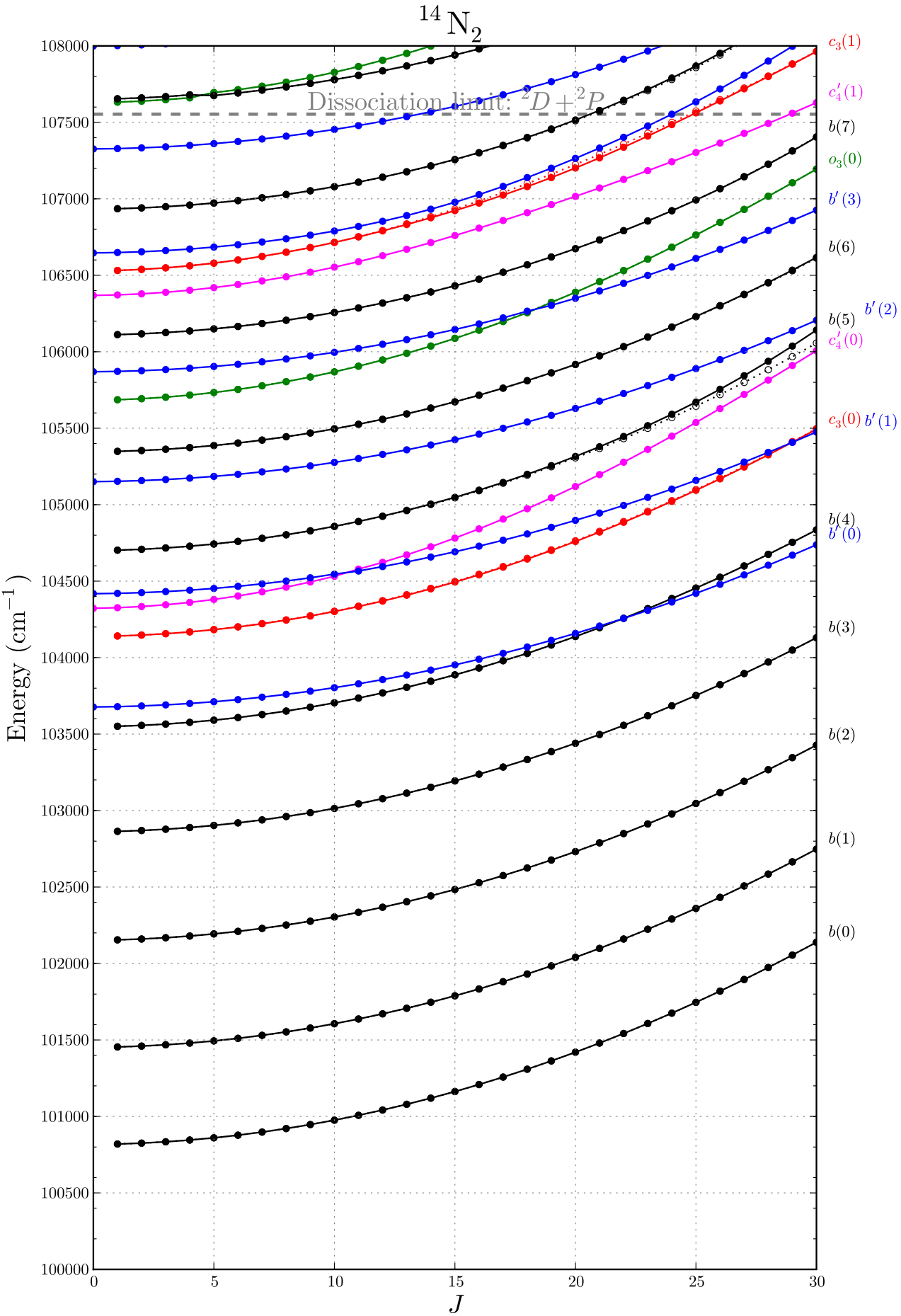
$^{14}N_2$
Dissociation limit: $^2D + {}^2P$
Energy (cm^{-1})
J
$c_3(1)$
$c_4'(1)$
$b(7)$
$o_3(0)$
$b'(3)$
$b(6)$
$b(5)$
$b'(2)$
$c_4'(0)$
$c_3(0)$
$b'(1)$
$b(4)$
$b'(0)$
$b(3)$
$b(2)$
$b(1)$
$b(0)$

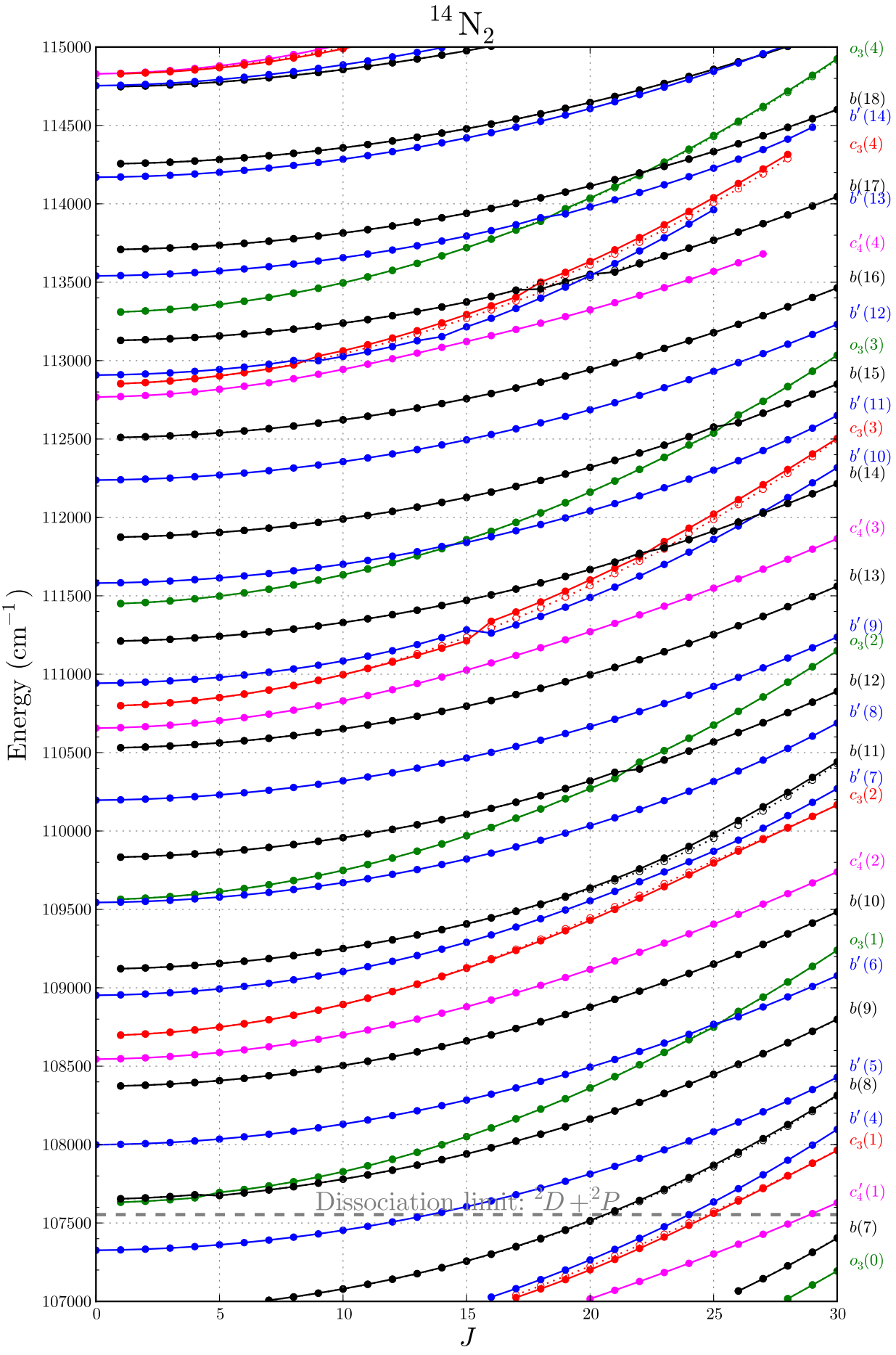
$^{14}N_2$
Energy (cm^{-1})
J
Dissociation limit: $^2D + ^2P$
$o_3(4)$
$b(18)$
$b'(14)$
$c_3(4)$
$b(17)$
$b'(13)$
$c_4'(4)$
$b(16)$
$b'(12)$
$o_3(3)$
$b(15)$
$b'(11)$
$c_3(3)$
$b'(10)$
$b(14)$
$c_4'(3)$
$b(13)$
$b'(9)$
$o_3(2)$
$b(12)$
$b'(8)$
$b(11)$
$b'(7)$
$c_3(2)$
$c_4'(2)$
$b(10)$
$o_3(1)$
$b'(6)$
$b(9)$
$b'(5)$
$b(8)$
$b'(4)$
$c_3(1)$
$c_4'(1)$
$b(7)$
$o_3(0)$

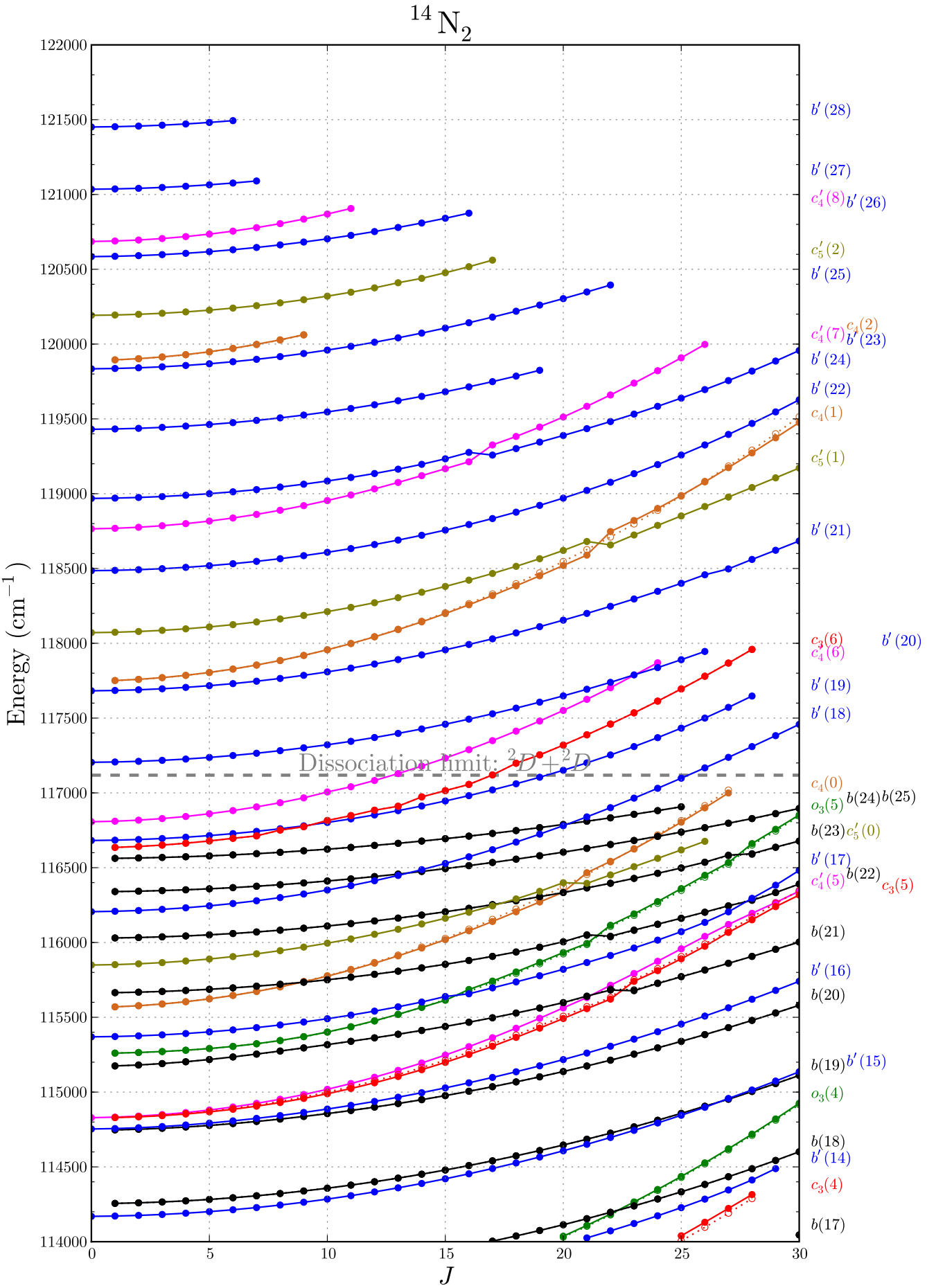
$^{14}N_2$
Energy (cm^{-1})
J
Dissociation limit: $^2D + ^2D$
$b'(28)$
$b'(27)$
$c_4'(8)$ $b'(26)$
$c_5'(2)$
$b'(25)$
$c_4'(7)$ $c_4(2)$ $b'(23)$
$b'(24)$
$b'(22)$
$c_4(1)$
$c_5'(1)$
$b'(21)$
$c_3(6)$ $c_4(6)$ $b'(20)$
$b'(19)$
$b'(18)$
$c_4(0)$
$o_3(5)$ $b(24)$ $b(25)$
$b(23)$ $c_5'(0)$
$b'(17)$
$c_4'(5)$ $b(22)$ $c_3(5)$
$b(21)$
$b'(16)$
$b(20)$
$b(19)$ $b'(15)$
$o_3(4)$
$b(18)$
$b'(14)$
$c_3(4)$
$b(17)$

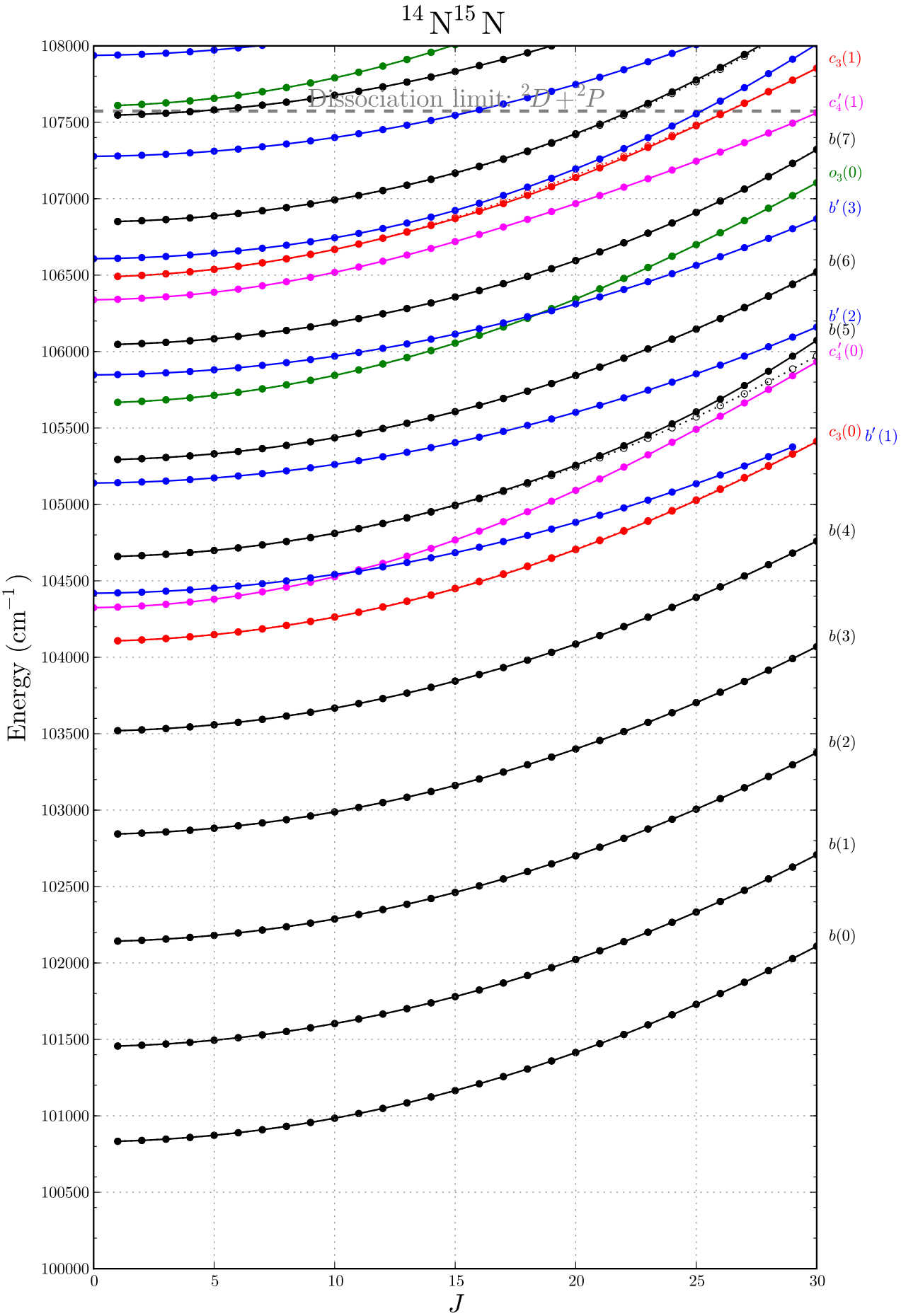
^{14}N^{15}N
Dissociation limit: $^2D+^2P$
$c_3(1)$
$c_4'(1)$
$b(7)$
$o_3(0)$
$b'(3)$
$b(6)$
$b'(2)$
$b(5)$
$c_4'(0)$
$c_3(0)$ $b'(1)$
$b(4)$
$b(3)$
$b(2)$
$b(1)$
$b(0)$
Energy (cm^{-1})
J
108000
107500
107000
106500
106000
105500
105000
104500
104000
103500
103000
102500
102000
101500
101000
100500
100000
0
5
10
15
20
25
30

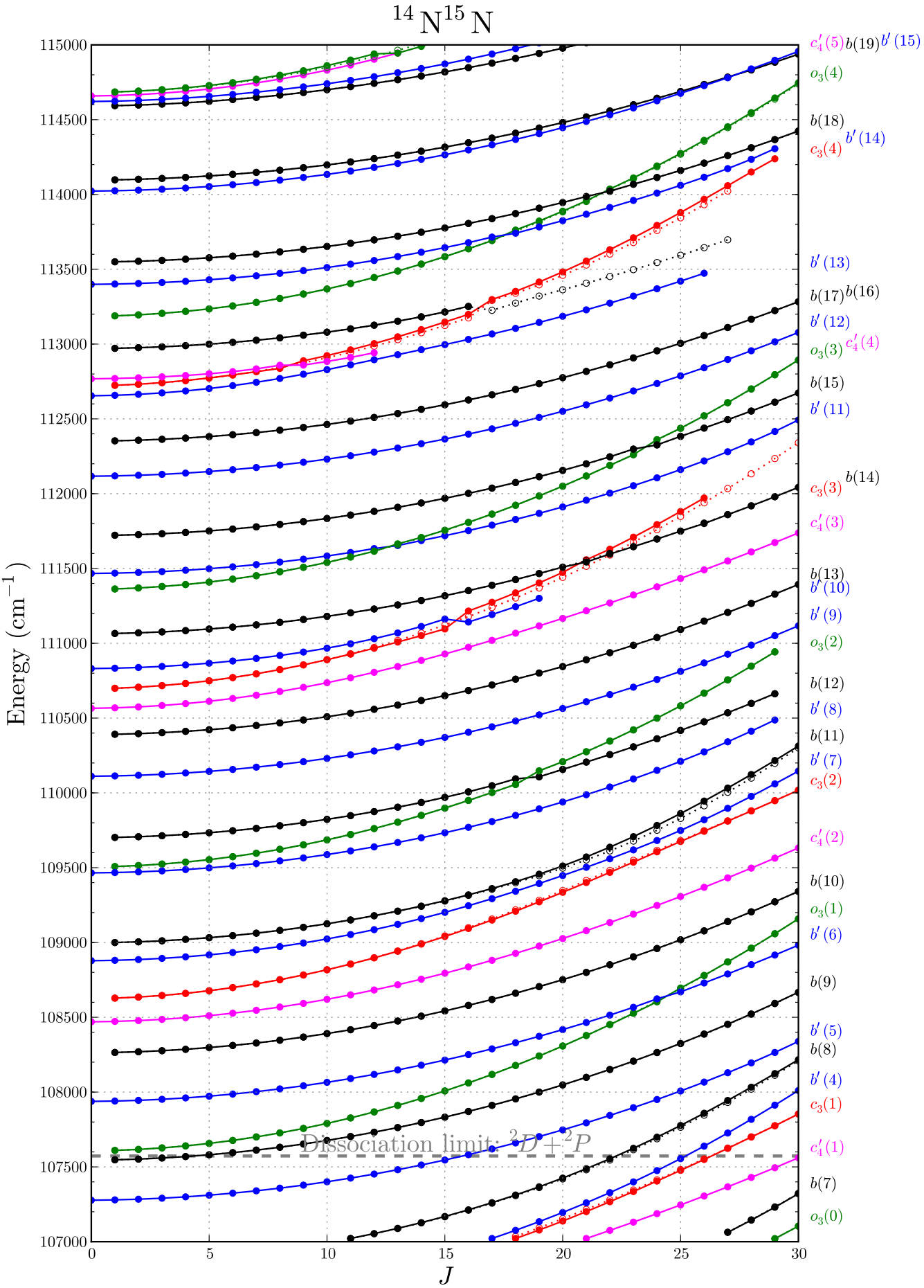
^{14}N^{15}N
Energy (cm^{-1})
J
Dissociation limit: $^2D + ^2P$
$c_4'(5)$ $b(19)$ $b'(15)$
$o_3(4)$
$b(18)$
$c_3(4)$ $b'(14)$
$b'(13)$
$b(17)$ $b(16)$
$b'(12)$
$o_3(3)$ $c_4'(4)$
$b(15)$
$b'(11)$
$c_3(3)$ $b(14)$
$c_4'(3)$
$b(13)$ $b'(10)$
$b'(9)$
$o_3(2)$
$b(12)$
$b'(8)$
$b(11)$
$b'(7)$
$c_3(2)$
$c_4'(2)$
$b(10)$
$o_3(1)$
$b'(6)$
$b(9)$
$b'(5)$ $b(8)$
$b'(4)$
$c_3(1)$
$c_4'(1)$
$b(7)$
$o_3(0)$

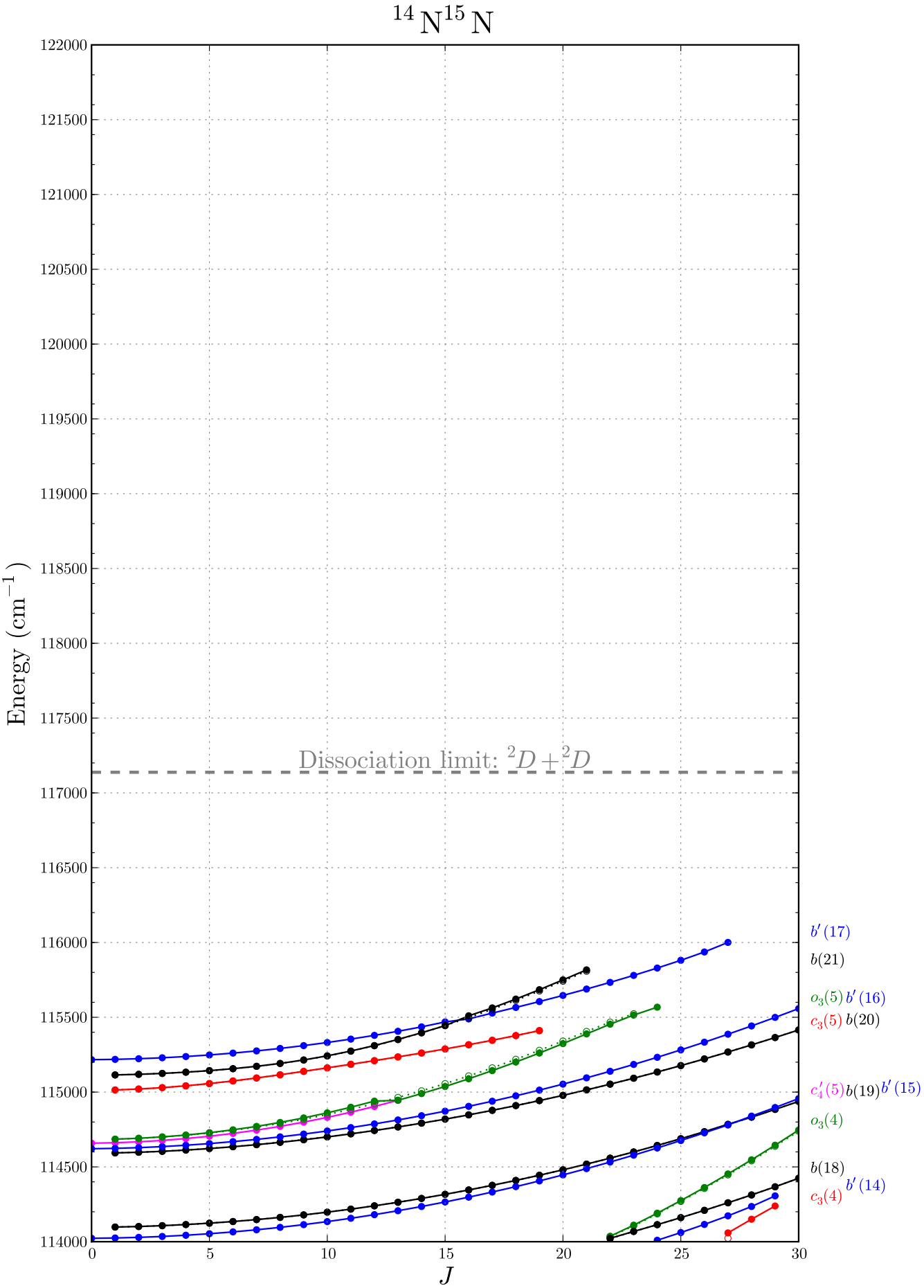
$^{14}N^{15}N$
Energy (cm^{-1})
J
Dissociation limit: $^2D + ^2D$
$b'(17)$
$b(21)$
$o_3(5)$ $b'(16)$
$c_3(5)$ $b(20)$
$c_4'(5)$ $b(19)$ $b'(15)$
$o_3(4)$
$b(18)$
$c_3(4)$ $b'(14)$

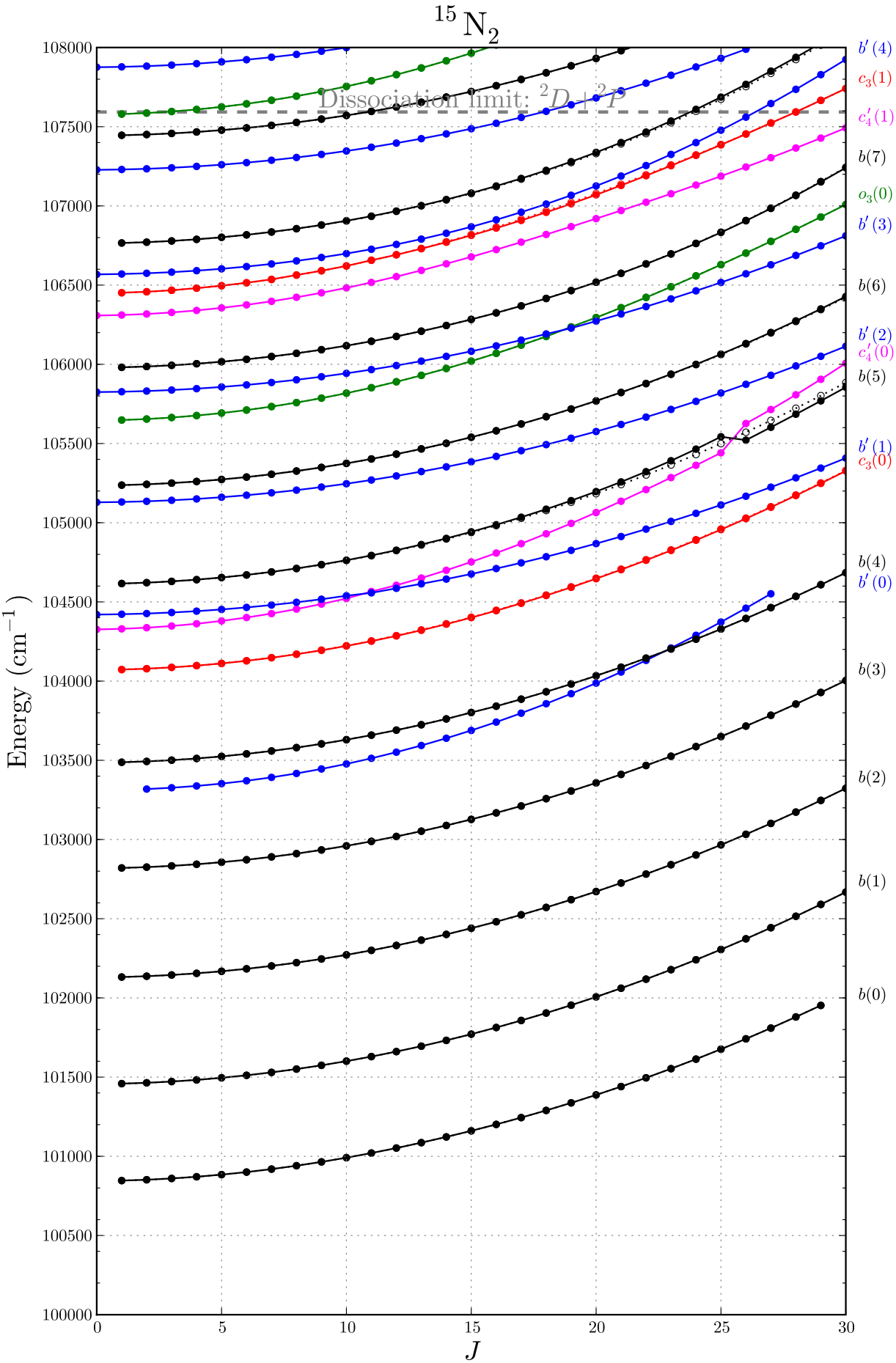
$^{15}N_2$
Dissociation limit: $^2D + ^2P$
Energy (cm^{-1})
J
$b'(4)$
$c_3(1)$
$c_4'(1)$
$b(7)$
$o_3(0)$
$b'(3)$
$b(6)$
$b'(2)$
$c_4'(0)$
$b(5)$
$b'(1)$
$c_3(0)$
$b(4)$
$b'(0)$
$b(3)$
$b(2)$
$b(1)$
$b(0)$

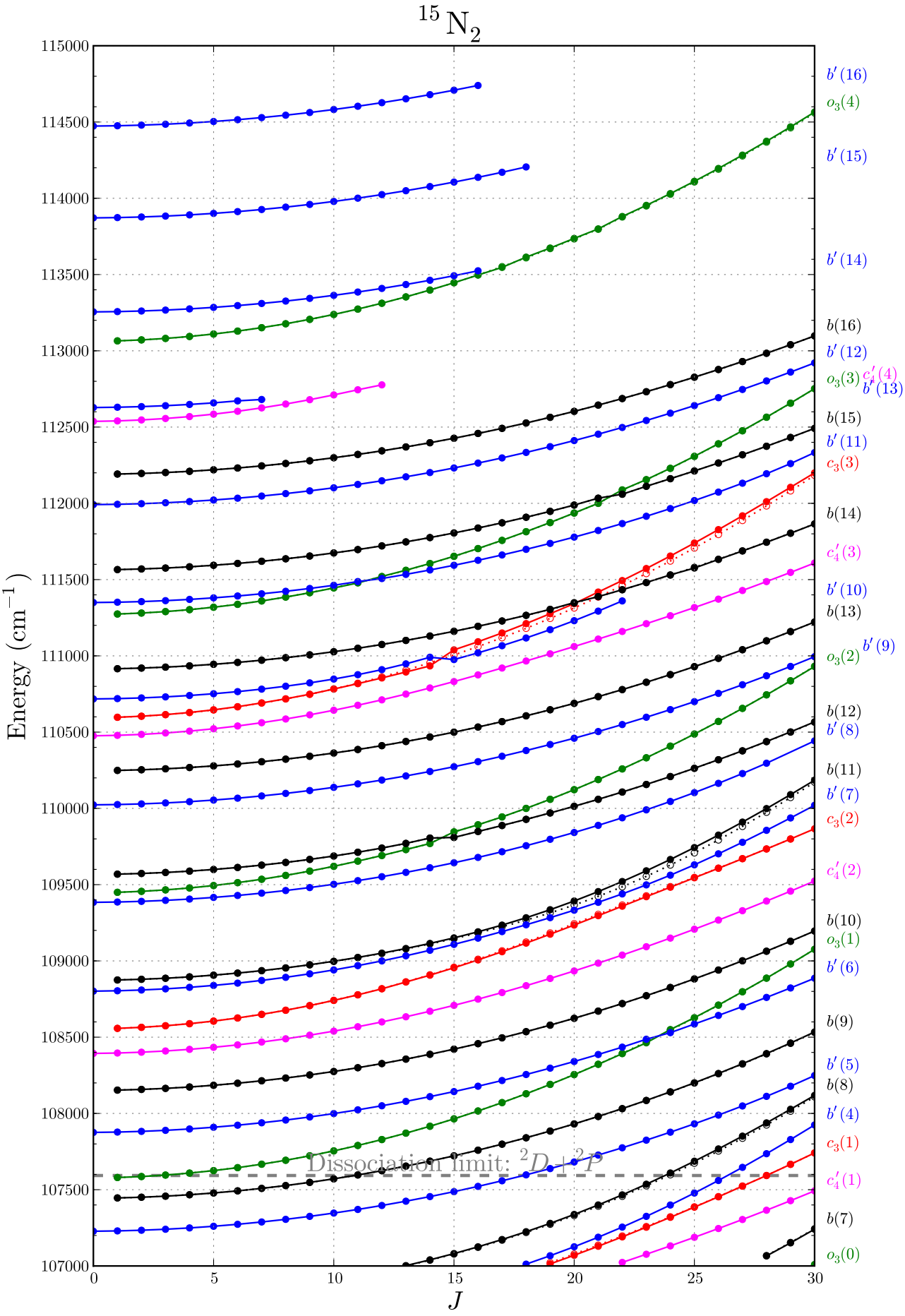
$^{15}N_2$
Energy (cm^{-1})
J
Dissociation limit: $^2D + ^2P$
$b'(16)$
$o_3(4)$
$b'(15)$
$b'(14)$
$b(16)$
$b'(12)$
$o_3(3)$
$c_4'(4)$
$b'(13)$
$b(15)$
$b'(11)$
$c_3(3)$
$b(14)$
$c_4'(3)$
$b'(10)$
$b(13)$
$o_3(2)$
$b'(9)$
$b(12)$
$b'(8)$
$b(11)$
$b'(7)$
$c_3(2)$
$c_4'(2)$
$b(10)$
$o_3(1)$
$b'(6)$
$b(9)$
$b'(5)$
$b(8)$
$b'(4)$
$c_3(1)$
$c_4'(1)$
$b(7)$
$o_3(0)$

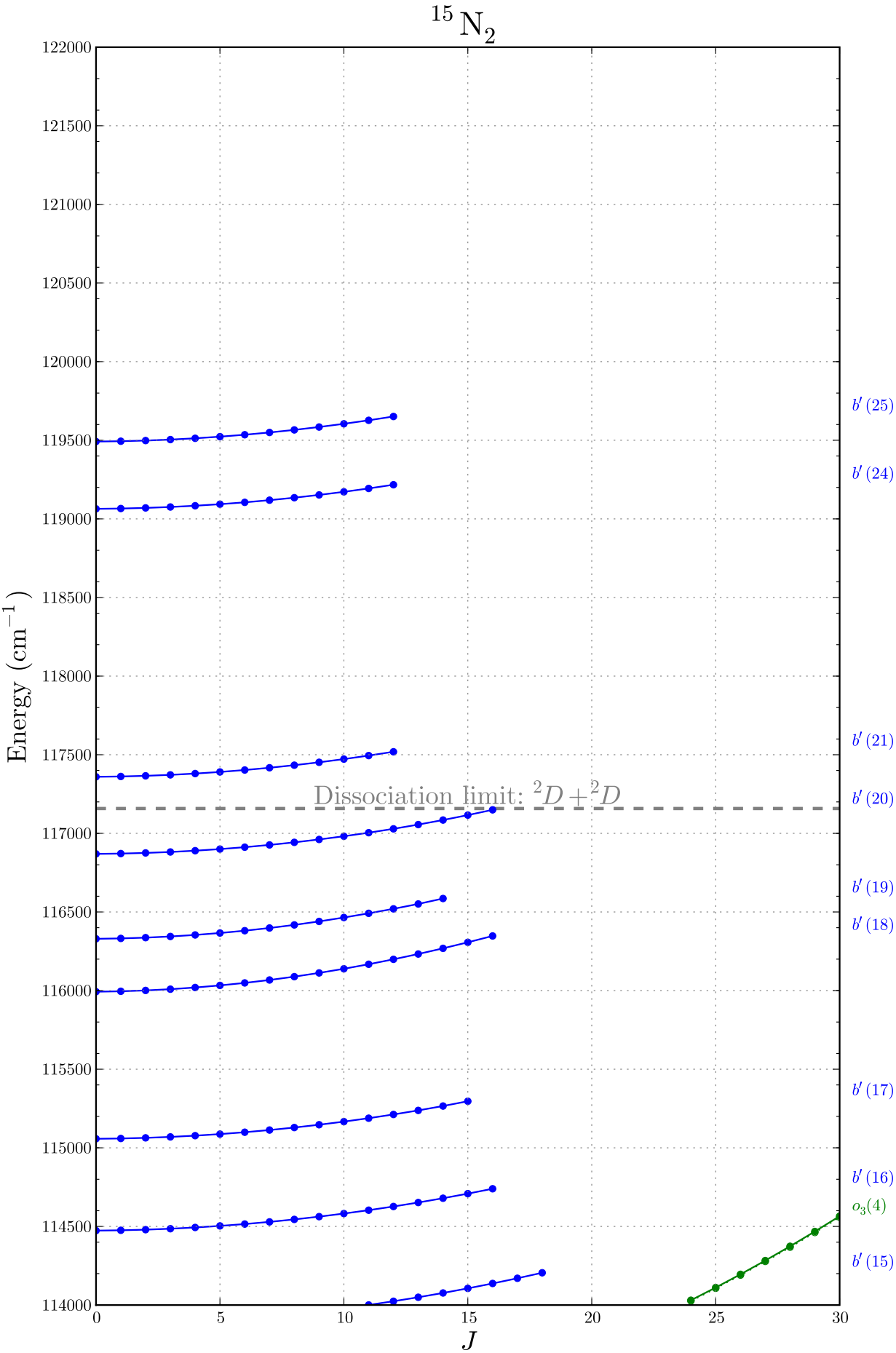
$^{15}N_2$
Energy (cm^{-1})
J
Dissociation limit: $^2D + ^2D$
$b'(25)$
$b'(24)$
$b'(21)$
$b'(20)$
$b'(19)$
$b'(18)$
$b'(17)$
$b'(16)$
$o_3(4)$
$b'(15)$

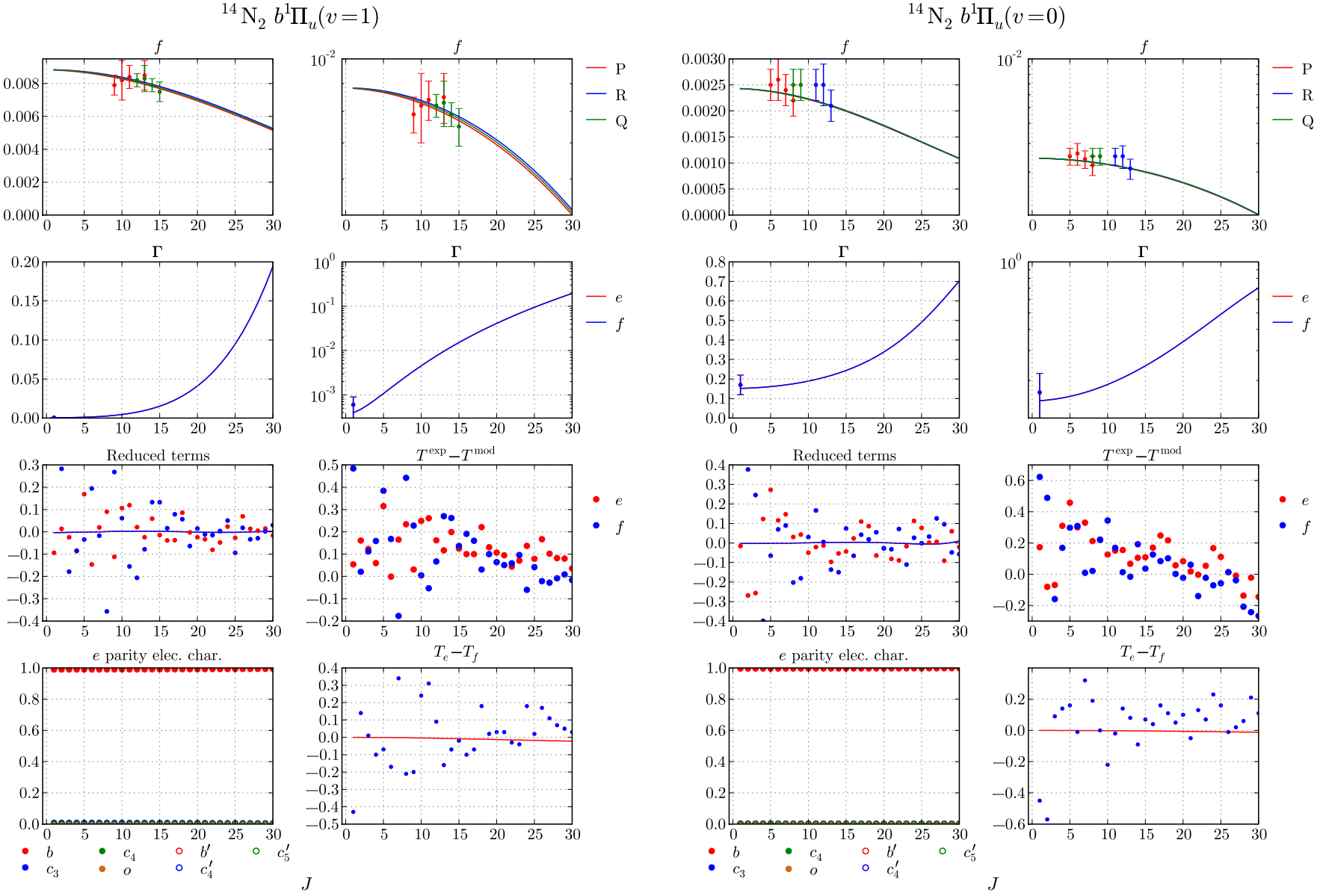
$^{14}N_2$ $b^1\Pi_u(v=1)$
$^{14}N_2$ $b^1\Pi_u(v=0)$
f
Γ
Reduced terms
$T^{exp}-T^{mod}$
e parity elec. char.
T_e-T_f
P
R
Q
e
f
b
c_3
c_4
o
b'
c_4'
c_5'
J

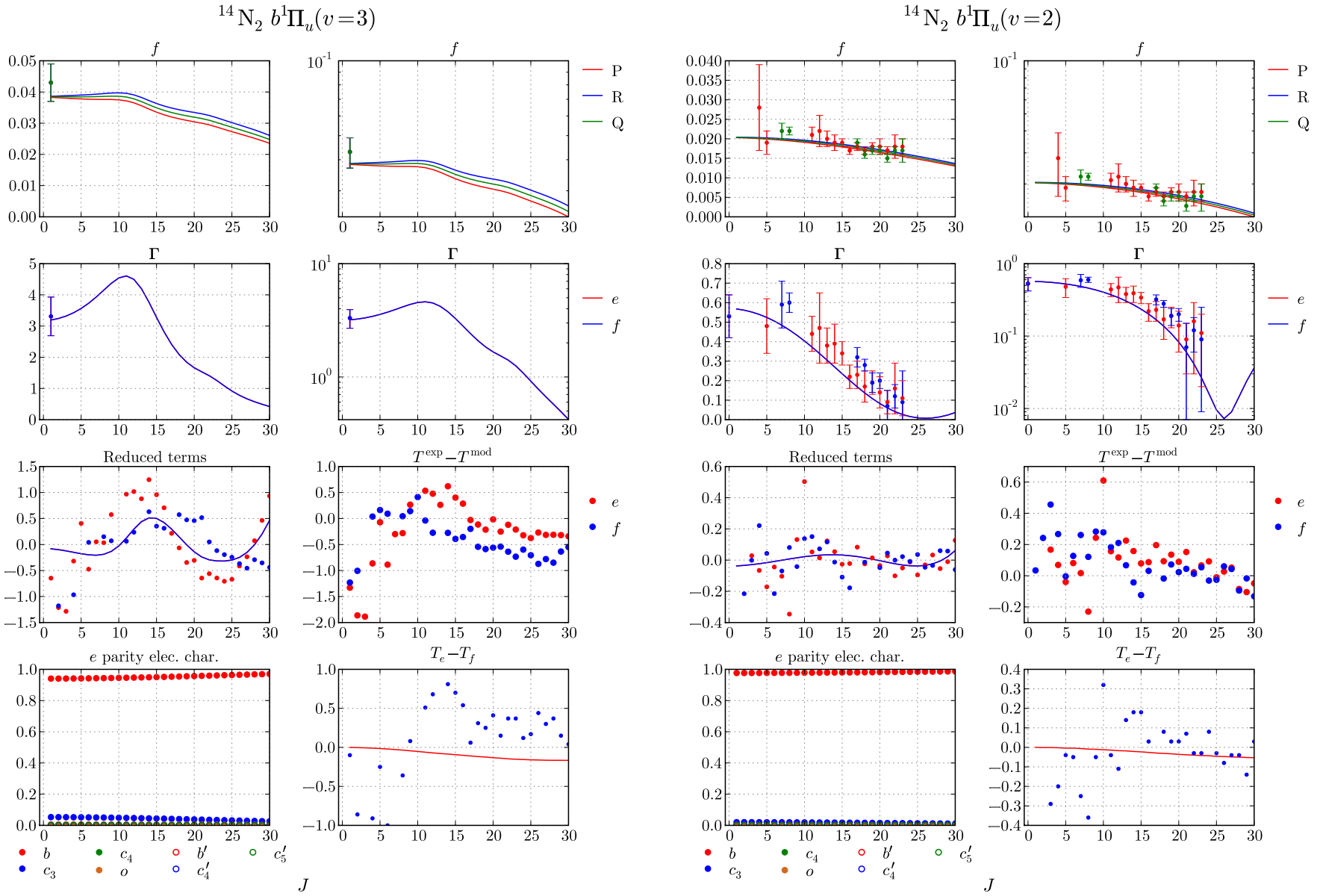
$^{14}N_2$ $b^1\Pi_u(v=3)$
$^{14}N_2$ $b^1\Pi_u(v=2)$
f
Γ
Reduced terms
$T^{exp}-T^{mod}$
e parity elec. char.
T_e-T_f
P
R
Q
e
f
b
c_3
c_4
o
b'
c_4'
c_5'
J

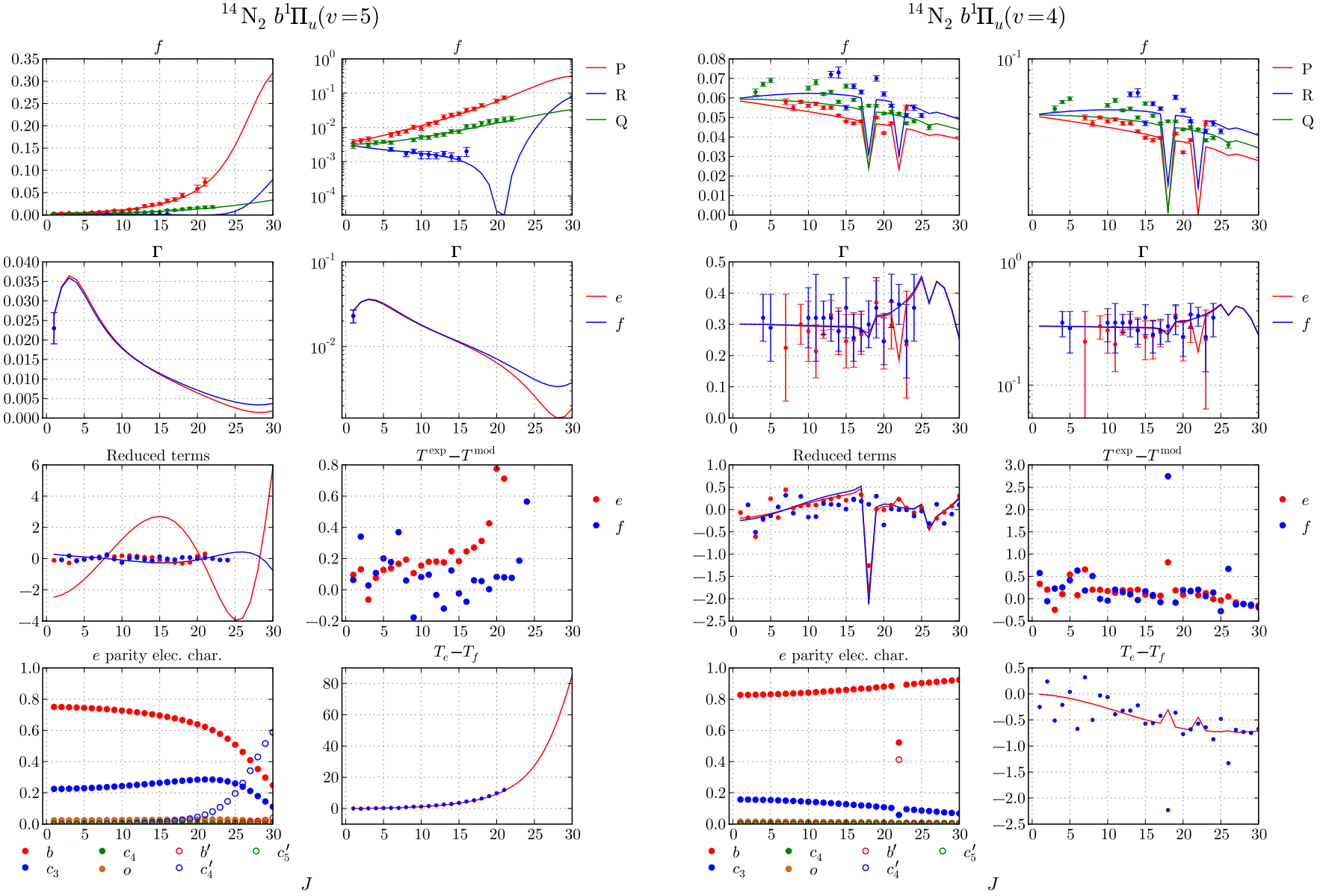
$^{14}N_2$ $b^1\Pi_u(v=5)$
$^{14}N_2$ $b^1\Pi_u(v=4)$
f
Γ
Reduced terms
$T^{exp}-T^{mod}$
e parity elec. char.
T_e-T_f
P
R
Q
e
f
b
c_3
c_4
o
b'
c_4'
c_5'
J

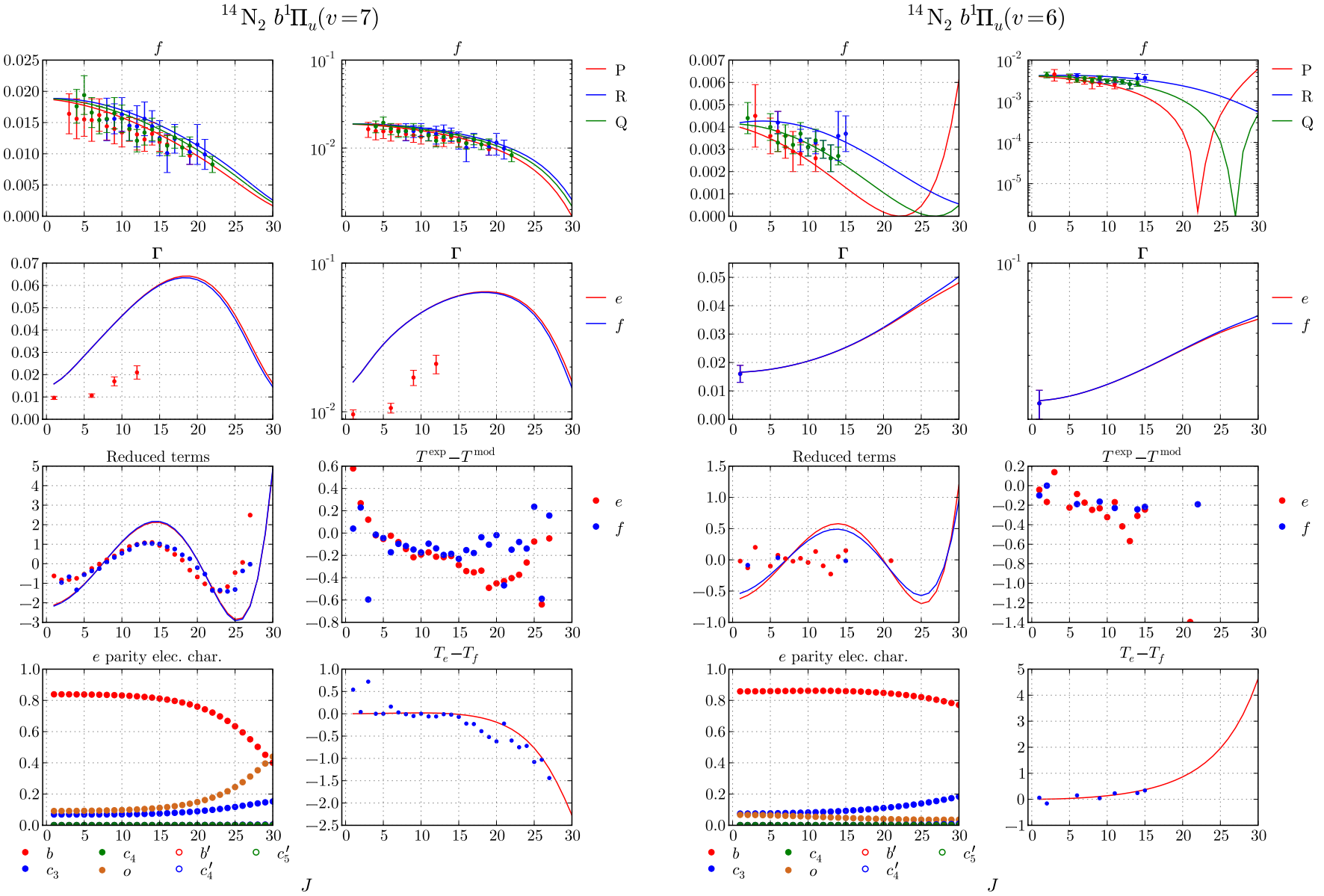
$^{14}\mathrm{N}_2$ $b\,^1\Pi_u(v=7)$
$^{14}\mathrm{N}_2$ $b\,^1\Pi_u(v=6)$
f
Γ
Reduced terms
$T^{\mathrm{exp}}-T^{\mathrm{mod}}$
e parity elec. char.
T_e-T_f
P
R
Q
e
f
b
c_3
c_4
o
b'
c_4'
c_5'
J

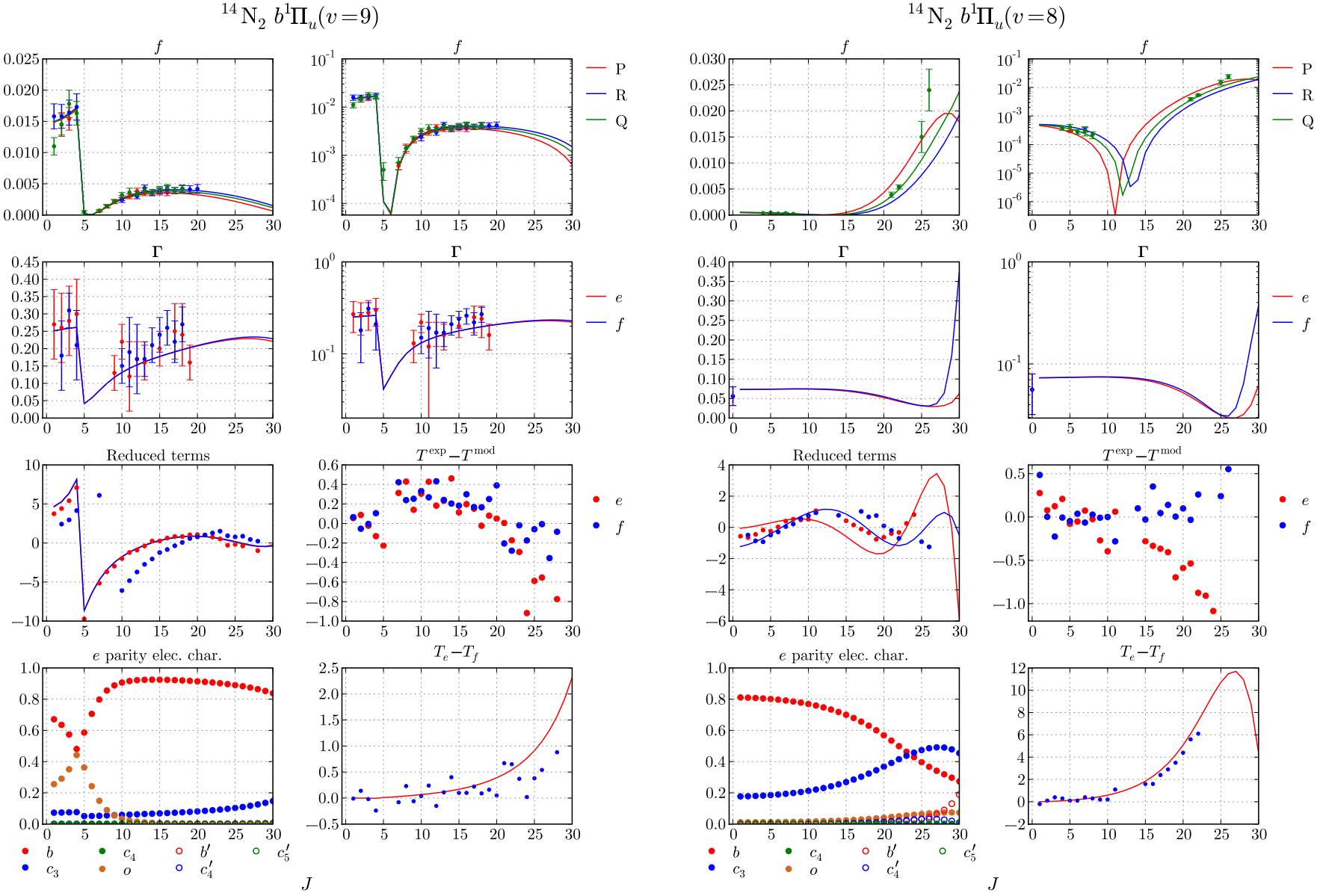
$^{14}N_2$ $b^1\Pi_u(v=9)$
$^{14}N_2$ $b^1\Pi_u(v=8)$
f
Γ
Reduced terms
$T^{exp}-T^{mod}$
e parity elec. char.
T_e-T_f
P
R
Q
e
f
b
c_3
c_4
o
b'
c_4'
c_5'
J

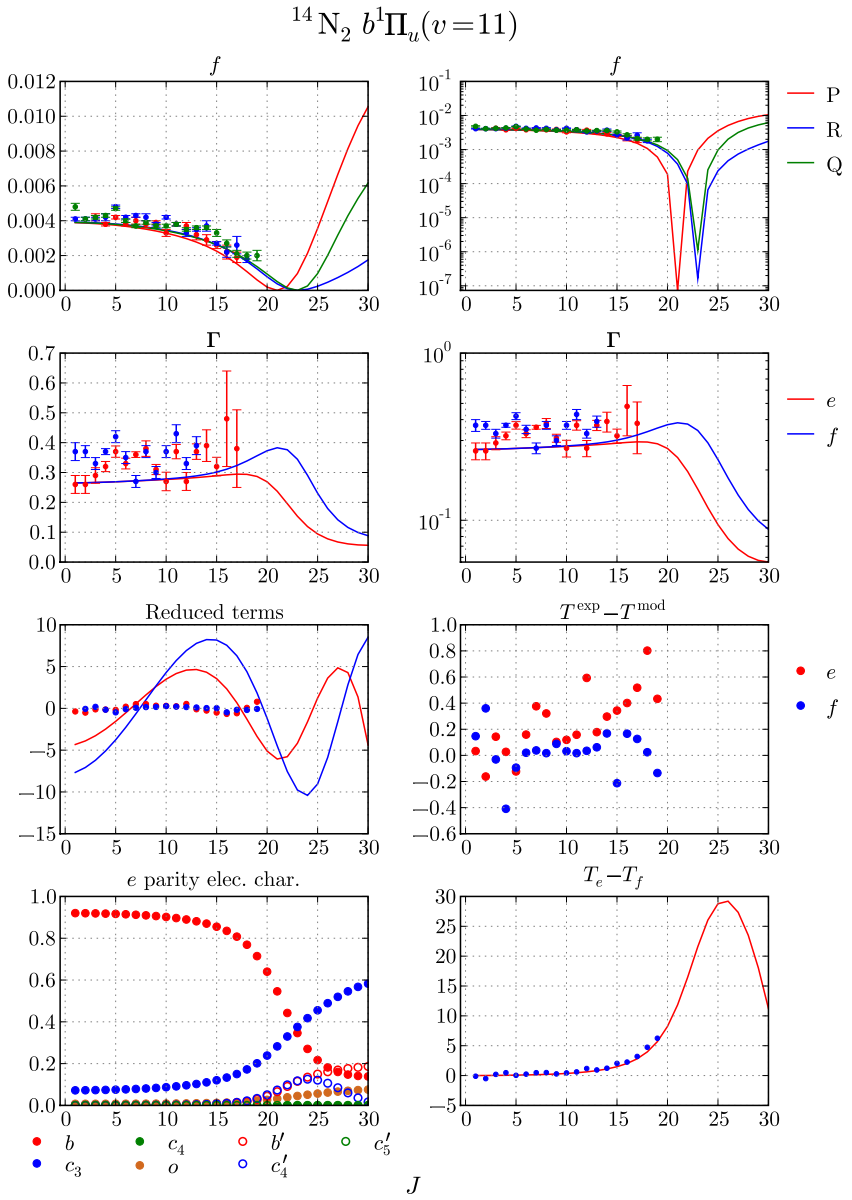
$^{14}\mathrm{N}_2$ $b^1\Pi_u(v=11)$
f
f
P
R
Q
Γ
Γ
e
f
Reduced terms
$T^{\mathrm{exp}}-T^{\mathrm{mod}}$
e
f
e parity elec. char.
T_e-T_f
b
c_3
c_4
o
b'
c_4'
c_5'
J

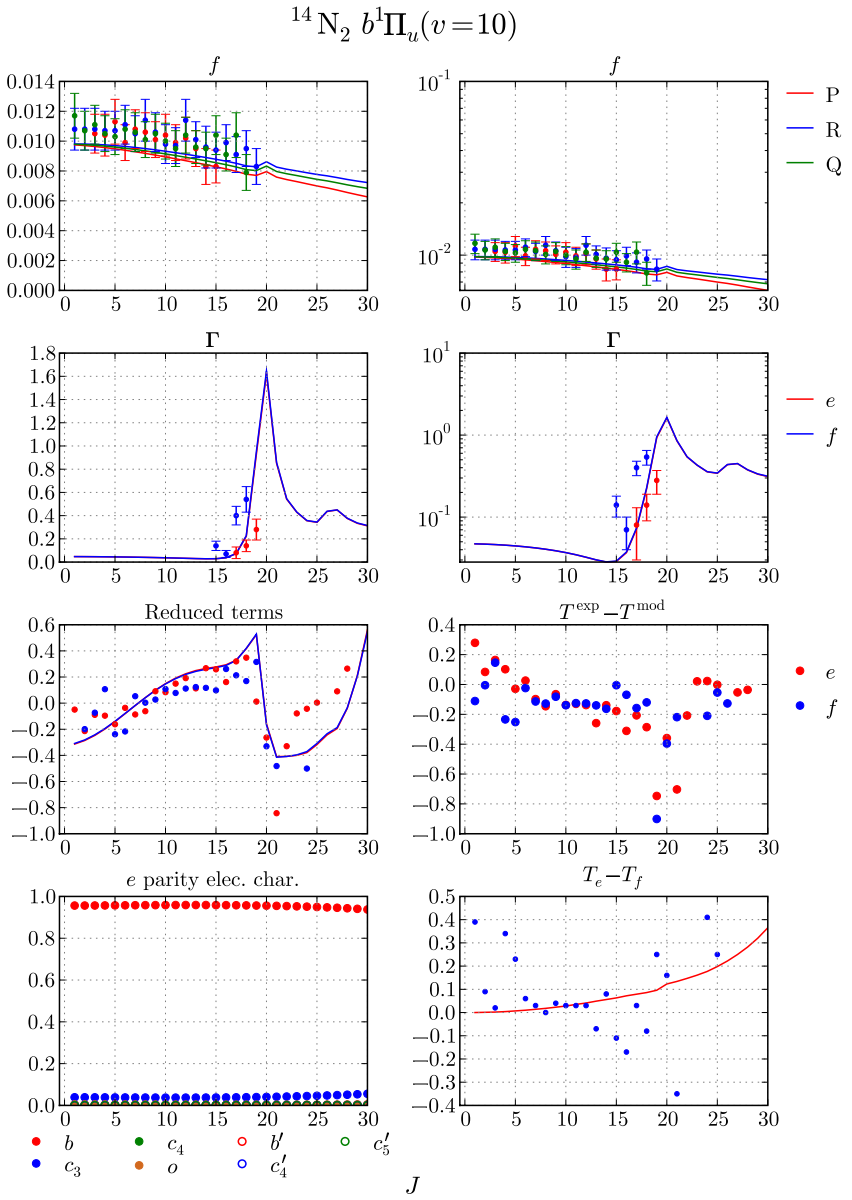
$^{14}\mathrm{N}_2$ $b^1\Pi_u(v=10)$
f
f
P
R
Q
Γ
Γ
e
f
Reduced terms
$T^{\mathrm{exp}}-T^{\mathrm{mod}}$
e
f
e parity elec. char.
T_e-T_f
b
c_3
c_4
o
b'
c_4'
c_5'
J

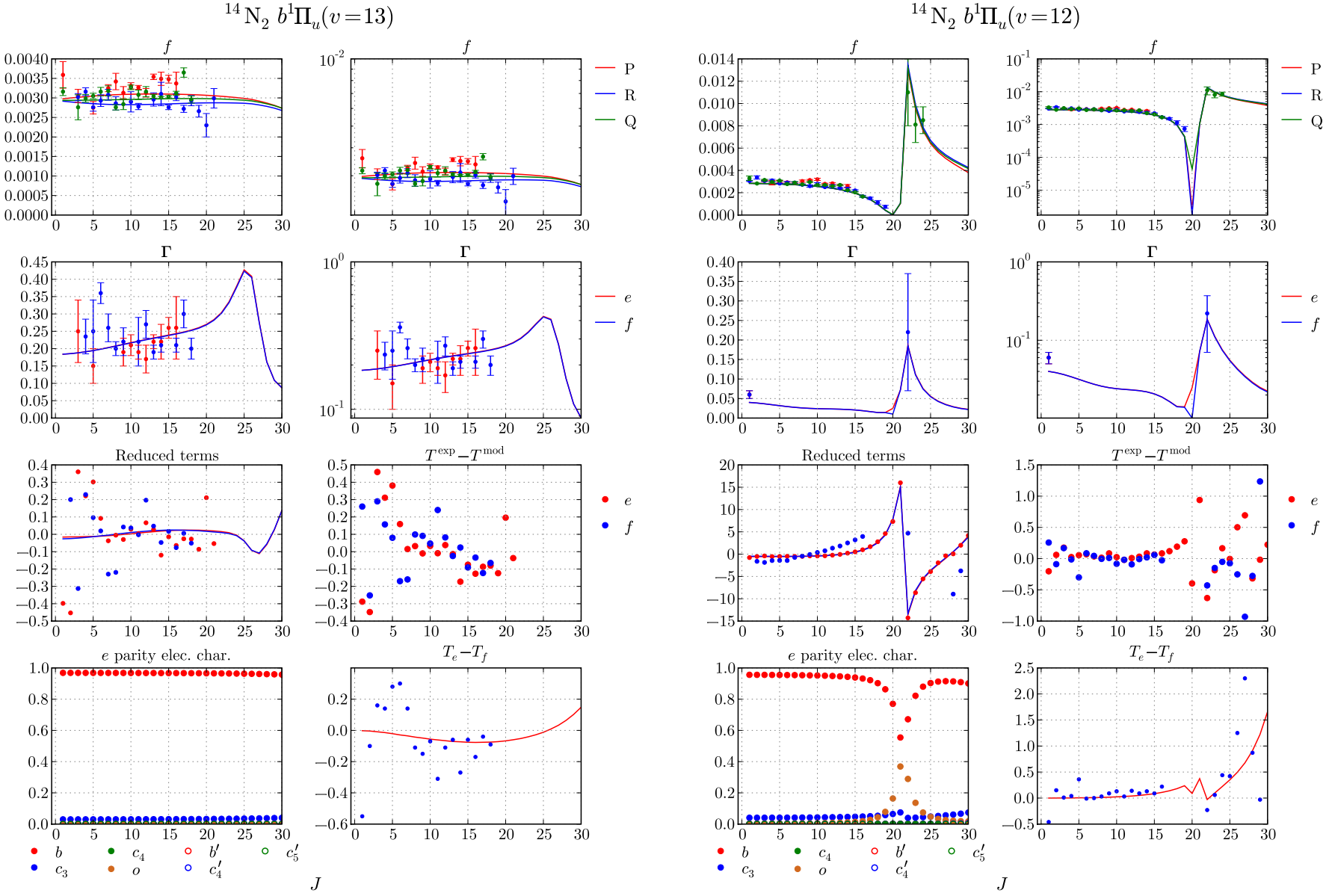
$^{14}N_2$ $b^1\Pi_u(v=13)$
$^{14}N_2$ $b^1\Pi_u(v=12)$
f
Γ
Reduced terms
$T^{exp}-T^{mod}$
e parity elec. char.
T_e-T_f
P
R
Q
e
f
b
c_3
c_4
o
b'
c_4'
c_5'
J

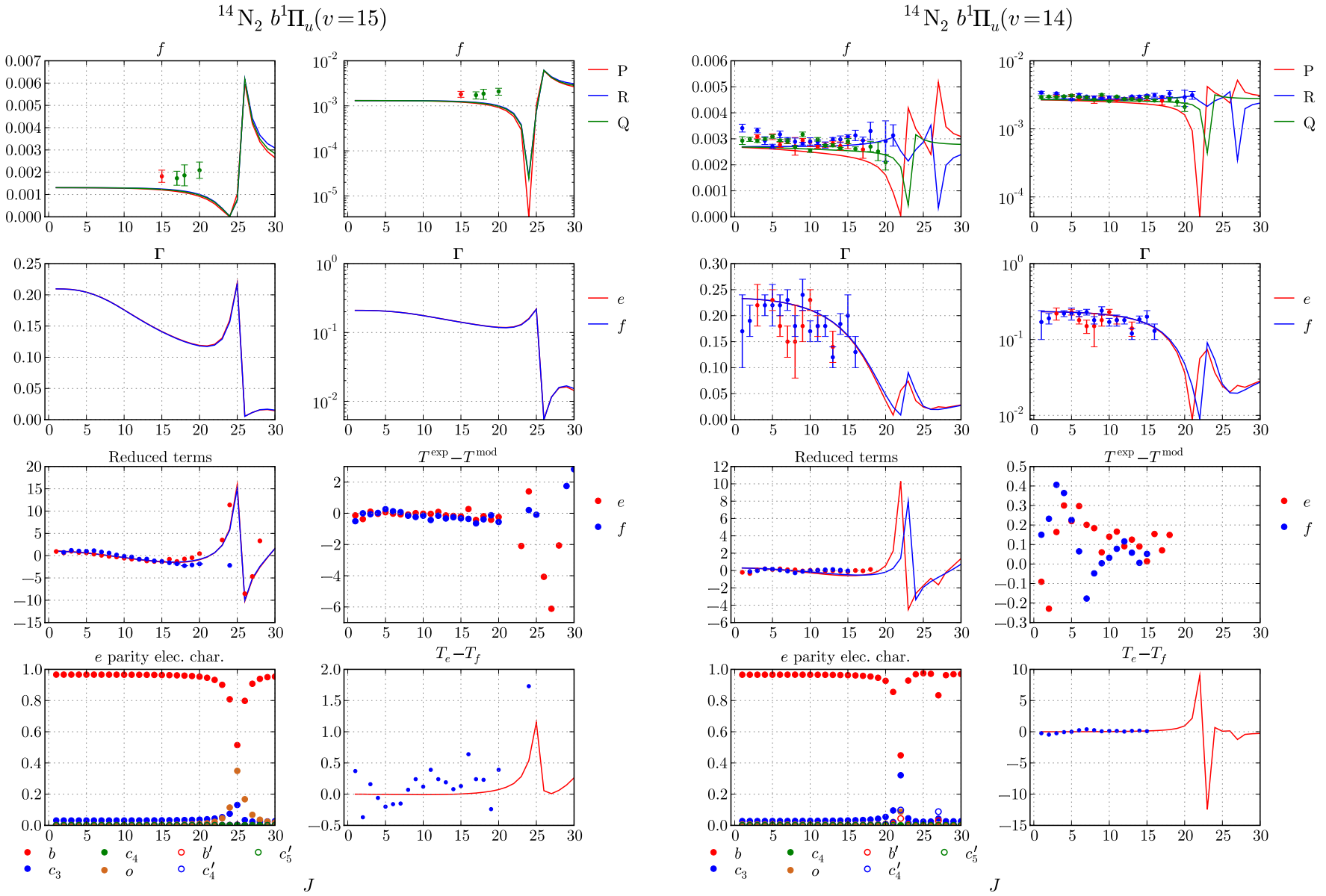
$^{14}\mathrm{N}_2$ $b^1\Pi_u(v=15)$
$^{14}\mathrm{N}_2$ $b^1\Pi_u(v=14)$
f
Γ
Reduced terms
$T^{\mathrm{exp}}-T^{\mathrm{mod}}$
e parity elec. char.
T_e-T_f
P
R
Q
e
f
b
c_3
c_4
o
b'
c_4'
c_5'
J

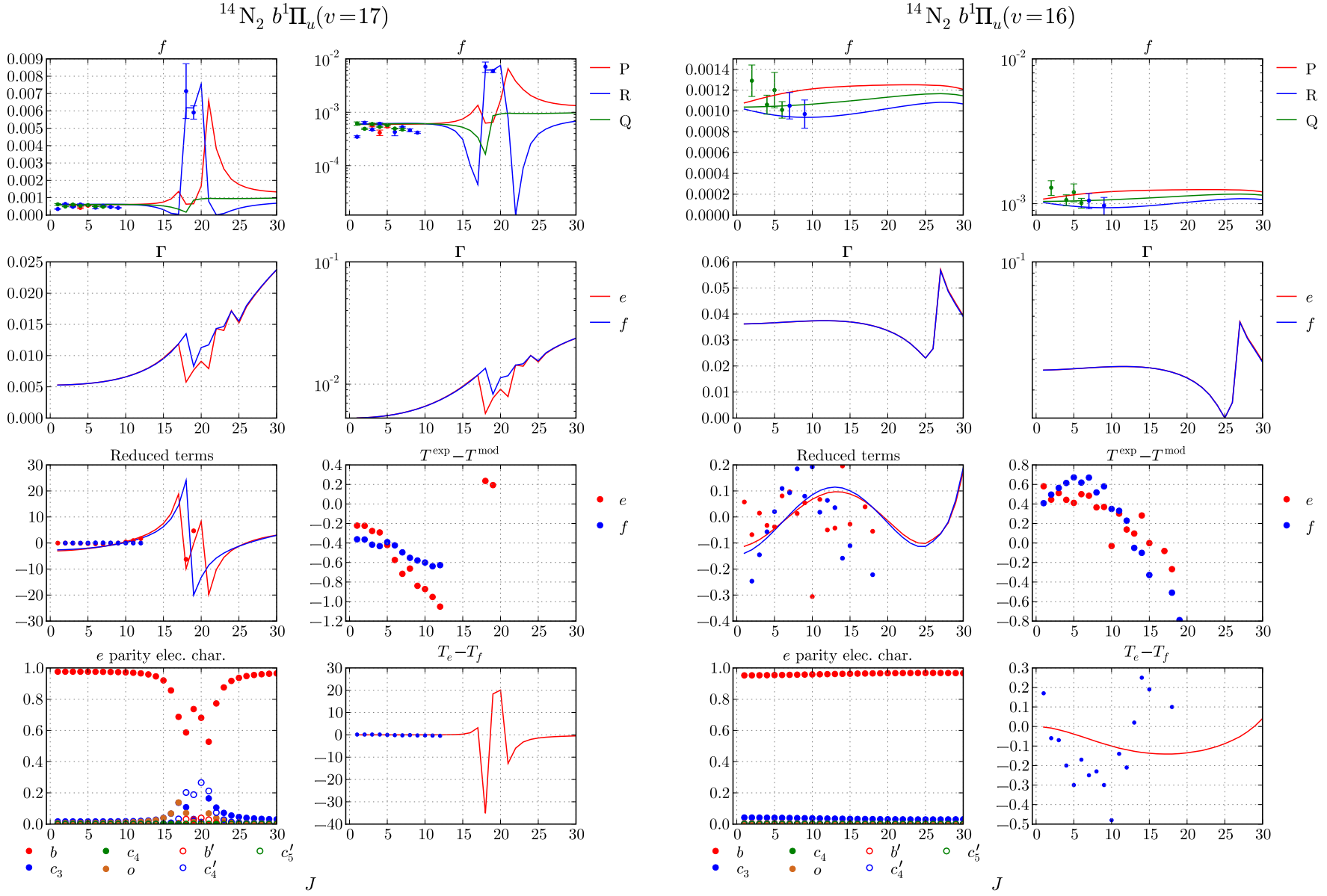
$^{14}N_2$ $b^1\Pi_u(v=17)$
$^{14}N_2$ $b^1\Pi_u(v=16)$
f
Γ
Reduced terms
$T^{exp}-T^{mod}$
e parity elec. char.
T_e-T_f
P
R
Q
e
f
b
c_3
c_4
o
b'
c_4'
c_5'
J

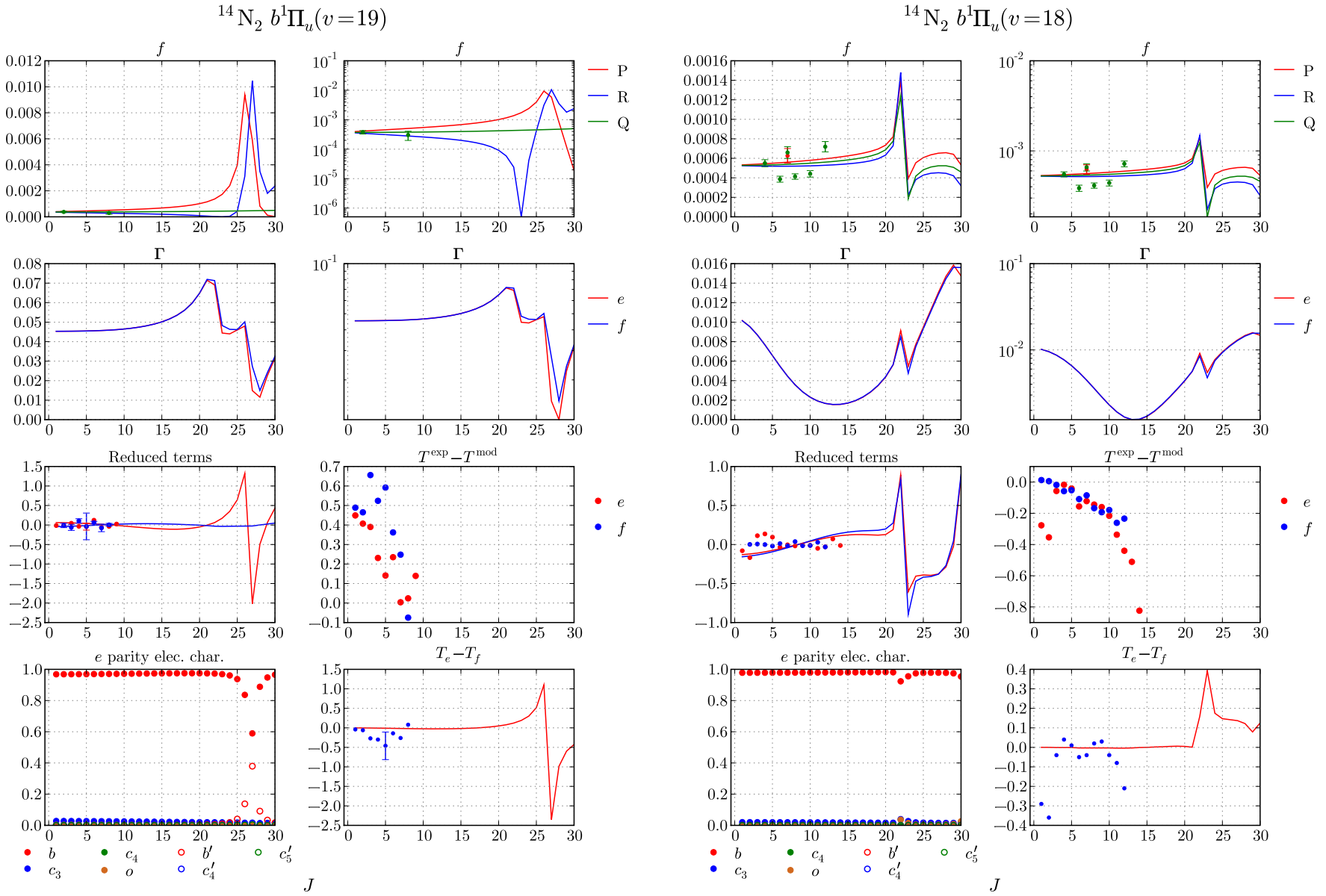
$^{14}N_2$ $b^1\Pi_u(v=19)$
$^{14}N_2$ $b^1\Pi_u(v=18)$
f
Γ
Reduced terms
$T^{exp}-T^{mod}$
e parity elec. char.
T_e-T_f
P
R
Q
e
f
b
c_3
c_4
o
b'
c_4'
c_5'
J

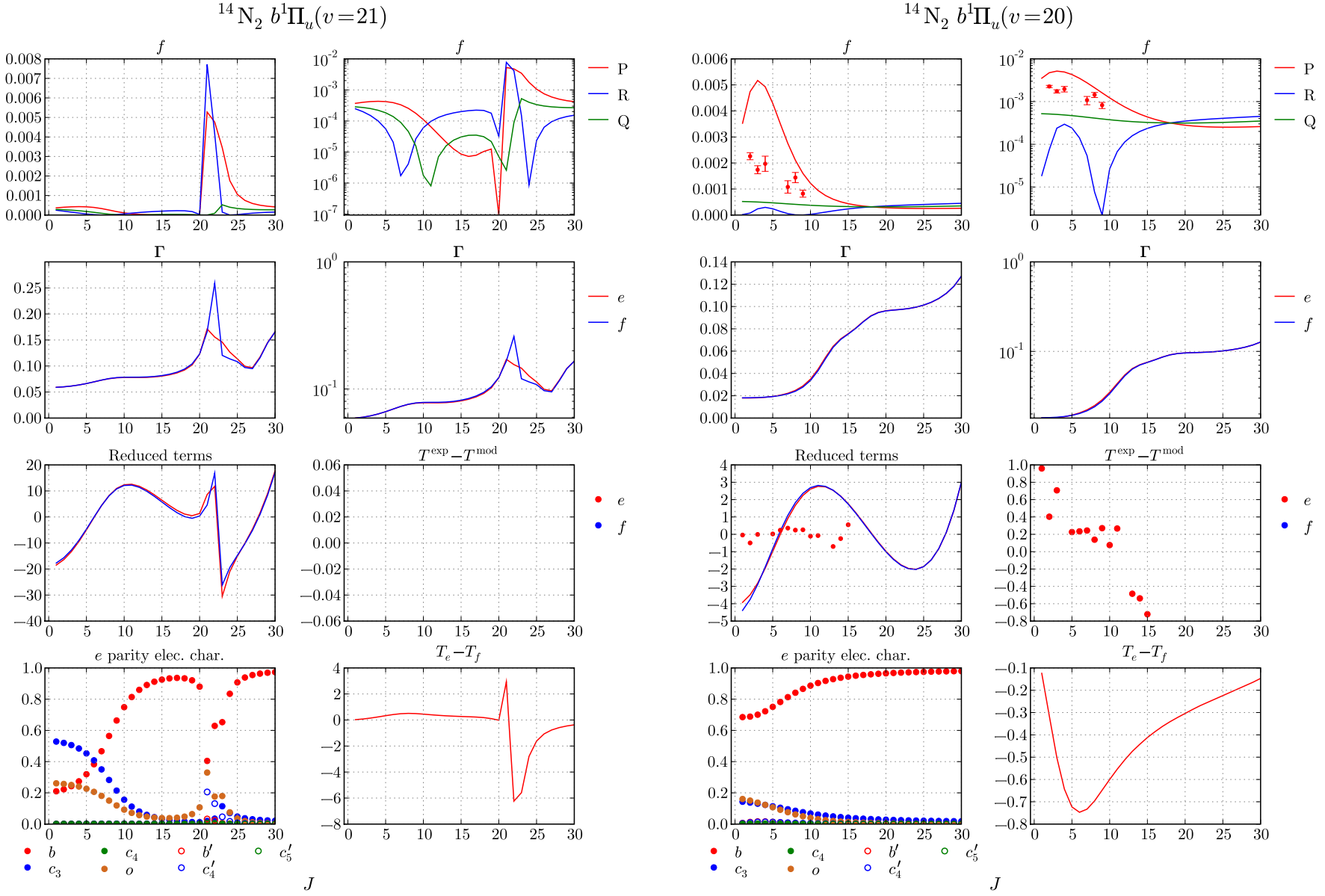
$^{14}N_2$ $b^1\Pi_u(v=21)$
$^{14}N_2$ $b^1\Pi_u(v=20)$
f
Γ
Reduced terms
$T^{exp}-T^{mod}$
e parity elec. char.
T_e-T_f
P
R
Q
e
f
b
c_3
c_4
o
b'
c_4'
c_5'
J

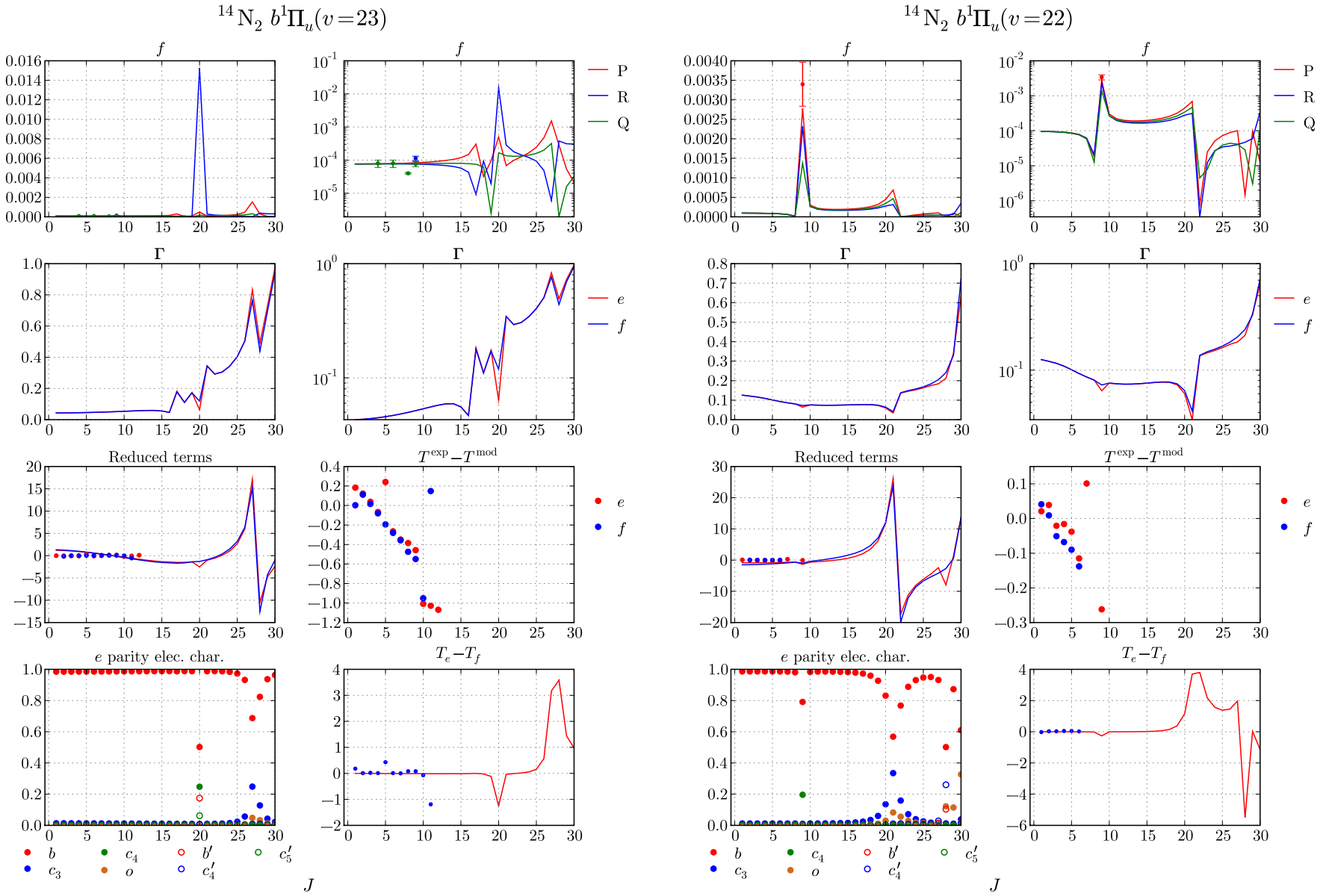
$^{14}\mathrm{N}_2$ $b^1\Pi_u(v=23)$
$^{14}\mathrm{N}_2$ $b^1\Pi_u(v=22)$
f
Γ
Reduced terms
$T^{\mathrm{exp}}-T^{\mathrm{mod}}$
e parity elec. char.
T_e-T_f
P
R
Q
e
f
b
c_3
c_4
o
b'
c_4'
c_5'
J

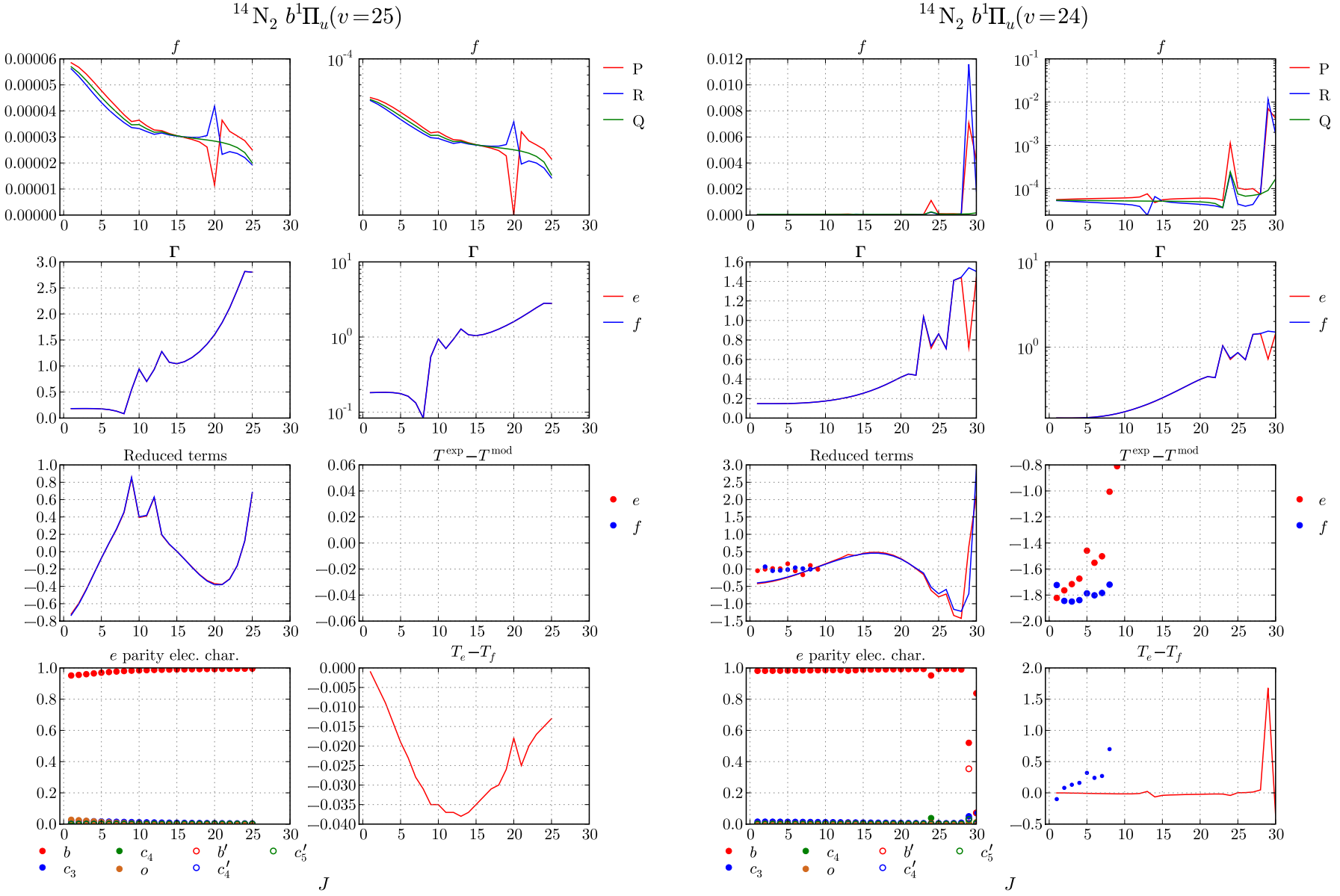
$^{14}N_2$ $b^1\Pi_u(v=25)$
$^{14}N_2$ $b^1\Pi_u(v=24)$
f
Γ
Reduced terms
$T^{exp}-T^{mod}$
e parity elec. char.
T_e-T_f
P
R
Q
e
f
b
c_3
c_4
o
b'
c_4'
c_5'
J

$^{14}\mathrm{N}_2$ $c_3{}^1\Pi_u(v=1)$
f
Γ
Reduced terms
e parity elec. char.
$T^{\mathrm{exp}}-T^{\mathrm{mod}}$
T_e-T_f
P
R
Q
e
f
b
c_3
c_4
o
b'
c_4'
c_5'
J
$^{14}\mathrm{N}_2$ $c_3{}^1\Pi_u(v=0)$
f
Γ
Reduced terms
e parity elec. char.
$T^{\mathrm{exp}}-T^{\mathrm{mod}}$
T_e-T_f
P
R
Q
e
f
b
c_3
c_4
o
b'
c_4'
c_5'
J

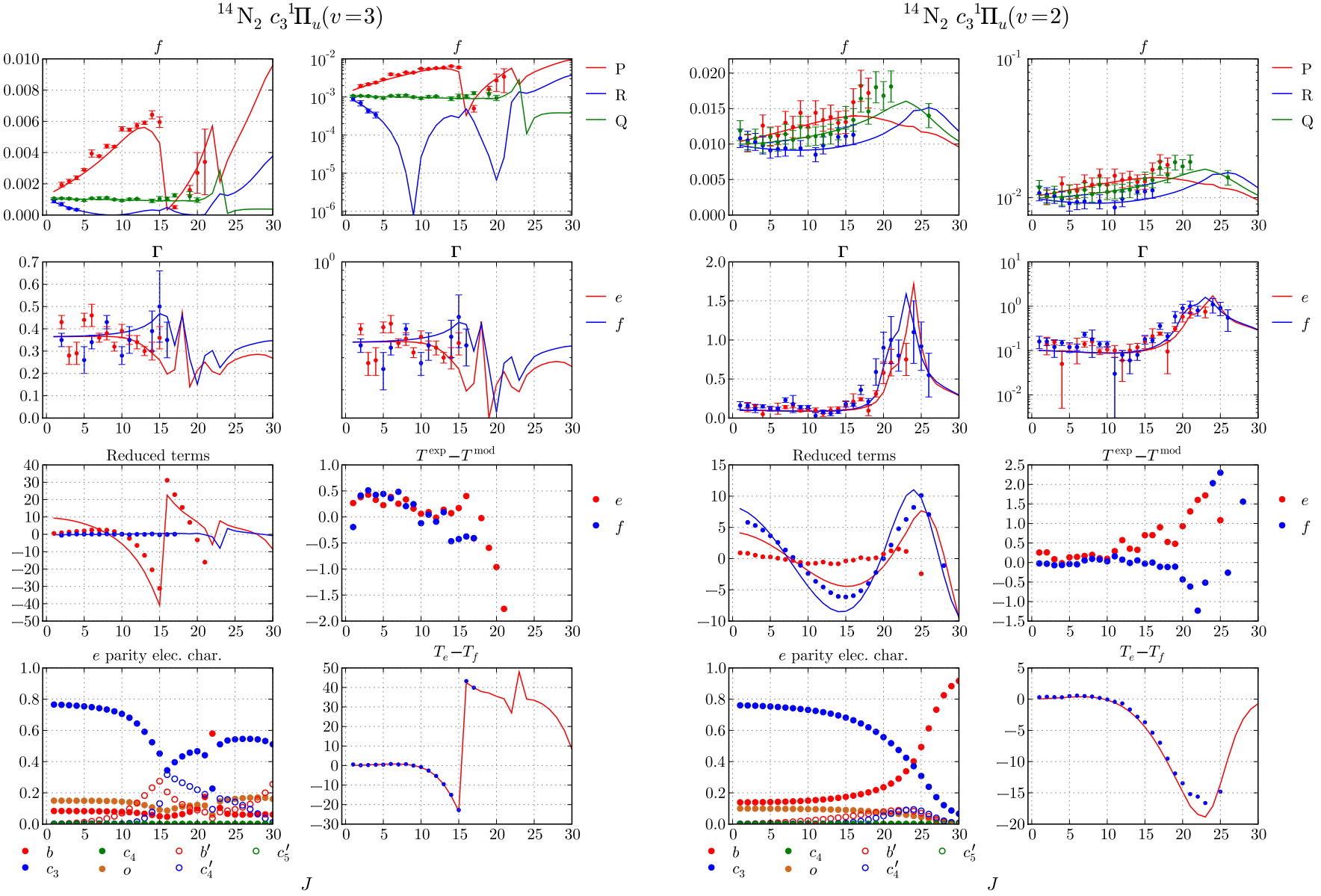
$^{14}N_2$ $c_3{}^1\Pi_u(v=3)$
$^{14}N_2$ $c_3{}^1\Pi_u(v=2)$
f
Γ
Reduced terms
$T^{exp}-T^{mod}$
e parity elec. char.
T_e-T_f
P
R
Q
e
f
b
c_3
c_4
o
b'
c_4'
c_5'
J

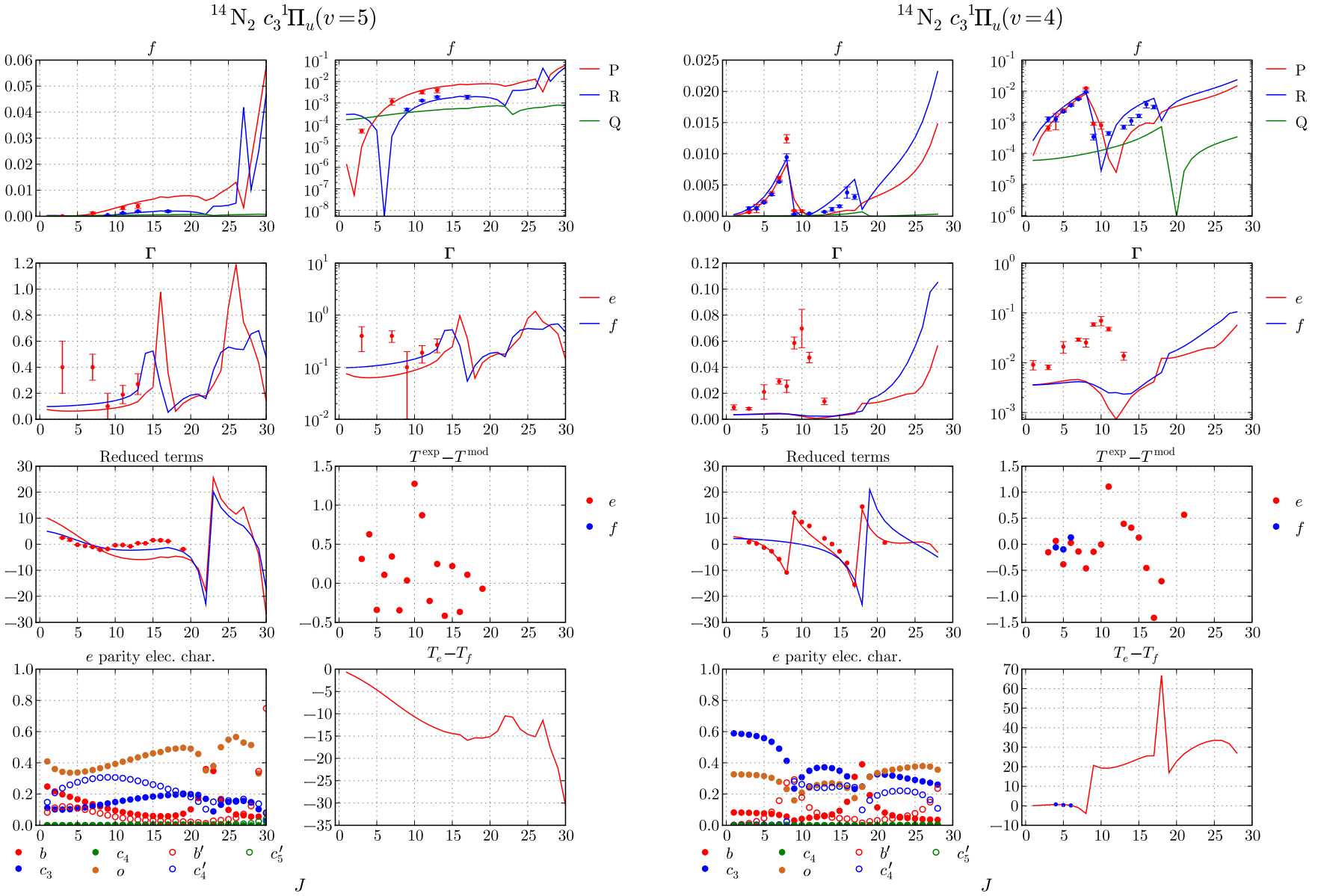
$^{14}N_2$ $c_3{}^1\Pi_u(v=5)$
$^{14}N_2$ $c_3{}^1\Pi_u(v=4)$
f
Γ
Reduced terms
$T^{exp}-T^{mod}$
e parity elec. char.
T_e-T_f
P
R
Q
e
f
b
c_3
c_4
o
b'
c_4'
c_5'
J

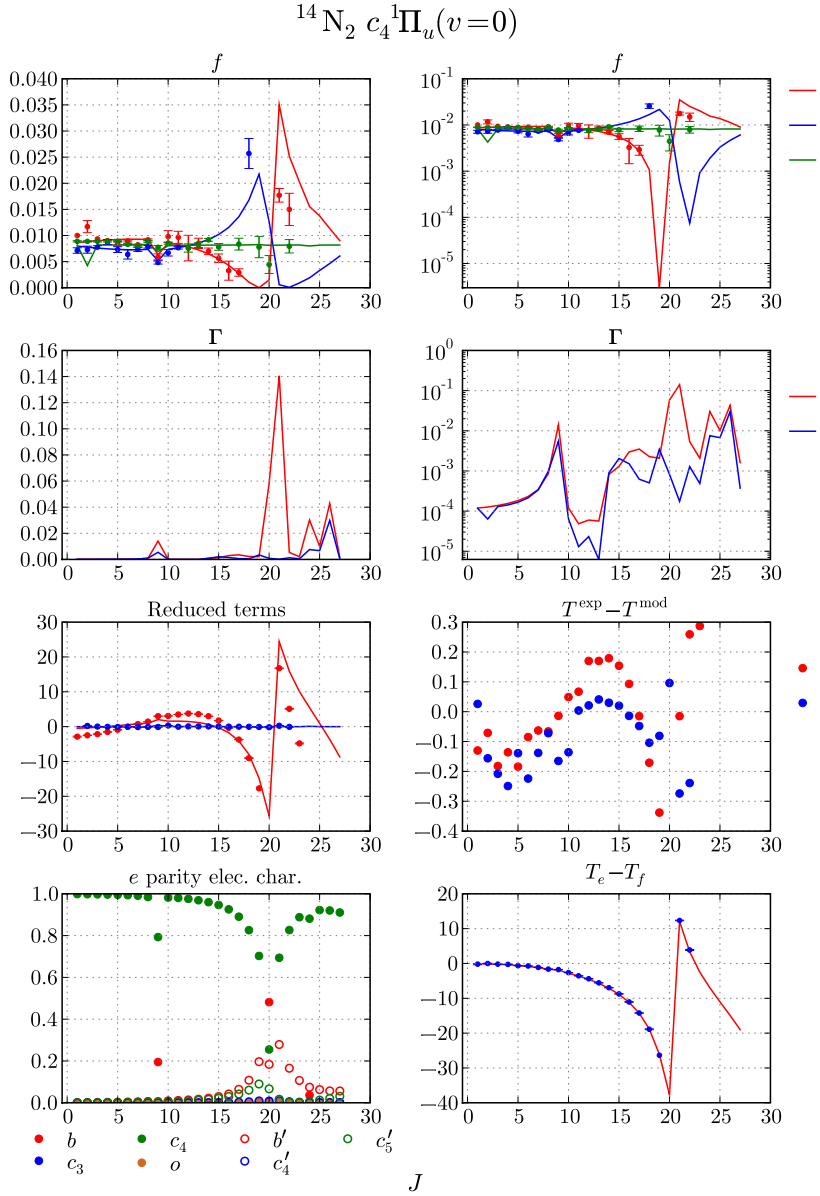
$^{14}N_2$ $c_4{}^1\Pi_u(v=0)$
f
Γ
Reduced terms
$T^{exp}-T^{mod}$
e parity elec. char.
T_e-T_f
P
R
Q
e
f
b
c_3
c_4
o
b'
c_4'
c_5'
J

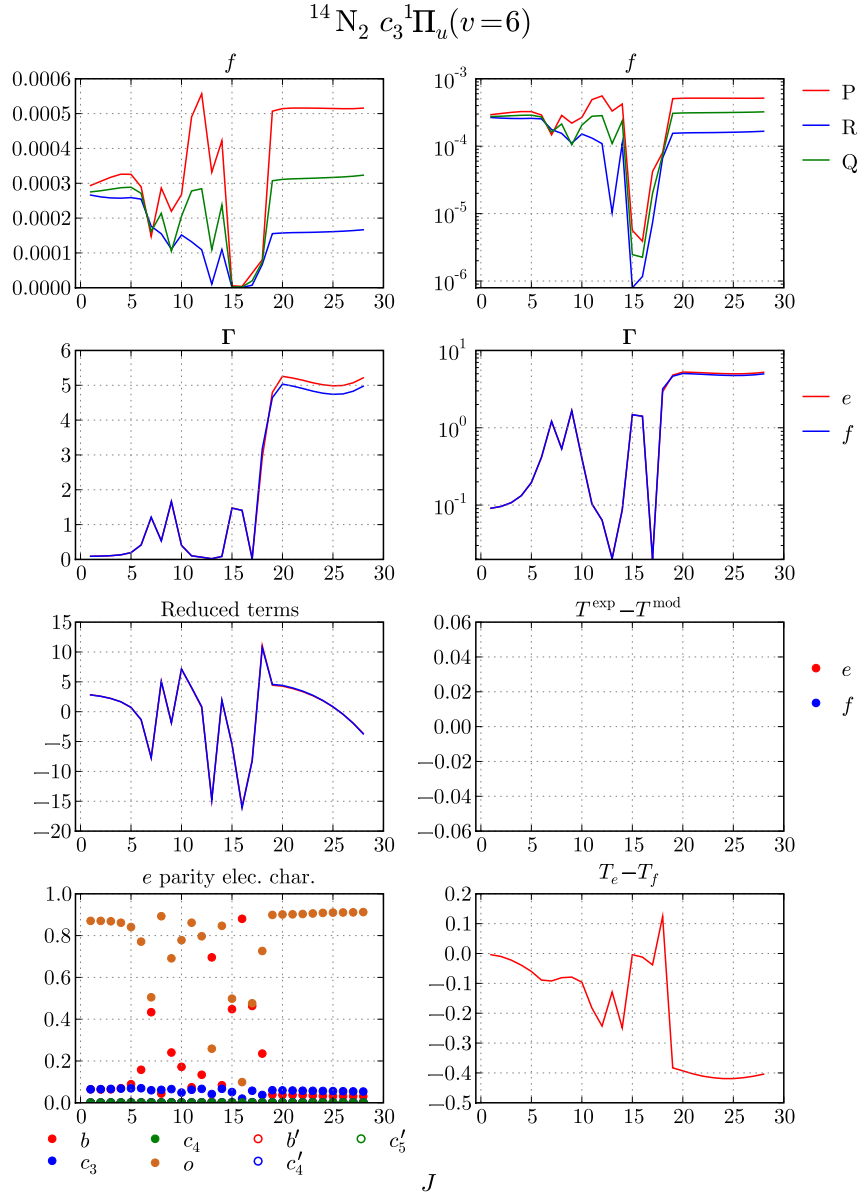
$^{14}N_2$ $c_3{}^1\Pi_u(v=6)$
f
Γ
Reduced terms
$T^{exp}-T^{mod}$
e parity elec. char.
T_e-T_f
P
R
Q
e
f
b
c_3
c_4
o
b'
c_4'
c_5'
J

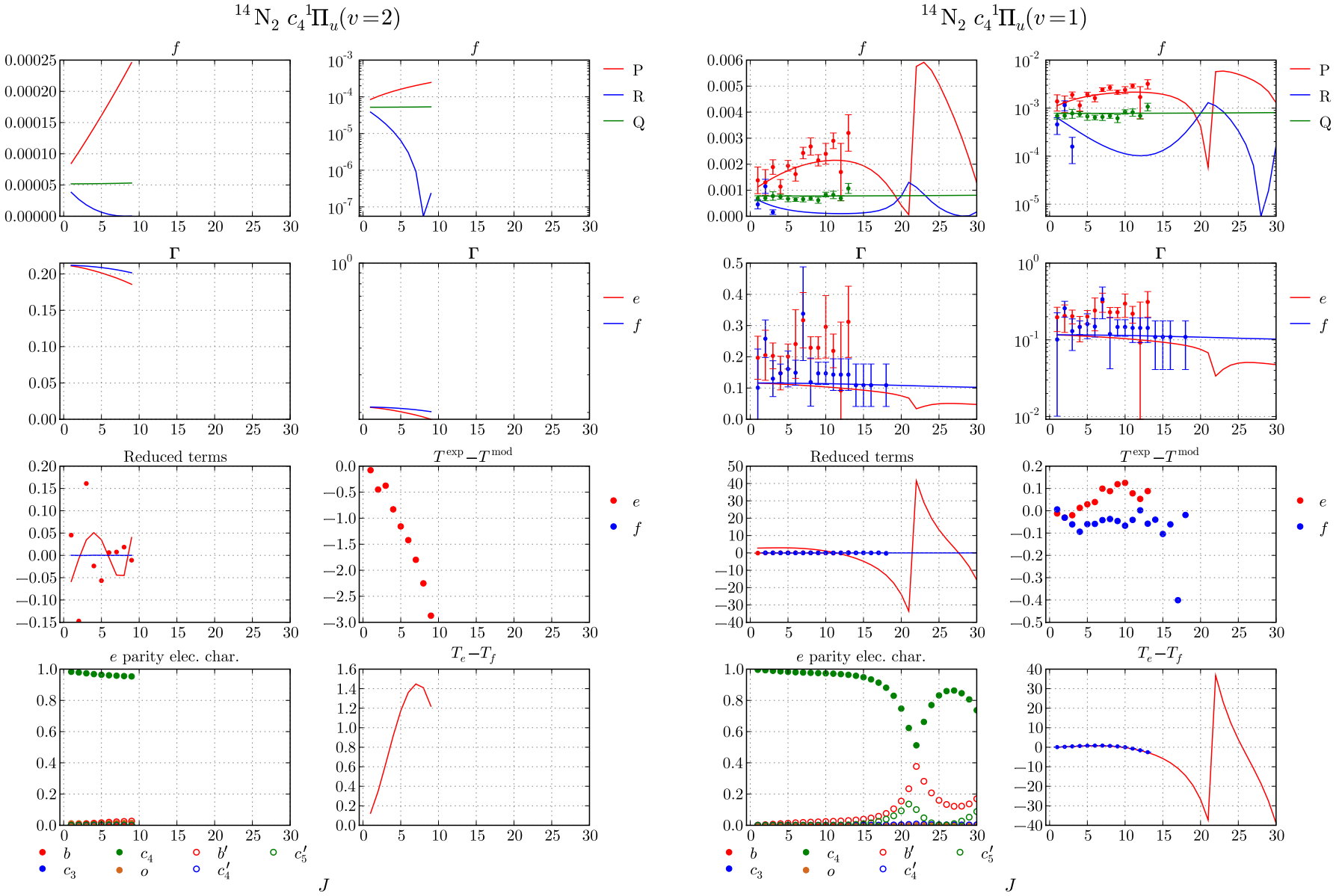
$^{14}N_2$ $c_4{}^1\Pi_u(v=2)$
$^{14}N_2$ $c_4{}^1\Pi_u(v=1)$
f
Γ
Reduced terms
$T^{exp}-T^{mod}$
e parity elec. char.
T_e-T_f
P
R
Q
e
f
b
c_3
c_4
o
b'
c_4'
c_5'
J

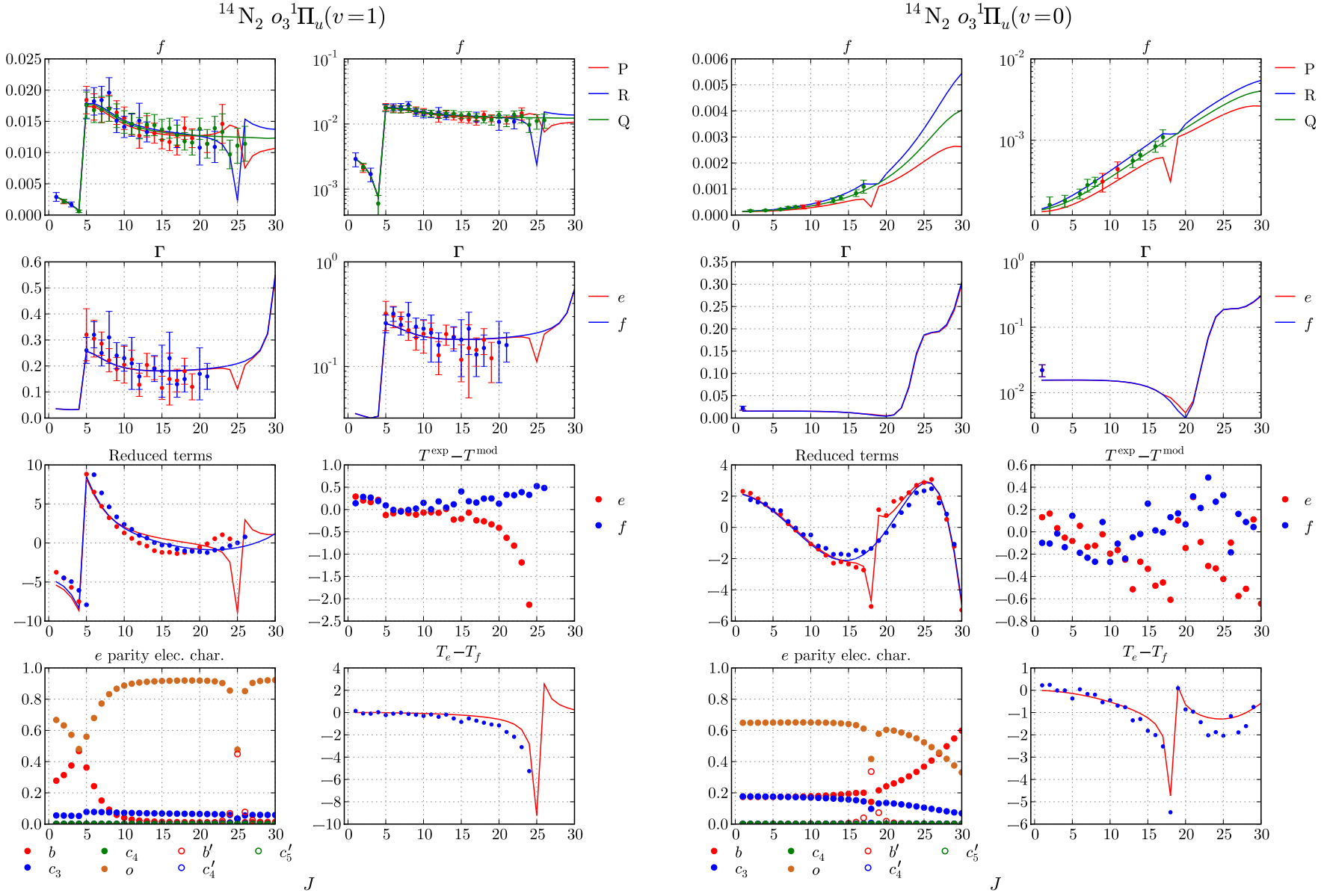
$^{14}N_2$ $o_3\,{}^1\Pi_u(v=1)$
$^{14}N_2$ $o_3\,{}^1\Pi_u(v=0)$
f
Γ
Reduced terms
$T^{\rm exp}-T^{\rm mod}$
e parity elec. char.
T_e-T_f
P
R
Q
e
f
b
c_3
c_4
o
b'
c_4'
c_5'
J

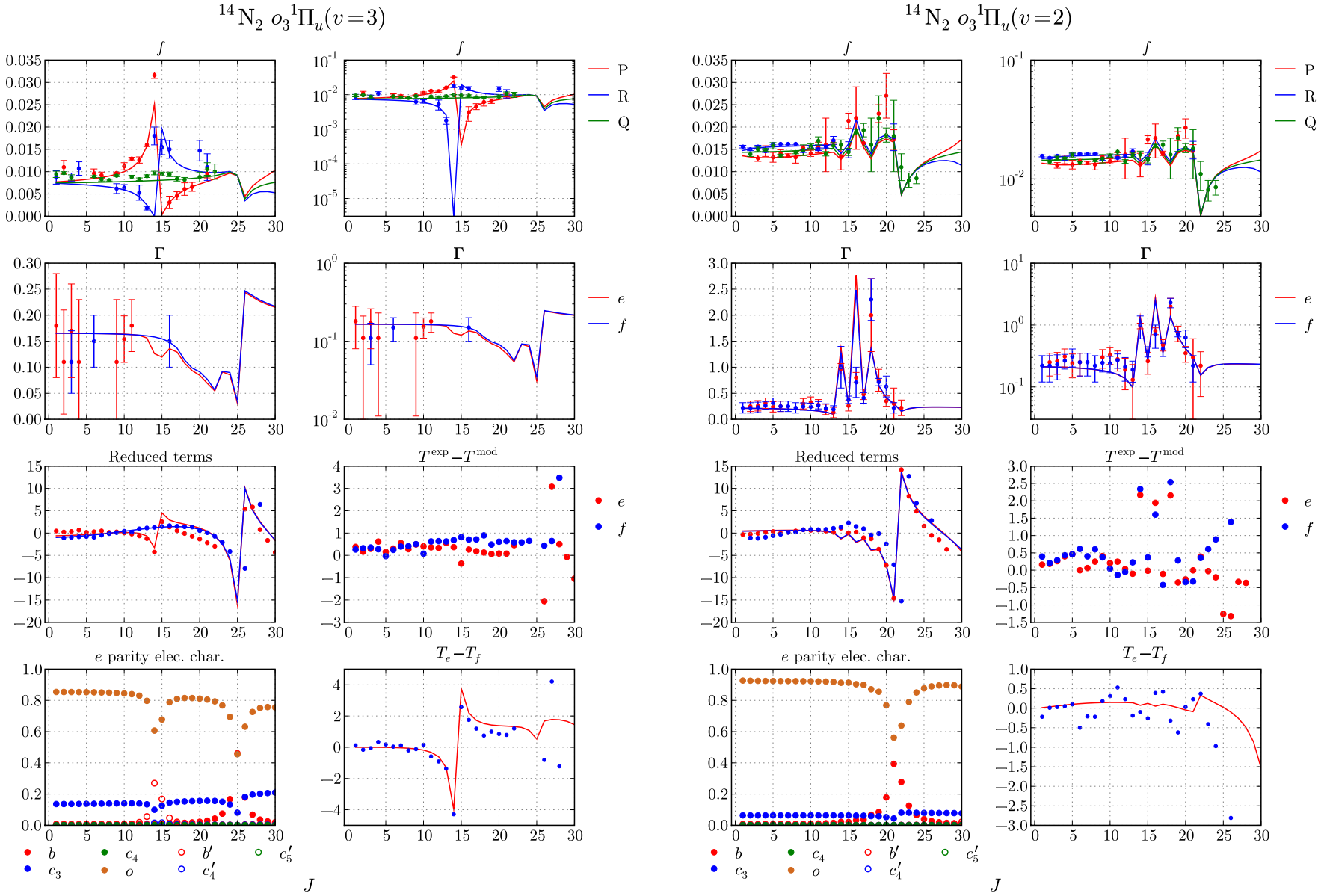
$^{14}\mathrm{N}_2\ o_3\,{}^1\Pi_u(v=3)$
$^{14}\mathrm{N}_2\ o_3\,{}^1\Pi_u(v=2)$
f
Γ
Reduced terms
$T^{\mathrm{exp}}-T^{\mathrm{mod}}$
e parity elec. char.
T_e-T_f
P
R
Q
e
f
b
c_3
c_4
o
b'
c_4'
c_5'
J

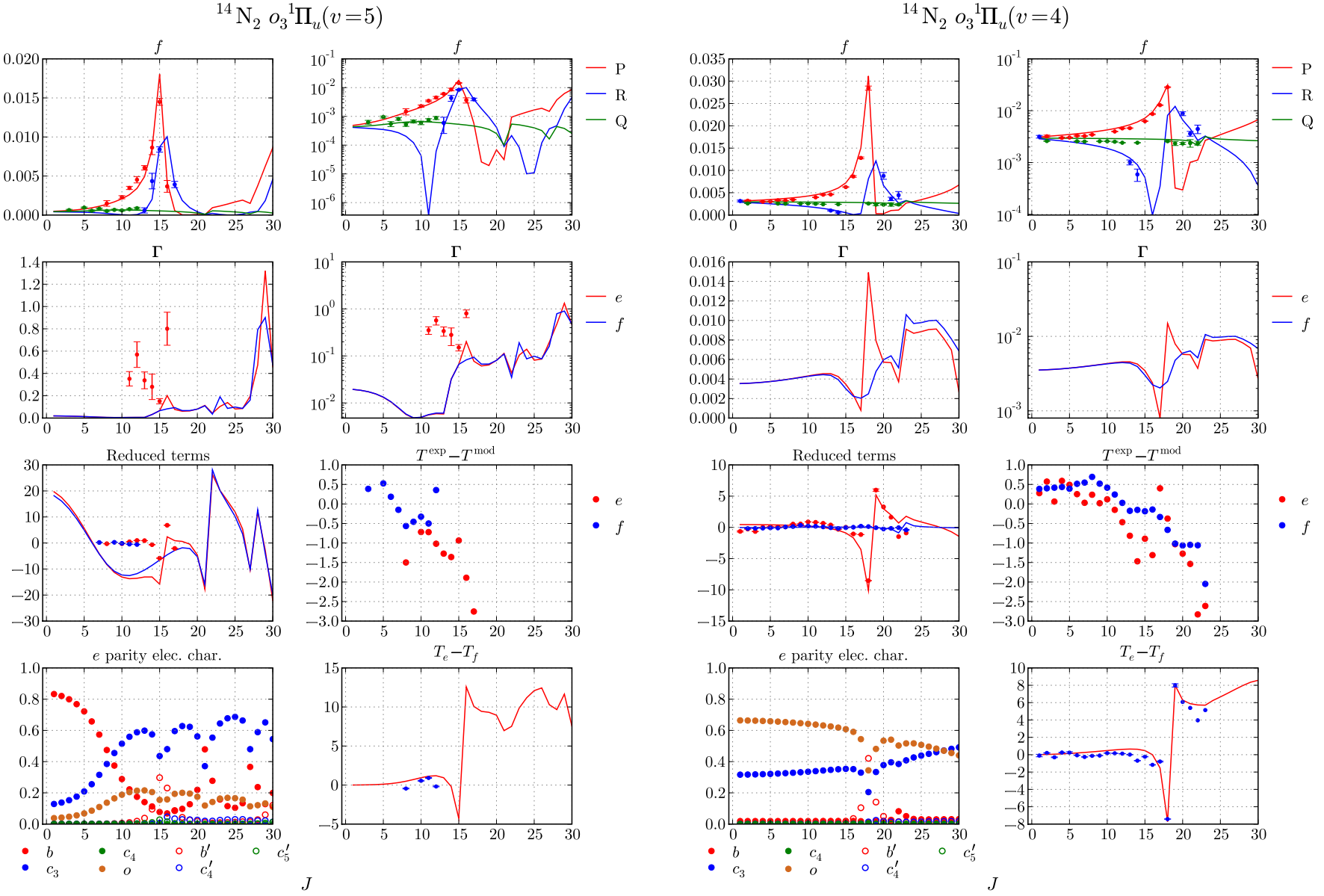
$^{14}N_2$ $o_3{}^1\Pi_u(v=5)$
$^{14}N_2$ $o_3{}^1\Pi_u(v=4)$
f
Γ
Reduced terms
$T^{exp}-T^{mod}$
e parity elec. char.
T_e-T_f
P
R
Q
e
f
b
c_3
c_4
o
b'
c_4'
c_5'
J

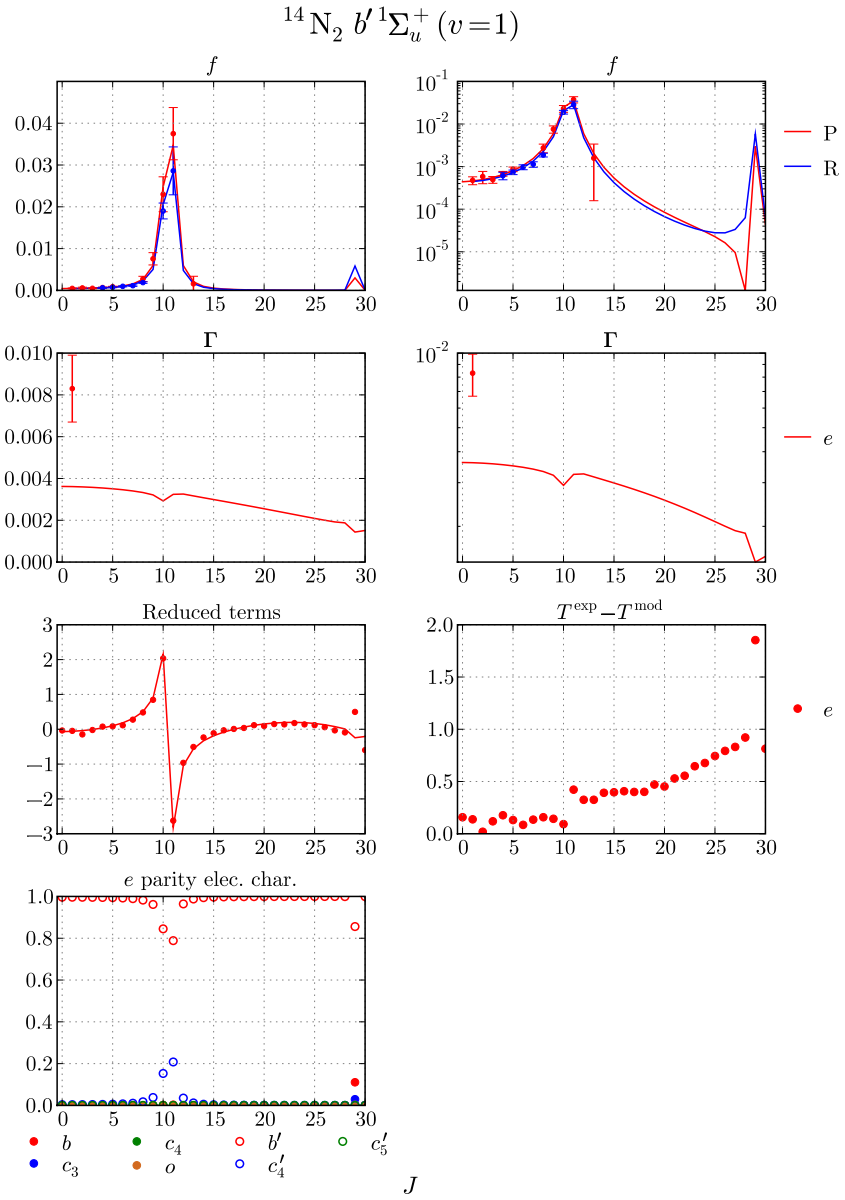
$^{14}N_2\ b'\,^1\Sigma_u^+\ (v=1)$
f
f
P
R
Γ
Γ
e
Reduced terms
$T^{exp} - T^{mod}$
e
e parity elec. char.
b
c_3
c_4
o
b′
c_4'
c_5'
J

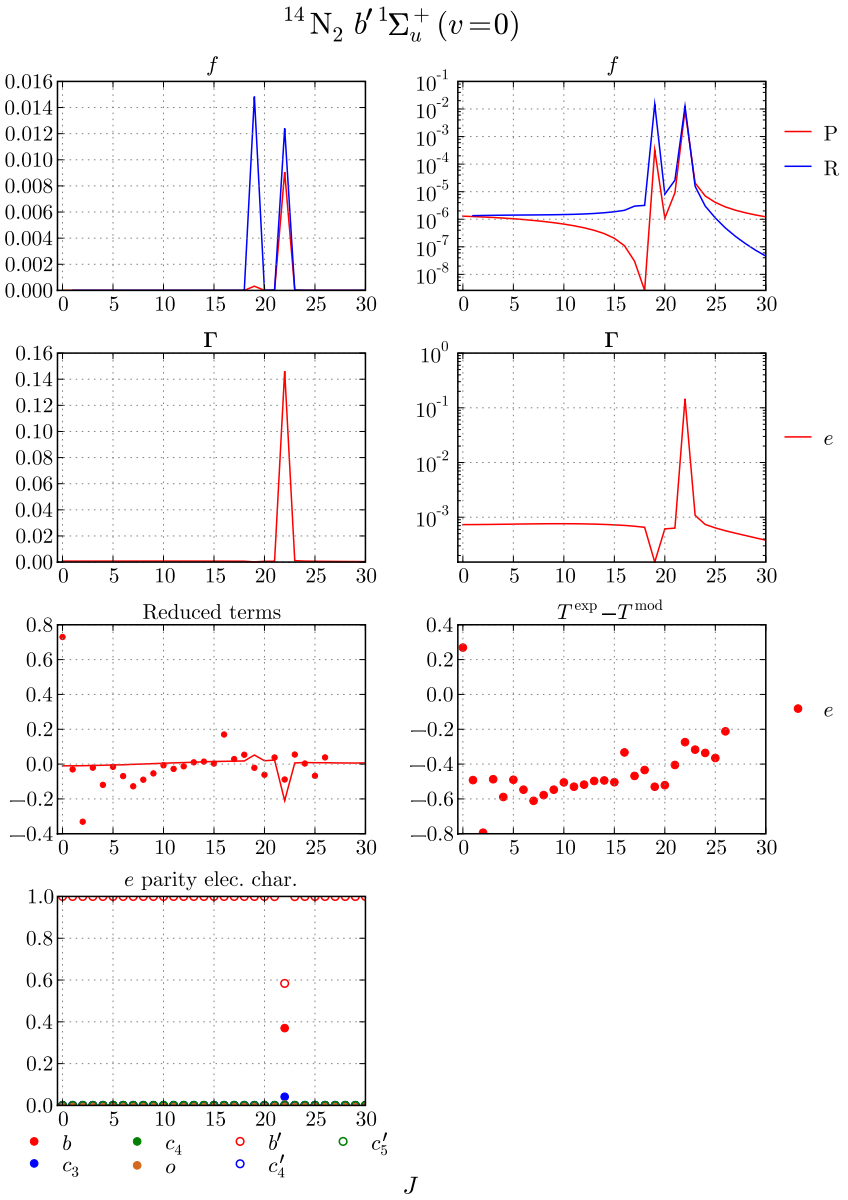
$^{14}N_2\ b'\,^1\Sigma_u^+\ (v=0)$
f
f
P
R
Γ
Γ
e
Reduced terms
$T^{exp} - T^{mod}$
e
e parity elec. char.
b
c_3
c_4
o
b′
c_4'
c_5'
J

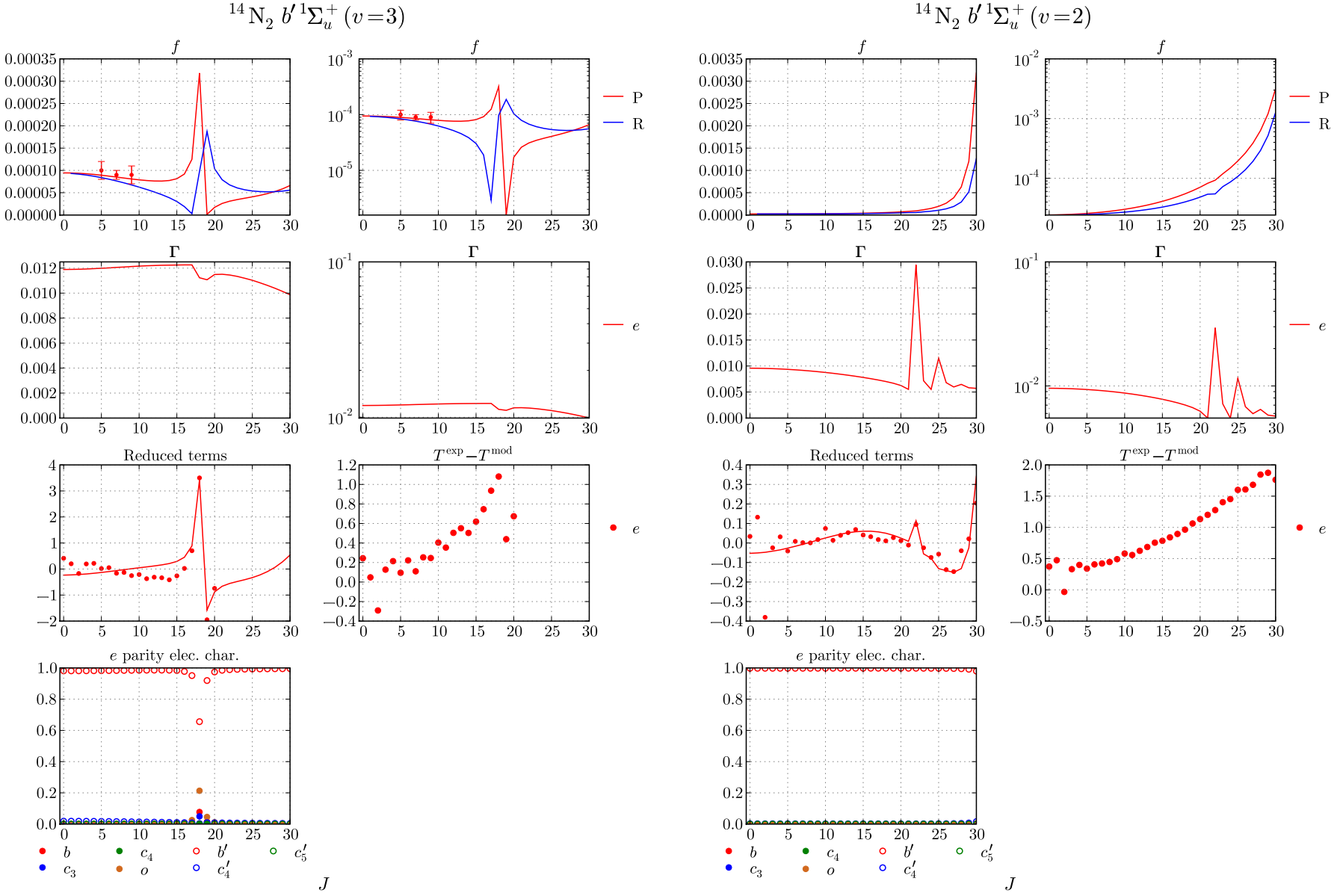
$^{14}N_2\ b'\,^1\Sigma_u^+\ (v=3)$
$^{14}N_2\ b'\,^1\Sigma_u^+\ (v=2)$
f
Γ
Reduced terms
$T^{exp}-T^{mod}$
e parity elec. char.
P
R
e
b
c_3
c_4
o
b′
c_4'
c_5'
J

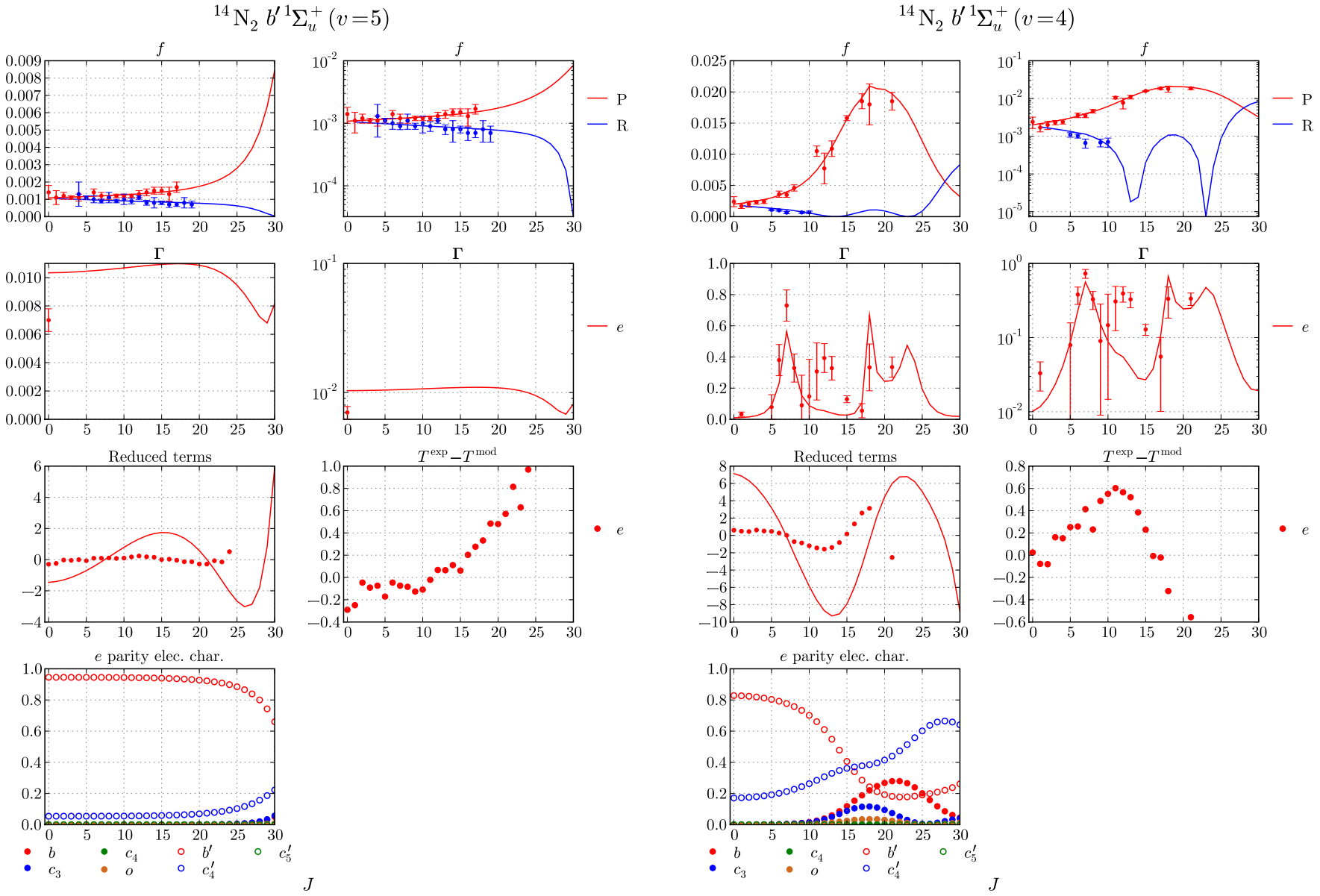
$^{14}N_2$ $b'\,^1\Sigma_u^+$ $(v=5)$
$^{14}N_2$ $b'\,^1\Sigma_u^+$ $(v=4)$
f
Γ
Reduced terms
$T^{exp}-T^{mod}$
e parity elec. char.
P
R
e
b
c_3
c_4
o
b′
c_4'
c_5'
J

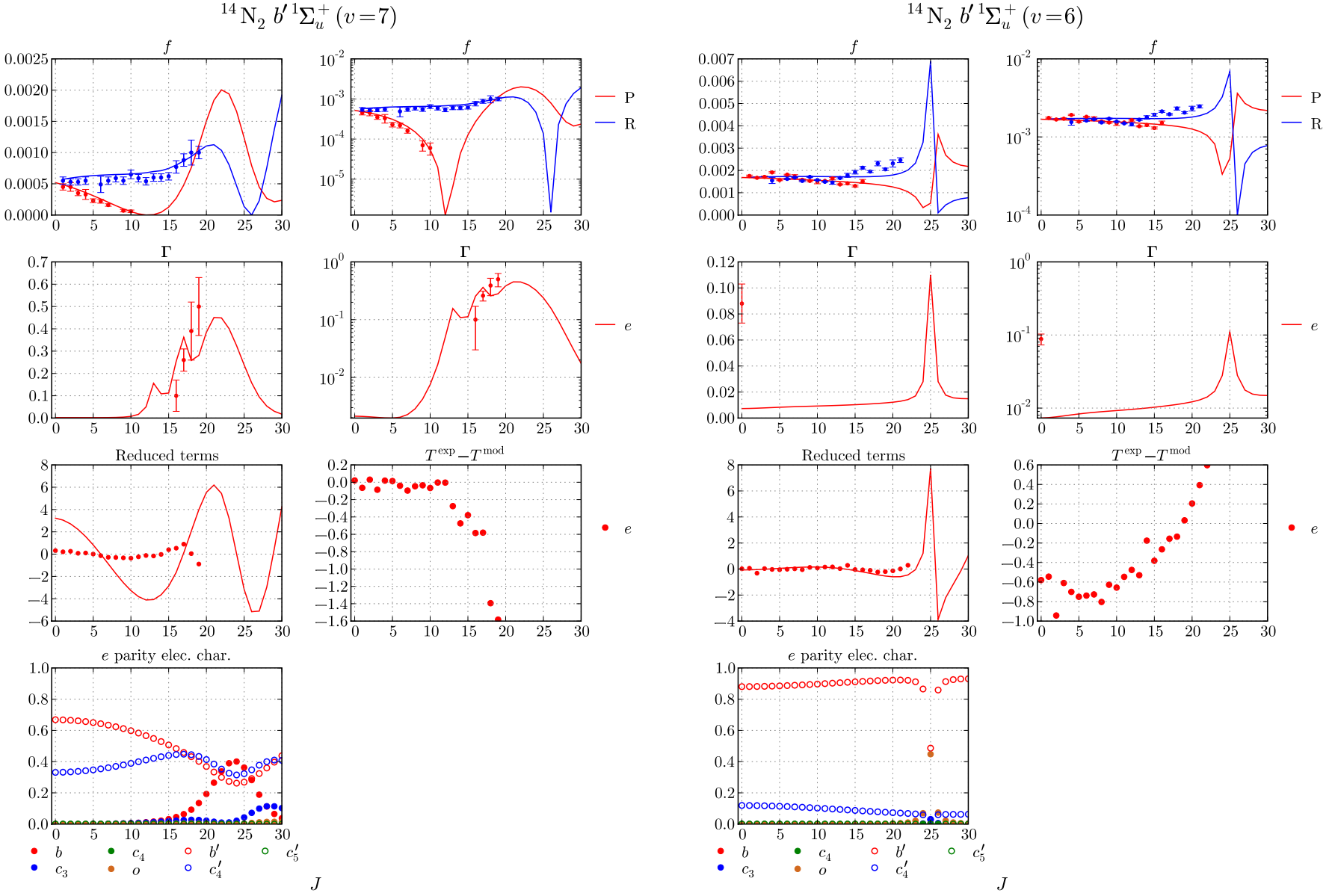
$^{14}N_2\ b'\,^1\Sigma_u^+\ (v=7)$
$^{14}N_2\ b'\,^1\Sigma_u^+\ (v=6)$
f
Γ
Reduced terms
$T^{exp}-T^{mod}$
e parity elec. char.
P
R
e
b
c_3
c_4
o
b'
c_4'
c_5'
J

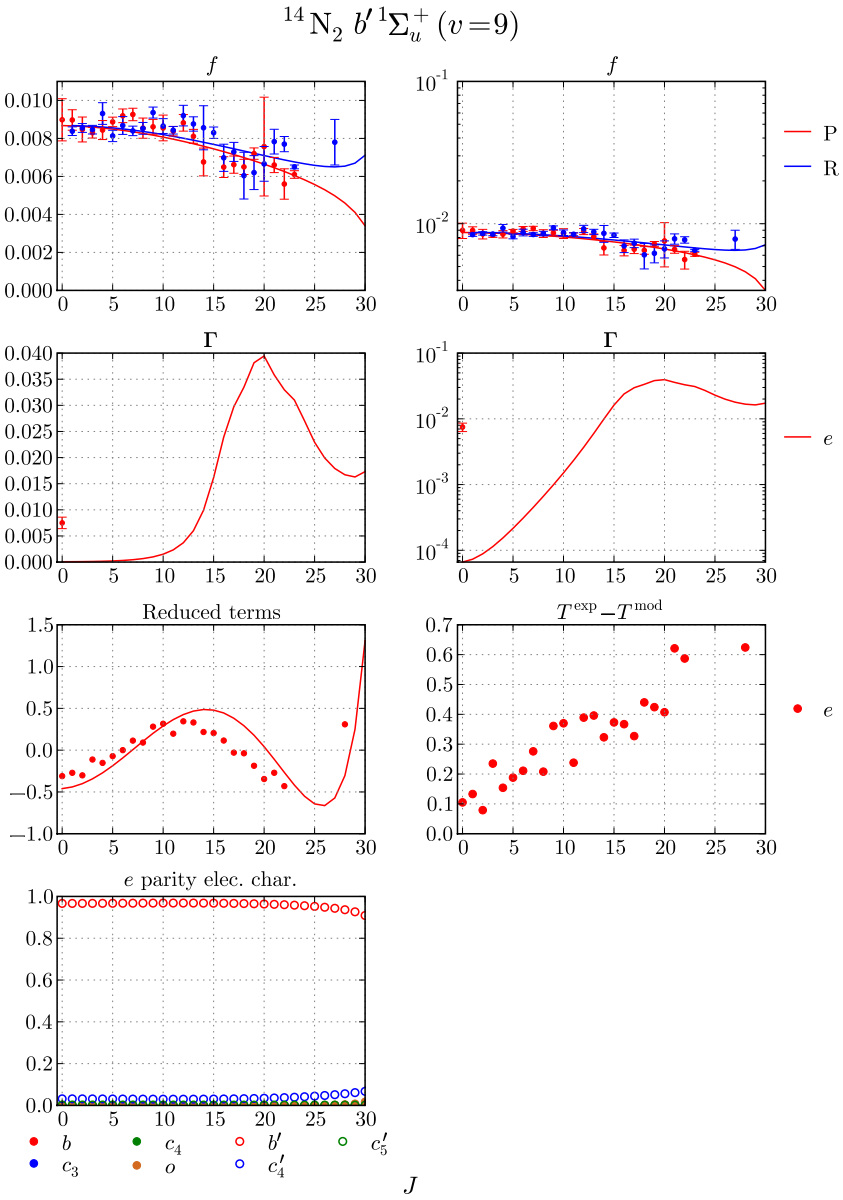
$^{14}N_2\ b'\,^1\Sigma_u^+\ (v=9)$
f
Γ
Reduced terms
$T^{exp} - T^{mod}$
e parity elec. char.
P
R
e
b
c_3
c_4
o
b′
c_4'
c_5'
J

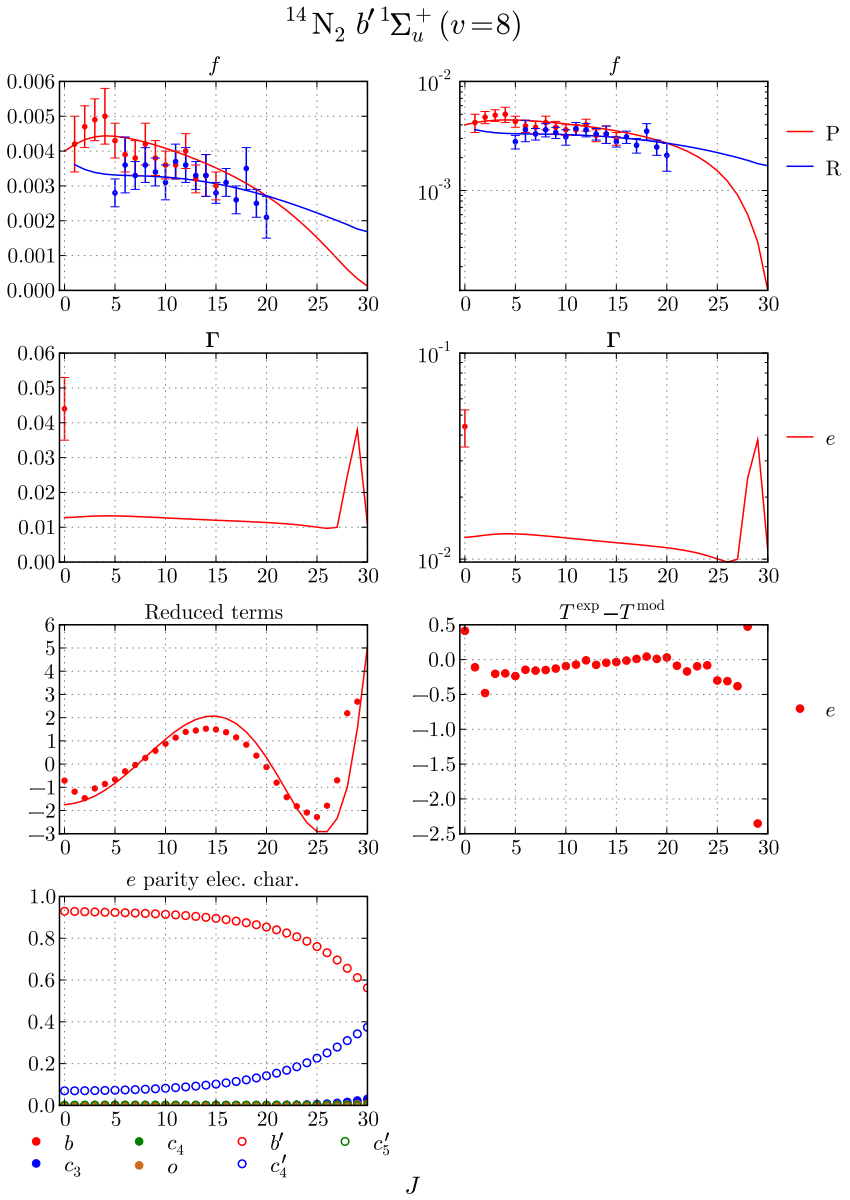
$^{14}N_2\ b'\,^1\Sigma_u^+\ (v=8)$
f
Γ
Reduced terms
$T^{exp} - T^{mod}$
e parity elec. char.
P
R
e
b
c_3
c_4
o
b′
c_4'
c_5'
J

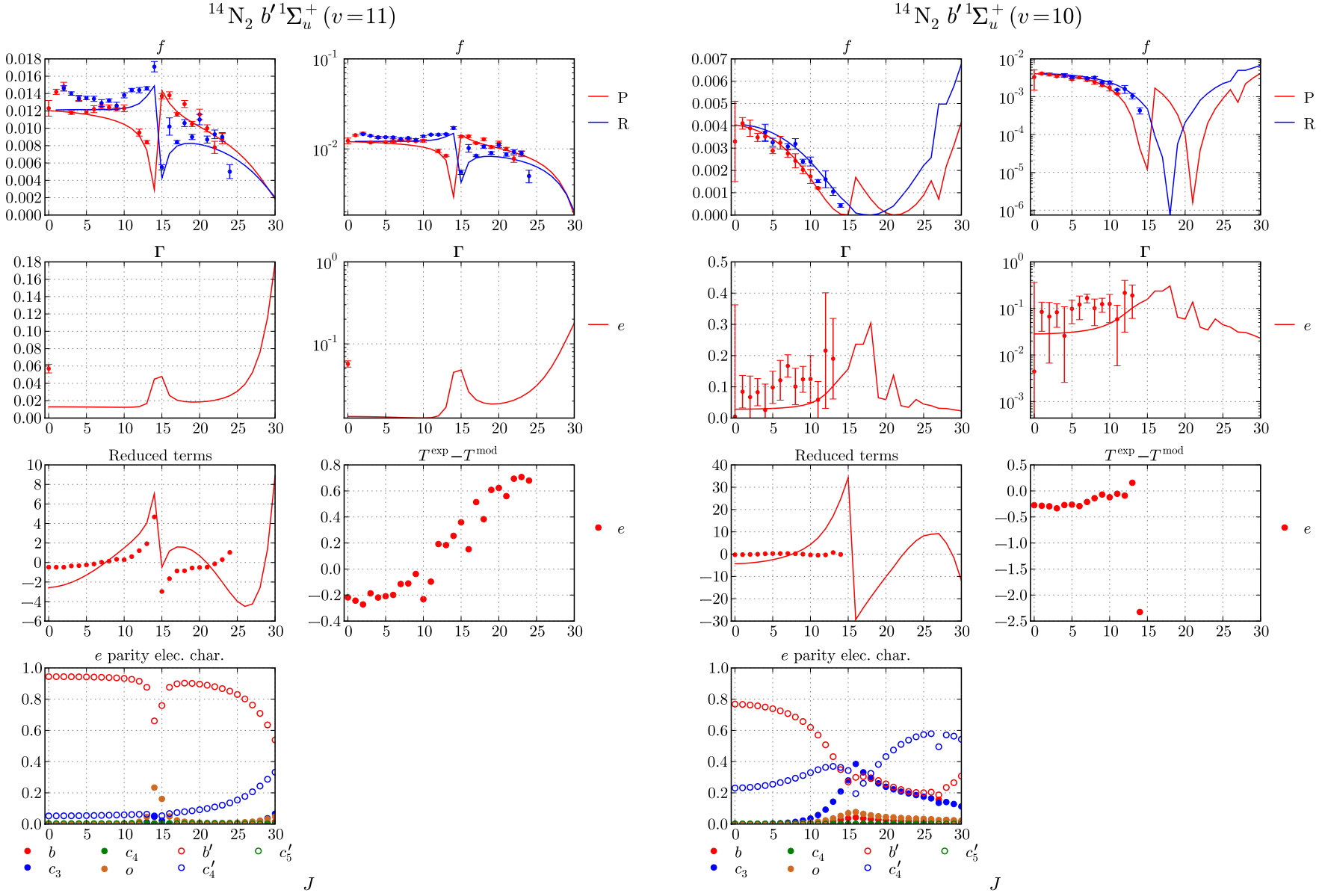
$^{14}N_2$ $b'^1\Sigma_u^+$ ($v=11$)
$^{14}N_2$ $b'^1\Sigma_u^+$ ($v=10$)
f
Γ
Reduced terms
$T^{exp}-T^{mod}$
e parity elec. char.
P
R
e
b
c_3
c_4
o
b'
c_4'
c_5'
J

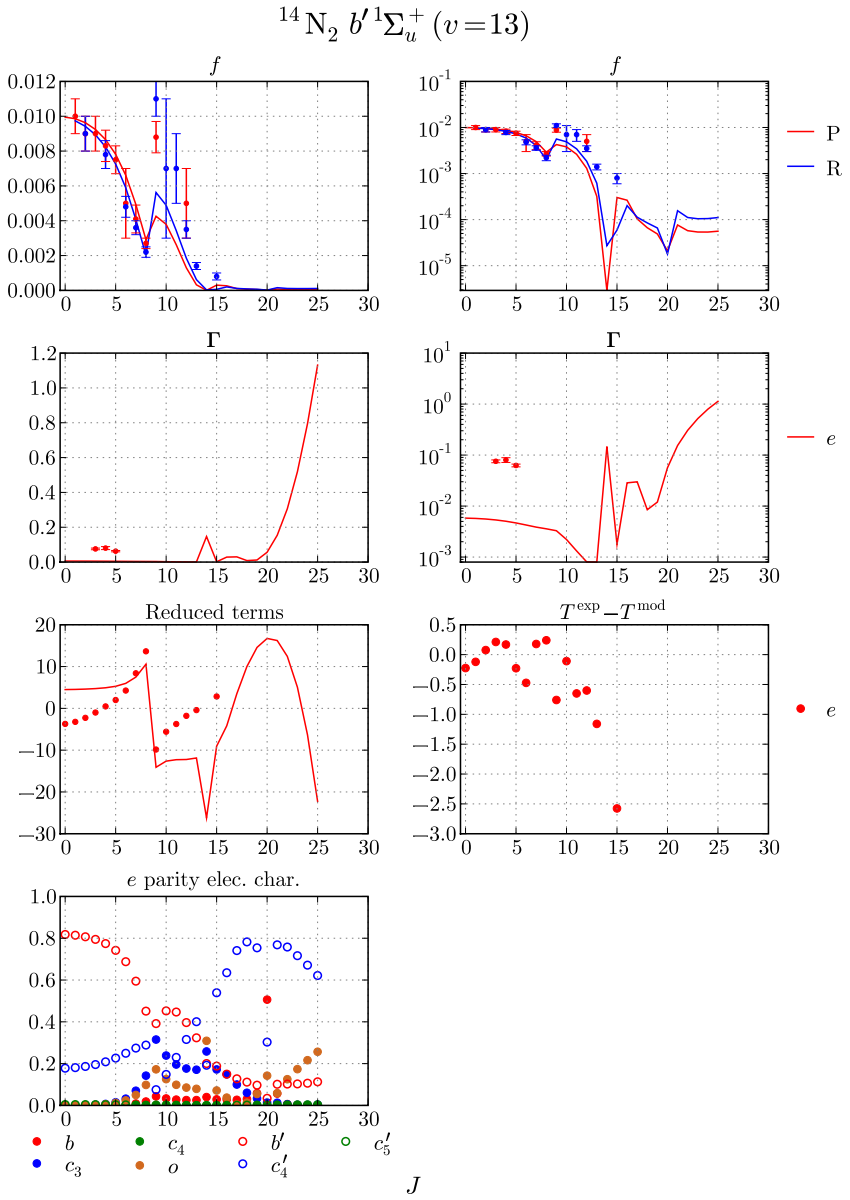
$^{14}N_2\ b'\,^1\Sigma_u^+\ (v=13)$
f
f
P
R
Γ
Γ
e
Reduced terms
$T^{exp}-T^{mod}$
e
e parity elec. char.
b
c_3
c_4
o
b′
c_4'
c_5'
J

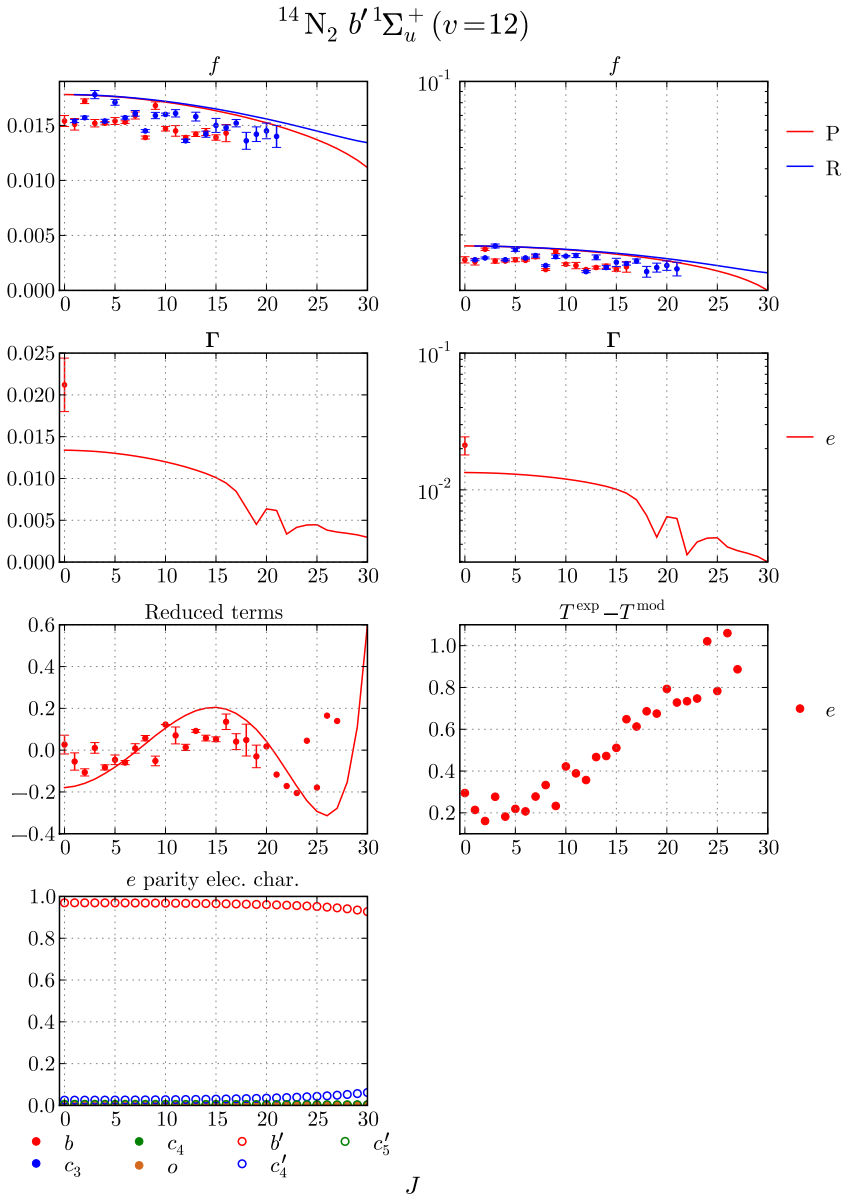
$^{14}N_2\ b'\,^1\Sigma_u^+\ (v=12)$
f
f
P
R
Γ
Γ
e
Reduced terms
$T^{exp}-T^{mod}$
e
e parity elec. char.
b
c_3
c_4
o
b′
c_4'
c_5'
J

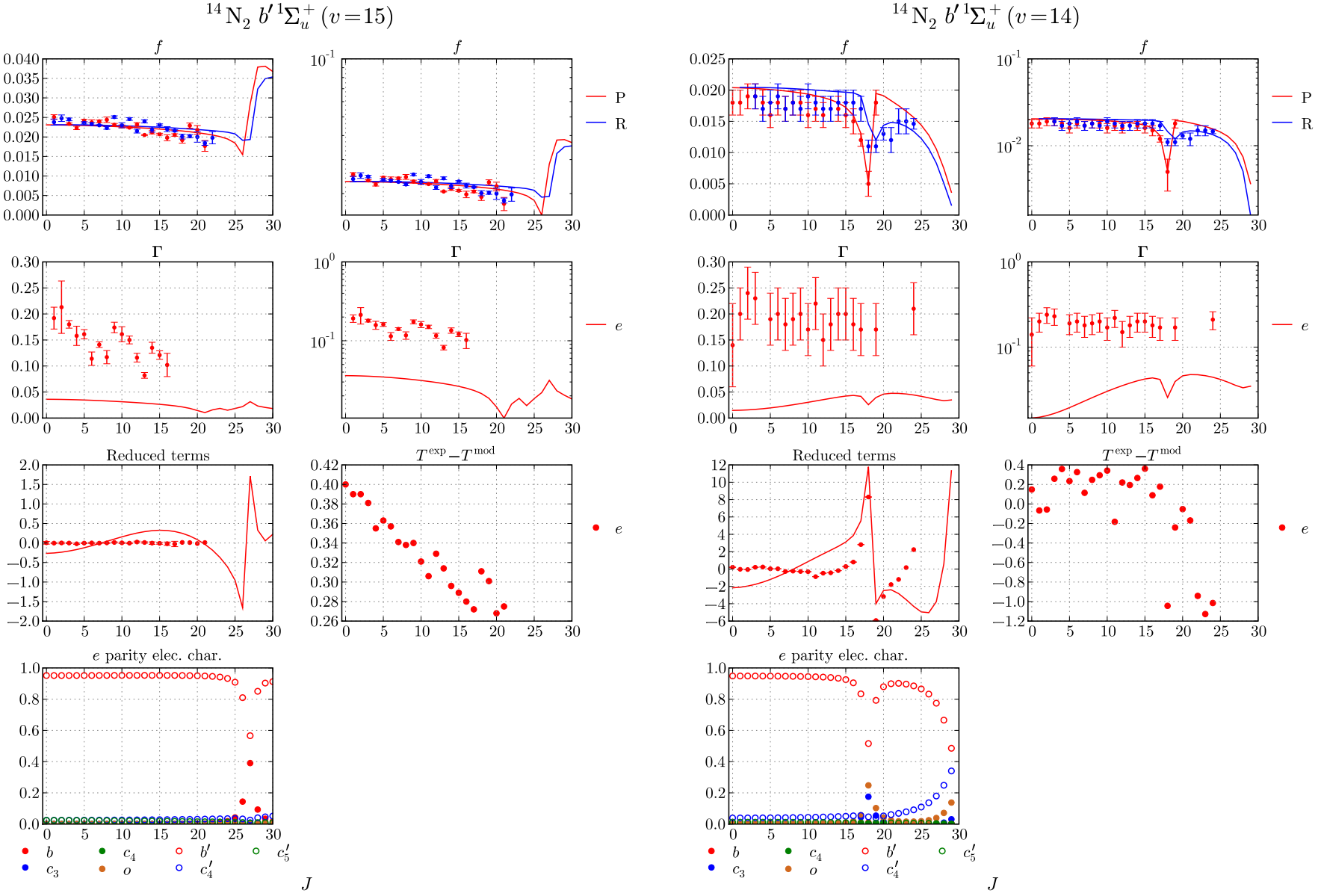
$^{14}N_2$ $b'^1\Sigma_u^+$ ($v=15$)
$^{14}N_2$ $b'^1\Sigma_u^+$ ($v=14$)
f
Γ
Reduced terms
$T^{exp}-T^{mod}$
e parity elec. char.
P
R
e
b
c_3
c_4
o
b'
c_4'
c_5'
J

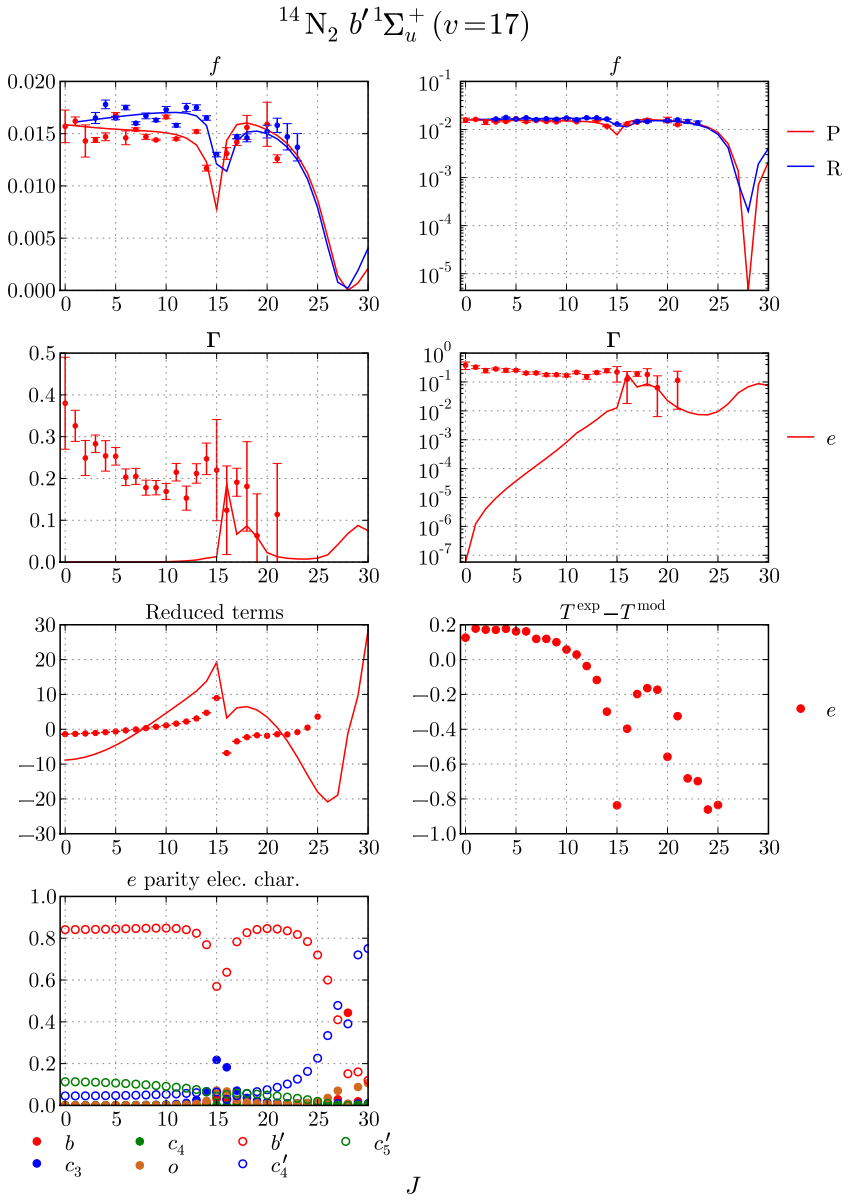
$^{14}N_2$ $b'\,^1\Sigma_u^+$ ($v=17$)
f
Γ
Reduced terms
$T^{exp}-T^{mod}$
e parity elec. char.
P
R
e
b
c_3
c_4
o
b'
c_4'
c_5'
J

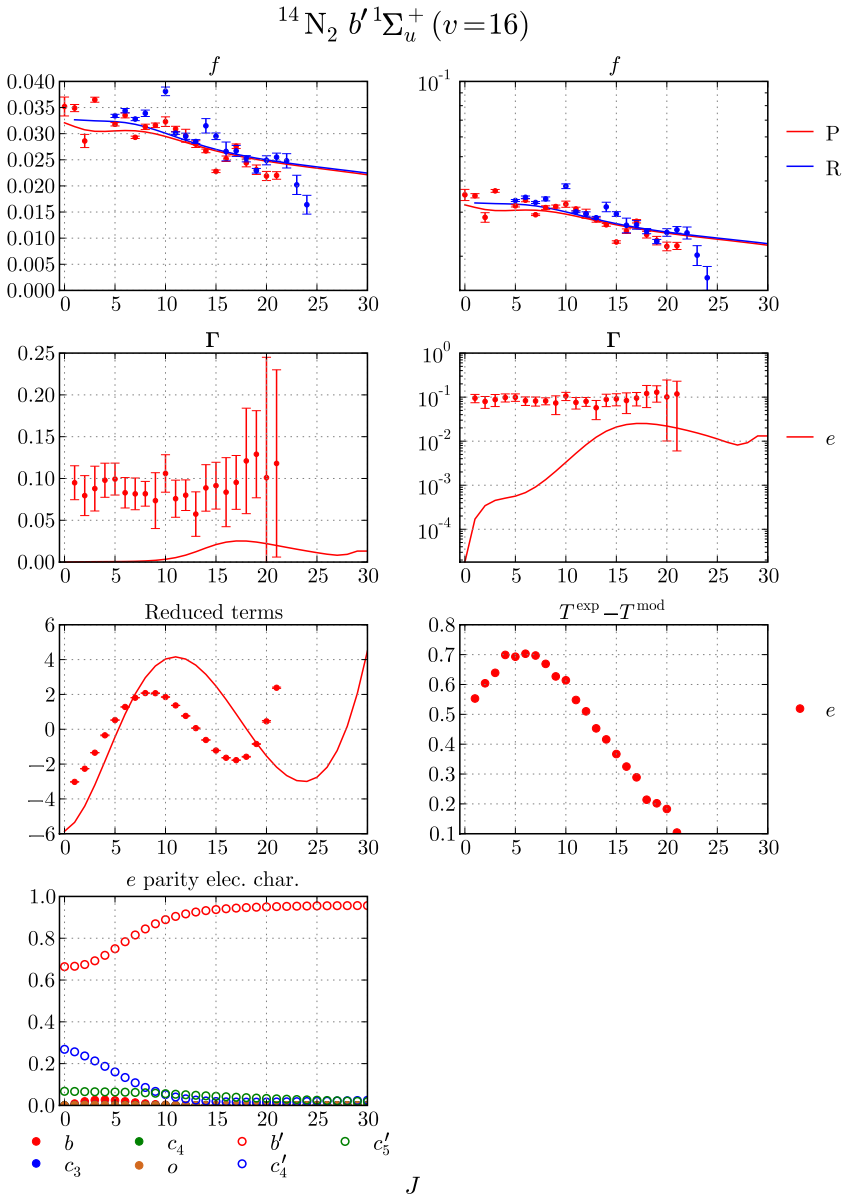
$^{14}N_2$ $b'\,^1\Sigma_u^+$ ($v=16$)
f
Γ
Reduced terms
$T^{exp}-T^{mod}$
e parity elec. char.
P
R
e
b
c_3
c_4
o
b'
c_4'
c_5'
J

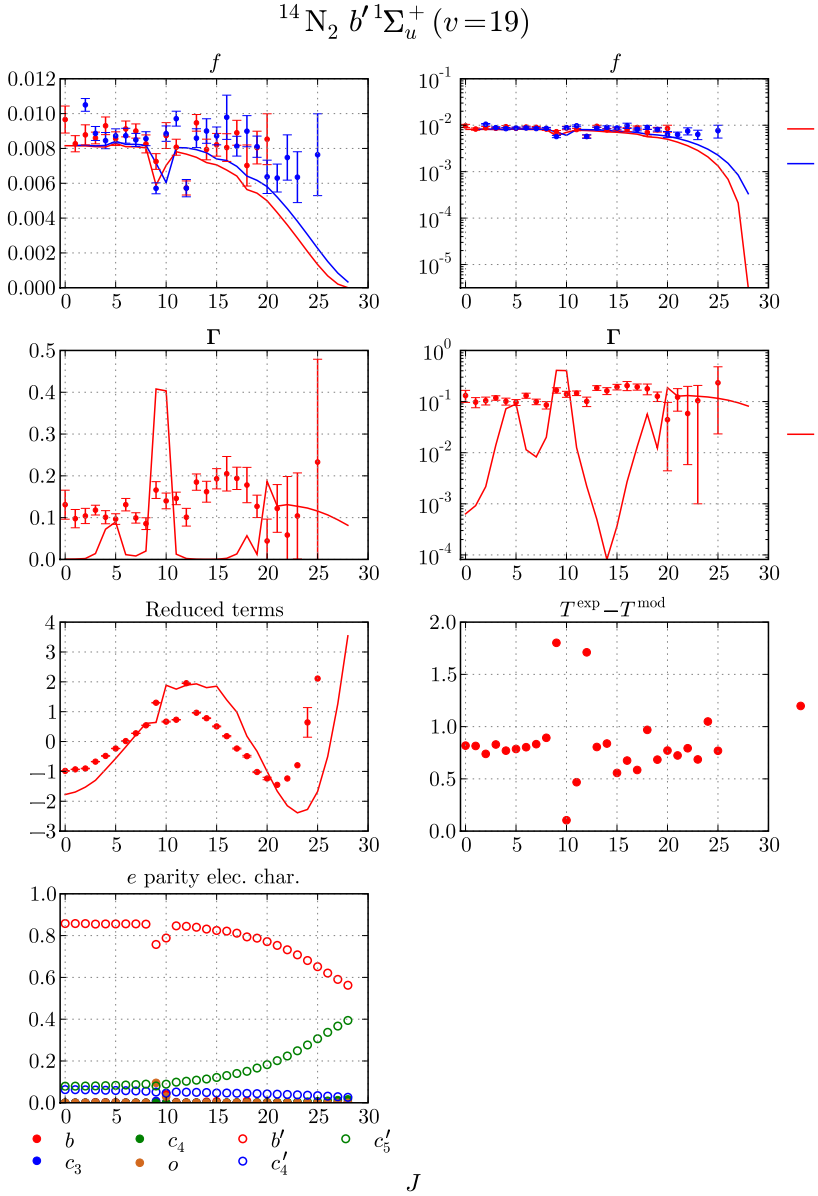
$^{14}N_2\ b'^1\Sigma_u^+\ (v=19)$
f
Γ
Reduced terms
e parity elec. char.
$T^{exp}-T^{mod}$
P
R
e
b
c_3
c_4
o
b′
c_4'
c_5'
J

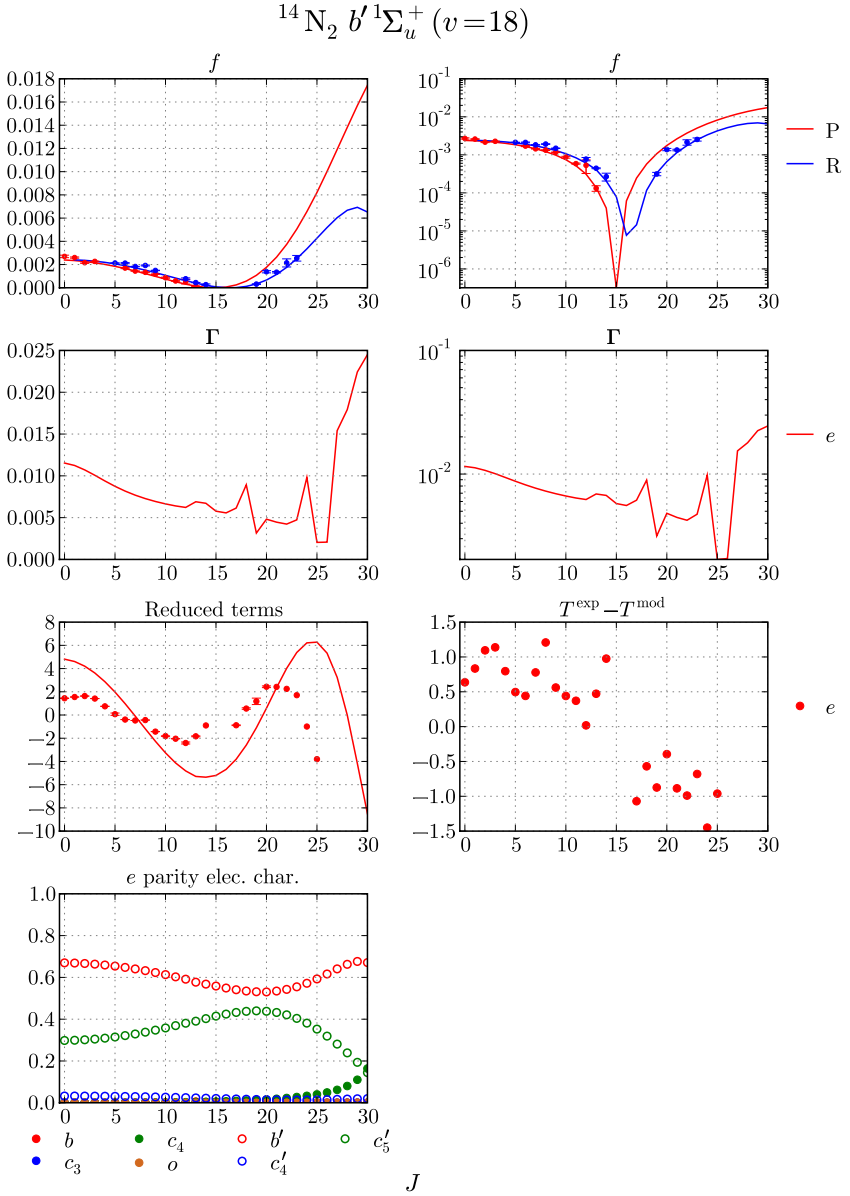
$^{14}N_2\ b'^1\Sigma_u^+\ (v=18)$
f
Γ
Reduced terms
e parity elec. char.
$T^{exp}-T^{mod}$
P
R
e
b
c_3
c_4
o
b′
c_4'
c_5'
J

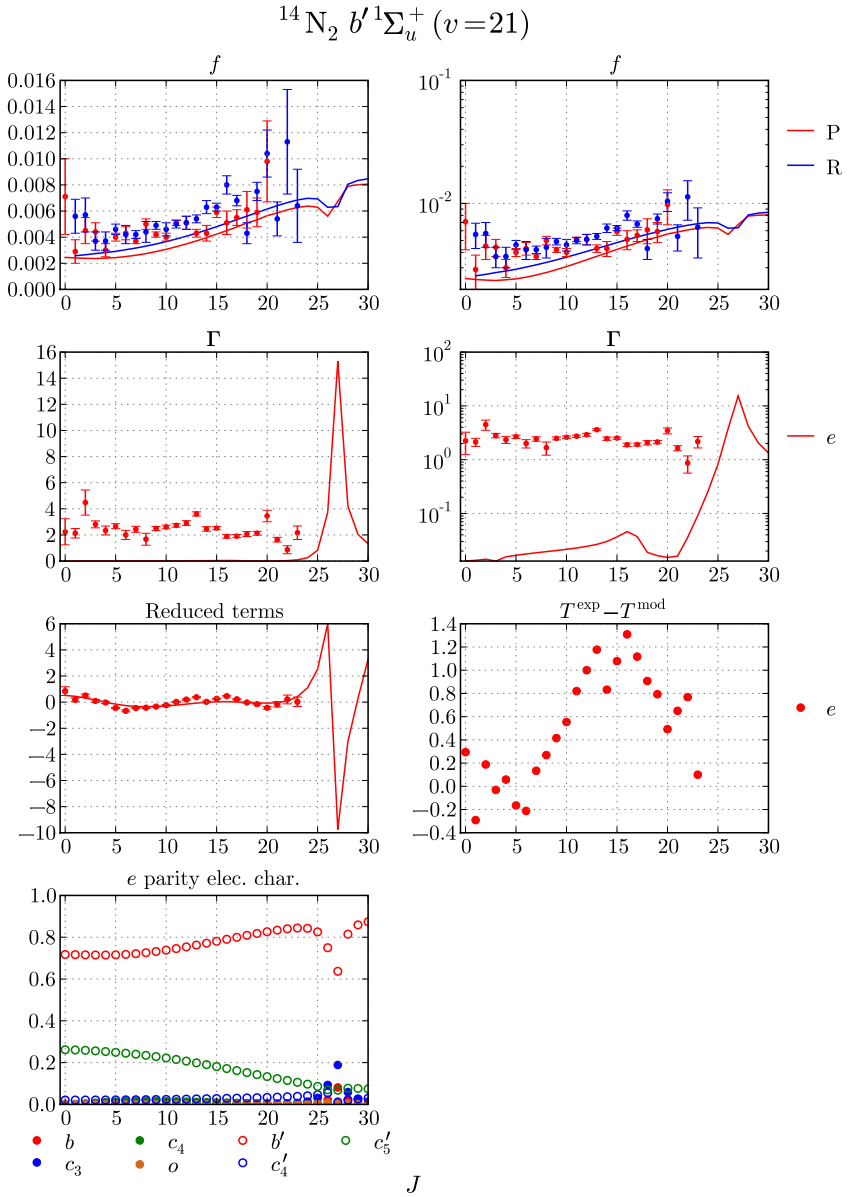
$^{14}N_2$ $b'\,^1\Sigma_u^+$ ($v=21$)
f
Γ
Reduced terms
$T^{exp}-T^{mod}$
e parity elec. char.
P
R
e
b
c_3
c_4
o
b'
c_4'
c_5'
J

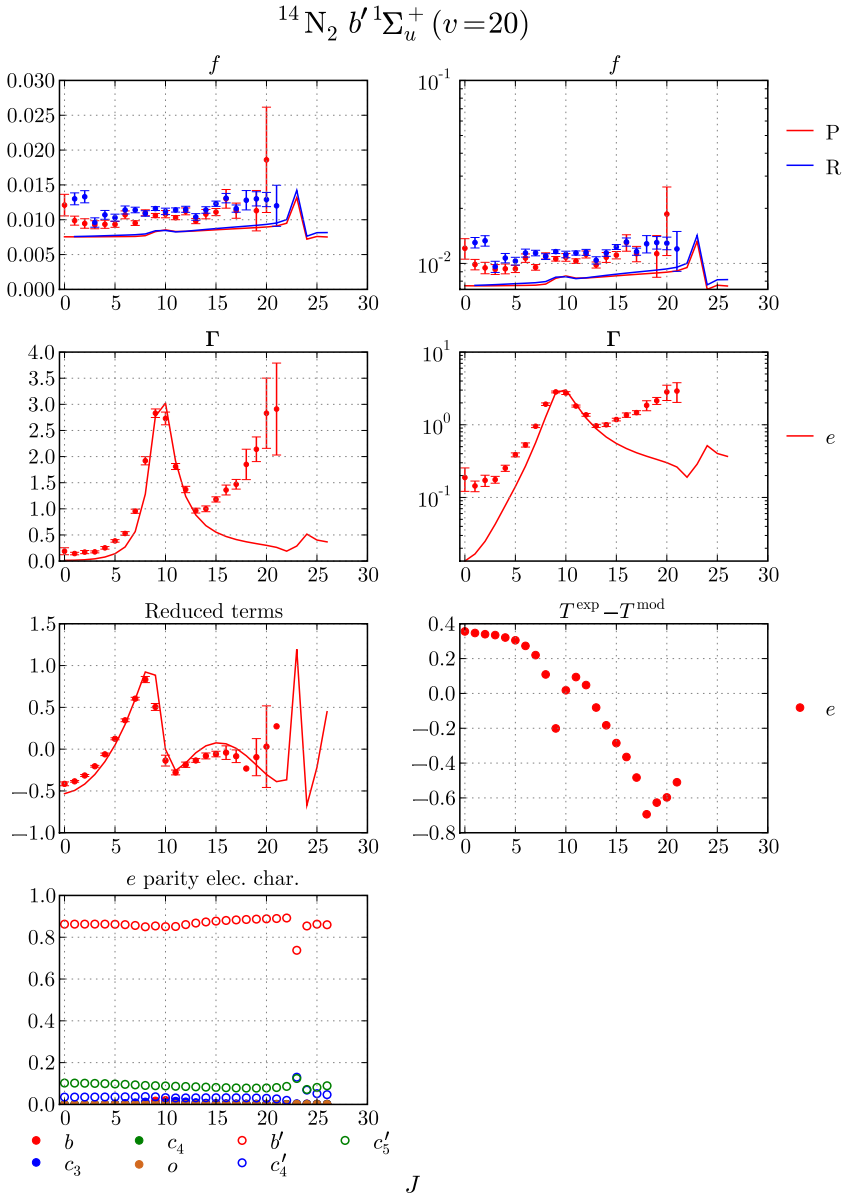
$^{14}N_2$ $b'\,^1\Sigma_u^+$ ($v=20$)
f
Γ
Reduced terms
$T^{exp}-T^{mod}$
e parity elec. char.
P
R
e
b
c_3
c_4
o
b'
c_4'
c_5'
J

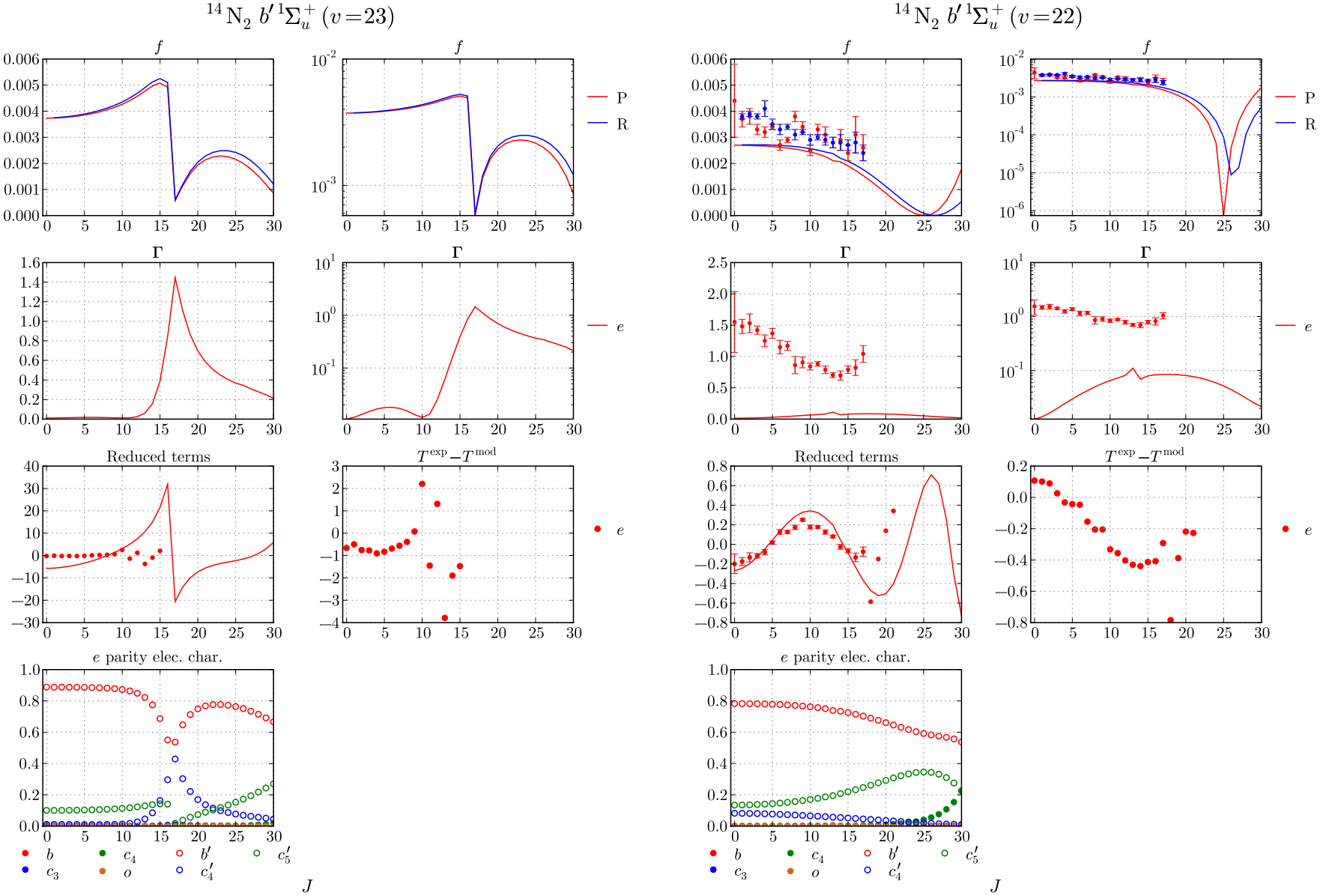
$^{14}N_2\ b'^1\Sigma_u^+\ (v=23)$
$^{14}N_2\ b'^1\Sigma_u^+\ (v=22)$
f
Γ
Reduced terms
$T^{exp}-T^{mod}$
e parity elec. char.
P
R
e
b
c_3
c_4
o
b'
c_4'
c_5'
J

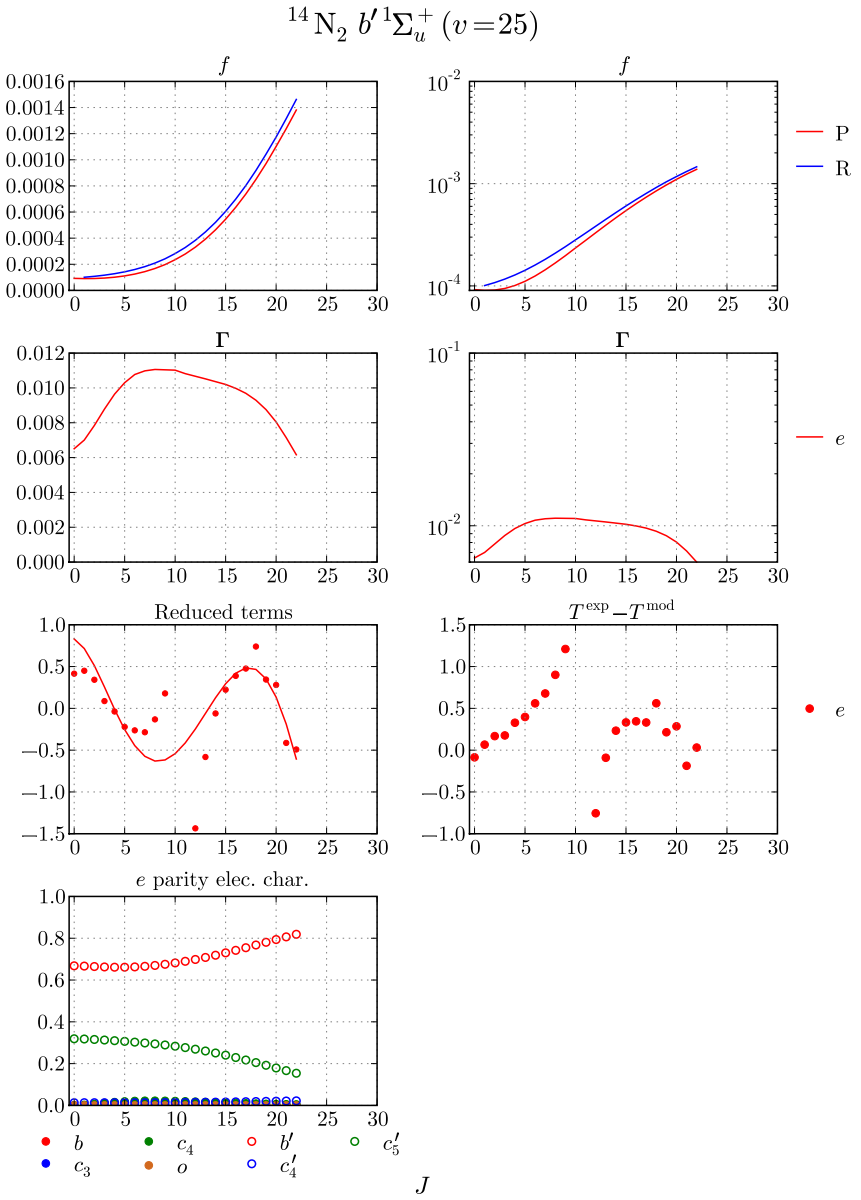
$^{14}N_2\ b'^1\Sigma_u^+\ (v=25)$
f
Γ
Reduced terms
$T^{exp}-T^{mod}$
e parity elec. char.
P
R
e
b
c_3
c_4
o
b'
c_4'
c_5'
J

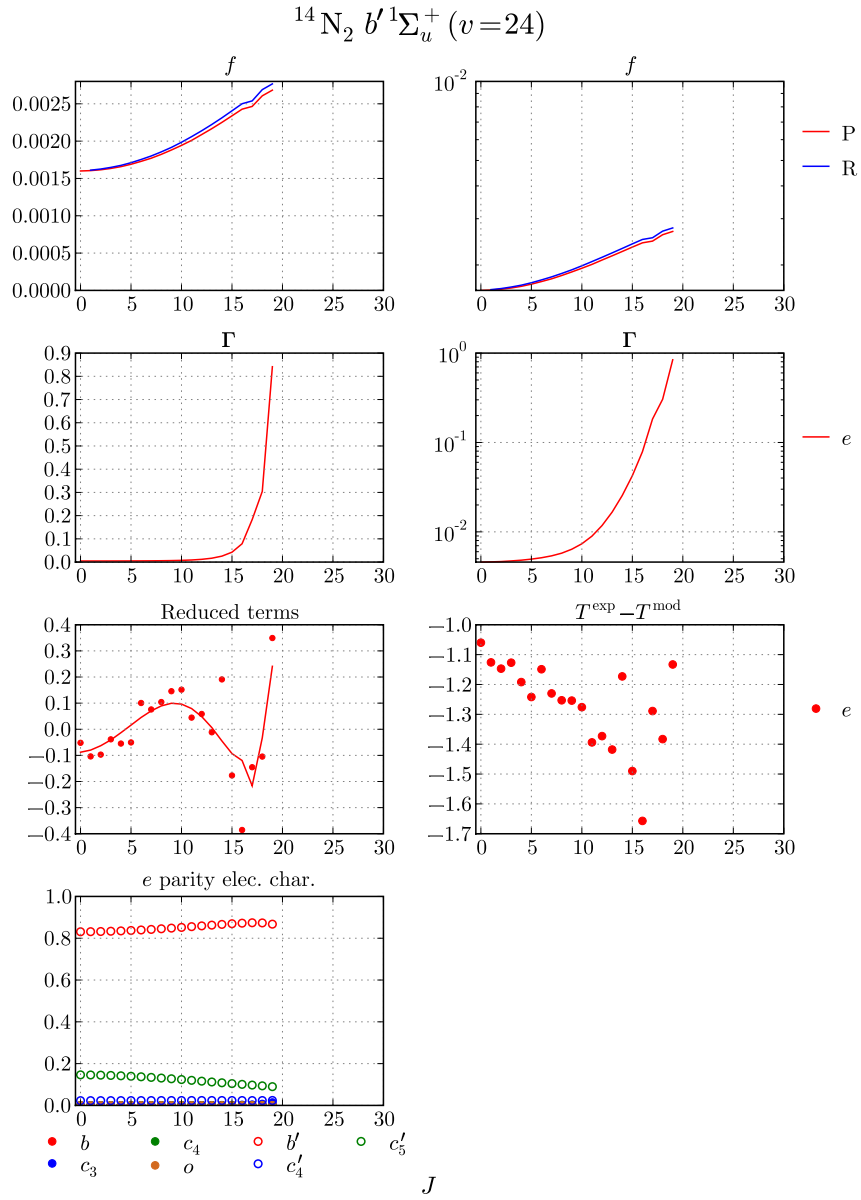
$^{14}N_2\ b'^1\Sigma_u^+\ (v=24)$
f
Γ
Reduced terms
$T^{exp}-T^{mod}$
e parity elec. char.
P
R
e
b
c_3
c_4
o
b'
c_4'
c_5'
J

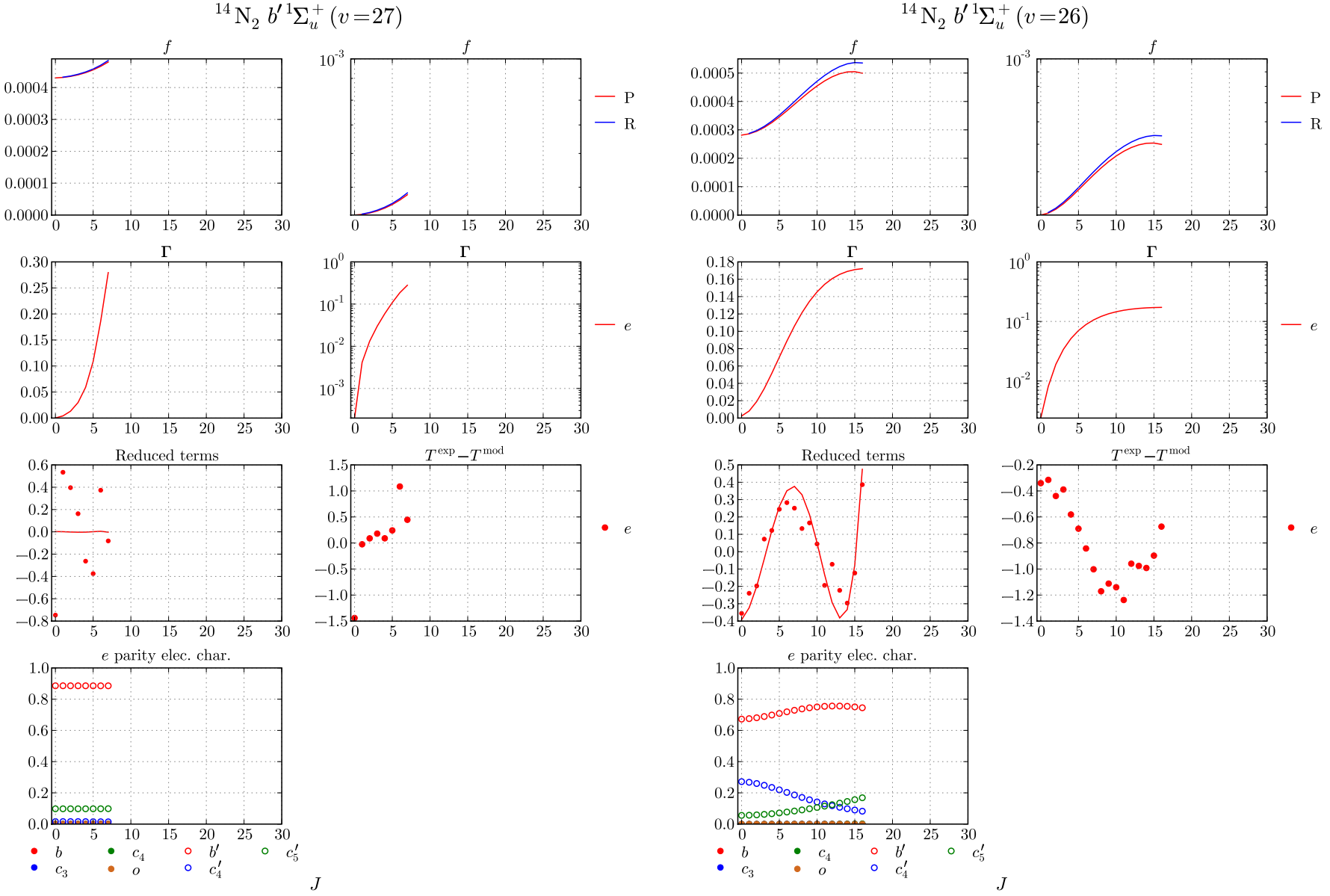
$^{14}N_2$ $b'^1\Sigma_u^+$ ($v=27$)
$^{14}N_2$ $b'^1\Sigma_u^+$ ($v=26$)
f
Γ
Reduced terms
$T^{exp}-T^{mod}$
e parity elec. char.
P
R
e
b
c_3
c_4
o
b'
c_4'
c_5'
J

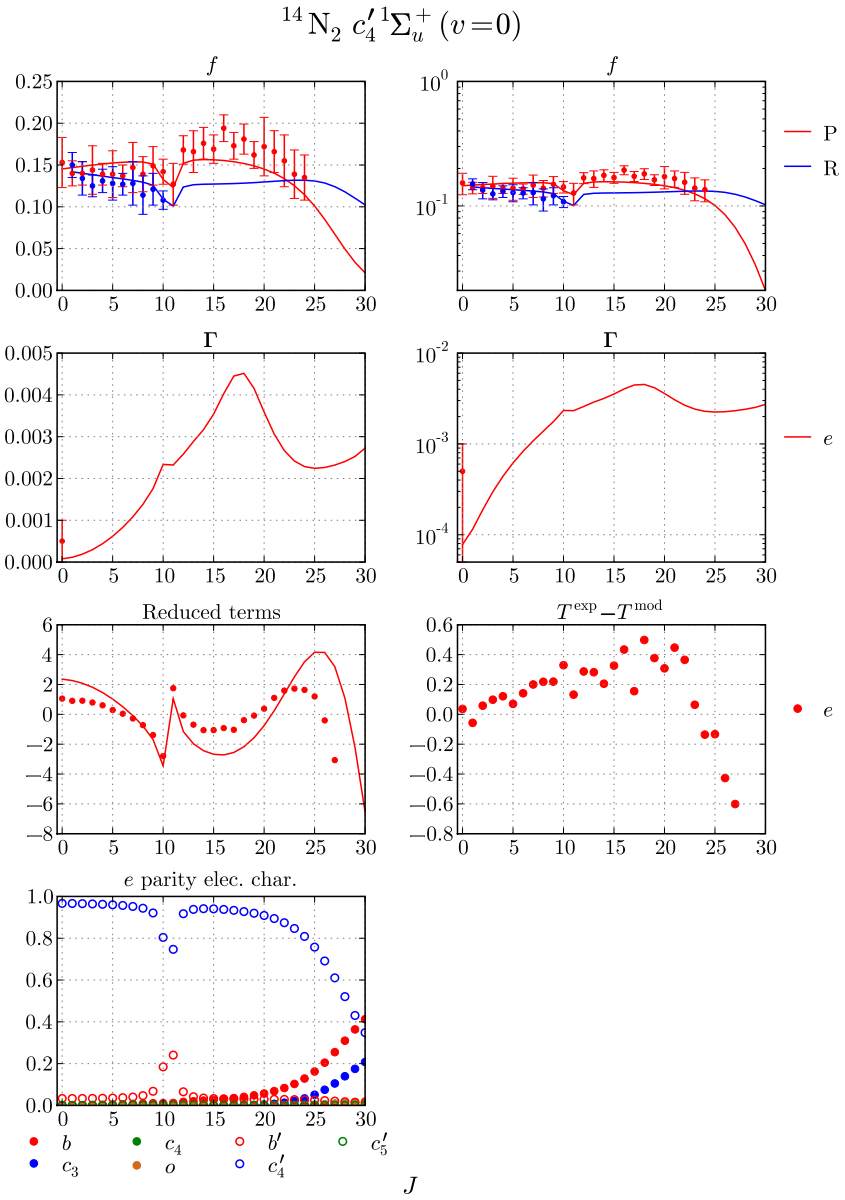
$^{14}N_2\ c_4'\,^1\Sigma_u^+\ (v=0)$
f
f
P
R
Γ
Γ
e
Reduced terms
$T^{exp}-T^{mod}$
e
e parity elec. char.
b
c_3
c_4
o
b'
c_4'
c_5'
J

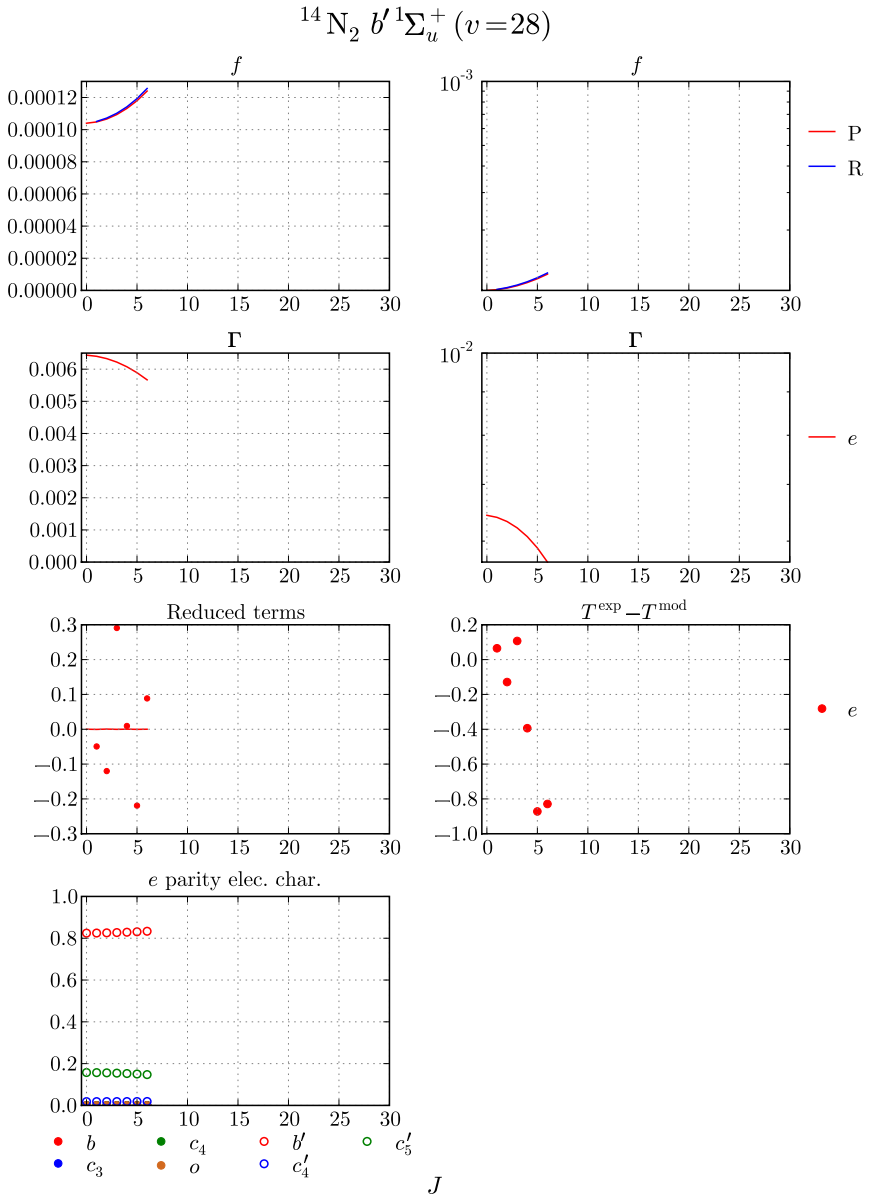
$^{14}N_2\ b'\,^1\Sigma_u^+\ (v=28)$
f
f
P
R
Γ
Γ
e
Reduced terms
$T^{exp}-T^{mod}$
e
e parity elec. char.
b
c_3
c_4
o
b'
c_4'
c_5'
J

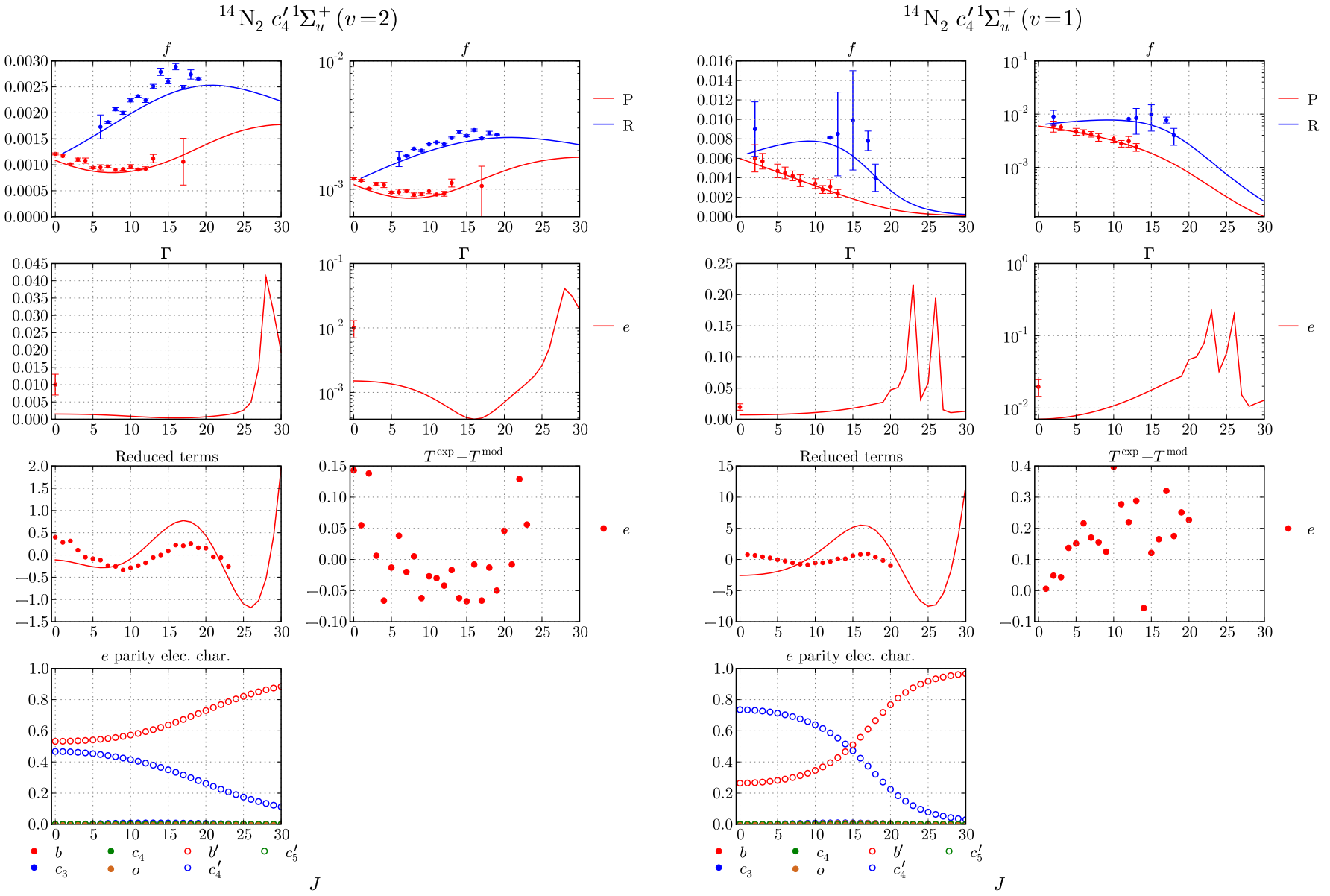
$^{14}N_2$ $c_4'\,^1\Sigma_u^+$ $(v=2)$
$^{14}N_2$ $c_4'\,^1\Sigma_u^+$ $(v=1)$
f
Γ
Reduced terms
$T^{\rm exp}-T^{\rm mod}$
e parity elec. char.
P
R
e
b
c_3
c_4
o
b'
c_4'
c_5'
J

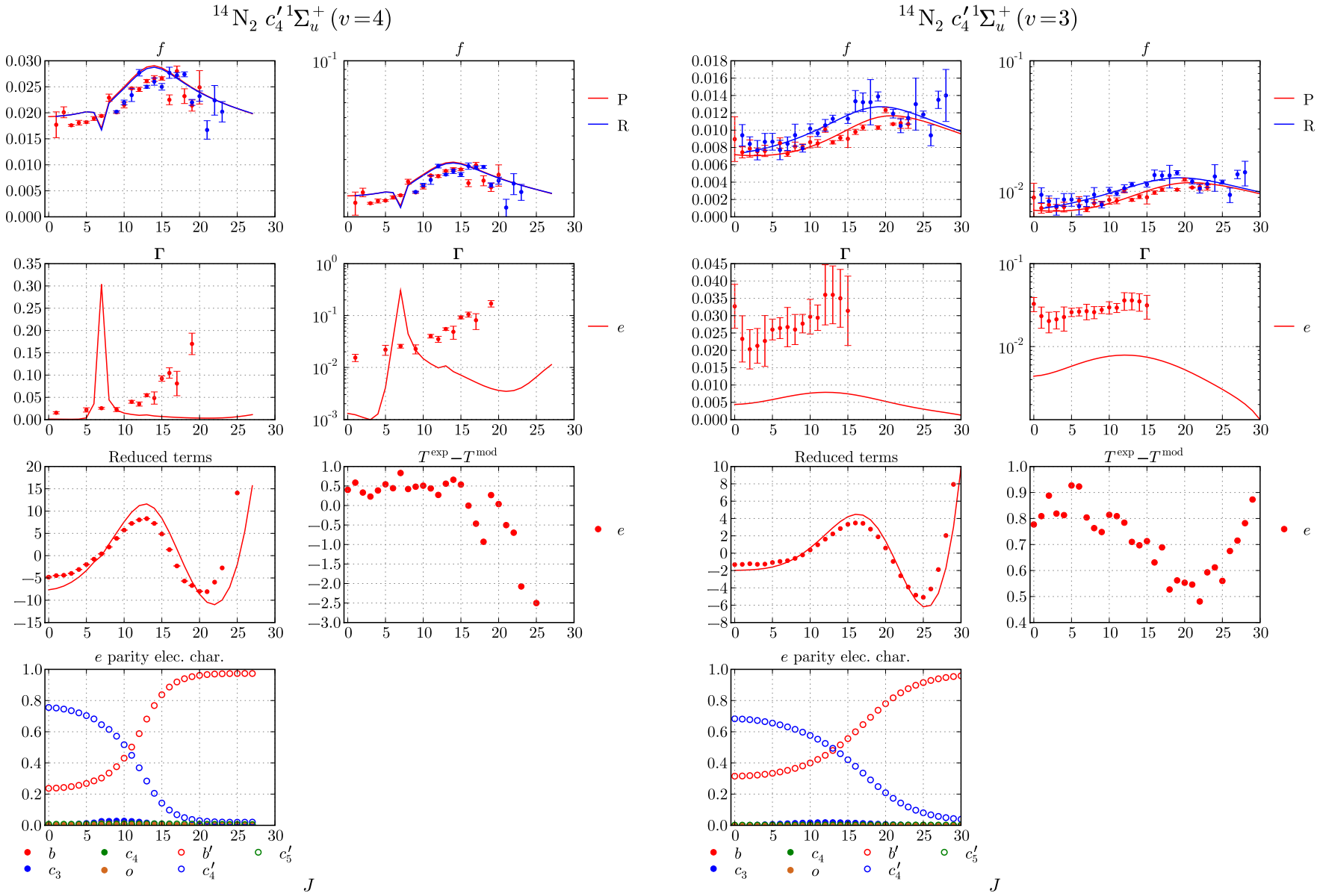
$^{14}N_2$ $c_4'^1\Sigma_u^+$ ($v=4$)
$^{14}N_2$ $c_4'^1\Sigma_u^+$ ($v=3$)
f
Γ
Reduced terms
$T^{exp}-T^{mod}$
e parity elec. char.
P
R
e
b
c_3
c_4
o
b'
c_4'
c_5'
J

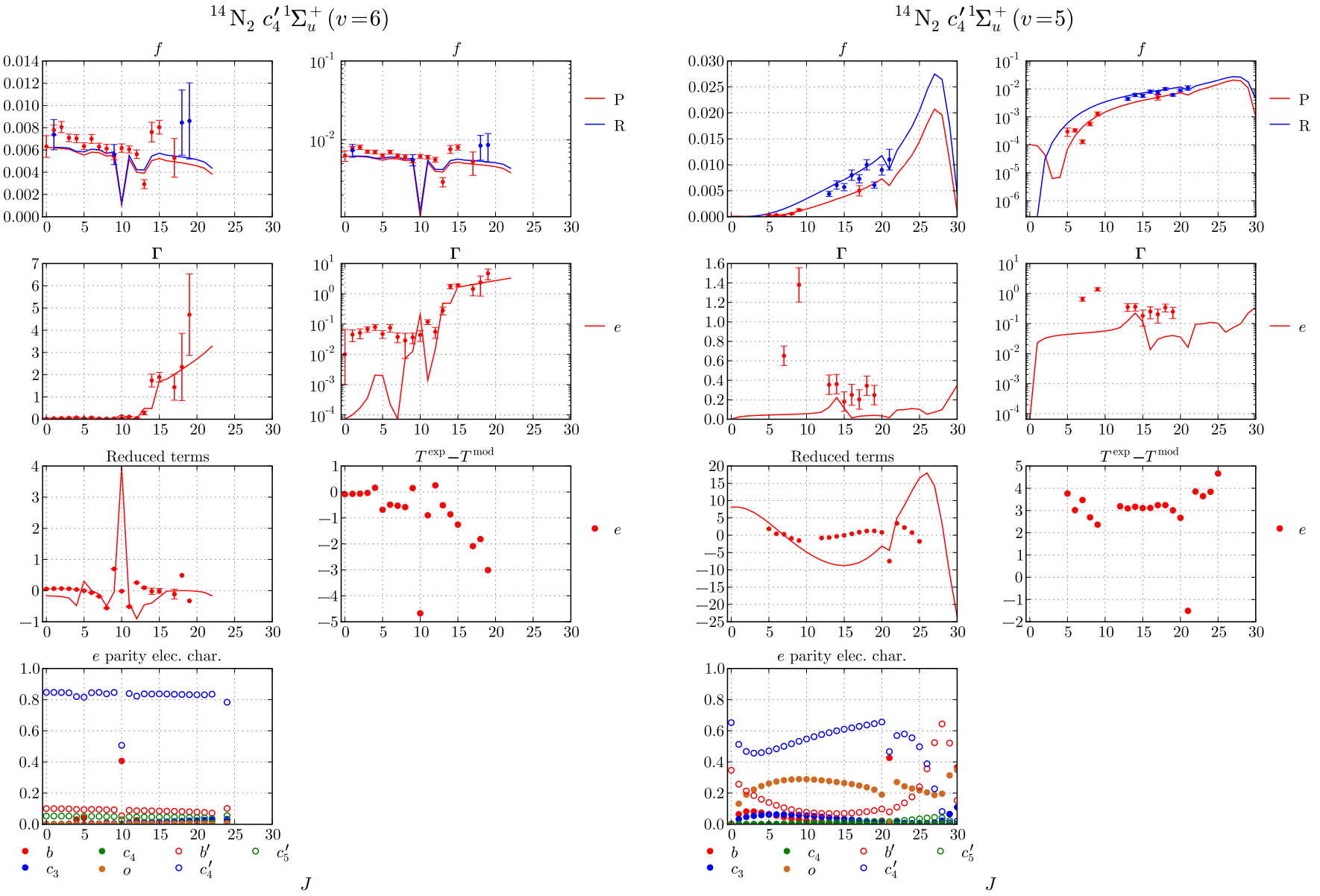
$^{14}N_2$ $c_4'\,^1\Sigma_u^+$ $(v=6)$
$^{14}N_2$ $c_4'\,^1\Sigma_u^+$ $(v=5)$
f
Γ
Reduced terms
$T^{\rm exp}-T^{\rm mod}$
e parity elec. char.
P
R
e
b
c_3
c_4
o
b'
c_4'
c_5'
J

$^{14}\mathrm{N}_2\ c_4'\,{}^1\Sigma_u^+\ (v=8)$
f
Γ
Reduced terms
e parity elec. char.
f
Γ
$T^{\mathrm{exp}}-T^{\mathrm{mod}}$
P
R
e
b
c_3
c_4
o
b'
c_4'
c_5'
J

$^{14}\mathrm{N}_2\ c_4'\,{}^1\Sigma_u^+\ (v=7)$
f
Γ
Reduced terms
e parity elec. char.
f
Γ
$T^{\mathrm{exp}}-T^{\mathrm{mod}}$
P
R
e
b
c_3
c_4
o
b'
c_4'
c_5'
J

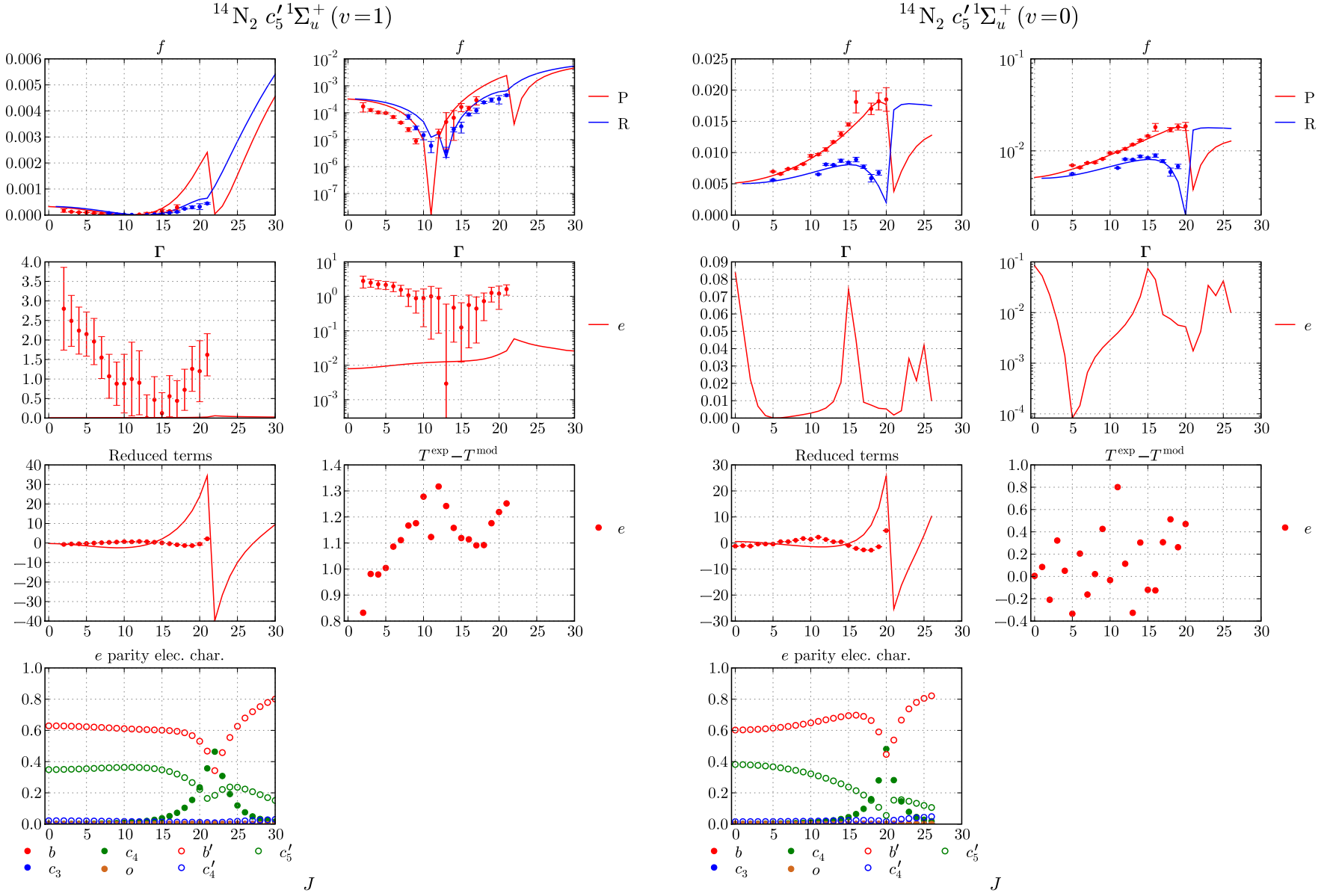
$^{14}N_2$ $c_5'\,^1\Sigma_u^+$ $(v=1)$
$^{14}N_2$ $c_5'\,^1\Sigma_u^+$ $(v=0)$
f
Γ
Reduced terms
$T^{exp}-T^{mod}$
e parity elec. char.
P
R
e
b
c_3
c_4
o
b'
c_4'
c_5'
J

$^{14}N^{15}N\ b^1\Pi_u(v=0)$
f
Γ
Reduced terms
e parity elec. char.
$T^{exp}-T^{mod}$
T_e-T_f
P
R
Q
e
f
b
c_3
c_4
o
b'
c_4'
c_5'
J

$^{14}N_2\ c_5'^1\Sigma_u^+\ (v=2)$
f
Γ
Reduced terms
e parity elec. char.
$T^{exp}-T^{mod}$
P
R
e
b
c_3
c_4
o
b'
c_4'
c_5'
J

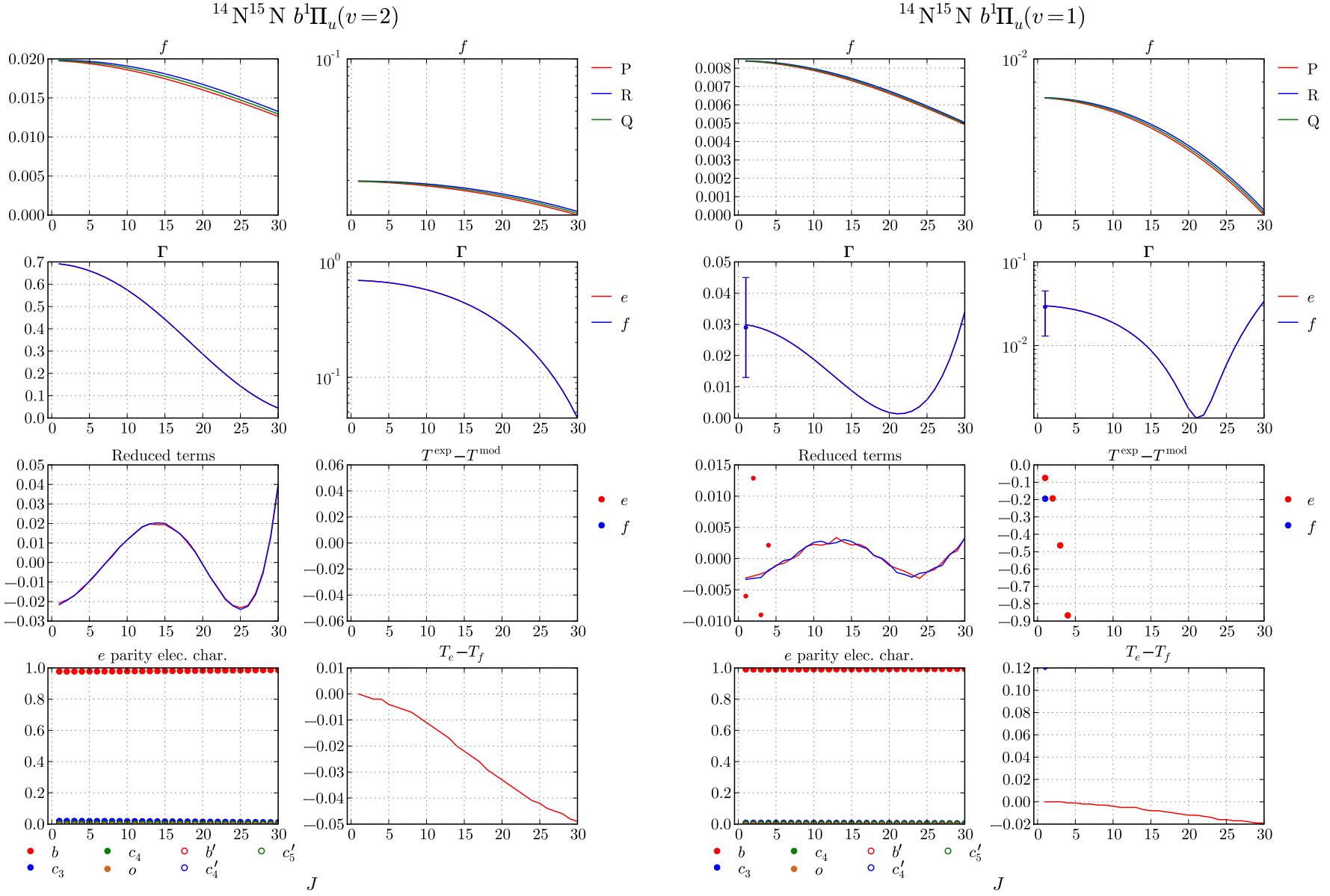
^{14}N^{15}N $b^1\Pi_u(v=2)$
^{14}N^{15}N $b^1\Pi_u(v=1)$
f
Γ
Reduced terms
$T^{\rm exp}-T^{\rm mod}$
e parity elec. char.
T_e-T_f
P
R
Q
e
f
b
c_3
c_4
o
b'
c_4'
c_5'
J

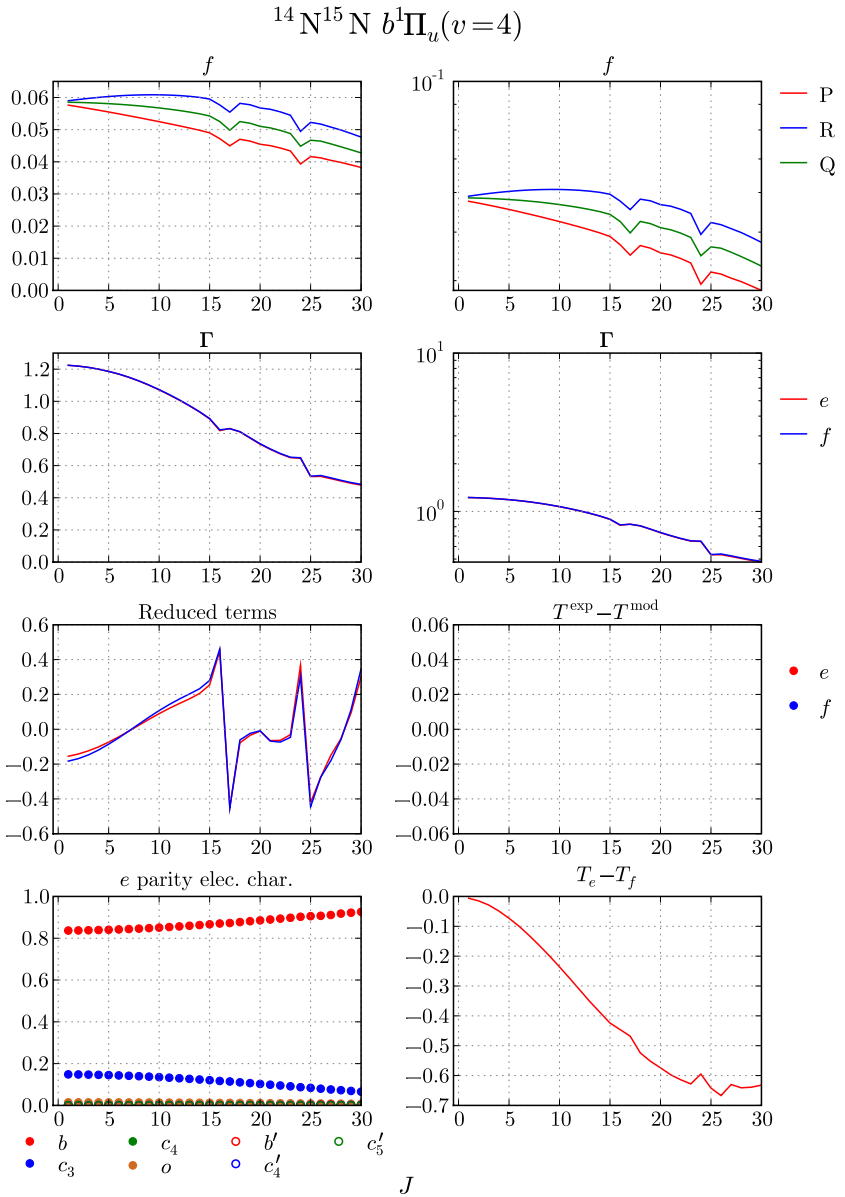
^{14}N^{15}N $b^1\Pi_u(v=4)$
f
Γ
Reduced terms
e parity elec. char.
$T^{\rm exp}-T^{\rm mod}$
T_e-T_f
P
R
Q
e
f
b
c_3
c_4
o
b'
c_4'
c_5'
J

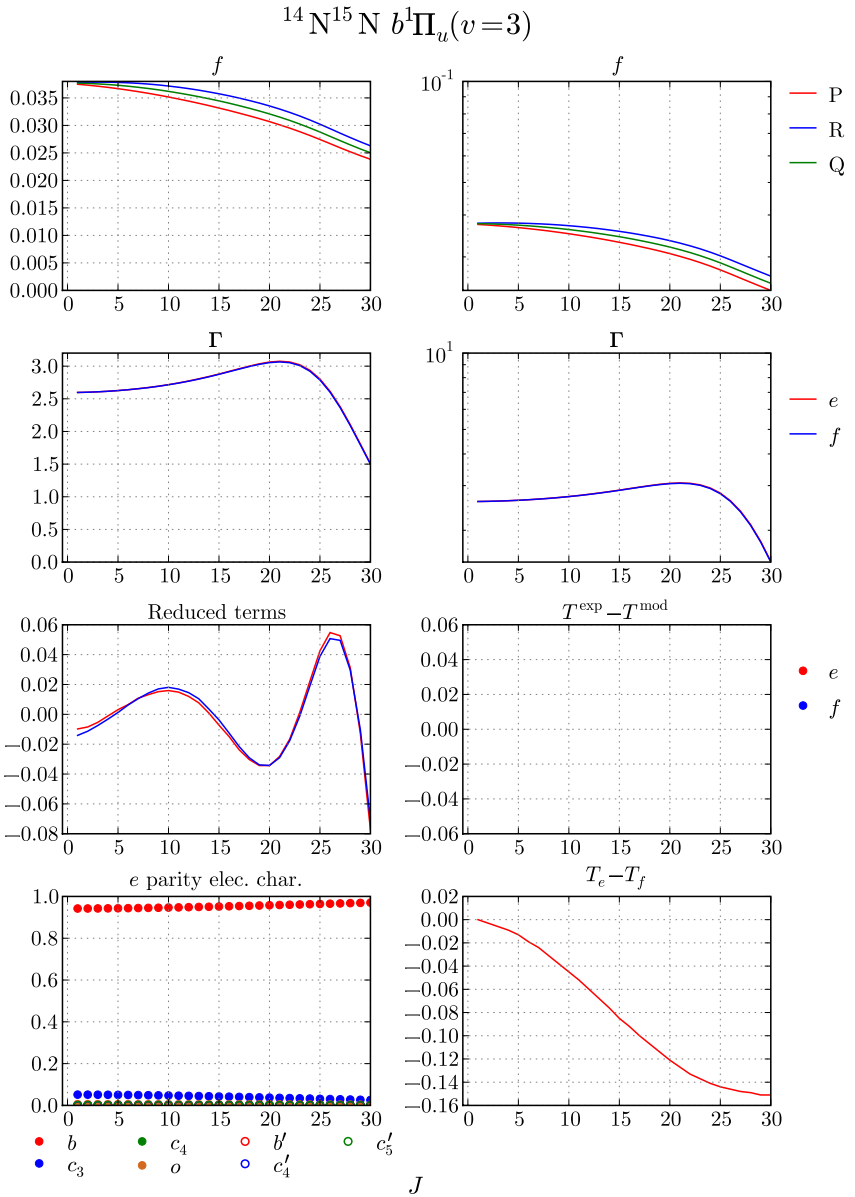
^{14}N^{15}N $b^1\Pi_u(v=3)$
f
Γ
Reduced terms
e parity elec. char.
$T^{\rm exp}-T^{\rm mod}$
T_e-T_f
P
R
Q
e
f
b
c_3
c_4
o
b'
c_4'
c_5'
J

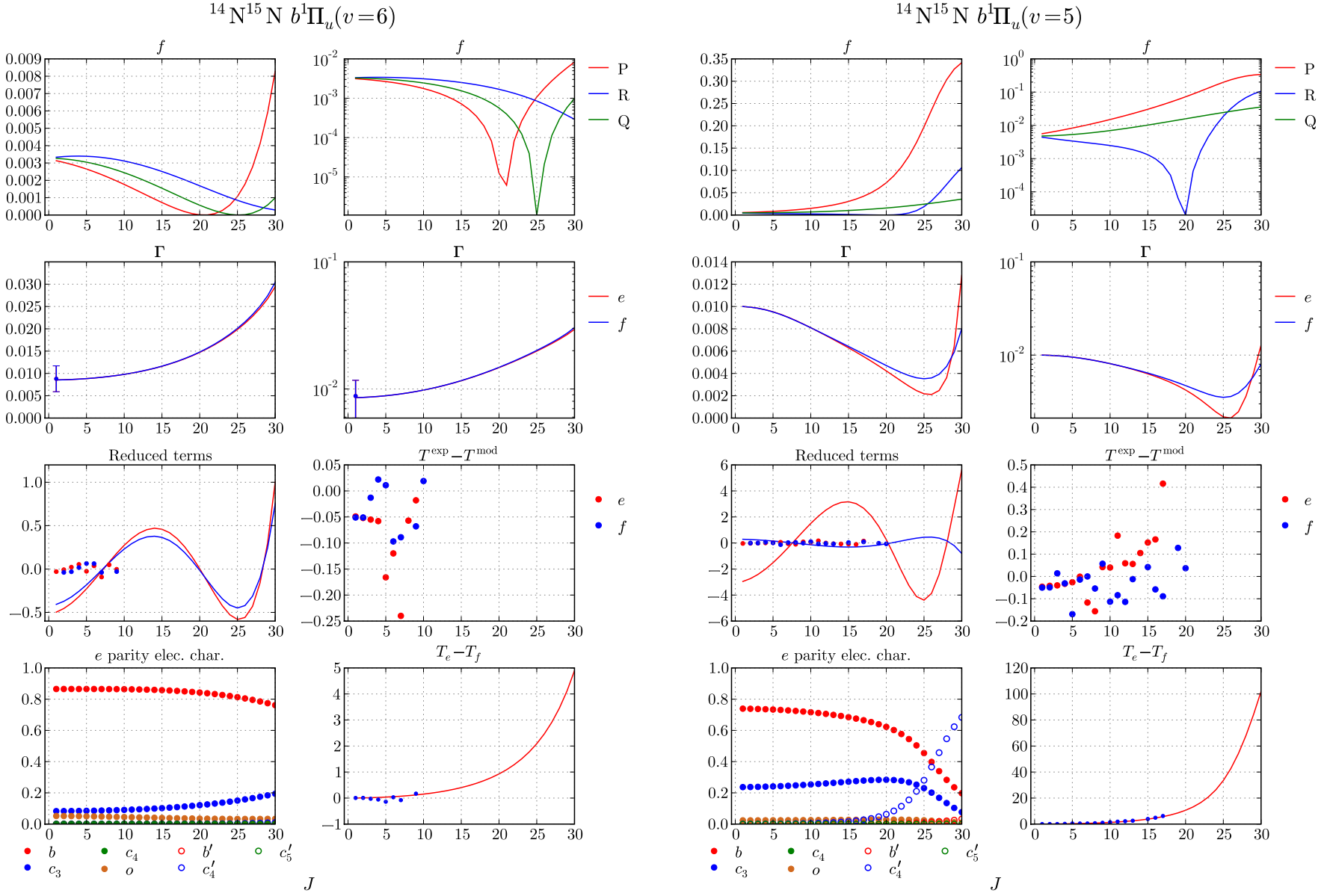
^{14}N^{15}N $b^1\Pi_u(v=6)$
^{14}N^{15}N $b^1\Pi_u(v=5)$
f
Γ
Reduced terms
$T^{\rm exp}-T^{\rm mod}$
e parity elec. char.
T_e-T_f
P
R
Q
e
f
b
c_3
c_4
o
b'
c_4'
c_5'
J

^{14}N^{15}N $b^1\Pi_u(v=8)$
f
Γ
Reduced terms
e parity elec. char.
$T^{\rm exp}-T^{\rm mod}$
T_e-T_f
P
R
Q
e
f
b
c_3
c_4
o
b'
c_4'
c_5'
J

^{14}N^{15}N $b^1\Pi_u(v=7)$
f
Γ
Reduced terms
e parity elec. char.
$T^{\rm exp}-T^{\rm mod}$
T_e-T_f
P
R
Q
e
f
b
c_3
c_4
o
b'
c_4'
c_5'
J

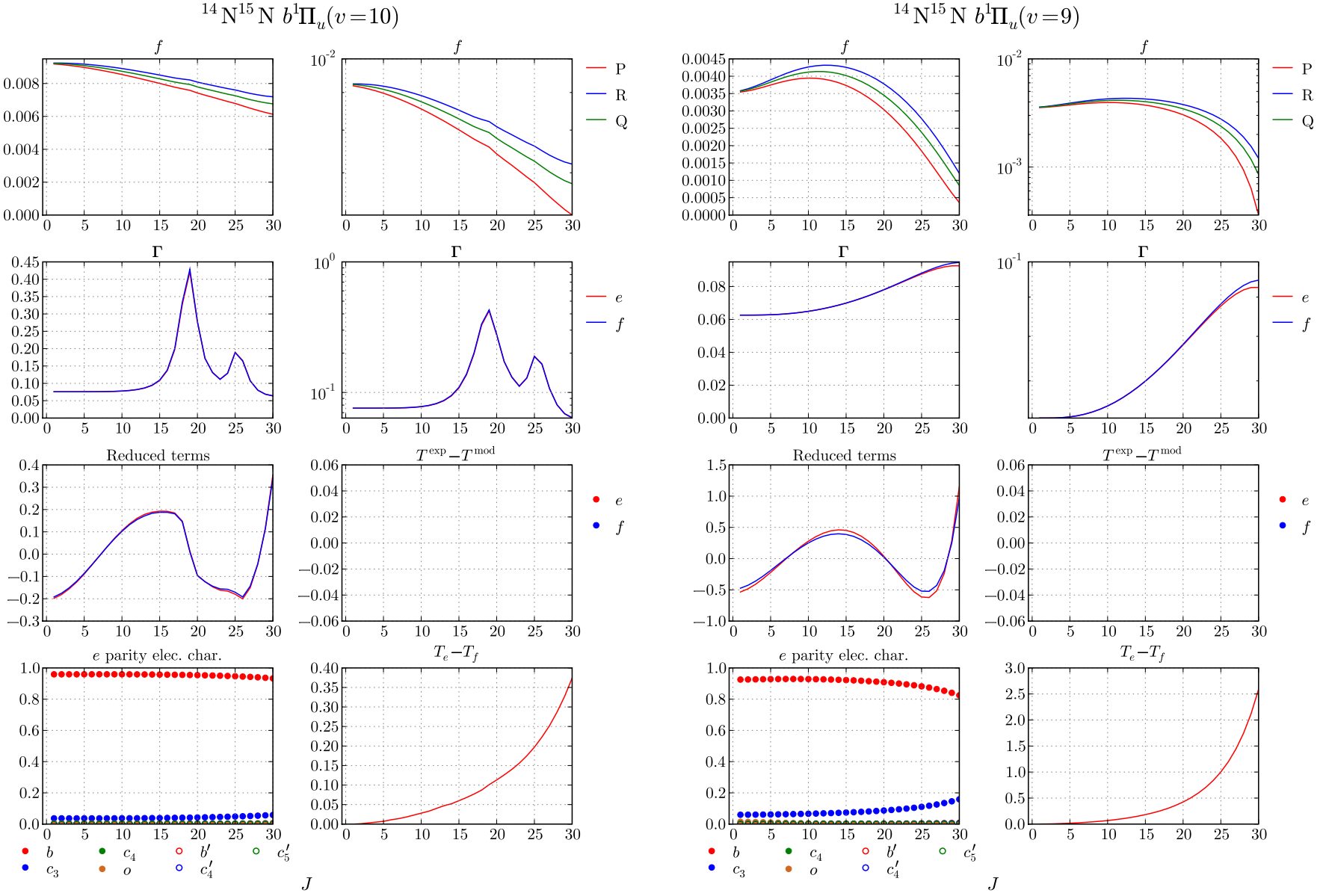
^{14}N^{15}N $b^1\Pi_u(v=10)$
f
Γ
Reduced terms
$T^{\rm exp}-T^{\rm mod}$
e parity elec. char.
T_e-T_f
P
R
Q
e
f
b
c_3
c_4
o
b'
c_4'
c_5'
J
^{14}N^{15}N $b^1\Pi_u(v=9)$
f
Γ
Reduced terms
$T^{\rm exp}-T^{\rm mod}$
e parity elec. char.
T_e-T_f
P
R
Q
e
f
b
c_3
c_4
o
b'
c_4'
c_5'
J

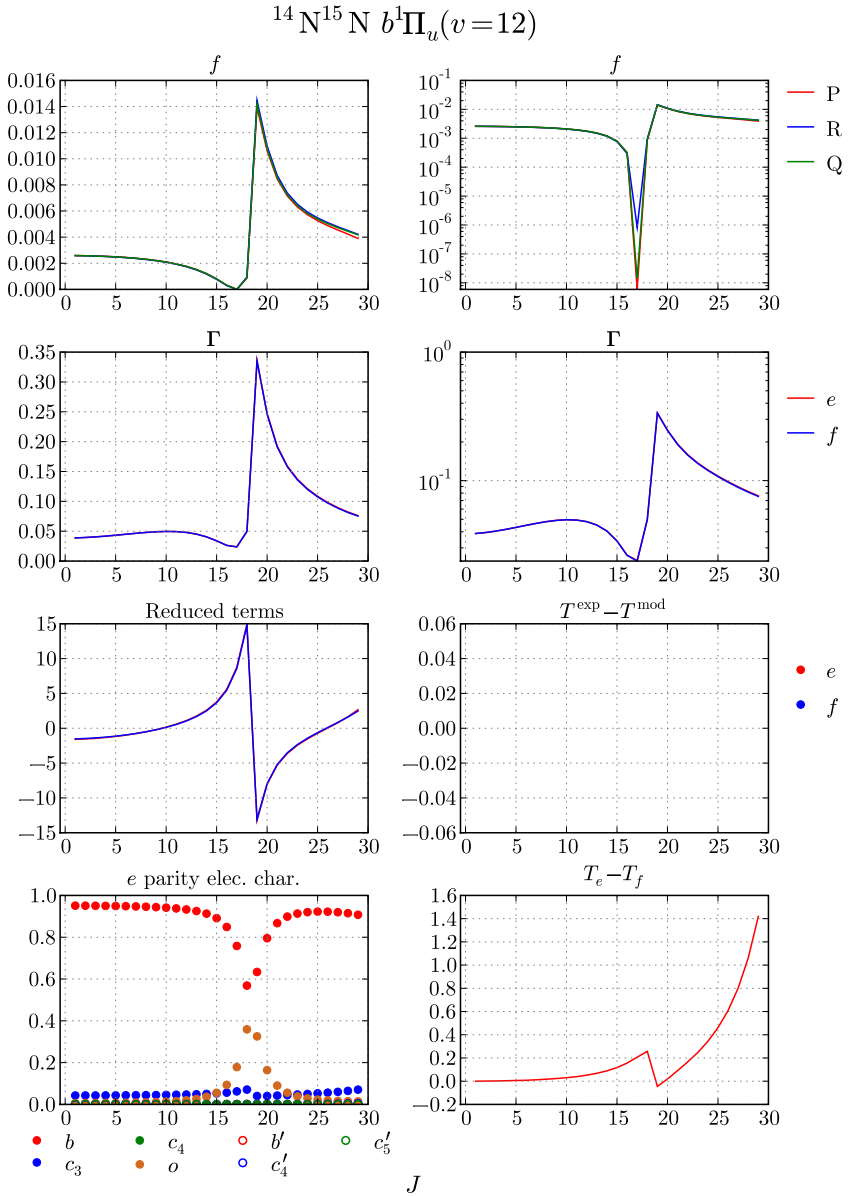
^{14}N^{15}N $b^1\Pi_u(v=12)$
f
Γ
Reduced terms
e parity elec. char.
$T^{\rm exp}-T^{\rm mod}$
T_e-T_f
P
R
Q
e
f
b
c_3
c_4
o
b'
c_4'
c_5'
J

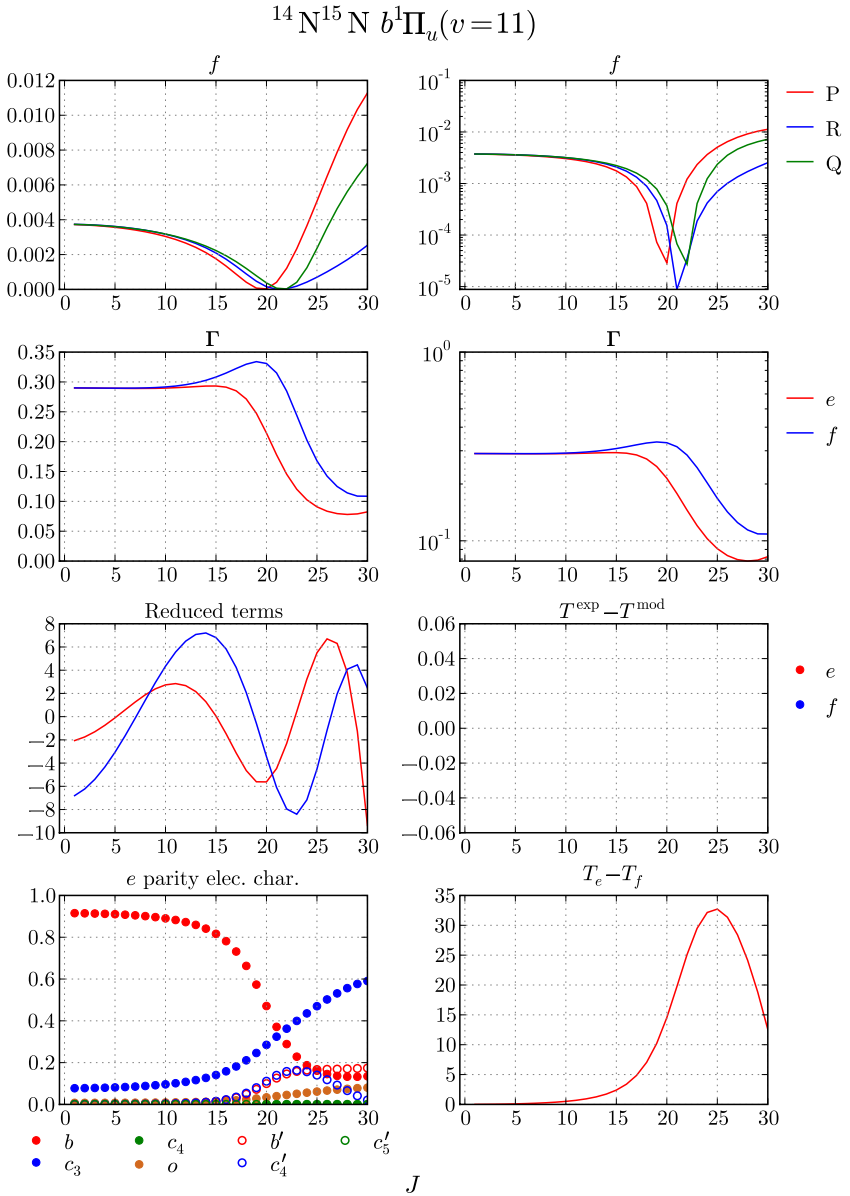
^{14}N^{15}N $b^1\Pi_u(v=11)$
f
Γ
Reduced terms
e parity elec. char.
$T^{\rm exp}-T^{\rm mod}$
T_e-T_f
P
R
Q
e
f
b
c_3
c_4
o
b'
c_4'
c_5'
J

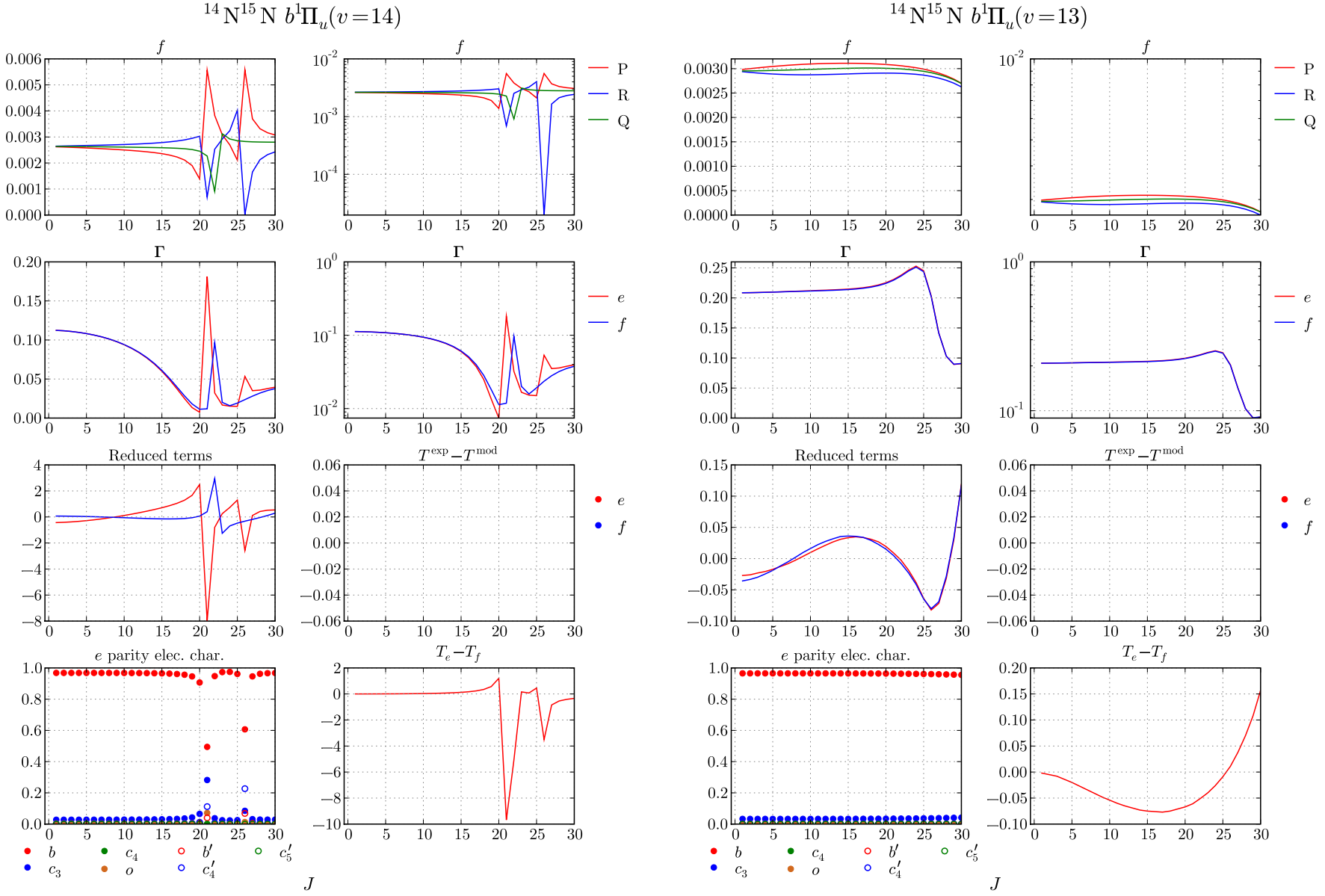
^{14}N^{15}N $b^1\Pi_u(v=14)$
^{14}N^{15}N $b^1\Pi_u(v=13)$
f
Γ
Reduced terms
$T^{\mathrm{exp}}-T^{\mathrm{mod}}$
e parity elec. char.
T_e-T_f
P
R
Q
e
f
b
c_3
c_4
o
b'
c_4'
c_5'
J

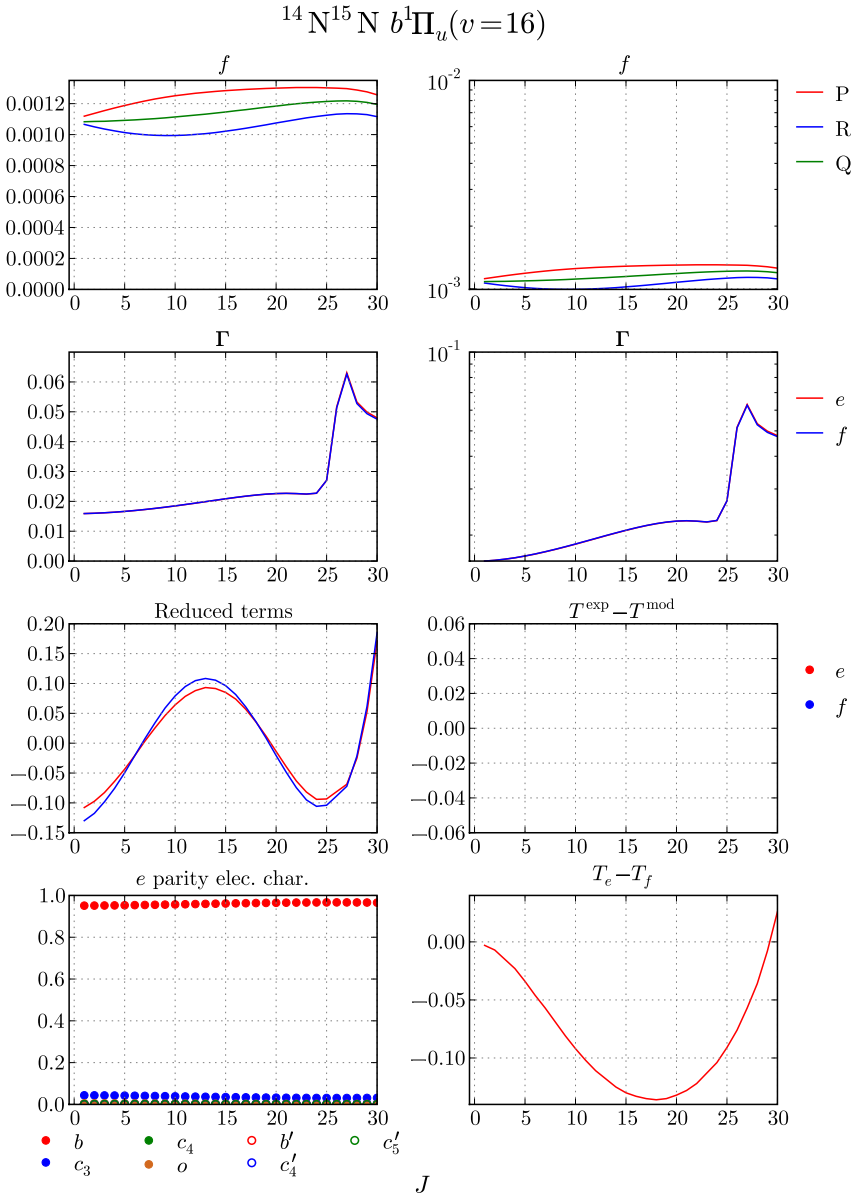
^{14}N^{15}N $b^1\Pi_u(v=16)$
f
Γ
Reduced terms
e parity elec. char.
P
R
Q
e
f
$T^{\rm exp}-T^{\rm mod}$
T_e-T_f
b
c_3
c_4
o
b'
c_4'
c_5'
J

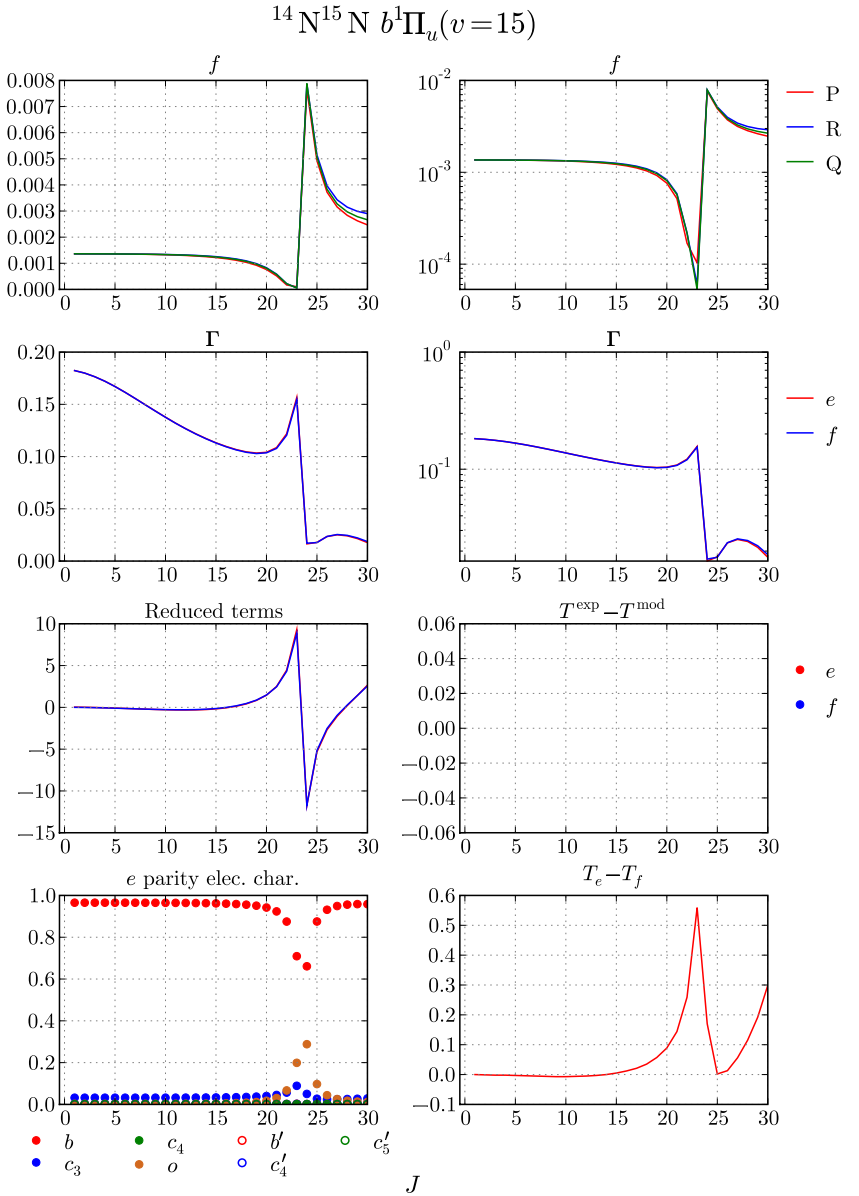
^{14}N^{15}N $b^1\Pi_u(v=15)$
f
Γ
Reduced terms
e parity elec. char.
P
R
Q
e
f
$T^{\rm exp}-T^{\rm mod}$
T_e-T_f
b
c_3
c_4
o
b'
c_4'
c_5'
J

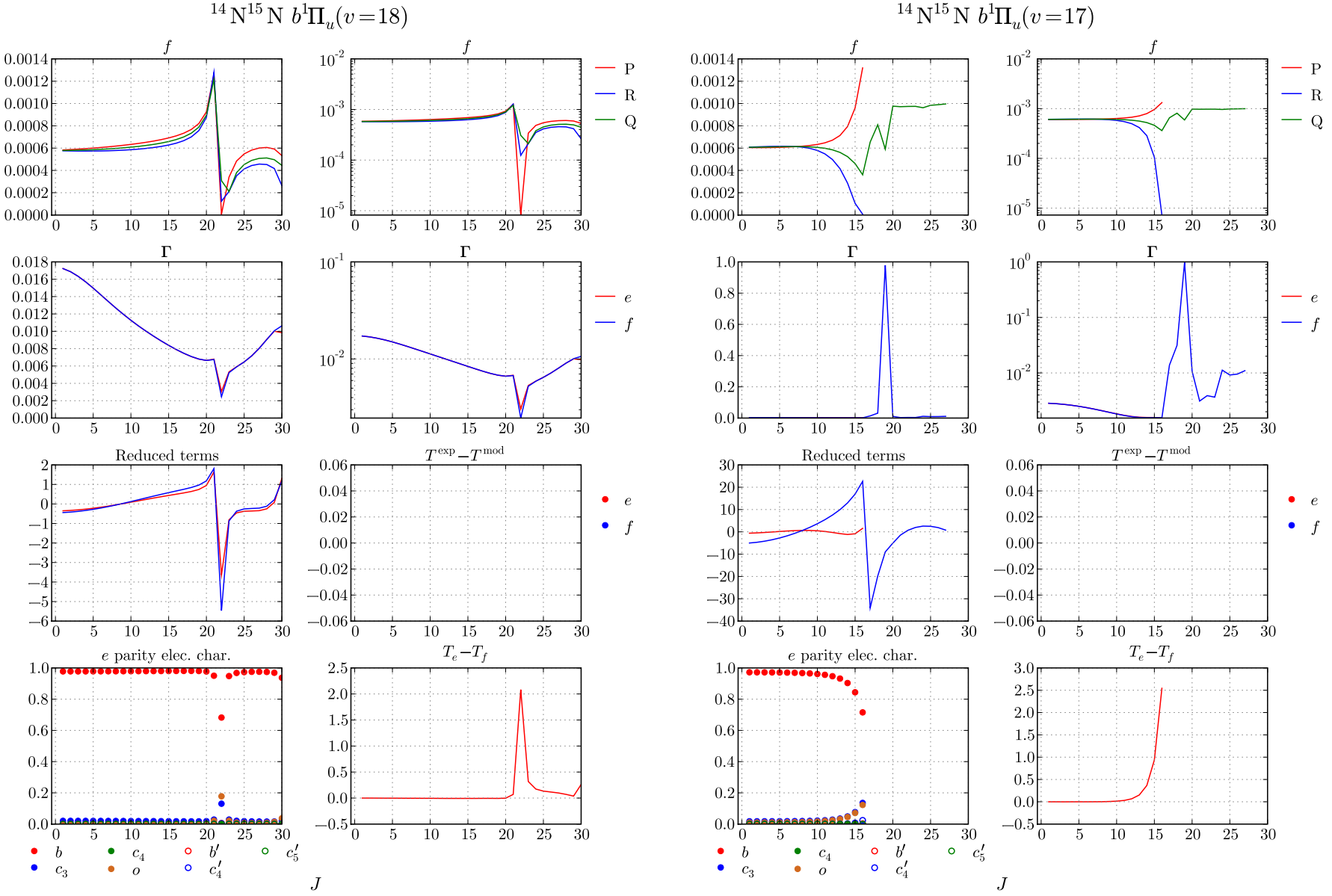
^{14}N^{15}N $b^1\Pi_u(v=18)$
^{14}N^{15}N $b^1\Pi_u(v=17)$
f
Γ
Reduced terms
$T^{\rm exp}-T^{\rm mod}$
T_e-T_f
e parity elec. char.
P
R
Q
e
f
b
c_3
c_4
o
b'
c_4'
c_5'
J

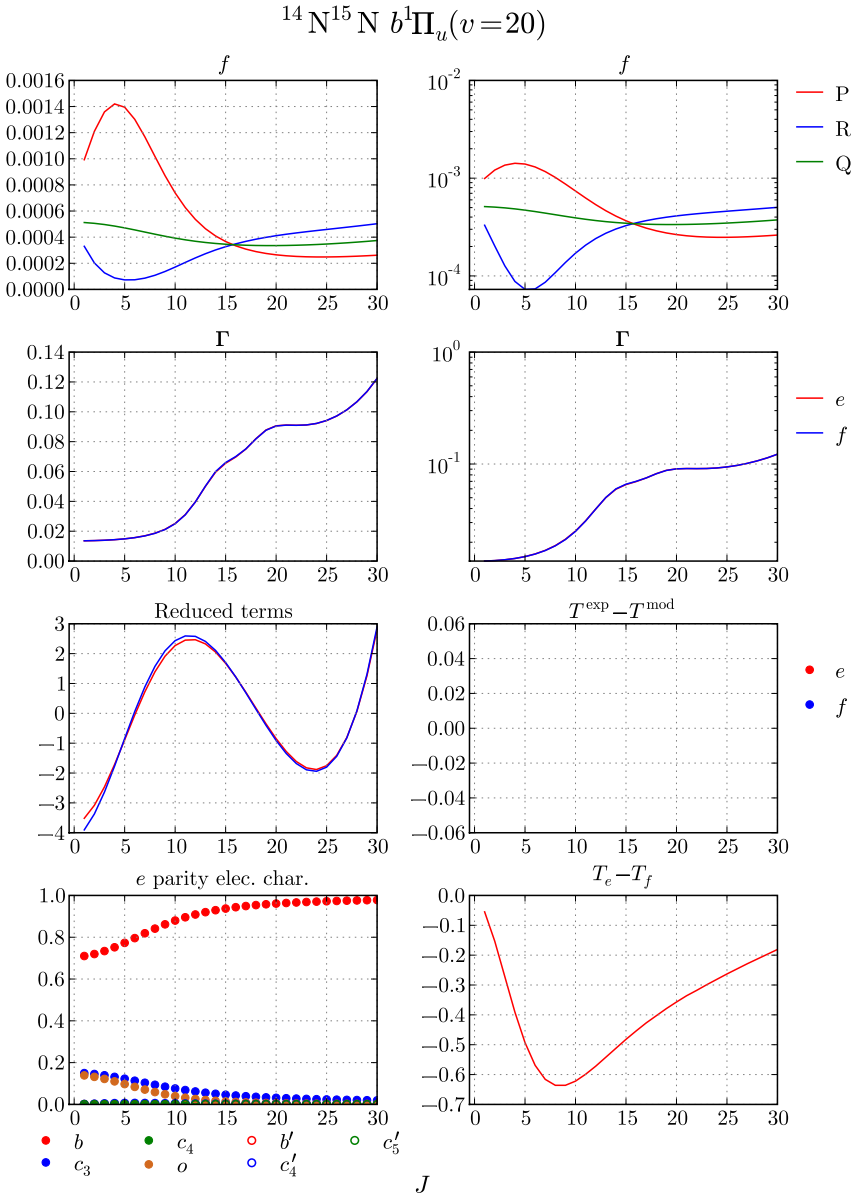
^{14}N^{15}N $b^1\Pi_u(v=20)$
f
f
P
R
Q
Γ
Γ
e
f
Reduced terms
$T^{\rm exp}-T^{\rm mod}$
e
f
e parity elec. char.
T_e-T_f
b
c_3
c_4
o
b'
c_4'
c_5'
J

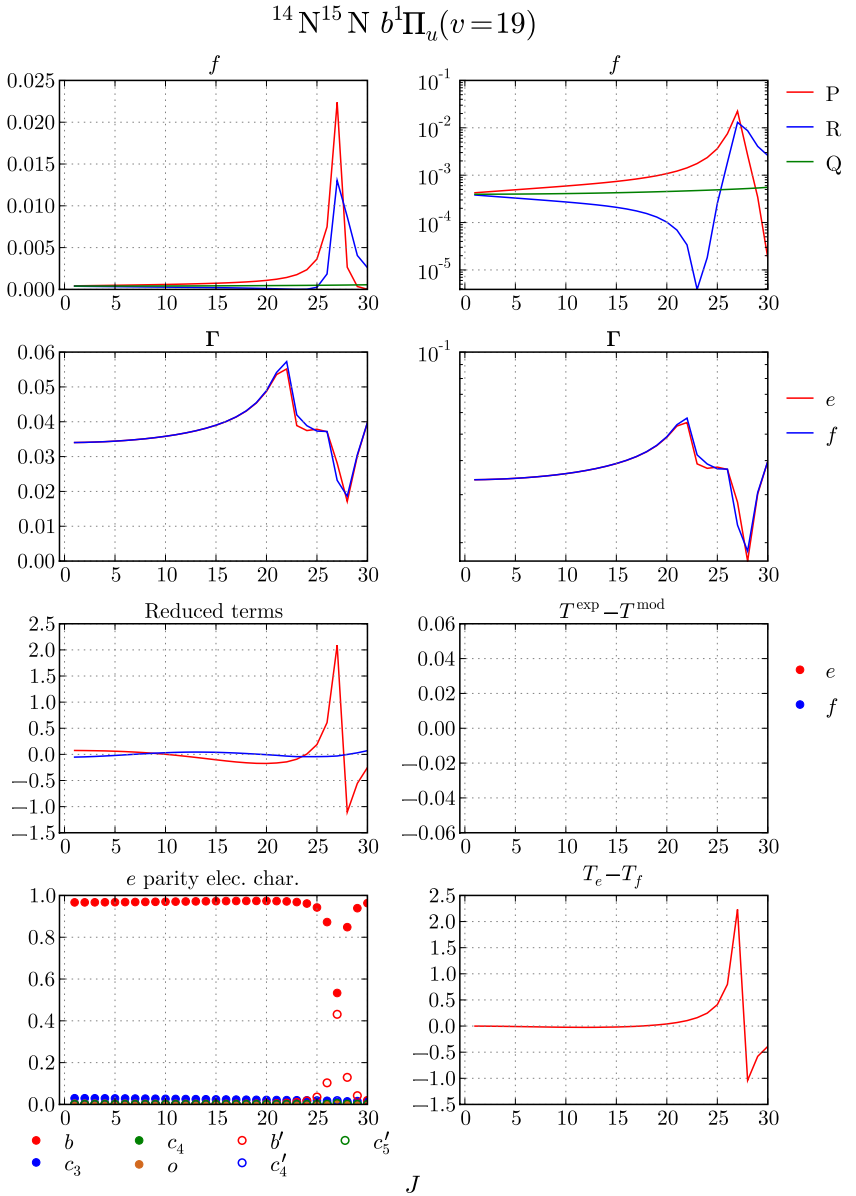
^{14}N^{15}N $b^1\Pi_u(v=19)$
f
f
P
R
Q
Γ
Γ
e
f
Reduced terms
$T^{\rm exp}-T^{\rm mod}$
e
f
e parity elec. char.
T_e-T_f
b
c_3
c_4
o
b'
c_4'
c_5'
J

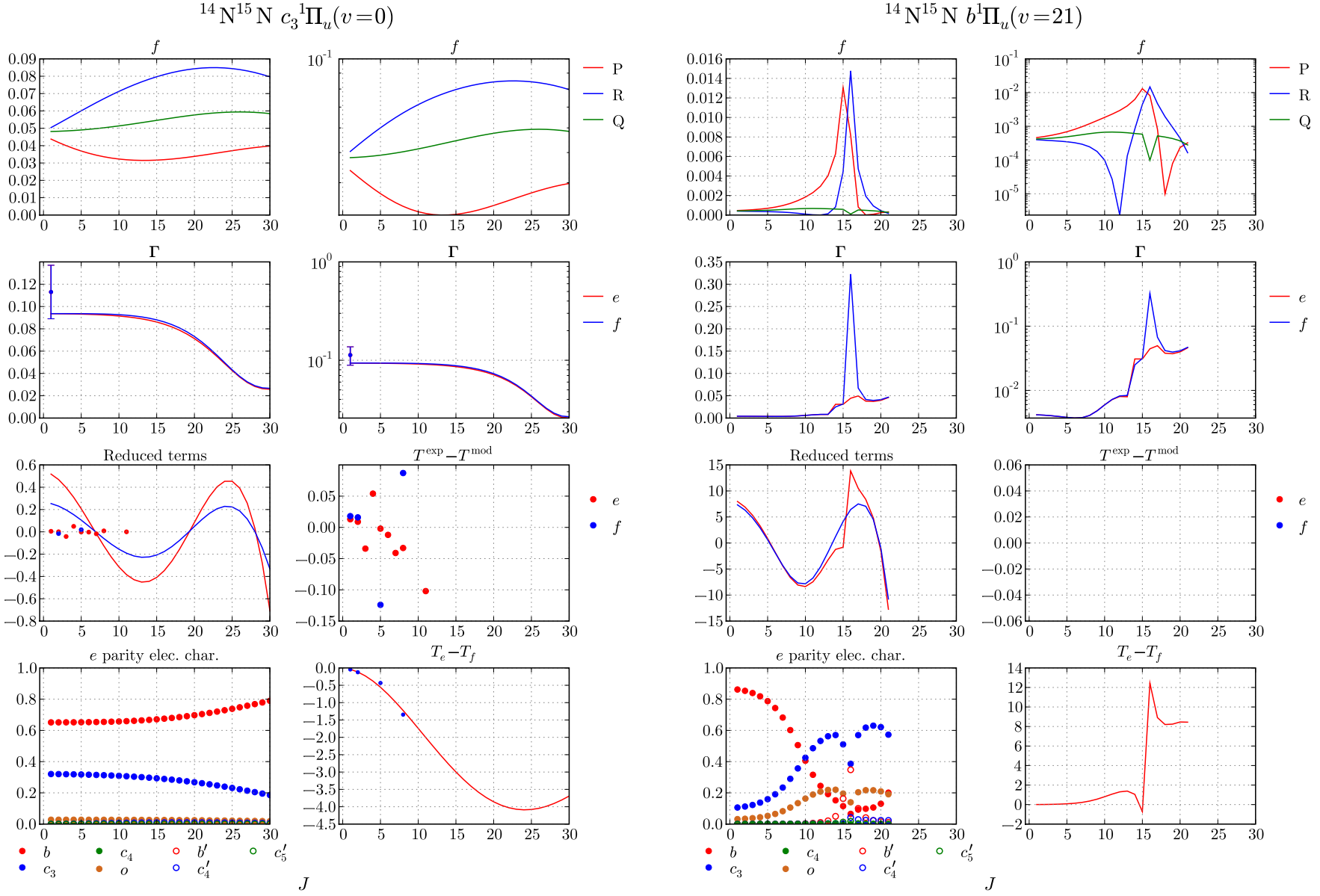
^{14}N^{15}N $c_3{}^1\Pi_u(v=0)$
^{14}N^{15}N $b^1\Pi_u(v=21)$
f
Γ
Reduced terms
$T^{exp}-T^{mod}$
e parity elec. char.
T_e-T_f
P
R
Q
e
f
b
c_3
c_4
o
b'
c_4'
c_5'
J

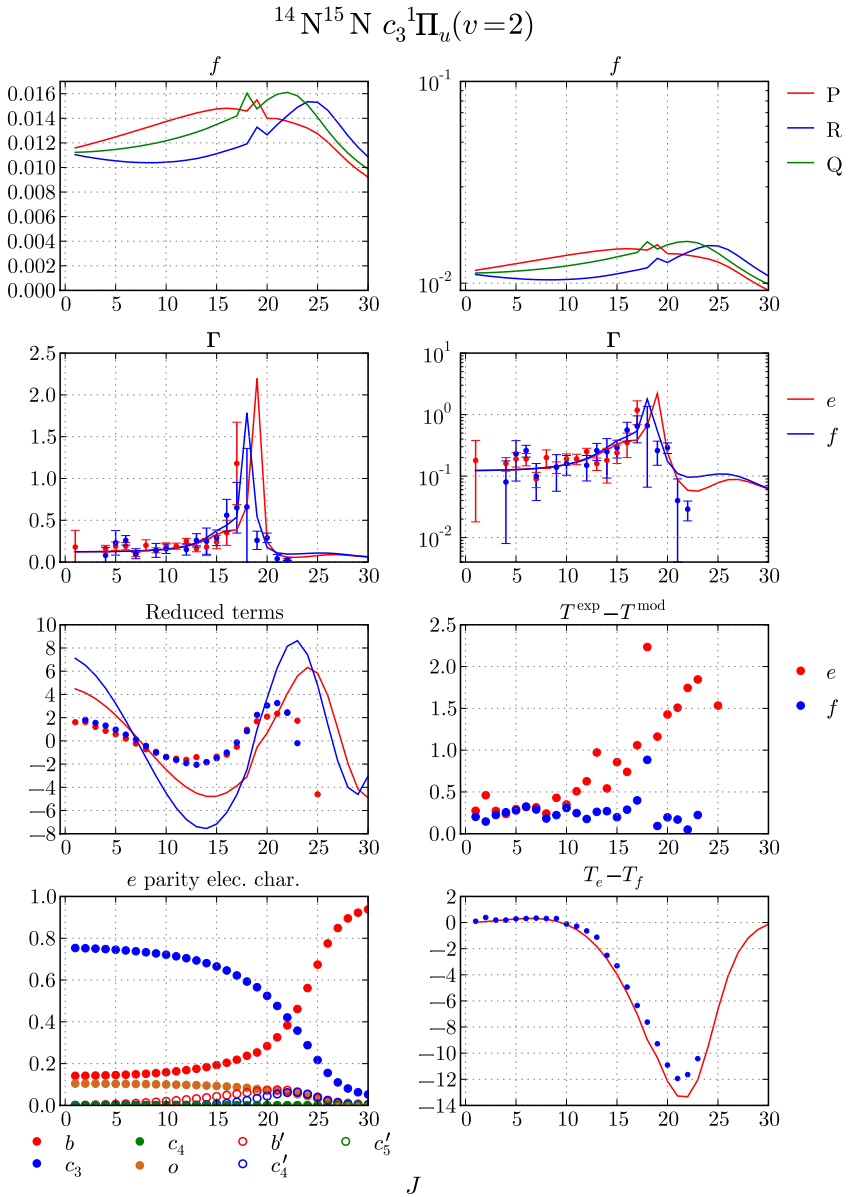
^{14}N^{15}N $c_3\,{}^1\Pi_u(v=2)$
f
Γ
Reduced terms
$T^{\rm exp}-T^{\rm mod}$
e parity elec. char.
T_e-T_f
P
R
Q
e
f
b
c_3
c_4
o
b'
c_4'
c_5'
J

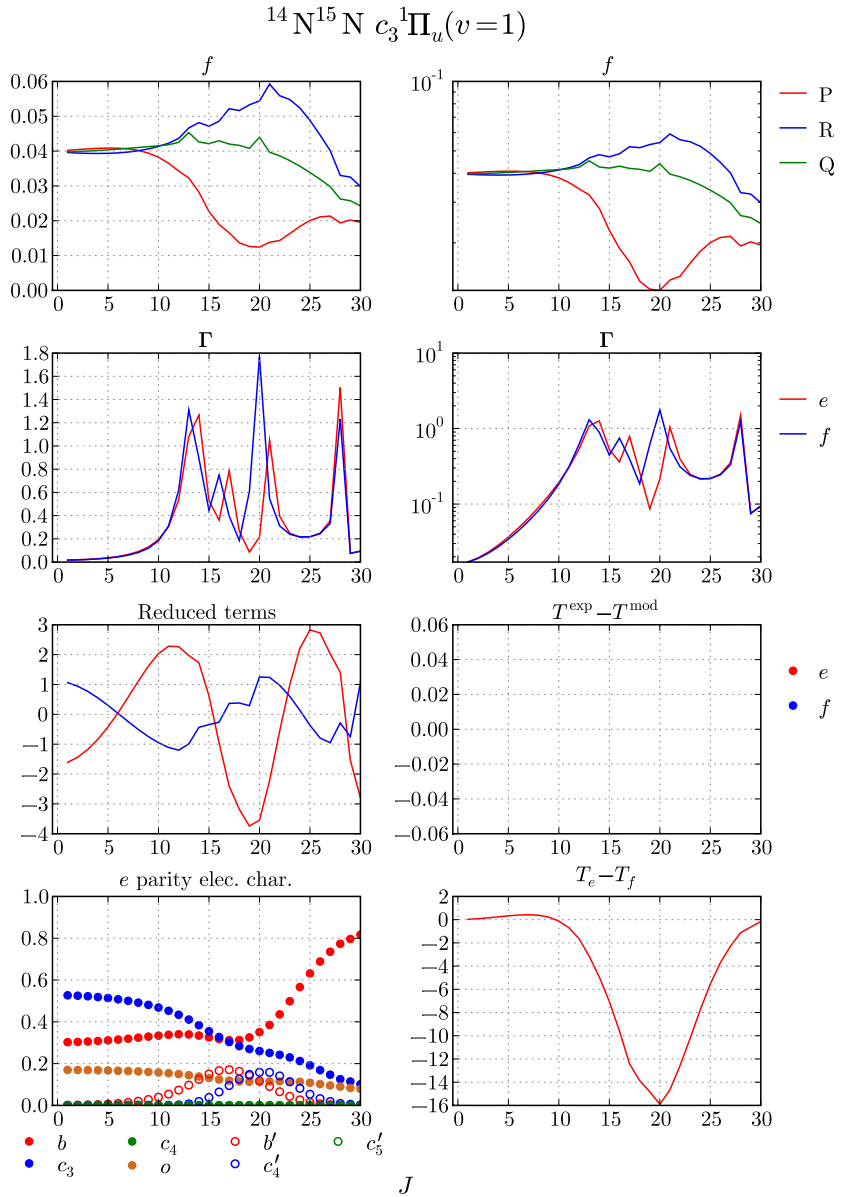
^{14}N^{15}N $c_3\,{}^1\Pi_u(v=1)$
f
Γ
Reduced terms
$T^{\rm exp}-T^{\rm mod}$
e parity elec. char.
T_e-T_f
P
R
Q
e
f
b
c_3
c_4
o
b'
c_4'
c_5'
J

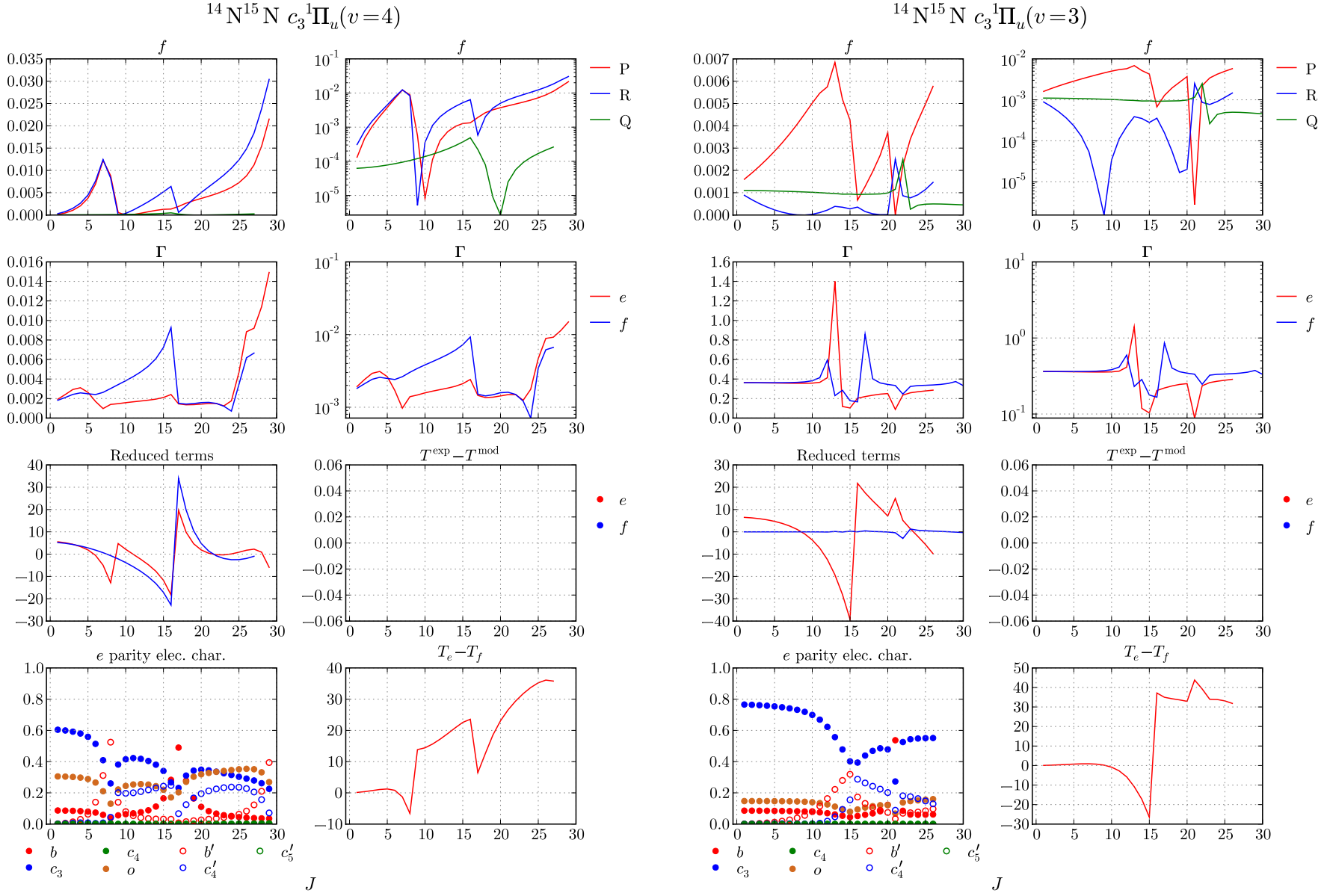
^{14}N^{15}N $c_3{}^1\Pi_u(v=4)$
^{14}N^{15}N $c_3{}^1\Pi_u(v=3)$
f
Γ
Reduced terms
$T^{\rm exp}-T^{\rm mod}$
e parity elec. char.
T_e-T_f
P
R
Q
e
f
b
c_3
c_4
o
b'
c_4'
c_5'
J

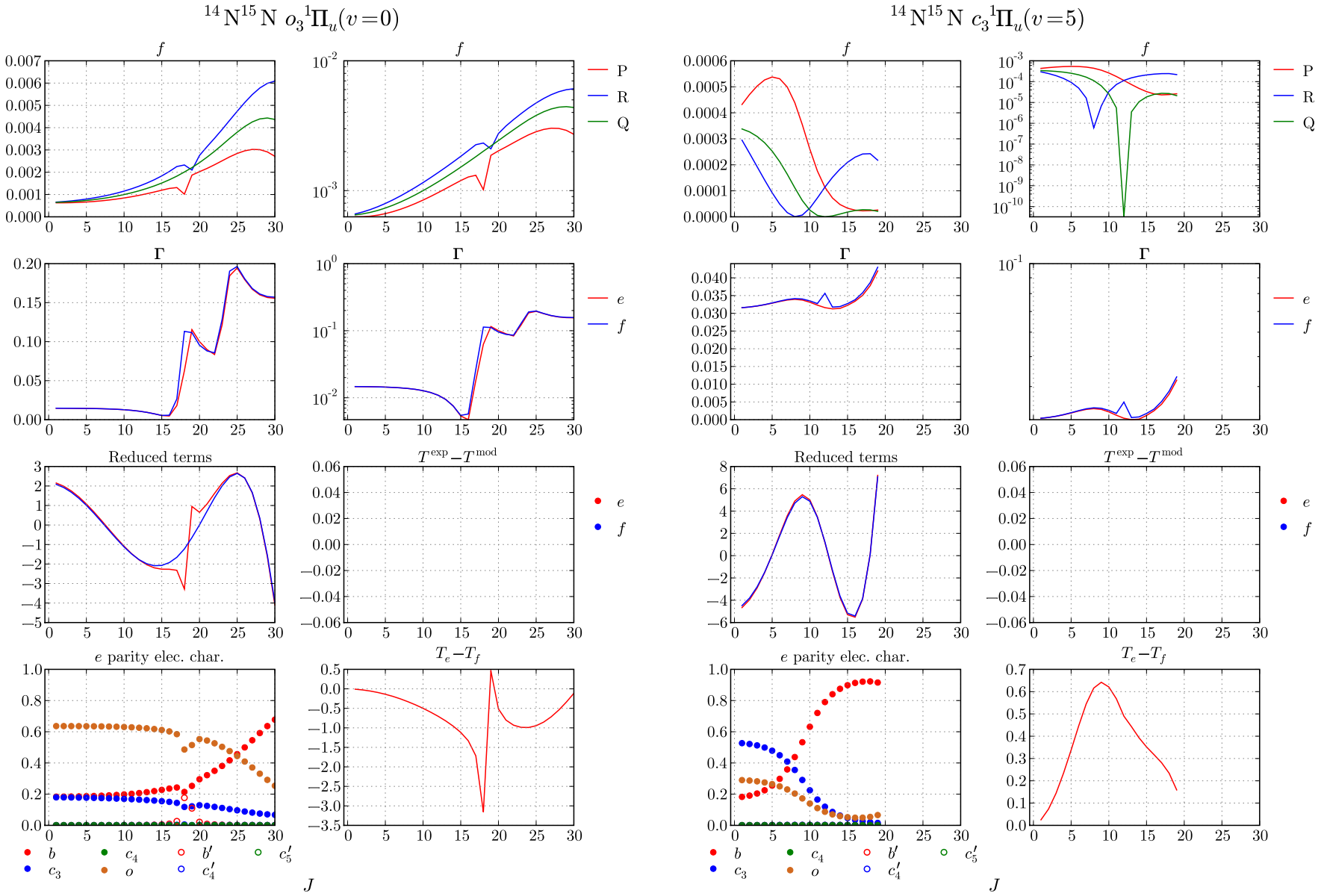
^{14}N^{15}N $o_3\,{}^1\Pi_u(v=0)$
^{14}N^{15}N $c_3\,{}^1\Pi_u(v=5)$
f
Γ
Reduced terms
$T^{\rm exp}-T^{\rm mod}$
e parity elec. char.
T_e-T_f
P
R
Q
e
f
b
c_3
c_4
o
b'
c_4'
c_5'
J

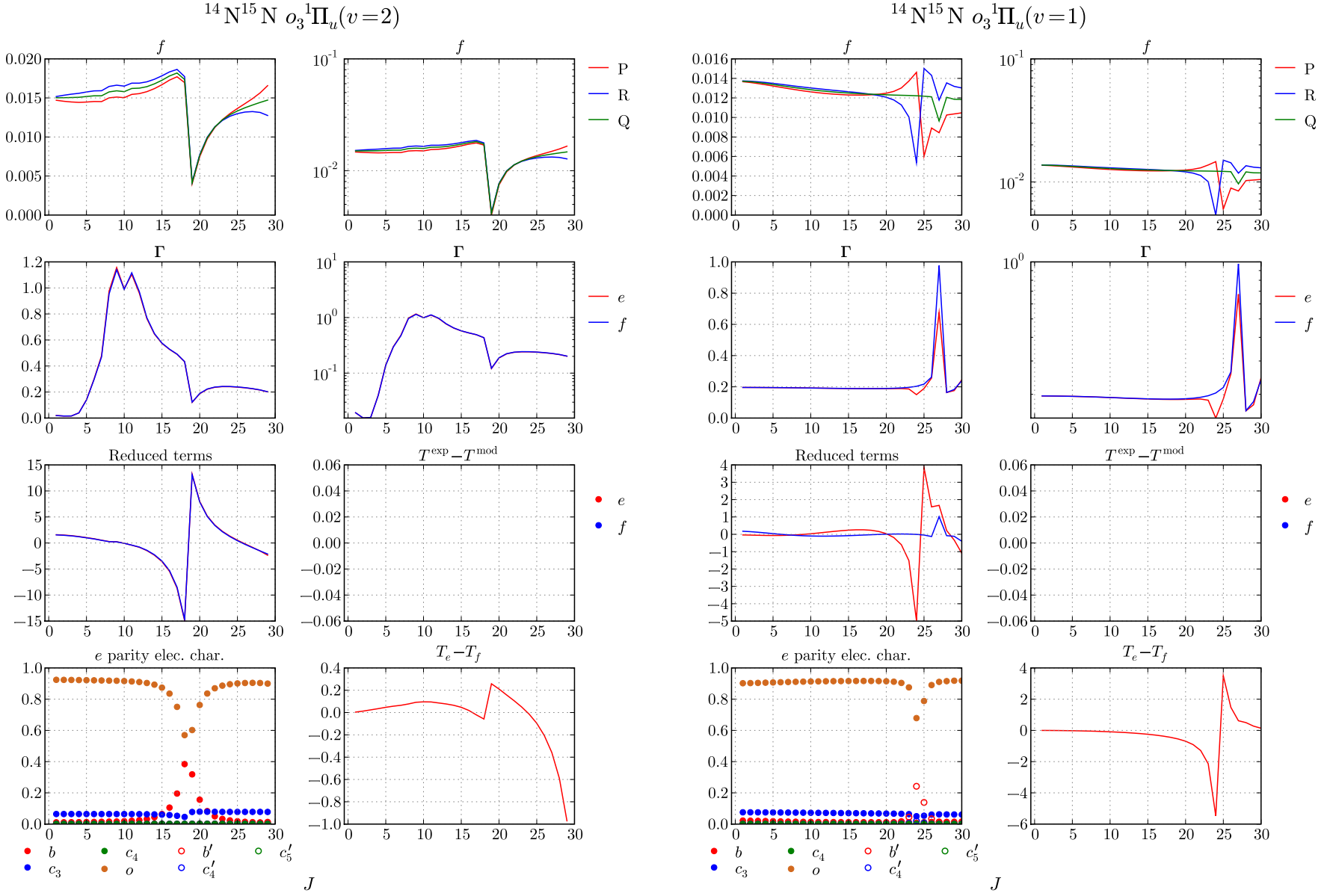
^{14}N^{15}N $o_3\,{}^1\Pi_u(v=2)$
^{14}N^{15}N $o_3\,{}^1\Pi_u(v=1)$
f
Γ
Reduced terms
$T^{\rm exp}-T^{\rm mod}$
e parity elec. char.
T_e-T_f
P
R
Q
e
f
b
c_3
c_4
o
b'
c_4'
c_5'
J

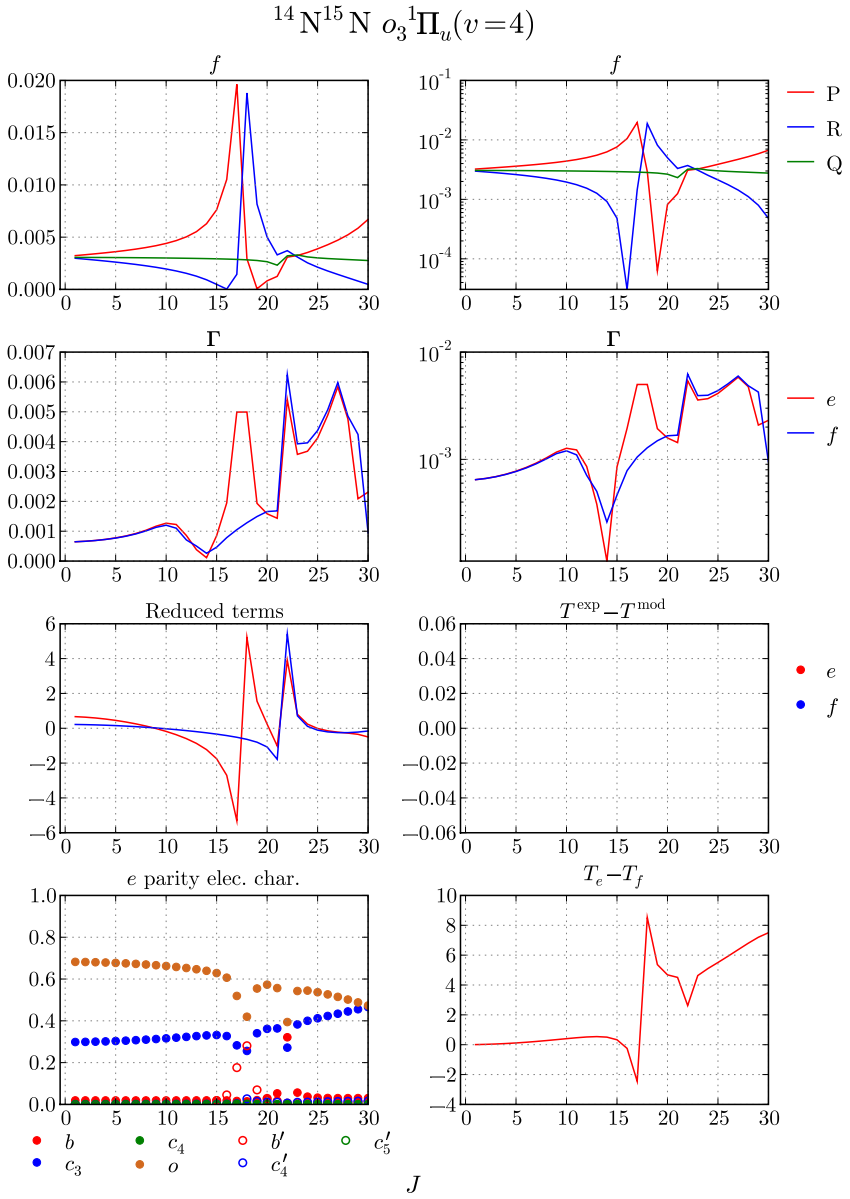
^{14}N^{15}N $o_3\,{}^1\Pi_u(v=4)$
f
Γ
Reduced terms
$T^{\rm exp}-T^{\rm mod}$
e parity elec. char.
T_e-T_f
P
R
Q
e
f
b
c_3
c_4
o
b'
c_4'
c_5'
J

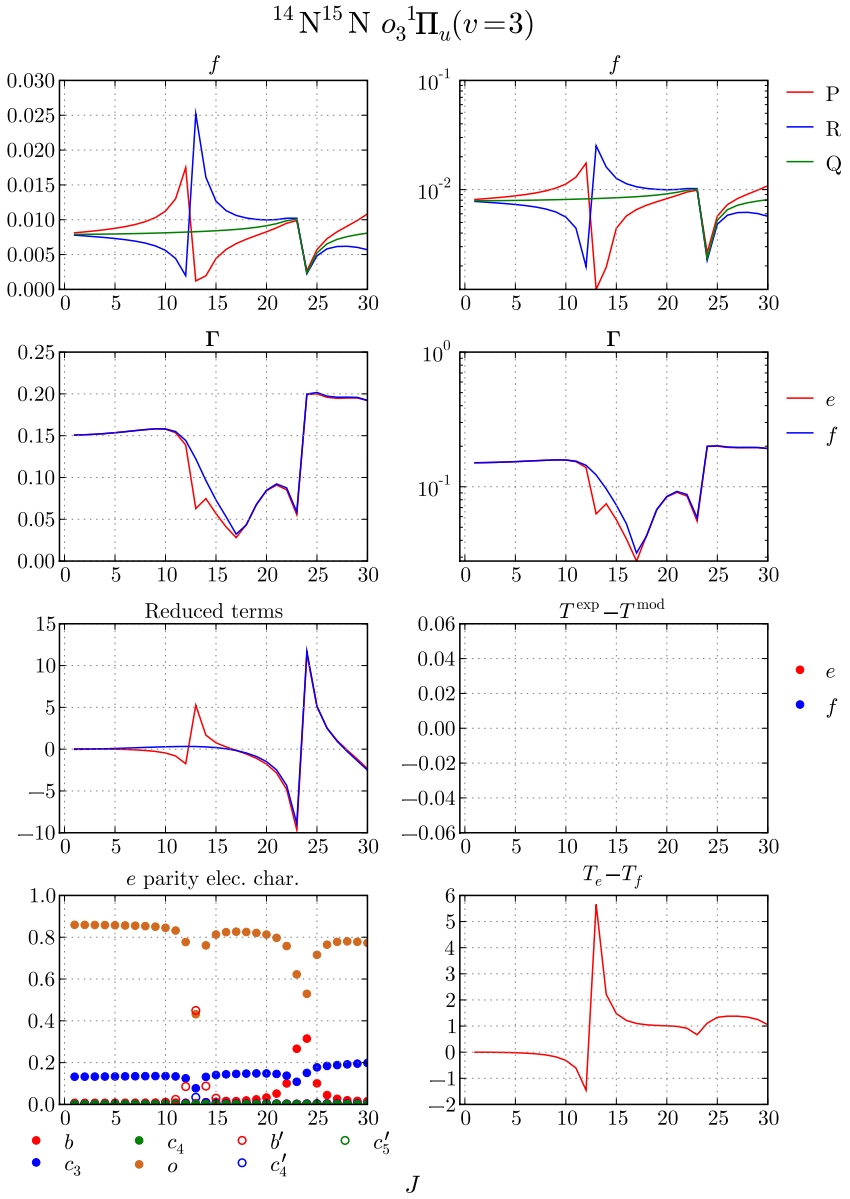
^{14}N^{15}N $o_3\,{}^1\Pi_u(v=3)$
f
Γ
Reduced terms
$T^{\rm exp}-T^{\rm mod}$
e parity elec. char.
T_e-T_f
P
R
Q
e
f
b
c_3
c_4
o
b'
c_4'
c_5'
J

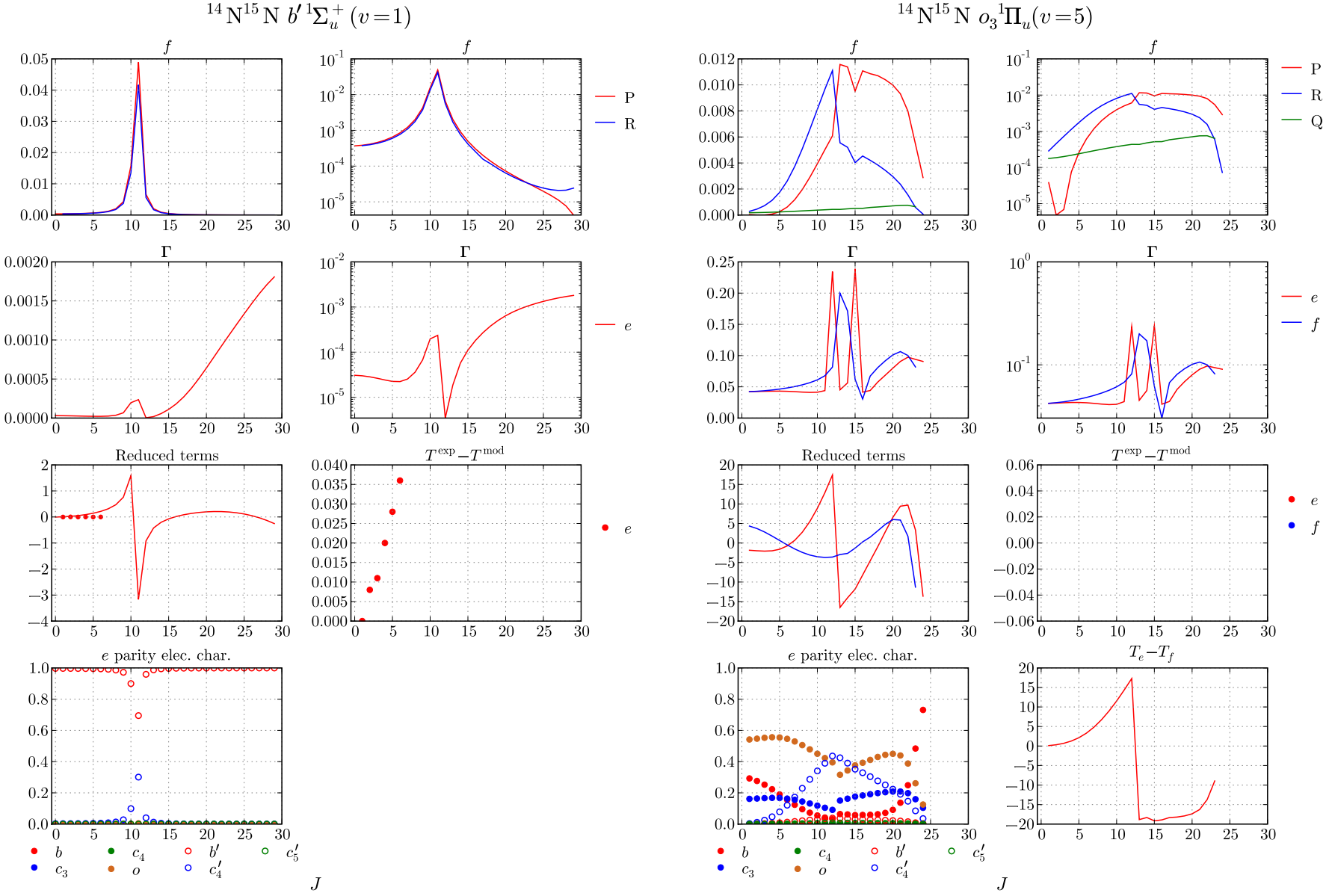
^{14}N^{15}N $b'\,^1\Sigma_u^+$ (v=1)
^{14}N^{15}N $o_3\,^1\Pi_u$(v=5)
f
Γ
Reduced terms
$T^{\rm exp}-T^{\rm mod}$
e parity elec. char.
T_e-T_f
P
R
Q
e
f
b
c_3
c_4
o
b'
c_4'
c_5'
J

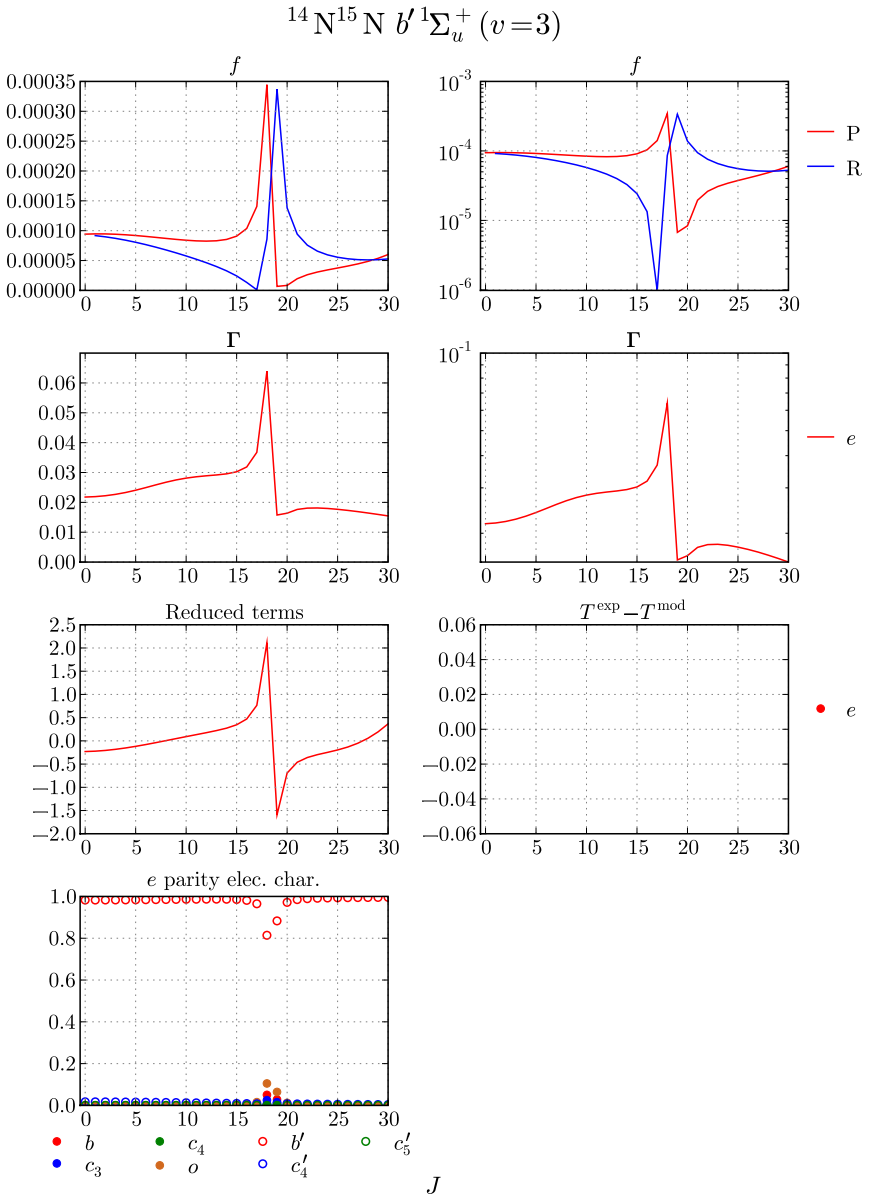
^{14}N^{15}N $b'\,^1\Sigma_u^+$ ($v=3$)
f
f
P
R
Γ
Γ
e
Reduced terms
$T^{\rm exp}-T^{\rm mod}$
e
e parity elec. char.
b
c_3
c_4
o
b'
c_4'
c_5'
J

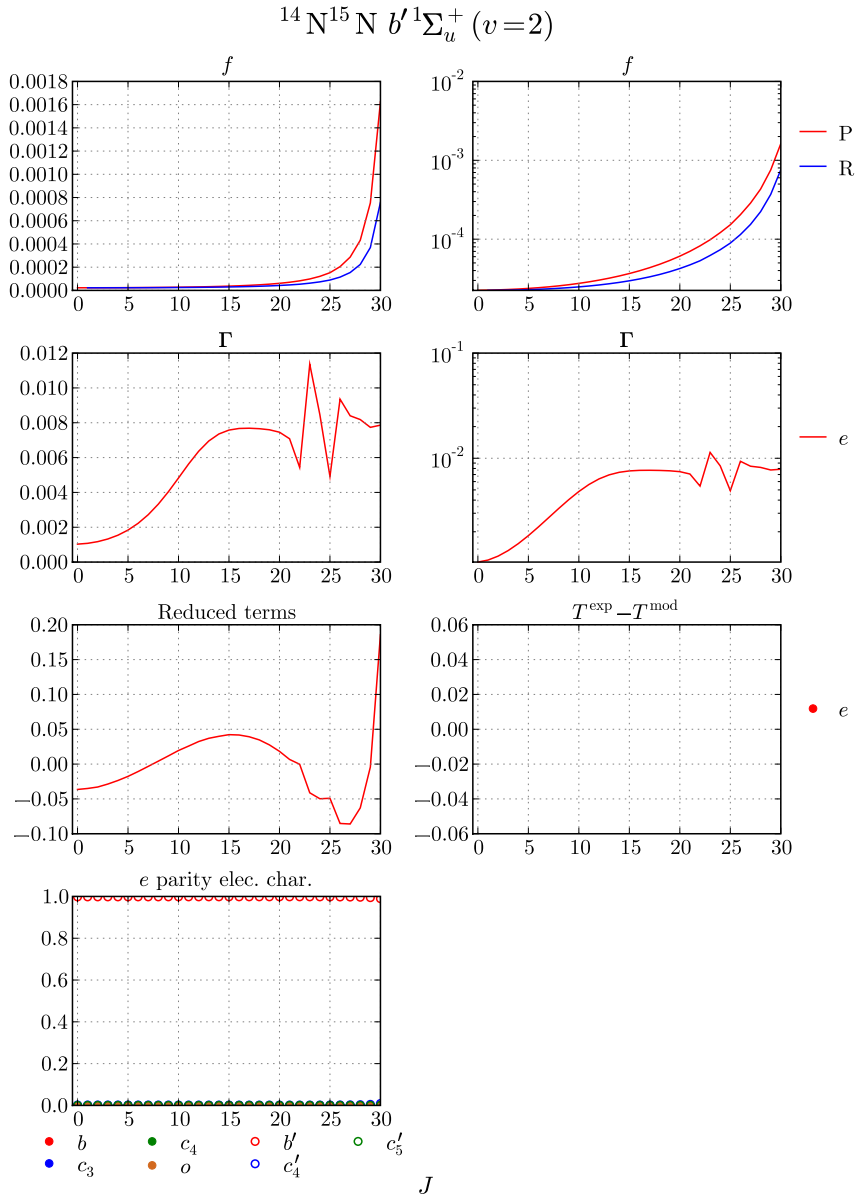
^{14}N^{15}N $b'\,^1\Sigma_u^+$ ($v=2$)
f
f
P
R
Γ
Γ
e
Reduced terms
$T^{\rm exp}-T^{\rm mod}$
e
e parity elec. char.
b
c_3
c_4
o
b'
c_4'
c_5'
J

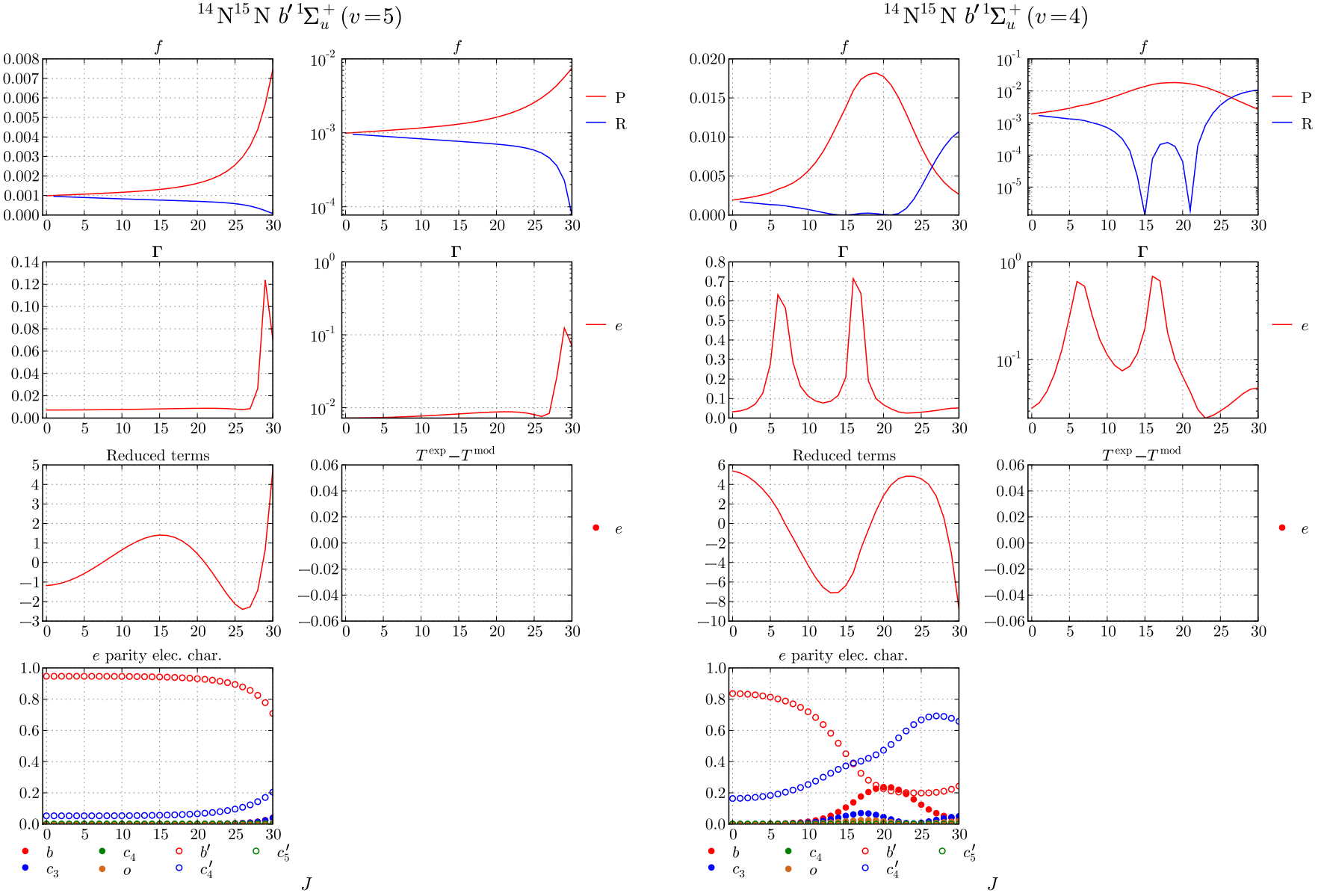
^{14}N^{15}N $b'\,^1\Sigma_u^+$ ($v=5$)
f
Γ
Reduced terms
$T^{\rm exp}-T^{\rm mod}$
e parity elec. char.
P
R
e
b
c_3
c_4
o
b'
c_4'
c_5'
J
^{14}N^{15}N $b'\,^1\Sigma_u^+$ ($v=4$)
f
Γ
Reduced terms
$T^{\rm exp}-T^{\rm mod}$
e parity elec. char.
P
R
e
b
c_3
c_4
o
b'
c_4'
c_5'
J

$^{14}\mathrm{N}^{15}\mathrm{N}\ b'\,^1\Sigma_u^+\ (v=7)$
f
Γ
Reduced terms
$T^{\mathrm{exp}}-T^{\mathrm{mod}}$
e parity elec. char.
P
R
e
b
c_3
c_4
o
b'
c_4'
c_5'
J

$^{14}\mathrm{N}^{15}\mathrm{N}\ b'\,^1\Sigma_u^+\ (v=6)$
f
Γ
Reduced terms
$T^{\mathrm{exp}}-T^{\mathrm{mod}}$
e parity elec. char.
P
R
e
b
c_3
c_4
o
b'
c_4'
c_5'
J

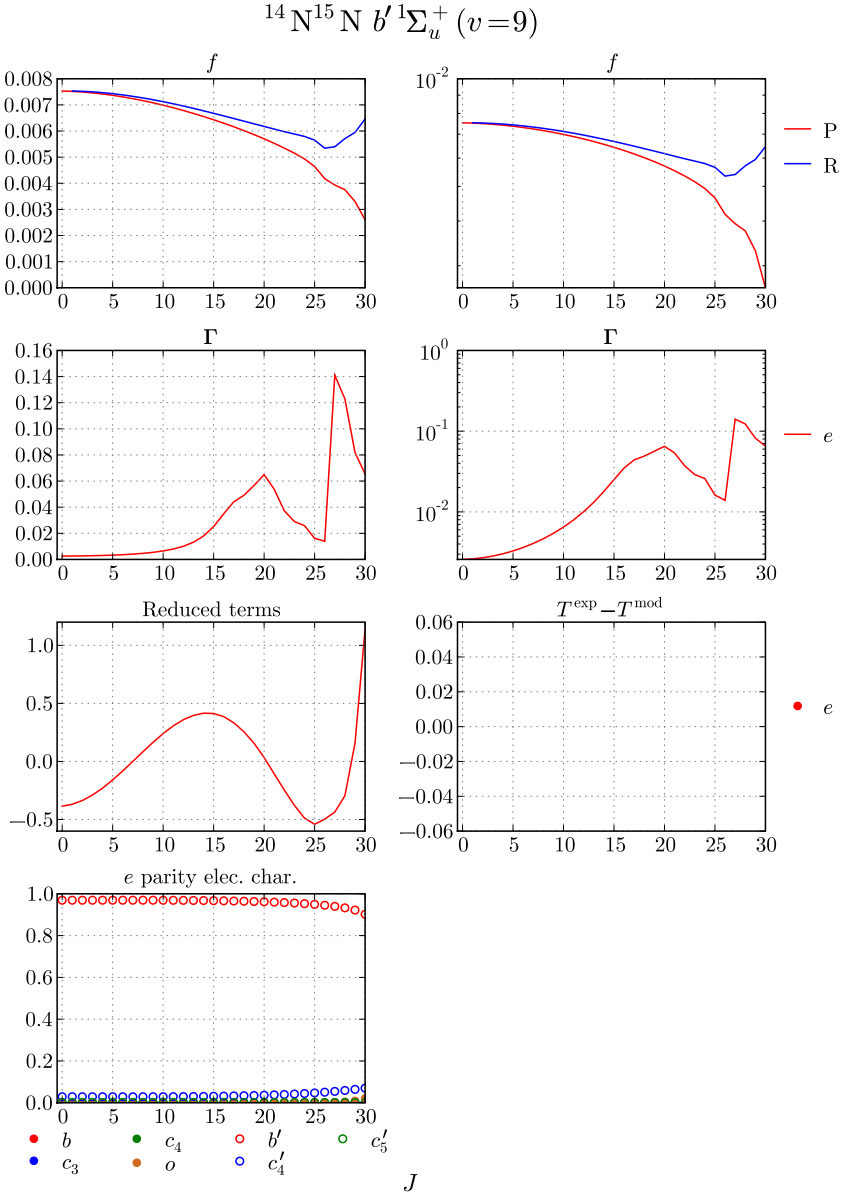
^{14}N^{15}N $b'\,^1\Sigma_u^+$ ($v=9$)
f
Γ
Reduced terms
$T^{\rm exp}-T^{\rm mod}$
e parity elec. char.
P
R
e
b
c_3
c_4
o
b'
c_4'
c_5'
J

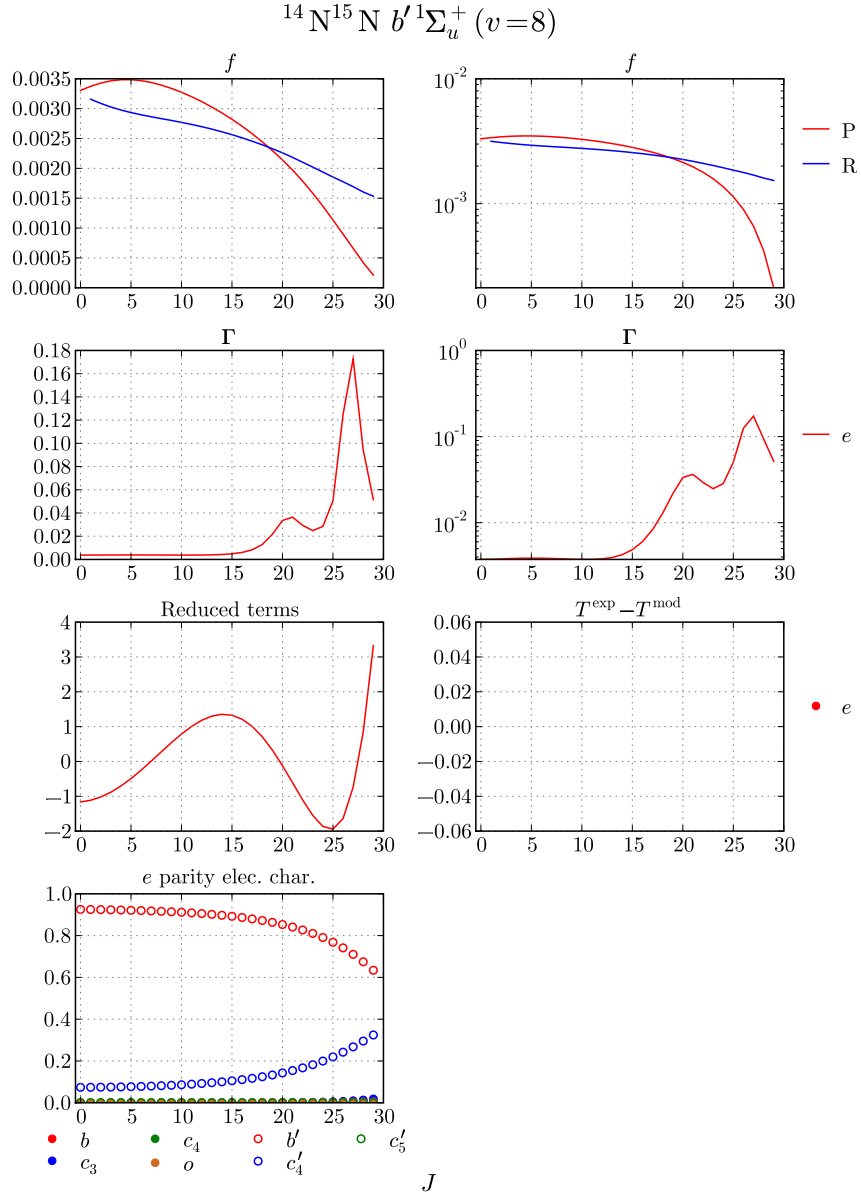
^{14}N^{15}N $b'\,^1\Sigma_u^+$ ($v=8$)
f
Γ
Reduced terms
$T^{\rm exp}-T^{\rm mod}$
e parity elec. char.
P
R
e
b
c_3
c_4
o
b'
c_4'
c_5'
J

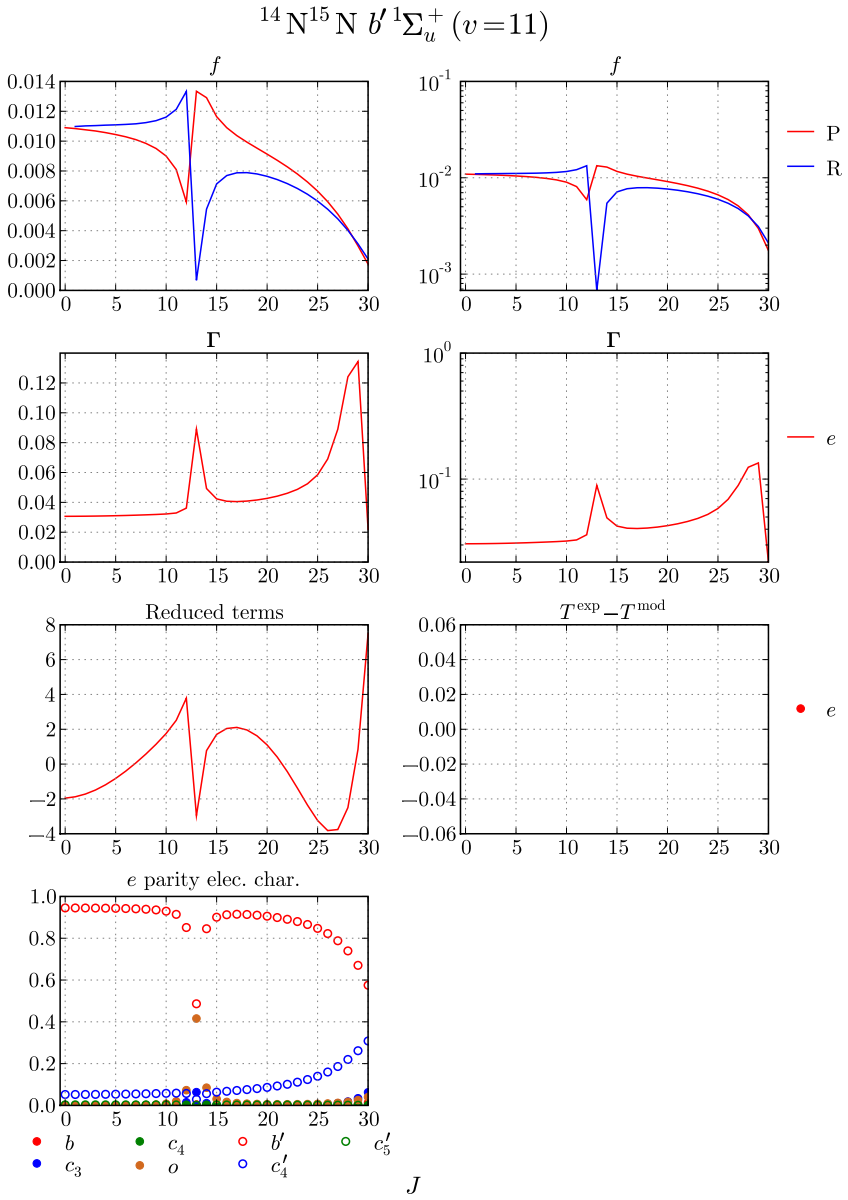
^{14}N^{15}N $b'\,^1\Sigma_u^+$ ($v=11$)
f
Γ
Reduced terms
$T^{\rm exp}-T^{\rm mod}$
e parity elec. char.
P
R
e
b
c_3
c_4
o
b'
c_4'
c_5'
J

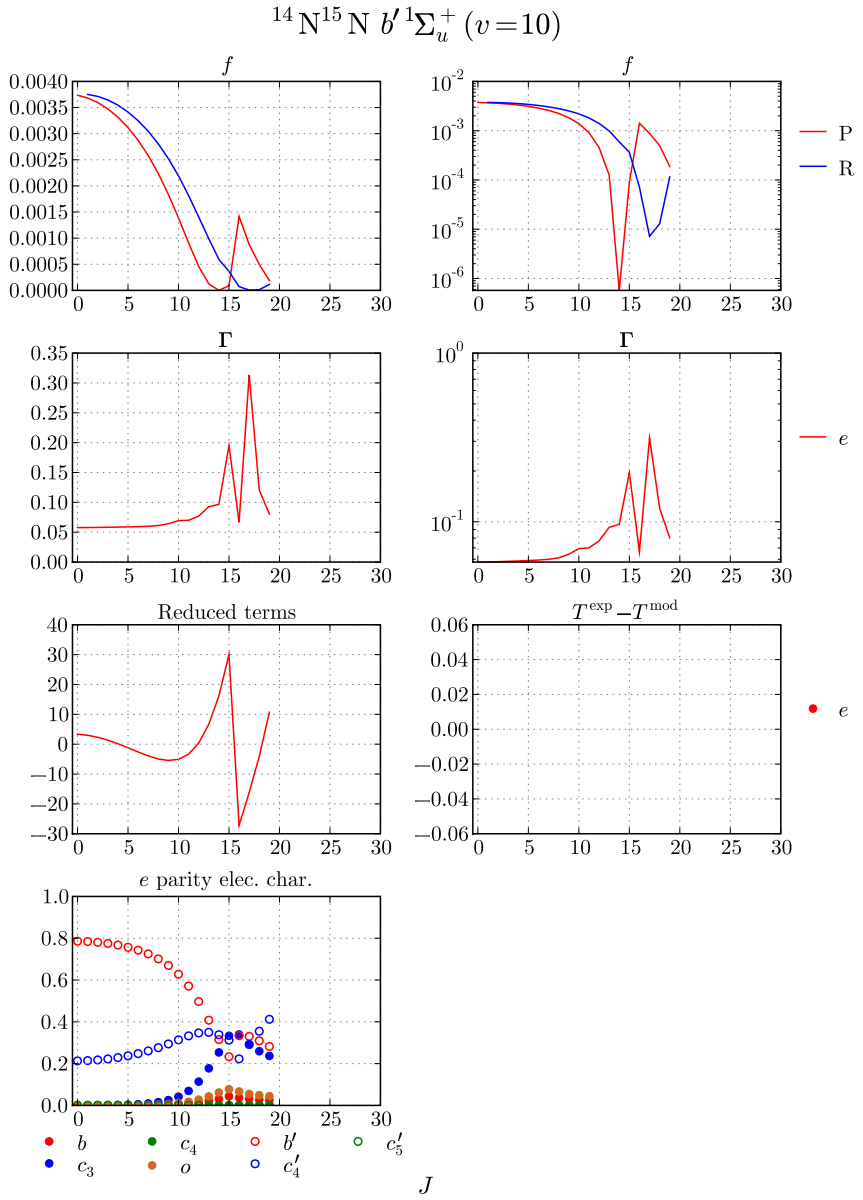
^{14}N^{15}N $b'\,^1\Sigma_u^+$ ($v=10$)
f
Γ
Reduced terms
$T^{\rm exp}-T^{\rm mod}$
e parity elec. char.
P
R
e
b
c_3
c_4
o
b'
c_4'
c_5'
J

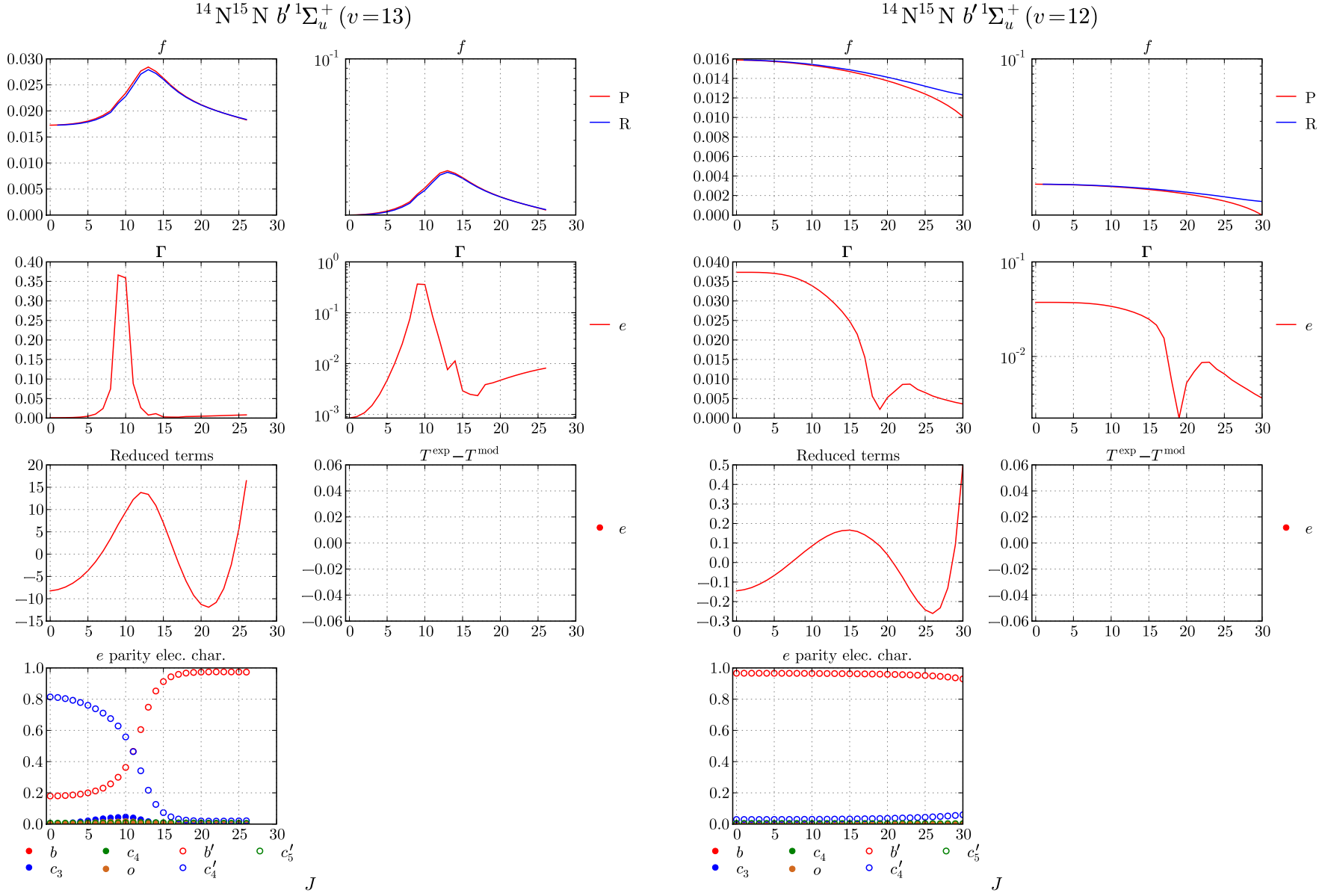
^{14}N^{15}N $b'\,^1\Sigma_u^+$ ($v=13$)
^{14}N^{15}N $b'\,^1\Sigma_u^+$ ($v=12$)
f
Γ
Reduced terms
$T^{\rm exp}-T^{\rm mod}$
e parity elec. char.
P
R
e
b
c_3
c_4
o
b'
c_4'
c_5'
J

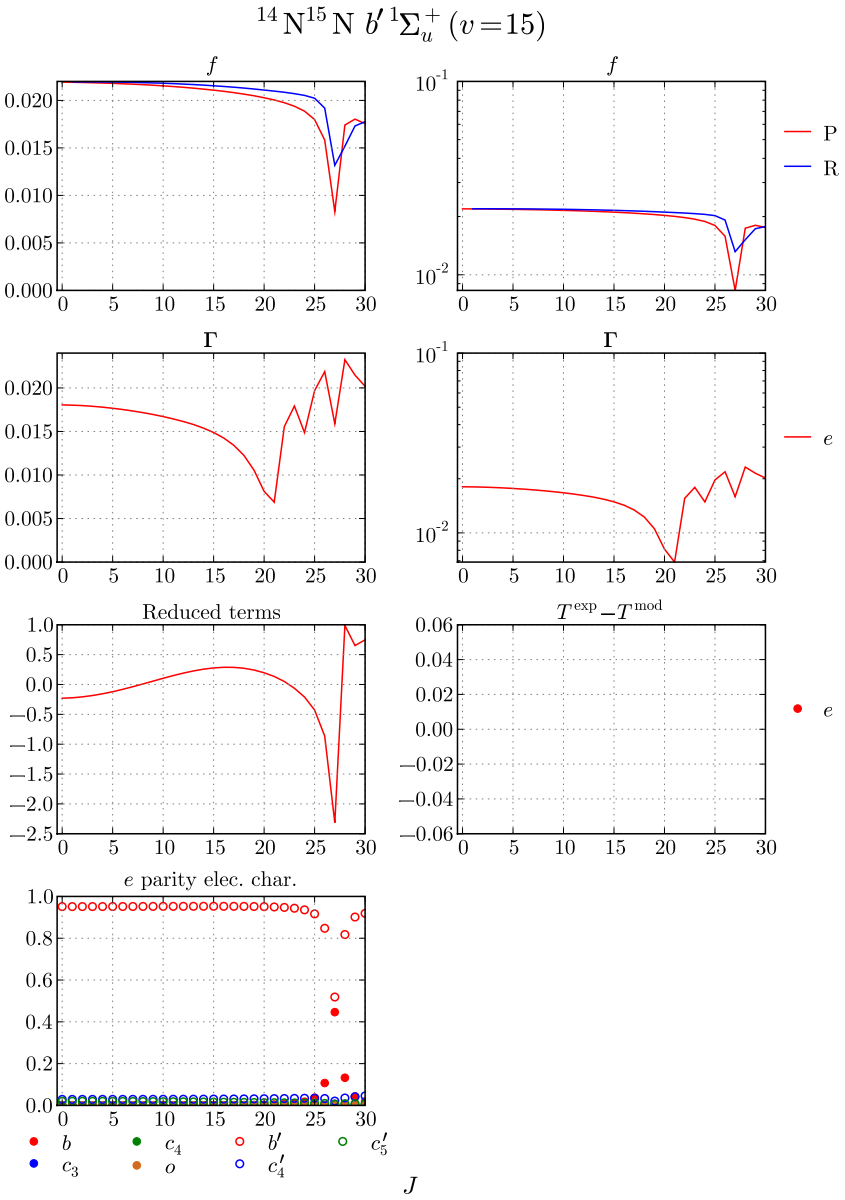
^{14}N^{15}N $b'\,^1\Sigma_u^+$ ($v=15$)
f
f
P
R
Γ
Γ
e
Reduced terms
$T^{\rm exp}-T^{\rm mod}$
e
e parity elec. char.
b
c_3
c_4
o
b'
c_4'
c_5'
J

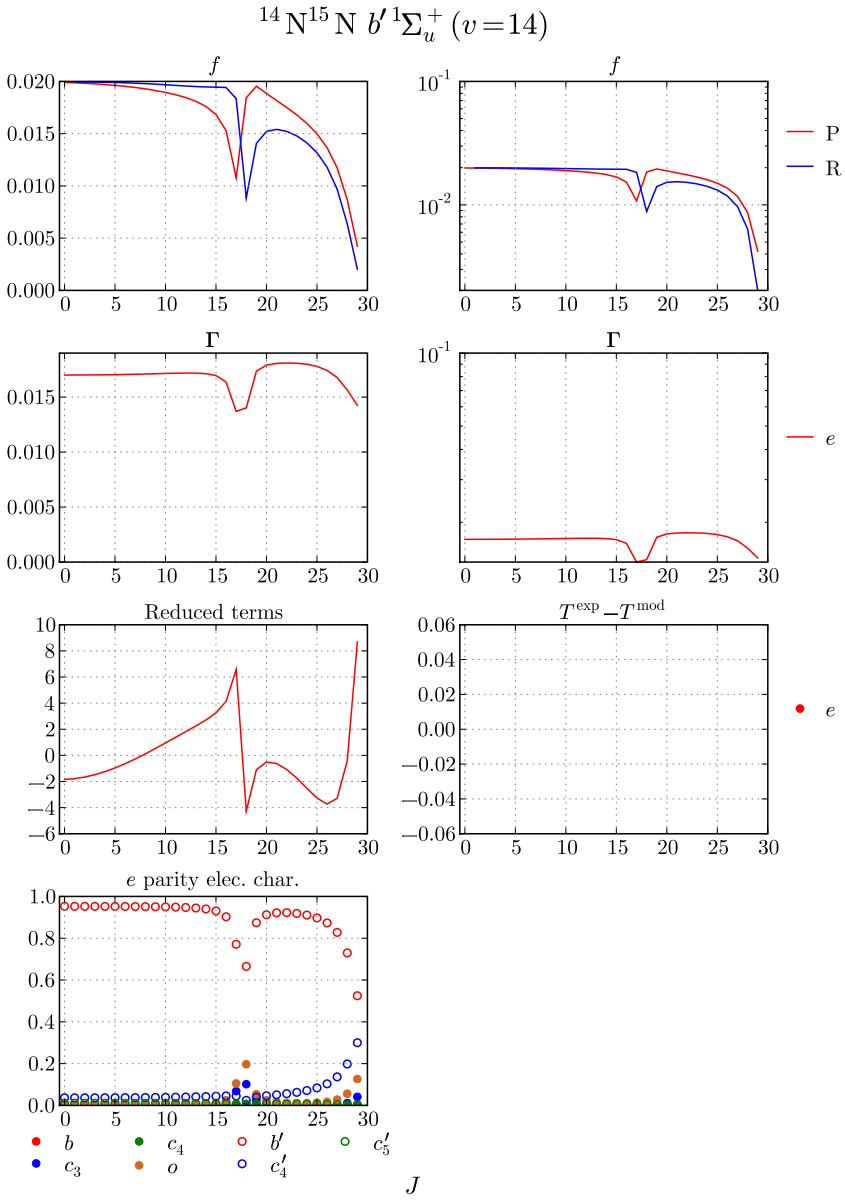
^{14}N^{15}N $b'\,^1\Sigma_u^+$ ($v=14$)
f
f
P
R
Γ
Γ
e
Reduced terms
$T^{\rm exp}-T^{\rm mod}$
e
e parity elec. char.
b
c_3
c_4
o
b'
c_4'
c_5'
J

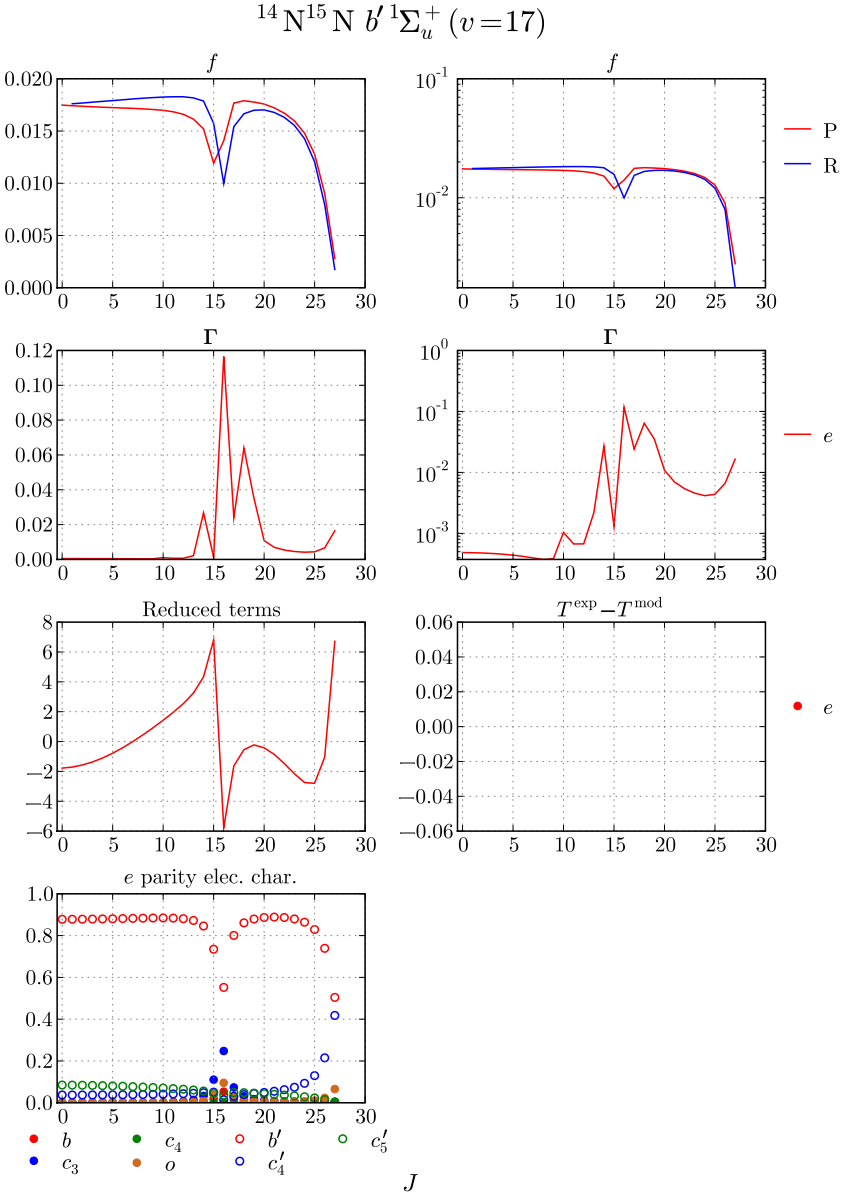
^{14}N^{15}N $b'\,^1\Sigma_u^+$ ($v=17$)
f
f
P
R
Γ
Γ
e
Reduced terms
$T^{\rm exp}-T^{\rm mod}$
e
e parity elec. char.
b
c_4
b'
c_5'
c_3
o
c_4'
J

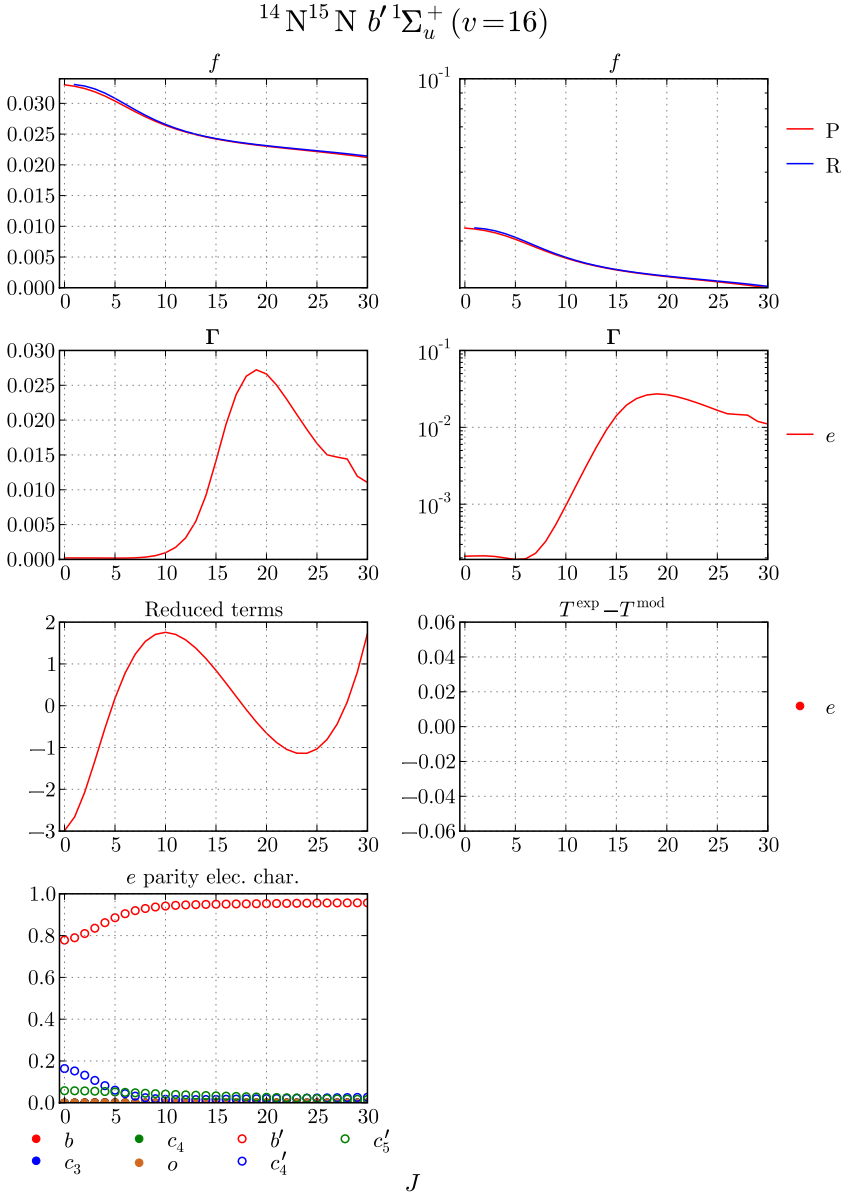
^{14}N^{15}N $b'\,^1\Sigma_u^+$ ($v=16$)
f
f
P
R
Γ
Γ
e
Reduced terms
$T^{\rm exp}-T^{\rm mod}$
e
e parity elec. char.
b
c_4
b'
c_5'
c_3
o
c_4'
J

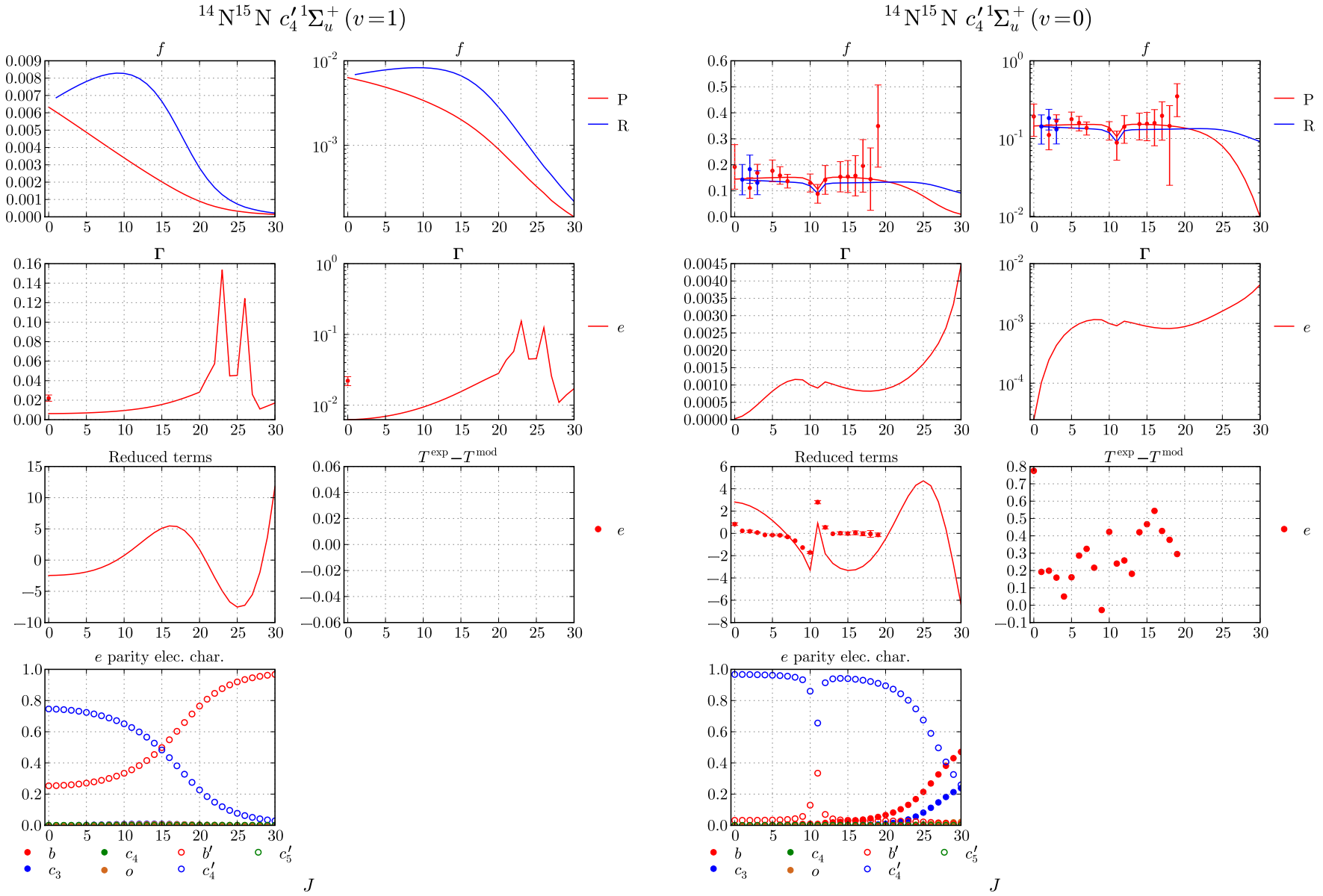
^{14}N^{15}N $c_4'\,^1\Sigma_u^+$ ($v=1$)
^{14}N^{15}N $c_4'\,^1\Sigma_u^+$ ($v=0$)
f
Γ
Reduced terms
$T^{\rm exp}-T^{\rm mod}$
e parity elec. char.
P
R
e
b
c_3
c_4
o
b'
c_4'
c_5'
J

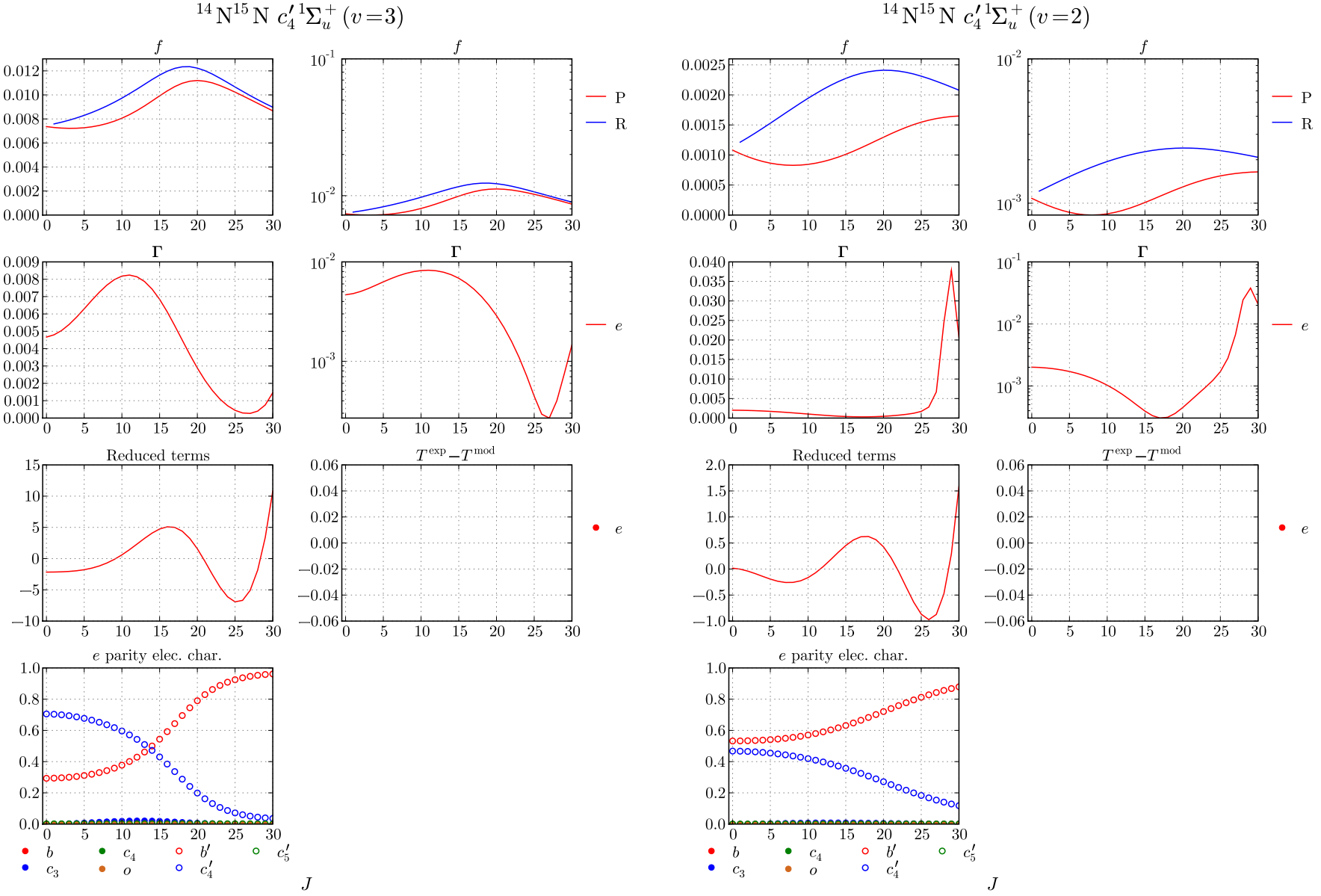
^{14}N^{15}N $c_4'\,^1\Sigma_u^+$ $(v=3)$
f
Γ
Reduced terms
$T^{\rm exp}-T^{\rm mod}$
e parity elec. char.
P
R
e
b
c_3
c_4
o
b'
c_4'
c_5'
J
^{14}N^{15}N $c_4'\,^1\Sigma_u^+$ $(v=2)$
f
Γ
Reduced terms
$T^{\rm exp}-T^{\rm mod}$
e parity elec. char.
P
R
e
b
c_3
c_4
o
b'
c_4'
c_5'
J

$^{14}\mathrm{N}^{15}\mathrm{N}\ c_4'\,^1\Sigma_u^+\ (v=5)$
f
Γ
Reduced terms
$T^{\mathrm{exp}}-T^{\mathrm{mod}}$
e parity elec. char.
P
R
e
b
c_3
c_4
o
b'
c_4'
c_5'
J

$^{14}\mathrm{N}^{15}\mathrm{N}\ c_4'\,^1\Sigma_u^+\ (v=4)$
f
Γ
Reduced terms
$T^{\mathrm{exp}}-T^{\mathrm{mod}}$
e parity elec. char.
P
R
e
b
c_3
c_4
o
b'
c_4'
c_5'
J

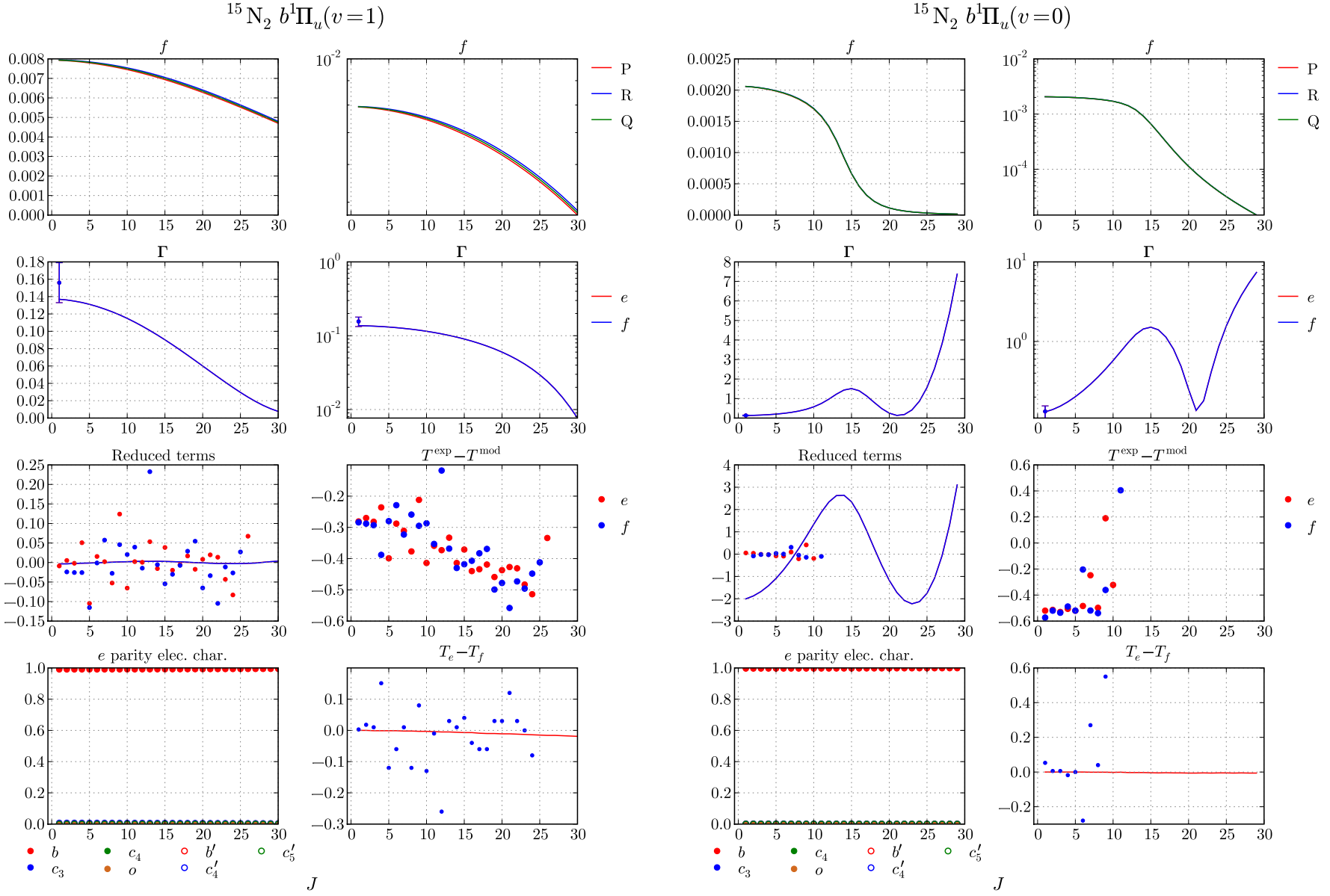
$^{15}N_2$ $b^1\Pi_u(v=1)$
$^{15}N_2$ $b^1\Pi_u(v=0)$
f
Γ
Reduced terms
$T^{exp}-T^{mod}$
e parity elec. char.
T_e-T_f
P
R
Q
e
f
b
c_3
c_4
o
b'
c_4'
c_5'
J

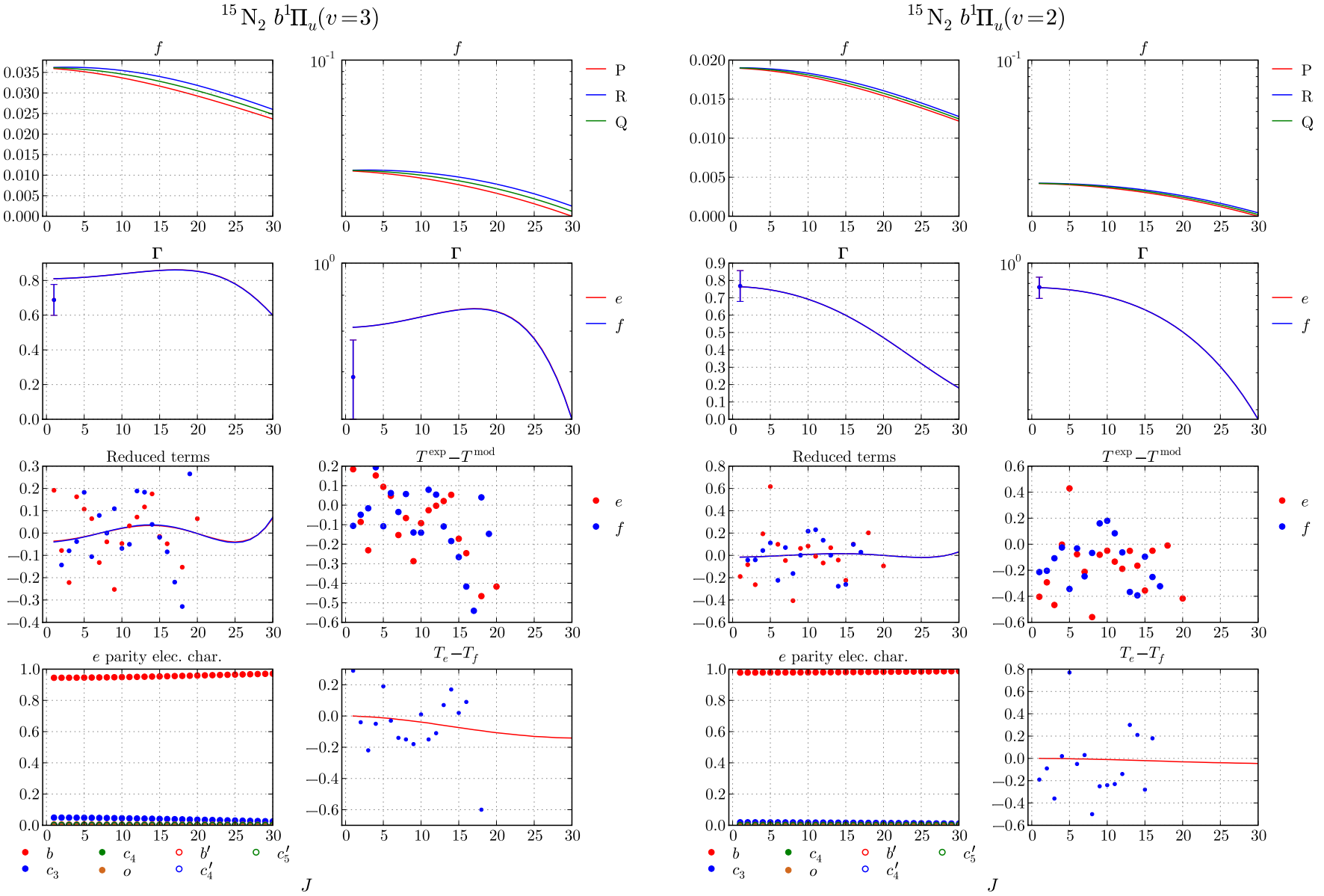
$^{15}N_2$ $b^1\Pi_u(v=3)$
$^{15}N_2$ $b^1\Pi_u(v=2)$
f
Γ
Reduced terms
$T^{exp}-T^{mod}$
e parity elec. char.
T_e-T_f
P
R
Q
e
f
b
c_3
c_4
o
b'
c_4'
c_5'
J

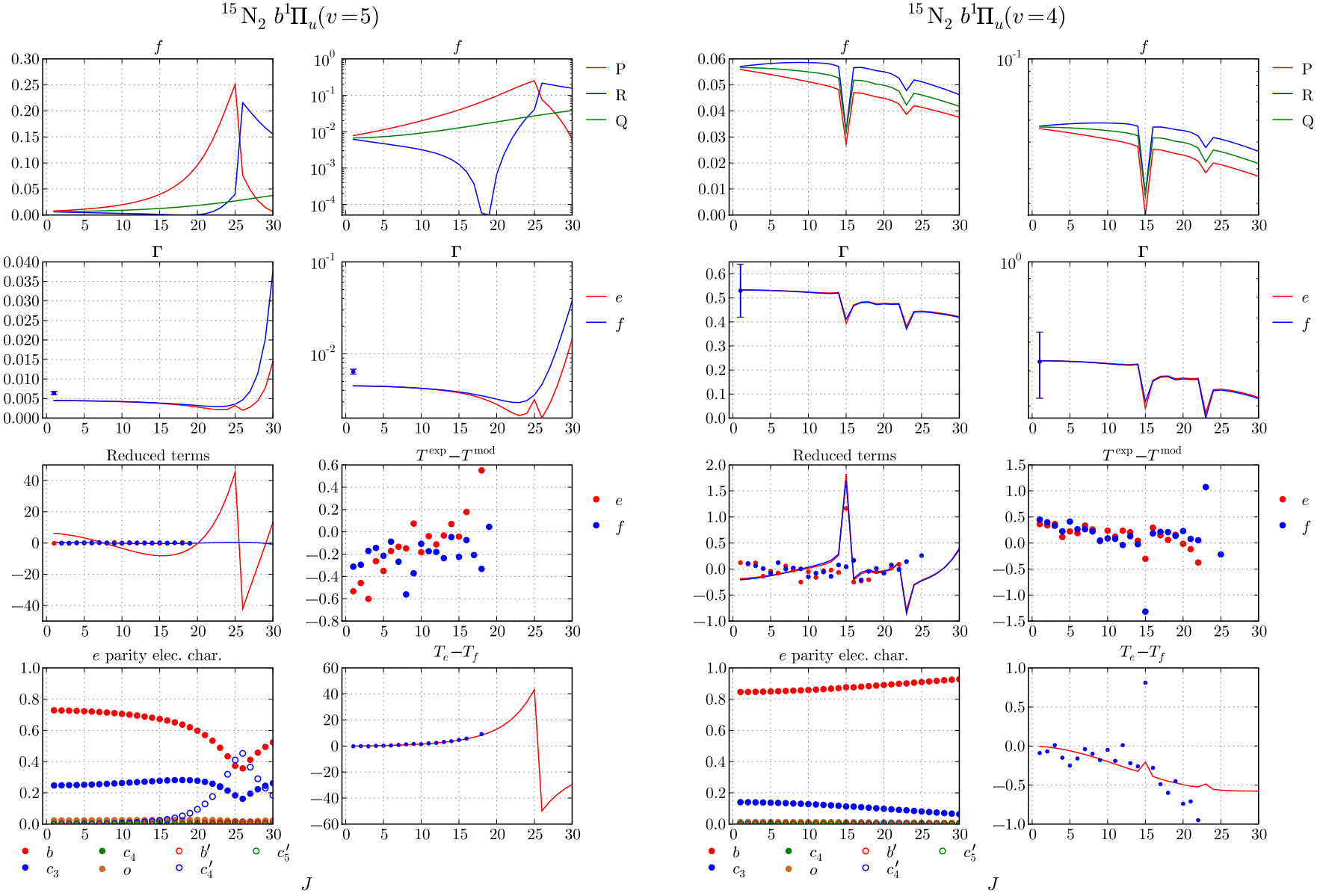
$^{15}N_2$ $b^1\Pi_u(v=5)$
$^{15}N_2$ $b^1\Pi_u(v=4)$
f
Γ
Reduced terms
$T^{exp}-T^{mod}$
e parity elec. char.
T_e-T_f
P
R
Q
e
f
b
c_3
c_4
o
b'
c_4'
c_5'
J

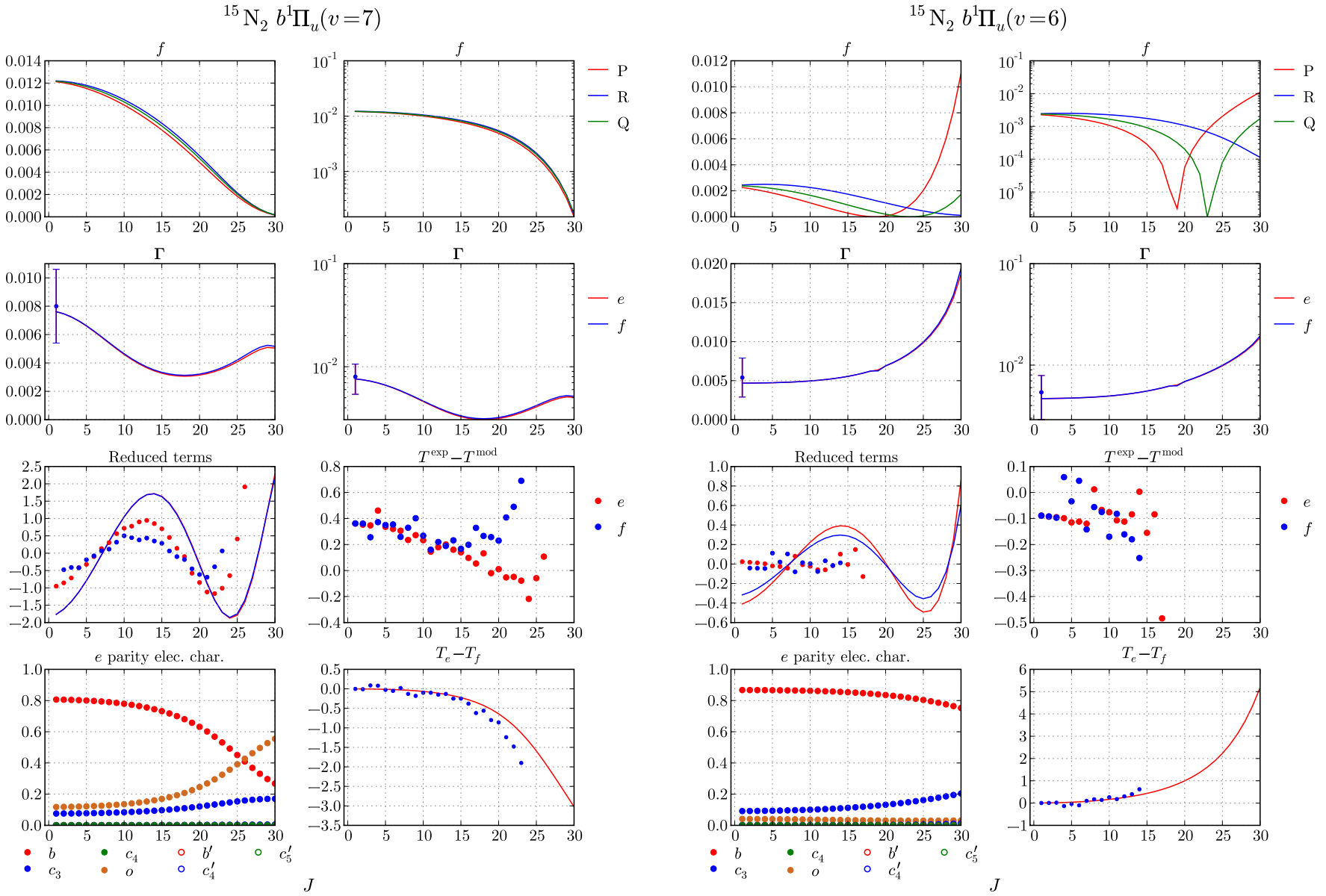
$^{15}\mathrm{N}_2$ $b^1\Pi_u(v=7)$
$^{15}\mathrm{N}_2$ $b^1\Pi_u(v=6)$
f
Γ
Reduced terms
$T^{\mathrm{exp}}-T^{\mathrm{mod}}$
e parity elec. char.
T_e-T_f
P
R
Q
e
f
b
c_3
c_4
o
b'
c_4'
c_5'
J

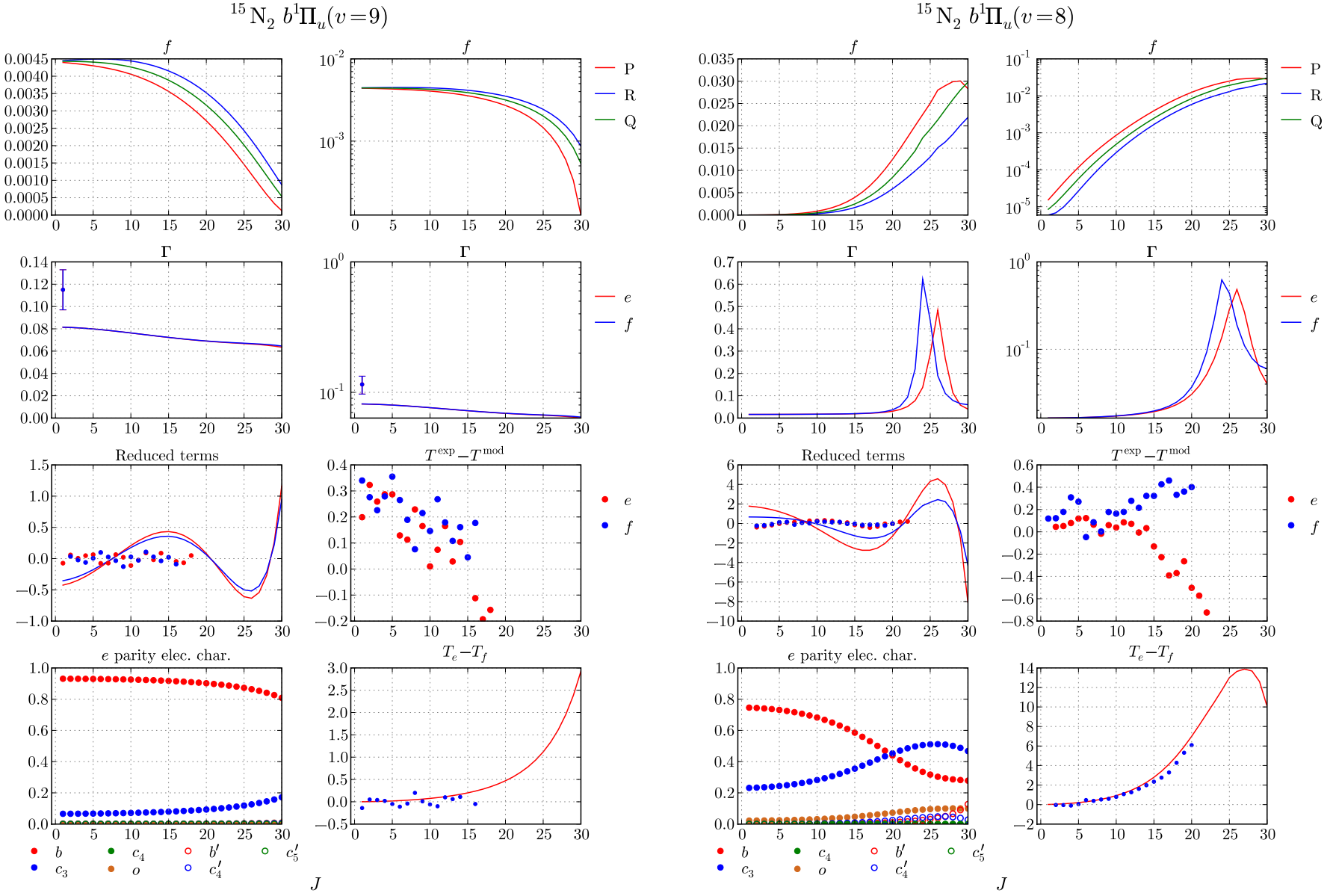
$^{15}N_2$ $b^1\Pi_u(v=9)$
$^{15}N_2$ $b^1\Pi_u(v=8)$
f
Γ
Reduced terms
$T^{exp}-T^{mod}$
e parity elec. char.
T_e-T_f
P
R
Q
e
f
b
c_3
c_4
o
b'
c_4'
c_5'
J

$^{15}\mathrm{N}_2$ $b^1\Pi_u(v=11)$
f
f
P
R
Q
Γ
Γ
e
f
Reduced terms
$T^{\mathrm{exp}}-T^{\mathrm{mod}}$
e
f
e parity elec. char.
T_e-T_f
b
c_3
c_4
o
b'
c_4'
c_5'
J
$^{15}\mathrm{N}_2$ $b^1\Pi_u(v=10)$
f
f
P
R
Q
Γ
Γ
e
f
Reduced terms
$T^{\mathrm{exp}}-T^{\mathrm{mod}}$
e
f
e parity elec. char.
T_e-T_f
b
c_3
c_4
o
b'
c_4'
c_5'
J

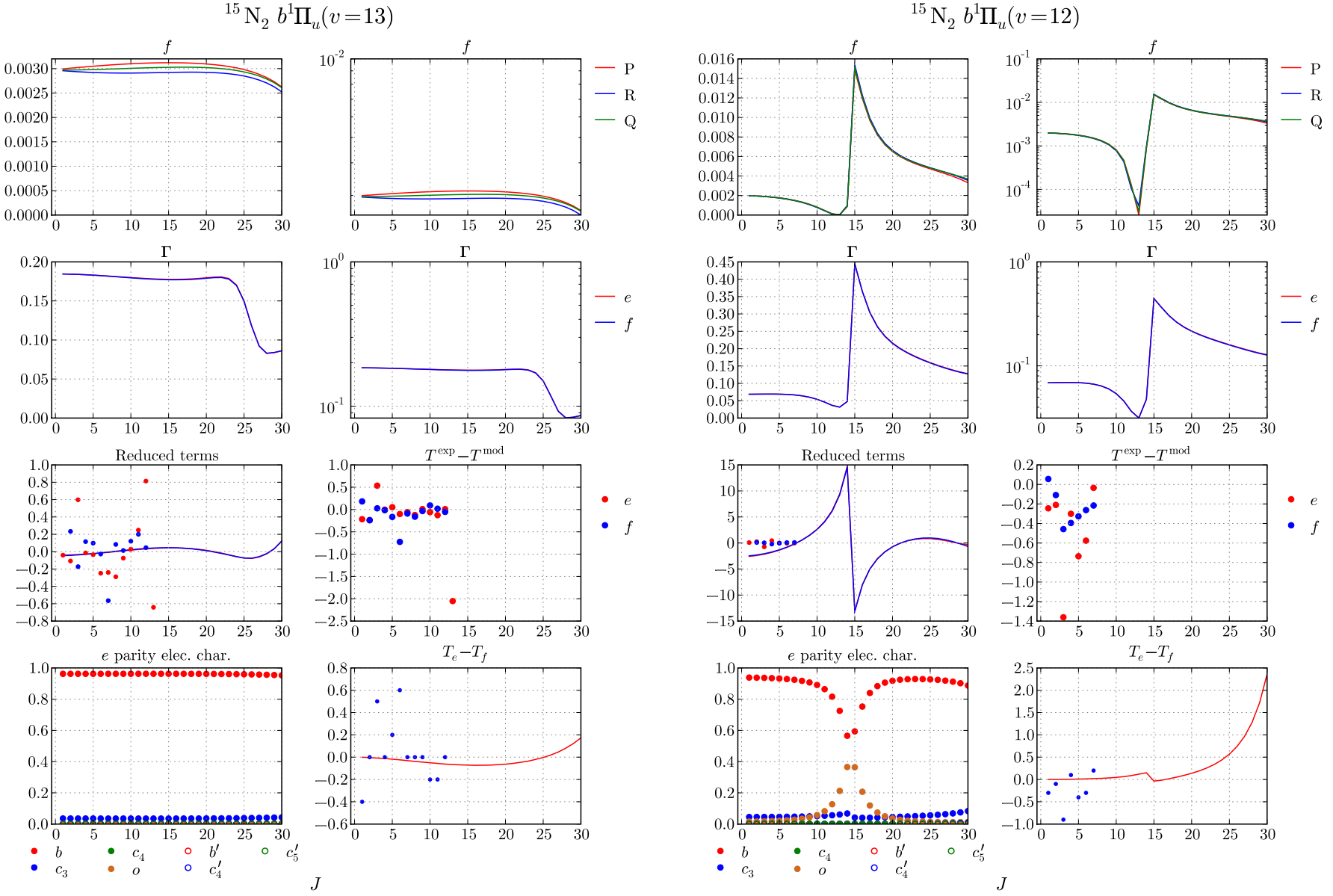
$^{15}N_2$ $b^1\Pi_u(v=13)$
$^{15}N_2$ $b^1\Pi_u(v=12)$
f
Γ
Reduced terms
$T^{exp}-T^{mod}$
e parity elec. char.
T_e-T_f
P
R
Q
e
f
b
c_3
c_4
o
b'
c_4'
c_5'
J

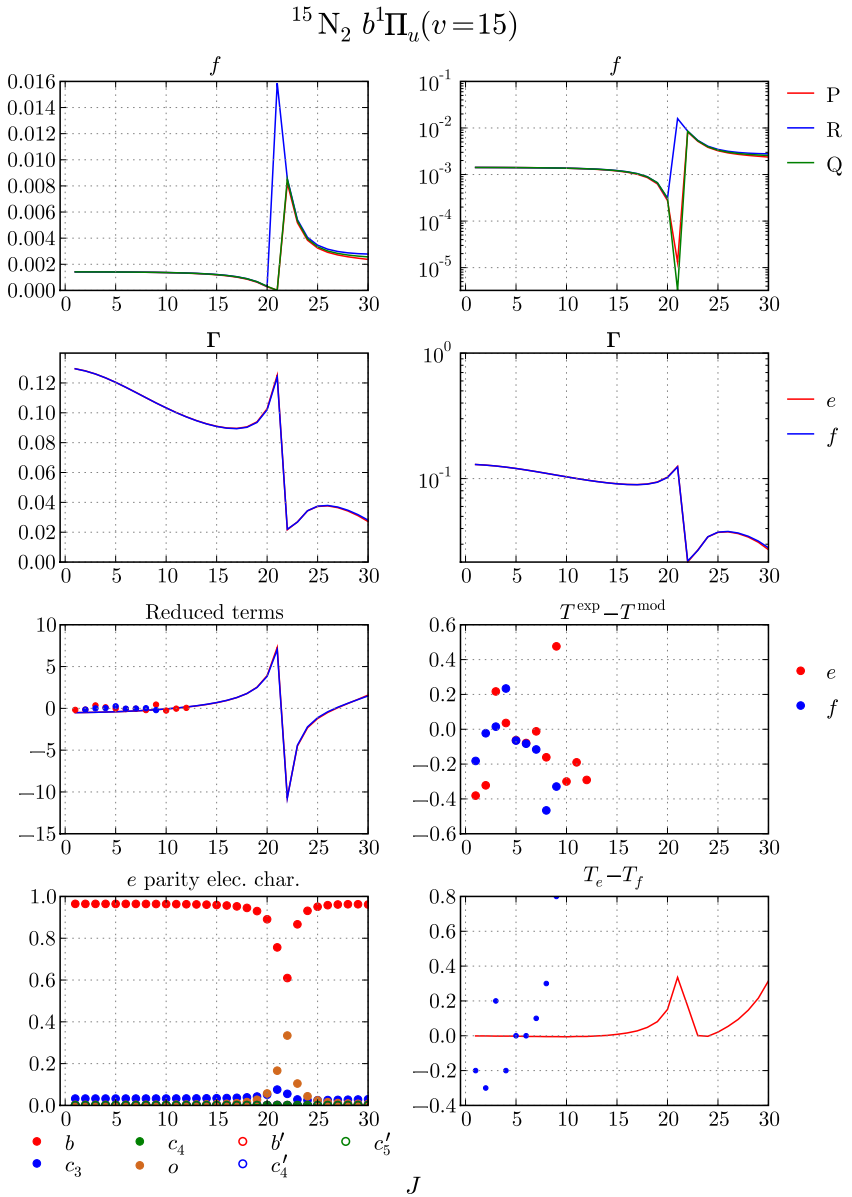
$^{15}N_2$ $b^1\Pi_u(v=15)$
f
f
P
R
Q
Γ
Γ
e
f
Reduced terms
$T^{exp}-T^{mod}$
e
f
e parity elec. char.
T_e-T_f
b
c_3
c_4
o
b′
c_4'
c_5'
J

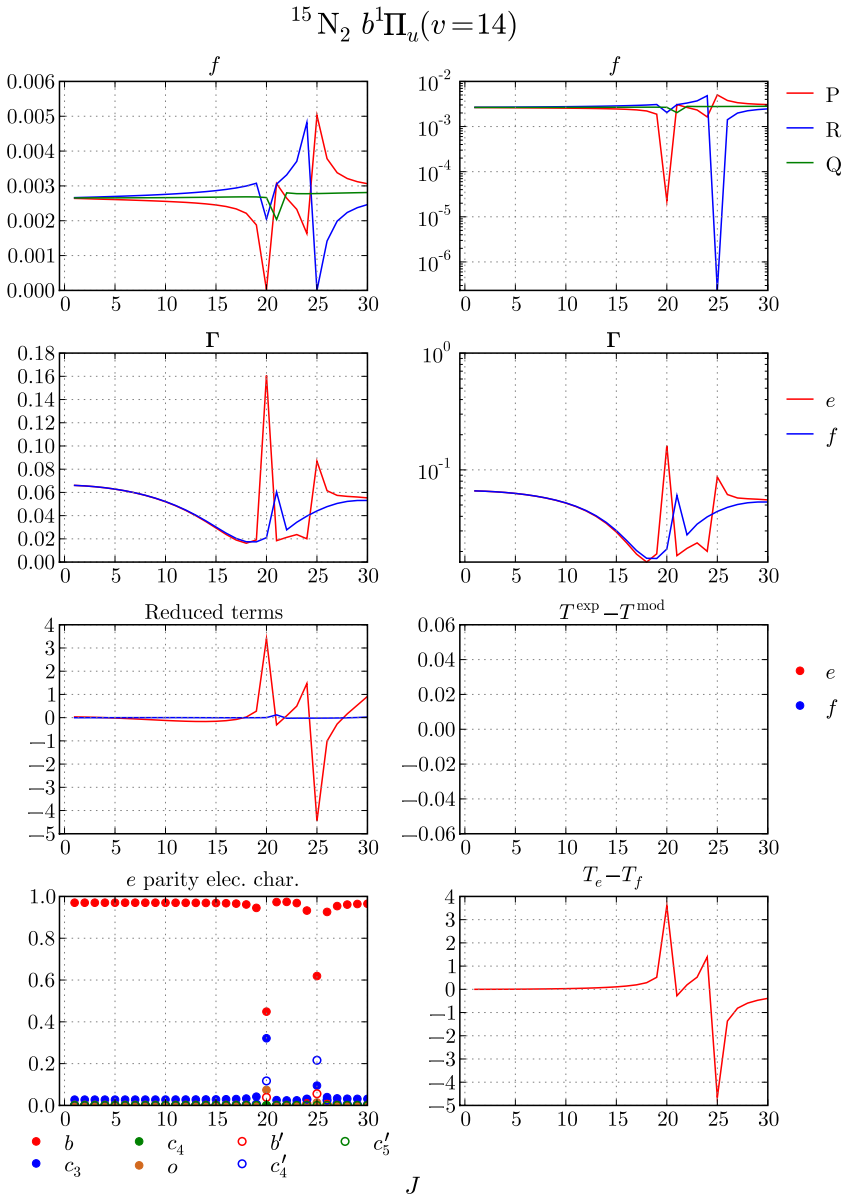
$^{15}N_2$ $b^1\Pi_u(v=14)$
f
f
P
R
Q
Γ
Γ
e
f
Reduced terms
$T^{exp}-T^{mod}$
e
f
e parity elec. char.
T_e-T_f
b
c_3
c_4
o
b′
c_4'
c_5'
J

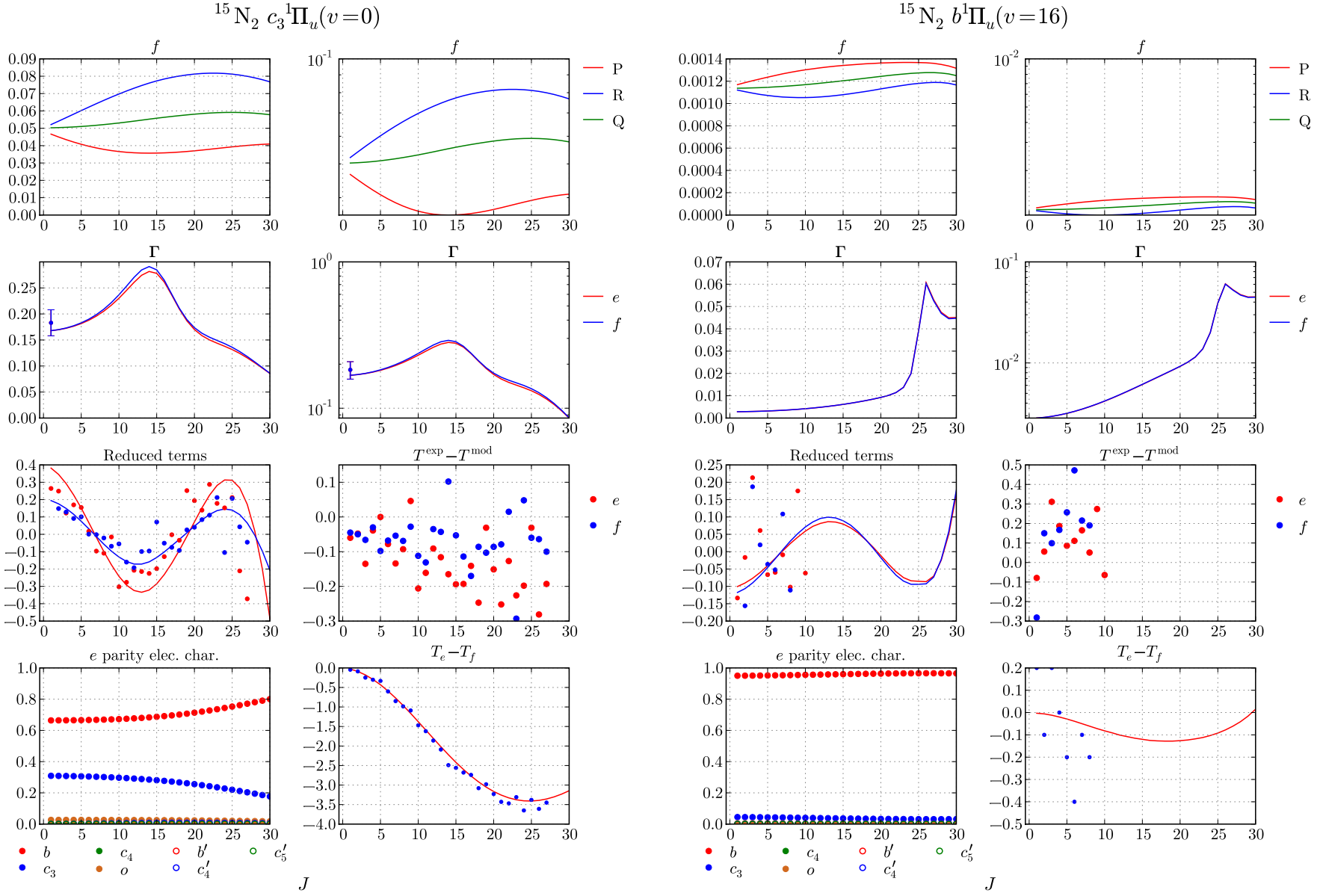
$^{15}N_2$ $c_3{}^1\Pi_u(v=0)$
$^{15}N_2$ $b^1\Pi_u(v=16)$
f
Γ
Reduced terms
$T^{exp}-T^{mod}$
e parity elec. char.
T_e-T_f
P
R
Q
e
f
b
c_3
c_4
o
b'
c_4'
c_5'
J

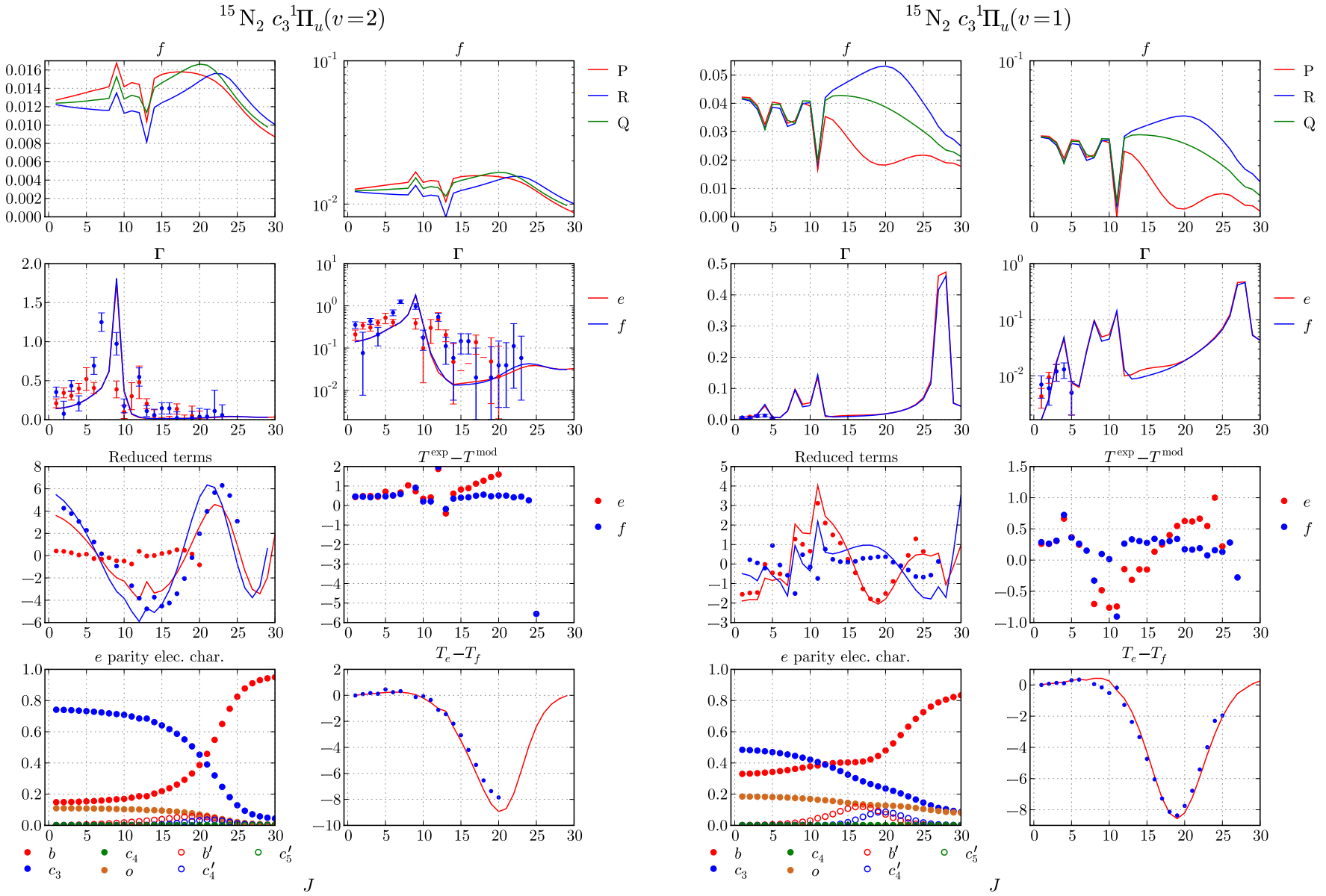
$^{15}N_2$ $c_3{}^1\Pi_u(v=2)$
$^{15}N_2$ $c_3{}^1\Pi_u(v=1)$
f
Γ
Reduced terms
$T^{\mathrm{exp}}-T^{\mathrm{mod}}$
e parity elec. char.
T_e-T_f
P
R
Q
e
f
b
c_3
c_4
o
b'
c_4'
c_5'
J

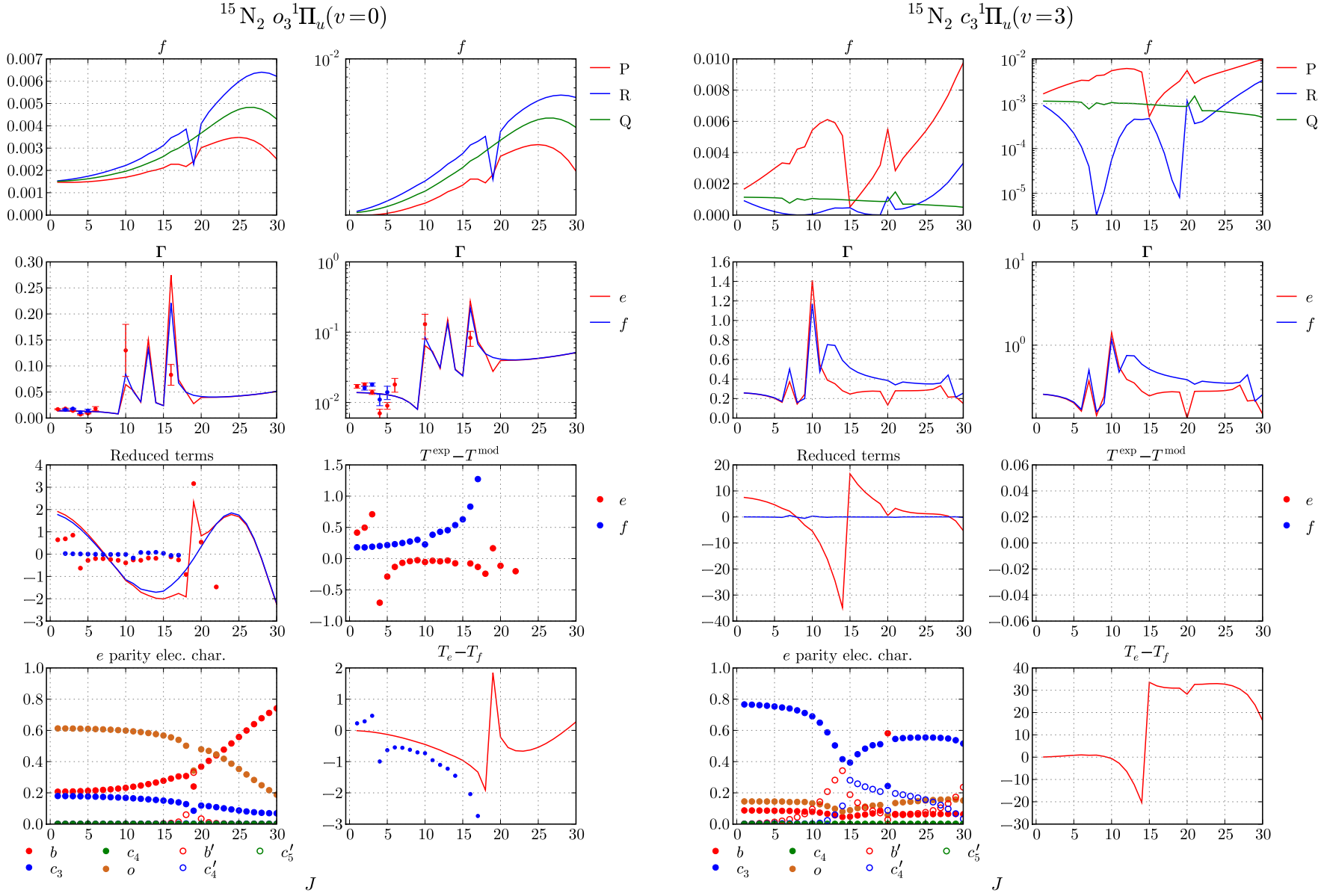
$^{15}N_2$ $o_3\,^1\Pi_u(v=0)$
$^{15}N_2$ $c_3\,^1\Pi_u(v=3)$
f
Γ
Reduced terms
$T^{exp}-T^{mod}$
e parity elec. char.
T_e-T_f
P
R
Q
e
f
b
c_3
c_4
o
b'
c_4'
c_5'
J

$^{15}\mathrm{N}_2$ $o_3\,{}^1\Pi_u(v=2)$
f
f
P
R
Q
Γ
Γ
e
f
Reduced terms
$T^{\mathrm{exp}}-T^{\mathrm{mod}}$
e
f
e parity elec. char.
T_e-T_f
b
c_3
c_4
o
b'
c_4'
c_5'
J
$^{15}\mathrm{N}_2$ $o_3\,{}^1\Pi_u(v=1)$
f
f
P
R
Q
Γ
Γ
e
f
Reduced terms
$T^{\mathrm{exp}}-T^{\mathrm{mod}}$
e
f
e parity elec. char.
T_e-T_f
b
c_3
c_4
o
b'
c_4'
c_5'
J

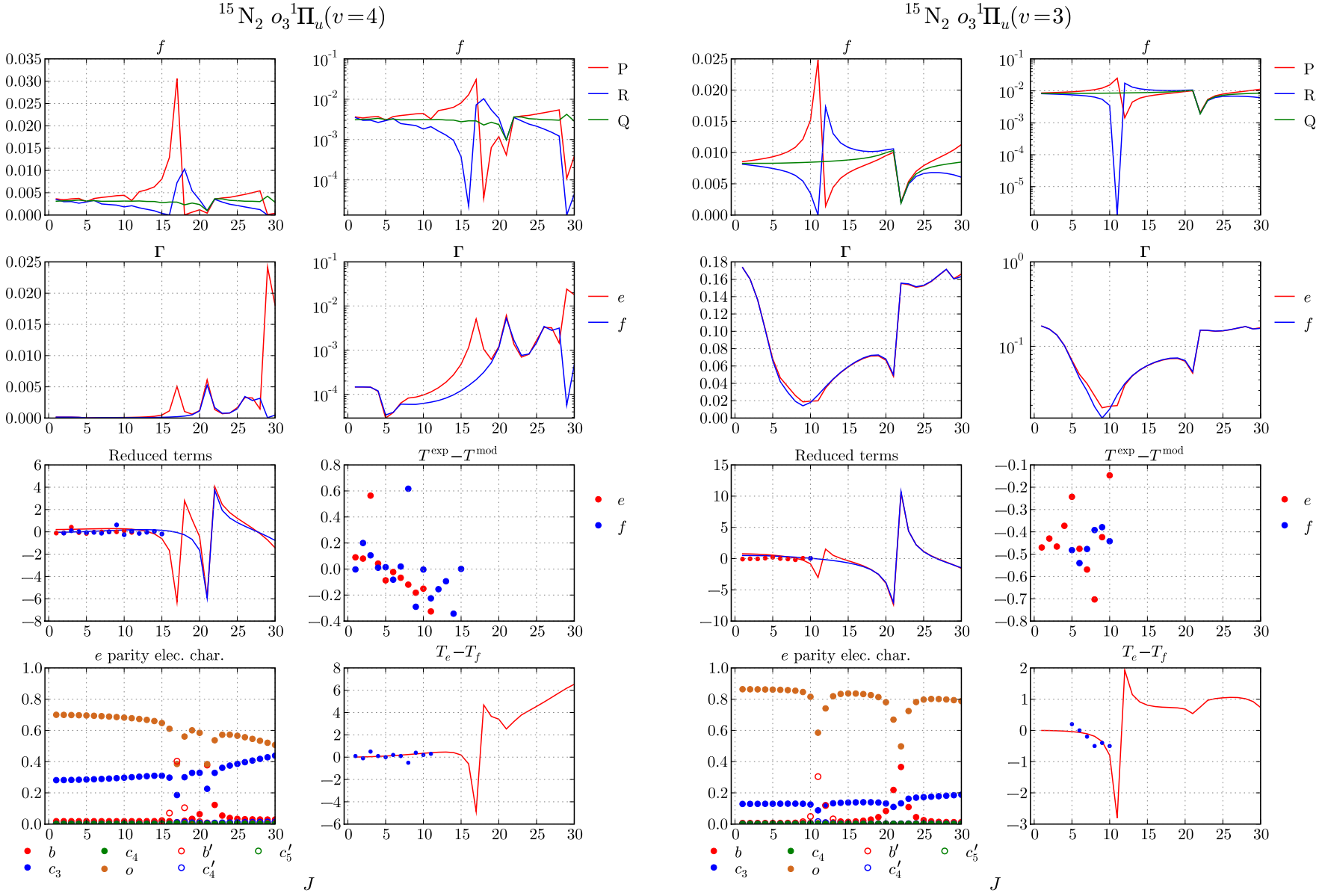
$^{15}N_2$ $o_3{}^1\Pi_u(v=4)$
$^{15}N_2$ $o_3{}^1\Pi_u(v=3)$
f
Γ
Reduced terms
$T^{exp}-T^{mod}$
e parity elec. char.
T_e-T_f
P
R
Q
e
f
b
c_3
c_4
o
b'
c_4'
c_5'
J

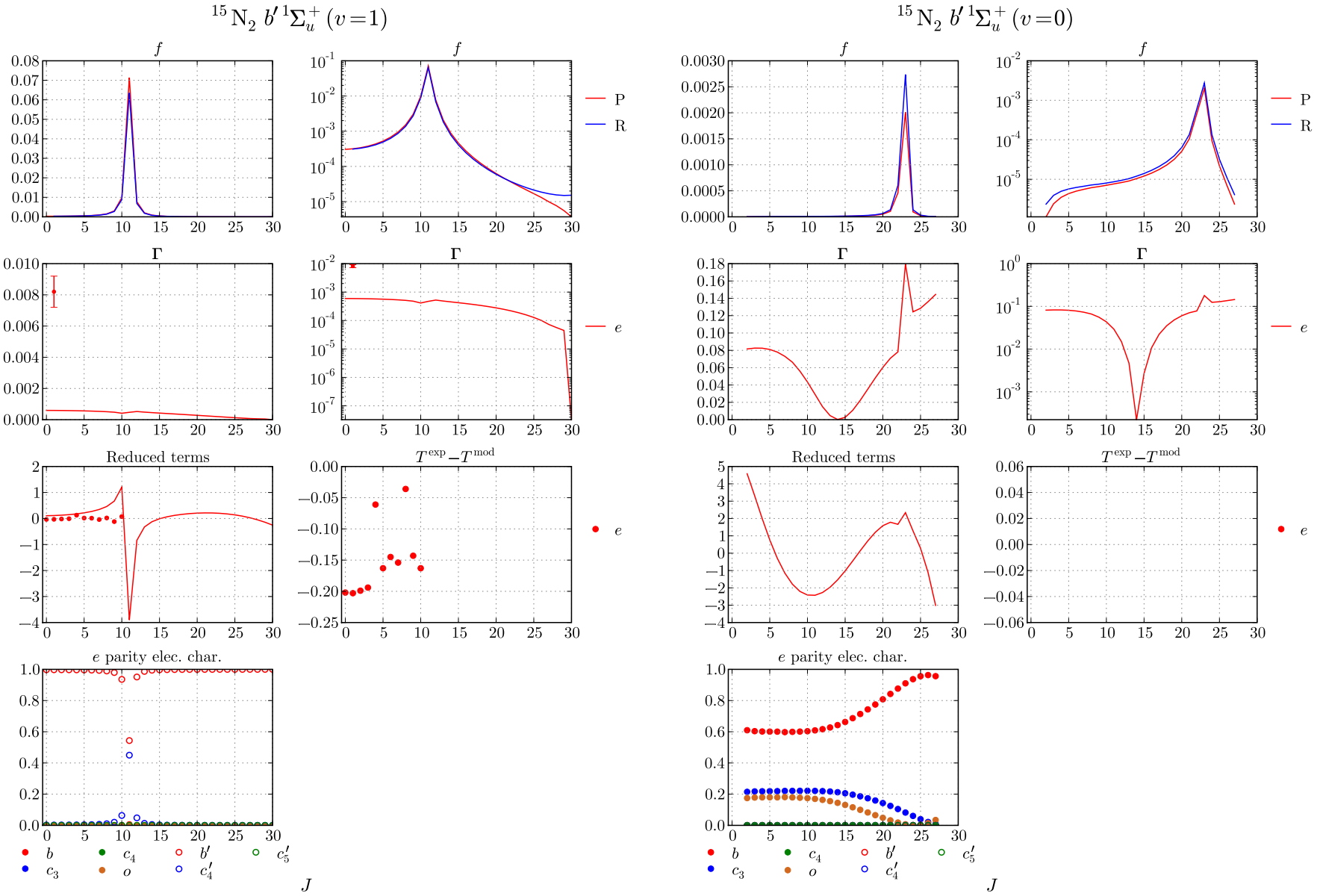
$^{15}N_2\ b'\,^1\Sigma_u^+\ (v=1)$
$^{15}N_2\ b'\,^1\Sigma_u^+\ (v=0)$
f
Γ
Reduced terms
$T^{\mathrm{exp}}-T^{\mathrm{mod}}$
e parity elec. char.
P
R
e
b
c_3
c_4
o
b'
c_4'
c_5'
J

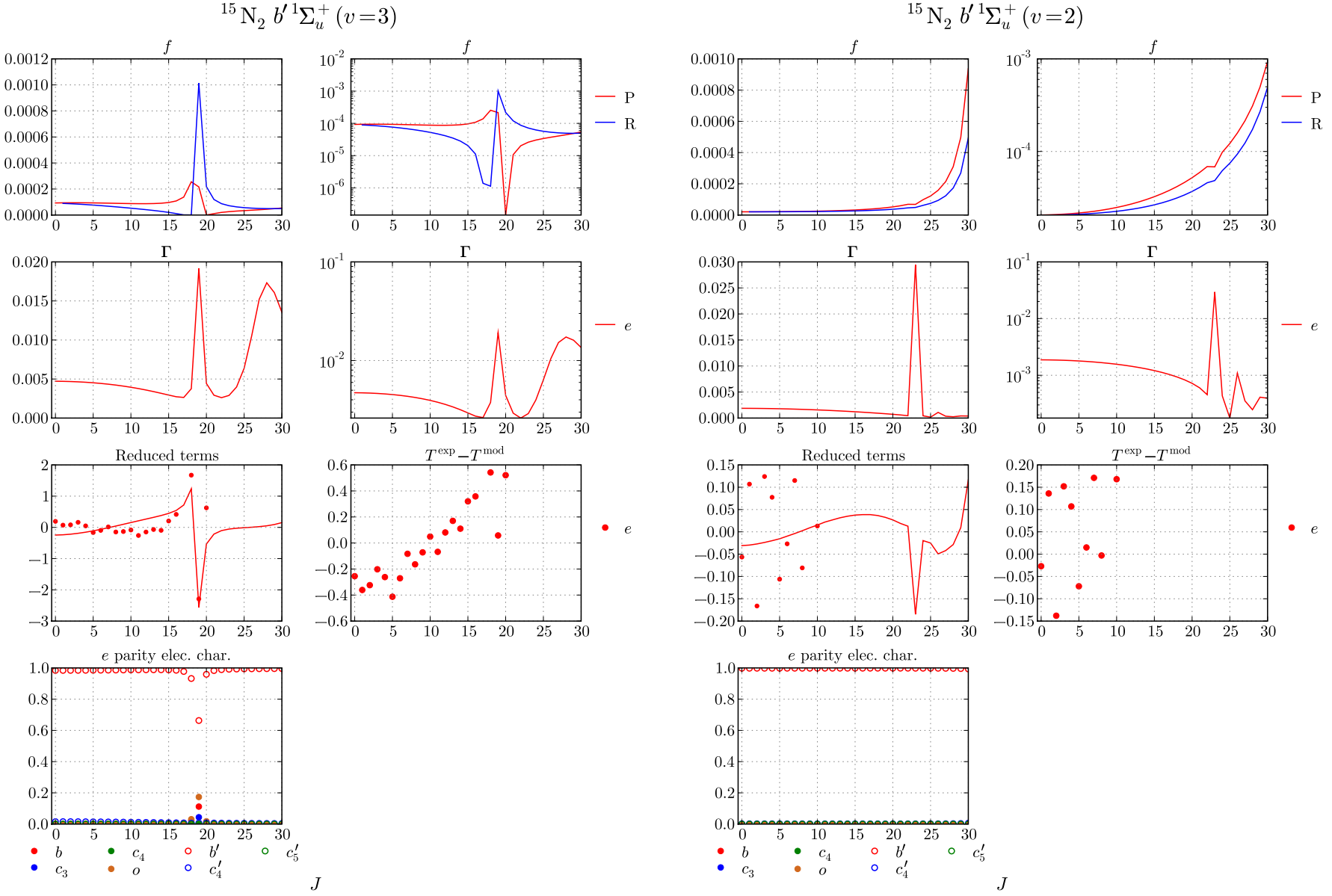
$^{15}N_2\ b'\,^1\Sigma_u^+\ (v=3)$
$^{15}N_2\ b'\,^1\Sigma_u^+\ (v=2)$
f
Γ
Reduced terms
$T^{\rm exp}-T^{\rm mod}$
e parity elec. char.
P
R
e
b
c_3
c_4
o
b'
c_4'
c_5'
J

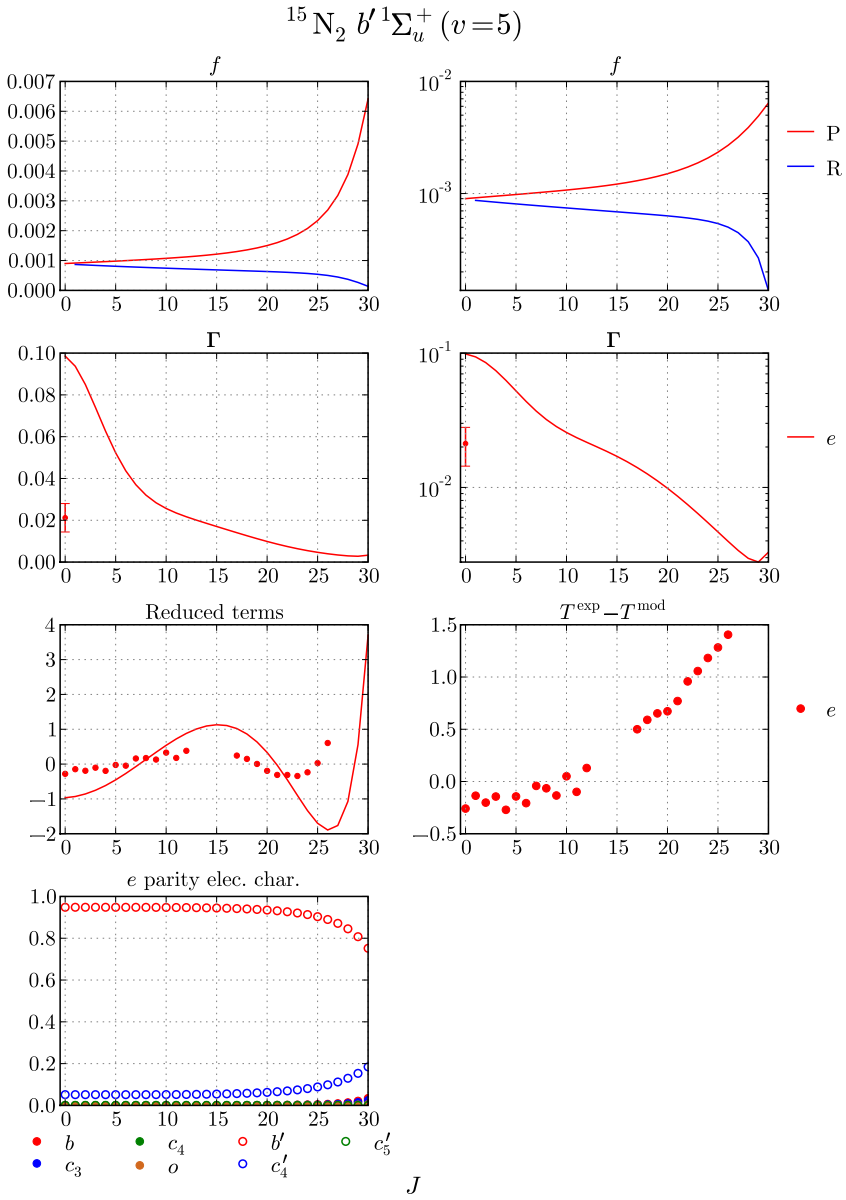
$^{15}N_2\ b'\,^1\Sigma_u^+\ (v=5)$
f
Γ
Reduced terms
$T^{exp} - T^{mod}$
e parity elec. char.
P
R
e
b
c_3
c_4
o
b′
c_4'
c_5'
J

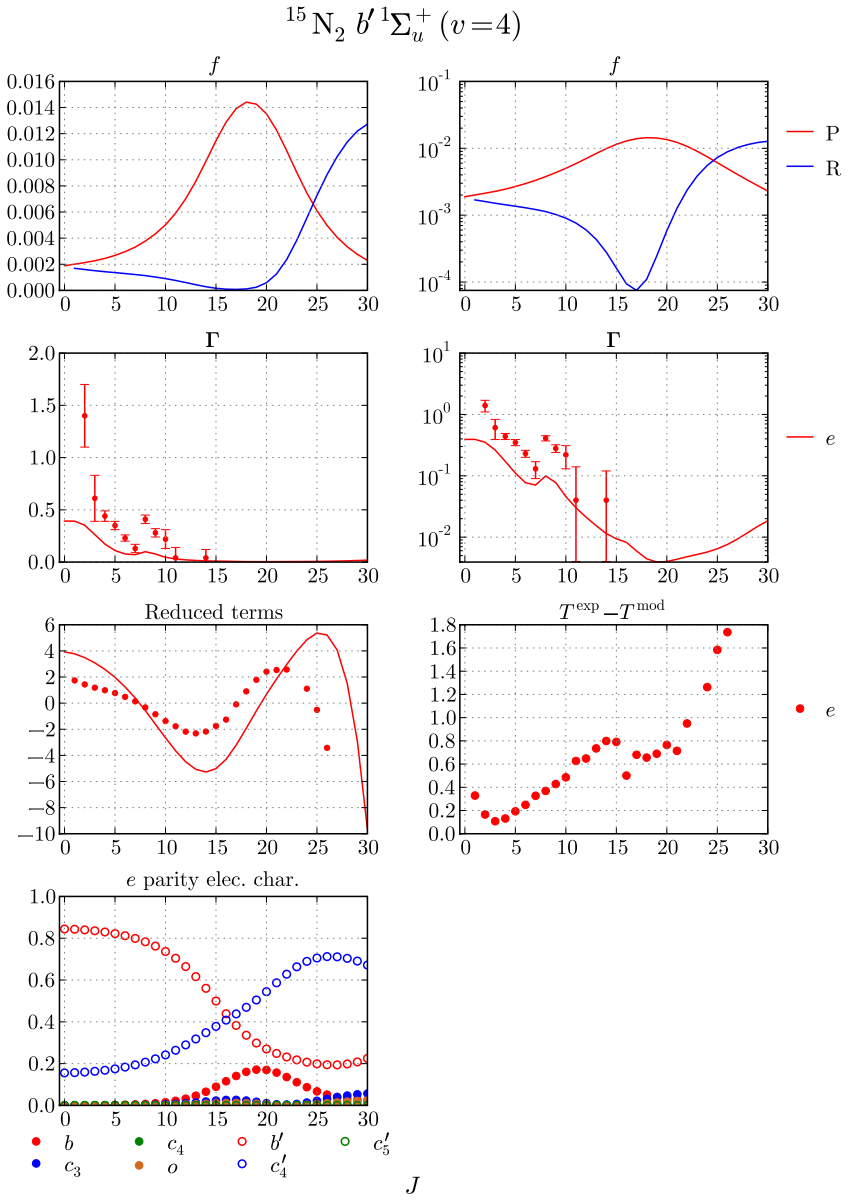
$^{15}N_2\ b'\,^1\Sigma_u^+\ (v=4)$
f
Γ
Reduced terms
$T^{exp} - T^{mod}$
e parity elec. char.
P
R
e
b
c_3
c_4
o
b′
c_4'
c_5'
J

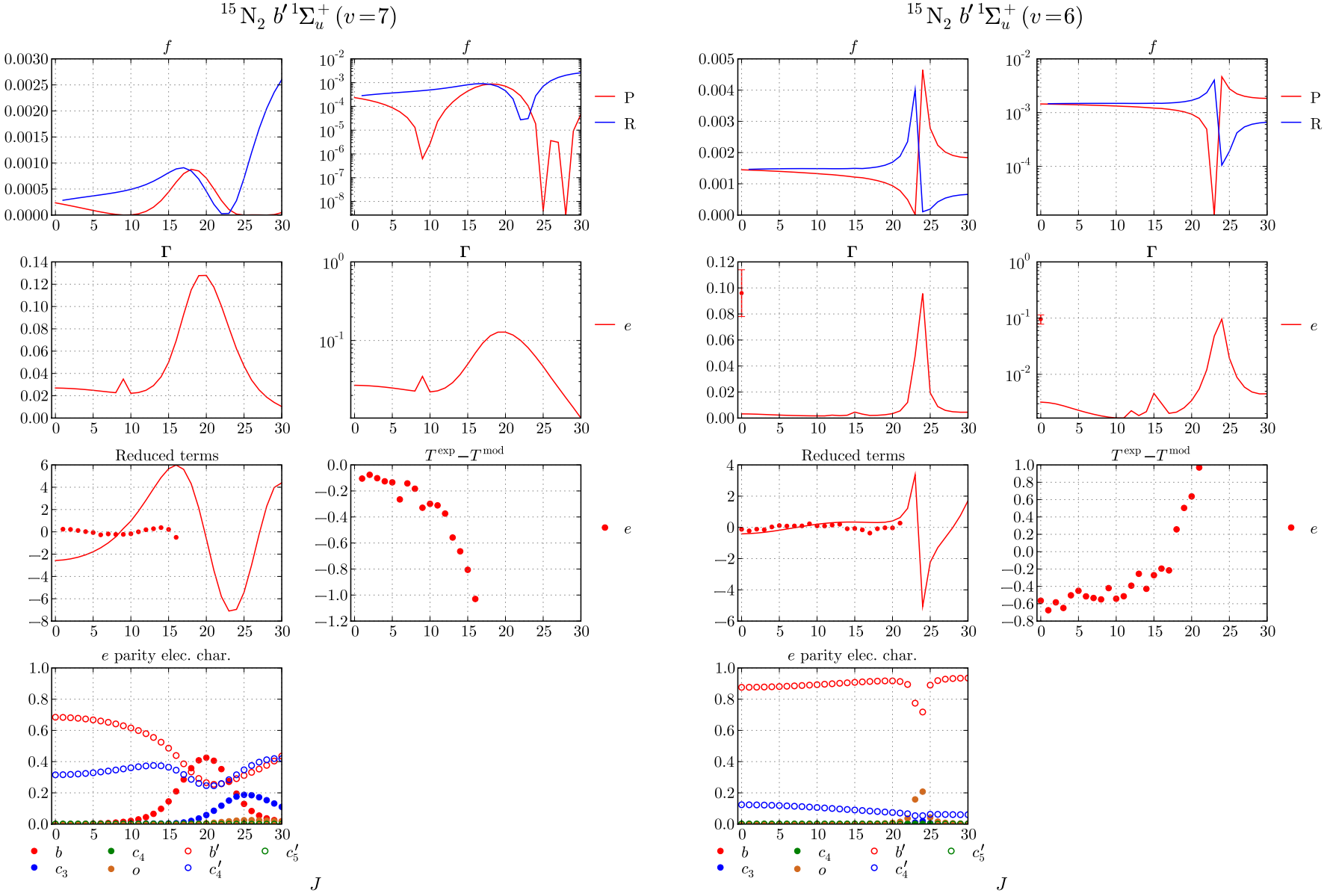
$^{15}N_2$ $b'\,^1\Sigma_u^+$ $(v=7)$
$^{15}N_2$ $b'\,^1\Sigma_u^+$ $(v=6)$
f
Γ
Reduced terms
$T^{\mathrm{exp}}-T^{\mathrm{mod}}$
e parity elec. char.
P
R
e
b
c_3
c_4
o
b'
c_4'
c_5'
J

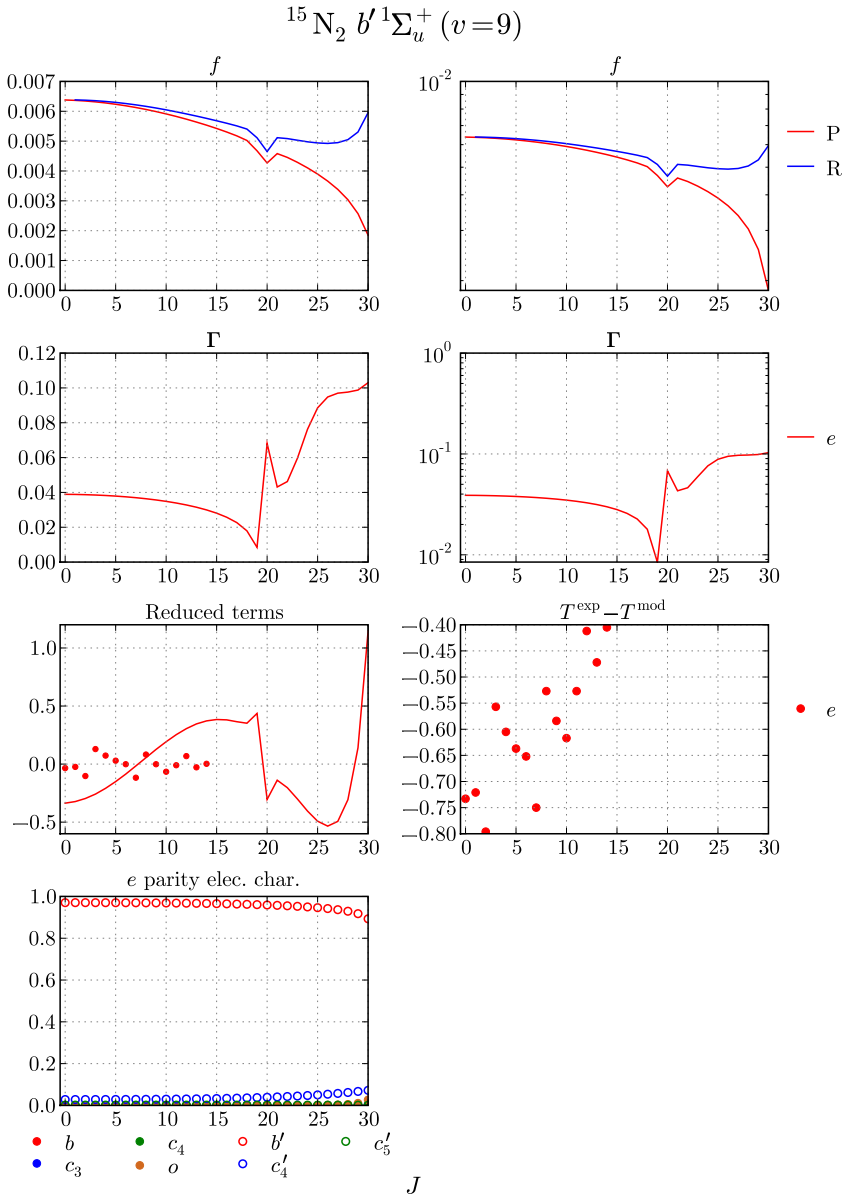
$^{15}N_2\ b'\,^1\Sigma_u^+\ (v=9)$
f
Γ
Reduced terms
$T^{exp}-T^{mod}$
e parity elec. char.
P
R
e
b
c_3
c_4
o
b′
c_4'
c_5'
J

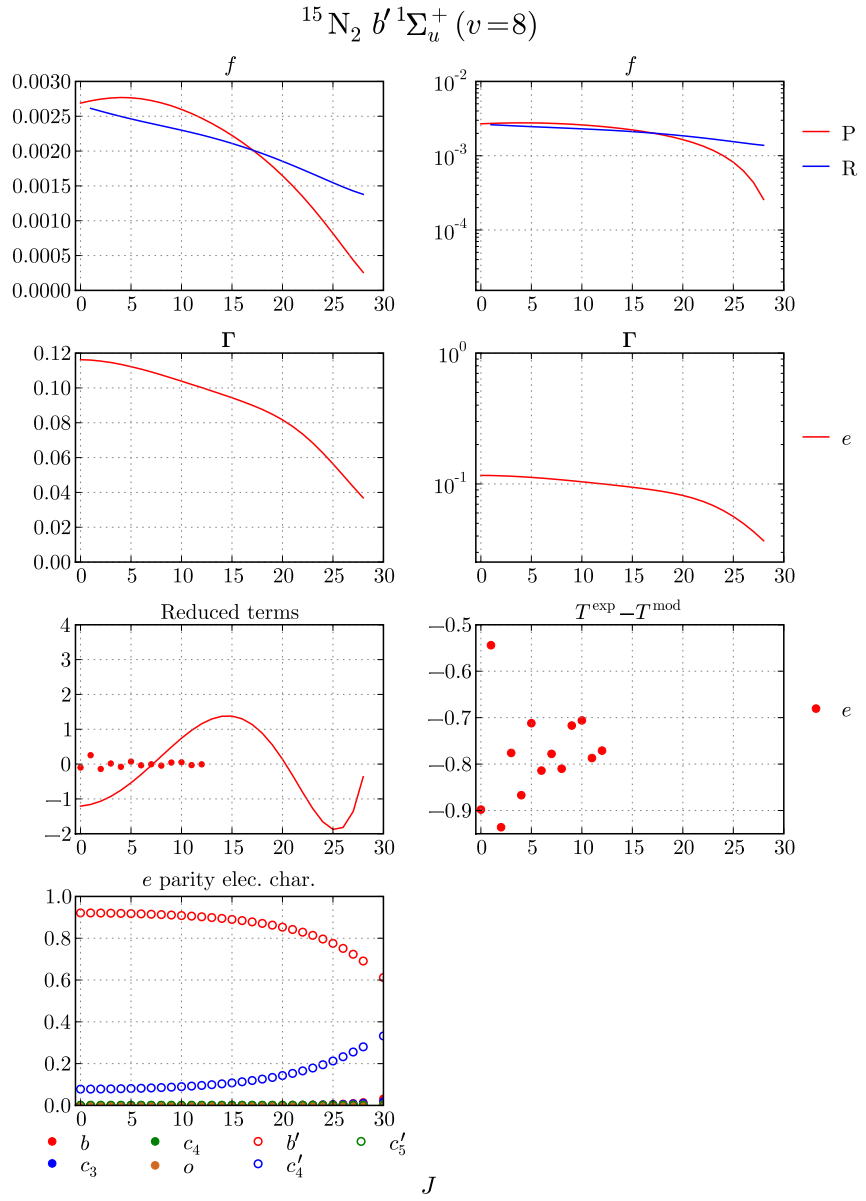
$^{15}N_2\ b'\,^1\Sigma_u^+\ (v=8)$
f
Γ
Reduced terms
$T^{exp}-T^{mod}$
e parity elec. char.
P
R
e
b
c_3
c_4
o
b′
c_4'
c_5'
J

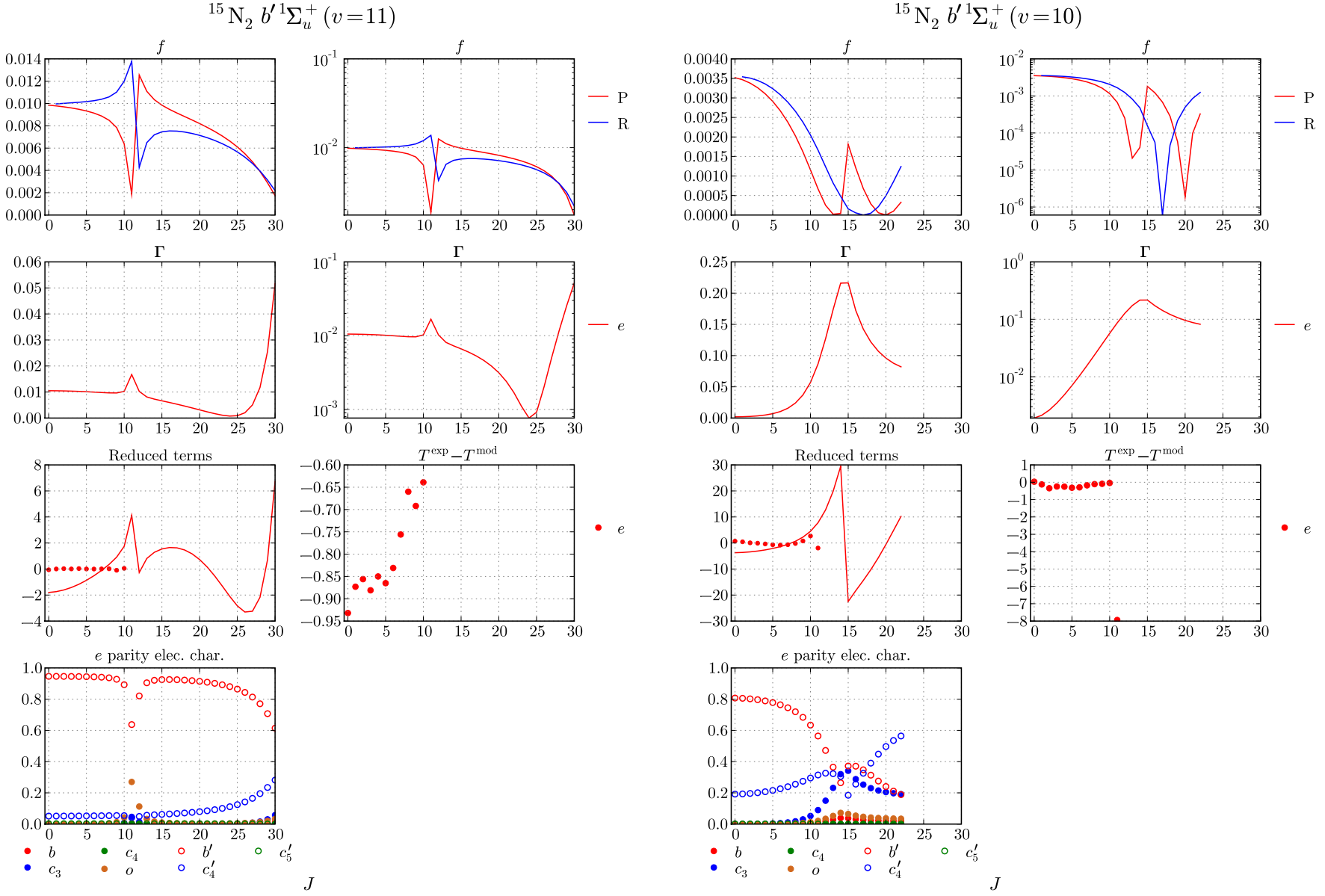
$^{15}N_2\ b'^1\Sigma_u^+\ (v=11)$
$^{15}N_2\ b'^1\Sigma_u^+\ (v=10)$
f
Γ
Reduced terms
$T^{exp}-T^{mod}$
e parity elec. char.
P
R
e
b
c_3
c_4
o
b'
c_4'
c_5'
J

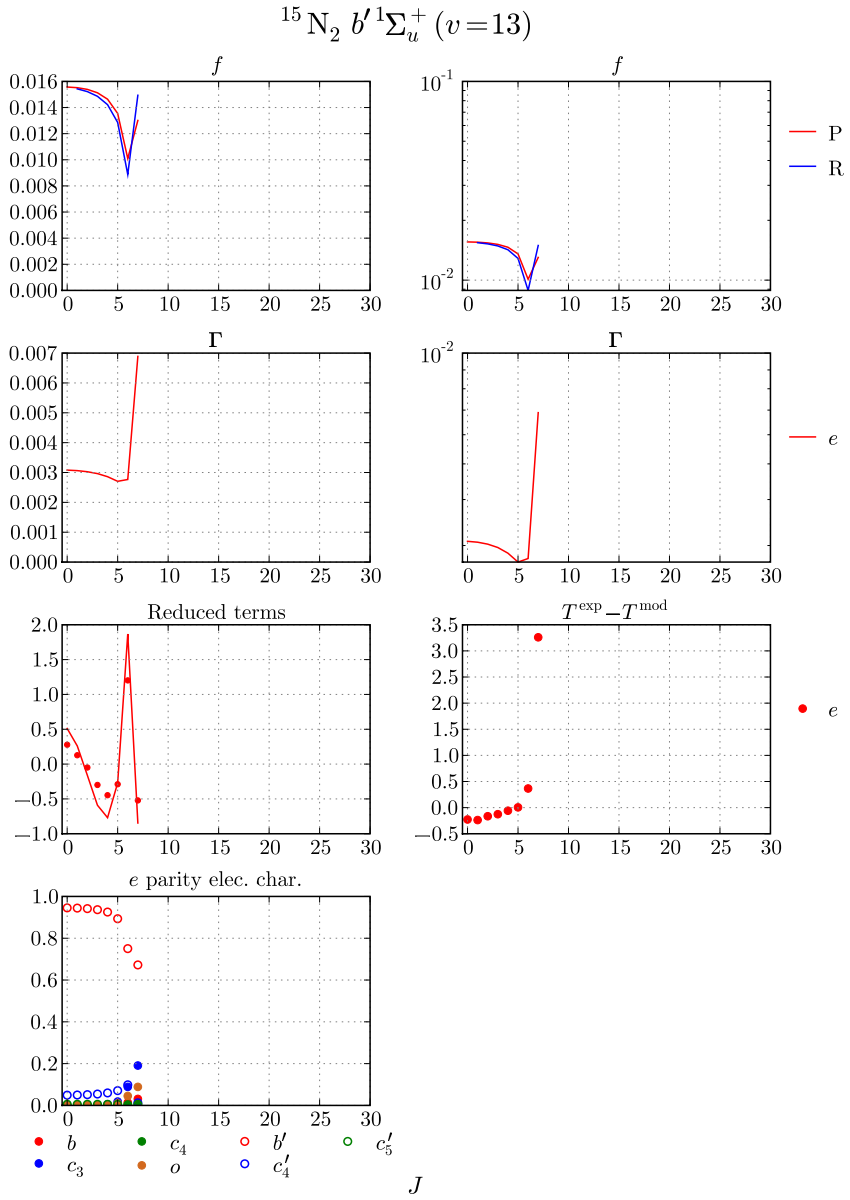
$^{15}N_2$ $b'\,^1\Sigma_u^+$ ($v=13$)
f
Γ
Reduced terms
$T^{\mathrm{exp}}-T^{\mathrm{mod}}$
e parity elec. char.
P
R
e
b
c_3
c_4
o
b'
c_4'
c_5'
J

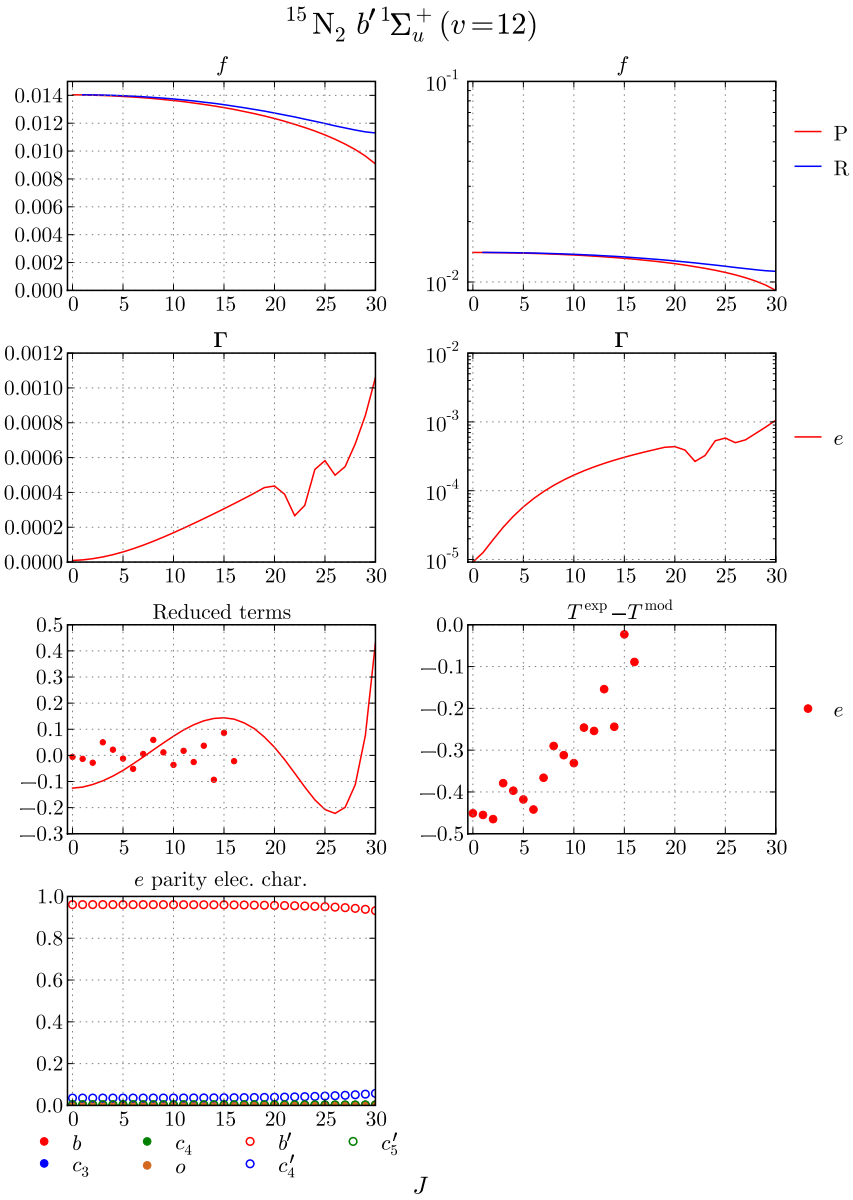
$^{15}N_2$ $b'\,^1\Sigma_u^+$ ($v=12$)
f
Γ
Reduced terms
$T^{\mathrm{exp}}-T^{\mathrm{mod}}$
e parity elec. char.
P
R
e
b
c_3
c_4
o
b'
c_4'
c_5'
J

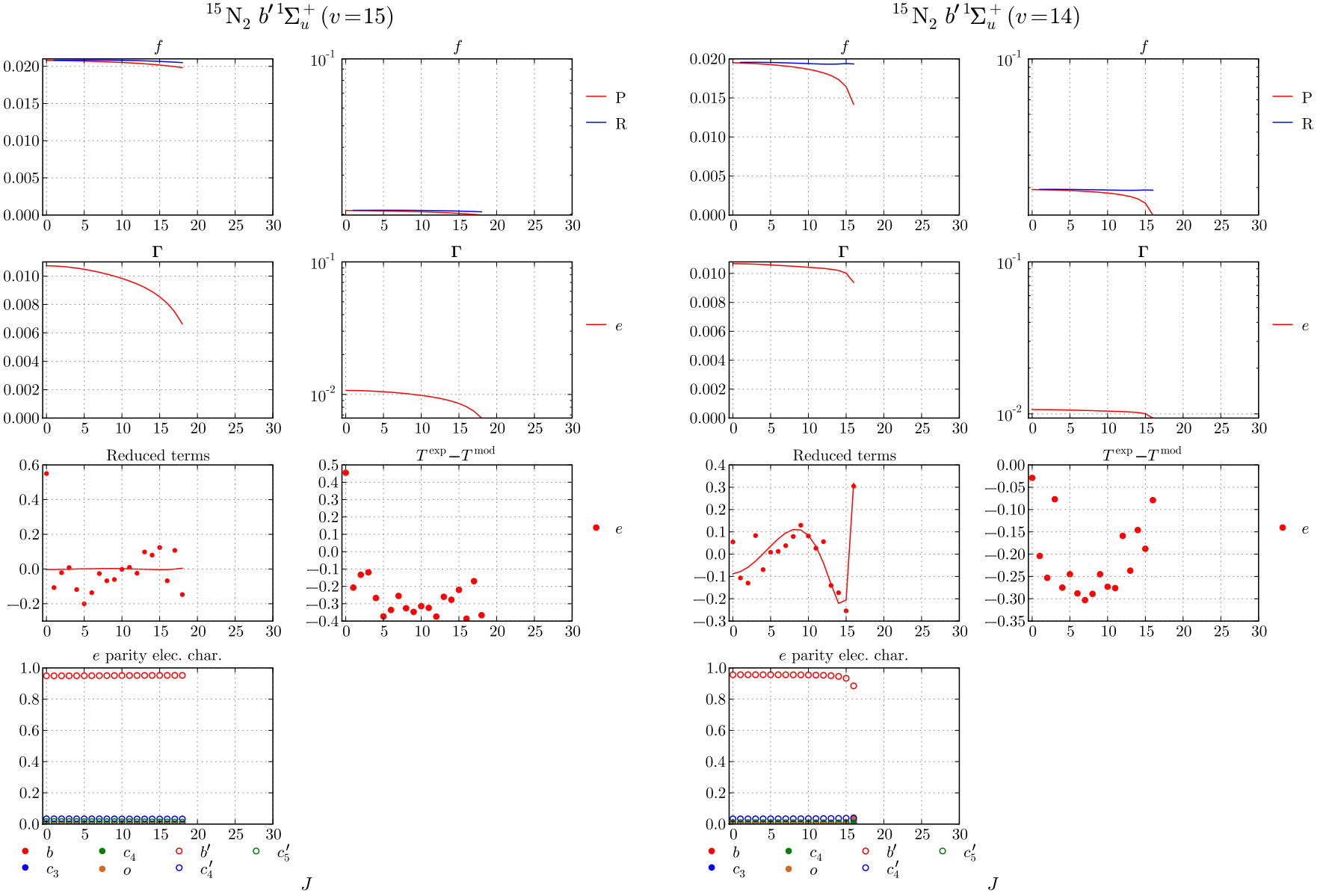
$^{15}N_2\ b'^1\Sigma_u^+\ (v=15)$
$^{15}N_2\ b'^1\Sigma_u^+\ (v=14)$
f
Γ
Reduced terms
$T^{exp}-T^{mod}$
e parity elec. char.
P
R
e
b
c_3
c_4
o
b'
c_4'
c_5'
J

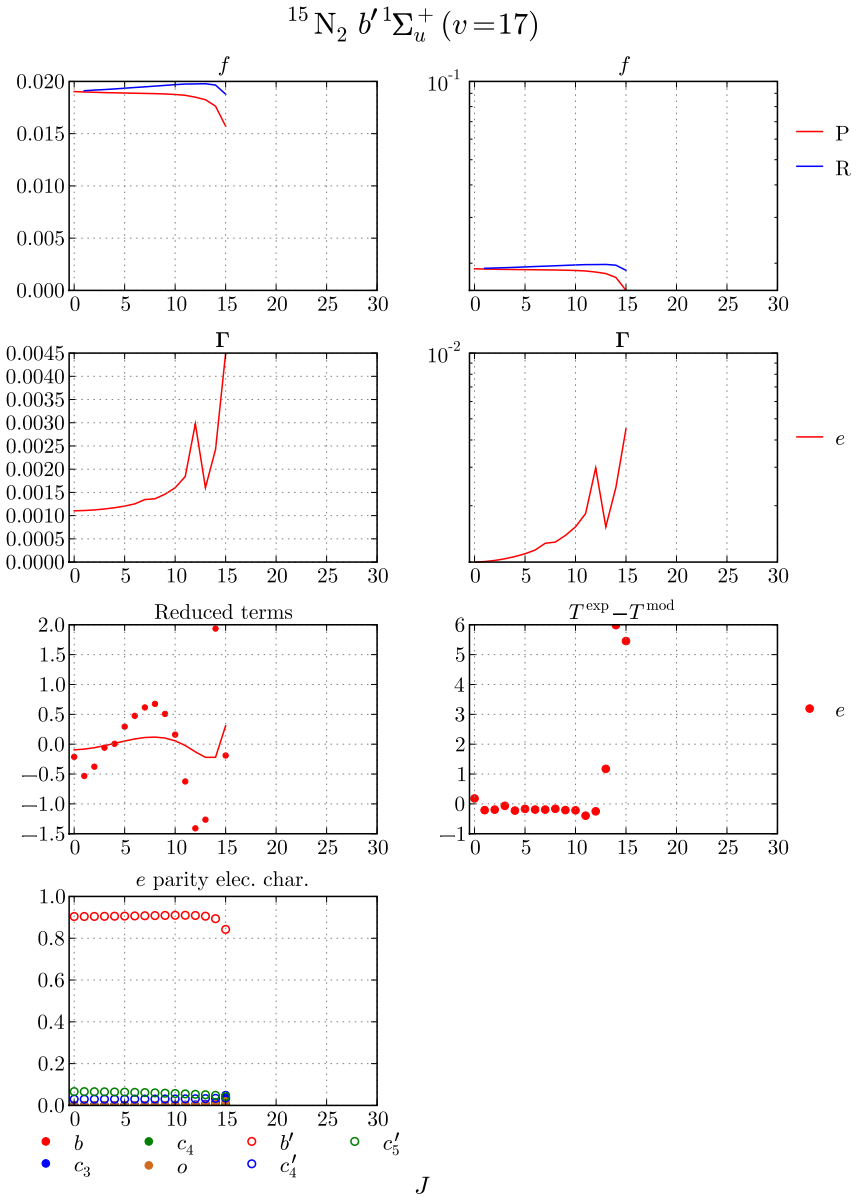
$^{15}N_2$ $b'\,^1\Sigma_u^+$ ($v=17$)
f
Γ
Reduced terms
$T^{\mathrm{exp}}-T^{\mathrm{mod}}$
e parity elec. char.
P
R
e
b
c_3
c_4
o
b'
c_4'
c_5'
J

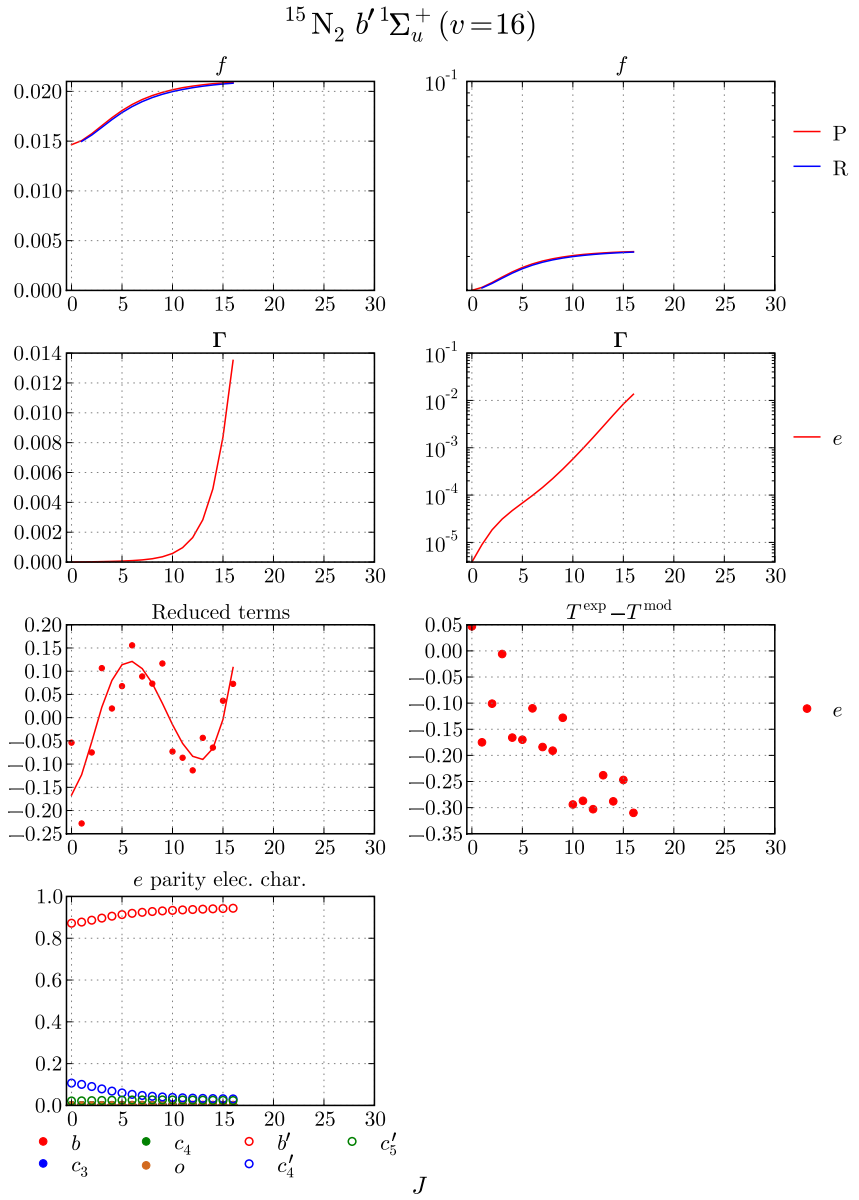
$^{15}N_2$ $b'\,^1\Sigma_u^+$ ($v=16$)
f
Γ
Reduced terms
$T^{\mathrm{exp}}-T^{\mathrm{mod}}$
e parity elec. char.
P
R
e
b
c_3
c_4
o
b'
c_4'
c_5'
J

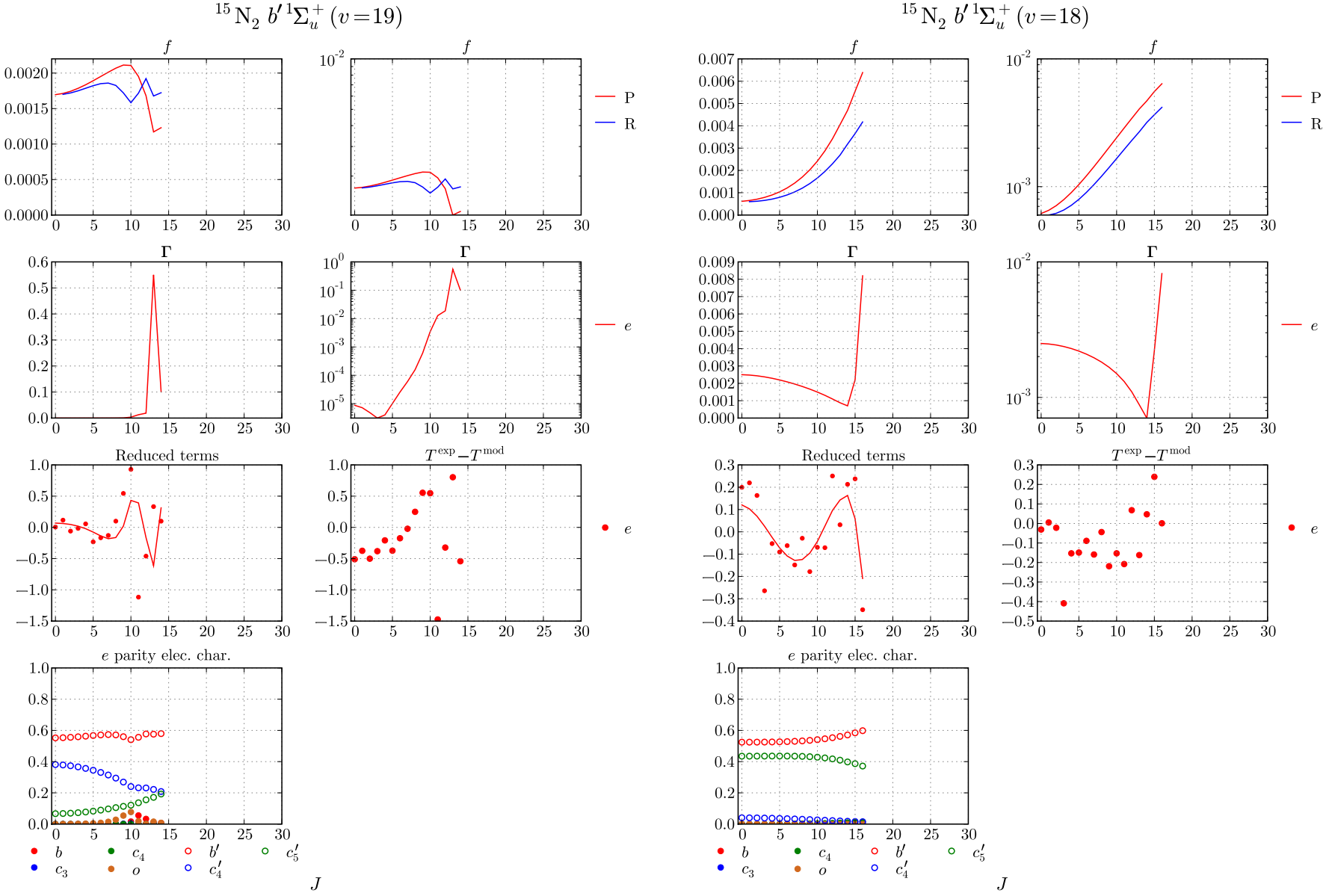
$^{15}N_2$ $b'^1\Sigma_u^+$ ($v=19$)
$^{15}N_2$ $b'^1\Sigma_u^+$ ($v=18$)
f
Γ
Reduced terms
$T^{exp}-T^{mod}$
e parity elec. char.
P
R
e
b
c_3
c_4
o
b'
c_4'
c_5'
J

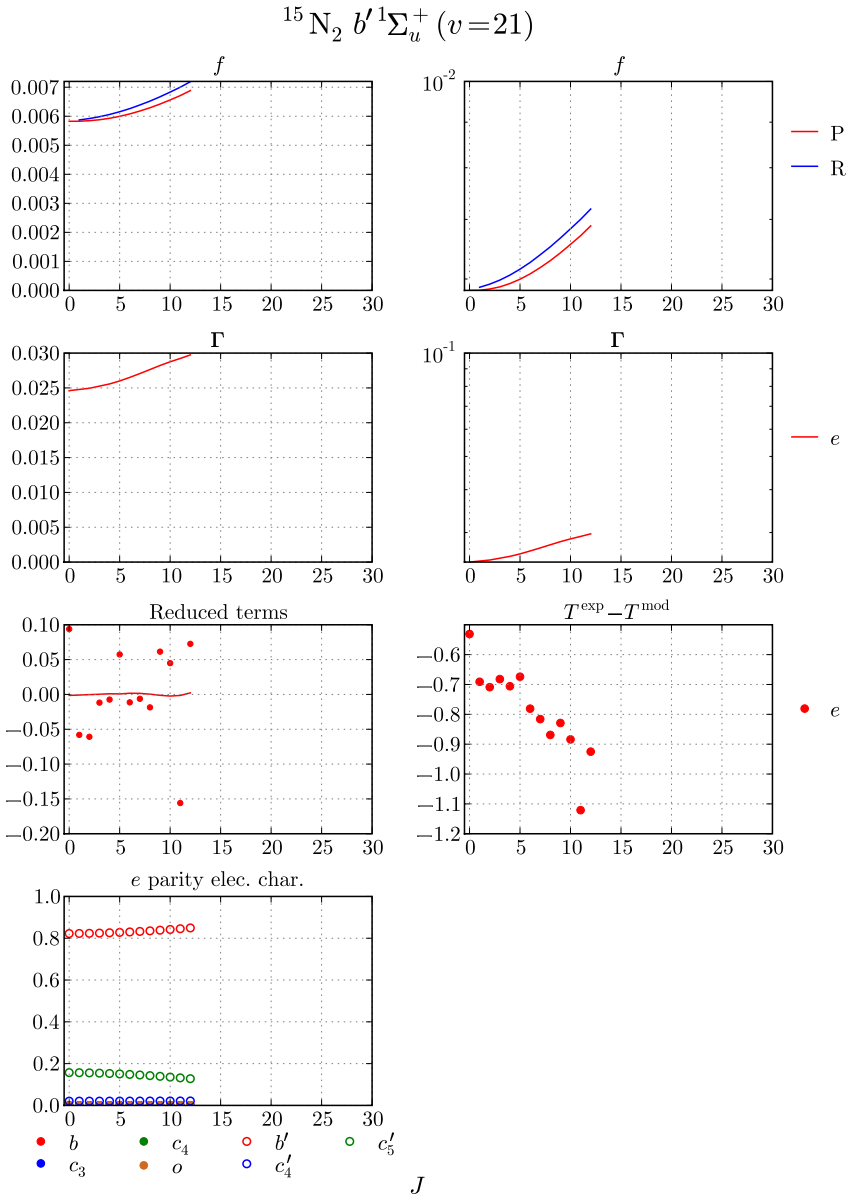
$^{15}N_2\ b'\,^1\Sigma_u^+\ (v=21)$
f
f
P
R
Γ
Γ
e
Reduced terms
$T^{exp}-T^{mod}$
e
e parity elec. char.
b
c_3
c_4
o
b′
c_4'
c_5'
J

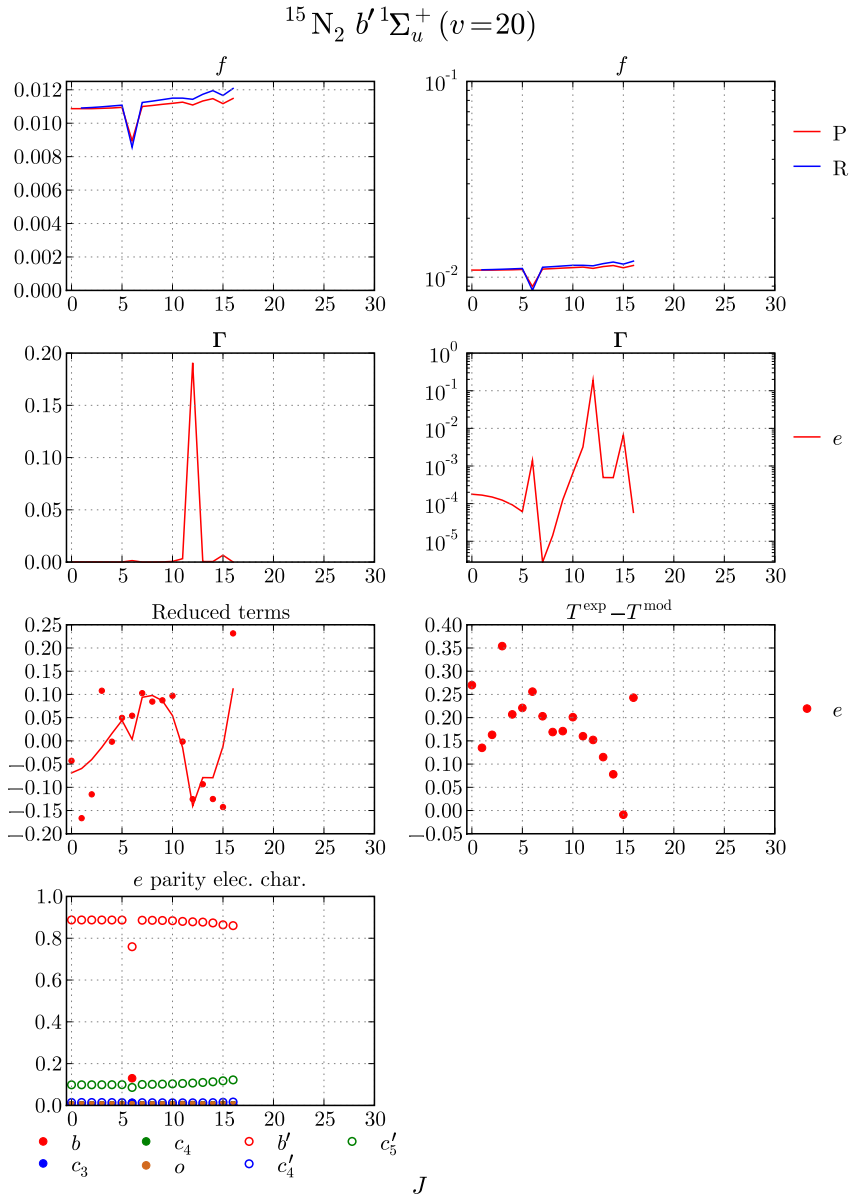
$^{15}N_2\ b'\,^1\Sigma_u^+\ (v=20)$
f
f
P
R
Γ
Γ
e
Reduced terms
$T^{exp}-T^{mod}$
e
e parity elec. char.
b
c_3
c_4
o
b′
c_4'
c_5'
J

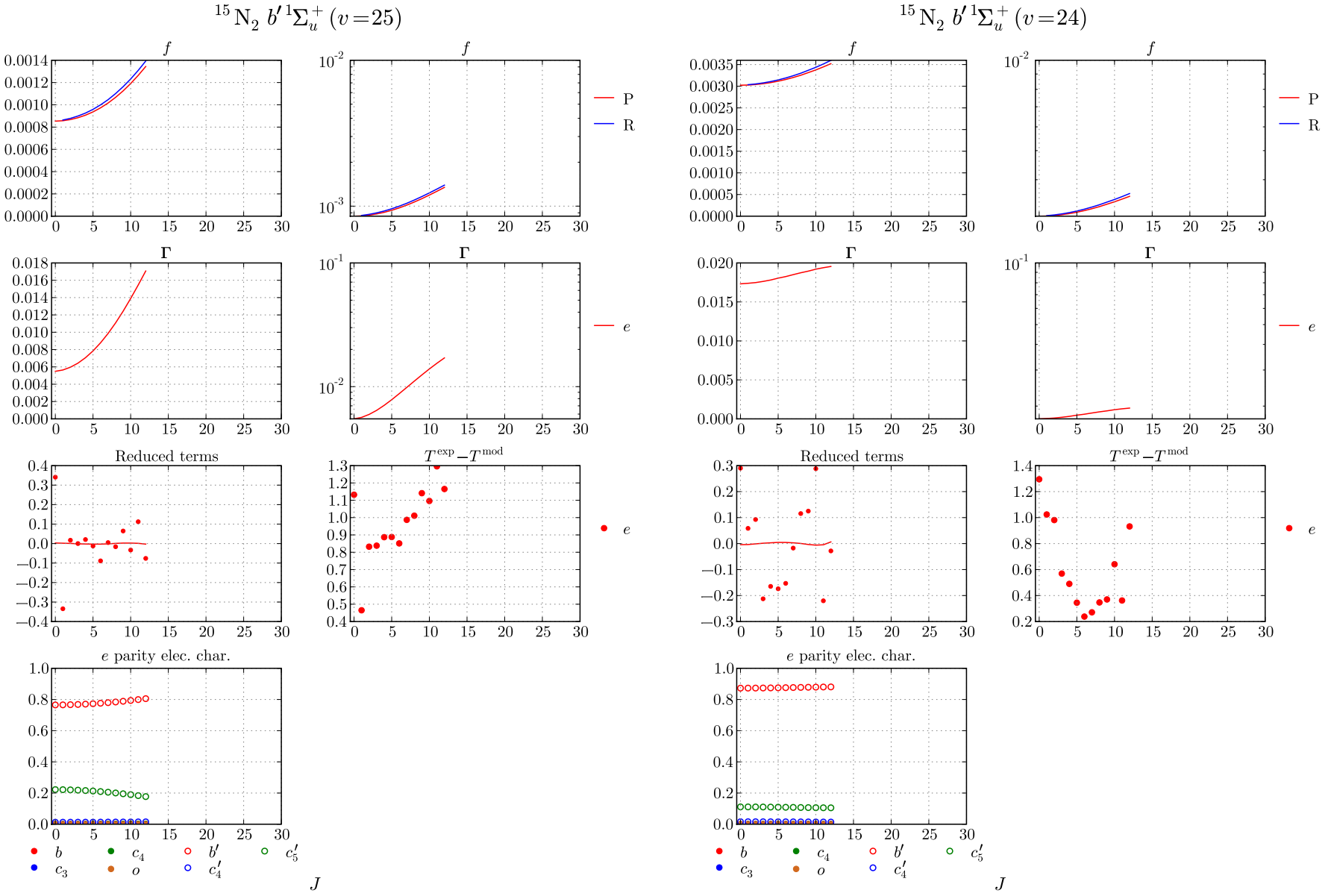
$^{15}N_2$ $b'^1\Sigma_u^+$ ($v=25$)
$^{15}N_2$ $b'^1\Sigma_u^+$ ($v=24$)
f
Γ
Reduced terms
$T^{exp}-T^{mod}$
e parity elec. char.
P
R
e
b
c_3
c_4
o
b'
c_4'
c_5'
J

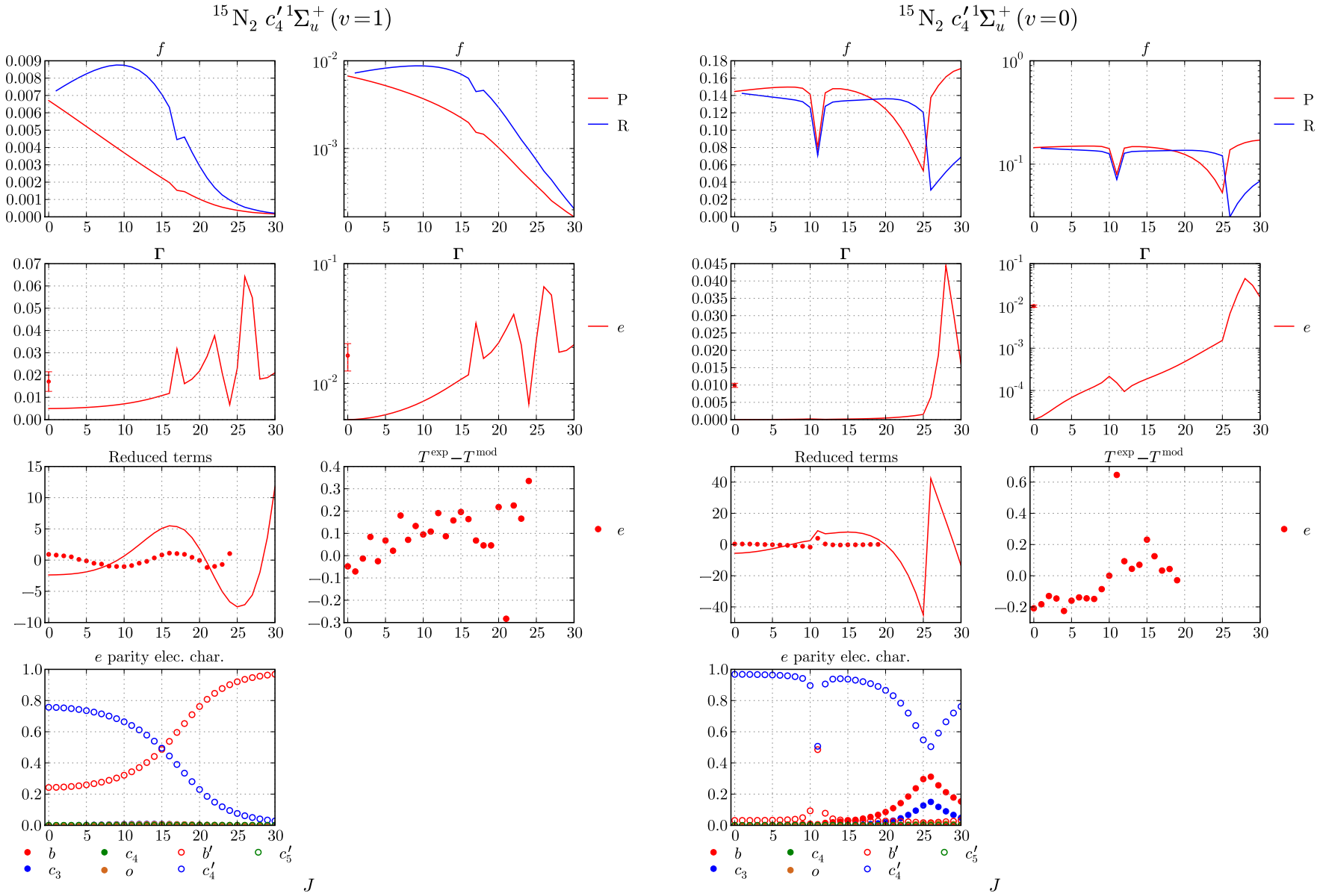
$^{15}N_2$ $c_4'^1\Sigma_u^+$ ($v=1$)
$^{15}N_2$ $c_4'^1\Sigma_u^+$ ($v=0$)
f
Γ
Reduced terms
$T^{\rm exp}-T^{\rm mod}$
e parity elec. char.
P
R
e
b
c_3
c_4
o
b'
c_4'
c_5'
J

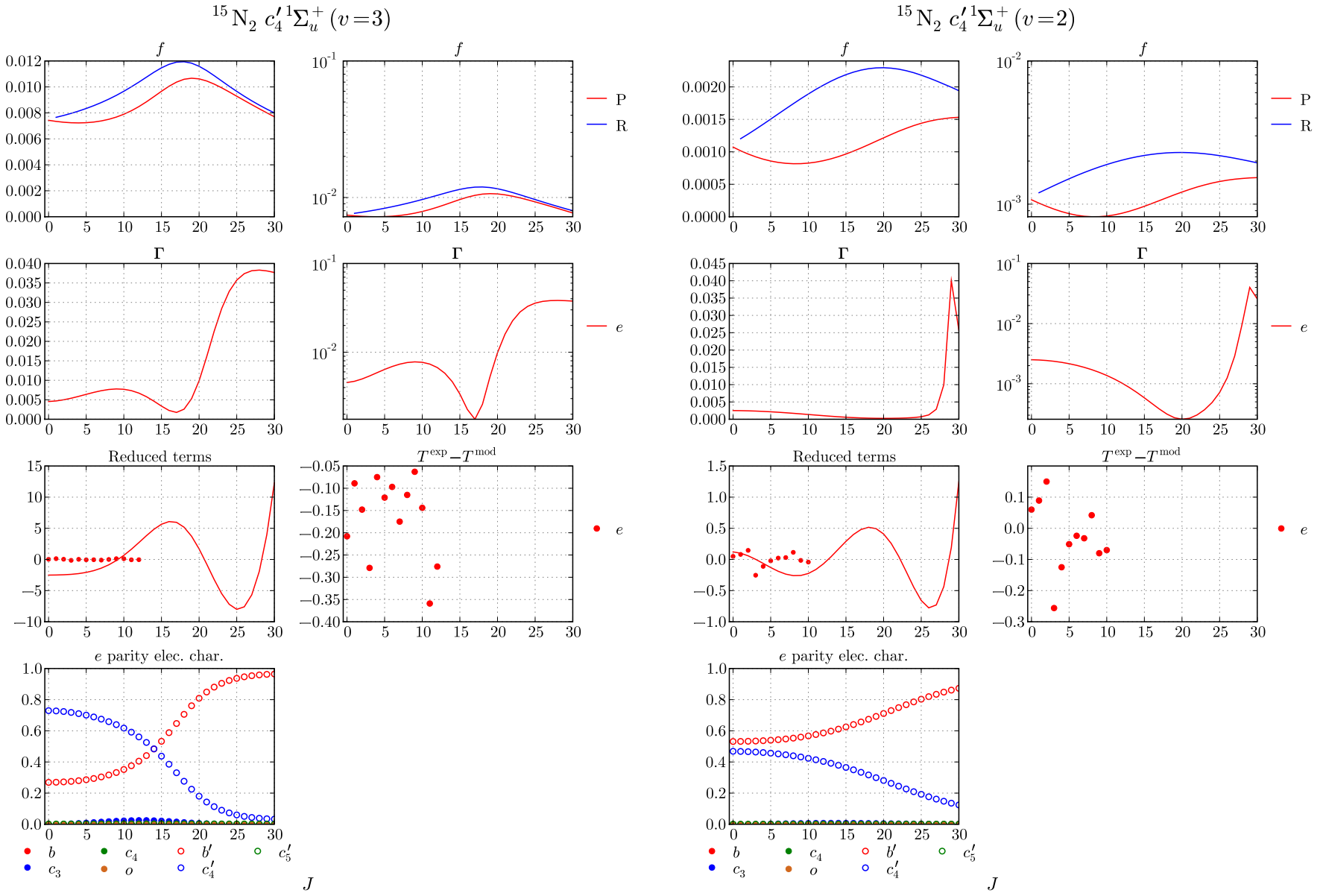
$^{15}N_2$ $c_4'\,^1\Sigma_u^+$ $(v=3)$
$^{15}N_2$ $c_4'\,^1\Sigma_u^+$ $(v=2)$
f
Γ
Reduced terms
$T^{exp}-T^{mod}$
e parity elec. char.
P
R
e
b
c_3
c_4
o
b'
c_4'
c_5'
J

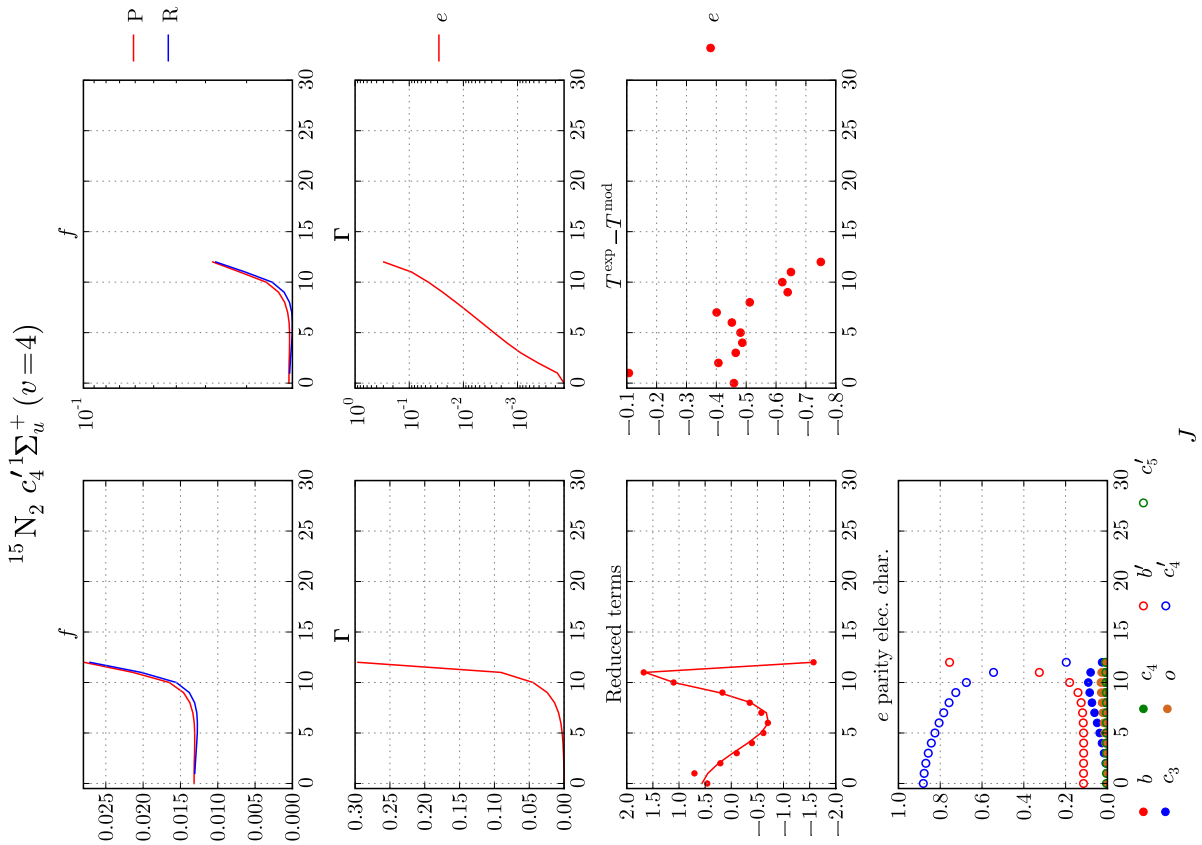
$^{15}N_2\ c_4'^1\Sigma_u^+\ (v=4)$
f
P
R
Γ
e
$T^{exp} - T^{mod}$
Reduced terms
e parity elec. char.
b
c_3
c_4
o
b'
c_4'
c_5'
J

Bibliography

[1] Ajello, J. M., James, G. K., Franklin, B. O., and Shemansky, D. E. (1989). Medium-resolution studies of extreme-ultraviolet emission from N_2 by electron-impact − Vibrational perturbations and cross-sections of the $c_4' \, ^1\Sigma_u^+$ and $b' \, ^1\Sigma_u^+$ states. *Phys. Rev. A*, 40(7):3524.

[2] Allison, A. C. and Dalgarno, A. (1971). Continuity at the dissociation threshold in molecular absorption. *J. Chem. Phys.*, 55(9):4342.

[3] Atabek, O., Lefebvre, R., and Requena, A. (1980). Semiclassical model for accidental predissociation in diatomic molecules. *J. Mol. Spectrosc.*, 82(2):364.

[4] Bakalian, F. (2006). Production of hot nitrogen atoms in the martian thermosphere. *Icarus*, 183(1):69.

[5] Bates, D. R. (1950). Dissociative recombination. *Phys. Rev.*, 78(4):492.

[6] Bendtsen, J. (2001). High-resolution Fourier transform Raman spectra of the fundamental bands of $^{14}N^{15}N$ and $^{15}N_2$. *J. Raman Spectrosc.*, 32(12):989.

[7] Bishop, J., Stevens, M. H., and Feldman, P. D. (2007). Molecular nitrogen Carroll-Yoshino $v' = 0$ emission in the thermospheric dayglow as seen by the Far Ultraviolet Spectroscopic Explorer. *J. Geophys. Res.*, 112(A10):A10312.

[8] Blume, M. and Watson, R. E. (1962). Theory of spin-orbit coupling in atoms. 1. Derivation of spin-orbit coupling constant. *Proc. R. Soc. London, Ser. A*, 270(1340):127.

[9] Bruna, P. J. and Grein, F. (2009). Theoretical study of electric moments, polarizabilities, and fine and hyperfine coupling constants of the $B \, ^3\Pi_g$, $C \, ^3\Pi_u$, $A' \, ^5\Sigma_g^+$, and $C'' \, ^5\Pi_u$ states of N_2. *Can. J. Phys.*, 87(5):589.

[10] Budó, A. (1935). Über die triplett-bandentermformel für den allgemeinen intermediären fall and anwendung derselben auf die $B^3\Pi_u$-, $C^3\Pi$-terme des N_2-moleküls. *Z. Phys.*, 96:219.

[11] Carroll, P. (1963). Structure of Goldstein-Kaplan bands of N_2. *Proc. R. Soc. London, Ser. A*, 272(1348):270.

[12] Carroll, P. K. (1973). Band structures in N_2 Rydberg complexes. *J. Chem. Phys.*, 58(9):3597.

[13] Carroll, P. K. and Collins, C. P. (1969). High resolution absorption studies of the $b^1\Pi_u \leftarrow X^1\Sigma_g^+$ system of nitrogen. *Can. J. Phys.*, 47:563.

[14] Carroll, P. K., Collins, C. P., and Yoshino, K. (1970). The high energy $^1\Sigma_u^+$ states of N_2. *J. Phys. B*, 3:L127.

[15] Carroll, P. K. and Hagim, K. I. (1988). Configuration interaction effects in molecular spectra. N_2: A case study. *Phys. Scr.*, 37(5):682.

[16] Carroll, P. K. and Mulliken, R. S. (1965). $^3\Pi$ levels and predissociations of N_2 near the 12.135 eV dissociation limit. *J. Chem. Phys.*, 43(7):2170.

[17] Carroll, P. K. and Yoshino, K. (1967). New Rydberg series of N_2. *J. Chem. Phys.*, 47(8):3073.

[18] Carroll, P. K. and Yoshino, K. (1972). The $c_n\,^1\Pi_u$ and $c'_n\,^1\Sigma_u^+$ Rydberg states of N_2: high resolution studies. *J. Phys. B*, 5:1614.

[19] Carter, V. L. (1972). High-resolution N_2 absorption study from 730 to 980 Å. *J. Chem. Phys.*, 56(8):4195.

[20] Chan, W. F., Cooper, G., and Brion, C. E. (1991). Absolute optical oscillator strengths for the electronic excitation of atoms at high resolution: Experimental methods and measurements for helium. *Phys. Rev. A*, 44(1):186.

[21] Chan, W. F., Cooper, G., Sodhi, R., and Brion, C. E. (1993). Absolute optical oscillator-strengths for discrete and continuum photoabsorption of molecular nitrogen ($11 - 200$ eV). *Chem. Phys.*, 170(1):81.

[22] Condon, E. U. and Shortley, G. H. (1957). *The theory of atomic spectra*, volume 1. Cambridge, London.

[23] Cosby, P. C. (1998). Personal communication to B.R. Lewis listing term values and predissociation branching ratios for many high energy $^1\Sigma_u^+$ and $^1\Pi_u$ bands.

[24] Cremaschi, P., Chattopadhyay, A., Madhavan, P., and Whitten, J. (1986). A theoretical-study of the Rydberg states of N_2 obtained from excitations of the valence $3\sigma_g$, $1\pi_u$, and $2\sigma_u$ levels. *Chem. Phys.*, 109(1):117.

[25] Dateo, C. (2004). Personal communication regarding *ab initio* calculations of some $^3\Pi_u$ and $^3\Sigma_u^+$ states of N_2.

[26] de Lange, A., Lang, R., van der Zande, W., and Ubachs, W. (2002). Highly excited states of gerade symmetry in molecular nitrogen. *J. Chem. Phys.*, 116(18):7893.

[27] de Oliveira, N., Joyeux, D., Phalippou, D., Rodier, J. C., Polack, F., Vervloet, M., and Nahon, L. (2009). A Fourier transform spectrometer without a beam splitter for the vacuum ultraviolet range: From the optical design to the first UV spectrum. *Rev. Sci. Instrum.*, 80(4):043101.

[28] DESIRS beamline (2010). Website the SOLEIL synchrotron facility. `http://www.synchrotron-soleil.fr/portal/page/portal/Recherche/LignesLumiere/DESIRS`.

[29] Douglas, A. E. (1953). Analysis of the $^2\Pi - ^2\Sigma$ bands of the N_2^+ Molecule. *Astrophys. J.*, 117:380.

[30] Dressler, K. (1969). The lowest valence and Rydberg states in the dipole-allowed absorption spectrum of nitrogen. A survey of their interactions. *Can. J. Phys.*, 47:547.

[31] Edwards, S., Roncin, J., Launay, F., and Rostas, F. (1993). The electronic ground-state of molecular nitrogen. *J. Mol. Spectrosc.*, 162(1):257.

[32] Edwards, S. A., Tchang-Brillet, W., Roncin, J. Y., Launay, F., and Rostas, F. (1995). Modeling the VUV emission-spectrum of N_2 − Preliminary results on the effects of rotational interactions on line-intensities. *Planet. Space Sci.*, 43(1-2):67.

[33] Ermler, W., McLean, A., and Mulliken, R. (1982). Ab initio study of valence state potential-energy curves of N_2. *J. Phys. Chem.*, 86(8):1305.

[34] Ermler, W. C., Clark, J. P., and Mulliken, R. S. (1987). Ab initio calculations of potential energy curves and transition moments of $^1\Sigma_g^+$ and $^1\Sigma_u^+$ states of N_2. *J. Chem. Phys.*, 86(1):370.

[35] Fano, U. (1961). Effects of configuration interaction on intensities and phase shifts. *Phys. Rev.*, 124(6):1866.

[36] Fano, U. and Cooper, J. W. (1968). Spectral distribution of atomic oscillator strengths. *Rev. Mod. Phys.*, 40(3):441.

[37] Feldman, P. D., Sahnow, D. J., Kruk, J. W., Murphy, E. M., and Moos, H. W. (2001). High-resolution FUV spectroscopy of the terrestrial day airglow with the Far Ultraviolet Spectroscopic Explorer. *J. Geophys. Res.*, 106(A5):8119.

[38] Geiger, J. and Schröder, H. (1969). Intensity perturbations due to configuration interaction observed in the electron energy-loss spectrum of N_2. *J. Chem. Phys.*, 50(1):7.

[39] Gerö, L. and Schmid, R. (1940). Rotationsanalyse der IV. positiven Banden des N_2-Moleküls. *Zeitschrift fr Physik A Hadrons and Nuclei*, 116:598.

[40] Gibson, S. T. and Lewis, B. R. (1996). Understanding diatomic photodissociation with a coupled-channel Schrödinger equation model. *J. Electron Spectrosc. Relat. Phenom.*, 80:9.

[41] Gordon, R. G. (1969). New method for constructing wavefunctions for bound states and scattering. *J. Chem. Phys.*, 51(1):14.

[42] Guberman, S. L. (1991). Dissociative recombination of the ground-state of N_2^+. *Geophys. Res. Lett.*, 18(6):1051.

[43] Guberman, S. L. (2009). Excited core states in the dissociative recombination of N_2^+. *J. Phys. Conf. Ser.*, 192(1):012001.

[44] Gurwell, M. (2004). Submillimeter observations of Titan: Global measures of stratospheric temperature, CO, HCN, HC_3N, and the isotopic ratios $^{12}C/^{13}C$ and $^{14}N/^{15}N$. *Astrophys. J.*, 616(1):L7.

[45] Hammond, P., King, G. C., Jureta, J., and Read, F. H. (1987). The threshold electron spectrum of molecular nitrogen. *J. Phys. B*, 20(16):4255.

[46] Hannemann, S., Hollenstein, U., van Duijn, E. J., and Ubachs, W. (2005). Production of narrowband tunable extreme-ultraviolet radiation by noncollinear resonance-enhanced four-wave mixing. *Opt. Lett.*, 30(12):1494.

[47] Harvard-Smithsonian Center for Astrophysics (2008). N_2 online archive. `http://www.cfa.harvard.edu/amp/ampdata/N2ARCHIVE/n2home.html`.

[48] Hashimoto, T. and Kanamori, H. (2006). A predissociative triplet Rydberg state of the nitrogen molecule studied by near-infrared diode laser kinetic spectroscopy. *J. Mol. Spectrosc.*, 235(1):104.

[49] Haverd, V., Lewis, B., Gibson, S., and Stark, G. (2005). Rotational effects in the band oscillator strengths and predissociation linewidths for the lowest $^1\Pi_u - X\,^1\Sigma_g^+$ transitions of N_2. *J. Chem. Phys.*, 123(21):214304.

[50] Heays, A. N., Lewis, B. R., Stark, G., Yoshino, K., Smith, P. L., Huber, K. P., and Ito, K. (2009a). Oscillator strengths and line widths of dipole-allowed transitions in $^{14}N_2$ between 86.0 and 89.7 nm. *J. Chem. Phys.*, 131(19):194308.

[51] Heays, A. N., Lewis, B. R., Stark, G., Yoshino, K., Smith, P. L., Huber, K. P., and Ito, K. (2009b). Oscillator strengths and line widths of dipole-allowed transitions in $^{14}N_2$ between 86.0 and 89.7 nm. Data archive. `http://netserver.aip.org/cgi-bin/epaps?ID=E-JCPSA6-131-061942`.

[52] Helm, H. and Cosby, P. C. (1989). Product branching in predissociation of the $e\,^1\Pi_u$, $e'\,^1\Sigma_u^+$, and $b'\,^1\Sigma_u^+$ states of N_2. *J. Chem. Phys.*, 90(8):4208.

[53] Helm, H., Hazell, I., and Bjerre, N. (1993). Lifetimes and Rydberg-valence state mixing of the $c'\,^1\Sigma_g^+(v=4)$ and $c\,^1\Pi_u(v=4)$ states of N_2. *Phys. Rev. A*, 48(4):2762.

[54] Herzberg, G. (1989). *Molecular Spectra and Molecular Structure I: Spectra of Diatomic Molecules*. Krieger Publishing Company, second edition.

[55] Hesser, J. E. and Dressler, K. (1966). Radiative lifetimes of ultraviolet molecular transitions. *J. Chem. Phys.*, 45(8):3149.

[56] Hougen, J. T. (1998). *The Calculation of Rotational Energy Levels and Rotational Line Intensities in Diatomic Molecules*. Physics Laboratory Publications, NIST.

[57] Huber, K. P. and Jungen, C. (1990). High-resolution jet absorption study of nitrogen near 800Å. *J. Chem. Phys.*, 92(2):850.

[58] Hudson, R. D. (1971). Critical review of ultraviolet photoabsorption cross sections for molecules of astrophysical and aeronomic interest. *Rev. Geophys. Space Phys.*, 9(2):305.

[59] Hudson, R. D. and Carter, V. L. (1968). Bandwidth dependence of measured UV absorption cross sections of argon. *J. Opt. Soc. Amer.*, 58(2):227.

[60] Hunten, D., Roach, F., and Chamberlain, J. (1956). A photometric unit for the airglow and aurora. *J. Atmos. Terr. Phys.*, 8(6):345.

[61] Inokuti, M. (1971). Inelastic collisions of fast charged particles with atoms and molecules − The Bethe theory revisited. *Rev. Mod. Phys.*, 43(3):297.

[62] Ito, K., Maeda, K., Morioka, Y., and Namioka, T. (1989). Performance of the 6VOPE high-resolution VUV spectroscopic facility in the photoelectric detection mode. *Appl. Opt.*, 28(10):1813.

[63] Ito, K., Namioka, T., Morioka, Y., Sasaki, T., Noda, H., Goto, K., Katayama, T., and Koike, M. (1986). High-resolution VUV spectroscopic facility at the Photon-Factory. *Appl. Opt.*, 25(6):837.

[64] James, G. K., Ajello, J. M., Franklin, B. O., and Shemansky, D. E. (1990). Medium resolution studies of extreme ultraviolet emission from N_2 by electron-impact − The effect of predissociation on the emission cross-section of the $b\,^1\Pi_u$ state. *J. Phys. B*, 23(12):2055.

[65] Johns, J. W. C. and Lepard, D. W. (1975). Calculation of rotation-electronic energies and relative transition intensities in diatomic molecules. *J. Mol. Spectrosc.*, 55(1-3):374.

[66] Johnson, B. (1977). New numerical-methods applied to solving the one-dimensional eigenvalue problem. *J. Chem. Phys.*, 67(9):4086.

[67] Johnson, B. R. (1978). The renormalized Numerov method applied to calculating bound states of the coupled-channel Schrödinger equation. *J. Chem. Phys.*, 69:4678.

[68] Johnson, P. V., Malone, C. P., Kanik, I., Tran, K., and Khakoo, M. A. (2005). Integral cross sections for the direct excitation of the $A\,^3\Sigma_u^+$, $B\,^3\Pi_g$, $W\,^3\Delta_u$, $B'\,^3\Sigma_u^-$, $a'\,^1\Sigma_u^-$, $a\,^1\Pi_g$, $w\,^1\Delta_u$, and $C\,^3\Pi_u$ electronic states in N_2 by electron impact. *J. Geophys. Res.*, 110(A11).

[69] Joyez, G., Hall, R. I., Reinhardt, J., and Mazeau, J. (1973). Low energy electron spectroscopy of N_2 in the 11.8−13.8 eV energy range. *J. Electron Spectrosc. Relat. Phenom.*, 2(2):183.

[70] Julienne, P. S. and Krauss, M. (1975). Predissociation of the Schumann-Runge bands of O_2. *J. Mol. Spectrosc.*, 56(2):270.

[71] Jungen, C., editor (1996). *Molecular applications of quantum defect theory.* IOP Publishing, London.

[72] K. P. Huber and G. Herzberg (1979). *Molecular spectra and molecular structure IV: Constants of diatomic molecules.* Van Nostrand, New York.

[73] Kam, A. W., Lawall, J. R., Lindsay, M. D., Pipkin, F. M., Short, R. C., and Zhao, P. (1989). Precise spectroscopy and lifetime measurement of electron-impact-excited N_2 − The $c'\,^1\Sigma_u^+(v=3)$ Rydberg level. *Phys. Rev. A*, 40(3):1279.

[74] Kanamori, H., Takashima, S., and Sakurai, K. (1991). Near-infrared diode laser spectroscopy of the nitrogen molecule in Rydberg states. *J. Chem. Phys.*, 95(1):80.

[75] Kawamoto, Y., Fujitake, M., and Ohashi, N. (1997). Near-infrared diode laser spectroscopy of the nitrogen molecule in Rydberg state: Analysis of the $c\,^1\Pi_u - a''\,^1\Sigma_g^+$, $v = 1 - 0$ band. *J. Mol. Spectrosc.*, 185:330.

[76] Khakoo, M. A., Johnson, P. V., Ozkay, I., Yan, P., Trajmar, S., and Kanik, I. (2005). Differential cross sections for the electron impact excitation of the $A\,^3\Sigma_u^+$, $B\,^3\Pi_g$, $W\,^3\Delta_u$, $B'\,^3\Sigma_u^-$, $a'\,^1\Sigma_u^-$, $a\,^1\Pi_g$, $w\,^1\Delta_u$, and $C\,^3\Pi_u$ states of N_2. *Phys. Rev. A*, 71(6).

[77] Khakoo, M. A., Malone, C. P., Johnson, P. V., Lewis, B. R., Laher, R., Wang, S., Swaminathan, V., Nuyujukian, D., and Kanik, I. (2008). Electron-impact excitation of $X\,^1\Sigma_g^+(v''=0)$ to the $a''\,^1\Sigma_g^+$, $b\,^1\Pi_u$, $c_3\,^1\Pi_u$, $o_3\,^1\Pi_u$, $b'\,^1\Sigma_u^+$, $c_4'\,^1\Sigma_u^+$, $G\,^3\Pi_u$, and $F\,^3\Pi_u$ states of molecular nitrogen. *Phys. Rev. A*, 77(1):012704.

[78] Klynning, L. and Pages, P. (1982). The band spectrum of N_2^+. *Phys. Scr.*, 25(4):543.

[79] Knauth, D. C., Andersson, B.-G., McCandliss, S. R., and Moos, H. W. (2004). The interstellar N_2 abundance towards HD 124314 from far-ultraviolet observations. *Nature*, 429:636.

[80] Kono, M., Lewis, B. R., Baldwin, K. G. H., and Gibson, S. T. (2003). Experimental verification of line- and band-shape asymmetry in the Schumann-Runge system of O_2. *J. Phys. Chem.*, 118(24):10924.

[81] Kurzweg, L., Egbert, G. T., and Burns, D. J. (1973). Lifetime of the $D^3\Sigma_u^+$ state of N_2. *J. Chem. Phys.*, 59(5):2641.

[82] Lawrence, G. M., Mickey, D. L., and Dressler, K. (1968). Absolute oscillator strengths of the strongest bands within the dipole-allowed absorption spectrum of nitrogen. *J. Chem. Phys.*, 48(5):1989.

[83] Le Roy, J. P. and Wallace, R. (1985). Renormalized Numerov method applied to eigenvalue equations: extension to include single derivative terms and a variety of boundary conditions. *J. Phys. Chem.*, 89(10):1928.

[84] Le Roy, R. J., Huang, Y., and Jary, C. (2006). An accurate analytic potential function for ground-state N_2 from a direct-potential-fit analysis of spectroscopic data. *J. Chem. Phys.*, 125(16):164310.

[85] Learner, R. C. M., Thorne, A. P., and Brault, J. W. (1996). Ghosts and artifacts in Fourier-transform spectrometry. *Appl. Opt.*, 35(16):2947.

[86] Ledbetter, J. (1977). A new band of N_2 and identification of the lower vibronic level of C', $v = 1$ and C, $v = 5$ $^3\Pi_u$ state interaction. *J. Chem. Phys.*, 67(7):3400.

[87] Ledbetter, J. W. and Dressler, K. (1976). Interaction of the $C'\,^3\Pi_u$ and $C\,^3\Pi_u$ states in $^{14}N_2$, $^{14}N^{15}N$, and $^{15}N_2$. *J. Mol. Spectrosc.*, 63(3):370.

[88] Lefebvre, R. (1992). Back rotation of complex rotated resonance wave functions: A numerical study. *Phys. Rev. A*, 46(9):6071.

[89] Lefebvre-Brion, H. (1969). Theoretical study of homogeneous perturbations. II. least-squares fitting method to obtain "deperturbed" crossing Morse curves. application to the perturbed $^1\Sigma_u^+$ states of N_2. *Can. J. Phys.*, 47:541.

[90] Lefebvre-Brion, H. and Field, R. W. (2004). *Perturbations in the spectra of diatomic molecules*. Academic Press, Amsterdam, Revised and enlarged edition.

[91] Lefebvre-Brion, H. and Lewis, B. R. (2007). Comparison between predissociation mechanisms in two isoelectronic molecules: CO and N_2. *Mol. Phys.*, 105(11-12):1625.

[92] Lefebvre-Brion, H. and Moser, C. M. (1965). Calculation of Rydberg levels in the nitrogen molecule. *J. Chem. Phys.*, 43(4):1394.

[93] Leoni, M. and Dressler, K. (1971). Predissociation probabilities and determination of a repulsive potential in the N_2 molecule. *J. Appl. Math. Phys.*, 22:794.

[94] Levelt, P. F. and Ubachs, W. (1992). XUV-laser spectroscopy on the $c_4'\,^1\Sigma_u^+(v = 0)$ and $c_3\,^1\Pi_u(v = 0)$ Rydberg states of N_2. *Chem. Phys.*, 163:263.

[95] Lewis, B., Gibson, S., Hawes, F., and Torop, L. (2001a). A new model for the Schumann-Runge bands of O_2. *Phys. Chem. Earth*, 26(7):519.

[96] Lewis, B., Gibson, S., Torop, L., and McCoy, D. (1998). Quantum interference in the Schumann-Runge bands of molecular oxygen. *Geophys. Res. Lett.*, 25(13):2457.

[97] Lewis, B. R., Baldwin, K. G. H., Heays, A. N., Gibson, S. T., Sprengers, J. P., Ubachs, W., and Fujitake, M. (2008a). Structure and predissociation of the $3p\sigma_u\, D\, ^3\Sigma_u^+$ Rydberg state of N_2: First extreme-ultraviolet and new near-infrared observations, with coupled-channels analysis. *J. Chem. Phys.*, 129(20):204303.

[98] Lewis, B. R., Baldwin, K. G. H., Sprengers, J. P., Ubachs, W., Stark, G., and Yoshino, K. (2008b). Optical observation of the C, $3s\sigma_g\, F_3$, and $3p\pi_u\, G_3\ ^3\Pi_u$ states of N_2. *J. Chem. Phys.*, 129(16):164305.

[99] Lewis, B. R., Banerjee, S. S., and Gibson, S. T. (1995). Asymmetric line shapes in the indirect predissociation of the $f^1\Sigma_u^+$ rydberg state of O_2. *J. Chem. Phys.*, 102(17):6631.

[100] Lewis, B. R., Berzins, L., and Carver, J. H. (1986). Oscillator strengths for the Schumann-Runge bands of $^{16}O_2$. *J. Quant. Spectrosc. Radiat. Transfer*, 36(3):209.

[101] Lewis, B. R., Dooley, P. M., England, J. P., Waring, K., Gibson, S. T., Baldwin, K. G. H., and Partridge, H. (1996). Observation of the second $^3\Pi_u$ valence state of O_2. *Phys. Rev. A*, 54(5):3923.

[102] Lewis, B. R., England, J. P., Gibson, S. T., Brunger, M. J., and Allan, M. (2001b). Electron energy-loss spectra of coupled electronic states: Effects of Rydberg-valence interactions in O_2 . *Phys. Rev. A*, 63(2):022707.

[103] Lewis, B. R., Gibson, S. T., Sprengers, J. P., Ubachs, W., Johansson, A., and Wahlström, C. (2005a). Lifetime and predissociation yield of $^{14}N_2\, b\, ^1\Pi_u(v = 1)$ revisited: Effects of rotation. *J. Chem. Phys.*, 123(23):236101.

[104] Lewis, B. R., Gibson, S. T., Zhang, W., Lefebvre-Brion, H., and Robbe, J. M. (2005b). Predissociation mechanism for the lowest $^1\Pi_u$ states of N_2. *J. Chem. Phys.*, 122:144302.

[105] Lewis, B. R., Heays, A. N., Gibson, S. T., Lefebvre-Brion, H., and Lefebvre, R. (2008c). A coupled-channel model of the $^3\Pi_u$ states of N_2: Structure and interactions of the $3s\sigma\, F_3{}^3\Pi_u$ and $3p\pi_u\, G_3{}^3\Pi_u$ Rydberg states. *J. Chem. Phys.*, 129(16):164306.

[106] Liang, M.-C., Heays, A. N., Lewis, B. R., Gibson, S. T., and Yung, Y. L. (2007). Source of nitrogen isotope anomaly in HCN in the atmosphere of Titan. *Astrophys. J.*, 664(2):L115.

[107] Liu, X., Heays, A. N., Shemansky, D. E., Lewis, B. R., and Feldman, P. D. (2009). Analysis of terrestrial-thermospheric N_2 $c_4'\, ^1\Sigma_u^+(0) \sim b'\, ^1\Sigma_u^+(1) - X\, ^1\Sigma_g^+$ by the Far Ultraviolet Spectroscopic Explorer. *J. Geophys. Res.*, 114:D07304.

[108] Liu, X., Shemanksy, D. E., Ciocca, M., Kanik, I., and Ajello, J. M. (2005). Analysis of the physical properties of the N_2 $c'^1\Sigma_u^+(0) - X^1\Sigma_g^+(0)$ transition. *Astrophys. J.*, 623:579.

[109] Liu, X. and Shemansky, D. E. (2006). A simple model for N_2 line oscillator strengths of the $b'\,^1\Sigma_u^+(1)$, $c_4'\,^1\Sigma_u^+(0)$, $b\,^1\Pi_u(4)$, $b\,^1\Pi_u(5)$, and $c_3\,^1\Pi_u(0) - X\,^1\Sigma_g^+(0)$ bands. *Astrophys. J.*, 645(2):1560.

[110] Liu, X., Shemansky, D. E., Malone, C. P., Johnson, P. V., Ajello, J. M., Kanik, I., Heays, A. N., Lewis, B. R., Gibson, S. T., and Stark, G. (2008). Experimental and coupled-channels investigation of the radiative properties of the N_2 $c_4'\,^1\Sigma_u^+ - X\,^1\Sigma_g^+$ band system. *J. Geophys. Res.*, 113(A2):A02304.

[111] Lofthus, A. and Krupenie, P. H. (1977). The spectrum of molecular nitrogen. *Journal of Physical Chemistry Reference Data*, 6(1):113.

[112] Malone, C. P., Johnson, P. V., Kanik, I., Ajdari, B., and Khakoo, M. A. (2009a). Electron-impact excitation of molecular nitrogen. I. Excitation of the $C\,^3\Pi_u$, $E\,^3\Sigma_g^+$, and $a''\,^1\Sigma_g^+$ states. *Phys. Rev. A*, 79(3):032704.

[113] Malone, C. P., Johnson, P. V., Kanik, I., Ajdari, B., Rahman, S. S., Bata, S. S., Emigh, A., and Khakoo, M. A. (2009b). Electron-impact excitation of molecular nitrogen. II. Vibrationally resolved excitation of the $C\,^3\Pi_u(v')$ state. *Phys. Rev. A*, 79(3):032705.

[114] Marquardt, D. W. (1963). An algorithm for least-squares estimation of nonlinear parameters. *SIAM J. Appl. Math.*, 11(2):431.

[115] Marten, A., Hidayat, T., Biraud, Y., and Moreno, R. (2002). New millimeter heterodyne observations of Titan: Vertical distributions of nitriles HCN, HC_3N, CH_3CN, and the isotopic ratio $^{15}N/^{14}N$ in its atmosphere. *Icarus*, 158(2):532.

[116] Meier, R. R. (1991). Ultraviolet spectroscopy and remote-sensing of the upper-atmosphere. *Space Sci. Rev.*, 58(1-2):1.

[117] Mies, F. H. (1980a). A scattering theory of diatomic molecules, expansion in adiabatic electronic-rotational states. *Mol. Phys.*, 41(5):973.

[118] Mies, F. H. (1980b). A scattering theory of diatomic molecules, general formalism using the channel state representation. *Mol. Phys.*, 41(5):953.

[119] Mies, F. H. (1984). A multichannel quantum defect analysis of diatomic predissociation and inelastic atomic scattering. *J. Chem. Phys.*, 80(6):2514.

[120] Mies, F. H. and Julienne, P. S. (1984). A multichannel quantum defect analysis of two-state couplings in diatomic molecules. *J. Chem. Phys.*, 80(6):2526.

[121] Mulliken, R. S. (1964). The Rydberg states of molecules. Parts I-V. *Journal of the American Chemical Society*, 80:3184.

[122] Ndome, H., Hochlaf, M., Lewis, B. R., Heays, A. N., Gibson, S. T., and Lefebvre-Brion, H. (2008). Sign reversal of the spin-orbit constant for the $C\,^3\Pi_u$ state of N_2. *J. Chem. Phys.*, 129(16):164307.

[123] Nicolaides, C. A. and Beck, D. R. (1978). The variational calculation of energies and widths of resonances. *Phys. Lett. A*, 65(1):11.

[124] Niemann, H., Atreya, S., Bauer, S., Carignan, G., Demick, J., Frost, R., Gautier, D., Haberman, J., Harpold, D., Hunten, D., Israel, G., Lunine, J., Kasprzak, W., Owen, T., Paulkovich, M., Raulin, F., Raaen, E., and Way, S. (2005). The abundances of constituents of Titan's atmosphere from the GCMS instrument on the Huygens probe. *Nature*, 438(7069):779.

[125] Oertel, H., Kratzat, M., Imschweiler, J., and Noll, T. (1981). Fluorescence from $^1\Pi_u$ and $^1\Sigma_u^+$ states of molecular nitrogen excited with synchrotron radiation between 12.4 and 18.8 eV. *Chem. Phys. Lett.*, 82(3):552.

[126] Owen, T. and Encrenaz, T. (2003). Element abundances and isotope ratios in the giant planets and Titan. *Space Sci. Rev.*, 106:121. 10.1023/A:1024633603624.

[127] Pack, R. and Hirschfelder, J. (1968). Separation of rotational coordinates from the N-electron diatomic Schrödinger equation. *J. Chem. Phys.*, 49(9):4009.

[128] Partridge, H. (1998). Personal communication regarding *ab initio* calculations of some $^3\Pi_u$ states of N_2.

[129] Philip, J., Sprengers, J. P., Cacciani, P., Lange, C. A. D., and Ubachs, W. (2004). Frequency-mixing scheme for the production of tunable narrowband XUV radiation (91-95nm): application to precision spectroscopy and predissocation in diatomic molecules. *Appl. Phys. B*, 78:737.

[130] Roncin, J. Y., Launay, F., Bredohl, H., and Dubois, I. (1999). The vacuum ultraviolet absorption bands of the pink afterglow spectrum of molecular nitrogen revisited at high resolution. *J. Mol. Spectrosc.*, 194(2):243.

[131] Roncin, J. Y., Launay, F., and Larzilliere, M. (1984). Evidence for predissociation of N_2 into $N(D_2)$+$N(D_2)$ from new high-resolution vacuum-ultraviolet emission bands. *Phys. Rev. Lett.*, 53(2):159.

[132] Roncin, J. Y., Launay, F., Subtil, J. L., and Yoshino, K. (1991). New emission bands in the high-resolution spectrum of molecular nitrogen between 107.7 and 124.2 nm. *Planet. Space Sci.*, 39(9):1301.

[133] Roncin, J. Y., Launay, F., and Yoshino, K. (1987). New emission bands in the high-resolution vacuum ultra-violet spectrum of molecular nitrogen. *Planet. Space Sci.*, 35(2):267.

[134] Roncin, J. Y., Launay, F., and Yoshino, K. (1989). Vacuum ultraviolet emission from highly excited-states of molecular nitrogen. *J. Mol. Spectrosc.*, 134(2):390.

[135] Roncin, J. Y., Subtil, J. L., and Launay, F. (1998). The high-resolution vacuum ultraviolet emission spectrum of molecular nitrogen from 82.6 to 124.2 nm: Level energies of 10 excited singlet electronic states. *J. Mol. Spectrosc.*, 188(2):128.

[136] Roux, F., Michaud, F., and Vervloet, M. (1989). High-resolution Fourier spectrometry of $^{14}N_2$: Analysis of the $(0-0)$, $(0-1)$, $(0-2)$, $(0-3)$ bands of the $C\,^3\Pi_u - B\,^3\Pi_g$ system. *Can. J. Phys.*, 67(2-3):143.

[137] Schinke, R. (1993). *Photodissociation Dynamics*. University Press, Cambridge.

[138] Schutte, C. J. H. (1976). *The theory of molecular spectroscopy*, volume I. North-Holland Publishing Company.

[139] Shemansky, D., Kanik, I., and Ajello, J. (1995). Fine-structure branching in N_2 $c'(4)\,^1\Sigma_u^+(0)$. *Astrophys. J.*, 452(1):480.

[140] Shore, B. W. (1973). Comparison of matrix methods applied to the radial Schrödinger eigenvalue equation: The Morse potential. *J. Chem. Phys.*, 59(12):6450.

[141] Simon, B. (1979). The definition of molecular resonance curves by the method of exterior complex scaling. *Phys. Lett. A*, 71(2-3):211.

[142] Slater, J. C. (1963). *Quantum theory of molecules and solids*, volume 1. McGraw Hill.

[143] Slater, J. C. (1968). *Quantum theory of matter*. McGraw Hill, 2 edition.

[144] Sommavilla, M. (2004). *Photoabsorptions-, Photoionisations- und Photoelektronen-spektroskopie von Atomen and kleinen Molekülen im VUV-Bereich*. PhD thesis, Eidgenössischen Technischen Hochschule, Zürich.

[145] Spelsberg, D. and Meyer, W. (2001). Dipole-allowed excited states of N_2: Potential energy curves, vibrational analysis, and absorption intensities. *J. Chem. Phys.*, 115(14):6438.

[146] Sprengers, J. P. (2006). *Extreme ultraviolet laser excitation of molecular nitrogen: Perturbations and predissociation*. PhD thesis, Vrije Universiteit.

[147] Sprengers, J. P., Johansson, A., L'Huillier, A., Wahlström, C. G., Lewis, B., and Ubachs, W. (2004a). Pump-probe lifetime measurements on singlet ungerade states in molecular nitrogen. *Chem. Phys. Lett.*, 389(4-6):348.

[148] Sprengers, J. P., Reinhold, E., Ubachs, W., Baldwin, K. G. H., and Lewis, B. R. (2005). Optical observation of the $3s\sigma_g F^3\Pi_u$ Rydberg state of N_2. *J. Chem. Phys.*, 123:144315.

[149] Sprengers, J. P. and Ubachs, W. (2005). Isotopic variation of experimental lifetimes for the lowest $^1\Pi_u$ states of N_2. *J. Chem. Phys.*, 122:144301.

[150] Sprengers, J. P. and Ubachs, W. (2006). Lifetime and transition frequences of several singlet *ungerade* states in N_2 between 106 000 and 109 000 cm^{-1}. *J. Mol. Spectrosc.*, 235:176.

[151] Sprengers, J. P., Ubachs, W., Baldwin, K. G. H., Lewis, B. R., and Tchang-Brillet, W.-U. L. (2003). Extreme ultraviolet laser excitation of isotopic molecular nitrogen: the dipole-allowed spectrum of $^{15}N_2$ and $^{14}N^{15}N$. *J. Chem. Phys.*, 119(6):3160.

[152] Sprengers, J. P., Ubachs, W., Johansson, A., L'Huillier, A., Wahlström, C.-G., Lang, R., Lewis, B. R., and Gibson, S. T. (2004b). Lifetime and predissociation yield of $^{14}N_2$ $b^1\Pi_u(v=1)$. *J. Chem. Phys.*, 120(19):8973.

[153] Stahel, D., Leoni, M., and Dressler, K. (1983). Nonadiabatic representations of the $^1\Sigma_u^+$ and $^1\Pi_u$ states of the N_2 molecule. *J. Chem. Phys.*, 79(6):2541.

[154] Stark, G., Huber, K. P., Yoshino, K., Chan, M. C., Matsui, T., Smith, P., and Ito, K. (2000). Line oscillator strength measurements in the $0-0$ band of the $c_4'\,{}^1\Sigma_u^+ \leftarrow X\,{}^1\Sigma_g^+$ transition of N_2. *Astrophys. J.*, 531(1):321.

[155] Stark, G., Huber, K. P., Yoshino, K., Smith, P. L., and Ito, K. (2005a). Oscillator strength and line width measurements of dipole-allowed transition in $^{14}N_2$ between 93.5 and 99.5nm. *J. Chem. Phys.*, 123:214303.

[156] Stark, G., Huber, K. P., Yoshino, K., Smith, P. L., and Ito, K. (2005b). Oscillator strength and line width measurements of dipole-allowed transition in $^{14}N_2$ between 93.5 and 99.5 nm. Data archive. `http://netserver.aip.org/cgi-bin/epaps?ID=E-JCPSA6-123-020544`.

[157] Stark, G., Lewis, B. R., Heays, A. N., Yoshino, K., Smith, P. L., and Ito, K. (2008a). Oscillator strengths and line widths of dipole-allowed transitions in $^{14}N_2$ between 89.7 and 93.5 nm. *J. Chem. Phys.*, 128(11):114302.

[158] Stark, G., Lewis, B. R., Heays, A. N., Yoshino, K., Smith, P. L., and Ito, K. (2008b). Oscillator strengths and line widths of dipole-allowed transitions in $^{14}N_2$ between 89.7 and 93.5 nm. Data archive. `http://netserver.aip.org/cgi-bin/epaps?ID=E-JCPSA6-128-012806`.

[159] Stark, G., Smith, P. L., Huber, K. P., Yoshino, K., Stevens, M. H., and Ito, K. (1992). Absorption-band oscillator-strengths of N_2 transitions between 95.8 and 99.4 nm. *J. Chem. Phys.*, 97(7):4809.

[160] Stevens, M. (2001). The EUV airglow of Titan: Production and loss of N_2 $c_4'(0)-X$. *J. Geophys. Res.*, 106(A3):3685.

[161] Strobel, D., Meier, R., Summers, M., and Strickland, D. (1991). Nitrogen airglow sources - comparison of Triton, Titan, and Earth. *Geophys. Res. Lett.*, 18(4):689.

[162] Tanaka, Y. and Jursa, A. (1961). A new method for producing auroral afterglow of nitrogen and its spectrum. *J. Opt. Soc. Amer.*, 51(11):1239.

[163] Tanaka, Y., Ogawa, M., and Jursa, A. S. (1964). Forbidden absorption-band systems of N_2 in the vacuum-ultraviolet region. *J. Chem. Phys.*, 40(12):3690.

[164] Thorne, A. P. (1991). Fourier transform spectrometry in the ultraviolet. *Anal. Chem.*, 63(2):57A.

[165] Tilford, S., JT, V., and PG, W. (1965). High-resolution absorption spectrum of nitrogen from 1060 to 1520 Å. V. the $C\,{}^3\Pi_u \leftarrow X\,{}^1\Sigma_g^+$ system. *Astrophys. J.*, 142(3):1203.

[166] Tilford, S., PG, W., Franklin, V., Naber, R., Benesch, W., and JT, V. (1966). Summary of observed absorption lines of room-temperature molecular nitrogen between 1060 and 1520 å. *Astrophys. J.*, S 13(Suppl. 115):31.

[167] Torop, L., Mccoy, D., Blake, A., Wang, J., and Scholz, T. (1987). Effects of the close approach of potential curves in photoabsorption by diatomic-molecules. 1. Theory and computational procedures. *J. Quant. Spectrosc. Radiat. Transfer*, 38(1):9.

[168] Ubachs, W. (1997). Predissociative decay of the $c_4'\,{}^1\Sigma_u^+(v=0)$ state of N_2. *Chem. Phys. Lett.*, 2568:201.

[169] Ubachs, W., Eikema, K. S. E., and Hogervorst, W. (1993). Narrow-band extreme-ultraviolet laser radiation tunable in the range 90.5–95nm. *Appl. Phys. B*, 57:411.

[170] Ubachs, W., Lang, R., Velchev, I., Tchang-Brillet, W.-L., Johansson, A., Li, Z. S., Lokhnygin, V., and Wahlström, C.-G. (2001). Lifetime measurements of the $c_4'\,^1\Sigma_u^+$, $v = 0$, 1 and 2 states of molecular nitrogen. *Chem. Phys.*, 270:215.

[171] Ubachs, W., Tashiro, L., and Zare, R. N. (1989). Study of the N_2 $b\,^1\Pi_u$ state via $1 + 1$ multiphoton ionization. *Chem. Phys.*, 130(1-3):1.

[172] Ubachs, W., Velchev, I., and De Lange, A. (2000). Predissociation in $b\,^1\Pi_u$, ($v = 1, 4, 5, 6$) levels of N_2. *J. Chem. Phys.*, 112(13):5711.

[173] van der Kamp, A. B., Cosby, P. C., and van der Zande, W. J. (1994). Charge-transfer production of predissociated N_2 states. 1. The $n = 3$ Rydberg state region ($12.8 - 14$ eV). *Chem. Phys.*, 184(1-3):319.

[174] van Dishoeck, E. F., van Hemert, M. C., Allison, A. C., and Dalgarno, A. (1984). Resonances in the photodissociation of OH by absorption into coupled $^2\Pi$ states: Adiabatic and diabatic formulations. *J. Chem. Phys.*, 81(12):5709.

[175] Veseth, L. (1970). Spin-orbit and spin-other-orbit interaction in diatomic molecules. *Theor. Chim. Acta*, 18(4):368.

[176] Vieitez, M., Ivanov, T., Ubachs, W., Lewis, B., and de Lange, C. (2008a). On the complexity of the absorption spectrum of molecular nitrogen. *J. Mol. Liq.*, 141(3):110.

[177] Vieitez, M. O. (2010). *XUV laser studies of Rydberg-valence states in N_2 and H^+H^- heavy Rydberg states*. PhD thesis, Vrije Universiteit.

[178] Vieitez, M. O., Ivanov, T. I., de Lange, C. A., Ubachs, W., Heays, A. N., Lewis, B. R., and Stark, G. (2008b). Interactions of the $3p\pi_u\,c^1\Pi_u(v = 2)$ Rydberg-complex member in isotopic N_2. *J. Chem. Phys.*, 128(13):134313.

[179] Vieitez, M. O., Ivanov, T. I., Sprengers, J. P., De Lange, C. A., Ubachs, W., Lewis, B. R., and Stark, G. (2007). Quantum-interference effects in the $o\,^1\Pi_u(v = 1) \sim b\,^1\Pi_u(v = 9)$ Rydberg-valence complex of molecular nitrogen. *Mol. Phys.*, 105(11-12):1543.

[180] Waite, J., Niemann, H., Yelle, R., Kasprzak, W., Cravens, T., Luhmann, J., McNutt, R., Ip, W., Gell, D., De La Haye, V., Muller-Wordag, I., Magee, B., Borggren, N., Ledvina, S., Fletcher, G., Walter, E., Miller, R., Scherer, S., Thorpe, R., Xu, J., Block, B., and Arnett, K. (2005). Ion Neutral Mass Spectrometer results from the first flyby of Titan. *Science*, 308(5724):982.

[181] Walter, C. W., Cosby, P. C., and Helm, H. (1993). $N(^4S_0)$, $N(^2D_0)$, and $N(^2P_0)$ yields in predissociation of excited singlet-states of N_2. *J. Chem. Phys.*, 99(5):3553.

[182] Walter, C. W., Cosby, P. C., and Helm, H. (1994). Predissociation quantum yields of singlet nitrogen. *Phys. Rev. A*, 50(4):2930.

[183] Walter, C. W., Cosby, P. C., and Helm, H. (2000). Photoexcitation and predissociation intensities of the $c'\,^1\Sigma_u^+$ ($v = 3$ and 4), $c\,^1\Pi_u$ ($v = 3$ and 4), and $b'\,^1\Sigma_u^+$ ($v = 10$ and 12, 13, and 15) states of N_2. *J. Chem. Phys.*, 112(10):4621.

[184] Whiting, E. E. (1968). An empirical approximation to the Voigt profile. *J. Quant. Spectrosc. Radiat. Transfer*, 8(6):1379.

[185] Whiting, E. E. and Nicholls, R. W. (1974). Reinvestigation of rotational-line intensity factors in diatomic spectra. *Astrophys. J. Suppl. Ser.*, 27:1.

[186] Yoshino, K. and Freeman, D. E. (1984). High resolution vacuum ultraviolet absorption spectrum of N_2: Perturbations in the $c_5'(0)^1\Sigma_u^+$ and $c_4(0)^1\Pi_u$ Rydberg levels. *Can. J. Phys.*, 62:1478.

[187] Yoshino, K., Smith, P. L., Parkinson, W. H., Thorne, A. P., and Ito, K. (1995). The combination of a VUV Fourier-transform spectrometer and synchrotron radiation. *Rev. Sci. Instrum.*, 66(2):2122.

[188] Yoshino, K. and Tanaka, Y. (1977). High resolution VUV absorption spectrum of N_2, homogeneous perturbations between $c_4'(0)^1\Sigma_u^+$ and $b'(1)^1\Sigma_u^+$. *J. Mol. Spectrosc.*, 66:219.

[189] Yoshino, K., Tanaka, Y., Carroll, P. K., and Mitchell, P. (1975). High resolution absorption spectrum of N_2 in the vacuum-UV region, $o_{3,4}(0)^1\Pi_u \leftarrow X\,^1\Sigma_g^+$ bands. *J. Mol. Spectrosc.*, 54:87.

[190] Zare, R. N., Schmelte, A. L., Harrop, W. J., and Albritto, D. L. (1973). Direct approach for reduction of diatomic spectra to molecular constants for construction of RKR potentials. *J. Mol. Spectrosc.*, 46(1):37.

[191] Zipf, E. C. and McLaughlin, R. W. (1978). Dissociation of nitrogen by electron-impact and by EUV photoabsorption. *Planet. Space Sci.*, 26(5):449.